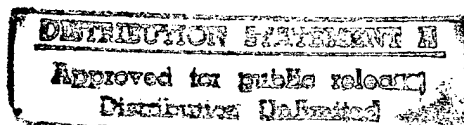# IGARSS'97

1997 International Geoscience and
Remote Sensing Symposium

03-08 August 1997

Singapore International Convention & Exhibition Centre • Singapore

Remote Sensing -- A Scientific Vision for Sustainable Development

19970801 015

Volume III

1997 IEEE INTERNATIONAL GEOSCIENCE AND REMOTE SENSING SYMPOSIUM

Editor: Tammy I. Stein
Production: IEEE Publications

Additional copies of this publication are available from the following source:

IEEE Operations Center
P. O. Box 1331
445 Hoes Lane
Piscataway, NJ 08855-1331 USA

1-800-678-IEEE
1-908-981-1393
1-908-981-9667 (FAX)
833-233 (Telex)
email: customer.services@ieee.org

IGARSS'97

1997 International Geoscience and Remote Sensing Symposium

03-08 August 1997

Sponsors

IEEE Geoscience and Remote Sensing Society

Centre for Remote Imaging, Sensing and Processing
   The National University of Singapore

National Aeronautics and Space Administration (NASA)

National Oceanic and Atmospheric Administration (NOAA)

Office of Naval Research (ONR)

International Union of Radio Science (URSI) ... Technical Sponsor

ORGANIZING COMMITTEE

Hock Lim
General Chairman

Tat Soon Yeo
Janet Nichol
Jian Kang Wu
Dayalan Kasilingam
Technical Co-Chairmen

Leong Keong Kwoh
Finance Chairman

Karen Wong
Publicity Chairman

Choong Weng Mak
Ngi Kun Chng
Exhibits Co-Chairmen

Jonnovan Hong
Chiat Keng Yew
Fen He
*Local Arrangements
Co-Chairmen*

Tammy Stein
*GRSS
Director of Conferences
and Information Services*

TECHNICAL COMMITTEE

Alpers, Werner
Aschbacher, Josef
Bechacq, Yves
Blanchard, Andrew J.
Boerner, Wolfgang-Martin
Cracknell, Arthur
Chan, Philip
Chappelle, Emmett W.
Chen, A.J.
Choi, Soon Dal
Chua, Poh Kian
Chuah, Hean Teik
Cumming, Ian
D'Aranjo, Wesley Gerard
Duchossois, G.
Durana, Jim
Forster, Bruce
Friedman, Ami Ben-Shalom
Fung, Adrian
Gasiewski, Albin J.
Gatlin, James A.
Goodenough, David
Guo, Huadong
Gupta, Avijit
Hallikainen, Martti T.
Hardesty, R. Michael
Ho, Anthony
Hong, Ye
Ishimaru, Akira
Jackson, Thomas J.
Kam, Suan-Pheng
Keydel, Wolfgang
Khazenie, Nahid
Khorram, Siamak
Kong, J.A.
Kuga, Yasuo
Lau, William K.M.
Le Toan, Thuy

Lee, Jong-Sen
Lewis, Anthony J.
Liew, Soo Chin
Lin, I-I
Lu, Yi Hui
Lui, Pao Chuen
Luther, Charles
Mariton, Michel
Massonet, Didier
Milne, Anthony K.
Moon, Wooil M.
Murai, Shunji
Nik Nasruddin Mahmood
Njoku, Eni
Ong, Jin Teong
Pampaloni, Paolo
Prati, C.
Quegan, Shaun
Quek, Gim Pew
Rais, Jacob
Reagan, John
Rees, W.G.
Salomonson, Vincent
Schumann, Robert
Shimoda, Haruhisa
Shu, Peter K.
Sieber, Alois
Singh, Kuldip
Su, Guaning
Takagi, Mikio
Tan, Bernard T.G.
Tilton, James C.
Tomiyasu, Kiyo
Tsang, Leung
Ulaby, Fawwaz
Wiesbeck, Werner
Winebernner, Dale
Zhang, Cheng Bo
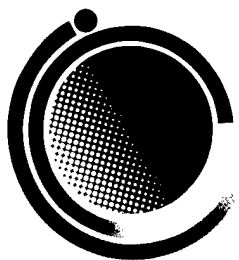
IGARSS'97

1997 International Geoscience and
Remote Sensing Symposium

03-08 August 1997

Table of Contents

"NA" indicates not available at time of printing.

Interactive Area 3: Applications of Remote Sensing

Interactive Area 4: Atmospheric Sounding

"NA" indicates not available at time of printing.

"NA" indicates not available at time of printing.

"NA" indicates not available at time of printing.

Interactive Area 15: Land Cover Applications

"NA" indicates not available at time of printing.

"NA" indicates not available at time of printing.

Interactive Area 19: Remote Sensing Techniques and Instrumentation

"NA" indicates not available at time of printing.

Interactive Area 21: Lidars

Interactive Area 22: SAR Interferometry

Interactive Area 23: SAR Techniques

"NA" indicates not available at time of printing.

"NA" indicates not available at time of printing.

Interactive 33: General Applications

"NA" indicates not available at time of printing.

"NA" indicates not available at time of printing.

"NA" indicates not available at time of printing.

"NA" indicates not available at time of printing.

"NA" indicates not available at time of printing.

"NA" indicates not available at time of printing.

"NA" indicates not available at time of printing.

C10: Monitoring Crops and Forests

"NA" indicates not available at time of printing.

D09: Surface Temperature: Observations and Applications

D09.01 Instrumentation for Land Surface Temperature Measurements   NA

Kahle, A.B.

D09.02 Temperature and Emissivity Separation from Advanced Spaceborne Thermal Emission and Reflection   NA
Radiometer (ASTER) Images

Gillespie, A.

D09.03 Application of the TES Algorithm to TIMS Data Aquired in HAPEX-Sahel   1233

Schmugge, T., S. Hook and C. Coll

D09.04 Hyperspectral TIR Remote Sensing of Fans and Bedrock Near Yuma, Arizona, USA   NA

Gillespie, A.

D09.05 Potential Interest of a Combined Use of MODIS and ASTER Data for the Determination of Surface   NA
Temperature and Emissivity

Becker, F., and Z.L. Li

D09.06 Lithologic Mapping in the Iron Hill, Colorado, USA Area Using Airborne Multispectral Thermal-Infrared   NA
Data and Simulated Advanced Spaceborne Thermal Emission and Reflection Radiometer (ASTER) Data

Rowan, L.C., and K. Watson

D09.07 An Overview of Volcanological Application of Infrared Remote Sensing   NA

Realmuto, V.J.

D09.08 ASTER Observations for the Monitoring of Land Surface Fluxes   1236

Schmugge, T.

D09.09 Application of High Resolution Side-Looking MSS Data to Heat Island Potential in Urban Area   1239

Hoyano, A., and A. Iino

D10: Data Standards and Distributions

D10.01 Derivative Analysis of Hyperspectral Data for Detecting Spectral Features   1243

Tsai, F., and W. Philpot

D10.02 Reading SAR Data: A New General Reader and a Proposed New Standard   1246

Pierce, L.

D10.03 Operational Performance of Radarsat's Canadian Data Processing Facility   NA

Jefferies, W.C., D.J. Wilson and R. Periard

D10.04 Standard Data Products form the MODIS Science Team   1249

Fishtahler, L.E.

D10.05 Intelligent Guide to Earth Observation - IGEOS   NA

Zingler, M.

D10.06 Towards a Common Language in Satellite Data Management: A New Processing Level Nomenclature   1252

Gutman, G., and A. Ignatov

D10.07 Innovations in Response to Floods of Data   1255

Ziskin, D.C., and P. Chan

D10.08 A Catalog-Browse System with Quick-Look Images for SPOT, ERS and RADARSAT Data Archives   1257

Kwoh, L.K.

"NA" indicates not available at time of printing.

"NA" indicates not available at time of printing.

E07: Terrain Scattering Models and Their Applications

E08: Advance Sensors and Sensor Calibration I

"NA" indicates not available at time of printing.

———————————— IGARSS'97 DIGEST VOLUME IV ————————————

F01: Global Monitoring and Remote Sensing for Climate Studies

F02: Clouds and Precipitation II

F04: Data Processing

F05: Remote Sensing of the Ocean by Radar Techniques

"NA" indicates not available at time of printing.

"NA" indicates not available at time of printing.

G05: Sea Surface Modelling

G06: SAR Intereferometry: Simulation and Noise Reduction

G07: Ecosystem Studies with Microwave Remote Sensing

G08: Remote Sensing of Clouds and Aerosols

"NA" indicates not available at time of printing.

"NA" indicates not available at time of printing.

"NA" indicates not available at time of printing.

H06: Application of SAR/INSAR in Forestry

H07: Atmospheric Radiation

H08: Advance Sensors and Sensor Calibration II

H09: Aerosols

"NA" indicates not available at time of printing.

H10: Weather Information Systems & Data Analysis Methods

I01: Soil and Vegetation Process Model

I02: Atmospheric Processing and Dynamics

I02.01 Examining the Influences of Water Vapor Profile on the SSM/I - Derived Column Water Vapor Over the Global Oceans   NA

Sohn, B.J.

I02.02 Simulataneous Measurements of Water Vapor Profiles from Airborne MIR and LASE   1969
Wang, J.R., P. Racette, M.E. Triesky, E.V. Browell, S. Ismail and L.A. Chang

I02.03 Volume Imaging Radar Observations of Atmospheric Boundary Layer Turbulence with Large Eddy Simulations   1972
Pollard, B.D., S.J. Frasier and R.E. McIntosh

I02.04 BIAS: A Straightforward Algorithm for the Retrieval of Tracegas Vertical Columns from Near Infra-Red Earthshine Measurements by the SCIAMACHY Remote Sensing Spectrometer   NA
Spurr, R.J.D.

I02.05 A Tomographic Infrared System for Monitoring Atmospheric Pollution in Urban Areas   1975
Giuli, D., F. Cuccoli, L. Facheris, and S. Tanelli

I02.06 Data Analysis of Lidar Measurements of Atmospheric Boundary Layer Aerosols from a Black Hawk Helicopter   NA
Karl, Jr., R.R., W.K. Grace, JR. Busse, J.G. Sutton, N.A. Kurnit, A. Koskelo,
O.G. Peterson and W.S. Huntgate

I02.07 A Study of Gravity Waves in the Atmospheric Boundary Layer Using Sodar and Microbarograph   NA
Reddy, K.K., and D.N. Rao

I02.08 Aerosol Atmospheric Pollution in Some Industrial Cities of Former Soviet Union   NA
Gorbarenko, E.V.

I03: Remote Sensing Research in China

I03.01 Remote Sensing in China: Techniques and Applications   1978
Huadong, G.

I03.02 Several Airborne Imaging Spectrometers Developed in China   NA
Wang, J., and Y. Xue

I03.03 Data Fusion of China Advanced Microwave Remote Sensor   1981
Zhang, X., and J. Jiang

I03.04 Research and Development on Synthetic Aperture Radar System in China   1984
Zhu, M.H.

I03.05 A New Airborne Remote Sensing Platform for Generating Geocoding Image Without Ground Control Point   1987
Li, S., Y. Xue and Z. Liu

I03.06 Short-Term and Imminent Earthquake Prediction and Satellite Remote Sensing Thermal Infrared Technology   NA
Zuji, Q., D. Changgong and L. Linzhi

I03.07 The Development of China's Meteorological Satellite and Satellite Meteorology   NA
Fang, Z., J. Xu and L. Guo

I03.08 GIS Development and Application in China   NA
Zhou, C.

"NA" indicates not available at time of printing.

I03.09 Mission Analysis of the China - Brazil Earth Resources Satellite (CBERS)   NA

Yiyuan, C.

I04: Data Compressson Techniques and Visualization

I04.01 Reversible Compression of Multispectral Imagery Based on an Enhanced Inter-Band JPEG Prediction   1990

Aiazzi, B., P.S. Alba, L. Alparone and S. Baronti

I04.02 A DCT-Based Adaptive Compression Algorithm Customized for Radar Imagery   1993

Andreadis, A., G. Benelli, A. Garzelli and S. Susini

I04.03 SPOT Image Compression Using Block Truncation Coding Techniques   1996

Ma, K.K., L. Huang, S. Zhu and A.T.S. Ho

I04.04 Effects on Image Quality for MPEG Video Over Satellite Channel   NA

Liren, Z.

I04.05 Lossless Compression of Satellite Images Using Nueral Network & Arithmetic Coding   NA

Yann, S.I., Y.C. Kiat and H.Y. Yi

I04.06 Construction of Multi-Resolution Terrain Models Using Hierarchical Delaunay Triangulated Irregular   1999
Networks

Huang, S.J., and D.C. Tseng

I04.07 Raw Data Compressing Technology Study in Spaceborne SAR   NA

Ru-liang, Y., and W.Y. Bai ping

I05: Sea Surface Temperature and Its Validation

I05.01 Wind Speed Forcing of the Bulk-Skin Sea Surface Temperature Difference as a Function of Wind Speed and   2002
Heat Flux

Emery, W.J., and C.J. Donlon

I05.02 Characteristics of the AVHRR-Derived Sea Surface Temperature in the Oceans Around Japan   2005

Kawamura, H., and Y. Kawai

I05.03 Global and Regional Pathfinder SST Fields: Characterization and Validation   2008

Casey, K., P. Cornillon, R. Evans and G. Podesta

I05.04 Spatial and Temporal Variability of Sea Surface Temperature in the Seas Around Korea Using Satellite Data   NA
(NOAA/AVHRR)

Park, K.A., and J.Y. Chung

I05.05 The Detection of the Diurnal Variation of SST by GOES   NA

Wu, X.Q.

I05.06 Investigation of Large-Scale Oceanographic Phenomena Using Data from ATSR on ERS-1 and Other   NA
Satellite Sensors

Llewellyn-Jones, D.T., S.P. Lawrence, Y. Xue and C.T. Mutlow

I05.07 The Retrieval and Validation of Ocean Color Products   NA

Lynch, M.

"NA" indicates not available at time of printing.

"NA" indicates not available at time of printing.

Soil Moisture Estimation under Sparse Vegetation Using Microwave radiometry at C-Band.

A. Chanzy (1), Y. Kerr (2), J.P. Wigneron (3) and J.-C. Calvet (4).

1) Corresponding author, INRA, unité de Science du sol, 84914 Avignon Cédex 9, France.
Tel: 04 90 31 61 29, Fax: 04 90 31 62 44, E-mail: achanzy@avignon.inra.fr
2) CESBIO, 18 Av. E. Belin, 31401 Touloulouse Cédex 4, France.
3) INRA, Unité de bioclimatologie, 84914 Avignon Cédex 9
4) J.-C. Calvet, Météo-France, CNRM, 42 Av. G Coriolis, 31057 Toulouse Cédex.

Abstract --The space borne microwave radiometer will have a lowest frequency in the C-band. We have to prepare the use of this band to estimate the soil moisture. This paper consider the case of sparsely vegetated areas encountered in semi-arid area. This paper is based on the HAPEX-Sahel data set. We show that the single scattering albedo could be neglected at C-band when the amount of vegetation is low. The vegetation transmission coefficient can be estimated from the polarization difference at 5.05 GHz and an angle of incidence of 45°. However the obtained relationship needs to be tested in various wetness conditions.

INTRODUCTION

It has been shown that the L band allows straight forward estimation of soil moisture on sparsely covered vegetation as the Sahelian Savannah or semi arid areas [1-2]. However, in a near future, spaceborne microwave radiometers will be operated with a lowest frequency located in the C-band. Therefore, it is important to prepare the use of the C band results for soil surface moisture assessment. Results obtained during the Hapex Sahel [1] experiment have shown that the vegetation influence should be accounted for to estimate the soil moisture accurately, even when the amounts of vegetation are low. The vegetation in the HAPEX-Sahel area was very complex to describe and the quantification of vegetation parameters as the Leaf Area Index or the vegetation water content was almost impossible to characterize in situ at the scale of microwave radiometer pixels. Therefore we chose to derive vegetation information from remotely sensed observation using the different configurations of the microwave radiometers involved in the experiment and the SPOT images collected during the airborne campaign. The aim of the presented study was to characterize the vegetation transmission coefficient (γ) and the single scattering albedo (ω) of the vegetation which are related to the brightness temperature (T_B) [3]:

$$T_{Bp} = (1 + \gamma \Gamma_p)(1 - \gamma)(1 - \omega)T_v + (1 - \Gamma_p)\gamma T_s \quad (1)$$

where p denotes the polarization, T_v and T_s are the vegetation and the soil temperature and Γ is the soil reflectivity. In order to extent the data set obtained during the Hapex Sahel experiment, we also used the data collected in the Avignon 93 experiment [4] over a sparse sorghum field which was sowed to reproduce a "Sahelian field".

MATERIEL AND METHOD

The HAPEX-Sahel and the Avignon 93 experiments were described in [1] and [4], respectively. It is important to note that the radiometric measurement were acquired by the French PORTOS CNES radiometer for both experiments. PORTOS is a multifrequency (1.4, 5.05, 10.65, 23.8, 36.5 and 90 GHz) and dual-polarized radiometer. The radiometer can be operated at different angles of incidence. The PORTOS radiometer was installed aboard the ARAT aircraft during HAPEX-Sahel experiment whereas it was mounted under a crane boom during the Avignon 93 experiment. As the PORTOS 1.4 GHz channel could not be operated with the airborne mode, we used the measurements collected by the Push Broom Microwave Radiometer (PBMR) which flew together with PORTOS at 3 dates.

To compute γ and ω at C-band, we estimated the Γ from the soil moisture in the top five millimeters of the soil [5]. The soil moisture (θ_s) is derived from the $T_B = f(\theta_s)$ relationship obtained at L-Band. Such a procedure was only applied when the soil footprints of the PBMR and PORTOS is located at same place with a tolerance of 50 m. A correction was done to account for the difference in penetration depth between the C and the L bands. We assumed that the soil and vegetation temperature were equal to the skin temperature measured by a thermal infrared thermometer.

RESULTS

Since the L-band was used to estimate the soil moisture, we have displayed in Figure 1 the $T_B = f(\theta_s)$ relationship at L band. The symbols corresponds to the

Avignon 93 data collected with PORTOS, whereas the lines are the regression lines computed with the PBMR measurements collected during the HAPEX-Sahel [1] and the Walnut Gulch experiments [2]. The Figures show that the vegetation does not influence the measurements when the amount of vegetation remains small (Vegetation water content {Wc} < 0.225 kg/m²). Moreover, Figure 1 shows that the data collected in three different areas in the world fall within a similar relationship. These results demonstrate the usefulness of the L-band which allows a straight forward estimation of the soil moisture over semi-arid areas. The relationships displayed in Figure 1 were then used to compute the soil moisture and the soil reflectivity.

In Table 1, we report the results of the transmission coefficient computed from the HAPEX-Sahel Data. γ was computed by inverting Equation 1 for different values of ω. ω influences significantly the γ results. γ can be related to Wc by the relationship [6-7] :

$$Wc=Log(\gamma)*cos(I)/b \qquad (2)$$

where I is angle of incidence and b an empirical parameter which depends on the frequency and the vegetation type. From the Avignon 93 data, Haboudane et al. [7] have found b=0.4 m²kg⁻¹. The most realistic value of Wc obtained from Eq. 2 were those computed with ω=0. This invite us to neglect the single scattering albedo. The γ values obtained for day 246 are significantly higher than those obtained for the day 239 which was wetter. Although we were in the middle of the rainy season, the vegetation growth can not explain the increase rate of γ. The instability in γ is likely the consequences of error propagation (error in T_B, error in soil moisture) which is more sensitive in dry condition, when the soil and the vegetation emissivities are similar.

In Figure 2, we have plotted the relationship between γ and different radiometric indices for the day 239. The Figures 2-abc show clearly that a polarization combination at 5.05 GHz offers the best correlation with γ while results obtained with the NDVI or with the microwave radiometer at 36.5 GHz are disappointing. The relationship between the polarization difference at 5.05 GHz and γ is however established for one day with a soil moisture varying from 0.10 to 0.15 m³/m³. We have now to analyze in which proportion this relationship varies with the soil wetness conditions. In figure 3, we have inverted the Equation 1 to retrieve the soil moisture. The inversion was performed with ω=0 and γ=f$(T_{Bv}-T_{BH})_{5.05}$ where f is the regression line through the Figure 2 scatter plot. The results of the inversion is encouraging.

CONCLUSIONS

This paper is devoted to the estimation of the vegetation properties for microwave emission and propagation in case of sparsely vegetated fields. It appears that the vegetation is mainly involved in the surface emission process at C-band through its transmission coefficient. This coefficient is clearly related to the polarization difference at 5.05 GHz. However this relationship have to be tested under various wetness conditions.

REFERENCES

[1] A. Chanzy, T.J. Schmugge, J.-C. Calvet, Y. Kerr; P. Van Oevelen, O. Grosjean and J.R. Wang, "Airborne microwave radiometry on a semi-arid area during Hapex-Sahel", J. Hydrology, in press, 1997

[2] T.J. Schmugge, T. Jackson, W.P. Kustas, R. Roberts, P. Parry, D. Goodrich, S. Amer, and Weltz, M.A., " PBMR observations of surface soil moisture in Monsoon 90", Water Resour. Res., 30, 1321-1327, 1994.

[3] D.R. Brunfeldt, and F.T. Ulaby, " Microwave emission from row crops" IEEE Transactions Geosci. Remote Sens., GE 24, Vol 3, 353-359, 1986.

[4] A. Chanzy , D. Haboudane, J.-P. Wigneron, J.-C. Calvet, and O. Grosjean, "Radiométrie micro-onde sur divers types de couverts végétaux : influence de l'humidité du sol", Colloque International ISPRS 'Mesures physiques et signatures en télédétection, Val d'Isère (FRA), 1994/01/17-21, pp 505-512, 1994.

[5] Suresh Raju, A. Chanzy, J.-P. Wigneron, J.-C. Calvet, Y. Kerr, and L. Laguerre, "Soil moisture and teperature profile effects on microwave emission at low frequencies", Remote Sens. Environ., 54: 85-97, 1995

[6] T.J. Jackson, and T.J. Schmugge, "Vegetation effects on the microwave emission of soils", Remote Sensing of Environ., 36: 203-212, 1991.

[7] D. Haboudane, A. Chanzy, J.-C. Calvet, J.-P. Wigneron, and F. Bonn, "Radiométrie Micro-onde dans le cas des couverts végétaux partiels : estimation de la teneur en eau du sol", Canadian J. of Remote Sens., vol 22, no 2, 208-217, 1996.

ACKNOWLEDGEMENT

TABLE 1 : Transmission coefficient at 5.05 GHz, H polarization and a 45° incidence angle. Data were collected during the HAPEX Sahel experiment

DOY	ω	γ_{min}	γ_{max}	Wc (γ_{min}) (Kg/m2)	Wc (γ_{max}) (Kg/m2)
239	0	0.76	0.95	0.48	0.08
239	0.02	0.7	0.93	0.62	0.13
239	0.05	0.61	0.84	0.87	0.31
239	0.1	0.41	0.71	1.56	0.61
246	0	0.57	0.85	0.98	0.28
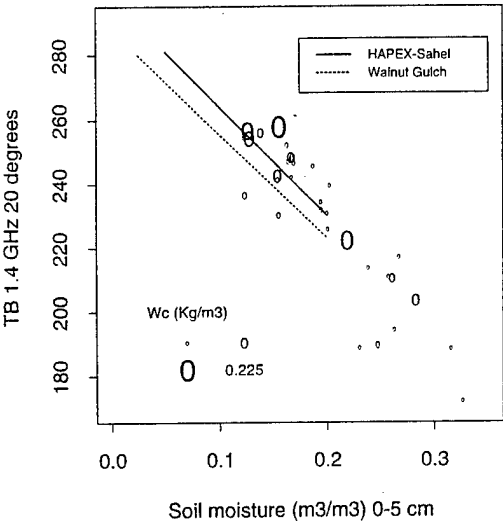
Figure 1 : T_B versus soil moisture. Avignon 93 experiment (sparse sorghum Field
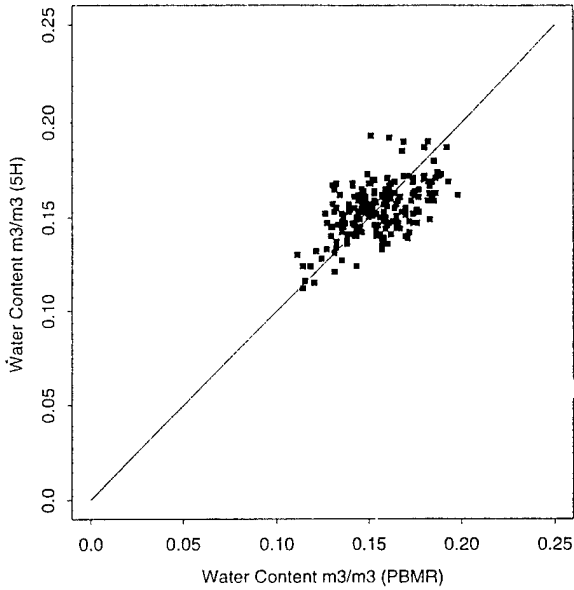
Figure 3 : Comparison of the soil moisture retreived from microwave observations at 5.05 GHz, 45° and H polarization and soil moisture derived from the L band PBMR radiometer.
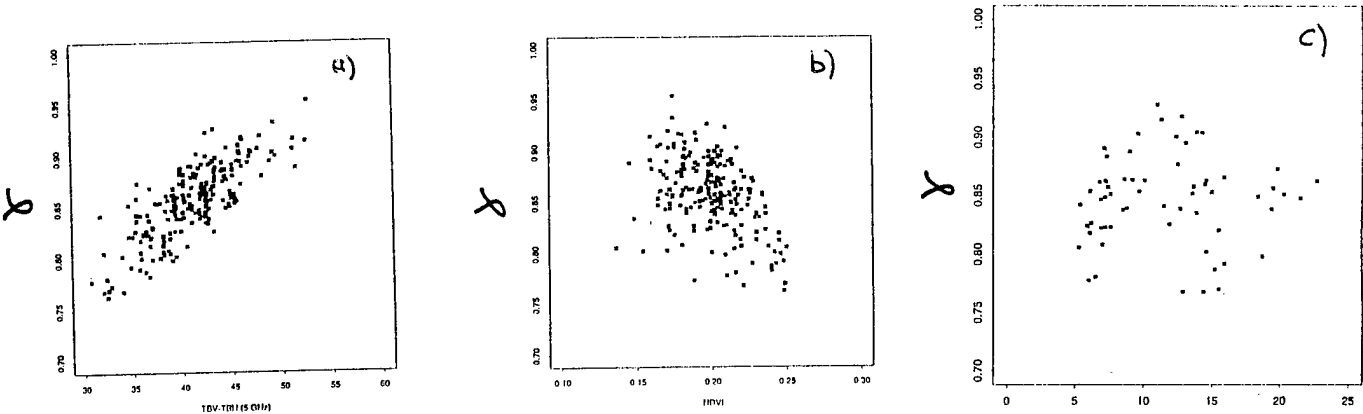
Figure 2 : Vegetation transmission coefficients versus a) (T_{BV}-T_{BH}) at 5.05 GHz; b) NDVI, c) (T_{BV}-T_{BH}) at 36.5 GHz

Microwave Remote Sensing of Soil Moisture for Estimation of Soil Properties

Nandish M. Mattikalli[*], and Edwin T. Engman
NASA Goddard Space Flight Center, Laboratory for Hydrospheric Processes
Hydrological Sciences Branch, Code 974 ([*]Hughes STX/Code 974)
Greenbelt, MD 20771, USA
Tel: (301) 286-7696 Fax: (301) 286-1758 E-mail: nandish@hydro5.gsfc.nasa.gov

Thomas J. Jackson
USDA Agricultural Research Service, Hydrology Laboratory
Beltsville, MD 20705, USA

Abstract -- Surface soil moisture dynamics was derived using microwave remote sensing, and employed to estimate soil physical and hydraulic properties. The L-band ESTAR radiometer was employed in an airborne campaign over the Little Washita watershed, Oklahoma during June 10-18, 1992. Brightness temperature (TB) data were employed in a soil moisture inversion algorithm which corrected for vegetation and soil effects. Analyses of spatial TB and soil moisture dynamics during the dry-down period revealed a direct relationship between changes in TB, soil moisture and soil texture. Extensive regression analyses were carried out which yielded statistically significant quantitative relationships between ratio of percent sand to percent clay (RSC, a term derived to quantify soil texture) and saturated hydraulic conductivity (Ksat) in terms of change components of TB and surface soil moisture. Validation of results indicated that both RSC and Ksat can be estimated with reasonable accuracy. These findings have potential applications for deriving spatial distributions of RSC and Ksat over large areas.

INTRODUCTION

Surface soil moisture is of great significance to hydrologic research for partitioning rainfall into runoff and infiltration. Soil properties such as soil texture and saturated hydraulic conductivity (Ksat) play a key role in the drainage and redistribution of soil moisture, but these properties are difficult to obtain in the field and/or laboratory. Therefore, methods based on remote sensing will have capabilities of deriving spatial distribution of Ksat. Earlier studies have employed brightness temperature (TB) data obtained from passive remote sensing and soil hydrology models for estimation of soil hydraulic parameters [1, 2]. Such approaches require information on several hydrologic and meteorological parameters, and therefore might not be ideally suited for application to large areas.

Reference [3] established highly significant relationships between changes in moisture content of the surface soil, 2 days after a thorough wetting, and average Ksat of the soil profile. The log-log transformations of an effective profile-average Ksat and the initial two-day drainage of the soil were valuable to obtain estimates of an average Ksat. These findings have a potential to obtain quick estimates of the spatial distribution of Ksat from the soil moisture contents if microwave remote sensing observations are made at two day temporal resolution after saturation [4]. The objective of the present study was to test the approach of [3] for the field conditions of a medium-sized watershed, and to evaluate if soil physical properties (viz. soil texture and Ksat) can be estimated from the temporal variability of microwave remotely sensed TB and soil moisture data.

MATERIALS AND METHODS

The Washita'92 research experiment was carried out during June 10-18, 1992 in the Little Washita watershed, Oklahoma. The climate of Little Washita region is moist and sub-humid with an average annual rainfall of about 750 mm [5]. During the experiment, land cover in the Little Washita watershed was dominated by pasture and senesced or harvested winter wheat with some other agricultural crops including corn and alfalfa [5]. Forest cover within the watershed is very sparse and constitutes a small proportion of the watershed.

Multitemporal airborne microwave data were collected using the L band (21 cm wavelength, or 1.4 GHz frequency) synthetic aperture Electronically Steered Thinned Array Radiometer (ESTAR) [6]. A large number of ground soil moisture measurements were carried out to support and validate microwave remotely sensed data. The study area experienced heavy rainfall (more than 30 mm) on June 5, 1992, and the rainfall continued till June 9, 1992. However, there was no rainfall in the watershed for the entire duration of the Washita'92 experiment [7]. Therefore, the hydrologic conditions in the watershed were ideal to follow a drying period from very wet (about 30%) to dry (about 10%) over a period of nine days.

Temporal soil moisture information was derived from the ESTAR TB images. The soil moisture retrieval algorithm corrects thermal emission records for vegetation cover and surface roughness, and estimates the real part of the soil dielectric constant based on the Fresnel assumptions [7]. Soil texture effects were corrected before inverting a dielectric mixing model for soil moisture determination. Vegetation parameters (i.e., type and water content) and soil texture data were derived from land-use data base and soils map, respectively. The ESTAR derived soil moisture values were validated by comparing them with the field measured soil moisture values, and the standard error of estimates were within 3.5% for the bare fields and 5.7% for the vegetated

fields for all days during the experiment [7].

Over a large corn field, which represented the densest vegetation cover encountered during the experiment (canopy height of 2.1 m; canopy water content of 4.05 kg/m^2), a match of predicted to measured soil moisture was excellent, with an average absolute error of less than 1.5% [8].

A change analysis was carried out using multitemporal TB and soil moisture data [9]. Georegistered data layers were employed in overlay and difference operations to quantify the changes. Change analysis was carried out for each soil texture class and eight temporal resolutions. To establish quantitative relationships between soil texture and temporal changes in TB and surface soil moisture, the ratio of percent sand to percent clay (RSC) has been computed. RSC was chosen because it numerically indicates soil texture such that an assumed value of 100 represents sand (although its theoretical value reaches ∞ for sand), and its decreasing values indicate higher clay contents. Percent sand and percent clay values were obtained from field measurements and data assembled in [10]. Validation of the statistical relationships was carried out by comparing predicted RSC and Ksat with those measured in the laboratory and also extracted from soil texture map for sites not incorporated in the development of relationships.

RESULTS

A comparative study of TB and soil moisture images with soil texture map clearly suggested that temporal variation of both TB and soil moisture was closely related to soil texture. This supports the hypothesis that remotely sensed TB and soil moisture and associated temporal changes can be employed to identify soil types and can be related to Ksat.

Relationships with soil texture

RSC holds a strong negative log-normal relationship with multitemporal changes in both TB and surface soil moisture (Table 1). Regression relationships are characterized by $r^2 >$ 0.6 for four temporal resolutions in the case of TB and for all temporal resolutions in the case of soil moisture (probably because soil moisture retrieval algorithm uses soil texture as input). Table 3 presents correlation coefficients of predicted and measured RSC values for various temporal resolutions. It is evident that the relationships yield RSC values close to the measured values although some deviations exist in the predictions. This suggests that RSC and hence the soil texture can be estimated with reasonable accuracy. Selection of a particular relationship is subject to the temporal data availability.

Relationships with Ksat

Regression analysis was carried out to establish relationships between Ksat and multitemporal changes in TB and surface soil moisture (Table 2). Evidently, Ksat also bears a negative log-normal relationship with changes of both TB and surface soil moisture. Similar to RSC, relationships for Ksat are characterized by $r^2 > 0.6$ in the case of 1-, 4-, 5- and 6-days resolution for TB change, and for all temporal

resolutions in the case of soil moisture change. Values of r^2 consistently greater than 0.8 suggest that temporal changes in soil moisture can be employed to estimate Ksat with reasonable accuracy. Validation of the relationships suggested (Table 3), despite minor errors in some cases, the relationships yielded acceptable Ksat values. Regression equations presented in Table 2 are invaluable for the quick estimation of Ksat using temporal remotely sensed TB and soil moisture data.

SUMMARY

Microwave remote sensing was employed to obtain spatial and multitemporal soil moisture data for the Little Washita watershed, OK. As part of the Washita'92 airborne campaign during June 10-18, 1992, the ESTAR instrument was flown each day to acquire TB data at a spatial resolution of 200 m, which were converted into soil moisture information. Data sets were georeferenced to monitor spatial and temporal variability of both TB and surface soil moisture.

Analysis of multitemporal TB and soil moisture maps with soils map suggested that remotely sensed TB and soil moisture and their associated changes could be employed to identify soil type and to estimate soil hydraulic properties. It was observed that temporal changes of TB and surface soil moisture held statistically significant negative log-normal relationships with RSC and Ksat, and validations of these relationships suggested that both soil properties could be estimated with acceptable accuracy. Quantitative regression relationships are invaluable to determine spatial distribution of Ksat which is typically not measured in the field. Further, such relationships can be used to indicate soil properties (percent sand and percent clay) from observed changes in remotely sensed TB and soil moisture patterns. These findings have significant long term potential of employing space borne microwave remotely sensed observations for identification of soil texture and derivation of soil physical properties over large spatial scales.

REFERENCES

[1] Camillo, P. J., O'Neill, P. E., and Gurney, R. J. (1986). Estimating soil hydraulic parameters using passive microwave data. IEEE Transactions on Geoscience and Remote Sensing, GE-24, 930-936.

[2] van de Griend, A. A. & O'Neill, P. E. (1986). Discrimination of soil hydraulic properties by combining thermal infrared and microwave remote sensing. Proc. IGARSS'86 Symp., 839-845.

[3] Ahuja, L. R., Wendroth, O., and Nielsen, D. R. (1993). Relationship between initial drainage of surface soil and average profile saturated conductivity. Soil Science Society America Journal, 57, 19-25.

[4] Mattikalli, N. M., Engman, E. T., Ahuja, L. R. & Jackson, T. J. (1995a). Estimating soil properties from microwave remote sensing of soil moisture. Proc. SPIE vol. 2585, 89-101.

Table 1: Relationships between RSC and mean temporal changes of TB and soil water content.

| Period of Change (days) | Estimation of RSC | | | | |
	From TB	r^2	From soil water content (SM)	r^2
1	$RSC = 1.3025 \times 10^{41} \times TB^{-45.81}$	0.95	$RSC = 5.5325 \times 10^5 \times SM^{-11.36}$	0.89
2	$RSC = 1.8563 \times 10^{25} \times TB^{-23.95}$	0.29	$RSC = 2.3374 \times 10^7 \times SM^{-11.39}$	0.76
3	$RSC = 2.2083 \times 10^{18} \times TB^{-16.64}$	0.45	$RSC = 2.1679 \times 10^6 \times SM^{-9.29}$	0.87
4	$RSC = 5.6156 \times 10^{17} \times TB^{-14.67}$	0.86	$RSC = 9.9705 \times 10^6 \times SM^{-8.84}$	0.90
5	$RSC = 2.2211 \times 10^{16} \times TB^{-12.98}$	0.83	$RSC = 1.1650 \times 10^7 \times SM^{-8.45}$	0.86
6	$RSC = 1.0450 \times 10^{17} \times TB^{-12.51}$	0.70	$RSC = 8.1714 \times 10^7 \times SM^{-8.46}$	0.86
7	$RSC = 1.0819 \times 10^{18} \times TB^{-12.46}$	0.40	$RSC = 8.4541 \times 10^8 \times SM^{-8.76}$	0.80
8	$RSC = 8.0543 \times 10^{20} \times TB^{-13.46}$	0.49	$RSC = 1.5315 \times 10^{10} \times SM^{-9.02}$	0.83

Table 2: Relationships between Ksat and mean temporal changes of TB and soil water content.

| Period of Change (days) | Estimation of Ksat | | | | |
	From TB	r^2	From soil water content (SM)	r^2
1	$Ksat = 1.1795 \times 10^{35} \times TB^{-39.45}$	0.94	$Ksat = 3.7860 \times 10^4 \times SM^{-9.69}$	0.86
2	$Ksat = 6.9265 \times 10^{23} \times TB^{-22.98}$	0.29	$Ksat = 3.0690 \times 10^6 \times SM^{-10.61}$	0.83
3	$Ksat = 1.9351 \times 10^{16} \times TB^{-15.10}$	0.40	$Ksat = 2.6070 \times 10^5 \times SM^{-8.48}$	0.91
4	$Ksat = 1.5414 \times 10^{15} \times TB^{-12.84}$	0.84	$Ksat = 7.7820 \times 10^5 \times SM^{-7.9}$	0.92
5	$Ksat = 9.1992 \times 10^{13} \times TB^{-11.36}$	0.85	$Ksat = 9.5030 \times 10^5 \times SM^{-7.58}$	0.90
6	$Ksat = 6.7263 \times 10^{14} \times TB^{-11.16}$	0.69	$Ksat = 6.2090 \times 10^6 \times SM^{-7.65}$	0.88
7	$Ksat = 1.0303 \times 10^{16} \times TB^{-11.31}$	0.41	$Ksat = 6.4010 \times 10^7 \times SM^{-8.02}$	0.83
8	$Ksat = 4.8968 \times 10^{18} \times TB^{-12.27}$	0.50	$Ksat = 9.3832 \times 10^8 \times SM^{-8.27}$	0.85

Table 3: Comparison between measured and estimated RSC and Ksat values from temporal changes of TB and soil water content (SM). Measured RSC and Ksat values were derived from laboratory experiment, soil texture map, and from data compiled in [10].

| Period of of Change (days) | No. of data points | r^2 between measured and estimated | | | |
| | | RSC from | | Ksat from | |
		TB	SM	TB	SM
1	36	0.96	0.98	0.96	0.98
2	30	0.77	0.90	0.77	0.92
3	24	0.88	0.98	0.90	0.96
4	24	0.96	0.98	0.98	0.98
5	18	0.98	0.98	0.98	0.98
6	18	0.98	0.96	0.96	0.96
7	12	0.90	0.98	0.94	0.96
8	6	0.98	0.98	0.96	0.98

[5] Allen, P. B., and Naney, J. W. (1991). Hydrology of the Little Washita River watershed, Oklahoma: data and analysis. USDA/ARS-90, 74 pages.

[6] Jackson, T. J. & Schiebe, F. R. (eds.) (1993). Hydrology data report: Washita'92. USDA-Agri. Res.Service, Nat. Agri. Water Quality Lab., NAWQL 93-1, Durant, OK.

[7] Jackson, T. J., Le Vine, D. M., Swift, C. T., Schmugge, T. J. & Schiebe, F. R. (1995). Large area mapping of soil moisture using the ESTAR passive microwave radiometer in Washita'92. Rem. Sens. Environ., 53, 27-37.

[8] O'Neill, P. E., Chauhan, N. S., Jackson, T. J., Le Vine, D. M. & Lang, R. H. (1994). Microwave soil moisture prediction through corn in Washita'92. Proc. IGARSS'94 Symp., 1585-1587.

[9] Mattikalli, N. M., Engman, E. T., Jackson, T. J. & Ahuja, L. R. (1996). Microwave remote sensing of temporal variations of surface soil moisture during Washita'92, and its application to the estimation of soil physical properties. Submitted to Water Resou. Research.

[10] Rawls, W. J. & Brakensiek, D. L. (1982). Estimating soil water retention from soil properties. Journal of the Irri. & Drain. Division, ASCE, 108, 166-171.

RETRIEVAL OF SOIL MOISTURE USING A DYNAMIC LEARNING NEURAL NETWORK TRAINED WITH A 1-DIMENSIONAL HYDROLOGY/RADIOBRIGHTNESS MODEL *

Yuei-An Liou[1], Y. C. Tzeng[1], and A. W. England[2]

1. Center for Space and Remote Sensing Research
National Central University, Chung-Li, Taiwan
Tel: +886-3-4227151 7631, Fax: +886-3-4254908, yueian@csrsr.ncu.edu.tw
2. Department of Electrical Engineering and Computer Science
The University of Michigan, Ann Arbor, Michigan 48109-2122, USA

ABSTRACT

We present a retrieval approach that uses satellite radiobrightness to infer surface parameters of prairie grassland based on a Dynamic Learning Neural Network (DLNN) trained with a 1-dimensional Hydrology/Radiobrightness (1dH/R) model. The parameters of interest include the temperatures and moisture contents of the soil and canopy. To evaluate the feasibility of the retrieval approach, we conduct two case studies. The first study is based on products from the 1dH/R model that are used for the model validation. The second study is based on results from a 60-day summer dry-down run of the 1dH/R model with a vegetation coverage of 100 %. In each case, we utilize about 95 % of the 1dH/R model predictions to train the DLNN and the rest of the predictions are used to evaluate the DLNN retrievals. The training data include horizontally- and vertically-polarized brightnesses at 1.4, 19, and 37 GHz, and the corresponding temperatures and moisture contents of the soil and canopy. In the first study, we find that differences between DLNN retrievals and desired quantities (1dH/R model products) are less than 0.1 Kelvin for the canopy temperature, 1.2 Kelvins for the soil temperature (uppermost 5 mm), 0.0001 kg/m^2 for the canopy water content, and 1.2 % for the soil moisture content (by volume). In the second study, the corresponding differences are smaller as expected.

INTRODUCTION

Land-air exchanges of moisture and energy are important boundary forcings of the atmospheric circulation models. These exchanges are governed by surface parameters, such as temperatures and water contents of the soil and canopy [1, 2]. Microwave emission is sensitive to temperature and moisture so that radiometry is useful in monitoring these parameters. Since microwave emission is non-linear dependent on the temperature and moisture, it is extremely difficult to retrieve the parameters by biophysically-based models without considerably-simplified approximations on the relation between measured quantities (e.g., radiobrightness) and desired variables (e.g., surface parameters)

In this paper, we examine a scheme that utilizes satellite radiobrightness to infer surface parameters without losing the nonlinearity between the measured quantities and desired variables. Our approach is to incorporate products from the 1dH/R model into the DLNN where the 1dH/R model describes the nonlinearity and the DLNN manages the nonlinear mappings.

THE 1dH/R MODEL

The 1dH/R model consists of two modules, a 1dH module and an R module. It has been developed for years ([3]-[6]). A series of Radiobrightness Energy Balance Experiments has been conducted to validate the model [7]. The 1dH module that treats energy and moisture exchanges between the land and atmosphere computes temperature and moisture profiles of the soil and canopy. The R module manages radiative transfer within canopy, and absorption from the canopy to estimate microwave emission.

Energy and moisture transfer in soil and canopy involves solving the 1-dimensional form of the coupled equations

$$\frac{\partial X_{m,k}}{\partial t} = -\nabla \cdot \vec{Q}_{m,k} \tag{1}$$

$$\frac{\partial X_{h,k}}{\partial t} = -\nabla \cdot \vec{Q}_{h,k}, \tag{2}$$

where the subscript k represents the soil or canopy, X_m is the total water mass per unit volume, kg/m^3, X_h is the total heat content per unit volume, J/m^3, t is the time, s, $\vec{Q}_m$ is the vector moisture (vapor and liquid) flux density, kg/m^2-s, and $\vec{Q}_h$ is the vector heat flux density, J/m^2-s. The constitutive relations, the boundary conditions, and the numerical solutions of temperature and moisture to Equations (1) and (2) are presented by Liou et al [6].

The R module follows the approach of England and Galantowicz [8]. The combined soil and canopy radiobrightness is

$$Tb = T_{s,e}(1 - R_p(\mu))e^{-\tau_0/\mu} + T_{c,e}(1 - e^{-\tau_0/\mu})$$
$$(1 + R_p(\mu)e^{-\tau_0/\mu}) \tag{3}$$

where $T_{s,e}$ is the effective emitting temperature of the soil [3, 4], K, R_p is the Fresnel reflectivity of the moist soil for polarization p, τ_0 is the optical thickness of the canopy, μ is the cosine of the SSM/I incidence angle of 53^0, and $T_{c,e}$ is the effective emitting temperature of the canopy, K.

THE DLNN

The DLNN is utilized to manage a nonlinear mapping relation between the radiobrightnesses and the surface parameters. Based on a polynomial basis function expansion [10], a multilayer perceptron network is modified so that at the output layer the functional form is linearized while the hidden layers remain nonlinear. The weighting functions in each layer are cascaded to form a long vector through which the outputs and inputs are related [9], i.e.,

$$y = Wx, \tag{4}$$

where the output vector y contains all the output nodes of a network, the long input vector x is formed by concatenating all the input and hidden nodes in the network, and the long output weight matrix W is formed by concatenating all the weights

that connected to each output node. This modification allows us to apply the dynamic Kalman filtering algorithm [11] to adjust the network weights with a recursive minimum least square error, which is very suitable for computer implementation [12]. The network, i.e, the DLNN, bears features such as fast learning and built-in optimization of a weighting function at little expense of the computer storage. The fast learning feature stems from the fact that the updating of the weights is accomplished in a global manner avoiding back-propagation, which usually makes the learning process very lengthy. The DLNN is presented by Tzeng et al [9].

RESULTS AND DISCUSSION

Fig. 1 shows temperatures and moisture contents of the soil and canopy from products of the 1dH/R model in a run for the model validation, and from the DLNN retrievals. In general, differences between the retrievals and desired variables are small — less than 0.1 Kelvin for the canopy temperature, 1.2 Kelvins for the soil temperature (uppermost 5 mm), 0.0001 kg/m^2 for the canopy water content, and 1.2 % for the soil moisture content. That is, the retrievals for the four parameters of interest are all better than 96 % accuracy. We do not show comparisons between results from the 1dH/R model for the dry-down case and the DLNN retrievals because the retrievals are all better than 98 % accuracy — less than 0.1 Kelvin for the canopy temperature, 0.8 Kelvin for the soil temperature (uppermost 5 mm), 0.00001 kg/m^2 for the canopy water content, and 0.3 % for the soil moisture content.

Fig. 1 also shows the inferred canopy temperature appears to match the corresponding variable much better than the other three parameters. Our interpretations include three aspects: 1. Emissions at 19 and 37 GHz are primarily from the canopy — about more than 90 % for the former and 95 % for the latter [6]; 2. Brightnesses at 19 and 37 GHz are almost linearly related to the physical temperature of the canopy; and 3. Brightnesses at 1.4, 19, and 37 GHz depend on the canopy moisture, and soil temperature and moisture content with a higher degree of nonlinearity than on the canopy temperature. Total effect of 1 to 3 permits the DLNN to infer the canopy temperature better than the other three parameters.

This study has shown that (1) the DLNN can relatively well infer the desired variables from the radiobrightnesses if the radiobrightnesses are sensitive to the variables, and, hence, most of the uncertainities or errors produced in the retrieving process might be from the training data; and (2) the retrieval scheme presented in the paper can be very powerful if one were using a reliable 1dH/R model.

References

[1] Rowntree, P. R., and J. R. Bolton, "Simulation of the atmospheric response to soil moisture anomalies over Europe," *Quart. J. Roy. Meteor. Soc.*, 109, 501–526, 1983.

[2] Cunnington, W. M., and P. R. Rowntree, "Simulation of the Saharan atmosphere–dependence on moisture and albedo," *Quart. J. R. Met. Soc.*, 112, 971–999, 1986.

[3] Liou, Y.-A., and A. W. England, "Annual temperature and radiobrightness signatures for bare soils," *IEEE Trans. Geosci. Remote Sensing*, 34, 981–990, July, 1996.

[4] Liou, Y.-A., and A. W. England, "A land surface process/radiobrightness model with coupled heat and moisture transport in soil," *IEEE Trans. Geosci. Remote Sensing* (in press), 1997.

[5] Liou, Y.-A., and A. W. England, "A land surface process/radiobrightness model with coupled heat and moisture transport for freezing soils," revised for *IEEE Trans. Geosci. Remote Sensing*, April, 1997.

[6] Liou, Y.-A., and A. W. England, "A land surface process/radiobrightness model with coupled heat and moisture transport for prairie grassland," submitted to *IEEE Trans. Geosci. Remote Sensing*, February, 1997.

[7] Liou, Y.-A., E. J. Kim, and A. W. England, "Radiobrightness of prairie soil and grassland during dry-down simulations," submitted to *Radio Sci.*, March 6, 1997.

[8] England, A. W., and J. F. Galantowicz, "Observed and modeled radiobrightness of prairie grass in early fall," *Proc. IGARSS'95 Symp.*, Florence, July 10-12, 1995.

[9] Tzeng, Y. C., K. S. Chen, W. L. Kao, and A. K. Fung, "A dynamic learning neural network for remote sensing applications," *IEEE Trans. on Geosci. and Remote Sensing*, 32, 1096-1102, Sept. 1994.

[10] Chen, M. S., and M. T. Manry, "Back-propagation representation theorem using power series," *Proc. Int. Joint Conference on Neural Network*, 295-300, 1991.

[11] Brown, R. G., and P. Y. C. Hwang, *Introduction to Random Signals and Applied Kalman Filtering*, 2nd Edition, NY:Wiley, 1983.

[12] Haykin, S., *Neural Networks*, Englewood Cliffs, NJ: Prentice-Hall, 1994.
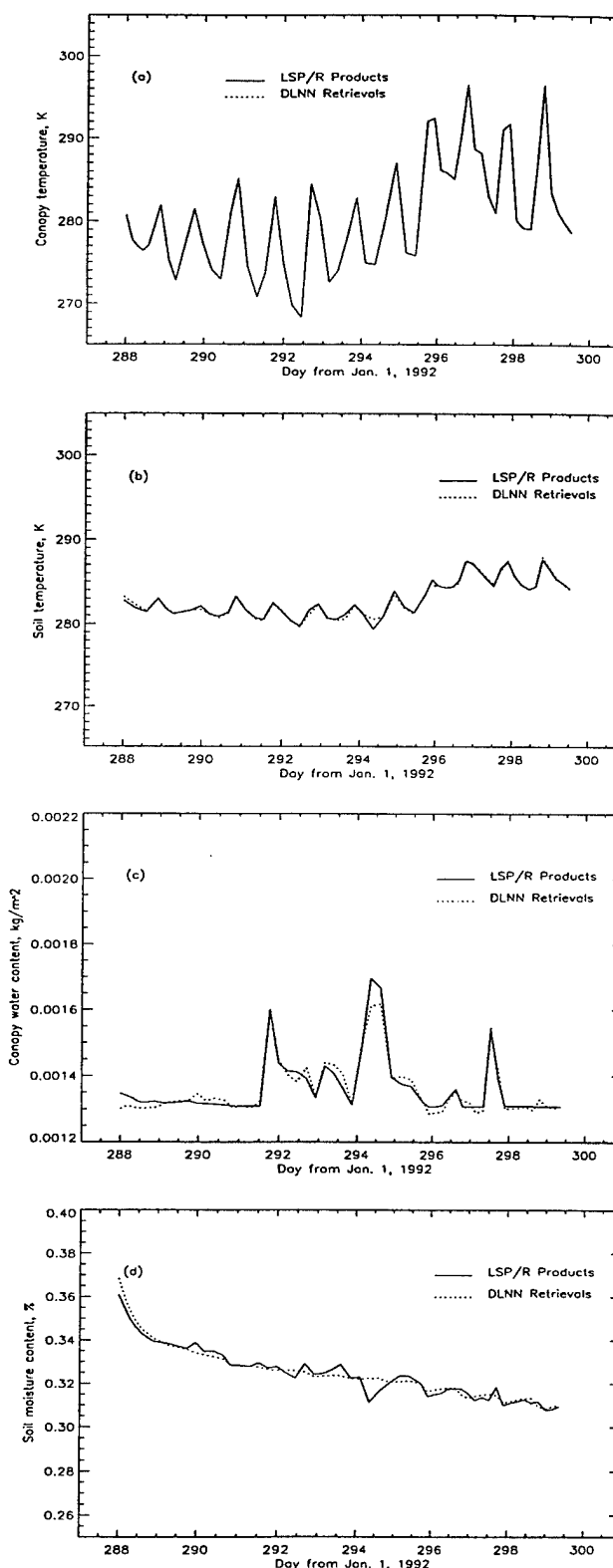
Figure 1: (a) Canopy temperature, (b) soil temperature, (c) canopy water content, and (d) soil moisture content from the products of the 1dH/R model and DLNN retrievals.

Passive Microwave Observation of Soil Water Infiltration

Thomas J. Jackson, Thomas J. Schmugge, Walter J. Rawls
USDA ARS Hydrology Lab
104 Bldg.. 007 BAR-West
Beltsville, MD 20705
(301) 504-8511
fax (301) 504-8931
tjackson@hydrolab.arsusda.gov

Peggy E. O'Neill
NASA Goddard Space Flight Center

Marc B. Parlange
Johns Hopkins University

Abstract -- Infiltration is a time varying process of water entry into soil. Experiments were conducted here using truck based microwave radiometers to observe small plots during and following sprinkler irrigation. Experiments were conducted on a sandy loam soil in 1994 and a silt loam in 1995. Sandy loam soils typically have higher infiltration capabilities than clays. For the sandy loam, the observed brightness temperature (TB) quickly reached a nominally constant value during irrigation. When the irrigation was stopped the TB began to increase as drainage took place. The irrigation rates in 1995 with the silt loam soil exceeded the saturated conductivity of the soil. During irrigation the TB values exhibited a pattern that suggests the occurrence of coherent reflection, a rarely observed phenomena under natural conditions. These results suggested the existence of a sharp dielectric boundary (wet over dry soil) that was increasing in depth with time.

INTRODUCTION

In this investigation the role of remote sensing in infiltration studies is considered. One reason for our interest is that remote sensing provides a spatially integrated measurement. Another is the increased availability of sensors which have the potential of providing soil water information, i.e. microwave. Previous research in this area has been very limited [1 and 2]. Several recent investigations have examined new approaches to estimating infiltration parameters which depend upon temporal observations of soil moisture {3, 4 and 5}.

The work described here focuses on the results obtained in a series of experiments using passive microwave radiometers installed on a truck based observing platform. Unique aspects of these studies include multi frequency microwave measurements, high temporal resolution (as compared with typical remote sensing field observations) and a spatial resolution on the order of 1 to 2 m.

S AND L BAND MICROWAVE RADIOMETER SYSTEM (SLMR)

The S and L Microwave Radiometer (SLMR) is a dual frequency passive sensor system operating at S band (2.65 GHz or 11.3 cm) and L band (1.413 GHz or 21.2 cm) [6]. For the 1994 experiments the SLMR system was mounted on a 1966 Ford hydraulic boom truck belonging to the Hydrological Sciences Branch at NASA's Goddard Space Flight Center. The antennas were mounted to observe horizontal polarization. At the nominal operating height of 5 m with the specified field of view of the radiometers (20°), the footprint size was 1.5 m at a viewing angle of 10° off nadir. The centers of the S and L band radiometers are offset by approximately 1 m in the installation, therefore, the centers of the ground footprints will be offset. The beams do overlap but there is the potential for some variation in target properties in the area contributing to the two individual measurements. In 1995, a different truck system was used. This was a 1990 Navstar hydraulic boom with a maximum height of 19 m. The observations in 1995 were made at a slightly higher elevation of 8 m which results in footprints closer to 2.5 m for the sensors.

EXPERIMENT DESCRIPTIONS

The experiments were conducted at two sites using sprinkler irrigation to apply water. In 1994, plots at the Beltsville Agricultural Research Center (BARC) were used. The soil was a sandy loam (70% sand, 6% clay) with a smooth surface. Bulk density averaged 1.45 g/cm^3. Hydraulic conductivity was measured using disc permeameters at 4 cm tension as 0.338 cm/hr. From this the saturated hydraulic conductivity was estimated as 22 cm/hr.

In 1995, the experiments were conducted at facilities of the University of California at Davis. Soil conditions were quite different from 1994. This was also a smooth bare soil. The particular area these measurements were conducted in was a Yolo

Silt Loam (20% sand and 20% clay). Bulk density was measured after irrigation as 1.4 g/cm³. Soil properties reported in [7] for the 30 cm layer are saturated water content 44%, saturated conductivity 0.44 cm/hr, and bulk density of 1.39 g/cm³.

RESULTS AND DISCUSSION

Beltsville 1994

Two sets of bare soil observations were made September 27 (bare) and October 3 (bare). Water applications amounts were estimated as 4.2 cm on September 27 and 2.5 cm October 3. Prior to September 27, there had been a rainfall event the previous night (> 2.5 cm) that left the soil wet at the outset of irrigation. A rainfall event on October 1 of more than 1 cm resulted in wet conditions for the October 3 observations.

Microwave data were collected every 2 minutes and integrated over a 15 second interval. Figure 1 shows the brightness temperature versus time plot for September 27 (similar results were observed October 3). There was a very rapid decrease in T_B after the start of water application. Second, in all cases the T_B then remains at a constant level for the balance of the irrigation. This level does vary between the S and L band. Visual observations indicated that ponding (water pooling on the surface) did not occur. Considering the high saturated conductivity of this soil this was to be expected under the relatively low water application rates possible with the sprinkler irrigation system. The T_B values would indicate a soil moisture close to saturation for this soil.

A close examination of the T_B curves at the end of irrigation shows indications of wavelength specific effects that reflect the differences in the contributing depth of the S and L bands. After the end of the irrigation, the water in the column should drain to the 1/3 bar (sometimes called field capacity) soil moisture. Without evaporation the soil moisture should remain at this nominal level. The results shown in Figure 1 indicate a more rapid increase in T_B for S band which would be expected because a shallower depth contributes to the measurement. The longer term variations involve diurnal (nighttime) temperature changes.

Davis 1995

The soil at the Davis site was very dry prior to the irrigation performed on June 12. Very limited sampling indicated the following soil moisture profile; 0-5 cm 6%, 5-10 cm 11%, and 10-15 cm 19%. Visual observation within the 0-5 cm layer indicated uniform conditions. For a silt loam soil, the 15 bar tension moisture content will be on the order of 10% and the 1/3 bar will be on the order of 35%.

The irrigation rate was approximately 0.5 cm/hr and was initiated in the early evening to minimize losses to evaporation and blowing. As opposed to the Beltsville experiment, the irrigation rate was on the order of the saturated conductivity for this soil (~0.44 cm/hr). Figure 2 shows the T_B trace observed for S and L band. At the outset of irrigation we observed large

decreases in T_B as expected. However, as time progressed an oscillation began to occur. The pattern of this oscillation was similar to that which is predicted using coherent radiative transfer models [8] for a layered media having a sharp dielectric boundary.

This is the first time that coherent reflection has been observed in soil moisture studies. Previous soil related investigations designed to verify this theory have utilized buried plate experiments [9 and 10]. In these studies a metal plate (which has a very high reflectivity) is buried at increasing depths in a uniform soil. As the soil depth increases, the oscillatory pattern predicted from coherent models has been observed. Since no field experiments have ever reported this phenomenon, it has been assumed that the sharp dielectric boundaries needed to produce the effect do not occur in nature with sufficient uniformity over an area the size of a radiometer field of view.

There are several features of the coherent reflectivity that can be readily observed in Figure 2. For an individual wavelength, the time between peaks is consistent and the magnitude of the oscillation decreases with each peak. The theory [8] predicts that the reflectivity will oscillate as the depth to the dielectric boundary increases and that the peaks will occur at fixed depth intervals $(\lambda/\varepsilon_{soil}^{0.5})/2$, where λ = wavelength and ε = dielectric constant. For L band and a wet soil, this oscillation interval would be on the order of 2 cm. The decrease in oscillation with time (or depth) is attributed to the decreasing impact of this layer interface as it gets deeper in the soil column and approaches a depth at which the profile can be treated as uniform.

In addition to the individual wavelength behavior, the L and S band results can be compared. It appears that the time period for S band is roughly half that of L band and that the oscillations appear to stop sooner than for L band. Both of these features would be expected from the coherent reflection.

SUMMARY

Experiments were conducted using truck based microwave radiometer to observe small plots during and following sprinkler irrigation. Data were collected using microwave radiometers operating at 1.41 (L band) and 2.65 (S band) GHz. horizontal polarization mounted on a boom type truck over a sandy loam soil in 1994 and a silt loam in 1995. For the soils with infiltration capabilities exceeding the water application rate, the observed brightness temperature quickly reached a nominally constant value during irrigation. When the irrigation was stopped the brightness temperature began to increase as drainage took place. The irrigation rates in 1995 with the silt loam soil exceeded the saturated conductivity of the soil. During irrigation the brightness temperature values exhibited a phenomena that had not been previously observed and identified. The temporal variation exhibited the pattern that is associated with coherent reflection.

REFERENCES

[1] Camillo, P. J., O'Neill, P. E., and Gurney, R. J. Estimating soil hydraulic parameters using passive microwave data. IEEE

Tran. on Geoscience and Remote Sensing, GE-24:930-936, 1986.

[2] Blanchard, B. J. and O'Neill, P. E. Estimation of the hydraulic conductivity of soils with passive microwave systems. Advances in infiltration, ASAE, 215-225, 1983.

[3] Ahuja, L. R., Wendroth, O., and Nielson, D. R. Relationship between the initial drainage of surface soil and average profile saturated hydraulic conductivity. Soil Science Society of America Journal 57:19-25, 1993.

[4] Mattikalli, N. M., Engman, E. T., Ahuja, L. R., and Jackson, T. J. Estimating soil properties from microwave measurements of soil moisture. SPIE Proceeding, 2585:89-101, 1995.

[5] Hollenbeck, K. J., Schmugge, T. J., Hornberger, G. M., and Wang, J. R. Identifying soil hydraulic heterogeneity by detection of relative change in passive microwave remote sensing observations, Water Resources Research, 32:139-148, 1996.

[6] Jackson, T. J., O'Neill, and Swift, C. T. Diurnal observations of soil moisture with microwave radiometers. IEEE Trans. Geoscience and Remote Sensing, in press, 1997.

[7] Buchter, B., Aina, P. O., Azari, A. S., and Nielsen, D. R. Soil spatial variability along transects. Soil Technology, 4:297-314. 1991.

[8] Ulaby, F. T., Moore, R. K., and Fung, A. K. Microwave remote sensing: active and passive, Vol. III, from theory to application. Artech House, Dedham, MA, 1986.

[9] Blinn, J. C. III, Conel, J. E., and Quade, J. G. Microwave emission from geological materials: observations of interference effects. J. Geophysical Research, 27:4366-4378. 1972.

[10] Paloscia, S., Pampaloni, P., Chiarantini, L., Coppo, P., Gagliani, S., and Luzi, G. Multi frequency passive microwave remote sensing of soil moisture and roughness. Int. J. of Remote Sensing, 14:467-483, 1993.
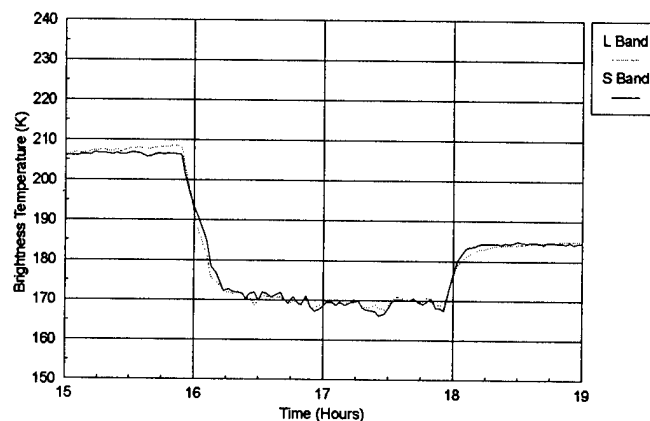
Figure 1. Observed brightness temperature during and after infiltration on Sept. 27, 1994 on a sandy loam soil at Beltsville, MD.
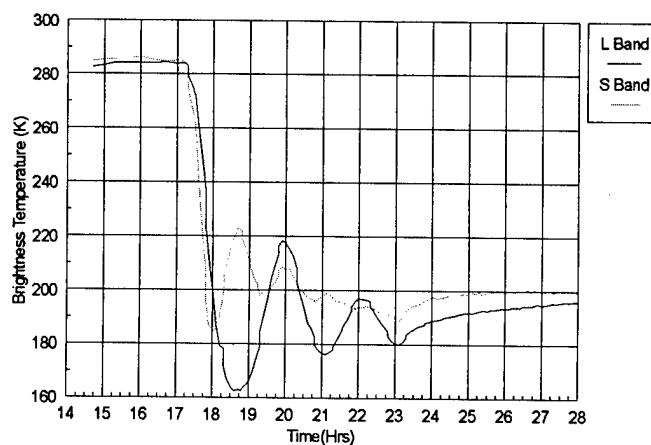
Figure 2. Observed brightness temperature during and after infiltration on June 12, 1995 on a silt loam soil at Davis, CA.

Land Surface Hydrological Processes Using Satellite Data

Venkataraman Lakshmi and Joel Susskind

Code 910.4, NASA/GSFC,
Greenbelt, MD 20771
(301)-286-9040; Fax: (301)-286-1757;
email: venkat@spectra.gsfc.nasa.gov

Abstract – Field experiments designed to support climate studies are of limited spatial and temporal coverage. Satellite data bridges the gap between field experiments and large scale modeling by aiding in model validation. The Tiros Operational Vertical Sounder (TOVS) Pathfinder Path A surface data of surface skin temperature, surface air temperature and the relative humidity will be used for the Red River Basin grid box in the GCIP LSA-SW region to simulate the surface fluxes, surface skin temperature and surface soil moisture. The surface skin temperatures simulated and observed by the TOVS will be compared.

BACKGROUND

Large scale studies of hydrology are greatly aided by the use of satellite data. Satellite data have repeat temporal and large scale spatial coverage and can be used in conjunction with station data to infer land surface - atmosphere interactions. The TIROS Operational Vertical Sounder (TOVS), comprised of the infrared and microwave sounders HIRS2 and MSU, have flown on the NOAA operational sun synchronous polar orbiting satellites TIROS N, NOAA 6-12 and NOAA 14 from late 1978 to the present day. These satellites view the earth twice daily at roughly 7:30 am/pm local crossing time or 2:30 am/pm local crossing time depending on the satellite. Susskind et. al., (1996) analyzed TOVS data for the period 1985-1991 to produce the Extended Pathfinder Path A data set which includes surface skin temperature, air temperature, specific humidity and microwave emis-sivity, atmospheric moisture and temperature profiles, as well as information about clouds, radiative fluxes and precipitation. The TOVS (Tiros Operational Vertical Sounder) Pathfinder Path A data of immediate interest are the surface skin and air temperatures, surface specific humidity, surface microwave emissivity and precipitation. Scientific studies using this data has been carried out (Lakshmi et. al. 1997d) and has shown that TOVS data is useful for land surface process studies.

METHODOLOGY AND RESULTS

The use of satellite data in land surface modeling requires developing a hydrological model with a thin upper layer to be compatible with the nature of the satellite observations and that would evaluate the soil moisture and soil temperature of a thin layer close to the surface. Such a model has been developed and validated using data from the Kings Creek catchment in Kansas (Lakshmi et. al. 1997a). This hydrological model has been used in a coupled model framework in order to simulate Special Sensor Microwave Imager (SSM/I) 19 and 37 GHz brightness temperatures as well as estimate the soil moisture over the Red River Basin grid box using the SSM/I observations (Lakshmi et. al. 1997b). The simulation region extends between $31°50'N, 36°N$ and $94°30'W, 104°30'W$ and the simulation time period is between August 1, 1987 and July 31, 1988. The coupled model is run on a hourly time step and the simulated values correspond to the SSM/I ascending overpass (approximately 6:00 am). The surface meteorological

data was obtained from 17 Surface Airways stations in the region. The rainfall was derived from the Manually Digitzed Radar, the vegetation index from the Advanced Very High Resolution Radiometer Global Vegetation Index (AVHRR-GVI) and the shortwave radiation was obtained using a topographic model of the region. An example of the SSM/I estimated soil moistures and the hydrological model simulated soil moistures as well as the simulated and the observed SSM/I average and polarization difference brightness temperatures are shown in Figure 1.

mospheric water budget and compared to that estimated using the SSM/I estimated surface soil moistures and the hydrological model estimated streamflows. This is shown in Figure 2.
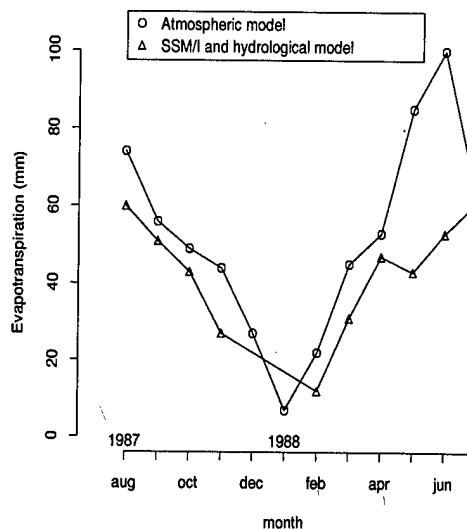
Figure 2: Monthly total evapotranspiration computed using atmospheric water vapor budgets and estimated using SSM/I and hydrological modeling

The comparisons are quite good considering the fact that the soil moisture estimates and the evaptranspiration comes from different sources.

USE OF SURFACE SATELLITE DATA

Figure 3 shows the comparisons between the TOVS derived surface air temperatures and the data measured at FIFE (First ISLSCP - International Satellite Land Surface Climatology Project, Field Experiment) corresponding to the NOAA 10 satellite. The NOAA 10 satellite is at 7:30am/pm only for the spots at the nadir. For spots viewed in the off-nadir portions of the scan, the local time can differ from 7:30am/pm by up to two hours. Accounting for this is extremely important when comparing a rapidly varying quantity such as surface skin temperature. In addition, since the HIRS2/MSU spot size is $60km \times 60km$, there may be more than one

Figure 1: Simulated and 19 GHz SSM/I brightness temperature derived soil moisture and average and polarization difference brightness temperature at the location $33.0°N$ and $104.25°W$

The monthly cumulative evapotranspiration has been computed using atmospheric data and the at-

spot in a $1°X1°$ box. In such a case, the average skin temperature at the mean time of the spots is used. The exact local time of satellite measurements in the $1°X1°$ grid box is used in comparing the am and the pm values of the derived surface skin temperature with the closest (with 15 minutes) AMS air temperatures. Results of daily comparisons are shown in Figure 3 separately for the nominal 7:30am and 7:30pm overpass. There has been no tuning or calibration in comparing these two sets of data. Furthermore, these two sets of data are derived from completely different sources with nothing in common. The comparison between the TOVS derived and the FIFE measured surface skin temperatures shows good agreement. This study is similar to the one carried out by Sugita et. al. (1993) except that this result has been carried out over more number of days. The dotted line is for the best fit regression line. More comparisons can be found in Lakshmi et. al. (1997c).

It is our desire to use the surface air temperatures and surface relative humidity from the TOVS data and perform the above simulations and make a three way comparison between the hydrological model estimates of soil moisture using station data, hydrological model using TOVS data and that derived using SSM/I brightness temperatures and TOVS data. This should help in future uses of TOVS and other satellite data in large scale hydrological modeling.

Figure 3: Surface air temperature measured in FIFE versus derived from NOAA 10

REFERENCES

[1] Lakshmi, V., E.F.Wood and B.J.Choudhury, A soil-canopy-atmosphere model for use in satellite microwave remote sensing, *J. Geophys. Res.*, 102(D6), 6911-6927, 1997a

[2] Lakshmi, V., E.F.Wood and B.J.Choudhury, Evaluation of SSM/I data for regional soil moisture estimation over the Red River basin, To appear in *J. App. Met.*, 1997b

[3] Lakshmi, V. and J. Susskind, Validation of TOVS Land Surface Parameters using Ground Observations, submitted to *J. Geophys. Res.*, 1997c

[4] Lakshmi, V. and J. Susskind, Determination of Land Surface Skin Temperatures and Surface Air Temperature and Humidity from TOVS HIRS2/MSU Data, To appear in *Adv. Space Res.*, 1997d

[5] Sugita, M. and W.Brutsaert, Comparison of Land Surface Temperatures Derived from Satellite Observations with Ground Truth During FIFE, *Int. J. Rem. Sen.*, 14, 1659-1676, 1993

[6] Susskind, J., P.Piraino, L.Rokke, L.Iredell and A.Mehta, Characteristics of the TOVS Pathfinder Path A Data Set, To appear in *Bull. Am. Met. Soc.*, 1997

Soil Moisture Profile Determination Using Remote Sensing Techniques

A.I.Timchenko, Yu.V.Gorishnya
Institute for Radiophysics and Electronics
National Academy of Sciences of Ukraine
Proscura 12, Kharkov, 310085, UKRAINE
Phone: 7-0572-448429/ Fax: 7-0572-441012/
E-mail:Timchenko@ire.kharkov.ua

Abstract -- This paper studies the behavior of the scattered intensity from the inhomogeneous medium bounded the rough surface. The theoretical analysis is based on an extension of the diagram and smoothing methods for the semi-transparent boundary. The series of numerical calculations for the various dielectric profiles which are typical for the different weather conditions have been made in the case of backscattering. The comparison between calculated intensity and remote sensing data shows a good correlation for the moistened soil before and after rainfalls. It was shown that the spatial variation experimental data of the rainfall zone can be related due to the variation in the soil moisture profile.

INTRODUCTION

The air– and space-borne radar sensing of the Earth can be an efficient source of the data on the soil conditions over vast areas. In this connection an adequate interpretation of remotely sensed data and estimation of the various hydrological parameters, such as soil moisture, is becoming increasingly important. In the recently developed models (see, for example, [1]) relating to the connection between the characteristics of the scattered radar signal and the soil moisture parameters the inhomogeneous moisture distributions were not usually taken into account. However, the natural media have an inhomogeneous profile with a depth for the moisture, density, salinity, etc. [2,3] and, as a consequance, the corresponding dielectric permittivity profile have a direct impact on the characteristics of the scattered signals.

In this paper we investigate the peculiar features of the radar signal scattered from depth-inhomogeneous medium as compared to the homogeneous one. Initially, we developed the theory of rough surface scattering for the semi-transparent boundary based on the smoothing and diagram methods which extends the range validity beyond the usual perturbation solution. The similar method has been proposed by Ishimaru for the conducting rough surface [4].

Next, we described the inhomogeneous moisture profile as an analytical function, whose parameters variation allows to describe the natural distribution of the soil moisture content and, at the same time, permits to apply the Witteker function for the analytical solution to the rough surface scattering problem. The calculating results of backscattering was compared with the remote sensing data.

THEORETICAL BACKGROUND

Consider the one-dimensional rough surface with the semi-transparent boundary. Let the incident electromagnetic wave have the s-polarization (E_y, H_x, H_z). For the upper half-space with the dielectric permittivity $\varepsilon_0 = 1$ the total electromagnetic field E_0 is the sum of incident and scattered fields. The propagation in the lower half-space with the dielectric permittivity ε_1 is described by the field E_1. The boundary conditions at the surface $z = h(x,y)$ is:

$$E_0 = E_1 \, , \; H_{0x} = H_{1x} \, , \tag{1}$$

where H_{0x}, H_{1x} are the x-components of the magnetic fields; k is the wave number.

Let us convert (1) into the equivalent boundary conditions at $z = 0$. For this purpose expand E_0 and E_1 about $z = 0$:

$$E_0 = \sum_{n=0}^{\infty} \frac{h^n}{n!} \left(\frac{\partial^n}{\partial z^n} E_0 \right)_{z=0} \, , \tag{2a}$$

$$E_1 = \sum_{n=0}^{\infty} \frac{h^n}{n!} \left(\frac{\partial^n}{\partial z^n} E_1 \right)_{z=0} \, , \tag{2b}$$

Substituting (2a) and (2b) into (1) we obtain the boundary conditions at $z = 0$. Note that h is considered to be a small quantity (ε h) and shown above are the terms up to ε^2.

Now we can obtain the Dyson equations set for dyadic Green's function G with the source placed in the upper half-space and satisfies the same wave equations set and the same boundary conditions than the electromagnetic field. We make use of the Greens' functions G_{0f}, G_{1f}, which are related to the upper and lower half-space correspondingly and satisfy the boundary condition at $h(x,y) = 0$.

Then apply Green's theorem to obtain

$G_x = G_{0x} - \int dx_1\, h(x_1)\, G_{0x}\, \hat{V}\, G_x$, (3a)

$G_y = G_{0y} - \int dx_1\, h(x_1)\, G_{0x}\, \hat{V}\, G_x$, (3b)

where: $G_x = G_0 + G_1$, $G_y = G_0 - G_1$, $G_{0x} = G_{0f} + G_{1f}$, $G_{0y} = G_{0f} - G_{1f}$, the indexes 0,1 are related to the values in the upper and lower half-space, respectively, $\hat{V} = \dfrac{\overset{\leftarrow}{\partial}}{\partial z_1}\, \dfrac{\overset{\rightarrow}{\partial}}{\partial z_1}$, and $\hat{V}$ means that it operates on the functions on the left and on the right side of V.

The Dyson's equation can be obtained for the average Green's function $\overline{G_x}$. Making use the first-order smoothing we get the bilocal approximation for $\overline{G_x}$, $\overline{G_y}$:

$\overline{G_x} = G_{0x} - \iint dx_1\, dx_2\, G_{0x}\, N_{12}(x_1, x_2)\, \overline{G_x}$, (4a)

$\overline{G_y} = G_{0y} - \iint dx_1\, dx_2\, G_{0y}\, N_{12}(x_1, x_2)\, \overline{G_y}$, (4b)

where N_{12} is

$N_{12} = \langle\, h(x_1)\, h(x_2)\, \rangle\, \hat{V}(z_1)\, G_{0x}(x_1, x_2)\, \hat{V}(z_2)$.

Next, express $\overline{G_i}$, G_{0i} and N_{12} ($i = x, y$) in terms of Fourier transform and substitute theirs into (4) we obtain the reflection and transmission coefficients:

In order to calculate the incoherent intensity we apply the Bethe-Salpeter equation. The first-order intensity I is obtained by taking the first-term of iteration. Also, we use the Fourier transform representation and evaluate intensity in the far field zone where $\rho = (x^2 + z^2)^{1/2}$ is large. Next, we obtain the scattering cross section σ, which is defined by Ishimaru [4] as $\sigma = 2\pi\rho\, I/x_c$, where x_c is the unit length of the rough surface. Finally, we have

$\sigma = (2\pi/k)\,\dfrac{k_{zi}^2\, k_{zs}^2\, T_{ai}^2\, T_{as}^2\, W(k_{xi} - k_{xs})}{(1 - Q_i)^2\,(1 - Q_s)^2}$, (5)

where $T_{ar} = 1 - R_{0r}$, $r = i, s$, R_{0r} is the reflection coefficient in the case of the flat surface $z = 0$, the indexes i, s are related to the incident and scattered angles θ_r, respectively; $Q_r = -k_{zr}(1 - R_{0r})\int dk_x\, k_z\,(1 - R_0)\, W(k_x - k_{xr})$; $k_{zr} = \sqrt{k^2 - k_{xr}^2}$, $k_{xr} = k\sin\theta_r$, $W(k)$ is the Fourier transform from the spectral density of the rough boundary.

CALCULATION RESULTS AND ANALYSIS

The moisture distribution in the soil between the land cover surface and the ground water level is dependent upon the soil type, meteorogical conditions, etc. [2,3]. The moisture is directly related to the soil dielectric permittivity value.

The experimental data from the study of the moisture content in the soil indicates that distribution ε, which corresponds to the moisture profile, may vary from smoothly decaying or rising in depth to the typically curved profile [2]. The last type of the vertical distribution has an extremum (maximum or minimum) located at a certain depth. The extremum value and its location depend on the soil type and meteorogical conditions.

To describe a uniform moisture distribution with depth (z-coordinate) an analytical function $\varphi(z)$ was chosen

$\varphi(z) = b_1 + b_2 \exp(-az) + b_3 \exp(-2az)$. (6)

Then the dielectric permittivity can be presented as $\varepsilon_1(z) = \varepsilon_s(1 - \varphi) + \varepsilon_w\varphi$, where $\varepsilon_s = \varepsilon_s' + i\,\varepsilon_s''$, $\varepsilon_w = \varepsilon_w' + i\,\varepsilon_w''$ are the dielectric permittivities for the dry soil and water correspondingly. The variation of the parameters b_1, b_2, b_3, a gives us a various profiles ε_1 which present a typical experimental moisture content distribution with a depth.

As regards the different profiles the numerical calculations were made for the angular and spectral-spatial characteristics. The comparison of the angular backscattering from the homogeneous and inhomogeneous moistened soil has shown that the only small quality difference between this cases are observed. More information can be obtained from the spatial distribution of the backscattering characteristics. Thus, we studied the scattered intensity dependence on the extremum profile location at a depth. Some typical results are presented in Fig. 1(a,b), 2(a,b) and 3. The backscattering behavior for the wavelength $\lambda = 3$ cm are shown in Fig.1(a), 2(a), and for $\lambda = 3$ cm and 21 cm in Fig.3; the corresponding profile of the moisture content are illustrated in Fig.1(b), 2(b). Calculation was carried out for the incident angle 30°, the correlation length is equal $l = 0.1/k$, and rms is $h = \lambda/6$. The data in Fig.1(a),2(a),3 are presented as K, where K is the ratio between σ_s for the dry soil and σ_i for the inhomogeneously moistened soil. The calculated K are plotted as a function of extremum profile location. The curves (1,2,3) in Fig.1(a) present K for the various values of the moisture content at the point of minimum, while the curves (4,6) are typical for the exponential profile and the curve (5) is typical for the profile with the maximum content. The curve (1) has the negative value K in the minimum location, i.e. the backscattering from the inhomogeneous soil is a smaller than it is from the dry soil. This result indicate that the transparency effect can be observed when the minimum location are compared with the effective wavelength in the medium. The study of the backscattering intensity for the various values of the moisture content has shown that for the
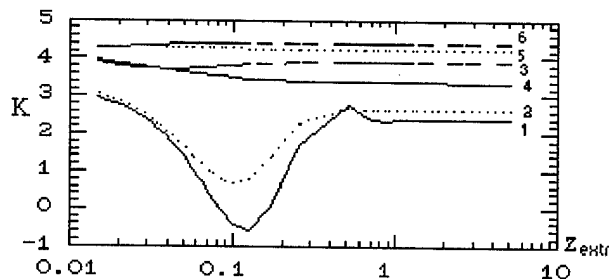
(a)
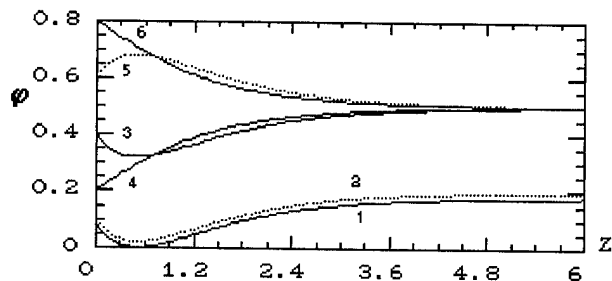
(b)

Fig.1.
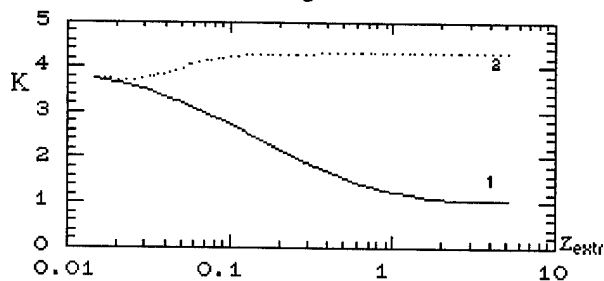
(a)
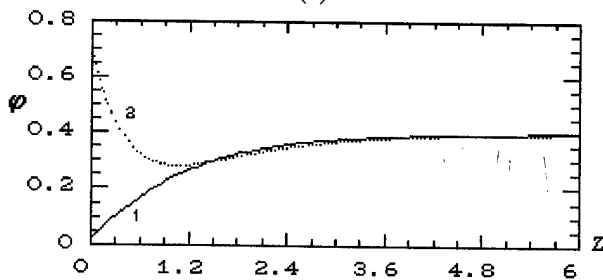
(b)

Fig.2.

wetter inhomogeneous soil the variation of K against the extremum profile is decreased. This fact is given in Fig.1(a) (curve 3).

Fig.3 present the comparison between the backscattering for the wavelength λ=3 cm(curve 1) and λ=21 cm (curve 2) for the profile of moisture content which was illustrated by curve 1 in Fig.1(b).
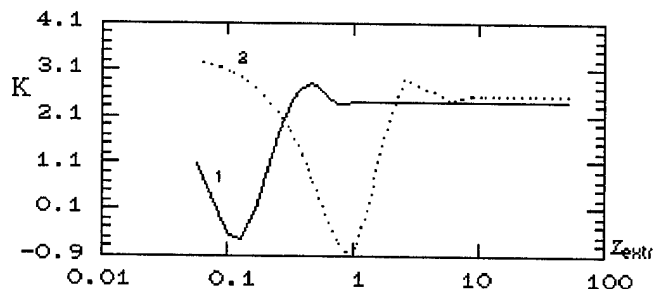
Fig.3

The typical situation describing the soil condition before and after rainfalls is presented in Fig.2. Since the top layer soil has a small moisture content w~2% (before the rainfall) and the w increases up to 70% (after the rainfall) the considerable difference for K is observed. Note that the curve (2) can describe the soil moisture profile directly after the rainfall while the only top layer soil becomes wetter.

The calculations results presented in Fig.2 were compared with the measured K values. The experimental data for K were obtained from the mapping of the soutern territory of Ukraine, which was performed using the SLR aboard the satellite "SICH-1" on April 1, 24, and 27 1996. The active rainfall zones are clearly seen on the images. The difference in K for the soil conditions before and after the rainfalls amounts to 5÷6 dB. However, the typical ratio K is on the order 3÷4 dB which is in agreement with the calculated K presented in Fig 2.

To summarize, the comparison of the calculating results and remote sensing data has shown that variations of the backscattering intensity due to the rainfall zone displacement can be determined by the variations in the soil moisture profile.

REFERENCES

[1] A.Beaudoin, T. Le Toan, and Q.H.J.Gwyn, "SAR observations and modeling of the C-band backscatter variability due to multiscale geometry and soil moisture," IEEE Trans. Geosci. Rem. Sensing, vol. 28, pp. 886-896, September 1990.

[2] J.R.Wang, "Microwave emission from smooth bare fields and soil moisture sampling depth," IEEE Trans. Geosci. Rem. Sensing, vol. 25, pp. 616-622, September 1987.

[3] A.M.Shutko, A Radiometry of the Water Surface and Soil. Moscow: Nauka, 1986, pp. 128-133.

[4] Akira Ishimaru, "The diagram and smoothing methods for rough surface scattering," The 1989 URSI International Symposium of Electromagnetic Theory, Stockholm, Sweden, 14-17 Aug. 1989 (Stockholm, Sweden; Royal. Inst. Technol., 1989, pp. 509-511).

Dielectric model of bound water in wet soils for microwave remote sensing

V.V.Tikhonov

Space Research Institute, Russian Academy of Sciences.
Profsojuznaya 84/32, Moscow 117810, Russia.
Fax. (7-095) 3331056, E-mail: kub@asp.iki.rssi.ru

INTRODUCTION

At present, modelling of dielectric properties of bound water in soil encounters significant obstacles. There are two main reasons: great variety of classifications of water in soils existing and controversial data on physical properties of water in contact with soil particles [1]. Classifying soil water, specialists of different fields propose different approaches taking as principal one or another feature of water and soil interaction [1]. Classification differences lead to different ways of estimation of the volume of bound water in soils for electrodynamic models of soils [2-4]: from one monomolecular layer of water covering soil particles to all non-gravity water in soil. As to physical characteristics of water, it is known, that the closer it is to the surface of a body, the more distorted its structure is compared to the structure of free water and ice [1]. Such structural distortions induce changes in water physical properties. However, available data on those characteristics are very controversial [1].

We believe, that determination of the volume of bound water in soils for electrodynamic models should be based on soil water dielectric properties and water should be considered bound if its permittivity differs from that of free water.

DIELECTRIC MODEL

To define volumetric content and permittivity of bound water in soils, let us first consider the following facts. Experiments described in [1] show, that bound water molecule relaxation time τ_{bw} differs from relaxation times of free water molecule τ_w and of ice molecule τ_i and $\tau_w < \tau_{bw} < \tau_i$. On the other hand, as noted in [1], with the increase of water content in clay minerals τ_{bw} approaches τ_w. In [1], through the analysis of nuclear magnetic resonance of bound water films in clay, upper limits of bound water molecule relaxation time at +27°C depending on the number of monomolecular layers covering water particles were determined. Those investigations show, that τ_{bw} falls with the increase of the number of monomolecular layers covering particles [5] and τ_{bw} is the same as τ_w at a film 10 layer thick.

Based on the facts given and assuming, that bound water permittivity, like that of free water, agrees with the

Debye model, we suggest the following statements:

1. With soil wetness increase, water in soil remains bound till a certain level of wetness.

2. The change of bound water volume results in different bound water dielectric properties induced by the change of bound water molecule relaxation time.

3. At a certain soil wetness, dielectric properties of bound water become similar to those of free water. Further increase of wetness brings no effect on the permittivity of bound water which remains equal to free water permittivity.

Using τ_{bw} obtained in [1], we defined an approximation of τ_{bw} depending on thickness h of water film covering soil particles. The dependence has the following form:

$$\tau_{bw}(+27) = \exp(-5.95 \times 10^{13} h^2 - 27.93 \exp(h) + \frac{1.52 \times 10^{-7}}{h} + 1.95 \times 10^7 h + 0.6), \quad (1)$$

where τ_{bw} is expressed in seconds, h - in centimetres. The dependence is worked out under the assumption that τ_{bw} becomes equal to τ_w at water film density h_{10} equal to 10 diameters of a water molecule (2.8×10^{-7} см [1]). I assume $\tau_{bw} = \tau_w$ at $h \geq h_{10}$.

To define bound water permittivity ε_{bw}, the relaxation model of free water permittivity [6] was used.

Given the bound water molecule relaxation time at +27°C from (1), it is easy to determine bound water relaxation wave length at the same temperature. Assuming that $\lambda_{bw}(+27°C)$, $\lambda_w(+27°C)$ and $\lambda_{bw}(t)$, $\lambda_w(t)$ are proportionally connected, we get:

$$\lambda_{bw}(t) = \lambda_{bw}(+27)\lambda_w(t) / \lambda_w(+27). \quad (2)$$

Then real and imaginary parts of bound water permittivity can be derived from expressions found in [6], where $\lambda_{bw}(t)$ is substituted for $\lambda_w(t)$:

$$\varepsilon'_{bw} = \varepsilon_\infty + \frac{(\varepsilon_s - \varepsilon_\infty)}{1 + (\lambda_{bw}(t)/\lambda)^2}, \quad \varepsilon''_{bw} = \frac{(\varepsilon_s - \varepsilon_\infty)(\lambda_{bw}(t)/\lambda)}{1 + (\lambda_{bw}(t)/\lambda)^2}, \quad (3)$$

here ε_s and ε_∞ are retrieved from the same formulas as for free water [6].

Thus, we can calculate ε_{bw} in soil depending on the thickness of bound water covering soil particles. The film thickness can be determined from the soil wetness and the soil model applied.

I used the wet soil model described in detail in [5].

According to it, the soil is an air medium with spherical granular inclusions divided in three fractions: sand, silt and clay. It is assumed that at volumetric soil wetness V_w ranging from 0% to max(V_{bw}), when bound water dielectric properties become similar to those of free water, water is distributed in the shape of spherical covers only on clay particles and is bound [1,2]. At soil wetness max(V_{bw}) $\leq V_w \leq V_{FC}$, water covers particles of all fractions and is free. Soil wetness V_{FC} is called field capacity and represents maximum quantity of capillary suspended water. According to [2], V_{FC} can be derived from the regression dependency given there. At soil wetness $V_w > V_{FC}$, surplus (gravity) water V_w-V_{FC} accumulates in the shape of spherical drops in soil pores. Effective permittivity ε_{cf} of wet soil is obtained from the equation given in [5].
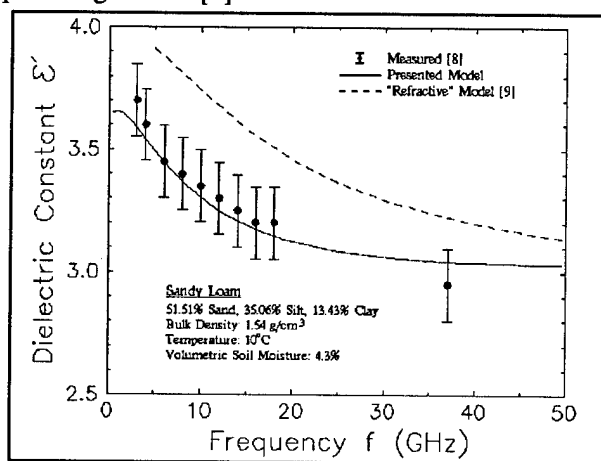
Fig.1 (a)
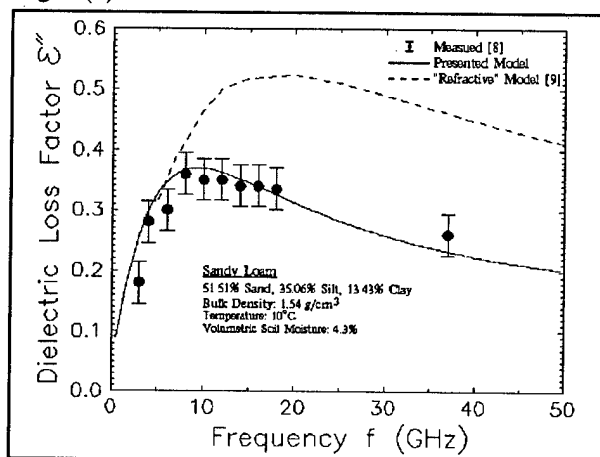
Fig.1 (b)

Model calculations of ε_{cf} of wet soils were compared to experimental data presented in [7,8]. Actual soil structural parameters were used in calculations. Comparisons gave good agreement between calculations and experimental data.

Figs. 1 and 2 present model calculations and experimental data [8] of real (a) and imaginary (b) parts of wet sandy loam depending on emission frequency. In agreement with the fractional composition of the soil and the model of soil bound water suggested, at low wetness (4.3%), all soil water is bound, while at high soil wetness (24.3%), it is free.
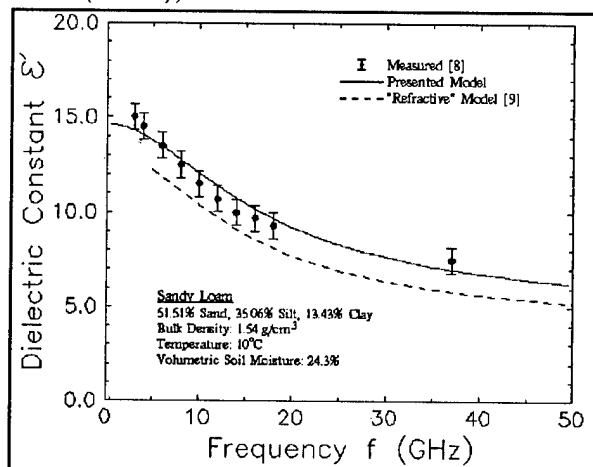
Fig.2 (a)
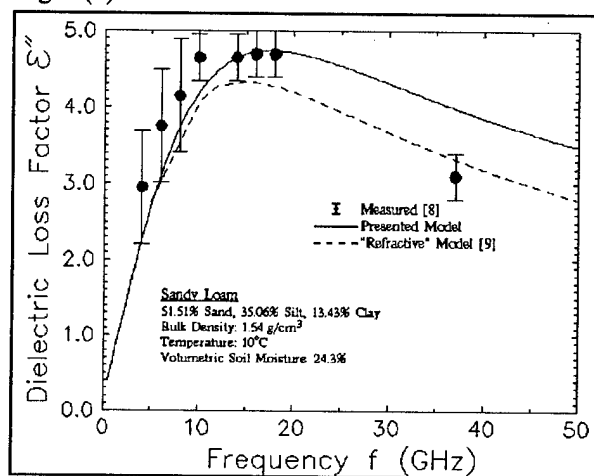
Fig.2 (b)

For comparison purpose, the figures also give dependencies calculated based on the "refractive" model, which does not take into account bound water in soil [9].

Analysis of Figs. 1 and 2 leads to the following conclusion. At low soil wetness, less than max(V_{bw}), bound water has to be taken into account in models for ε_{cf} of wet soil. This is confirmed by the difference of calculations made according to the present and "refractive" models at low wetness and their practical identity at high wetness.

Theoretical and experimental [7] dependencies of real and imaginary parts of ε_{cf} of silt loam on the soil volumetric wetness are presented in Fig. 3. Figures show two breaks of theoretical curves. The first one corresponds to that soil wetness at which bound water becomes free (V_t = max(V_{bw}) = 17.5%). This break is

placed in the so-called region of transitional moisture.
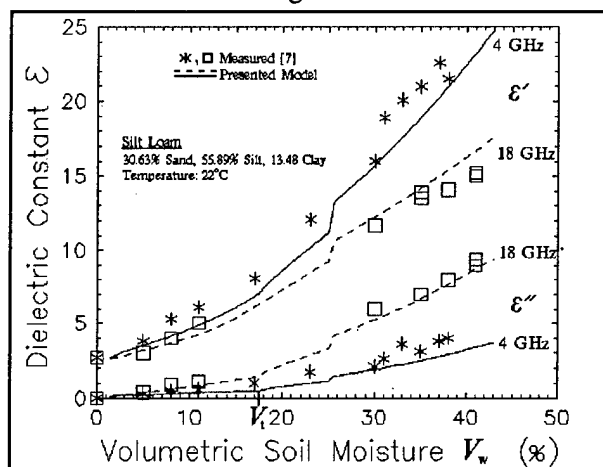
Fig.3

Most papers say this is the region of wetness where free water starts to appear. In the light of the models of ε_{cf} of soil and ε_{bw} in soil, this transitional region obtains new explanation as being region of wetness at which bound water becomes free. The second break of theoretical dependencies of soil permittivity on wetness relates to wetness where gravity water starts to appear in the soil. Experimental data, however, do not show such a break which, apparently, evidences that in reality water is simultaneously distributed as in film covers around soil particles as in drops in soil pores at wetness starting with V_t, which is much earlier than the calculated wetness V_{FC}.
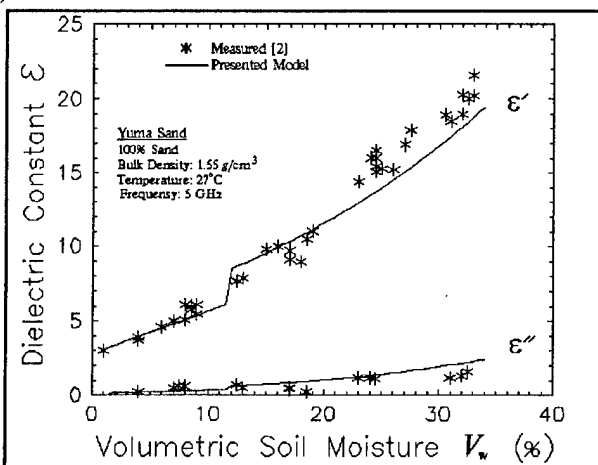
Fig.4

It is noteworthy that the model of soil ε_{cf} suggested assumes that bound water is found in soil only when the latter contains clay particles. In reality, bound water also covers other particles (sand and silt). However, given assumed maximum thickness of bound water of 10 monomolecular layers, estimations show that water covering sand and silt particles amounts to only 0.1% of total volume of water and is, hence, negligible. The statement is confirmed by Fig. 4 showing experimental

permittivities of sand [2] and calculated dependencies of ε_{cf} on wetness of the soil. Naturally, only sand fraction is present in the soil meaning, according to the model of ε_{cf}, that there is now bound water. Calculated and experimental dependencies agree well within the whole wetness range.

CONCLUSIONS

Calculations of ε_{cf} carried out based on the suggested model of ε_{cf} are in good agreement with experimental data for various soils. This agreement was reached due to the consideration of structural properties of soil in the model of ε_{cf} as well as due to the model of ε_{bw}. The suggested model of soil bound water permittivity allows to explain the region of transitional wetness and to describe dielectric properties of soils with low wetness.

ACKNOWLEDGEMENTS

REFERENCES

[1] E.D.Schukin, Surface water films in dispersed media, Moscow: ,1988, in russian.

[2] J.R.Wang, and T.J.Schmugge, "An Empirical Model for the Complex Dielectric Permittivity of Soils as a Function of Water Content," IEEE Trans. on Geosci.and Rem.Sens.,vol.18,№4,pp.288-295,1980.

[3] M.C.Dobson, F.T.Ulaby, M.T.Hallikainen, and M.A.El-Rayes, "Microwave Dielectric Behavior of Wet Soil -Part II: Dielectric Mixing Models, "IEEE Trans. on Geosci. and Rem. Sens., vol.23, №1, pp.35-46,1985.

[4] V.I.Spiridonov, "Relaxation Dielectric Model of Water in Heterogeneous Mixtures," Izmeritelnaya Tekhnika, № 5, pp. 68-70, 1982, in russian.

[5] V.V.Tikhonov, "Dielectric and Emissions Models for Salt Water-Soil Mixtures," Proc. of IGARSS'95, vol.I, pp. 9-11, Firenze, Italy, July, 1995.

[6] A.Stogrin, "Equations for calculating the dielectric constant of saline water," IEEE Trans. on Microwave Theory Tech., vol. MTT-19. pp. 733-736, 1971.

[7] M.T.Hallikainen,F.T.Ulaby,M.C.Dobson,M.A.El-Rayes, and Lin-Kun Wu, "Microwave Dielectric Behavior of Wet Soil - Part I: Empirical Models and Experimental Observations," IEEE Trans. on Geosci. and Rem. Sens., vol. GE-23, № 1, pp. 25-34, 1985.

[8] M.T.Hallikainen, F.T.Ulaby, M.C.Dobson, and M. A.El-Rayes, "Dielectric Measurements of Soils in the 3-to 37-GHz Band Between -50°C and 23°C," Proc. of IGARSS'84,pp.163-168, Strasbourg, August, 1984.

[9] J.R.Birchak, C.G.Gardner, J.E.Hipp, and J.M.Victor, "High Dielectric Constant Microwave Probes for Sensing Soil Moisture," Proceedincs IEEE, vol.62, № 1, pp. 115-121, 1974.

Rain/No-rain Discrimination for TRMM Precipitation Radar

Hiroshi Kumagai[1], Toshiaki Kozu[2], and Toshio Iguchi[2]

[1]Kashima Space Research Center, Communications Research Laboratory
893-1 Hirai, Kashima, Ibaraki, 314 Japan
TEL: +81 299 84 7117; FAX: +81 299 84 7157; e-mail: kumagai@crl.go.jp

[2]Communications Research Laboratory
4-2-1 Nukui-kita, Koganei, Tokyo, 184 Japan
TEL: +81 423 27 7543; FAX: +81 423 27 6666

Abstract—An algorithm for discrimination whether rain exists or not in the TRMM PR (Precipitation Radar) data is being developed. The rain/no-rain discrimination will provide us with useful information for on-line data processing, data storage control, and data analysis in post processing. A simple rain/no-rain discrimination with a flag output representing the possibility of rain is employed. The flag expresses the three states of rain as 'rain certain', 'rain possible', and 'rain little' at each PR footprint. Rain top height is also determined in this algorithm. The algorithm described here is implemented as one of TRMM standard algorithms.

1. INTRODUCTION

TRMM PR (Tropical Rainfall Measuring Mission/ Precipitation Radar) is the first spaceborne rain radar which objective is to achieve more quantitative rain measurement in global scale than ever made in tropical and sub-tropical regions. In the PR algorithms for the TRMM data system, an algorithm to discriminate whether rain exists or not has been developed. One of products of this algorithm is a flag representing the rain status for an footprint. This flag is used for the algorithms in downstream in the data system, reduction of storage data volume by eliminating data judged as rain-little, and data analysis in the post-processing.

The rain/no-rain discrimination is the statistical testing problem using thresholds in the radar received signal. The probability distribution function (PDF) of received signal describes both the detection probability and false alarm probability for some particular threshold. The PDF particularly with the mean value and standard deviation of weather radar signal has been studied by Zrnic [1]. The task to be solved here is to choose optimum thresholds to separate rain and no-rain condition effectively under the TRMM PR performance. The algorithm first compares the radar range data in an anglebin with threshold. Then, a flag output for the anglebin is generated by examining the result of range data comparison. The rain top height at each anglebin is also derived. The method in deriving these products and simulation study to find optimum parameters are discussed.

2. TRMM PR MEASUREMENT

TRMM PR is an active phased array radar which is composed of all solid state components. The electronic antenna beam scanning in cross-track direction performs contiguous rain mapping over the swath width of about 220 km on the earth surface. The antenna scan angle ranges ±17 deg centered at nadir. The footprint size is 4.3 km at nadir. The cross-track swath is filled with 49 footprints (anglebins). The range resolution (a rangebin size) in each anglebin is 250 m.

The signal to noise ratio (SNR) in the TRMM PR is generally poorer than typical ground-based radars due mainly to longer radar range. The designed and achieved PR sensitivity is given as S_n, which is the SNR per one pulse, being unity (0 dB) for the signal from 0.5 mm/h rainrate. In this case, the noise figure of the PR receiver is about 5 dB. Here, the following Z-R relation which is considered to be suitable to tropical rainfall is assumed,

$$Z = 372R^{1.54}. \qquad (2)$$

In the case of rain radar measurements from space or aircraft, ground (sea) surface echo is much intense than typical rain echo. Therefore, effect from the surface clutter to the rain discrimination must be considered. There are two causes for the surface clutter: one is caused from the PR antenna mainlobe. PR footprint size is 17 times larger than range resolution. Therefore, at the scan edge of ±17 deg, the clutter echo caused from the antenna mainlobe shoulder appears up to 1.6 km above the surface in the radar range. Because received level of mainlobe coupled clutter is much intense than rain echo, the rain discrimination can not be made where the mainlobe clutter appears. Another type of clutter is the antenna sidelobe-coupled clutter. After examination of the PR antenna radiation pattern, it is concluded that the sidelobe-coupled clutter level is low enough in usual surface conditions.

3. PR SIGNAL STATISTICS AND RAIN DISCRIMINATION METHOD

In the rain discrimination, PR data between the sea surface and 20 km above it are used, although the upper portion of data are not always available. This algorithm belongs to the Level-1 data processing in the TRMM data system. In this level, the instantaneous data in the anglebin-basis are processed. The rain discrimination is applied to each anglebin data and a flag is generated at anglebin by anglebin. The height (range) distribution of rain in each angle bin is used in this processing.

After logarithmic detection is applied, incoherent averaging of data is applied over 64 data for received power and 256 data for receiver noise in PR. Standard deviation of rain signal obtained in PR after integration is expressed as [1][2]

$$\sigma_s = \frac{\pi \overline{P_s}}{\sqrt{6}} \left[\frac{1}{N}\left(1 + \frac{1}{S_n}\right)^2 + \frac{1}{M}\left(\frac{1}{S_n}\right)^2 \right]^{\frac{1}{2}} \quad (2)$$

where, N and M are the integration number for received power and noise, respectively. $\overline{P_s}$ and S_n are the averaged signal power and SNR per pulse, respectively. A standard deviation in the case of no-rain ($\overline{P_s} = 0$) is given as,

$$\sigma_{s0} = \frac{\pi \overline{P_n}}{\sqrt{6}} \sqrt{\frac{1}{N} + \frac{1}{M}} \quad (3)$$

Although above discussion does not specify the PDF shape, PDF will be close to the normal distribution due to large number of integration.

To examine the PDF of the PR received signal, PDF is generated using random numbers. Fig. 1 shows the PDF of PR signal which is generated from 40000 random numbers simulating the PR signal processing: abscissa is scaled by radar reflectivity factor (Z). Fig. 1 shows two cases for different PR receiver noise level, that is, $S_n = 1$ at 0.5 mm/h rainrate signal and at 0.7 mm/h rainrate signal. Three curves representing no-rain case, and rain cases with rainrate of 0.5 mm/h and 0.7 mm/h. Dots represent simulation results and solid lines show the normal distribution with the standard deviation given from (2) and (3). Each simulated PDF is well consistent with corresponding normal distribution curve. It is noted, however, that the PDF from simulation is slightly asymmetric with its center and the probability in the upper skirt is a little higher than that of normal distribution.

It is postulated that the goal of this discrimination is to separate rain data at 0.5 mm/h effectively from receiver noise fluctuation. To achieve this, we can set a threshold at the upper 3σ point of no-rain PDF. The false alarm probability in this case is 0.4%. In the case (a), this threshold will work

well with relatively high detection probability (92 %) for 0.5 mm/h rain. However, in the case of the increased receiver noise (b), this threshold gives poor detection probability (about 59 %), which means that 41 % of rain data at 0.5 mm/h is left by oversight. To prevent this, the second (lower) threshold is set at upper 10 percentile of no-rain PDF with detection probability of 92% in (b). The rain state is considered as 'rain certain' for the signal above the higher threshold, 'rain possible' for that above the lower threshold, and 'rain little' for that below the lower threshold.
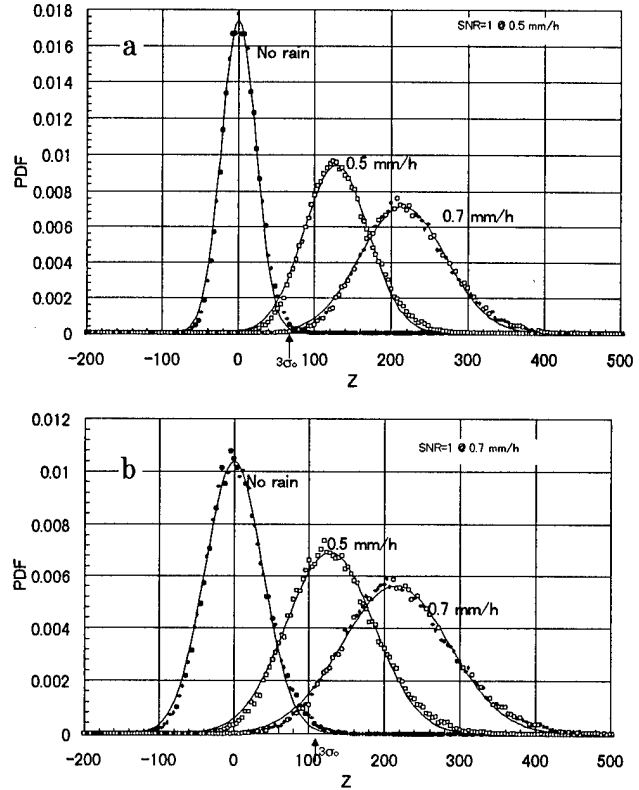
Fig. 1: PDFs of PR received signal for no-rain case, and rain cases with rainrate of 0.5 mm/h and 0.7 mm/h. (a) $S_n = 1$ at 0.5 mm/h rainrate signal and (b) at 0.7 mm/h rainrate signal.

4. SIMULATION OF RAIN DISCRIMINATION

Propriety of thresholds and flag derivation method is tested using simulation data. The data used for this simulation were originally obtained from airborne rain radar measurement of vertical rain distribution along flight track. Fig. 2(a) shows an example of original data with coordinate and resolution being modified to match those in TRMM PR. The data are first spatially averaged to meet the PR resolution with 250 in vertical and 4.3 km in horizontal, and then re-arranged to form the TRMM scan plane which consists of 49 anglebins

and about 80 rangebins. The PR scan plane is plotted in rectangular shape for simplicity. Black portion and white portion in the bottom are the ground and mainlobe-coupled clutter region, respectively. The noise fluctuation in this original plot is considered to be small enough because of higher SNR in the airborne radar measurement and very large number of integration in the averaging process.

Fig 2(b) shows the plot simulating PR data. Noise fluctuation expected in the PR SNR is added to the data in (a). Vertical pattern which appears in the plot is caused by the subtraction of constant noise level at an anglebin.

Comparison with threshold values is made over all rangebin and anglebin data. The results for (a) and (b) are shown in (c) and (d), respectively. The signal level at black and gray points are above the higher and lower thresholds, respectively. Here, the values of 2 and 1 are assigned to the black and gray points, respectively. The final product is the flag output for anglebin basis. Here, we introduce a concept of vertical correlation distance d to avoid the flag being ON due to noise fluctuation. The rule is that the anglebin flag is 2 or 1 only for the cases that at least d-consecutive rangebins are judged as 2, or larger than or equal to 1. The final anglebin flags derived are plotted with d value in (e). The result for $d = 0$ is the result obtained from the plot (c) and is the reference. Comparison of results from d=1 to 4 with that for d=0 suggests that the case of $d=2$ gives the best result among the 4 cases.

SUMMARY

Outline of an algorithm for rain/no-rain discrimination in the TRMM PR is described together with an example of algorithm performance test using simulation data. Preliminary test suggests that vertical correlation distance of 2-rangebin sizes gives the best discrimination performance. Parameter tuning and further algorithm improvement will be continued throughout the TRMM mission.

This study has been conducted under collaboration with NASDA based on the TRMM Joint Research Announcement.

REFERENCES

[1] D. S. Zrnic, "Measurements of estimated input power for finite sample averages of radar receiver outputs," IEEE Trans. Aerosp. Electron. Syst., AES-11, pp. 109-113, 1975.
[2] F. T. Ulaby, R. K. Moor, and A. K. Fung, Microwave remote sensing: active and passive, vol. 2, Chap. 7, Artech House, 1982.
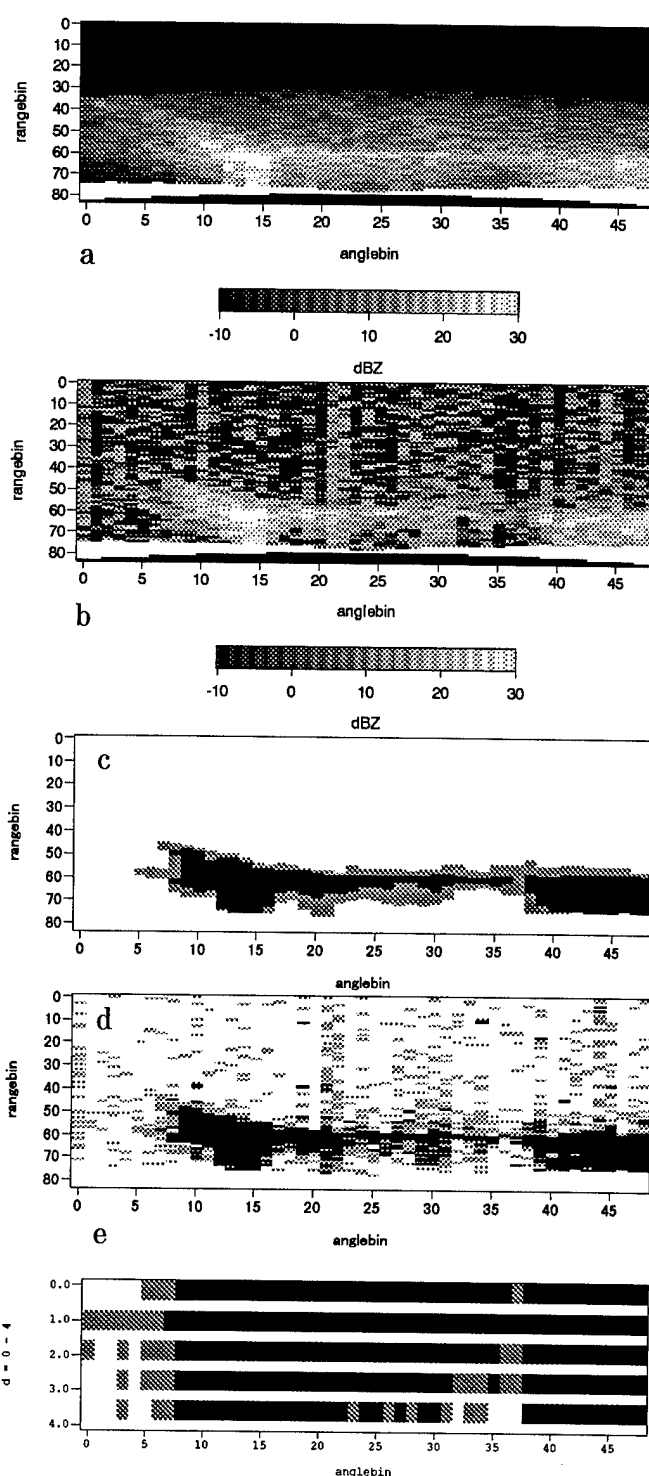
Fig. 2: Simulation results of rain/no-rain discrimination. (a) Original Z distribution on PR scan plane; (b) Noise fluctuation expected in PR is added; (c) Classification by thresholds for the plot (a); (d) Classification by thresholds for the plot (b); (e) Dependence of flag on the parameter d.

An Assessment of Multiparameter Radar Rain Rate Algorithms Using an Optimal Area Approach

S. Bolen
Rome Laboratory/OCSA
Rome, New York 13441

V.N. Bringi and V. Chandrasekar
Colorado State University
Fort Collins, Colorado 80523

Abstract – An optimal area method is described which is used as a basis for comparing Kdp, (Kdp,Zdr) and Zh based estimates of rain rates with gauge measured rain rates. This method differs from conventional methods which typically use a square L×L area centered on the gauge. The spatial structure of the rms error field, which is the difference between Kdp-based rain rate and gauge-measured rain rate is used in an objective manner to define the optimal area over which the radar data is averaged; additionally, an optimum time delay is calculated. Three convective rain events (with pea-to-marble sized hail) are analyzed using the data from the CSU-CHILL Radar and gauge data. In two cases, a young capacitance rain gauge installed in a chase van was used to record rainfall. The chase van was directed by radar for storm cell intercepts. Another radar algorithm using the principle of the optimal area was also developed relying on radar data only. In this algorithm radar data from different elevation angles are used to arrive at an optimal area and time delay. These rainfall estimates are then compared with gauge reports to provide an independent measure of accuracy and assessment of the various rain rate algorithms.

INTRODUCTION

Until recently there have been few opportunities to measure polarimetric radar parameters including differential propagation phase (Φdp) from which Kdp is estimated and to assess performance of algorithms based on (Kdp) or (Kdp,Zdr) [1][10]. Quantitative assessments of algorithms based on (Zh,Zdr) against distrometer and gauges have shown that fractional standard errors of (30-40%) are typical for these algorithms [2][3][5][6].

Radar-gauge comparisons are complicated by various error sources. The conventional approach is to construct an L×L square area centered over the gauge location and then to spatially average the radar data within this region [11]. Aydin, et al, [2] have suggested a method based on choosing an optimal area from a set of pre-determined sub-areas or swaths. Radar Zh and Zdr values are averaged within this optimal area before comparing to distrometer values. Swath areas are pre-defined and laid out in the path of storm motion relative to the distrometer location. Areas are chosen within each radar PPI scan that minimize the time-delayed cross-correlation between radar Zh and distrometer Zh. Such swaths would define an optimal area that likely contributed to the distrometer measurements and thus can be used to compare radar-distrometer rainfall estimates.

In this paper we present an approach similar to Aydin, et al, except that there are no predefined areas used to select the optimal area and no apriori knowledge of the storm motion is assumed. An objective procedure for locating an elliptically-shaped optimal area is described that minimizes the rms error difference between radar rain rate estimates and the gauge rain rate over an appropriate time interval. The dimensions of the ellipse are obtained from the spatial correlation structure of the rms error field.

DATA SOURCES

CSU-CHILL Radar

Radar data such as Zh, Zdr, and Φdp were available at resolution volumes spaced 150 m apart with a dwell time of 128 ms (64 horizontal/vertical polarized pulse pairs). Kdp was derived by post-processing the raw Φdp range profiles using an adaptive digital range filtering technique described in [8]. The resulting Kdp accuracy is estimated to be within ±0.5 deg km^{-1}.

Rain Gauges

For the 20 June 1994 storm event a tipping bucket was used for Gauge #1 and a weighing gauge was used for Gauge #2. Both gauges logged cumulative rainfall measurements at 5 minute intervals. The storm duration for this event was ~45 minutes over both gauges. The distance of Gauge #1 and #2 from the radar was 45.6 km and 40.6 km respectively.

For the 2 June 1995 and 6 July 1996 events, a Young capacitance rain gauge was used. The gauge was interfaced to a PC; cumulative rainfall was recorded every ~3 seconds. The distance of the gauges from the radar was 14.8 km and 24.1 km for the 2 June 1995 and the 6 July 1996 events

respectively. The duration of the 2 June 1995 event lasted ~30 minutes and the 6 July 1996 event a ~30 minutes.

OPTIMAL AREA METHOD - RADAR/GAUGE ELLIPSE

Data from the 2 June 1995 storm will be used as an example to describe the optimal area method. A time series of radar data is constructed through each resolution cell from multiple PPI scans. We use a 3.5 km radius circle centered over the gauge location as an observation area to study to reduce computation time.

The temporal and spatial variability of rainfall are important considerations in the development of the optimal area. Gauge data is used to determine the time interval that the optimal area can be matched to the gauge measurements. The autocorrelation of the gauge time series is taken and then best fit to a smooth exponential function. The time lag (τ_g) where the best fit curve is equal to 1/e is chosen to be the time interval of interest. The radar data time series are truncated to a window size equal to τ_g.

In turn, each radar time series are shifted incrementally in time across the gauge data. Increments of 1 second are used. At each successive increment the rms difference (RG_{rms}) between the radar and gauge measurements is computed. The minimum RG_{rms} value is then found from all of the time lag calculations:

$$\min(RG_{rms}) = \min \left\{ \frac{1}{n} \sum_{i=1}^{n} \left[R_{ri}(t+\tau) - R_{gi}(t) \right]^2 \right\}^{\frac{1}{2}} .$$

(1)

Next, the time lag of all the radar time series are set to the lag of the R-G time series pair that has the smallest rms value. RG_{rms} is then re-computed for all time series once more. The result is an rms difference field as shown in fig. 1. The physical dimensions of the ellipse are determined from the rms difference field. The center location of the ellipse is
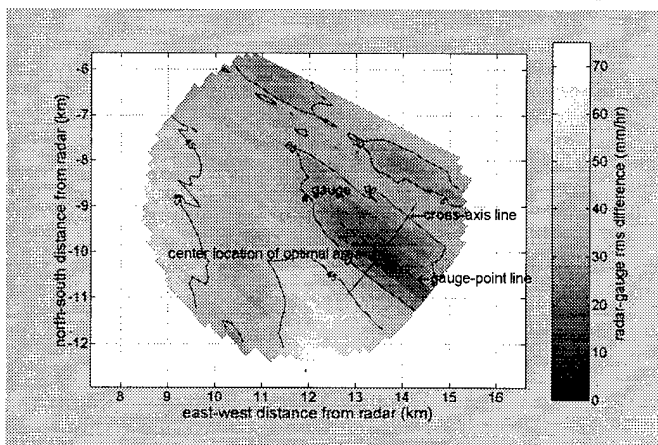
Fig. 1. RMS difference field (mm hr⁻¹) from the radar/gauge method is shown with gauge-point and cross axis lines as indicated. Data is from the 2 June 1995 event.
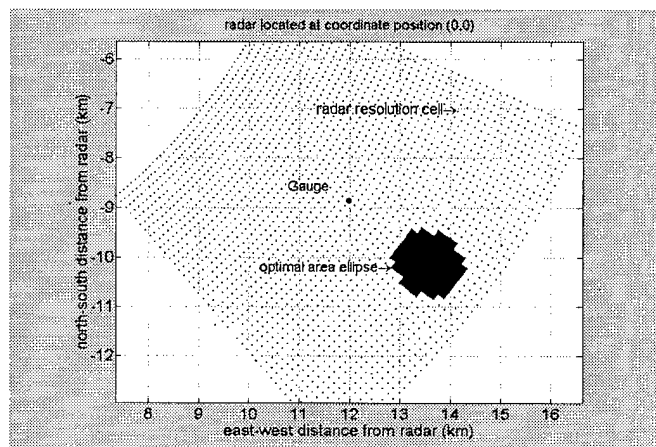
Fig. 2. Optimal area from radar/gauge method. Data is from 2 June 1995 event.

taken to be at the point location with the smallest rms value.

A gauge-point axis and orthogonal cross-axis line are drawn as shown in fig.1. The rms difference values profiled along each line are used to determine the axis lengths of the ellipse. Rather than using an arbitrary cutoff level of the error measure, an adaptive procedure is used. The autocorrelation of the rms error profile is taken for each line and the decorrelation value equal to 1/e is used to fix the spatial lag corresponding to the axis length. The optimal area for the 2 June 1995 event is shown in fig. 2. Radar data within the optimal area ellipse are averaged to form a composite radar value. The optimum time delay (T_{opt}) is taken as the time shift where the radar composite time series and gauge measurements have a minimum rms difference.

OPTIMAL AREA METHOD - RADAR/RADAR ELLIPSE

This method is similar to the previously described approach except that radar data alone is used to determine the optimal area ellipse. Data from two elevation levels are used to develop the ellipse area. Gauge data is substituted for radar data (R_{ref}) selected at the center of the observation area in one of the elevation planes (the reference plane). The other elevation plane represents a test a field to compare with the R_{ref}. The time interval, rms difference field, and ellipse axis lengths are computed exactly in the same manner as before except that the R_{ref} is used instead of the gauge data.

The point where the R-R_{ref} difference pair has the smallest rms value is used to calculate a *storm vector*. This vector is then used to find the displacement from the center location of the optimal area with respect to any desired location. Thus, a point on the ground can be matched to a point aloft by the projection of the storm vector. For comparison purposes, the ground point is chosen to be the gauge location.

Radar data are averaged within the optimal area to form a composite radar time series. To find T_{opt} all of the radar time series in the reference elevation are shifted ahead in time and

1115

series in the reference elevation are shifted ahead in time and the rms difference between these time series and the original R_{ref} at 0 time shift is computed. Again, the best $R(t+\tau)$-R_{ref} pair is found. The distance from this point and the time shift determine a *storm speed*. T_{opt} is then computed from storm speed and the distance from the center of the optimal area to the gauge location. The composite radar value and T_{opt} can be used to compare with the gauge reports on the ground.

RESULTS/CONCLUSIONS

Table 1 lists the rain rate estimators. Table 2 contains the results for the optimal area radar/gauge and radar/radar methods compared to the gauge reports. Radar/radar results are given only for the 2 June 1995 and 6 July 1996 events. The errors shown in Table 2 are in excellent agreement with theoretical predictions [10]. Further, our results support the conclusions of [1][10] that Kdp-based algorithms offer an excellent, physically based radar method for measuring rain rate in mixed phase precipitation.

ACKNOWLEDGMENTS

Table 1. Radar Algorithms of Rain Rate (mm hr⁻¹) and References

R(Kdp)	$= 40.5(Kdp)^{0.85}$	[4]
R(Kdp,Zdr,1)	$= 52.0[(Kdp)^{0.96}][(Zdr)^{-0.447}]$	[10]
R(Kdp,Zdr,2)	$= 67.152[(Kdp)^{0.956}](10)^{-0.125(Zdr)}$	[7]
R(Zh)	$= 0.017(Zh)^{0.714}$	[9]
R(Zh,55)	$= 0.017(Zh,55)^{0.714}$	-
R(Zh,53)	$= 0.017(Zh,53)^{0.714}$	-
R(Zh,51)	$= 0.017(Zh,51)^{0.714}$	-

note: Kdp in deg km⁻¹, Zdr in dB, and Zh in units of mm⁶m⁻³. Zh_55 means truncated at 55 (53,51 dBZ) respectively.

REFERENCES

[1] Aydin, K., V.N. Bringi, and L. Liu, "Rain-rate estimation in the presence of hail using S-band specific differential phase and other radar parameters", J. Of Applied Met., **34**, pp 404-410, 1995.

[2] −, H. Direskeneli, and T.A. Seliga, 'Dual polarization radar estimation of rainfall parameters compared with ground-based distrometer measurements: 29 October 1982, Central Illinois Experiment", IEEE Trans. On Geo. and Remote Sensing, **25**, pp 834-844, 1987.

[3] −, Yuan-Ming Lure, and T.A. Seliga, "Polarimetric radar measurements of rainfall compared with ground-based rain gauges during Maypole '84", IEEE Trans. On Geo. And Remote Sensing, **28**, pp 443-449, 1990.

[4] Chandrasekar, V., V.N. Bringi, N. Balakrishnan, and D.S. Zrnic, "Error structure of multiparameter radar and surface measurements of rainfall. Part III: specific differential phase shift', J. Atmos. And Oceanic Tech., **7**, pp 621-629, 1990.

[5] Goddard, J.W.F. and S.M. Cherry, 'The ability of dual-polarization radar (co-polar linear) to predict rainfall rate and microwave attenuation", Radio Sci., **19**, pp 201-208, 1984.

[6] Gorgucci, E., V. Chandrasekar, and G. Scarchilli, "Radar and surface measurement of rainfall during CaPE: 26 July 1991 case study', J. App. Met., **34**, pp 1570-1577, 1995.

[7] −, and G. Scarchilli, "A robust estimator of rainfall using differential reflectivity", J. Atmos. And Oceanic Tech., **11**, pp 586-592, 1994.

[8] Hubbert, J. and V.N. Bringi, 'An iterative filtering technique for the analysis of co-polar differential phase and dual-frequency radar measurements", J. Atmos. Oceanic Tech., **12**, pp 634-648, 1995.

[9] Kelsh, M., "An evaluation of the NEXRAD hydrology sequence for different types of convective storms in northeastern Colorado", Preprints, 24th Conf. on Radar Met., Tallahassee, FL, Amer., Met. Soc., pp 207-210, 1989.

[10] Ryzhkov, A.V. and D.S. Zrnic, "Comparison of dual-polarization radar estimators of rain", J. Atmos. and Oceanic Tech., **12**, pp 249-256, 1995.

[11] Zawadzki, I.I., "On-radar raingauge comparison", J. App. Met., **14**, pp 1430-1436.

Table 2. Radar Algorithms of Rain Rate (mm hr⁻¹) & Fractional Standard Error (%)

Algorithm	FSE (%)					
	20 June 1994 #1 radar/gauge	20 June 1994 #2 radar/gauge	2 June 1995 radar/gauge	2 June 1995 radar/radar	6 July 1996 radar/gauge	6 July 1996 radar/radar
R(Kdp)	10.80	10.72	11.27	13.78	06.13	12.18
R(Kdp,Zdr,1)	48.42	18.39	10.99	10.91	19.87	25.58
R(Kdp,Zdr,2)	44.81	25.00	17.61	16.07	33.69	37.34
R(Zh)	57.64	43.73	33.28	35.58	35.11	35.44
R(Zh,55)	-	-	-	-	-	35.41
R(Zh,53)	-	-	34.81	36.44	27.36	30.45
R(Zh,51)	-	-	39.45	41.85	30.16	31.83

note: Algorithms are as defined in Table 1. Dash indicates entry is the same as the above previous value.

Non-Uniform Beam Filling Correction for Spaceborne Rain Radar Measurement: A simulation Study Using Shipborne Radar Data over Tropical Pacific

Toshiaki Kozu and Toshio Iguchi
Communications Research Laboratory
4-2-1 Nukui-kita, Koganei Tokyo 184 Japan
Phone: +81-423-27-7543, Fax: +81-423-27-6666, e-mail: kozu@crl.go.jp

Abstract -- A method to correct spaceborne rain radar measurement for non-uniform beam filling (NUBF) is studied using a shipborne radar data set over tropical Pacific. Statistical analyses are made on spatial variabilities of rain rate. The result is reflected into estimating the variability in a radar IFOV which is then used to obtain a NUBF correction factor. Results indicate the usefulness of this method for reducing bias error in rain rate estimation.

INTRODUCTION

It is well known that the non-uniform beam-filling (NUBF) is a major error source in rainfall measurement with a spaceborne rain radar the foot-print size of which may be comparable to or greater than a typical convective cell size. The effect of NUBF depends on the algorithm used for a rain-parameter estimation. It has been shown that the use of the path-integrated attenuation (PIA) derived from the surface reference target (SRT) method suffers from stronger effect than the use of a Z-R relation [1,2]. However, the SRT method is also recognized as the most important algorithm to stabilize the rain attenuation correction in heavy rain. It is crucial to develop a method to correct the SRT-derived PIA for the NUBF effect.

We proposed a method for correcting the SRT-measured PIA for NUBF, and studied its feasibility using shipborne and ground-based radar data obtained in the TOGA/COARE campaign [3]. This method is based on a characteristic of spatial variability of rain rate, which has been used for the SSM/I rain retrieval algorithm [4]. In this method, the key point is to estimate the fine-scale rain rate variability (normalized standard deviation, NSD, NSD_H; SD divided by mean) in an instantaneous field-of-view (IFOV) from the large-scale NSD (NSD_L) that can be measured by radar. The concept of this process is shown in Fig. 1. The NSD_H in IFOV ($i = 5$) is estimated from the NSD_L obtained from the radar data measured at IFOVs ($i = 1$ - 9).

This paper presents a follow-up study of this method using a more comprehensive data set for statistical evaluation of this correction method.

FORMULATION OF THE PROBLEM

Referring to Figure 1, let R_i ($i = 1$ - 9) be the IFOV-averaged path-averaged rain rate which consists of n rain rate elements ($r_{j,i}, j = 1, n$) within the IFOV:

$$R_i = \sum_j r_{j,i} / n \qquad (1)$$

The path-integrated attenuation we should obtain when rain is uniform in the IFOV, A_i (dB), is:

$$A_i = 2L \, \alpha R_i^{\beta} \approx 2L\alpha R_i \qquad (2)$$
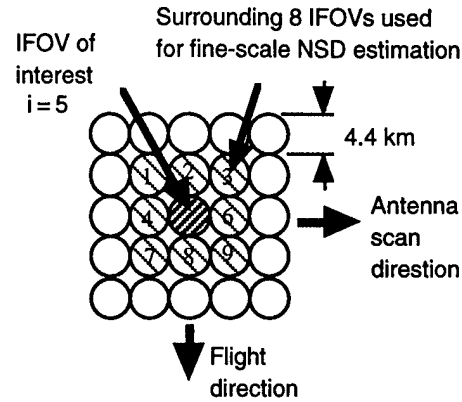
Fig. 1 Concept of estimating fine-scale variability from large-scale one

where α and β are coefficient and the exponent of the k-R relation, and L is the rain depth. The exponent β depends upon the frequency and dropsize distribution, but fairly close to unity for the frequency range of interest (10 - 35 GHz). Similar to $r_{j,i}$, PIA element $a_{j,i}$ is expressed as

$$a_{j,i} = 2L \, \alpha \, r_{j,i}^{\beta} \approx 2L\alpha \, r_{j,i} \qquad (3)$$

The SRT-measured PIA (A_m) is given by

$$A_{m,i} = -10\log(\sum_j \exp(-\ln 10\alpha \, r_{j,i} \, L/5)) \qquad (4)$$

The $NSD_{H,i}$ is given by

$$NSD_{H,i} = \left[(1/n)\sum_j (r_{j,i} - R_i)^2 \right]^{1/2} / R_i \qquad (5)$$

As an estimate of NSD of spatially averaged rain rate (NSD_L), we use samples of A_m surrounding the IFOV of interest ($i = 5$) as shown in Fig. 1.

$$NSD_L = \left[(1/n)\sum_i (A_{m,i} - <A_m>)^2 \right]^{1/2} / <A_m> \qquad (6)$$

where $<A_m>$ is the average of $A_{m,1}$ through $A_{m,9}$. Note that $A_{m,i}$ and NSD_L can be obtained from spaceborne radar measurement. First we estimate $NSD_{H,5}$ from NSD_L. Next, we estimate A_5 from $A_{m,5}$ and $NSD_{H,5}$ using a relation between $A_{m,5}$ and A_5 for a given $NSD_{H,5}$ assuming a pdf model within the IFOV.

RAIN RATE VARIABILITY

We may expect that, if we see high variability in large-scale rain field, fine-scale variability is also high. Such a correlation may be related to the statistical properties of spatial variability of rain rate. The statistical properties are

studied using 42 rain fields that are classified into four categories; Type-1 (squall line system), Type-2 (randomly spread convective), Type-3 (wide-spread stratiform), and Type-4 (mixed stratiform/convective).

To characterize the spatial variability of rain rate, the spatial auto-correlation function (ACF) is calculated. If the ACF is stable, it is expected that the magnitudes of fine-scale and large-scale rain rate variabilities is also stable. It is found that the 1-D normalized auto-correlation function, $\rho(x)$, obtained from the averaging of the values of a 2-D auto-correlation function at an equi-distance, x, is well approximated by

$$\rho(x) = \exp(-ax^b). \tag{7}$$

From regression analyses of all rain fields, a and b values and the correlation distance, x_{dec} (the distance at which $\rho(x_{dec})$ is e^{-1}) are obtained. Results show that a, b, and x_{dec} vary significantly, and x_{dec} somewhat correlates with the coefficient c relating NSD_H to NSD_L (Eq.8).

For each rain field, pairs of NSD_H of rain rate and NSD_L of A_m are calculated, and a regression analysis is performed to relate NSD_H to NSD_L with

$$NSD_H = c\ NSD_L \tag{8}$$

The results for Types 1, 2, and 4 are shown in Fig. 2, in which correlation coefficient (r) and the coefficient c are shown as histograms. It is found that there is a reasonable degree of correlation between NSD_H and NSD_L, and that c is fairly stable. As for stratiform rain, r and c are slightly lower than convective rain, suggesting the necessity of classifying rain type in the NUBF correction.

It is known that the probability density function (pdf) of rain rate is well approximated by a log-normal distribution combined with a delta function representing "no rain" region, when the area is sufficiently wide. In this case, however, the area of interest is as small as several tens of square kilometers, and the pdf may not be stable enough to apply a single pdf model. To investigate the log-normality

of such area, χ^2 tests are applied for 7km by 7km rainy areas in each rain field. Percentage of areas judged non-lognormal is a measure of non-lognormality of the rain field. The result is summarized in Fig. 3. For convective rains, about half the areas appear to be judged non-lognormal as anticipated. For the simulation described later, however, we assume the log-normal pdf for simplicity. More study is needed for the statistical characterization of rain field within the spatial domain related to the problem we consider here.

SIMULATION OF NUBF CORRECTION

Using the relationship between NSD_L and NSD_H (Eq.8, with $c = 0.73$), a simulation is performed. A flowchart of the simulation is shown in Fig. 4. we start with the conversion of the 1-km spatial resolution Z-factor map to the corresponding rain rate and PIA. Next, we calculate the rain rate and PIA of 4-km resolution. At the same time, we calculate NSD_H using Eq. 5 and NSD_L using Eq. 6. The simulation starts with looking at the radar measurement (A_m) of each IFOV. For a specific IFOV, we obtain A_m and NSD_L. The NSD_L is then converted to NSD_H using Eq.8. A_m and the estimated NSD_H are input to the look-up table to obtain a corrected A_m (an estimate of A). This result is finally compared with the "uniform" PIA (A) directly calculated from the 1-km resolution data.

An example of the simulation result is shown in Fig.5, where scattergrams of (a) "Uniform" PIA (A) vs "Apparent" PIA (A_m), (b) A vs. NUBF-corrected PIA using NSD_H estimated from NSD_L, and (c) A vs. NUBF-corrected PIA with "true" NSD_H are plotted. It is clear that the NUBF correction reduces bias errors; however, some "over-correction" appears in some cases.
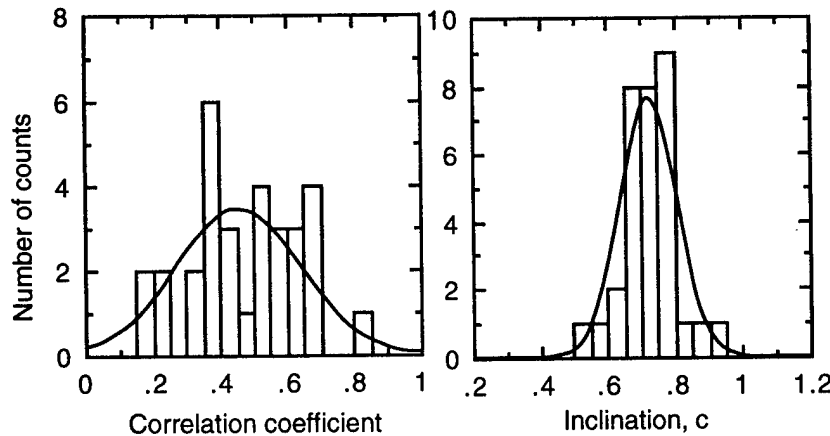
Fig. 2 Results of linear regression analysis of NSD_H vs. NSD_L relation for Type 1, 2 and 4 rains. (Rain rate corresponding to $A_5 > 5$ mm/h)
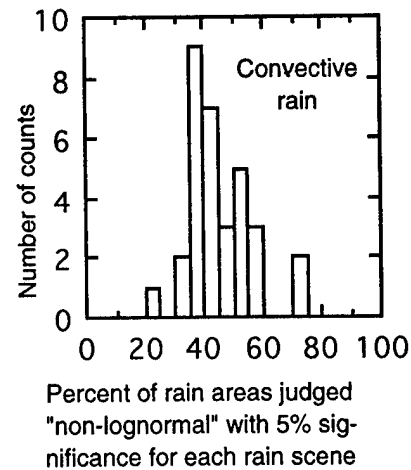
Fig. 3 Result of χ^2 test to evaluate "non-lognormality" of rain rate pdf.

When we use "true" NSD_H, random errors in the corrected PIA are reduced; however, there remains some underestimation. This is probably due to the assumption of log-normal pdf. In Fig. 6, errors in estimating rain rate cumulative distribution (CDF) are compared. In this figure, the ordinate is the percent difference between the NUBF-corrected (or without correction) CDF versus "Uniform" PIA CDF. It is shown that the NUBF correction reduces the bias error except for very small PIA range (< 2 dB).

SUMMARY

The NUBF correction method presented here appears to work reasonably well to reduce the bias error. Care should be given, however, to the possible "over-correction" caused by the over-estimation of NSD_H. This method is currently implemented in the TRMM PR standard algorithm for range profiling [5]. The usefulness of this method in this algorithm needs to be evaluated.

REFERENCES

[1] K. Nakamura. *J. Atmos. Ocean. Tech*, **8**, 363-373, 1991.

[2] P. Amayenc, M. Marzoug and J. Testud. *IEEE Trans.*, **GE-31**, 417-425, 1993.

[3] T. Kozu and T. Iguchi. *IEICE Trans. Comm.*, **E79-B**, 763-769, 1996.

[4] C. Kummerow and L. Giglio. *J. Appl. Meteor.*, **33**, 3-18, 1994.

[5] T. Iguchi, T. Kozu, R. Meneghini and K. Okamoto. *IGARSS'97*, Singapore, 1997.
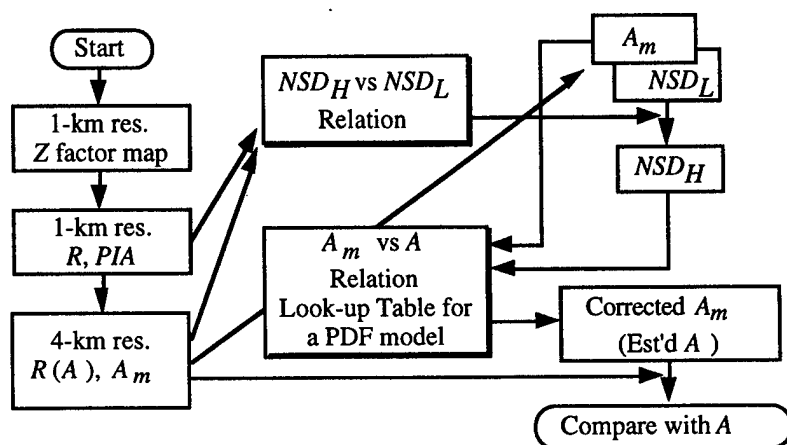
Fig.4 Flowchart of NUBF correction simulation.
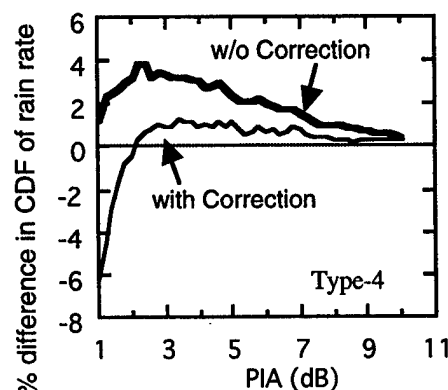
Fig.6 Errors in estimating CDF of rain rate.

Y = .259 + .814 * X; R=0.973

Y = .064 + .972 * X; R =0.981

Y = .195 + .91 * X; R = 0.992
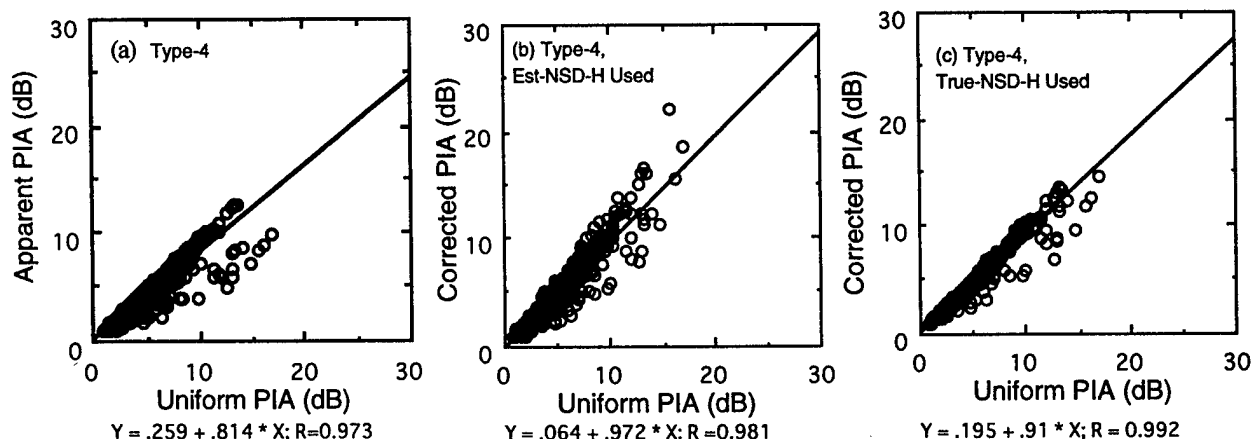
Fig.5 Results of NUBF correction for Type-4 rains: (a) "Uniform" PIA (A) vs "Apparent" PIA (A_m), (b) A vs. NUBF-corrected PIA using NSD_H estimated from NSD_L, and (c) A vs. NUBF-corrected PIA with "true" NSD_H.

Space-borne Remote Sensing of Cloud Liquid Water Content by Combined Radar-Radiometer*

Jinli Liu, Ling Zhang and Daren LU
LAGEO, Institute of Atmospheric Physics, CAS
Beijing, 100029, P.R. CHINA
Tel:86 10 62048922 Fax:86 10 62028604 Email:ludr@sun.ihep.ac.cn

Abstract -- In this paper, a retrieval method of remote sensing of cloud liquid water content by space-borne combined radar-radiometer is suggested. A 3-layer vertical cloud model is chosen to represent the typical stratified precipitating cloud. The retrieval method mainly follow our previously suggested scheme[1] with minor modification. Numerical comparative study shows that in space-borne remote sensing of liquid water content the combined method is much better than by radar only; Also the retrieval accuracy of liquid water content may increase when using the 3-layer cloud model in combined method.

INTRODUCTION

Global precipitation distribution at earth surface and vertical structure of precipitating cloud are of vital important in global energy and water cycle. It is well known that the global precipitation measurement can only be made from space. Passive microwave techniques such as SSMR and SSM/I have been used in global precipitation remote sensing with preliminary success. In principle it is very difficult to remote sensing the vertical structure of the liquid water content (LWC) in precipitating cloud. Combined radar-radiometer will be the best arrangement to solve this problem. For ground-based situation we have shown that remote sensing of precipitation and LWC distribution with a combined radar-radiometer system is better than that with only a radar[1,2]. In comparison with ground-based remote sensing of horizontal rainfall distribution where only the lowest part of cloud is concerned, space-borne remote sensing of precipitating cloud is necessary to consider the vertical structure of whole cloud, surface rainfall and surface situation. In this paper, we will discuss the retrieval method of space-borne remote sensing of precipitating cloud structure with combined radar-radiometer and give some preliminary simulation results.

CLOUD MODEL AND RETRIEVAL METHOD

Cloud Model

A three layer (ice layer, mixed layer and liquid layer) stratified cloud model is assumed. Fig 1. is a schematic view of the model which is deduced from the field observation of stratified precipitating cloud in China. H_1, H_4, H_3, H_2 are cloud bottom(for cloud with rainfall $H_1 = 0$), cloud top, height of -10 ℃ and 0.3 km below the freezing level respectively, H_3, H_2 are determined by radio sounding data, H_4 and H_1 may be obtained by radar observation.

Retrieval Algorithm

In the retrieval, reflectivity Z_e, attenuation coefficient σ_e are related in an empirical exponential manner. Those coefficient in the empirical relationship are different for different cloud particle size distribution (DSD). it is assumed that the fraction of cloud LWC/IWC (ice water content) Mq/Mi in mixed layer is known in prior.

The retrieval method suggested here is similar to the method for the situation of ground-based remote sensing described in detail in [1,2]. The main procedures are as follow: 1)We may derive the distribution of attenuation coefficient $\sigma(r)$ from radar reflectivity along ray path with empirical regressive relation $(Ze = c\sigma^d)$ between radar
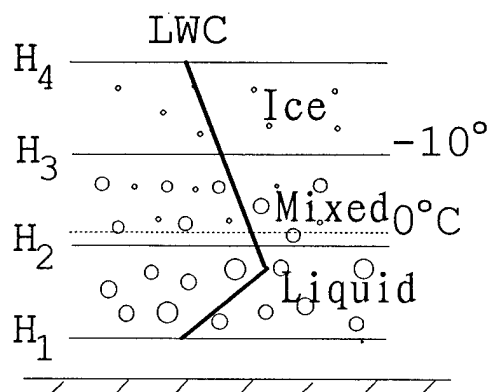
Fig.1 A schematic view of the stratified cloud model.

reflectivity and attenuation coefficient for liquid and ice droplet respectively; 2)Using MW radiative transfer model to calculate the brightness temperature Tb with $\sigma(r)$ from 1) and compare with observed Tb; 3) Adjust the derived $\sigma(r)$ by adjusting the empirical coefficient so as the calculated Tb approximating to observed Tb with in the required error; 4) derived LWC and surface rainfall R with respective relationships of $\sigma - M$ and $\sigma - R$. The details of this retrieval method can be found in our paper [1,2], the only difference is the constraint factor, we used total attenuation rather than the brightness temperature in that paper.

NUMERICAL SIMULATION AND RESULTS

By using radar equation and MW radiative calculation code, we may establish the 'observation' $Z_e(r)$ and Tb with input of different cloud parameters and surface condition.

In this calculation we choose calm ocean as ground surface and 9.364GHz (X-band) for the frequency .

Variations with Different Drop Size Distribution

From the field observations we know that in mature stage the LWC profile mostly has the pattern indicated in Fig. 2. Here we only consider this kind of LWC vertical profile. Four kinds of cloud drop size distribution are chosen: Type 1, M-P DSD in all three layer; Type 2, Γ DSD for ice droplets and M-P for liquid drop; Type 3, SS DSD for liquid drops derived from stratified precipitating clouds of South China, Γ DSD for ice droplets; Type 4, CS DSD for liquid drops derived from convective precipitating clouds of South China, Γ DSD for ice droplets.

For comparative study, with the original LWC vertical profile which we used in simulation procedure the one-layer structure and the single radar(without radiometer observation) method are also calculated. All the results show that the combined method is much better than single radar method; And the 3-layer model is better than the 1-layer for various drop size distributions. especially when the value of LWC is small.

For investigating the influence of drop size distribution, different type of DSD are chosen between the simulation and retrieval calculations. One of the results is given in Fig 2. it can be seen that 3-layer cloud model is much better than 1-layer, especially for mixed layer (4.6-6.8 km) and the ice layer (6.8-8.0 km).

The relative deviations of root-mean-square(rms) are given in Table 1. It shows that the accuracy of retrieval LWC can be increased when using combined method than single radar method , even comparing with the 1-layer structure, it may increase about 70 %; When we use 3-layer instead of 1-layer structure in combined method, the increased accuracy would be about 20-30 % .

Variation with the Fraction of Mq and Mi in Mixed Layer

As we know that to obtain the real fraction of Mq and Mi in the mixed layer is very difficult and it plays important role in measuring LWC with combined method.

We change the proportion of Mq and Mi in simulation and retrieval calculations, it is found that larger deviations exist in retrieving LWC vertical profile, especially when overestimated Mi is in retrieval calculation. For example, when Mi/Mq=1 is chosen in the simulation calculation and Mi/Mq=2 in retrieval calculation, the results are shown in Table 2. It is indicated that the deviations of 3-layer may increase, but it still better than 1-layer situation. When
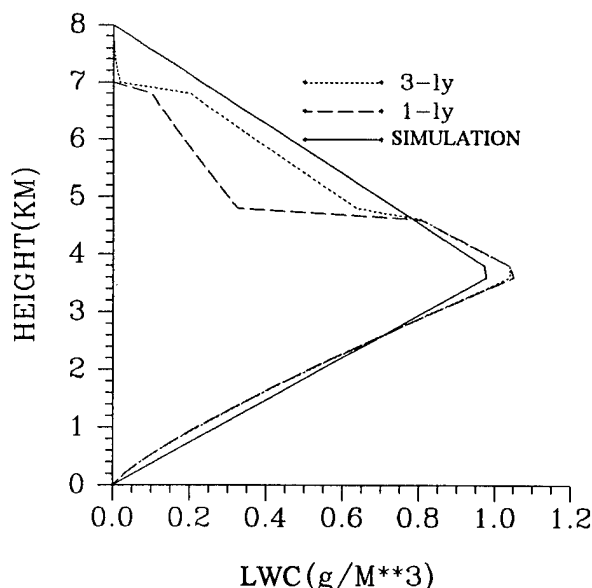
Fig.2 Vertical profile of LWC obtained with different cloud models,   Mq/Mi=1/1, $\overline{LWC}$=0.5 g/m^3. M-P DSD in simulation and CS DSD in retrieval.

Table 1. The relative rms deviation in LWC vertical profile calculation by 1-layer , 3-layer model with combined method and single radar method   for different $\overline{LWC}$, Mq/Mi=1/1, M-P DSD in simulation and Γ DSD in retrieval.

$\overline{LWC}$	0.1	0.2	0.3	0.4	0.5	0.6	0.7	0.8	0.9	1.0
1-ly	.491	.451	.443	.440	.438	.437	.437	.436	.436	.436
3-ly	.232	.169	.157	.152	.149	.147	.145	.143	.142	.140
radar	1.19	1.19	1.19	1.19	1.19	1.20	1.20	1.21	1.21	1.22

Table 2. Same as Table 1, but for Γ DSD, Mq/Mi=1/1 in simulation and Mq/Mi=1/2 in retrieval.

$\overline{LWC}$	0.1	0.2	0.3	0.4	0.5	0.6	0.7	0.8	0.9	1.0
1-ly	.424	.425	.425	.425	.426	.426	.426	.426	.425	.425
3-ly	.386	.383	.379	.374	.370	.370	.369	.367	.365	.363
radar	.425	.428	.433	.438	.445	.454	.464	.476	.490	.504

Table 3. Same as Table 1 but for Γ DSD, the difference of surface albedo is 0.01 between simulation and retrieval calculation.

$\overline{LWC}$	0.1	0.2	0.3	0.4	0.5	0.6	0.7	0.8	0.9	1.0
1-ly	.685	.442	.413	.410	.410	.412	.413	.415	.416	.417
3-ly	.732	.303	.178	.120	.088	.068	.055	.047	.041	.038
radar	.425	.428	.433	.438	.445	.454	.464	.476	.490	.504

Mi/Mq is taken as > 3 in retrieval calculation it is found that the rms of 3-layer model mostly larger than 1-layer structure. The reason is that, the retrieval method(retrieval calculation) is based on both radar return and radiative absorption of cloud particles, the contribution of ice particles to radar reflectivity is larger than water drops for the same LWC while the contribution of ice particles is smaller to radiative absorption. When Mi overestimated, through constraining the brightness temperature obtained by radiometer and radar reflectivity vertical distribution, it would result in larger overestimation of the retrieval LWC in the mixed layer, also in ice layer.

Variation with Surface Albedo

For understanding the influence of surface albedo , 0.01 difference of surface albedo is chosen between simulation and retrieval calculation, the results is given in Table 3. It shows that the rms versus LWC are very changeable by using combined method. When LWC is small, e.g. LWC=0.1g/m^3, the rms of 3-layer is larger than 1-layer and single radar method, but when LWC is getting larger the deviation of 3-layer may better than the others, when LWC $\geq$ 0.5 g/m^3, the deviation of rms may decrease to $\leq$ 0.8 %.

REFERENCES

[1]Liu, Jinli & Ling Zhang "Remote sensing of liquid water content with combined radar-radiometer system" ATMOSPHERIC RESEARCH, Elsevier,vol 34,pp 145-152, June 1994.

[2]Lu, Daren & Hai Lin "Comparison of radar and microwave radiometer in precipitation measurements and their use" Scientia Atmospherica Sinica, Vol.4, No.1, pp30-39, 1980

Attenuation Compensation Technique for an X-band Polarimetric Weather Radar

Gaspare Galati[1] , Gabriele Pavan[1] , Gianfranco Scarchilli[2]

[1]Università degli Studi di Roma "Tor Vergata" and Centro "Vito Volterra"
Via della Ricerca Scientifica 00133, Roma - Italy -
Phone: +39 6 72597417, Fax: +39 6 2026266, e-mail: galati@disp.utovrm.it

[2]Istituto di Fisica dell'Atmosfera CNR
Piazza L. Sturzo, 31 00144 Roma - Italy -
Phone: +39 6 59293026, Fax: +39 6 5915790

Abstract: There is an increasing interest for a low cost X-band radar systems to be used for urban rainfall monitoring, for airport weather surveillance or other short range purposes. However at X-band the reflectivity measurements are significantly affected by attenuation due to the precipitation, an attenuation correction is needed and some related techniques are described.

INTRODUCTION

In the modern applications of weather radar, the absolute and differential reflectivity techniques to improve the rainfall rate estimation are of increasing interest.

It is possible to estimate the rainrate using radar polarimetric observables, for example employing relationships between the rainrate r and the reflectivity factor Z_H and the differential reflectivity Z_{DR}, or between the rainrate r and the differential phase shift K_{DP}.

Existing X-band radar are not polarimetric but the low cost of RF components in this band makes an enhancement to dual polarization (H on transmit, H and V on receive) affordable in some cases. Even a coherentization can be proposed as a further enhancement.

However at X-band the reflectivity measurements (absolute Z_H and differential Z_{DR}) are significantly affected by attenuation due to the precipitation [1]. In fact experimental measurements have shown that the absolute specific attenuation (one way) at horizontal polarization α_H and differential specific attenuation α_D are around 0.37 dB/Km and 0.06 dB/Km respectively when the rainfall rate r is equal to 20 mm/h and increase to 1.2 dB/Km and 0.22 dB/Km for $r = 50$ mm/h.

A computer simulation has been carried on to evaluate the sensitivity of attenuation correction algorithms based on a cumulative scheme in which the absolute and differential attenuation, at n^{th} range cell, are estimated using the attenuation-corrected reflectivity at previous the cells [2].

The quantities α_H and α_D are estimated using a non linear best-fit with (Z_H, Z_{DR}), or, if phase measurements are available (i.e. the radar is coherent and has adequate processing) by linear best-fit relationships with the differential specific phase shift K_{DP}.

The propagation path is supposed equal to 20 Km, and a triangular rainfall path model has been considered to take account the variability of the rainfall rate along the horizontal direction. A comparison between the *true* profile, the *attenuated* profile and the *corrected* profile is shown.

METEOROLOGICAL RADAR OBSERVABLES

The meteorological radar observables are defined as follow [1]:

Rainfall rate (*mm/h*)

$$r = 0.6 \cdot 10^{-3} \cdot \pi \cdot \int D^3 \cdot v(D) \cdot N(D) \cdot dD \qquad (1)$$

Reflectivity at horizontal and vertical polarization (*dBZ*)

$$Z_{H,V} = 10 \cdot log_{10} \left[\frac{\lambda^4}{\pi^5 \cdot |K|^2} \cdot \int \sigma_{H,V}(D) \cdot N(D) \cdot dD \right] \quad (2)$$

Differential reflectivity (*dB*)

$$Z_{DR} = Z_H - Z_V \qquad (3)$$

Specific differential phase shift (*deg/Km*)

$$K_{DP} = \frac{180}{\pi} \cdot \lambda \cdot Re \left\{ \int \int \left[f_H(D) - f_V(D) \right] \cdot N(D) \cdot dD \right\} \quad (4)$$

Specific attenuation (*dB/Km*)

$$\alpha_{H,V} = 8.686 \cdot \lambda \cdot Im \left\{ \int \int f_{H,V}(D) \cdot N(D) \cdot dD \right\} \qquad (5)$$

Specific differential attenuation (*dB/Km*)

$$\alpha_D = \alpha_H - \alpha_V \qquad (6)$$

Where D is the equivolumetric spherical diameter of a raindrop.

In (1), (2), (4) and (5) $N(D)$ is the number of raindrops per unit volume per unit size interval (D to $D+\Delta D$) and can be adequately described by a Gamma model given by:

$$N(D) = N_o \cdot D^\mu \cdot exp\left(-\frac{3.67 + \mu}{D_o} \cdot D\right) \qquad (7)$$

where the parameter N_o, D_o and μ of the Drop Size Distribution (DSD) are made to vary over a wide range as suggested by Ulbrich [3].

In (1) $v(D)$ is the fall speed of raindrop. In (2) $\sigma_{H,V}(D)$ represent the radar cross sections at horizontal and vertical polarization respectively, λ is the wavelength and $K = \frac{m^2-1}{m^2+2}$ where m is the complex refractive index of water (for a fixed temperature). In (4) and (5) $f_{H,V}(D)$ are the forward scatter amplitudes at H and V polarization, respectively.

ATTENUATION COMPENSATION AND RAINFALL RATE ESTIMATION

The radar signal attenuation in the range direction is a cumulative process. Then the *measured* (*m*) reflectivity factor Z_H (*dBZ*) and the differential reflectivity Z_{DR} (*dB*) at the nth range cell are related to *true* (*t*) values as [4]:

$$\left[Z_H^{(m)}\right]_n = \left[Z_H^{(t)}\right]_n - 2 \cdot \sum_{i=1}^{n-1} \alpha_{H_i} \cdot \Delta x_i \qquad (8)$$

$$\left[Z_{DR}^{(m)}\right]_n = \left[Z_{DR}^{(t)}\right]_n - 2 \cdot \sum_{i=1}^{n-1} \alpha_{D_i} \cdot \Delta x_i \qquad (9)$$

where Δx_i is the length of the ith range cell, α_{H_i} and α_{D_i} are the specific attenuation (one way) at the ith range cell.

Using an iterative correction scheme the *attenuation-corrected* (*c*) values of the horizontal reflectivity and the differential reflectivity can be estimated as [4],[5]:

$$\left[Z_H^{(c)}\right]_n = \left[Z_H^{(m)}\right]_n + 2 \cdot \sum_{i=1}^{n-1} \hat{\alpha}_{H_i} \cdot \Delta x_i \qquad (10)$$

$$\left[Z_{DR}^{(c)}\right]_n = \left[Z_{DR}^{(m)}\right]_n + 2 \cdot \sum_{i=1}^{n-1} \hat{\alpha}_{D_i} \cdot \Delta x_i \qquad (11)$$

where $\hat{\alpha}_{H_i}$ and $\hat{\alpha}_{D_i}$ are the estimates of the specific attenuation:

$$\hat{\alpha}_H = a_1 \cdot 10^{a_2 \cdot Z_H} \cdot 10^{a_3 \cdot Z_{DR}} \qquad (12)$$

$$\hat{\alpha}_D = b_1 \cdot 10^{b_2 \cdot Z_H} \cdot 10^{b_3 \cdot Z_{DR}} \qquad (13)$$

where the reflectivity Z_H and Z_{DR} are in (*dBZ*) and (*dB*) respectively, while $\hat{\alpha}_H$ and $\hat{\alpha}_D$ are expressed in (*dB/Km*).

The coefficients of the equations (12) and (13) change with the temperature but their variation is not very large. In the following we will consider the coefficients at $T = 20\ °C$. Scarchilli at X-band has obtained:

$a_1 = 7.03 \cdot 10^{-5}$, $a_2 = 0.098$, $a_3 = -0.321$;
$b_1 = 8.38 \cdot 10^{-6}$, $b_2 = 0.1$, $b_3 = -0.278$.

The specific absolute and differential attenuation can be also estimated using the relations related to the differential phase shift K_{DP} as:

$$\hat{\alpha}_H = \gamma_1 \cdot K_{DP} \qquad (14)$$

$$\hat{\alpha}_D = \gamma_2 \cdot K_{DP} \qquad (15)$$

where K_{DP} is in (*deg/Km*). At X-band we have obtained $\gamma_1 = 0.1836$ and $\gamma_2 = 0.0319$.

In the iterative scheme for attenuation compensation the absolute attenuation and the differential attenuation at i^{th} range cell are estimated using *attenuation-corrected values* of the reflectivity factor and differential reflectivity related to the $(i-1)^{th}$ range cell. Then the first cell is not attenuated through the propagation path. After attenuation corrected reflectivity Z_H and Z_{DR}, the *corrected* rainfall rate (*mm/h*) is derived to apply the following relationship:

$$r = c_1 \cdot 10^{c_2 \cdot Z_H} \cdot 10^{c_3 \cdot Z_{DR}} \qquad (16)$$

where, at X-band: $c_1 = 9.1074 \cdot 10^{-3}$, $c_2 = 0.0984$, $c_3 = -0.4833$ with Z_H and Z_{DR} are in (*dBZ*) and (*dB*) respectively.

The rainfall rate can be also estimated using the best-fit relationship at X-band:

$$r = \gamma_3 \cdot K_{DP} \qquad (17)$$

where $\gamma_3 = 11.57$.

In the latter way the rainfall rate is estimated using a non attenuated radar observable. However it should be noted here that K_{DP} is composed by two terms related to the forward and to the back scattering; in this work the back scattering contribution is neglected. Moreover, K_{DP} estimates are poor in low Signal-to-Noise conditions.

In Fig. 1 are shown the Percent Error PE and the Fractional Standard Error FSE of (16) and (17).

RAIN MODEL AND ERROR SOURCES IN RAINFALL RATE ESTIMATION ·

The effectiveness of the correction technique for improving rainrate estimates is related to the rainfall path between measurement cell and radar. In our analysis we have considered a triangular rainfall path. In this model the rainfall rate along the propagation path has a triangular profile, where, along the path, the *Drop Size Distribution* parameters N_o and μ are varied randomly following the Ulbrich's range [3], while D_o is calculated from the inversion of the rainfall rate equation. In this model the rainrate is decorrelated from cell to cell.

The correction attenuation scheme above described is affected by a set of errors that we can classify as [6]:

- *Random error sources* related to the physical variability (DSD variation) and statistical variability of the radar observables.

- *Systematic error sources*, for example bias in the Z_H measurements related to the calibration system, or bias in the Z_{DR} measurements due to the mismatching between the radiation pattern at horizontal polarization and the one at vertical polarization.

In our analysis, to evaluate the best-fit relationship errors, the statistical signal fluctuations are neglected;. in any case these errors can be minimized using suitable time-space average. Then the random errors can be decomposed in:

1) best-fit (16) errors related to rainfall rate estimation; 2) best-fit (12), (13) or (14), (15) related to attenuation estimation; 3) best-fit relation errors related to attenuation estimated by attenuation corrected values of Z_H and Z_{DR} instead than by the true values.

We point out that the correction procedure is not a linear procedure, then the total error is not the sum of errors.

CONCLUSION

For X-band dual polarization radar we have analyzed by computer simulations an attenuation compensation techniques.

The iterative procedure to correct the radar observables Z_H, Z_{DR} from the absolute and differential attenuation is based on the best-fit relationships between (Z_H, Z_{DR}) or K_{DP} and the specific absolute and differential attenuation (α_H, α_D).

A triangular rain path model has been introduced varying the drop size distribution parameters (N_o, D_o, μ) from cell to cell. The *random* errors due to the variation of the DSD have been analyzed. Fig. 2 shown the comparison between the true profile and the attenuated and corrected profiles, the latter obtained using (12), (13) and (14), (15) to estimate the absolute and differential attenuation.

The results have been shown that the application of the attenuation compensation technique produces a negative bias in the rainfall rate estimation. The bias increases when the propagation path and the rainfall rate increase, while it is little sensitive to the number of cells along the propagation path with a fixed range.

In conclusion the examined attenuation-corrected technique based on Z_H, Z_{DR} measurements, generally, has shown a good behaviour. Operational limits are presented when the rainrate is very high, then, in this case, the best-fit relationships are affected by high errors. The direct use of K_{DP} (observable no affected by attenuation) to estimate the rainrate is useful particularly when the rainfall rate is very high.
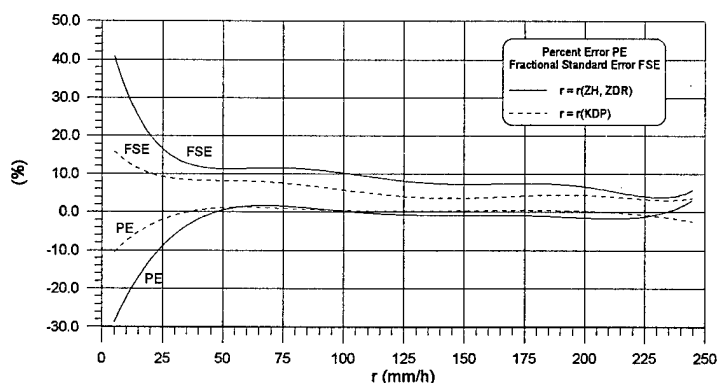
Fig. 1 Percent Error (PE) and Fractional Standard Error (FSE) of the rainfall rate estimation (16) and (17).
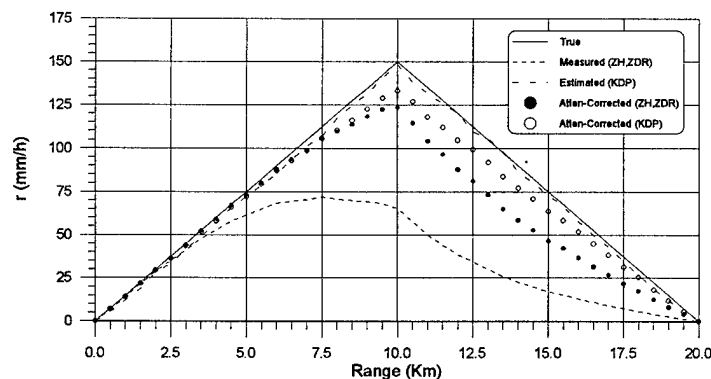
Fig. 2 Triangular rain profile: true; measured (16); estimated (17); corrected (16), (12), (13); corrected (16), (14), (15).

RFERENCES

[1] R.J. Doviak and D.S. Zrnic, "Doppler radar and weather observation", Academic Press, INC, 1984, pp. 39-42.

[2] K. Aydin, T.A. Seliga and Y. Zhao, "A self correction procedure of attenuation due to rain for C band dual linear polarization radars", 23rd Conf. Radar Meteorol., Amer. Meteor. Soc., vol. 3 pp. JP337-JP341, 1986.

[3] C.W. Ulbrich, "Natural variations in the analytical form of raindrop size distribution", J. Climate Appl. Meteor., vol. 22, pp. 1774-1775, 1983.

[4] E. Gorgucci, G. Scarchilli and V. Chandrasekar, "Radar and raingage measurements of rainfall over the Arno basin", AMS Conference on Hydrology, 15-20 January 1995, Dallas.

[5] G. Scarchilli, E. Gorgucci, V. Chandrasekar and T.A. Seliga, "Rainfall estimation using polarimetric techniques at C-band frequencies", J. of App. Meteor., vol.32, n.6, pp 1150-1160, 1993.

[6] G. Galati, G. Pavan, G. Scarchilli and E. Gorgucci, "Rainfall rate estimation using C-band dual polarisation radar: attenuation compensation technique", Proceedings of RADME96, Rome 11-12 June 1996, pp. 175-196.

Dual Polarisation and Multifrequency Measurements of Rain Rate and Drop Size Distribution by Ground-Based Radar and Radiometers

A. Hornbostel and A. Schroth

DLR, Deutsche Forschungsanstalt fuer Luft- und Raumfahrt
Institut fuer Hochfrequenztechnik
D-82230 Oberpfaffenhofen, P.O. Box 1116, Germany
. Tel.: ++ 49 8153 28 2318/2325, Fax.: ++ 49 8153 28
Email: achim.hornbostel@dlr.de, arno.schroth@dlr.de

B.G. Kutuza and A. Evtuchenko
Russian Academy of Sciences
Institute of Radio Engineering and Electronics
Moscow, Mokhovaya St. 11, Russia
Tel: ++7095 203 47 93, Fax ++7 095 203 84 14
email: kutuza@mail.cplire.ru, eandrey@mail.cplire.ru

Abstract -- Polarisation effects can be observed as well in radar as in radiometer data of stratiform and convective rain. These polarisation effects are due to different influences, e. g. the oblateness of large rain drops and path inhomogeneities. The dual polarisation technique is well known in radar meteorology. The emphasis in this contribution is therefore on the event based and statistical accuracy of the derived rain rate and on different sources of errors. In the passive remote sensing of rain the use of two polarisations is a new subject. By such measurements also drop size distributions can be derived, which improve the rain rate determination.

INTRODUCTION

Rain rate estimation by ground based weather radar is a widely used technique today. Although many operational radars still use only one polarisation, dual polarisation techniques have been developed and experimentally approved, which allow the determination of the shape, distribution and type of the hydrometeors, and finally the rain rate with more precision. However, there are a many sources of errors, which have to be taken into account carefully.

In the rain rate estimation by microwave radiometers there are two principle ways: absorption (emission) measurements using frequencies below 30 GHz and scattering measurements using higher frequencies up to 90 GHz. The second approach is in particular useful for spaceborne applications, where the reduction of the surface emission due to the scattering by rain or clouds can be measured. For ground-based applications with low background radiation from space the absorption technique seems to be preferable.

A dual polarisation technique for radiometers was developed in [1]. Similar to the radar differential reflectivity technique, the drop size distribution is determined, which allows then a more precise calculation of the rain rate or of propagation parameters along the path. Drop size
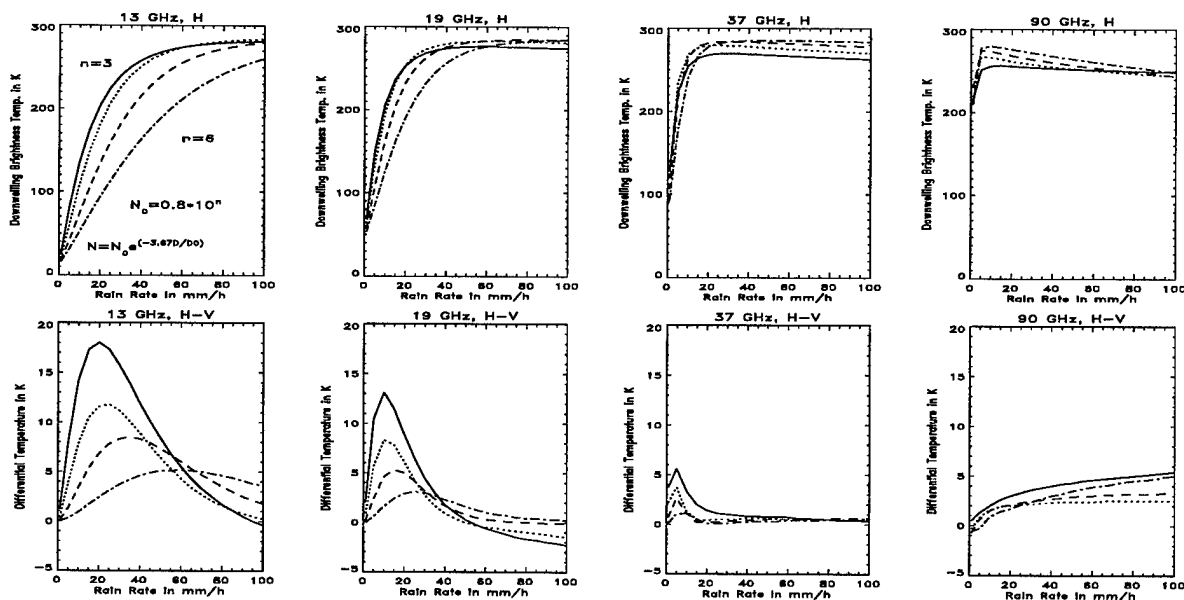
Fig. 1: Brightness temperature and differential temperature versus rain rate (elevation 27.3°, rain height 2.5km).

distributions, derived from such passive measurements, are coincident with radar and distrometer measurements [1]. The effectiveness of this technique is also demonstrated in this paper.

BRIGHTNESS TEMPERATURE AND DIFFERENTIAL TEMPERATURE

The dependence of brightness temperature (TB) and its difference between horizontal and vertical polarisation , the differential temperature ($TD = TB_H - TB_V$) was investigated by numerical solution of the vector radiative transfer equation. Fig. 1 shows downwelling TB and TD, which is seen by a ground based radiometer under an elevation of 27.3°. A plane-parallel rain slab with 2,5 km height and a temperature lapse rate of -6.5 K/km above a land surface with temperature 288 K and emissivity 0.96 was assumed. Absorption by water vapour and oxygen is included. The simulations have been carried out for oblate rain drops with Pruppacher-Pitter axial ratio and different two parameter drop size distributions of the form

$$N(D) = N_0 \exp(-3.67 D / D_0), \qquad (1)$$

where $N_0 = 0.8 * 10^n$ m^{-3}mm^{-1}. The parameter $n=4$, for instance, corresponds to the well know Marshall-Palmer distribution with $N_0 = 8000$ m^{-3}mm^{-1}. The curves show that

- TD can reach values up to 15-20 K at 13 and 19 GHz,
- TD decreases with frequency,
- the relations of TB and TD to the rain rate depend clearly on the drop size distribution,
- TB is saturated for rain rates higher 10 mm/h for 37 and 90 GHz.
- At 90 GHz TB decreases for high rain rates due to scattering effects, where TD slightly grows but still remains small.

DUAL POLARISATION TECHNIQUE

In the classical Radar dual polarisation technique, the drop size distribution parameter D_0 is derived from the differential reflectivity Z_{DR} and N_0 then with the aid of the effective reflectivity factor Z. For constant N_0 the rain rate is directly related to the second drop size distribution parameter D_0.

Fig . 1 shows that a similar approach is also possible for dual polarisation radiometer measurements. Although, here the differential temperature does not depend directly on D_0 but also on N_0, both parameters (or equivalently N_0 and the rain rate) can be determined, if TB and TD are measured simultaneously. Practically, this is done by a search and interpolation algorithm and a look-up table. The resolution and accuracy of this algorithm is best at 13 and 19 GHz up to rain rates of 30 - 40 mm/h, where TD has measurable values and a good sensitivity to the drop size distribution and TB is not saturated. For 37 and 90 GHz the values of TD are too small.
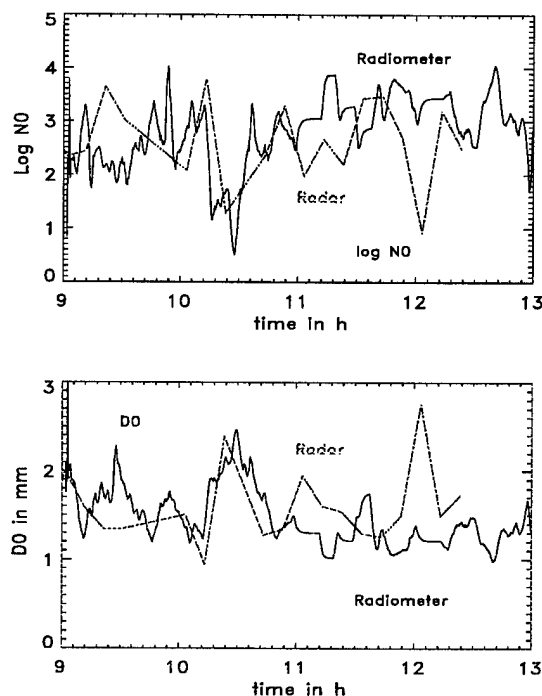
Fig. 2: Drop size parameters N_0 and D_0 for stratiform rain.

Fig. 2 represents an example of D_0 and N_0 for stratiform rain, which have been derived from radiometer measurements at 19 GHz, in comparison with path averaged values obtained from 5.5 GHz radar measurements .

RAIN RATE MEASUREMENTS

The effectiveness of the dual polarisation technique is demonstrated in Fig. 3. The rain rate was determined by the dual polarisation technique from 19 and 13 GHz radiometer data and are compared with the rain rate measured by a rain gauge located near the radiometer antennas. The rain rate was also calculated from TB only, assuming a Marshall-Palmer distribution with constant $N_0 = 8000$ m^{-3}mm^{-1}.

The figure shows a significant improvement of the rain rate estimation by the dual polarisation technique, in particular by the 13 GHz radiometer and for the second peak of rain rate. Comparing the 13 and 19 GHz results, one have to take into account the very different beamwidths of the two radiometers of 15° for 13 GHz and 1.2° for 19 GHz.

ERROR SOURCES

Calibration Errors
The calibration of the radiometer can be performed with a cold and a hot load or by clear sky measurements. In the first case the losses and mismatches of the connections from the load to the receiver must be measured exactly. These connections can change the effective temperature of a liquid nitrogen load by 10 K and more, respectively [2]. In the

1127
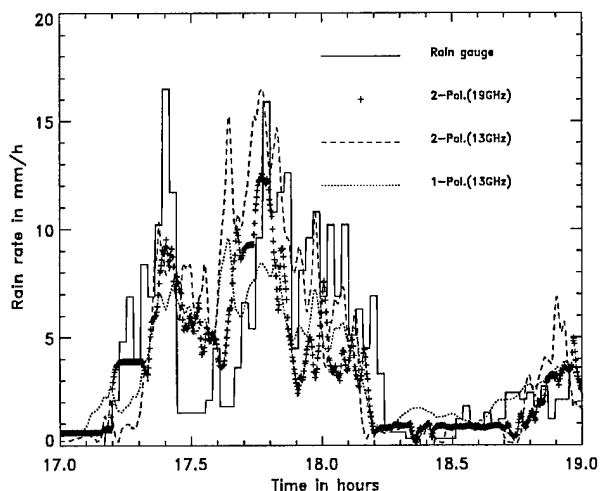
Fig. 3: Comparison of rain rate estimation by radiometers.

second case the reference temperature of the clear sky must be calculated with the help of models and meteorological information. The error can be reduced by performing clear sky measurements at different elevations. By a combination of the different methods, accuracies of 1 K for the absolute and differential temperature are possible [2].

For the calibration of the radar constant and radar polarisation states often a metallic sphere is used as a target. For the differential reflectivity a calibration accuracy of 0.1 dB is possible. However, due to uncertainties about the antenna gain, transmit power, antenna pattern and internal calibration of the amplifiers, the overall accuracy of the radar constant and the effective reflectivity factor is only 1-2 dB. Therefore, the radar may be additionally (or alternatively) calibrated statistically by comparison with rain rate measurements.

Instrument Errors

Even with a good calibration errors can occur due to statistical signal fluctuations, non-perfect linearity of the amplifiers and quantisation effects in the signal processing chain. A major source of errors are also instrument instabilities, e. g. temperature drifts of the amplifier coefficients, if there is no good temperature stabilization.

Path Inhomogeneity and Beam Filling

Radiometers measure integral values of the emission along the total path through the atmosphere. Therefore, when comparing point rain rates measured by a rain gauge with radiometer measurements, the agreement will be best for homogeneous paths. For rain rates above 10 mm/h, normally rain cells exist with dimensions smaller than the path length. If a rain cell is located near the antenna and fills the total antenna beamwidth, the rest of the path do not contribute much and the error will be small. On the other hand the radiometer can detect rain cells, which do not pass the rain gauge.

For the radar, the problem of path inhomogeneity exists on a first view only, if the rain rate is inhomogeneous within the scale size of the radar pulse volume. However, when the average rain rate along the radar beam (path) or a radar scan volume is compared with a rain gauge, similar problems as for the radiometer exist.

Model Errors

For the conversion of brightness temperature to rain rate a plane-parallel atmosphere was assumed here. Besides the problem of the path inhomogeneity the rain height (altitude of the rain area above ground) must be estimated, which is probably the major error source of the model. Other error sources are connected with the modeling of the hydrometeors itself, e.g. their shape and orientation. Also the two parameter drop size distribution is only an approximation.

It has been found that the distribution of the drop canting angle (even with a zero mean) reduces the measured Z_{DR} values and leads to values of N_0, which are too high. Also the existence of hail or other hydrometerors can produce large errors in the radar rain rate, if they are not detected and not taken into consideration [3]. The radiometric emission measurements seem to be less sensitive to these types of errors in comparison to the radar backscatter measurements.

CONCLUSIONS

The performance of rain rate estimation by radiometers shows the same (or even better) accuracy than radar measurements. Both active and passive dual polarisations measurements allow the determination of the drop size distribution. The knowledge of the drop size distribution can improve the rain rate estimation significantly. Additionally, it opens the door to many other applications, e. g. the complete transmission matrix of a path including differential propagation parameters like differential attenuation and XPD can be calculated for satllite communication links.

Radar measurements provide a good spatial resolution and can cover large areas. In contrast, the advantages of the radiometer measurements are high temporal resolution and their principal simplicity. By combining dual polarisation and multi-frequency measurements the accuracy of the rain rate estimation by radiometers may be still improved.

REFERENCES

[1] A. Hornbostel, A. Schroth and B. G. Kutuza, "Polarimetric Measurements and Model Calculations of Downwelling Rain Brightness Temperatures," Microwave Radiometry and Remote Sensing of the Environment, VSP 1995, pp. 242-252.

[2] OPEX Reference Book on Radiometry and Meteorological Measurements, WPP-083, 1994, pp. 44-47.

[3] A. Hornbostel, and A. Schroth, "Statistical and Event Based Analysis of 20 GHz Attenuation on the Earth-Olympus Path," ICAP 1993, Conf. Proc No 370, Part 1, pp. 131-134.

Indian Doppler Weather Radar System-An Overview

G.Viswanathan & Members of Project Team
Doppler Weather Radar Project
Indian Space Research Organization(ISRO)
ISRO Telemetry Tracking & Command Network(ISTRAC)
Peenya Industrial Estate,Peenya ,Bangalore -560058,India
Telephone:#91-80-8394261,Fax:#91-80-8398257, e mail:geevee@hotmail.com & geevee@istrac.ernet.in
and
R.C.Bhatia, V.P.Kamble, .& S.Rajesh Rao
India Meteorological Department
Mausam Bhavan,Lodhi Road,New Delhi-11003,India
Phone;#91-11-4611451,Fax:#91-11-4699216.

Abstract --India Meteorological Department (IMD) is the nodal agency for weather service in India.IMD Operates a chain of conventional weather radars along the peninsular coastline for the Cyclone detection & charecterization of severe weather.This chain of Cyclone Detection Radar (CDR) systems is now being replaced by Pulse Doppler Radar systems known as Doppler Weather Radar (DWR) systems.As part of this program IMD entered into a Memorandum of Understanding with the Indian Space Research Organisation (ISRO) for the design, development and commissioning of an operational DWR system.The overall system level and detailed subsystem level specifications for this radar were arrived at by IMD & ISRO after detailed deliberations with experts in the fields of radar meteorology and radar system design.This paper describes the salient features of the Indian Doppler Weather Radar.

INTRODUCTION

IMD has a distinguished service spanning two centuries providing weather forecasts & severe weather alerts over peninsular India.Cyclonic storms especially over the east coast of India cause wide spread damage & destruction to life & property. Radar systems have played a major role in charecterisation of cyclones & other severe weather systems.Use of radar systems for this purpose is well established & documented[1],[2].Advances in Pulse Doppler Radar systems made them ideal choice for severe weather charecterisation.Development & operationalisation of WSR-88 (also known as NEXRAD) by National Weather Service(NWS) in USA, has set the trend for the use of Doppler Weather Radar for operational weather forecasting. An inter agency program between IMD & ISRO was initiated to design & develop a Doppler Weather Radar System in S band to meet the specific requirements of IMD in the area of Cyclone detection & charecterisation of severe weather systems.Based on the sytem level performance specifications,and subsystem requirements projected by IMD, the DWR Project team at ISRO/ISTRAC carriedout a detailed design study. After detailed design review by a committee of experts the DWR system is being realised to be integrated,tested & commissioned by the first quarter of 1999, thus making it a Weather Radar for the 21st century.The following is an overview of this DWR system:

SYSTEM SPECIFICATIONS & FUNCTIONAL REQUIREMENTS

Table 1 summarises the system level performance specifications.

Table.1

	Reflectivity	Velocity	Sp Width
1. Range (Km)	500	250	250
2. Resolution (m)	300	300	300
3. Accuracy @23 dBZ @ 2 rpm	2 dB	1 m/s	1 m/s

Unambiguous maximum velocity ± 30 m/s for 125 Km
Ambiguity Resolution techniques to extend velocity to ± 60 m/s for 125 Km or ± 30 m/s for 250 Km.

DOPPLER WEATHER RADAR SYSTEM DESCRIPTION

With the design approach adopted the DWR system was configured as shown in Fig.1. DWR employs a low sidelobe antenna enclosed in a rigid spherical radome employing curved sandwich panels.Radome is designed to withstand winds of 200Km/hr gusting to 300Km/hr.The antenna drive system employs a position loop servo with digital compensator to provide accurate scan functions including a programmable volumetric scan.Provision for vertical scan at selected Azimuth can generate quick RHI display. A coherent transmit / receive system employs a master reference oscillator with very low phase noise,to phaselock the COHO & STALO synthesisers.Transmitter waveform selected for a given observation is modulated on the buffered COHO , upconverted & given to the transmitter input. Transmitter with a hard tube modulator employs a klystron as power amplifier to generate a nominal peak power of 1MW,with an average power around 2KW.Receiver with LNA (~1dB NF)
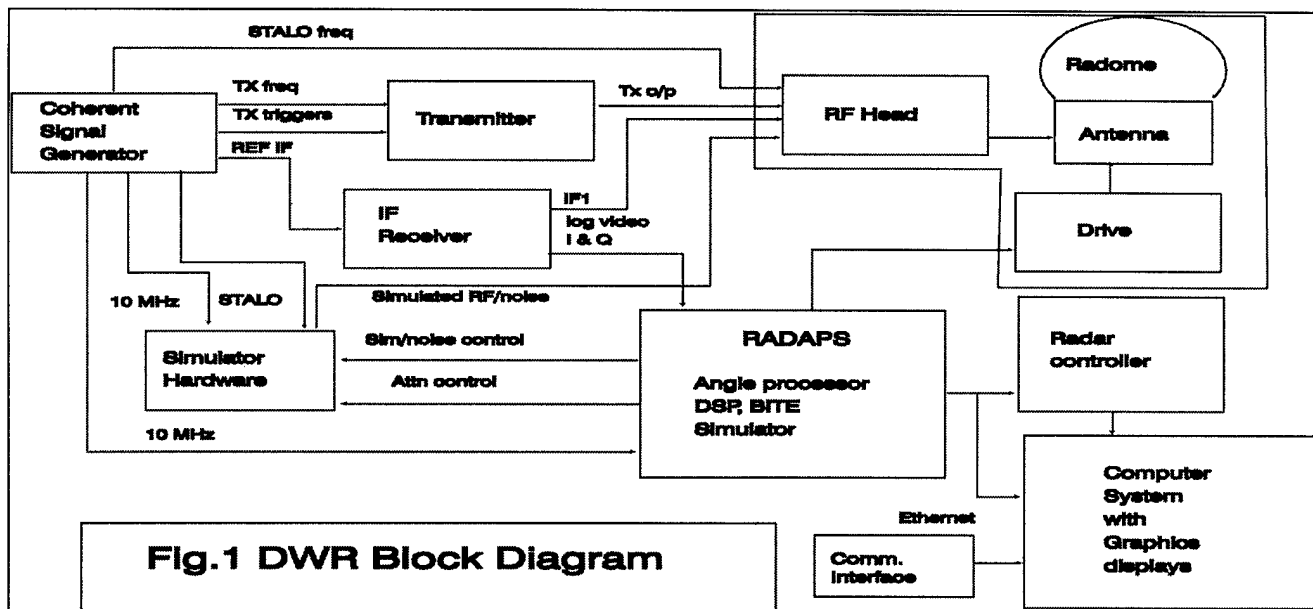
Fig.1 DWR Block Diagram

and a mixer preamplifer located along with TR limiter right at the antenna hub provides a sytem noise temperature close to 300 Kelvin. IF portion of the receiver is split into LOG & LINEAR channels.LOG channel is used to cover the entire dynamic range of 95 dB and provide a control voltage to set the IAGC to the proper level to avoid saturation of the LIN channel. I & Q outputs of the LIN channel are digitised with 14 bit resolution Data & fed to a modular DSP system to derive base products,viz the three moments of the time series,thus providing signal power,mean Doppler & spectrum width. DSP is programmable to provide the moments either directly using the popular Pulse Pair algorithm,or in certain special situations by obtaining power spectrum using FFT.Provision exists to dispaly the base products on the graphical workstations or on a simple PC monitor.

RADAR DATA ACQUISITION AND PROCESSING SYSTEM

The DSP subsystem uses PCI bus compatible boards for the ADC and DSP and these boards are pluggable on to a general purpose PC. This option is cost-effective and also uses the PCI bus which is prefered for I/O applications due to its bandwidth and throughput capabilities. The Computer System for the Doppler Weather Radar uses the distributed computing environment in which a powerful file server is connected to three workstations on a high speed Ethernet bus along with a Radar Controller and the Radar Data Acquisition & Processing System (RADAPS) as in Fig.2. The Radar Controller is a PC which provides the graphical use interface (GUI) for the operator to operate the radar. The data acquired and processed by the RADAPS is sent to the server which in turn makes the data available on the ethernet to the workstations for displaying higher order data products.Server maintains the data archive. Options exist for the user to further process the data and display any· of the

Data Products on a remote workstation. The Data Products are classified as follows.

1. Base Products ---- Z, V and σ
2. Primary Products
   a) X-Z cross-section
   b) CAPPI (Constant Altitude PPI)
   c) Echotop image display
   d) Rainfall intensity
   e) Rainfall Accumulation
   f) Vertically Integrated Liquid Water Content
   g) Hail Warning
   h) Velocity Volume Products
3. Derived Products.
   a) Track Forecast
   b) Height of Tidal Waves
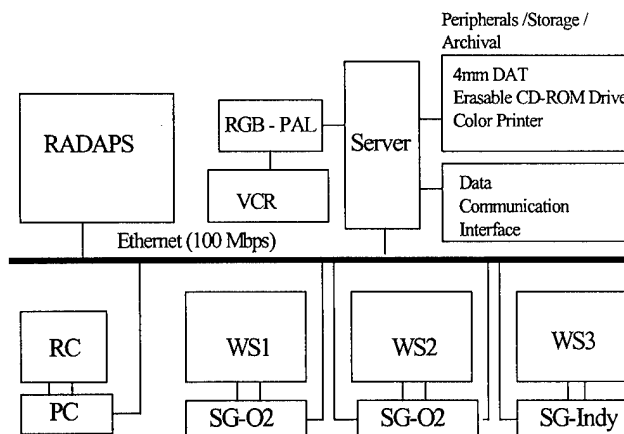
Fig.2 Computer System for DWR

SYSTEM PERFORMANCE SIMULATION

Overall system performance was evaluated for different precipitation levels using the classical PROBERT JONES equation. The resultant signal to noise ratio as a function of slant range for different values of reflectivities is plotted in Fig 3. Estimation of accuracies for measurement of reflectivity , Mean Doppler velocity & Spectrum width for antenna rotation at 2 rpm were made for relevant prf values using estimators given by Doviak & Zrnic[2]. Results are tabulated as Table.2. It can be seen that the accuracies meet specifications.

Table -2.

PRF	Std deviation m/s at SNR of	
	0 dB	20 dB
250 Hz	1.02	0.5
1200 Hz	0.93	0.44

SCAN STRATEGIES

Scan strategies are worked out for three typical cases and are shown in Table.3. Presently a two prt/prf method for resolving Range - Doppler ambiguities is effected.Efforts are on to include a phase coded waveform which can yield better resolution of such ambiguities.

Table 3

Parameters	Severe Weather	Precipitati-on	Cyclone
El steps	15	5	3 , 15
Total time	5 min	2 min	i) 1 min ii) 5 min
AZ Rate	3 rpm	3 rpm	3 rpm
PRF	i) 1200 Hz ii) Dual PRF 800 Hz, 600 Hz	250 Hz	i) 250 Hz ii)Dual PRF 600 Hz, 450 Hz
Pulse Width	2 μ sec	2 μ sec	1 or 2 μ sec
Data Products	Base Products Echo top VIL, Hail Severe weather probability, storm track CAPPI X-Z cross section	Base Products VIL, Hail Echo top Strom track CAPPI X-Z cross section	i)Precip products ii)Volume scan products

PROJECT TEAM

DWR Project is an interagency program between ISRO & IMD.Different subsystems are subcontracted to work centres like Society for Advanced Microwave & Electronic Engg & Research, Indian Institute of Technology, Electronics & Radar Development Establishment, National Aerospace Laboratory and Thumba Equatorial Rocket Launching Station, System design & Engg being the responsibility of ISRO-ISTRAC.
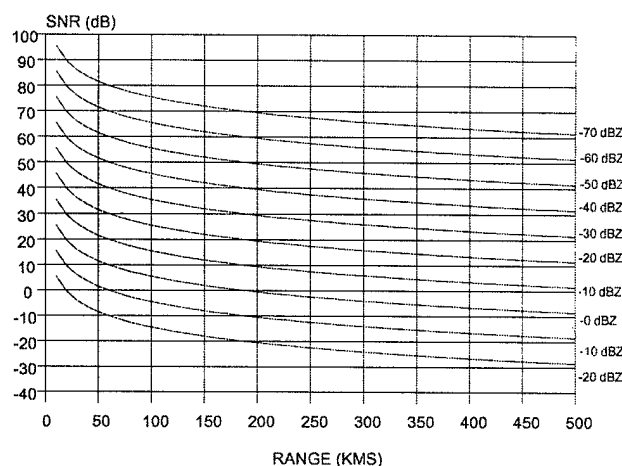
Fig 3.

REFERENCES

[1].D.Atlas, "Radar in Meteorology", American Meteorological Society, Boston, 1990.

[2]. R.J Doviak and D.S Zrnic, "Doppler Radar and Weather Observations", New York: Acadamic, 1993.

Simulation of Close-In & Stand-Off Mine Detection

Anh H. Trang
US Army CECOM, Night Vision & Electronic Sensors Directorate, AMSEL RD NV CD MD
10221 Burbeck Rd Suite 430, Ft. Belvoir VA 22060-5806
Tel: (703) 704-2456/ Fax: (703) 704-2467/ Email: atrang@nvl.army.mil

Henry G. Irion, Jr.
George Mason University
21830 Atlantic Blvd., Dulles VA 20166
Tel: (703) 406-5848/ Fax: (703) 406-5579/ Email: hirion@osf1.gmu.edu

Abstract -- A simple model for normal incident angle and close-in detection was developed and presented at the SPIE conference in 1996. Complex models that include normal and oblique incident angles and stand-off detection are included in this paper. The models and algorithms are based on electromagnetic and radar equations. Electromagnetic equations determining transmission and reflection coefficients, attenuation factors, and wave numbers, as well as radar equations involving power and radar cross-section are used in the simulation. Variables included in the models are operating frequencies, three and four boundary models, two detection techniques, four mine types, different environments, and four incident angles.

INTRODUCTION

The purpose of this paper is to model the detection of buried metallic and non-metallic land mines in snow and ice as well as in dry and moist soil, while attempting to simulate some of the real conditions that an actual detector, using monostatic Ground Penetrating Radar (GPR), might encounter. A detection algorithm is designed and implemented using the engineering programming software MATLAB.

The mine detection process is simulated by using the concept of pulse transmission, reflection and attenuation in each medium. Each medium layer, through which the transmitting signal pulse propagates, is modeled as a characteristic impedance, derived from the electrical properties of that medium. Then reflection and transmission coefficients are calculated based on these impedances and the attenuation constant is calculated using the properties of the medium.

Simulations are presented for a GPR radiating into a three- boundary (antenna/air, air/soil, soil/mine) and a four-boundary (antenna/air, air/snow, snow/soil, soil/mine) environment. Both near-field (close-in) and far-field (stand-off) techniques consider four anti-tank mines: two non-metallic and two metallic. Operating frequencies in the range from 200 MHz to 4 GHz (200 MHz incremental step) and four incident angles: 0^0 (normal), 30^0, 60^0, and 90^0 are considered.

CONCEPTS

Simulation techniques for near-field and far-field mine detection are modeled mainly by using the concept of pulse reflections and transmissions at surface boundaries and pulse attenuations in the media through which the signal propagates. The main difference between the two techniques is the calculation in air medium (i.e., between the antenna and ground).

Assume as illustrated in Fig. 1, a monostatic GPR looks directly into multi-layers of different materials such as air, snow or ice, soil and a mine.
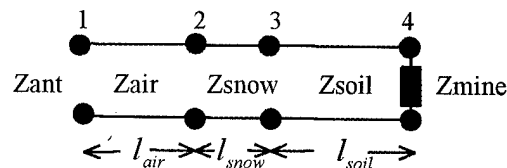
Fig. 1. An analogous transmission line with load

According to the model, a GPR produces a short pulse of magnitude $V_{Initial}$ which propagates along the transmission line as indicated in Fig. 1. At each junction, an incident pulse splits into reflected and transmitted pulses. The magnitude of the pulses after each encounter with each junction is indicated by τ and ρ the transmission and reflection coefficients. For example, the pulse traveling sequentially through each junction from the antenna to the mine and back to the antenna has a magnitude of $(\tau_1 \tau_2 \tau_3 \rho_4 \tau_{3'} \tau_{2'} \tau_{1'}) V_{Initial}$. This amplitude attenuates by $(e^{-2\alpha_{air}l_{air}} e^{-2\alpha_{snow}l_{snow}} e^{-2\alpha_{soil}l_{soil}})$. We assume that the attenuation of the soil is large enough so that multiple reflections within a material reduce to zero. The backscattered signal reduces to the product of $(\tau_1 \tau_2 \tau_3 \rho_4 \tau_{3'} \tau_{2'} \tau_{1'})(e^{-2\alpha_{air}l_{air}} e^{-2\alpha_{snow}l_{snow}} e^{-2\alpha_{soil}l_{soil}}) V_{Initial}$.

MODELING AND ALGORITHMS

Technique 1

The method used to find the backscattered signal returned from a mine buried in dry soil or moist soil covered with snow (or ice), involves calculating the characteristic impedances Z, the transmission coefficients τ, the reflection coefficients ρ, and attenuation factors.

The characteristic impedance $Z(\Omega)$ of $73+j42.5$ is chosen for the antenna while $Z(\Omega)$ of the air, snow, ice, soil, and mines are computed using

$$Z = \frac{E_Y}{H_Z} = \sqrt{\frac{j\omega\mu_0\mu_r}{\sigma + j\omega\varepsilon_0\varepsilon_r}} \qquad (1)$$

where

$\omega = 2\pi f$ = radian frequency of operation (f = frequency of operation)

$\mu = \mu_0\mu_r$ = permeability of medium

$\varepsilon = \varepsilon_0\varepsilon_r$ = permittivity of medium

$\varepsilon_r = \varepsilon_r{'} - j\varepsilon_r{''}$ = complex relative permittivity of medium

σ = conductivity of medium

The impedances of adjacent media are used to compute the reflection coefficient using

$$\rho = \frac{Z_2 - Z_1}{Z_2 + Z_1} \qquad (2)$$

Using ρ from equation (2), the transmission coefficient at a given junction from <u>left to right</u> is

$$\tau_j = 1 + \rho \qquad (3)$$

whereas the transmission coefficient at a given junction from <u>right to left</u> is

$$\tau_{j'} = 1 - \rho \qquad (4)$$

The propagation constant of waves in a given medium is computed using

$$\gamma_{med} = \sqrt{(\sigma_{med} + j\omega\varepsilon_0\varepsilon_{rmed})(j\omega\mu_0\mu_{rmed})} \qquad (5)$$

and the attenuation constant is simply corresponding

$$\alpha_{med} = real(\gamma_{med}) \qquad (6)$$

Waves attenuate according to

$$e^{-2\alpha_{med}l_{med}} \qquad (7)$$

where l_{med} is the thickness or depth of the medium.

Finally, the signal reflected from the mine is given by

$$V_{Final} = (\tau_1\tau_2\tau_3\rho_4\tau_{3'}\tau_{2'}\tau_{1'})*$$
$$(e^{-2\alpha_{air}l_{air}}e^{-2\alpha_{snow}l_{snow}}e^{-2\alpha_{soil}l_{soil}})*V_{Initial} \qquad (8)$$

Oblique angle

In the event that the incident wave propagates in a direction that is not perpendicular to the boundary, the incident wave (from medium 1) makes an angle θ_i with the y axis (y is orthogonal to the surface of the ground), the reflected wave (medium 1) makes an angle of θ_r with the y axis, and the transmitted wave (medium 2) makes an angle of θ_t with the negative y axis. In this model, it is assumed that the electric field is perpendicular to the plane of incidence (the xy plane) and the antenna does not receive the reflected wave from the ground. Using Snell's law, the sine of the angle of transmission is equal to

$$\sin\theta_t = \frac{k_1}{k_2}\sin\theta_i \qquad (9)$$

where k_1 is wave number of medium 1 and k_2 is wave number of medium 2.

The wave number in a high-loss medium, k_{HL}, is computed using

$$k_{HL} = \sqrt{-j\omega\mu_r{'}\mu_0(\sigma + j\omega\varepsilon_r{'}\varepsilon_0)} \qquad (10)$$

whereas the wave number in a low-loss medium, k_{LL} is given by

$$k_{LL} = \omega\sqrt{\mu_r{'}\mu_0\varepsilon_r{'}\varepsilon_0(1 - j\tan\delta)} \qquad (11)$$

If the medium is lossless then

$$k_{NL} = \omega\sqrt{\mu_r{'}\mu_0\varepsilon_r{'}\varepsilon_0} \qquad (12)$$

The characteristic impedance $Z(\Omega)$ of the medium when incident angle is oblique is given by

$$Z_{oblique} = Z_{normal}/\cos(\theta) \qquad (13)$$

where Z_{normal} is obtained from equation (1) and θ can be either the incident or transmit angle.

For a wave incident at an oblique angle, the reflection coefficient becomes

$$\rho_{oblique} = \frac{Z_{2\_oblique} - Z_{1\_oblique}}{Z_{2\_oblique} + Z_{1\_oblique}} \qquad (14)$$

then equations (3) through (8) are used to obtain the backscattered signal, V_{Final}.

For oblique incident angles, the scattered field returned to the antenna follows the same path as the incident wave.

Technique 2

Technique 2 is used to simulate far-field or stand-off mine detection. The modeling and the simulation process are similar to technique 1 with a few exceptions. Technique 2 uses the power equation while technique 1 uses the coefficient equations and attenuation constants in the boundary between the antenna and air. Also, technique 1 assumes an infinite boundary of the detection area, while technique 2 assumes a finite boundary, which is equal to the circular flat surface area of an anti-tank mine, in this case a radius of 17 cm.

A far-field mine detection model can be used because the standoff operating ranges (5 to 30 m) qualify as far-field by the criterion

$$R = \frac{2D^2}{\lambda} \qquad (15)$$

where R (m) is the distance to the boundary between the radiating near-field and far-field regions, D is the largest dimension (0.5 m) of a horn antenna aperture and λ is the wavelength (0.075 to 1.5 m for the above frequency range).

The mean received power P_r (W) in air (between antenna and ground) is given by

$$P_r = P_t \frac{A_P^2 \sigma_{rcs}}{4\pi\lambda^2 d^4} \qquad (16)$$

where P_t is the transmit power, A_P is the physical aperture of the horn antenna, σ_{rcs} is the radar cross-section as obtained from equation (17) below, λ is the wavelength, and d is the distance from the radar to the ground. In order for equation to be valid, several assumptions are made, namely: the gain of the receive antenna is the same as the gain of the transmit antenna (both equal to $4\pi A_P /\lambda^2$), and furthermore, the size of the mine is large compared to the wavelength.

The radar cross-section (m^2) of the circular flat mine is given by

$$\sigma_{rcs} = \frac{16\pi^3 r^4}{\lambda^2} \cos^2 \theta (\frac{J_1(4\pi r \sin\theta / \lambda)}{4\pi r \sin\theta / \lambda})^2 \qquad (17)$$

where r is the radius of the ground area, which is equal to the surface area of the mine, and θ is the oblique incident angle to the ground.

The backscattered signal in mediums other than air are computed using equation (8) of technique 1; the backscattered signal (dB) in all mediums except air is

$$S_{11} = 20 * \log_{10} [(\tau_2 \tau_3 \rho_4 \tau_{3'} \tau_{2'})*$$
$$(e^{-2\alpha_{snow} l_{snow}} e^{-2\alpha_{soil} l_{soil}})] \qquad (18)$$

Total power received (dB) by the antenna:

$$P_{total} = S_{11} (dB) + 10 \log_{10}(\frac{P_r}{P_t}) \qquad (19)$$

CONCLUSION

In the near-field detection, the results from technique 1 agree with the experimental results when the targets are buried in dry soil. However, when the targets are buried in moist and wet soil, the simulated results only partially agree with the experimental results. For far-field detection, the experimental results are not available; hence, no comparison is made. However, when they are available, they will be presented at the symposium.

Simulated data for oblique angles shows that the received power is strongest when the incident wave propagates normally to the boundary.

Results confirm that non-metallic mines are very hard to detect in dry soil. This is so because the dielectric constant of the mines is similar to that dry sand (low contrast). However, the simulated data shows that when the soil is moist or the dry sand is covered with snow or ice, the non-metallic mines are less difficult to detect. However, the increased moisture content in the dry soil does not help to detect the metallic mines.

Although the models presented here are not completely rigorous, they have the advantage of being computationally efficient. Under certain condition, results were obtained which were in reasonable agreement with measured data. The work is presented mainly as a starting point from which a more sophisticated analyses may depart.

REFERENCES

[1] A. H. Trang and H. G. Irion, "Computer models simulating the detection of buried metallic and dielectric mines", pp. 1-20, December 1996, unpublished.

[2] A. H. Trang, "Simulation of mine detection over dry soil, snow, ice, and water", SPIE Proceedings, Vol. 2765, pp. 430-440, April 1996.

[3] J. D. Kraus and K. R. Carver, "Electromagnetics", McGraw-Hill Book Company, Second Edition, 1973, pp. 117, 201, 404, 446, 447, 453-456, 498, 516-519, and 671.

[4] Other references can be found in [1] and [2].

Exploration of Innovative Radar Sensing Schemes
for Subsurface Object Detection

Kevin O'Neill
U.S. Army Cold Regions Research and Engineering Laboratory (CRREL)
72 Lyme Rd   Hanover, NH 03755   USA
603-646-4312   koneill@crrel.usace.army.mil

The problem of abandoned landmines and unexploded ordnance is particularly acute when these objects are near the surface, so that their radar returns cannot easily be separated from the ground surface response. To address this, we pursue simulations here designed to test methods of sensor deployment and data processing that exploit angular, positional, and frequency diversity for detection of metallic targets that are on the order of the subsurface wavelength in size. Rigorous 2-D computations were performed and results processed for the angular correlation function (ACF) approach, in which one performs a coherent average of received signals from two incidence and observation angles. Simulations pursue the behavior of the ACF under realistic ground roughness and moisture content, target geometry, and highest practical resolution GPR frequencies. To achieve an expanded ensemble of cases, given a single subject ground surface, we average both over frequencies and overlapping incident beam locations.

INTRODUCTION

The investigations discussed here are part of a larger study in which measurements and simulations are pursued to test innovations in sensing strategy for detection of buried objects. A principal motivation is to improve methods for detecting abandoned landmines or unexploded ordnance. These objects pose an enormously widespread and urgent problem worldwide, and also put extraordinary burdens on subsurface sensing methods. This is partly because the criteria applied must be extremely strict, requiring an absolute minimum of both false positive and false negative judgments as to the presence of a target sought. This is particularly challenging in as much as the targets of interest typically reside in randomized environments. Simply increasing the sensitivity of sensors tends to inundate the record with irrelevant clutter. One must pursue creative sensing strategies, by which we mean the totality of sensor configuration, combination, deployment, and data processing methods.

The nature of the problem is illustrated in Figure 1, which shows bistatic results from 2-D numerical solutions for radar reflection from metallic targets embedded in a moist soil with randomly rough surface. The two targets are approximately the same size, one elliptically shaped and the other having a mine-like geometrical cross section (Figure 2). Radar cross section values are shown, arbitrarily but consistently scaled, in negative scattering directions, i.e. back into the quadrant occupied by the transmitter. For these re-

sults from a single frequency, incidence angle, and beam position, one sees that relative visibility of the subsurface target depends very much on which target one considers and which observation angle he chooses.

Bistatic cross sections on arithmetic scale
for 1600 MHz with $\Theta_i = 50°$
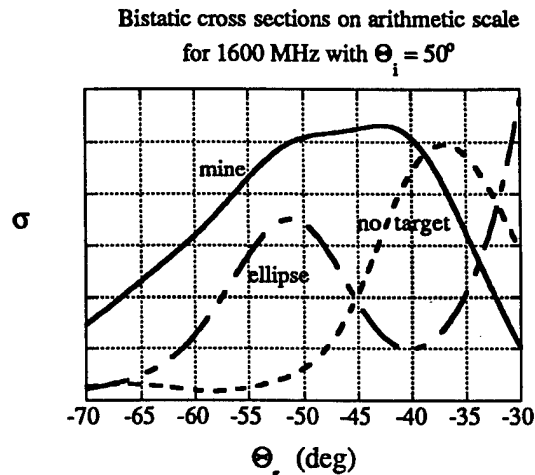
Figure 1. Bistatic radar cross sections at 1600 MHz for rough ground with and without buried target.

We must pool data to ascertain ways in which any of a variety of targets will stand out, reliably and over a broad range of angular and environmental conditions. Because our targets of concern are quite localized, one's options are limited for achieving an ensemble of sensor data for processing. We proceed by defining a particular scene (Figure 2) and solving for the scattered response over a broad frequency band, variety of incidence and observation angles, and beam position combinations. We then investigate the behavior of ACF processing schemes when applied to that data.

SIMULATION AND PROCESSING APPROACH

The example target (Fig. 2) is 10 cm high, 22 cm wide at the base, buried with its top 5 cm below the mean surface. We treat only horizontal polarization here (E field into the page). The taper of the beam is illustrated by the E field solution magnitudes shown for total field along the soil surface. Environmental randomness is expressed through the rough soil surface, which is otherwise homogeneous. The real part of the soil dielectric constant is 9, typical of a moist soil, and its electrical conductivity is 10^{-3} S/m.

1135
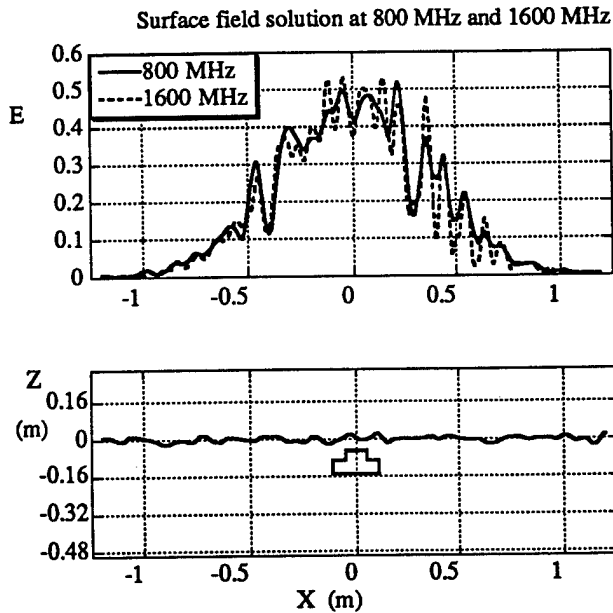
Figure 2. Example target and surface geometry, with ground surface field solution.

The random surface is generated by selecting a parent distribution Fourier transform $Z(K)$ of its height profile, corresponding to a power spectrum $W(K)$ in the form of a Rayleigh distribution.

$$W(K) = \frac{\pi \ell^2 h^2}{2} |K| \exp\left(\frac{-\pi K^2 \ell^2}{2}\right) \qquad (1)$$

where h is the root mean square height and ℓ the correlation length. This suppresses low frequency surface shape components and produces many relatively small bumps, as shown. We choose $Z(K)$ proportional to $\sqrt{W(K)}$ for each K, but then randomize the phase of the component. This produces an ensemble in which each member surface is different but has the same specified h and ℓ equal here to 1 cm and 3 cm respectively. The E field is obtained from numerical solution of an integral equation in the manner of [1], for each electromagnetic frequency, beam position, and surface.

To achieve positional diversity we shift the beam from side to side over five positions: centered over the target, and centered over points $\pm$ 25cm and $\pm$50cm from there. Thus the target remains at least generally within the main beam, and with each shift of the beam we change the sample of the surface by a significant amount. Examination of amplitude and phase of backscatter suggests that this is the best we can do with these surface parameter/ radar wavelength relations. Larger shifts would take us away from the target. Scattering data are pooled from nine frequencies equally spaced between 800 MHz and 1600 MHz. This appears optimal from

the point of the view of the angular correlation study over this band. That is, a coarser frequency division shows angular correlation effects poorly; a finer division produces samples that are less independent, thus bringing no improvement. Altogether, with five shifts and nine frequencies, we achieve an ensemble of 45 cases for each surface surveyed, over a total ensemble with 25 such surfaces.

Recent work suggests that angular correlation function analysis (ACF) may succeed in suppressing scattered signal clutter from random surface irregularities, relative to the effect of the target [2]. One computes the complex product of fields scattered in directions Θ_{s1} and Θ_{s2} produced by incident waves from directions Θ_{i1} and Θ_{i2}, respectively.

$$ACF = \langle E(\Theta_{s1}, \Theta_{i1}) E^*(\Theta_{s2}, \Theta_{i2}) \rangle \qquad (2)$$

When the averaging $\langle ... \rangle$ is performed over samples of a statistically homogeneous domain, the fields will decorrelate except along the "memory line," determined by the angular relations $\sin(\Theta_{s2}) - \sin(\Theta_{s1}) = \sin(\Theta_{i2}) - \sin(\Theta_{i1})$. This applies for any statistically appropriate source of random reflection in the medium. The effect of the target represents an underlying coherence that will not decorrelate in the same way over the sample space. Here we take care to choose a relevant target with irregularities on the order of the surface perturbations, in part to see whether its effect simply averages out as if it were tantamount to another surface variation. We will proceed by selecting Θ_{i1}, Θ_{i2}, and Θ_{s1}, viewing the results over Θ_{s2}. A major quiestion has been the width of the memory line, i.e of the region where surface effects may correlate, obscuring the hopefully high ACF value from the target. This relates to our preoccupation with reliability: how decisively (and when) will the target case ACF be larger than that from the surface alone. The ACF/ memory line phenomenon was originally shown to occur for ensembles of spatial samples. Here we must rely more on sampling over frequencies.

Figure 3 shows bistatic ACF bounds computed with frequency averaging but without space shifting. The ACF magnitude is calculated for each surface, with and without buried target; the bounds defined as +/- one standard deviation from ensemble average are determined at each Θ_{s2}. While peaks appear at the memory line angle of -4.5°, they are quite diffuse and ill-defined. In any case, the locus of ACF magnitudes with target present is generally higher than without a target. Next we consider both frequency and spatial averaging. Figure 4 shows quite distinct peaks directly at the memory line angle. Given the range of positions and the frequency band at our disposal, this is about as narrow a memory line as can be achieved. At observation angles Θ_{s2} around -60°, the target would usually though not always be distinguishable. However for Θ_{s2} between about -20° and -55° the distributions overlap badly. Note also that in both target and non-target cases there is a prominent secondary lobe; detectability of the target is distinctly better over these lobes, *including the memory line lobe*. Detection

performance is not better in Θ_{s2} regions that show maximum decorrelation behavior ($\Theta_{s2} \sim$ -30°). The target seems primarily to intensify the non-zero correlation at the memory line and secondary lobes.
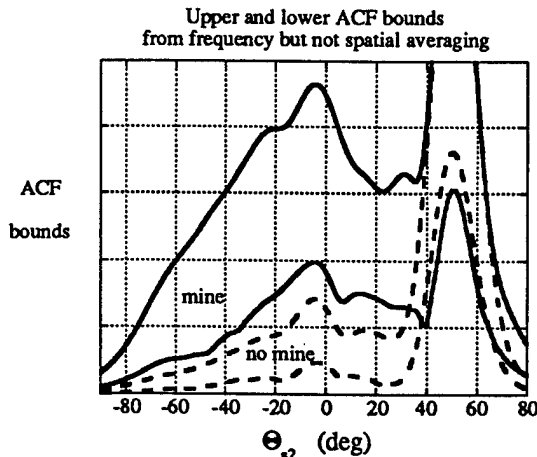
Figure 3. ACF bounds: $\Theta_{i1} = 25°$, $\Theta_{s1} = $ -25°, $\Theta_{i2} = 50°$.
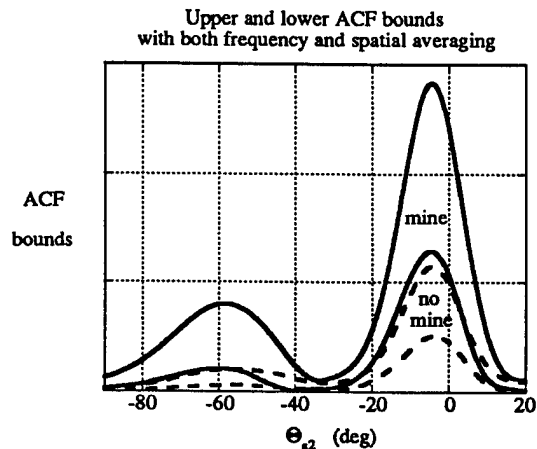
Figure 4. ACF bounds: $\Theta_{i1} = 25°$, $\Theta_{s1} = $ -25°, $\Theta_{i2} = 50°$.

As a second case we reverse the angular selections, with results shown in Figure 5. In this diffuse ACF pattern our angular selection has pushed the memory line to the left beyond real Θ_{s2}. When data from space shifts is included we obtain Figure 6 where the lobes do not correspond to theoretically identifiable memory effects. Again we note primary and secondary off-specular lobes, with an undesirable amount of overlap between the target and no-target distributions over much of the angular range.

CONCLUSION

The promising new technique of angular correlation function analysis has been applied to simulation cases involving realistic soil parameters and roughness relative to high reso-

lution GPR wavelengths. A fundamental ACF problem lies in obtaining a profitable ensemble of averaging samples pertaining to a single spot of ground. In general, increasing the sample pool by including overlapping space shifts as well as frequency diversity has improved definition and isolation of the memory line relative to frequency averaging alone. At the same time, this has not improved buried target detection performance in the cases investigated. Ironically, it provided less evidence of the presence of the target in angular zones of maximum noise decorrelation. Interestingly, it seems more to intensify target case ACF response in memory line and secondary lobe regions, relative to the no-target case.
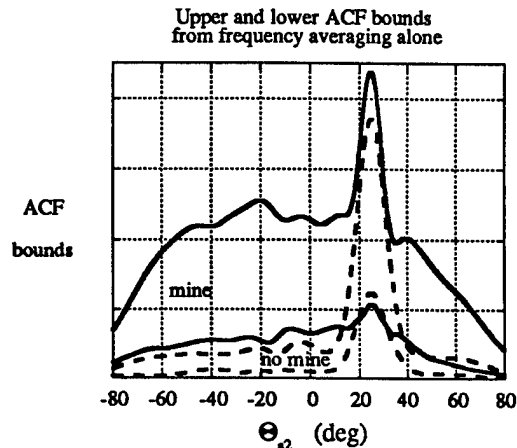
Figure 5. ACF bounds: $\Theta_{i1} = 50°$, $\Theta_{s1} = $ -50°, $\Theta_{i2} = 25°$.
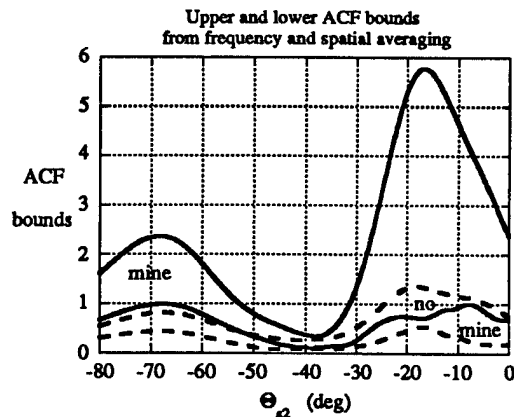
Figure 6. ACF bounds: $\Theta_{i1} = 50°$, $\Theta_{s1} = $ -50°, $\Theta_{i2} = 25°$.

REFERENCES

[1] K. O'Neill, R.F. Lussky, and K.D. Paulsen, "Scattering from a metallic object embedded near the randomly rough surface of a lossy dielectric," IEEE Trans.Geosci. Remote Sensing, vol 34, pp367-376, 1996.

[2] G. Zhang, L. Tsang, and Y. Kuga, "Studies of the angular correlation function of scattering by random rough surfaces with and without a buried object," IEEE Trans. Geosci. Remote Sensing, vol 35, pp444-453, 1997.

Feasibility Study on Localized Subsurface Imaging Using
Circular Synthetic Aperture Radar and Angular Correlation Function Measurement

Tsz-King Chan, Yasuo Kuga, and Akira Ishimaru
Department of Electrical Engineering
University of Washington, Box 352500
Seattle, WA 98195-2500, USA
Telephone: (206)543-0478, Fax:(206)543-3842, Email: kuga@ee.washington.edu

Abstract — The traditional linear synthetic aperture radar (LSAR) flying along a linear flight path is modified to circular synthetic aperture radar (CSAR) flying along a circular flight path. When operating in down-looking spotlight mode for imaging purposes, CSAR, in comparison with LSAR, can provide higher pixel resolutions on any confocally focused plane within the volume illuminated by the antenna beams. By combining this 3D imaging technique with the circular angular memory effect, it is possible to reconstruct volume radar images in localized subsurface imaging applications where poor signal-to-noise ratio (SNR) is a critical issue. Laboratory experiments at X-band (7–13 GHz) and W-band (75–100 GHz) frequencies were conducted to illustrate the capability of CSAR to perform 3D imaging, and the analytical basis of circular angular memory effect due to random surface scattering based on the first-order Kirchhoff approximation.

INTRODUCTION

Since its emergence in the late 1950's, synthetic aperture radar (SAR) has been popular for imaging applications among civilian and military users [1]. In a manner similar to the beam-forming process of phased array antennas, SAR operates on the principle of synthesizing a large antenna aperture by proper coherent summation of the pulses produced by the transmitting and receiving antennas temporally located along a sequence of known positions. The sharp beam resulting from this synthesis process allows one to use it as a 'flashlight probe' to obtain a 2D mapping (image) of the received echoes with moderately fine pixel resolution.

Traditionally, most SAR-based systems for geophysical remote sensing operate by launching an airborne SAR sensor along a straight flight path [1], with the synthesized beam scanning in stripmap mode or spotlight mode, depending on the tradeoff between pixel resolution and the size of the region under surveillance that a SAR user has to make. For brevity, these traditional SAR-based systems will be referred to as linear SARs (LSARs) in the following discussion, signifying the fact that the SAR sensors move along a linear path.

Although useful for many applications, the images produced by a LSAR system are projection images which are 2D in nature. Therefore, for a given illuminated structure, the portion of its scattering which takes place along a common wavefront but at different altitudes will all be mapped as one projection image pixel only, with no resolution in vertical dimension.

Among other alternatives such as interferometric SARs that aim at extracting the altitude information of the illuminated structures, SAR systems that move along a circular orbit, referred to in Fig. 1 as circular SARs (CSARs), can perform altitude-mapping imaging together with a number of unique features not found in LSARs. First, CSAR, which moves along a circular path circumferential to the illuminated spot, provides a full-rotation 2D view of the illuminated structure. Second, the spotlight nature of its operation makes CSAR capable of achieving pixel resolution on the order of λ (principally lower-bounded by diffraction limit as in optics research), where λ is the center wavelength of the wideband radiation produced by the pulse-sending SAR system. Third, the path differences between scattering points lying along a common wavefront but different altitudes can be resolved using SAR measurements made in front-looking, back-looking and/or side-looking directions, thus making it possible for 3D image reconstruction of the object at microwave frequencies in a way similar to confocal imaging in medical applications at optical and ultrasound frequencies. Last but not least, the circular geometry of operating CSAR also makes it a practical means for hardware implementation using airborne wideband radar systems.

Before proceeding to the details of performing 3D imaging using CSAR, it is perhaps a suitable point of digression to understand a correlation phenomenon with which CSAR can combine: circular angular memory effect.

CIRCULAR ANGULAR MEMORY EFFECT

Recently, it was shown analytically, experimentally, and numerically that under a phase matching condition for the transverse wave components, there exists a novel correlation phenomenon known as the angular memory effect for waves multiply scattered by random media [2]. Simply stated, this effect predicts that there is non-zero angular correlation between waves observed at different scattering angles in response to a change in incident angles under the phase matching condition mentioned above, but close-to-zero angular correlation otherwise. For scattering (2D scattering)

Figure 1: Geometry of CSAR

Figure 2: Circular angular memory signature due to scattering by 2D random rough surface. (a) Kirchhoff approximation. (b) Millimeter-wave experiments

which takes place at variable scattering angles θ but a fixed azimuth angle ϕ, this phase matching condition [2] can be expressed as

$$\sin(\theta_i) - \sin(\theta_s) = \sin(\theta'_i) - \sin(\theta'_s) \qquad (1)$$

where the unprimed quantities represent the *reference* incidence and scattering angles and the primed quantities represent the *variable* incidence and scattering angles. Equation (1) represents a straight line of slope +1 for a given reference antenna configuration represented by (θ_i, θ_s).

In contrast, for scattering (3D scattering) which takes place at variable azimuth angles ϕ but a fixed scattering angle θ, however, the phase matching condition can be shown, using the classical first-order Kirchhoff approximation, to be

$$\{[\cos(\phi_s) - \cos(\phi_i)] - [\cos(\phi'_s) - \cos(\phi'_i)]\}^2$$
$$+ \{[\sin(\phi_s) - \sin(\phi_i)] - [\sin(\phi'_s) - \sin(\phi'_i)]\}^2 = 0 \qquad (2)$$

Unlike (1), (2) can represent anything from straight line to spread spots, depending on the choice of the reference antenna configuration represented by (ϕ_i, ϕ_s). Since locus for the variable antenna positions describes a circular path, the resulting memory effect is appropriately known as the circular angular memory effect. For transmitting and receiving antennas located in the backscattering direction [(ϕ_i, ϕ_s) = (0°,180°)], the corresponding circular angular memory signature, predicted using Kirchhoff approximation and confirmed by experiments on scattering by 2D perfectly conducting Gaussian random rough surfaces (correlation lengths = 2λ, rms height = 1λ) at W-band (75–100 GHz) frequencies, are shown in Fig. 2. The significance of circular angular memory effect for this experiment is this: it exhibits strong angular correlation between multiply scattered waves under the phase matching condition, but very low correlation otherwise. The rate of decorrelation is inversely proportional

to the size of the illumination footprint and is *independent* of the surface roughness [2]. Since the traditional cross-section (intensity) measurement forces the reference antenna configuration to be equal to the variable antenna configuration (i.e. $\phi_i = \phi'_i$ and $\phi_s = \phi'_s$), the phase matching condition, as in (2), is satisfied. Therefore, the traditional detection/imaging techniques, which rely on cross-section measurement, will automatically contain a strong contribution (in the form of undesirable radar clutter) from multiple-scattering components produced by the scattering media, resulting in poor SNR.

With this viewpoint on clutter existence based on the concept of angular correlation, it is relatively easy to devise a measurement scheme that could suppress the clutter in CSAR application: perform field measurements at a specific set of angular positions around the circular scanning path and correlate them in such a manner that the azimuth angles represented by individual measurements are located at the far end of the decorrelation tail of the memory signature in Fig. 2. The clutter-rejection capability of this correlation technique in buried object detection at X-band frequencies has been reported in the literature [3].

CONFOCAL IMAGING USING CSAR

To illustrate the principle of CSAR in performing confocal imaging, and hence extracting the altitude information of the illuminated structure, laboratory experiments were performed at X-band frequencies in an anechoic chamber. The transmitting and receiving antennas were positioned in the backscattering direction and oriented at 45° below the horizon.

At a slant reference range of 140 cm the dimension of the illuminated volume is about 37.4 cm. Within the illuminated volume, spheres were supported by two thick styrofoam sheets. The lower sheet supported three uniformly spaced

metal spheres of different diameters (one of 2" and two of 1", with a 4" separation) and the upper sheet supported one metal sphere with a diameter of 2.5". The lower sheet was separated from the upper sheet by a vertical distance of 7.5". A frequency-domain SAR measurement was made at every 5° along the circular path over a frequency band of 7–13 GHz. The experimental setup is shown in Fig. 3.

CSAR PROCESSING AND RESULTS

To process the SAR measurement, the illuminated volume was first discretized into 77 x 77 x 9 cubes (pixel resolution: 6 points/wavelength). To each of these cubes, a unique set of time-domain, Kaiser-based tracking filter functions was computed and applied to each of the measurements made along the circular path. The resulting gated measurements were then magnitude-phase adjusted and coherently added for beamforming. Since this spotlight-mode focusing process can be done on any plane within the illumination volume, the 3D images can be obtained by focusing one slice at a time. With the help of software that can perform surface or volume rendering, it is possible to stack up all the image slices for 3D image reconstruction.

The processed data are presented as contour plots in Fig. 4. As evident from the contour plots, CSAR has the capability of focusing at a given plane with all other planes within the illumination volume being defocused. This confocal imaging feature should make CSAR a suitable candidate in practical subsurface 3D imaging applications.

CONCLUSION

In this paper, the confocal imaging capability of CSAR is experimentally demonstrated at X-band frequencies. Although we did not make a quantitative effort to link the uses of CSAR and circular angular memory effect in this research work, we expect that, with previous successful demonstration of the clutter-rejection feature of angular memory effect in target detection applications, similar ideas of enhancing SNR could be extended to imaging applications. For further studies on the combination of CSAR and circular angular memory effect in practical settings, efforts are being made to construct an indoor wideband bistatic X-band radar system capable of performing SAR measurement for a natural soil surface at any azimuth angle along a circular path. It is expected that successful combination of these techniques could result in a 3D imaging system particularly useful in low-SNR applications.
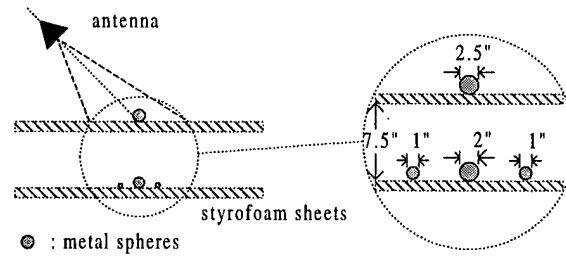
Figure 3: Experimental setup for confocal imaging using CSAR
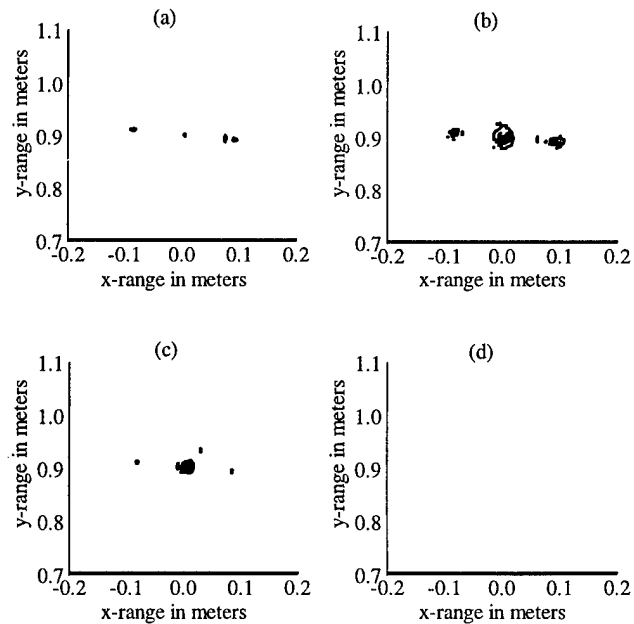
Figure 4: Confocal contour plots for image slices located at different altitudes. (a) below the lower styrofoam layer (no sphere). (b) lower styrofoam layer (3 spheres). (c) upper styrofoam layer (1 sphere). (d) above upper styrofoam layer (no sphere)

[1] F. T. Ulaby, R. K. Moore, and A. K. Fung, *Microwave Remote Sensing*, Vols. 1, 2, and 3. London: Addison-Wesley, 1981.

[2] C. Le, Y. Kuga, and A. Ishimaru, "Angular correlation function based on the second-order Kirchhoff approximation and comparison with experiments," *J. Opt. Soc. Am.*, 13(5), pp. 1057–1067, 1996.

[3] T. K. Chan, Y. Kuga, and A. Ishimaru, "Subsurface Detection of a Buried Object Using Angular Correlation Function Measurement," *Waves in Random Media*, in press.

Application of Angular Correlation Function of Wave Scattering by a Random Rough Surface and Random Discrete Scatterers in Target Detection

Guifu Zhang, Leung Tsang*, and Yasuo Kuga
Electromagnetics and Remote Sensing Laboratory
Department of Electrical Engineering
Box 352500
University of Washington, Seattle, WA 98195-2500
Telephone: (206)685-7537 Fax: (206)543-3842

Abstract

In this paper, we study the angular correlation function (ACF) of a rough surface and volume scattering and apply it to the detection of a target embedded in the clutter. Both the 2-D and 3-D ACF are studied by using numerical simulations with frequency averaging and circular azimuthal angle averaging techniques. The 3-D case has an increase of degree of freedom over the 2-D case. This increase of freedom makes the circular azimuthal angle averaging more successful in suppressing the clutter, making the technique attractive in real life implementation.

1. Introduction

Wave scattering by random rough surfaces and random scatterers has been studied extensively using analytic techniques, laboratory experimental measurements, and numerical simulations[1,2]. Most of the studies have utilized the bistatic scattering intensities to characterize the scattering results.

In 1988, a paper by Feng et al. demonstrated the existence of memory effects by taking the angular correlation of wave scattering [3]. The angular correlation function (ACF) is the correlation function of two scattered fields in directions θ_{s2} and θ_{s1} corresponding to two incident waves in directions θ_{i2} and θ_{i1}, respectively (Fig. 1). A strong correlation, called the angular memory effect, is exhibited on the memory line. The values of the ACF are very small for the angle pairs away from the memory line. This has been verified by theoretical models and experiments. For volume scattering, the same phase matching condition holds for the horizontal direction, $sin\theta_{i1} - sin\theta_{s1} = sin\theta_{i2} - sin\theta_{s2}$. For the case of a thick layer, an additional phase matching condition is $cos\theta_{i1} + cos\theta_{s1} = cos\theta_{i2} + cos\theta_{s2}$. The existence of the second condition makes the memory line shorter.

Recently, the ACF has been applied to the detection of a buried object [4,5,6]. For the detection of a target embedded in random scatterers under a rough surface, the scattering of waves by the target is often obscured by clutter such as rough surface scattering and random medium scattering. This makes the detection of a target difficult based on scattering intensity. However, by making use of the ACF, one can show that the contribution of clutter to the angular correlation function is minimal away from the memory line making the contribution of the buried object more conspicuous by many dB.

In this paper, we study the ACF of wave scattering by a random rough surface and random discrete scatterers for 2-D and 3-D scattering problems. In the ACF for detection of buried object, the target is associated with one realization of the random rough surface and random medium, therefore realization averaging is meaningless. In the 2-D ACF, we have been using averaging over frequency and angular averaging over zenithal angle θ. These averaging techniques are moderatally successful because the scattering properties are strongly dependent on frequency and the zenithal angle θ. However, in the 3-D case, there is an increase in the degree of freedom.

2. Formulation

2.1. General Definition

The general definition of the ACF is the correlation between two scattered waves corresponding to the

two incident waves, given by

$$\Gamma(\hat{k}_{s1}, \hat{k}_{i1}; \hat{k}_{s2}, \hat{k}_{i2}) = < F(\hat{k}_{s1}, \hat{k}_{i1}) F^*(\hat{k}_{s2}, \hat{k}_{i2}) >$$

(1)

where $F(\hat{k}_s, \hat{k}_i)$ is the total scattering amplitude (or normalized scattered field), $\hat{k}$ (θ, ϕ) is the direction of wave propagation. The ensemble average is usually calculated over many realizations in experiments and numerical simulations, written as

$$\Gamma_r(\hat{k}_{s1}, \hat{k}_{i1}; \hat{k}_{s2}, \hat{k}_{i2}) = \frac{1}{N_r} \sum_{n=1}^{N_r} F(\hat{k}_{s1}, \hat{k}_{i1}, n)$$
$$F^*(\hat{k}_{s2}, \hat{k}_{i2}, n)$$

(2)

There are eight variables in the ACF defined by (1) and (2). The ACF only exists on the angular pairs which are controlled by the three phase match conditions, which is called memory effect. The study of the ACF can be simplified for the specific problem.

2.2. 2-D ACF Based on Frequency Averaging

Consider a problem of a target embedded in discrete random scatterers below a rough surface as shown in figure 1. The target and the scatterers are all cylinders for the 2-D scattering problem. We formulate the problem by using the integral equation method. The equations are solved numerically using the method of moments, giving an exact solution of Maxwell's equations. Then, the normalized far field scattered field in direction θ_s is obtained.

Consider incident waves at two incident directions θ_{i1} and θ_{i2} with corresponding scattered waves at θ_{s1} and θ_{s2} respectively. Since the target is under a single realization of rough surface and random scatterers, we use frequency averaging with the angular correlation function (ACF) defined by

$$\Gamma_f(\theta_{s1}, \theta_{i1}; \theta_{s2}, \theta_{i2}) = \frac{1}{N_f} \sum_{n=1}^{N_f} F(\theta_{s1}, \theta_{i1}, f_n)$$
$$F^*(\theta_{s2}, \theta_{i2}, f_n)$$

(3)

where f_n is the frequency. The averaging is taken over the frequency range with center frequency f_o.

2.3. 3-D ACF Based on Circular Averaging

To calculate the 3-D ACF, we consider the wave scattering by a volume consisting of many scatterers (small spheres). The total scattering amplitude is calculated by using coherent addition approximation. The 3-D ACF can be studied in various

ways depending on different applications. For the target detection purpose, we illustrate our studies on the back-scattering configuration which reduces the eight variables into four. The 3-D ACF can be defined in ways similar to the 2-D ACF. After studying the 3-D scattering problem, a way of calculating the 3-D ACF is by circular averaging,

$$\Gamma_c(\theta_1, \phi_1; \theta_2, \phi_2) = \frac{1}{N_c} \sum_{n=1}^{N_c} F(\theta_1, \phi_1 + \phi_n)$$
$$F^*(\theta_2, \phi_2 + \phi_n)$$

(4)

The circular averaging defined in Eq. (4) is to take an average by changing the azimuth angles. Therefore, the circular SAR data can be used for ACF processing.

3. Numerical Results

In the 2-D scattering problem, we use 300 circular cylinders with radius of $a = 0.05\lambda_o$ to model the random scatterers and an elliptical cylinder with size of $b = 0.7\lambda_o$ and $c = 1.0\lambda_o$ as the target. We use a single random rough surface with the height profile plotted in figure 1, and a rough surface of length $L = 40\lambda_o$ with rms height $h = 0.25\lambda_o$ and correlation length $l = 0.5\lambda_o$. The target elliptical cylinder is placed at a depth $d = 2\lambda_o$. The 2-d ACF with fixed $\theta_{i1} = 20^o$ and $\theta_{s1} = -20^o$ is calculated by frequency averaging over a frequency band $0.5f_o$ to $1.5f_o$ as defined in Eq. (3). The ACF is plotted as a function of $sin\theta_{i2}$ and $sin\theta_{s2}$, as shown in figure 2. We see a strong correlation on the angle pairs of memory.

To show the effectiveness of using ACF in the 3-D case which has real life applications, we calculate the 3-D ACF of wave scattering by a target sphere embedded in 500 small spheres by using the circular averaging. The results are shown in figure 3. The 3-d ACF is plotted as a function of the incident angle θ_2 with fixed $\theta_1 = 20^o$ and $\phi_1 = \phi_2 = 0^o$. We can see a peak at $\theta_2 = 20^o$, which we call "memory dot". At the memory dot, the values of the ACF with and without the target are almost the same. This means that the random scatterers dominate the back-scattered intensity (self-correlation). Away from the memory dot, however, the ACF with the target is 10 to 20dB larger than that without the target. Therefore, the ACF is useful in the detection of target embedded in clutter. The technique works much better in 3-D real life situations.

4. References

1. A. Ishimaru, *Wave Propagation and Scattering in Random Media*, New York, Academic Press, 1978.

2. L. Tsang, J.A. Kong and R.T. Shin, *Theory of Microwave Remote Sensing*, New York, Wiley Interscience, 1985.

3. S. Feng, C. Kane, P. A. Lee, and A. D. Stone, "Correlations and fluctuations of coherent wave transmission through disordered media," *Phys. Rev. Lett.*, vol. 61, pp. 834-837, 1988.

4. Y. Kuga, T.-K. Chan, and A. Ishimaru, "Detection of a target embedded in clutter using the angular memory effect," submitted for publication in *IEEE Transactions on Antennas and Propagation*, 1995.

5. L. Tsang, G. Zhang, and K. Pak, "Detection of a buried object under a single random rough surface with angular correlation function in EM wave scattering", *Microwave and Optical Technology Letters*, to appear in April 1996.

6. G. Zhang, L. Tsang, and Y. Kuga, "Studies of angular correlation function of scattering by random rough surfaces with and without a buried object," *IEEE Transactions on Geoscience and Remote Scening*, vol. 35, no. 2, pp. 444-453, 1997.
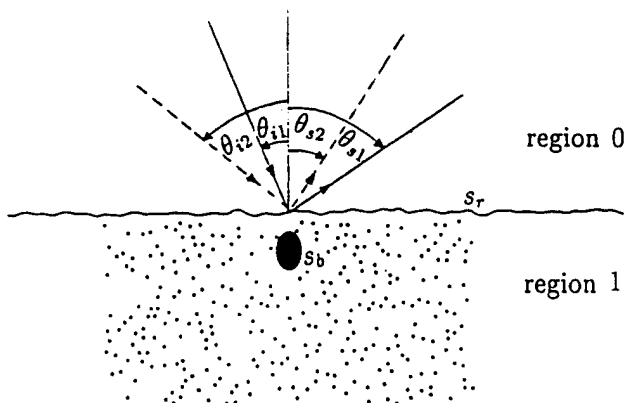
Figure 1: *Configuration of ACF of wave scattering by a target embedded in small scatterers under a rough surface .*
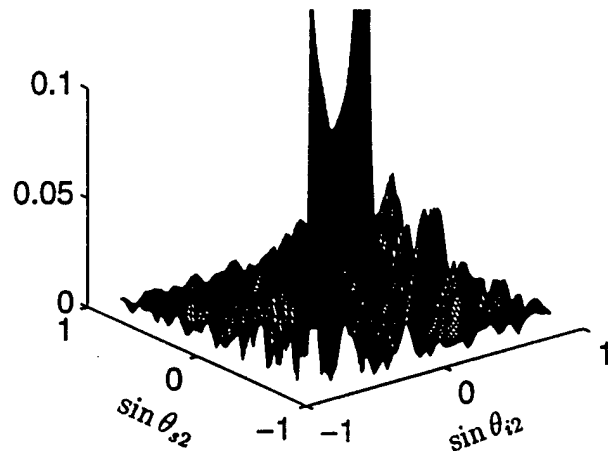
Figure 2: *3-D plot of 2-D ACF by frequency averaging for wave scattering from a rough surface and random scatterers with a target. Averaging band is $(0.5f_o - 1.5f_o)$. $\theta_{i1} = 20^o$, $\theta_{s1} = -20^o$. $\epsilon_1 = 3.7 + 0.13i$, $\epsilon_s = 16.67 + 1.15i$ $a = 0.05\lambda_o$. Rough surface parameters are $L = 40\lambda_o$, $g = L/4$. $h = 0.25\lambda_o$, $l = 0.5\lambda_o$*
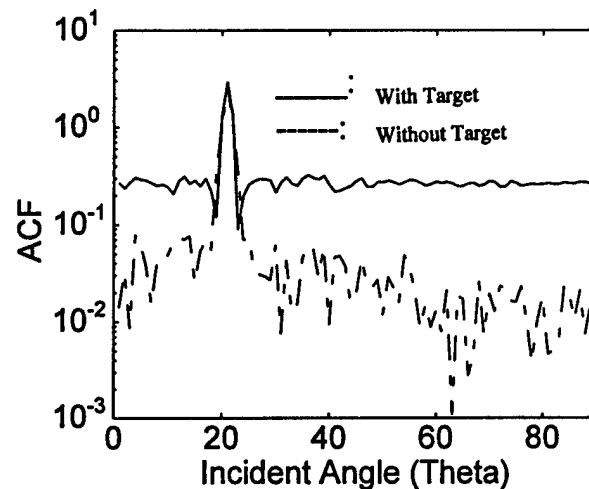
Figure 3: *3-D ACF by circular averaging for wave scattering by a target sphere embedded in randomly distributed 500 scatterers. Parameters are $\theta_1 = 20^o$, $\phi_1 = \phi_2 = 0^o$, $\epsilon_r = 3.23 + 0.36i$. $a_t = 0.3\lambda_o$, $a_s = 0.15\lambda_o$, $R = 10\lambda_o$ and $H = 20\lambda_o$.*

Remote Sensing of Buried Objects: An Analysis Using FD-TD Simulation

Saibun Tjuatja, Adrian K. Fung, Shr-Hua Wu, Ping Zhou, and Zhi-Jian Li

Wave Scattering Research Center
Department of Electrical Engineering
University of Texas at Arlington
Box 19016, Arlington, TX 76019, U.S.A.
Phone: (817) 272-3974   Fax: (817) 272-3443   Email: tjuatja@uta.edu

Abstract – A numerical modeling algorithm is developed and used to compute the scattering from objects buried under an irregular ground surface. The algorithm integrates object scattering with scattering from a rough surface above these objects.The algorithm will support two modes of operation: (a) return signal strength as a function of system, geometry, ground and object parameters and (b) angle and frequency diverse image as a function of system, geometry, ground and object parameters. The technique to be used for this effort will be a combination of the standard finite difference time domain (FD-TD) method, a randomly rough surface generation routine and an image generation routine developed at the University of Texas At Arlington (UTA). Such an algorithm should be useful for predicting the return signal as a function of the radar system parameters and the ground condition. It also offers the potential to find an optimum choice of system and geometric parameters for detecting buried objects under a given situation.

INTRODUCTION

Many sensors have been utilized (or proposed for use) in the detection of buried objects such as land mines. They include metal detector, ground penetrating radar (GPR), polarimetric microwave imaging, forward looking infrared (thermal) sensor (FLIR), video, and ultraviolet (UV) sensor. Accurate detection of land mine in a cost effective manner requires the right mix of sensors and the associated processing algorithms. An understanding of land mine signature characteristics and detectability is needed in order to determine the optimum sensor combination, sensor parameters, and the associated processing algorithms. In this study we investigate the scattering characteristics of buried objects in the microwave region using a numerical modeling approach.

For a medium with buried object as shown in Fig. 1 there are discontinuities at the object-medium boundary and the air-medium boundary. An impinging wave will experience multiple scattering between the object and the medium boundary as well as within the object. We expect complex wave, object and medium boundary interactions to occur. Except for special, idealized cases, analytical methods are ineffective for such problems. Numerical methods designed to solve frequency domain problems such as moment methods are also not suit-

able because of the wide band nature of the problem. On the other hand, the finite difference time domain method (FD-TD) offers many advantages as an electromagnetic modeling, simulation, and analysis tool with capabilities including [1,2] broadband response predictions; arbitrary 3-D model geometries; and interaction with an object of any conductivity.

The formulation of the FD-TD method is summarized in the following section. The implementation of a window function to obtain the scattering coefficient of a randomly rough surface with buried object are given in the subsequent section. Numerical results and summary are presented in the last two sections.

FD-TD: A SCATTERED FIELD APPROACH

The FD-TD approach has many formulations: scattered field, total field, potential, implicit etc. [1]. For scattering calculations where the amplitude of the scattered field is significantly smaller than the incident, it is particularly advantageous to use the scattered field formulation. This section summarizes the scattered field FD-TD formulation starting with the Maxwell's equations and then a conversion of them to finite difference forms. The conditions for acceptable time and spatial increments are also given.

A set of governing equations for the scattered fields in the medium defined by μ and ε are

$$\nabla \times \vec{E}^s = -\mu\frac{\partial}{\partial t}\vec{H}^s - \sigma_m\vec{H}^s - \sigma_m\vec{H}^i - (\mu - \mu_0)\frac{\partial}{\partial t}\vec{H}^i \qquad (1)$$

$$\nabla \times \vec{H}^s = \varepsilon\frac{\partial}{\partial t}\vec{E}^s + \sigma\vec{E}^s + \sigma\vec{E}^i + (\varepsilon - \varepsilon_0)\frac{\partial}{\partial t}\vec{E}^i \qquad (2)$$

where the superscript i and s denote the incident and scattered fields, respectively. Applying the central difference approximation to the differential operations in (2), we obtain three scalar difference equations for $\vec{H}^s$, and one of them is given by

$$H_{sx}^{n+1/2}\{i, j, k\} = \left(\frac{2\mu - \sigma_m\delta t}{2\mu + \sigma_m\delta t}\right)H_{sx}^{n-1/2}\{i, j, k\}$$

$$+ \left(\frac{-2\delta t/\delta y}{2\mu + \sigma_m\delta t}\right)[E_{sz}^n\{i, j+1, k\} - E_{sz}^n\{i, j, k\}]$$

$$+ \left(\frac{-2\delta t/\delta z}{2\mu + \sigma_m\delta t}\right)[-E_{sy}^n\{i, j, k+1\} + E_{sy}^n\{i, j, k\}]$$

$$+\left(\frac{-2\sigma_m\delta t}{2\mu + \sigma_m\delta t}\right)H_{ix}^n\{i, j + 1/2, k + 1/2\}$$

$$+\left(\frac{-2(\mu - \mu_0)\delta t}{2\mu + \sigma_m\delta t}\right)H_{ix}^n\{i, j + 1/2, k + 1/2\} \tag{3}$$

where a sampled scalar function of time and space is denoted as $F^n\{i, j, k\} = F\{i\delta x, j\delta y, k\delta z, n\delta t\}$, and δt, δx, δy, and δz are the time and spatial sampling periods respectively. The three scalar difference equations for $\vec{E}^s$ are also obtained using a similar procedure. Note that in this formulation, the transmitted field below the rough interface is the sum of the incident and scattered fields.

To ensure an algorithm which is stable and accurate, the conditions on the spatial increment and the time increment δt are given in [2]. The spatial sampling periods, δx, δy, and δz are chosen to be $\lambda/16$. δt is chosen to satisfy the inequality

$$\delta t \leq \frac{1}{c}\left[\frac{1}{(\delta x)^2} + \frac{1}{(\delta y)^2} + \frac{1}{(\delta z)^2}\right]^{-1/2} \tag{4}$$

Truncation Condition

A radiation boundary condition or truncation boundary condition is needed at the boundary of the FD-TD computation domain (grid). The first order Mur's radiation boundary conditions [3] is used in this study.

THE RADAR CROSS SECTION, SCATTERING COEFFICIENT, AND ISAR IMAGING

The Radar Cross Section (RCS)

To utilize the existing frequency-domain near-to-far field transformation method, a discrete Fourier transform is first applied to the time domain near fields, i.e., the FD-TD solutions, giving the frequency domain near fields. The equivalent surface currents are determined using the frequency domain near fields by applying the equivalence theorem. The equivalent currents on the virtual surface above the rough boundary are given by

$$\vec{J}_{Seq} = \hat{n} \times \vec{H}^s(\omega) \quad \text{and} \quad \vec{M}_{Seq} = -\hat{n} \times \vec{E}^s(\omega) \tag{6}$$

where $\hat{n}$ is the outward unit normal vector of the surface. The scattered far fields (in frequency domain) are obtained by transforming the equivalent currents over free space Green's function [5]. The radar cross section is computed using

$$RCS = \lim_{r \to \infty} 4\pi r^2\left[\frac{E_{\phi \text{ far}}^2 + E_{\theta \text{ far}}^2}{E_{\phi \text{ inc}}^2 + E_{\theta \text{ inc}}^2}\right] \tag{7}$$

where $E_{\phi \text{ inc}}$ and $E_{\theta \text{ inc}}$ are the components of the incident (excitation) plane wave.

Window Function And Scattering Coefficient

To reduce the error due to boundary reflection and finite

surface size, a window (or weighting) function is applied to the truncated surface such that field near the surface edges are weighted down in the scattered far-field calculations. A Gaussian window function [4] with 60 dB attenuation at the edges of truncated surface is used in this study.

The window is applied to the fields (in frequency domain) prior to the near-to-far field transformation. Following the transformation, the radar cross section (RCS) is calculated using the scattered far fields. The scattering coefficient is obtained by normalizing the RCS to the effective area of the truncated surface.

Bistatic Inverse Synthetic Aperture Radar (ISAR) Imaging

The scattered far-fields from FD-TD simulation are used as inputs to the bistatic ISAR imaging algorithm developed at UTA. The 2-D complex reflectivity image can be written as

$$I(x, y) \approx \int_{k_x} \int_{k_y} E^s(k_x, k_y)\exp(jk_xx + jk_yy)dk_xdk_y \tag{8}$$

where k_x and k_y are the x- and y-component of free-space propagation vector.

NUMERICAL RESULTS

Case 1: bistatic scattering coefficients

Fig. 2 shows the bistatic scattering coefficients of the medium with rough boundary for VV polarization. The rough boundary has Gaussian correlation function and height distribution with $k\sigma = 0.35$ and $kL = 5.5$, where k is the free space wave number. The medium parameters are $\varepsilon_r = 2.1$ and $\sigma = 10^{-6}$ [S/m]. An incident wave with an incident angle of $30°$ and wavelength, λ, of 10 cm are used in the calculations.

A perfect conducting object (a rectangular box) with dimensions $l_x = l_y = 60$ cm and $l_z = 10$ cm is introduced into the lower medium. The object is 3 cm below the mean height of the boundary. Fig. 3 shows the bistatic scattering coefficients of the medium with buried object for VV polarization. Note that the difference between Fig. 2 and Fig. 3 is caused by the presence of the buried object only.

Case 2: 2-D ISAR Imaging

Fig. 4 and Fig. 5 show the 2-D ISAR images for the flat surface without and with a buried object, respectively. The images are constructed using the V-polarized scattered far-fields generated by the FD-TD simulation. The medium parameters are $\varepsilon_r = 2.5$ and $\sigma = 10^{-5}$ [S/m]. Dimensions of the perfect conducting object are $l_x = l_y = 24$ cm and $l_z = 16$ cm. The object is 8 cm below the surface. An incident wave with an incident angle of $0°$ and wavelength, λ, of 16 cm are used in the calculations. Note that the Gaussian window used in the FD-TD calculations is clearly observed in both figures. The presence of rectangular shaped buried object is also discernible in Fig. 5.

SUMMARY

FD-TD simulation of scattering from object embedded in a medium with either plane or rough boundary has been carried out in this study. Simulation results which show the effects of buried object on the scattering pattern of medium with rough boundary are presented in this paper.

REFERENCES

[1] Kunz, K.S., and Luebbers, J., *The finite difference time-domain method for electromagnetics*, CRC Press, Boca Raton, FL, 1993.

[2] Taflove, A., *Computational Electrodynamics*, Artech House, Norwood, MA, 1995.

[3] Mur, G., "Absorbing boundary conditions for the Finite-difference approximation of the time-domain electromagnetic field equations," *IEEE Trans. Electromagnetic Compatibility*, EMC-23, pp. 377-382, 1981.

[4] Chen, M.F., and Bai, S.Y., "Computer simulation of wave scattering from a dielectric random surface in two dimensions - Cylindrical case," *J. Elec. Waves Appl.*, vol. 4, no. 10, pp. 963-982, 1990.

[5] Ramo, S., Whinnery, J., and Van Duzer, T., Fields and Waves in Communication Electronics, 3rd ed., John Wiley & Sons, 1994.
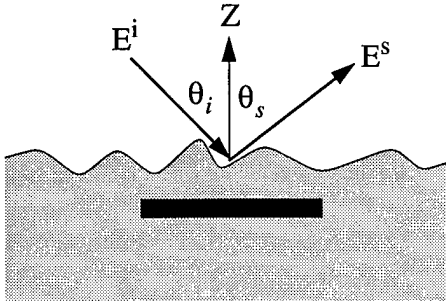
Figure 1. Geometry of the scattering from rough surface with buried object.
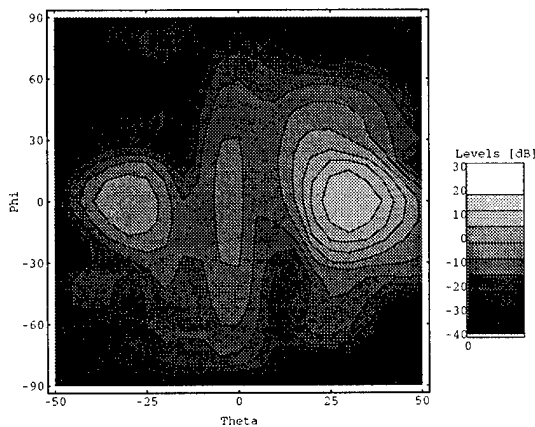
Figure 2. Bistatic scattering coefficients from the ran- . domly rough surface (VV).
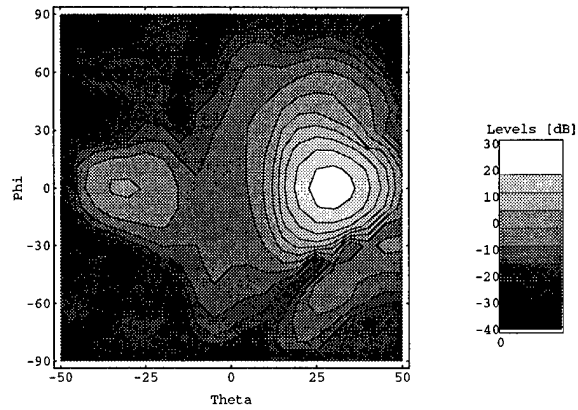
Figure 3. Bistatic scattering coefficients from the randomly rough surface with buried object (VV).
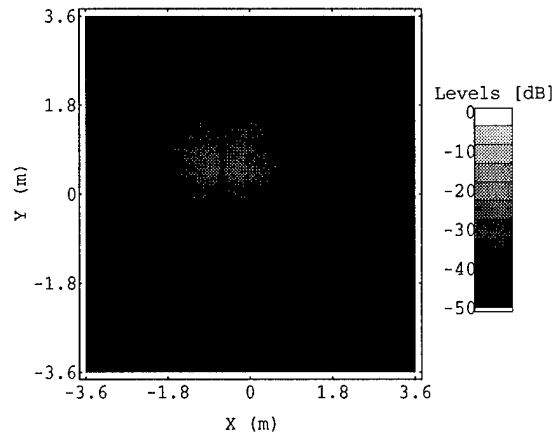
Figure 4. 2-D ISAR image of the flat surface; Gaussian windowed illumination and V-polarized fields.
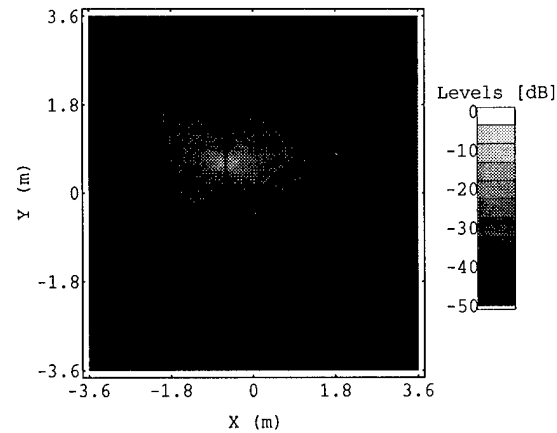
Figure 5. 2-D ISAR image of the flat surface with a buried object; Gaussian windowed illumination and V-polarized fields.

Using GPR and Seismic Reflection Measurements to Characterize Buried Objects: Large-Scale Simulations

Q. H. Liu*

Klipsch School of Electrical and Computer Engineering
New Mexico State University
Las Cruces, NM 88003, USA
Phone: (505) 646-5976; Fax: (505) 646-1435
Email: qhliu@nmsu.edu

ABSTRACT

Using ground-penetrating radar (GPR) and seismic reflection measurements simultaneously can give a much better characterization of buried objects than a stand-alone measurement since electromagnetic and seismic measurements provide complementary information of the buried objects and the surrounding environment. However, successful interpretation and processing of these measurements in large-scale problems rely on fast simulations. In this work we use the pseudospectral time-domain (PSTD) method newly developed by the author together with the finite-difference time-domain (FDTD) method to perform large-scale simulations of ground penetrating radar (GPR) and seismic reflection measurements. The PSTD method uses the fast Fourier transform (FFT) together with the perfectly matched layer (PML) to solve the partial-differential equations. It requires only two cells per wavelength regardless of the problem size. For multidimensional problems, the PSTD method is 4^D–32^D times more efficient than the conventional FDTD method. Hence, the PSTD algorithm is ideal for large-scale problems. The FDTD method, on the other hand, is used to model structures with fine details below 1/8 wavelength. Both the FDTD and PSTD algorithms are developed for conductive and viscous media, and thus can be used to model realistic losses in the subsurface media.

1. INTRODUCTION

Electromagnetic and acoustic measurements are widely used for detection and characterization of buried objects and voids, for examples in land-mine detection and identification and in nuclear waste-site characterization and monitoring. These measurements provide complementary information, namely the electromagnetic and mechanical properties, of the buried objects and the surrounding environment.

The electromagnetic field is more sensitive to the fluid contents in the pore space, while acoustic waves are more sensitive to the rock matrix. Therefore, we combine both measurements in this work for better detection and characterization of buried objects.

The emphasis of this work is to perform large-scale simulations of ground penetrating radar (GPR) and seismic reflection measurements using both the finite-difference time-domain (FDTD) method and the pseudospectral time-domain (PSTD) method recently developed by the author. The PSTD method uses the Fourier transform through an FFT fast Fourier transform) algorithm, instead of finite differences in the FDTD method, to represent the spatial derivatives in the partial differential equations. The wraparound effect due to the use of FFT is eliminated by using a perfectly matched layer (PML) as an absorbing boundary condition. The PSTD method requires only two cells per wavelength to obtain a comparable accuracy as the FDTD method with 8-16 cells per wavelength for a moderate size problem. For larger problems, the FDTD method requires much smaller cells, and hence the advantage of the PSTD method becomes even more profound.

Thus, the PSTD method is ideal for large-scale problems where the minimum structure of inhomogeneities is at least in the order of half wavelength. For other problems where the structure has fine details below 1/8 wavelength, we still use the FDTD method, since in order to resolve such small details in the geometrical representation, the PSTD method also needs a fine discretization and a smaller time step. In this sense the FDTD method is complementary to the new PSTD method for problems with very fine details. Both the FDTD and PSTD algorithms are developed for conductive and viscous media, and thus can be used to model realistic losses in the subsurface media. We will show various results using both algorithms for large-scale multidimensional problems. The development of the new PSTD method provides an important simulation tool for many large-scale electromagnetic and acoustic problems which are currently unsolvable with con-

ventional methods.

2. THE PSTD AND FDTD ALGORITHMS

For simulations of GPR and seismic measurements, Maxwell's equations and scalar acoustic equation are solved numerically using both the new PSTD and the conventional FDTD algorithms. The absorbing boundary condition used at the computational edge is the new perfectly matched layer (PML) [1]. In order to formulate the problem with PML, let us consider the acoustic equation using a coordinate-stretching variable $e_\eta = a_\eta + i\frac{\omega_\eta}{\omega}$. Following [2], we can derive the split acoustic equations as

$$a_\eta \rho \frac{\partial v_\eta}{\partial t} + \omega_\eta \rho v_\eta = -\frac{\partial p}{\partial \eta}, \qquad (1)$$

$$a_\eta \frac{\partial p^{(\eta)}}{\partial t} + (a_\eta \gamma c^2 + \omega_\eta) p^{(\eta)}$$

$$+\omega_\eta \gamma c^2 \int_{-\infty}^{t} p^{(\eta)}(\mathbf{r}, t') dt' = -\rho c^2 \frac{\partial v_\eta}{\partial \eta} + f_s^{(\eta)}(\mathbf{r}, t). \qquad (2)$$

It is worthwhile to note the following important difference between an acoustic PML and an elastic PML: In the acoustic PML, there is no need to split the particle velocity $\mathbf{v}$ into $\mathbf{v}^{(\eta)}$ as in the elastic PML. This is simply because that the second-rank stress tensor in the elastic case collapses into a zero-rank tensor (i.e., a scalar pressure field) in the acoustic case. Equations (1) and (2) consist of a total of 6 scalar equations. Similarly, split Maxwell's equations can be derived for conductive media [3–5].

These partial differential equations can be solved by using the conventional FDTD methods where both the spatial and temporal derivatives are approximated by finite differences. In contrast, in the newly developed PSTD method, the FFT algorithm is used to represent the spatial derivative in (1) and (2). For example, from (1) we have

$$a_\eta \rho \frac{\partial v_\eta}{\partial t} + \omega_\eta \rho v_\eta = \mathcal{F}_\eta^{-1}\{ik_\eta \mathcal{F}_\eta[p]\}, \qquad (3)$$

where $\mathcal{F}_\eta$ and $\mathcal{F}_\eta^{-1}$ denote forward and inverse FFT in the η direction which are calculated by FFT's. A similar result can be obtained for (2) as well as the split Maxwell's equations [5]. FDTD methods have also been developed for elastic wave propagation in multidimensional problems [6, 7].

The important difference between the PSTD method and the FDTD method is the approximation of spatial derivatives. The spatial derivatives

have an infinite order of accuracy in the PSTD algorithm, while a second-order accuracy in the conventional FDTD method. In addition, in contrast to the standard Yee's algorithm, the PSTD method uses a spatially centered grid where all field components are located at the same points. This provides an important advantage over the Yee's algorithm since the material properties are not altered by the presence of the staggered grid. The temporal grid, however, is staggered in the same way as in the FDTD method. In the PSTD algorithm, perfectly matched layers are implemented at the outer edge as the absorbing boundary condition to eliminate the wraparound effect. The dispersion relations and the stability condition in the PSTD algorithm are analyzed in [5].

3. NUMERICAL RESULTS

Theoretical analysis and numerical experiments confirm that the PSTD algorithm requires only two cells per minimum wavelength, i.e., the minimum Nyquist sampling rate, regardless of the problem size [5]. In contrast, the conventional FDTD method requires 10–20 cells per wavelength for a problem of moderate size. As the problem size grows, the FDTD requires increasingly finer discretization to maintain the accuracy.

As an example of the applications of the PSTD algorithm, we simulate subsurface radar and seismic reflection measurements of two buried objects as shown in Fig. 1(a) at the cross section of $y = 4.875$ m. The two rectangular objects extend from $y = 3.675$ to $y = 6.075$ m. The half-space is truncated to $0 \le y \le 9.6$ m by the PML absorbing boundary condition. The electromagnetic source and the seismic source are location at the center of the earth surface, and they operate at a center frequency of $f_c = 100$ MHz and $f_c = 2.667$ kHz respectively. With respect to the background medium in the earth, the object on the left has a large contrast in its electromagnetic properties, and a small contrast in its acoustic properties, and vise versa for the object on the right. At the highest frequency ($f_h = 2.5 f_c$) beyond which the energy is negligible, this 3-D problem has a size of $32\lambda \times 32\lambda \times 32\lambda$ (where λ is the wavelength in the earth). Using the PSTD method, we need a grid with only $64 \times 64 \times 64$ cells. Figs. 1(b) and 1(c) display the electromagnetic and acoustic waveforms measured at an array of receivers on the ground. Clearly, the two sets of measurements provide complementary information about the buried objects. If the conventional FDTD method had been used, this problem would have to be discretized by a grid with roughly 256–512 cells in each dimension in order to achieve a comparable accuracy. Therefore, for this problem, the

PSTD algorithm is about two orders of magnitude more efficient than the FDTD method. More numerical examples will be shown in the presentation.

4. CONCLUSIONS

The ground-penetrating radar and seismic reflection measurements can be used together to enhance the ability to characterize buried objects. We have developed pseudospectral time-domain and finite-difference time-domain algorithms to simulate large-scale problems encountered in GPR and seismic measurements for lossy media. The PSTD algorithm has an infinite-order of accuracy in the spatial representation, and hence requires only two cells per wavelength (Nyquist rate) to obtain accurate results. It is a factor of 4^D–32^D times more efficient than FDTD methods (where D is the dimensionality of the problem) for a problem of size 32λ to 512λ in each dimension. In terms of the spatial sampling rate, the PSTD algorithm is an optimal solution to time-domain Maxwell's equations and acoustic equations. The FDTD method, on the other hand, can be used for simulations of structures with fine details much smaller than half a wavelength.

REFERENCES

[1] J.-P. Berenger, "A perfectly matched layer for the absorption of electromagnetic waves," *J. Computational Physics*, vol. 114, pp. 185–200, 1994.

[2] Q. H. Liu, and J. Tao, "The perfectly matched layer (PML) for acoustic waves in absorptive media," *Technical Report*, NMSU-ECE-97-003, New Mexico State University, March 1997.

[3] Q. H. Liu, "A spectral-domain method with perfectly matched layers for time-domain solutions of Maxwell's equations," 1996 URSI Meeting, Baltimore, MD, July 1996.

[4] Q. H. Liu, "An FDTD algorithm with perfectly matched layers for conductive media," *Micro. Opt. Tech. Lett.*, vol. 10, no. 2, pp. 134–137, 1997.

[5] Q. H. Liu, "The PSTD algorithm: a time-domain method requiring only two cells per wavelength," *Microwave Opt. Tech. Lett.*, vol. 10, no. 6, June 1997.

[6] Q. H. Liu, F. Daube, C. Randall, E. Schoen, H. Liu, and P. Lee, "A three-dimensional finite difference simulation of sonic logging," *J. Acoust. Soc. Am.*, vol. 100, 72–79, 1996.

[7] W. C. Chew, and Q. H. Liu, "Perfectly matched layers for elastodynamics: A new absorbing boundary condition," *J. Computational Acoust.*, vol. 4, no. 4, 72–79, 1996.
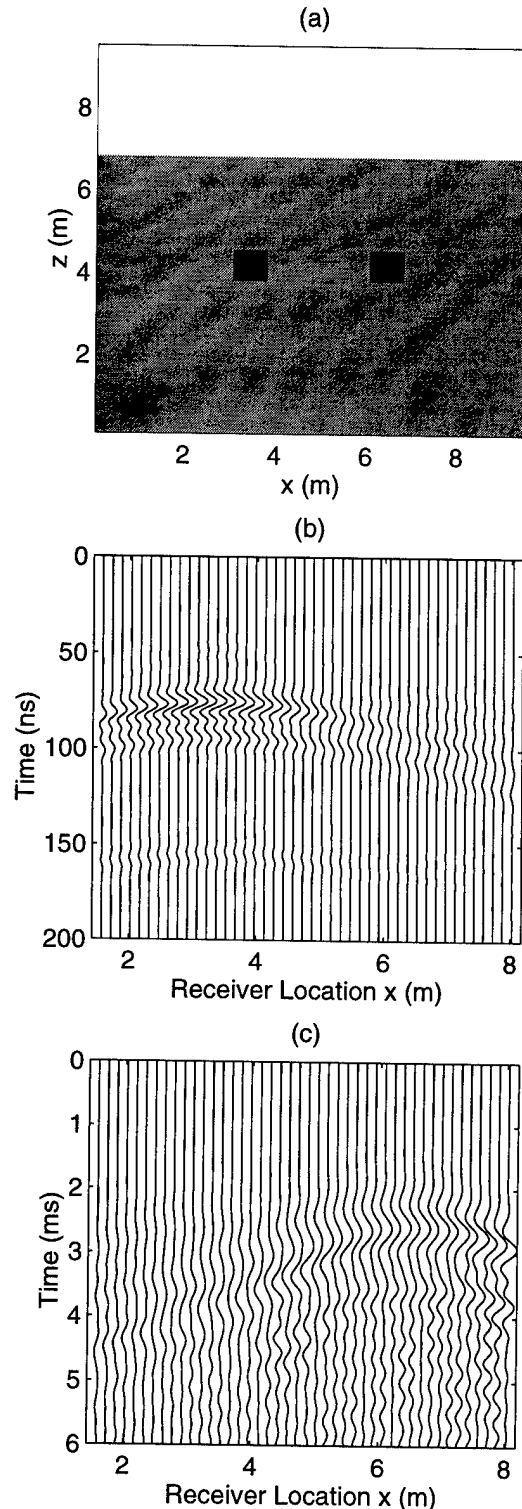
Fig. 1. A 3-D problem of size $32\lambda \times 32\lambda \times 32\lambda$. (a) Geometry of two buried objects having different sensitivities to electromagnetic and acoustic waves. Scattered electromagnetic field (b) and scattered acoustic field (c) at an array of receivers.

CLIMACS: Design of a High Radiometric Resolution SAR for Land and Sea Ice Applications

V.Adrian, N.Suinot
ALCATEL ESPACE, 26 av J.F Champollion, 31037 Toulouse Cedex, France
Telephone (33) 5 61 19 61 08, Fax (33) 5 61 19 61 63, Email FRDK8XC8@ibmmail.com

C.C.Lin
ESTEC, PO Box 299, 2200 AG Nordwijk, The Netherlands
Telephone (31) 71 565 5813, Fax (31) 71 565 4696, Email clin@estec.esa.nl

ABSTRACT

CLIMACS (Climate studies of Land surfaces and Ice using Microwave ACtive Sensing) is a synthetic aperture radar and is intended to be an element of a mission dedicated to global observation of land surfaces and ice. CLIMACS will provide relevant information for the studies related to climate change. In addition further expected applications are in the areas of disaster monitoring, ice reconnaissance and forest monitoring. In order to obtain valuable geophysical products for these applications, SAR images with modest spatial resolution but very high radiometric accuracy and high temporal sampling are desirable.

INTRODUCTION

In the context of the Earth Observation Preparatory Program, ESA is looking for a modest spatial resolution wide fixed swath SAR instrument for global monitoring of the Earth. This is the CLIMACS instrument which is intended to be an element of a global land and sea ice monitoring mission [1].

ESA has awarded two parallel prephase A studies at industrial level in order to design a SAR for CLIMACS purpose. This paper is related to the feasibility study leaded by ALCATEL ESPACE with CASA, SAAB ERICSSON SPACE, Oerlikon Contraves and Ylinen Electronics as subcontractors. We first recall the main mission objectives and the origin of the main instrument requirements. Then the remarkable features of the instrument and the main performance are reported with special emphasis on coverage, radiometric performances and needed resources. The final budgets show the compliance with small satellite mission and low cost program.

MISSION OBJECTIVES

The land surfaces act as a part of the coupled boundary to the global heat exchanges, to the general atmospheric circulation and to the global hydrological cycle. Their role is complex due to their heterogeneous nature and to their short time scale response. Although, the part played by the land is smaller than the one played by the ocean, it is over the land that many of the apparently irreversible changes occur. Hence it is a good indicator of any climatic changes which are taking place over the lifetime of the Earth.

Furthermore the radar measurements are independent of cloud coverage, illumination by the sun and atmospheric disturbances, hence provide uninterrupted observations with high temporal sampling rate.

CLIMACS will provide relevant information for the studies of:

- Climate change in terms of global carbon cycle and global energy cycle,
- Processes monitoring,
- Interactions between human activities and ecological systems.

In addition, further expected applications are in the areas of:

- Operational ice reconnaissance,
- Operational large scale hydrology,
- Large scale disaster monitoring,
- Large scale crop monitoring,
- Forest monitoring.

INSTRUMENT REQUIREMENTS

In order to obtain valuable geophysical products for the above applications, SAR images with modest spatial resolution, but high radiometric accuracy are desirable. Furthermore, the objective of global Earth monitoring with high temporal resolution leads to an ambitious coverage requirement (more than 95% of earth surface within 5 days) which in turn implies a very large swath instrument. In addition, since the land surfaces and polar regions are rather of heterogeneous nature, a multiple frequency (2 among P, L, C, X band) and multiple polarization system is desirable. This is the basis of the instrument requirements [2].

We have to notice that the absolute radiometric accuracy includes the radiometric resolution (speckle contribution) but also all the errors (calibration, mispointing, radar drift, ambiguities...). Finally we have to point out that the requirements are given in terms of final image quality (multi look spatial resolution, absolute radiometric accuracy) thus leading to a more open definition of the instrument.

The first challenge of such a radar is to design a very large swath instrument in order to be compliant with the coverage requirement. The second challenge is on one hand to be able to generate a great number of looks and on the other hand to

have a good calibration scheme in order to be compliant with the absolute radiometric accuracy requirement. The third challenge, which is not negligible, is to design a low mass and low power consumption dual frequency and dual polarization concept.

INSTRUMENT DESIGN

In order to reach the challenging design objective a coupled parametric orbital mission and radar system study was first performed. This phase was followed by a trade-off among the main promising concepts [3]. Finally the selected design is based on a ScanSAR mode (Fig 1) with 4 sub-swaths ensuring a total swath width of 430 km. Each sub-swath is illuminated twice during the SAR integration time in order to reduce the radiometric variation.
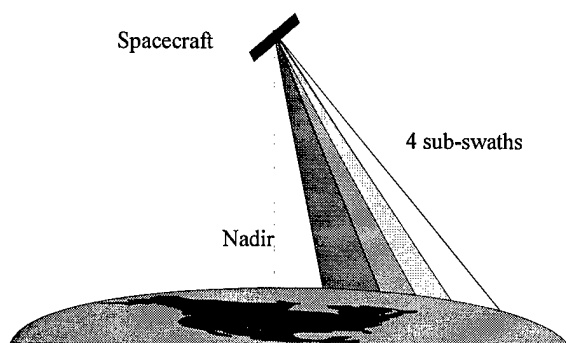
Figure 1: ScanSar Concept for CLIMACS

The instrument synoptic is given Fig 2. It includes separated antennas and HPA (High Power Amplifier) subsystems, but common RF (RadioFrequency) and digital subsystems. In order to limit the antenna size and the mass, C and X-band are selected. An absolute radiometric accuracy of 0.65 dB is obtained by averaging of a great number of looks (430) and by using a stable calibration scheme. In turn the multi-look spatial resolution is modest (2 km) in order to limit the needed resources. A complete cold redundancy scheme is included in order to ensure continuous operation during 5 years.

A low risk and low cost approach is followed for the design by selecting as far as possible mature technologies and techniques.

The remarkable features of the CLIMACS instrument are:

- Digital chirp generator ensuring versatility,
- Demodulator using sub-harmonic sampling scheme,
- Centralized distribution using one 1800 W RF peak power TWT in C-band, and one 400 W RF peak power TWT in X-band,
- Blass matrices in order to ensure beam steering capability (4 sub-swaths),
- X-band single polarization antenna using waveguide technology,
- C-band dual polarization antenna using waveguide distribution and triplate radiating elements,
- Raw data reduction using BAQ algorithm,
- Solid state mass memory with 90 Gbits capacity.

The fully passive multi-beam antenna design (Fig 3), ensures low losses, low mass and high stability. The Blass matrices are of particular importance in order to ensure the beam steering capability necessary for the ScanSar mode.
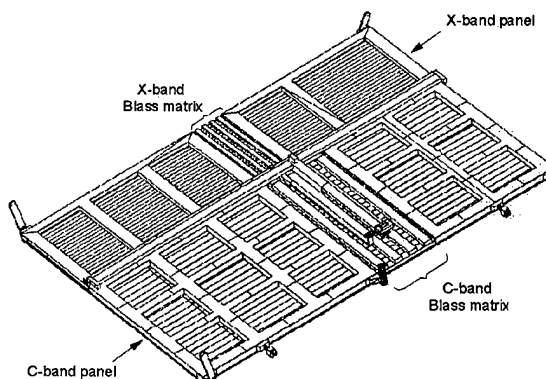
Figure 3: Antenna panel (with Blass matrices)

Figure 2: Instrument synoptic (redundancy not shown)

INSTRUMENT PERFORMANCES

COVERAGE   ■ 3 DAYS   ■ 5 DAYS
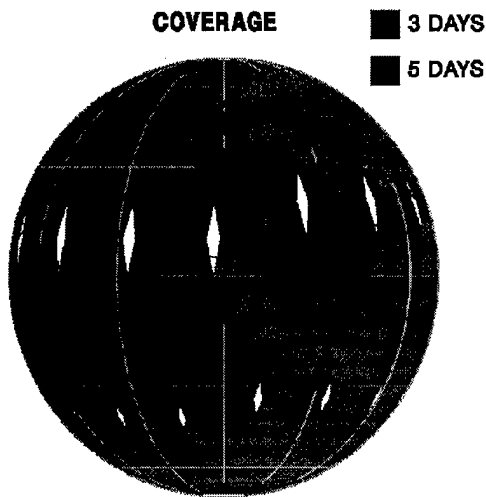
Figure 4: Coverage performance

The main performance and budget characteristics are given in Table 1 and Table 2. In addition the coverage obtained within 3 days and 5 days is shown Fig 4. These rather good figures are obtained mainly due to the orbit choice and radar swath width. We have to notice that the frequency choice (X and C band) is of importance in the coverage performance. In fact for a given antenna height requirement, the high frequency choice allows a larger swath and thus a better coverage performance. For example the L band choice could not lead to such a swath width.

Table 1: Performances summary

Orbit	Polar sun-synchronous
Altitude	510 km
Coverage	80 % within 3 days 98% within 5 days Global within 6 days
Swath width	430 km
Incidence range	12 to 50 deg
Frequency	C and X band
Polarization	C band: HH and VV X band: VV
Spatial resolution	2 km * 2 km
Radiometric accuracy	≤ 0.65 dB for 2*2 km² spatial resolution
Radiometric resolution	≤ 0.40 dB for 2*2 km² ≤ 0.76 dB for 1*1 km² ≤ 1.40 dB for 0.5*0.5 km²
Ambiguity ratio	20 dB
ISLR	19 dB
PSLR	25 dB

The absolute radiometric accuracy is better than 0.65 dB for a spatial resolution of 2 km by 2 km. This figure includes the radiometric resolution contribution (0.4 dB) and all the instrument errors. We can notice that, depending on the user needs, we can simply trade the radiometric resolution with the spatial resolution. This allows a very flexible final product.

The needed resources are rather low for a multiple frequency and multiple polarization instrument. In addition the stowed size of the antenna (5 panels) is compatible with various types of launchers and platforms. These figures are compatible with a small satellite mission. On the other hand the design being based on mature technology, the technical risks are very limited. This leads to a low cost mission.

Table 2: Budget summary

Antenna size	12m * 1.6 m
Mass	230 kg
Power consumption	350 W
In flight operation	5 years continuous
Reliability	0.9
Data rate	15 Mbit/s
Mass memory unit	90 Gbits
Launcher compatibility	ARIANE 4 DELTA III PROTON 1D ATLAS MPF

CONCLUSION

The proposed CLIMACS instrument offers:

- Good coverage performance (global within 6 days and better than 95% within 5 days),
- Good radiometric accuracy thanks to the number of looks (430) and the calibration,
- Rather low budget figures (mass, power consumption, and antenna size),
- Compatibility with various types of launchers,
- Uncriticallity of necessary technology,
- Continuous operation.

This instrument will ensure continuity of C band data availability (ERS, ASAR) enhanced by a X band channel.

In addition the design is compatible with small satellite mission and low cost program.

REFERENCES

[1] C.C. Lin, P. Mancini, "A SAR Instrument for Global Monitoring of Land Surfaces and Polar Ice", Proc IGARSS'94, Pasadena, pp 1525-1528, Aug 1994.

[2] C. Regolo, C.C Lin, P. Mancini, "CLIMACS: A medium/low resolution SAR for global monitoring of land surfaces and sea ice", Proc EUSAR 96, Konigswinter, Germany, 1996, pp 305-308.

[3] V. Adrian, N. Suinot, C.C. Lin, "CLIMACS prephase A, Design of a medium resolution SAR for land applications", SPIE Vol 2958, pp 406-411, Sept 1996.

Coastal Wind Field Retrievals from ERS SAR Images

E. Korsbakken[1], J. A. Johannessen[2] and O.M. Johannessen[3]

[1]Nansen Environmental and Remote Sensing Center (NERSC), Edvard Griegs vei 3a, N-5037 Solheimsviken, Bergen Norway.
e-mail: Erik.Korsbakken@nrsc.no, WWW: http://www.nrsc.no:8001/~erikk/

2ESTEC, European Space Agency, P.O. Box 299, 2200 AG Noordwijk, The Netherlands
phone:+31 71 56 55 959, fax:+31 71 56 55 675, email: jjohanne@estec.esa.nl

[3]NERSC/Geophysical Institute, University of Bergen

ABSTRACT

A unique series of ERS-1/2 C-band SAR images was obtained off the southern coast of Norway during the COAST WATCH'95 experiment in September 1995. In this paper we carry out a systematic analysis of the mesoscale coastal wind field conditions expressed in the SAR images. Four different categories of phenomena including wind rows, fetch limited seas, wind fronts and oceanographic fronts are examined and discussed. The quantitative retrievals of the wind field are based on examination of the backscatter characteristics and the spectral properties of the SAR image. Results are compared and validated against coincident ship and buoy data providing independent observations of the oceanographic and meteorological conditions.

INTRODUCTION

In order to better quantify SAR imaging of upper ocean and atmospheric boundary layer processes, an experiment, COAST WATCH'95 [1], was carried out off the southwest coast of Norway during September 1995 as a ERS-1 and ERS-2 tandem announcement of opportunity experiment. The tandem operation provided a unique SAR coverage of the experiment area consisting of 148 SAR images (frames). Meteorological and oceanographical in situ observations were provided from the research vessel R/V Håkon Mosby of University of Bergen, and an advanced metocean buoy from the Naval Postgraduate School, Monterey.

The main study objective reported in this paper is to demonstrate the optimum wind retrieval from SAR images. We will use the procedure outlined in [2] and [3].

WIND RETRIEVAL ALGORITHMS

The two SAR wind retrieval algorithms used are based on the extraction of the wind field from different parts of the ocean surface wave spectrum, in particular the medium wind wave regime and the small centimeter scale regime. Fig. 1 shows a conceptual overview of the wind field estimation as further described below.

SAR Wind Algorithm (SWA)

In case of a fully developed sea (no fetch limitation) the empirical SWA relation, based on evaluation of 1200 SAR wave-mode imagettes with a central incidence angle of 20.2° is given by [4] as

$$U_{10} = 4.75 \left(ms^{-1} \right) \left(\frac{\lambda_c - 30}{110} \right) \left(\frac{m}{m} \right)$$

where U_{10} is the wind speed at 10 m above the surface and λ_c is the azimuth cut-off wave length. Assuming a Gaussian shaped low pass filter for the azimuth cut-off the cut-off wavelength can be estimated from the auto covariance function (ACF) derived from an inverse Fourier transform of the SAR image power spectrum.

The CMOD4 model

The CMOD4 wind retrieval model [5] is developed for the ERS-1 C-band scatterometer but it is also shown to give good estimates of wind speed when applied to ERS-1 SAR images

The CMOD4 model provides σ_0 values as a function of relative wind direction ($\phi=0$ for a wind blowing toward the radar), wind speed and incidence angle, expressed as

$$\sigma_0 = B_0[1 + B_1 \cos(\phi) + B_2 \cos(2\phi)]$$

The coefficients B0, B1 and B2 depend on the local incidence angle of the radar beam and wind speed.

In this paper we also emphasize that the wind direction can be estimated from the CMOD4 model for different incidence angles provided the wind speed, derived from the SWA method, can be associated with the corresponding measured backscatter (σ_0). In such cases we will show that four solutions, i.e. two pairs, each with a 180° ambiguity can be
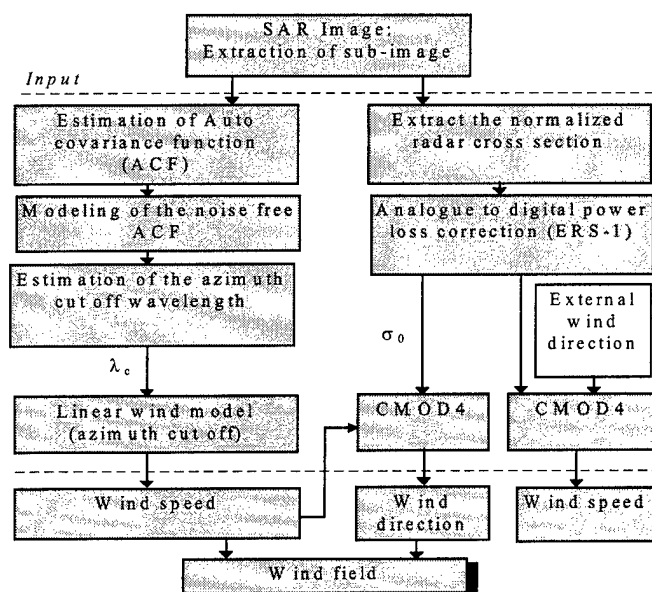
Figure 1 Conceptual overview of wind retrieval models. The external wind direction may be obtained from wind rows in the SAR image.

found, except in the cases when the direction is close to upwind (the wind blowing towards the radar) or downwind, for which only one pair is found.

COAST WATCH'95 Analysis

Two case studies from the Coast Watch'95 data base are presented including: a) wind rows under fetch limited conditions and b) oceanic front (jet) together with a local wind front:

a) The ERS-1 SAR images are from 17 September 1995 shows a characteristic pattern of wind rows aligned in the wind direction of about 110°. In particular, the northernmost area, west of the coast, lacks of expressions features, while the southern areas are recognized with wind rows with an west-northwestward orientation of 110°. There is also a gradual increase in the backscatter towards south.. The wind
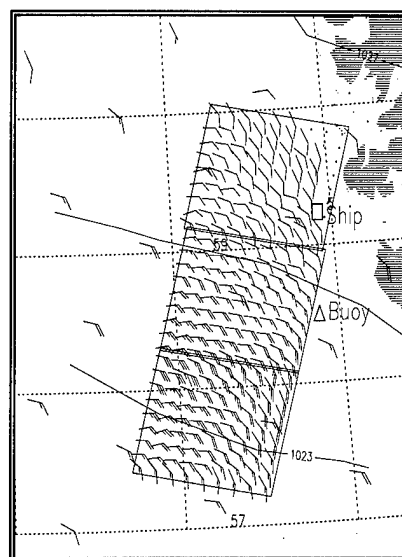
Figure 2 SAR image scatter plot and wind vector map from 17 September 1995

speed obtained in vicinity of the ship is about 13 m/s, and reveals a clear north west gradient as expected. The obtained wind direction is in good agreement with the isobars from the hindcast model. Wind retrievals from a total of 238 sub-images were compared for the 17 September images. The CMOD4 - SWA wind speed difference was less than 2 m/s for about 90 % of the sub images. The scatter plot in Fig. 2 (right) shows good agreement between the SWA and the CMOD4 derived wind speeds in the range of 3 to 15 m/s for all three images.

b) The final case study is based on the SAR images from 27 September 1995 which shows a westward flowing coastal jet bounded by two distinct, some places parallel fronts. A local, 5-10 km wide wind feature is also running diagonally across the image, in the second image. A total of 144 sub images were analyzed for the 27 September image of which only 8 % have a wind speed difference of less than 2 m/s in the range from 3 to 15 m/s. From the SAR image power spectrum (SIPS) analysis a strong peak in the energy occurs
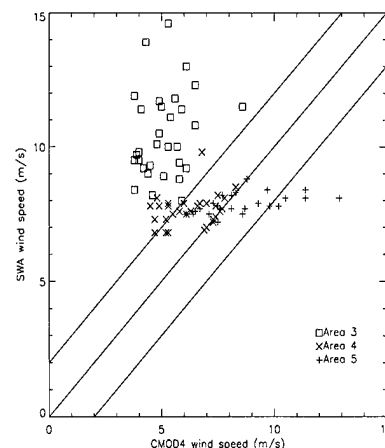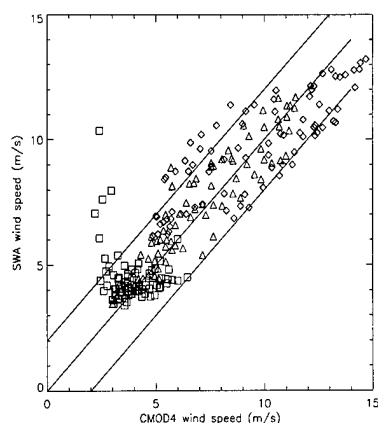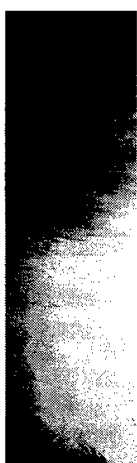
Figure 3

between 150 and 300 m wavelength, 30° to 50° to the range axis, in the SIPS. This peak in the SIPS is most likely caused by a corresponding peak in the real ocean wave spectrum suggesting the presence of incoming swell. The swell seems to affect the wind field results, in particular the SWA wind speed and the directional estimates. A shift of about 1.5 m/s to 2 m/s in the CMOD4 wind speed is observed across the jet. In contrast to CMOD4 wind speeds there is a large spread in the SWA derived wind speed for the areas. However, no evidence of wind shifts are found across the fronts.

Fig.3 (right) shows that the SWA wind speed is up to 10 m/s higher than the CMOD4. Particularly no correlation is therefore present. In comparison to the previous results, in particular from Case a, the results are poor. The SWA is consistently larger than CMOD4 by at least 4 m/s and completely without any correlation for the conditions encountered in Case b.

since the first method uses radar backscatter values while the latter uses spectral characteristics. But as mentioned in the analysis of the 17 September image, the SWA method is limited to SAR images containing clear wave modulation from which the azimuth cut-off can be derived. In the case of very low wind conditions (lower than approximately 3 m/s) or in presence of slicks the SWA method will therefore breakdown. But these conditions will also effect the CMOD4 since the threshold wind speed for C-band waves is around 3 m/s [6].

Hence, by combining the SWA and CMOD4 methods, the limitations encountered by each individually, can be suppressed. Moreover, this combination allows the wind direction to be retrieved independently thus offering a system for quantitative estimation of wind speed and direction at a resolution of about 10 km.

SUMMARY

In this paper we have shown that the radar backscatter and spectral signatures of the ocean surface obtained from ERS-1,2 SAR images can provide valuable and quantitative information on near surface wind speed and wind direction. 5 ERS SAR images, from 17 and 27 September 1995 have been examined by studying their σ_0 and spectral properties. Two different wind retrieval models, SWA and CMOD4, have been applied to the data. We have found by comparing the SWA and CMOD4 wind speed retrievals that about 90 % of the sub images gives a wind speed difference less than 2 m/s for case a) and about 8 % for case b).

It is demonstrated that the surface conditions impact on the performances of the different wind field retrieval methods and their corresponding results. The presence of homogenous wind rows are clearly favored. For fetch limited seas and in vicinity of wind fronts, on the other hand, the SWA method underestimates the wind speed. For fetch limited seas the waves are not in equilibrium with the near surface wind speed. Hence, the distribution of the velocity field of surface scatters, as introduced by the orbital velocity of the waves will be narrower than for fully developed seas leading to underestimation. Moreover the relatively large relaxation rate for the longer wind waves allows these waves to propagate across a wind front. Hence they will maintain their original equilibrium state over some distance away from the front. In turn, the wind front will not be resolved properly by the SWA method. For the same reason, the presence of swell may cause an increase in the derived wind speed. In contrast the CMOD4 method is not limited by these conditions.

While absolute image calibration is necessary for the CMOD4 method, it is not required for the SWA method

REFERENCES

[1] Johannessen O. M., Johannessen J. A., Jenkins A. D., Davidson K., Lyzenga D. R., Shuchman R., Samuel P., Espedal H. A., Knulst J., Dano E. and Reistad M., 'COAST WATCH-95 ERS-1,2 SAR Applications of Mesoscale Upper Ocean and Atmospheric Boundary Layer Processes off the coast of Norway', Proceedings of IGARSS'96 Lincoln, Nebraska, 1996.

[2] Korsbakken E. 'Quantitative Wind Field Retrievals from ERS SAR Images' YGT report. Available at the Ocean and Sea Ice Unit, Earth Sciences Division, ESTEC, ESA, 1996 a.

[3] Korsbakken E and Johannessen J. A. 'Quantitative Wind Field Retrievals from ERS SAR Images' in proceedings of the Third ERS Workshop IFREMER/BREST, June 18-20, 1996 b

[4] Chapron B., Fouhaily T. E. and Kerbaol V. 'Calibration and Validation of ERS Wave Mode Products' IFREMER March 95 Document DRO/OS/95-02, 1995.

[5] Stoffelen A. and Anderson D.L.T. 'ERS-1 Scatterometer Data and Characteristics and Wind Retrieval Skills' Proceeding of first ERS-1 Symposium, ESA SP-359, March, 1993.

[6] Johannessen J.A., Vachon P.W. and Johannessen O.M. 'ERS-1 SAR imaging of marine boundary layer processes' Earth Observation Quarterly, ESA, 1995.

CLIMATOLOGY OF WIND AND WAVES FROM SATELLITE ALTIMETERS

Paul A. Hwang, William J. Teague, and Gregg A. Jacobs
Oceanography Division, Naval Research Laboratory, Stennis Space Center, MS, 39529 USA
Phone: (601)6884708; Fax: (601)6884843; email: phwang@nrlssc.navy.mil

Abstract – Based on comparisons with buoy data, the wind speed and wave height measured by satellite altimeters are in excellent agreement with in-situ measurements. In regions of low swell effects, the combination of wind speed and wave height further yields the information of wave period. The long-term monitoring of these wave parameters from satellite altimeters can be used to study the wave climate of the world oceans. Examples from application to the Gulf of Mexico and the Yellow and East China Seas are presented. Using three years of TOPEX/POSEIDON continuous data, the annual and seasonal maps of the wind and wave climatology of the two regions can be constructed. Many mesoscale features can be clearly identified, and the geometric effects on the wave pattern can be seen from the wind and wave distributions.

INTRODUCTION

Satellite remote sensing provides an efficient way for monitoring global and regional oceanographic parameters. Spaceborne altimeters following their many generations of development have provided high-quality data on the sea state with an unusually high spatial density. For example, TOPEX/POSEIDON (hereafter referred. to as TOPEX) provides wind and wave information every second, corresponding to approximately a 7-km resolution along the satellite tracks. The spacing of the tracks is nominally 316 km (127 revolutions per repeat cycle) at the equator and much smaller at higher latitudes. The revisiting period of each track is 9.9156 days [1]. With such high density coverage, we can study the regional wave climatology using the TOPEX altimeter data output of wind and wave parameters. In this paper, the measurement accuracy of the wind and wave parameters from the TOPEX altimeter is validated with in-situ ocean buoy data

COMPARISON OF WIND AND WAVE PARAMETERS FROM ALTIMETERS WITH IN-SITU BUOY DATA

Comparisons of TOPEX significant wave heights (H) and wind speed (U) with in-situ measurements from surface buoys have shown very positive agreement [2-3]. In particular, Ref. [3] presents a comprehensive comparison of wind speed and wave height between the TOPEX altimeters and 14 moored buoys along the west coast of Canada, of which 3 are in the deep ocean, approximately 400 km west of the British Columbia coast; 6 are in the exposed positions within 100 km from the coast, and 5 are in sheltered coastal waters. Detailed statistical comparisons of these three groups of buoys with all three altimeters (NASA Ku- and C-band altimeters and CNES Ku-band solid state altimeter) are performed. Excellent agreement between the altimeter and buoy measurements of the significant wave height is found for the nine buoys in exposed positions. For coastal regions, the agreement is clearly not as good. The large variation in the coastal comparison is attributed to the local variation of the wave conditions due to the close proximity to the shoreline. Ref. [3] further shows that in the exposed locations, the rms data scatter is greatly reduced when the spatial distance between TOPEX and buoy observations is reduced to 10 km. For the three outer buoys and 6 inner buoys, the rms differences in wave height reduce to 0.14 and 0.15 m, respectively.

The excellent agreement on the wave height measurement is also confirmed in the Gulf of Mexico stations. A detailed statistical comparison of 6 data sets in the Gulf of Mexico is presented in [4]. The results pertaining to the three key properties of a wave field, the significant wave height, significant wave period and wind speed, are shown in Figs. 1a-c, which display the comparisons of the significant wave height, wind speed and characteristic (average) wave period derived from the TOPEX Ku-band altimeter and NDBC buoy. Only data points within 10 km spatial lags are used. The measurements from the two systems are essentially equivalent. The average ratio and one standard deviation of the wave heights, wind speeds, and characteristic wave periods are 1.01±0.14, 0.95±0.11, 1.06±0.13, respectively. The distributions of these ratios are displayed in Figures 1d-f, showing very narrow spreading.

WIND AND WAVE CLIMATOLOGY

Gulf of Mexico (GoM)
There are fourteen ground tracks from TOPEX in the GoM. The wind speed and wave height derived from the altimeters can be used to construct synoptic views of the regions. In addition, wave period and large scale surface steepness due to wave motion can be calculated from the wind speed and wave height parameters. In forming the climatological maps, the TOPEX data are averaged over one-degree squares. TOPEX data from one or more tracks that fall within any part of a square are used in the average for that square. The TOPEX data have high spatial resolution of about 7 km along track. The across-tracks (approximately 300 km) and temporal (10 days repeat cycle) resolutions are relatively coarse, so the shortest averaging period used at this stage is 90 days. The results reveal the seasonal and annual variations of the wind and wave climate in the regions [5]. Fig. 2 shows an example of the three-month (January to March, 1994) average of the wind speed, wave height, wave period and wave steepness in the GoM. Other seasons, and annual as well as three-year averages are also processed but not shown here. A few common features of the wind and wave climate in the GoM include: (1) The long-term average of the mean wave height increases from east to west. For example, the wave height range of the three-year average is from 0.5 m off the coast of Florida to 1.5 m off the coast of Texas. Similarly, mean wind speed, wave period and wave steepness show a trend of increasing from east to west. (2) Superimposed on the westward increasing trend, there is an oscillatory components, such that there are one to two local maximum values of the wind and wave parameters in longitudinal direction. The length scale of the oscillatory component is on the order of 300 to 600 km.

The GoM is a deep (more than 4000 m in the deepest region) semi-enclosed sea with the opening in the SE corner. Although the entrance to the GoM is partially blocked by the islands of Cuba and the Yucatan Peninsula, the Equatorial

Current enters the GoM through the Caribbean Sea and Yucatan Channel, forming the Loop Current with a transport of approximately 30×10^6 m^3/s. The Loop Current traces an anticyclonic path and exits the GoM through the Florida Straits and eventually becomes a principal component of the Gulf Stream [7]. Frequently, eddies are shedded from the Loop Current and propagate westward. The Loop Current in the gulf forms a very dynamic and active region. From examining the seasonal, annual and three-year average of the climatology maps, it is found that one of the dominant locations of the local highs is near the center of the eastern gulf in the area of Loop Current instabilities [6]. This local high is relatively stationary (compare the three-month average in Fig. 2 and the three-year average in Fig. 3) and may be an indication of active air-sea interactions in the region of the Loop Current instabilities.

Yellow and East China Seas (YES)

In the YES, there are seven TOPEX tracks passing through the region. The same procedure to construct the climatology maps of the GoM is applied to the YES. Fig. 4 shows an example of the three-month average (January to March, 1994) wind and wave climatology, which is distinctively different from that in the Gulf of Mexico. The distribution of the wind speed or wave parameters is almost stratified and follow closely the local bathymetry. For the long-term average, a north-south stratification of the distribution is evident (Fig. 5 shows an example of the 1994 averages). The oscillatory component is much weaker.

The YES are on a large and shallow continental shelf, with depths less than 100 m on the shelf. The major current system in the region is the Kuroshio, which enters YES just southeast of Taiwan and exits from southwest of Japan. The main axis of the Kuroshio is usually just outside of the 200 m contour line. The Kuroshio may intrude onto the shelf through two major regions. The first is through the Taiwan Strait during the winter months when the Taiwan Warm Current is weak [8]. The second source is the branching of the Tsushima Current from the Kuroshio [9] and the subsequent intrusion of the Yellow Sea Warm Current northward into the Yellow Sea [10]. One of the driving forces of the Yellow Sea Warm Current and the flux of open ocean properties onto the continental shelf is the northerly wind bursts during the winter season. Due to the shallow water depth, the wind events are capable of creating large sea level changes, which produce horizontal pressure gradients that drive the subsurface currents [11].

Interestingly, the ranges of wind speeds, wave heights, waver periods and wave steepnesses in the GoM and YES are quite similar (compare Figs. 2-3 with Figs. 4-5). The dynamic processes and the circulation patterns in the two regions are obviously different. These may contribute to the very different climatology of wind and waves in the two regions.

SUMMARY AND CONCLUSIONS

Using the TOPEX altimeter output of wind speed and wave height, the regional distributions of the wind and wave characteristics in the Gulf of Mexico and in the Yellow and East China Seas are investigated. The distributions of wind and wave parameters in the Gulf of Mexico is characterized by an oscillatory mode in the longitudinal direction. The Loop Current appears to have a strong influence on the dynamics of the region; this effect shows up in the presence of a stationary local high in the distributions of wind speeds,

wave heights, wave periods and wave steepnesses. In the Yellow and East China Sea, although the ranges of wind and wave parameters are very similar to those observed in the Gulf of Mexico, the climatology of the region is predominately a stratified distribution in the north-south orientation, and closely follows the local bathymetry.

REFERENCES

[1] Fu, L.-L, E.J. Christensen, and C.A. Yamarone, TOPEX /POSEIDON mission overview, *J. Geophys. Res.*, 99, 24369-24381, 1994.

[2] Ebuchi, N., and H. Kawamura, Validation of wind speeds and significant wave heights observed by the TOPEX altimeter around Japan, *J. Oceanography*, 50, 479--487, 1994.

[3] Gower, J.F.R., Intercomparison of wave and wind data from TOPEX/POSEIDON, *J. Geophys. Res.*, 101, 3817-3829, 1996.

[4] Hwang, P. A., W. J. Teague, G. A. Jacobs, and D. W. Wang, A statistical comparison of wind speed, wave height and wave period derived from satellite altimeters and ocean buoys, subm. *J. Geophys. Res.*, 1997.

[5] Teague, W. J., P. A. Hwang, D. W. Wang, G. A. Jacobs, A three-year climatology of waves and winds in the Gulf of Mexico, subm. *J. Atm. and Oceanic Tech.*, 1997.

[6] Leben, R., G. H. Born, J. D. Thompson, and C. A. fox, Mean sea surface and variability of the Gulf of Mexico using Geosat altimetry data, *J. Geophys. Res.*, 95, 3025-3032, 1990.

[7] Thompson, J. D., G. H. Born, G. A. Maul, Collinear-track altimetry in the Gulf of Mexico from SEASAT: Measurements, models, and surface truth, *J. Geophys. Res.*, 88, 1625-1636, 1983.

[8] Chuang, W. S., and W. D. Liang, Seasonal variability of intrusion of the Kuroshio water across the continental shelf northeast of Taiwan, *J. Oceanogr.*, 50, 531-542, 1994.

[9] Lie, H. J., and C. H. Cho, On the origin of the Tsushima Warm Current, *J. Geophys. Res.*, 99, 25081-25091, 1994.

[10] Hu, D. X., Some striking features of circulation in the Huanghai Sea and East China Sea, *Oceanology of China Sea*, 1, 27-28, 1994.

[11] Hsueh, Y., Recent current observations in the Eastern Yellow Sea, *J. Geophys. Res.*, 93, 6875-6884, 1988.
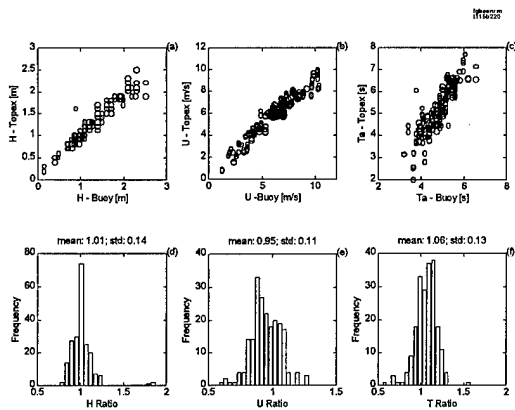
Fig. 1. Comparison of the altimeter and buoy measurements of the significant wave height (a), wind speed (b), and average wave period (c). The ratios (TOPEX divided by buoy) of these three wave parameters are shown in (d), (e) and (f), respectively [4].
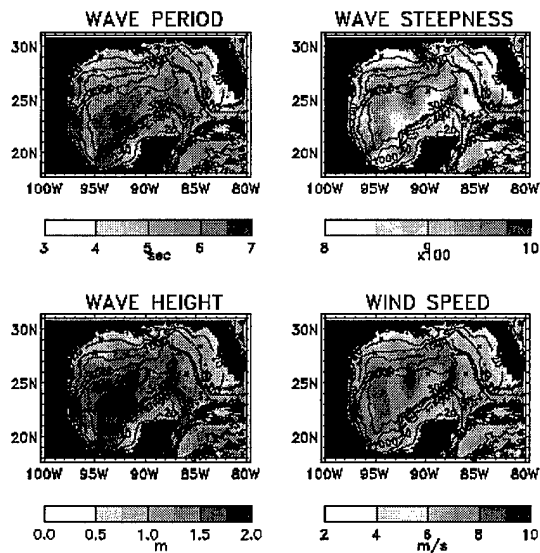
Fig. 2. The three-month (January to March, 1994) average of the wind and wave climatology in the Gulf of Mexico.
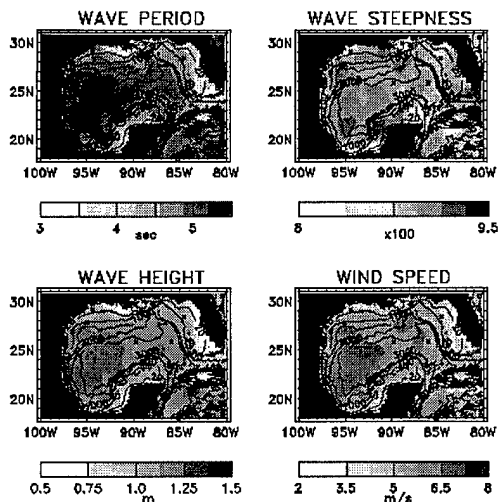
Fig. 3. The three-year (93-95) average of the wind and wave climatology in the Gulf of Mexico.
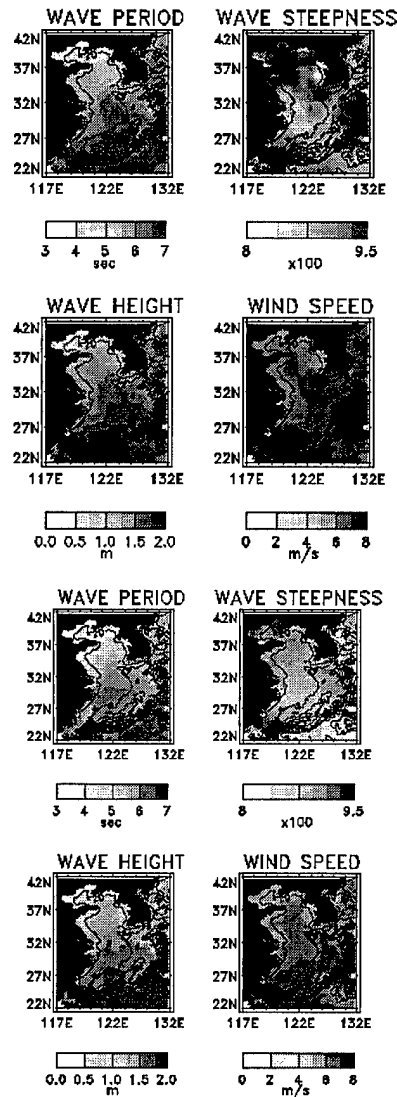
Fig. 4. The three-month (January to March, 1994) average of the wind and wave climatology in the Yellow and East China Seas.

Fig. 5. The annual average (1994) of the wind and wave climatology in the Yellow and East China Seas.

1158

Towards Extracting Fine-Scale Winds from Synthetic Aperture Radar Images

Pierre D. Mourad
Applied Physics Laboratory, University of Washington
1013 NE 40th St., Seattle, WA 98105
pierre@apl.washington.edu (w) 206-543-6921 (f) 206-543-6785

Abstract – Tower- and aircraft-based research over the last three decades has shown that the spatial or temporal averages of radar backscatter from the ocean surface at radar wavelengths that sample the gravity-capillary part of the ocean's surface-wave spectrum are proportional to nearly the square of the mean wind speed. During the last 15 years, analyses of satellite-based scatterometer images of the ocean surface (that is, radar images whose pixels measure 25 km to a side) show atmospheric frontal features and other, synoptic atmospheric structures. With these images, researchers have created images of the spatial distribution of wind (with extra work, they get both speed and direction) associated with those synoptic structures. Going down in scale, recent research has shown that synthetic aperture radar (SAR) images of the oceans (snapshots of the radar-backscatter patterns of the ocean surface with pixels measuring 100 m or 12.5 m to a side) manifest signatures of atmospheric turbulence - scales of motion on the order of hundreds of meters to tens of kilometers. These facts raise the following question: "(How) can one use SAR images of the ocean surface to infer fine-scale winds, that is wind patterns on scales of atmospheric turbulence?" The present work represents a step towards answering that question, by asking a related question, namely: "How much spatial averaging of backscatter is required to define a stable, convergent backscatter value for a given area, so that that value can then be translated into a wind speed?" The answer is based on the hypothesis that the statistics of radar backscatter patterns created by atmospheric turbulence should be related to the statistics of the atmospheric turbulence that generated the roughness patterns on the ocean surface.

BACKGROUND

As an example, [1] describes the multiscale structure of SAR backscatter seen in an image made by the ERS-1 SAR system and interprets this structure as the impression on the surface of the ocean of three scales of interacting atmospheric turbulence: quasi-two-dimensional roll vortices, boundary-layer scale thermals, and gust microfronts. Figure 1 is a repeat of their Figure 5 showing a binary image of the radar-backscatter patterns exhibited within the Bering Sea adjacent to its ice pack at the time of a cold air outbreak. (In this image, backscatter greater than a given value is colored gray, while backscatter less than that value is whited out. See Plate 1 from [1] for more detailed images. Also, a linear trend has been removed

from the original image, so the average backscatter value of the entire image is zero.) This low resolution (100~m pixel diameter) SAR image shows linear trends of enhanced radar backscatter or SAR-streaks, aligned with the mean surface-layer wind (10 m/s here). They have a dominant cross-wind scale of about 5 km (five times the boundary layer depth), and down-wind lengths of many tens of kilometers. These are argued [1] to be due to quasi-two-dimensional atmospheric roll vortices. Note that the linear features are actually created by linear arrangements of two-dimensional backscatter regions. These are argued [1] to be the footprints of boundary-layer scale thermals. A higher resolution image (12.5 m pixel diameter) of the same area shows even smaller-scale, two-dimensional structure in the radar backscatter image. The average and range of intensity of these features are significantly greater within than outside of the kilometer-scale enhanced backscatter regions. These backscatter patterns compare favorably [1] in both scale and effect to observations of the modulation of microfronts in the atmospheric surface layer by boundary-layer scale thermals, themselves modulated by roll vortices.

RESULTS

The hypothesis of this work is that if backscatter patterns are created by spatially and temporally-evolving atmospheric turbulence, then the amount of spatial averaging of a SAR image required to define a stable and convergent backscatter value for a given area should be related to if not identical to the amount of averaging required to define well the mean stress (hence, via modeling, a mean wind) associated with that atmospheric turbulence. When atmospheric rolls are present, the rule of thumb is that one must average an in-situ time series for 20--60 minutes (or 1200 to 3600 s) to get a convergent stress, while for aircraft data flown across the wind (and therefore across the axes of the rolls), one must capture about five to ten realizations of the roll vortices. In terms of the present image and the hypothesis of this work, one should therefore spatially average that image for (10 m/s)*(1200 to 3600 s) = 12 to 36 km in a direction along the SAR-streak axes, and 25—50 km in the cross-roll direction. The next figures demonstrate those calculations.

Figure 2 shows three panels that contain the results of averaging the backscatter values in the 520 columns centered within Fig. 1 and leaning slightly so that they are

aligned with the roll-vortex signatures. The averages start from the bottom and stop at an ever-increasing distance from the bottom. With 100 m pixels, this is equivalent to collecting "time series" of radar backscatter from 520 adjacent stations within the roll field across the centered 52 km of the SAR image, and assuming that the backscatter pattern of Fig. 1 advects by each of those stations for a given amount of time. (For example, the center panel shows the column averages of the bottom 240 pixels – equivalent to the bottom 24 km of the imaged region.) Along the left-hand side of each sub-figure is the range of relative backscatter averaged along the roll axes. The right-hand side of each sub-figure gives the percentage change of those backscatter, values from the cumulative, across-roll average. The rate of convergence of the column averages is qualitatively similar to that of in-situ time series of atmospheric turbulence, consistent with the hypothesis of this paper.

Note the across-roll variability in the along-roll *average* backscatter. This shows that a series of adjacent in-situ measurements of average backscatter, equivalent here to adjacent, in-situ measurements of averaged, turbulence-induced stress or wind, will differ from each other because of the intrinsic anisotropy of the atmospheric turbulence field. Thus, those differences in average quantities would not represent relative *errors*, but instead reflect the real effects of structured atmospheric turbulence. Also, not shown here is the fact that if one did these same calculations with rows rather than columns one would produce row-averages (across the rolls) that would converge when one included the backscatter associated with five to ten roll-vortex signatures. Such averages exhibit the same intrinsic variability shown in the column averages of Fig. 2, due again to the anisotropic backscatter field caused, in turn, by the anisotropic atmospheric-turbulence field.

Defining a convergent spatial average from the SAR image will subsume the variability shown in the adjacent line averages presented in Fig. 2. This is done in Figure 3, which is also motivated by the fact that SAR images resolve subgrid scale backscatter patterns that are averaged

together into scatterometer images. In particular, Fig. 3 shows the average backscatter found within coincident ever-increasing square areas taken from the same region of the SAR image used to create the line averages of Fig. 2. The lengths of the sides of these areas marks the horizontal axis. (The average backscatter value for this part of the entire image is slightly greater than zero, which balances off the blank, low-backscatter region in the upper right-hand corner of Fig. 1 which is caused by ice in the original imaged area.) One needs to average over squares of at least about 30 km to a side in order to get close to a convergent backscatter value associated with this segment of the SAR image. It is of interest that the pixels in scatterometer images measure 25 km to a side: the kind of analysis here shows that the structured sub-grid scale variability in surface roughness is a source of intrinsic variability in scatterometer pixels.

CONCLUSIONS

Averaging lengths required to generate convergent backscatter coefficients from SAR images whose backscatter variability is caused by atmospheric turbulence parallel the averaging lengths required to get convergent mean stress values associated with atmospheric turbulence. Thus, in order to extract well-defined wind fields within SAR images, one must carefully spatially average subsets of the image with attention to the source of the backscatter variability in those images.

REFERENCES

[1] P. D. Mourad, "Inferring multiscale structure in atmospheric turbulence using satellite-based synthetic aperture radar imagery," J. Geophys. Res., vol. 101(C8), pp.18,433-18,449.
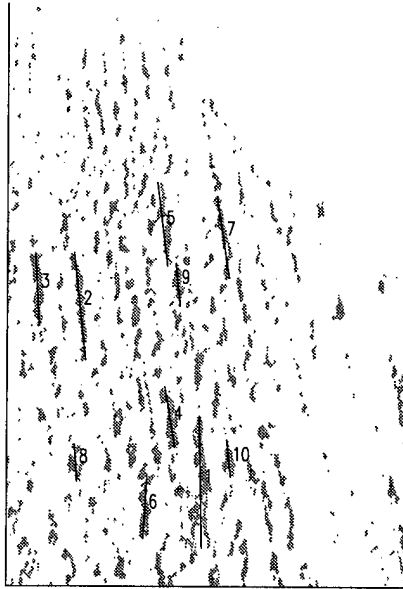
Fig. 1, from [1], showing a binary form of a SAR image which contains linearly-aggregated features in radar backscatter created by the impression on the ocean surface of three-dimensional, boundary-layer thermals herded by quasi-two-dimensional atmospheric roll vortices.

Average backscatter vs. position within roll field
for average wind speed of 10 m/s
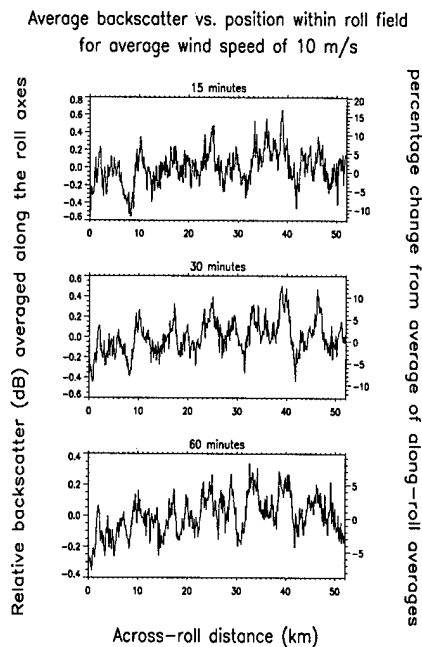
Fig. 2. Shows column averages of the bottom portion of the original SAR image corresponding to Fig. 1. Each panel shows the result of averaging over adjacent columns starting from the bottom of the image, for different

"times" that correspond to different distances from the bottom.
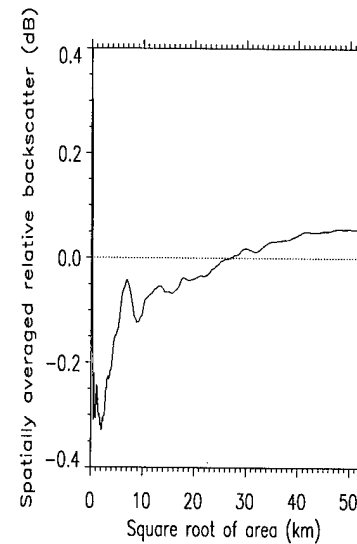
Fig. 3 shows the average backscatter from ever-increasing squares of the SAR image centered near the bottom of the SAR image. The length of those squares mark the horizontal axis of the plot. When one averages enough SAR pixels to form a square on the order of the size of pixels in scatterometer images (25 km to a side), the average backscatter converges to its final value.

Study of Atmospheric Boundary Layer Rolls Near Spitsbergen by Using ERS SAR Images of the Sea Surface and a Numerical Model

Werner Alpers
Institute of Oceanography, University of Hamburg
Troplowitzstr. 7, D-22529 Hamburg, Germany
Phone: +49 40 4123 5432 Fax: +49 40 4123 5713 E-Mail: alpers@ifm.uni-hamburg.de

Gerd Müller and Burghard Brümmer
Meteorological Institute, University of Hamburg
Bundesstr. 55, D-20146 Hamburg, Germany
Phone: +49 40 4123 5086 Fax: +49 40 41173-350

Abstract -- An ERS 1 SAR image of the Greenland Sea showing sea surface manifestations of atmospheric boundary layer rolls is used to determine the orientation and spacing of the rolls as well as the variation of the sea surface wind speed associated with the secondary flow. Furthermore, the sea surface wind field associated with these rolls is simulated by using a 3-dimensional atmospheric model. It is shown that the model reproduces well the roll spacing and the sea surface wind speed derived from the ERS 1 SAR image intensity.

INTRODUCTION

Atmospheric boundary layer rolls are helical circulation patterns in the atmospheric boundary layer which are superimposed on the mean wind field. The flow pattern associated with atmospheric boundary layer rolls is depicted schematically in Fig. 1 [1]. These rolls can be generated either by thermal instability (Rayleigh-Bénard instability) when the layer is heated from below or cooled from above, or by dynamic instability (inflection point instability) when the wind velocity changes with height in such a way that an inflection point occurs in the wind component normal to the roll axis. The axes of the boundary layer rolls are oriented between the directions of the mean surface wind and the geostrophic wind above the boundary layer. In the case of a thermal instability, the aspect ratio, i.e., the horizontal wavelength of the roll pattern (roll spacing), λ, divided by the roll height, h, is 2.8 according to the linear Rayleigh-Bénard convection. However, the most frequently observed values range
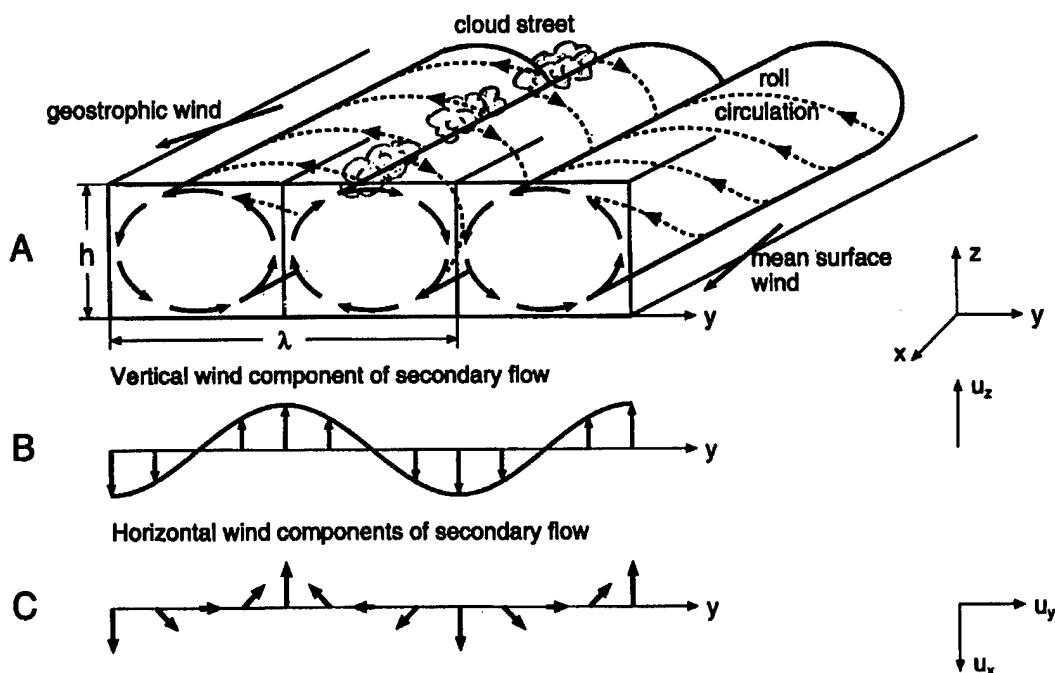
Fig. 1: Schematic plots of secondary flow pattern associated with atmospheric boundary layer rolls. Panel A: Perspective view of the three-dimensional flow; Panel B: Variation of the vertical component u_z of the wind velocity along the y direction; Panel C: Variation of the horizontal components u_x and u_y (in the x-y plane).

between 2 and 6, but also values of 15 have been reported [2].

If the moisture conditions are favorable, cloud streets may be formed in the upward rising branches of the roll circulation.

In this paper we analyze a radar image which was acquired by the synthetic aperture radar (SAR) aboard the First European Remote Sensing satellite over the Greenland Sea during a cold air outbreak on which sea surface manifestations of atmospheric boundary layer rolls are visible. At the time of the SAR data acquisition a meteorological experiment took place in this area in which data were collected which are needed as input for model calculations.

ERS 1 SAR IMAGE OF ATMOSPHERIC BOUNDARY LAYER ROLLS

Figure 2 shows an ERS 1 SAR image that was acquired over the Greenland Sea near Spitsbergen on March 24, 1993, at 19:54 UTC (orbit 8833, frames 1611 and 1629). In the upper part of the image, the fissured ice edge can be delineated. Areas covered with sea ice have a low normalized radar cross section (NRCS) and thus appear dark on the SAR image. The area exhibiting a streaky pattern is open-water area. The streaky pattern is caused by variations of the short-scale sea surface roughness induced by the atmospheric boundary layer rolls.

Figure 3 shows the variation of the NRCS along the scanline A-B marked in Figure 2. From this scan we see that the wavelength of the roughness pattern varies between 2.7 km and 4.6 km and that the average wavelength is 3.5 km. We have also made scans in several other areas of the SAR image and found that the average wavelength increases continuously with distance from the ice edge: from 1.3 km near the ice edge to 3.5 km at a distance of 140 km downwind.

If the wind direction at the sea surface is known, then the NRCS values can be converted into wind speed by using a wind scatterometer model. Here we assume that the mean wind direction as well as the main component of the wind speed fluctuation associated with the boundary layer rolls are parallel to the direction of the wind streaks visible on the SAR image. For the conversion of NRCS values into sea surface wind speeds we use the CMOD4 model [4]. Exactly speaking, this wind scatterometer model converts NRCS values into wind speeds at a reference height of 10 m above the sea surface for a neutrally stable air-sea interface. In the present case, the air-sea interface was highly unstable since at the ice edge the air-sea temperature difference was around -30 K and decreased to about -20 K at a distance 140 km downwind from the ice edge. However, the CMOD4 model can also be applied in this case because, the NRCS does not change
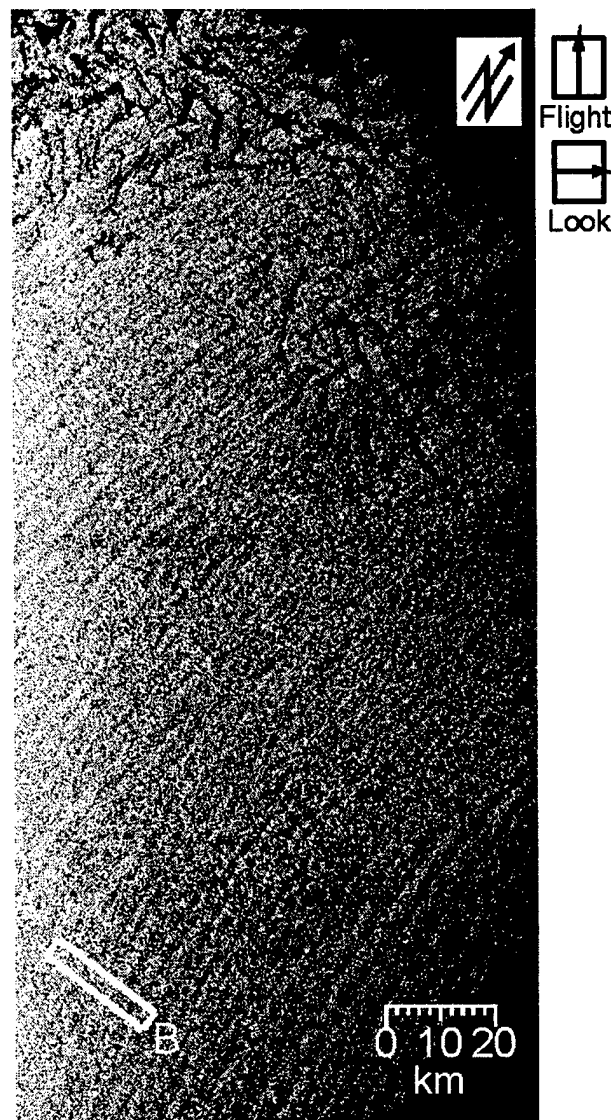
Fig. 2: ERS 1 SAR image acquired over the Greenland Sea near Spitsbergen (Corner coordinates: 79.93° N, 0.88° E / 80.47° N, 5.07° E / 78.47° N, 6.88° E / 78.95° N, 10.55° E) on 24 March, 1993, at 19:54 UTC showing sea surface manifestations of atmospheric boundary layer rolls.

significantly when the air-sea interface changes from neutrally stable to unstable.

The wind speed calculated in this way is depicted on the right-hand vertical coordinate axis in Figure 3. Note that the curve in Figure 3 is tilted because, at constant wind speed, the NRCS increases with decreasing incidence angle. We see from Figure 3 that the average wind speed decreases slightly from 17 m/s at point A to 16 m/s at point B. The maximum (minimum) wind speed in direction of the streaks is approximately 19 m/s (15.5 m/s).
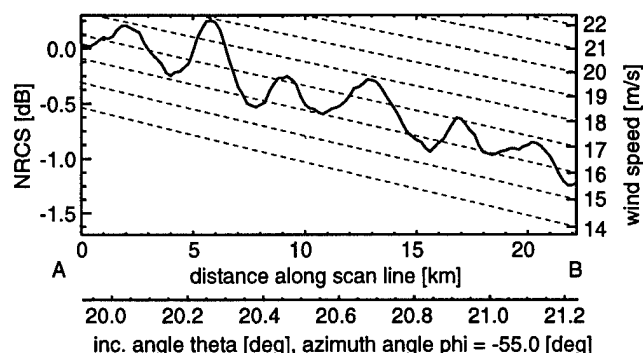
Fig. 3: Variation of the mean NRCS obtained from a scan from A to B in the area marked in Figure 2. The right-hand vertical axis shows the associated sea-surface wind speed calculated from the CMOD4 wind scatterometer model. The dashed lines are lines of constant wind speed.
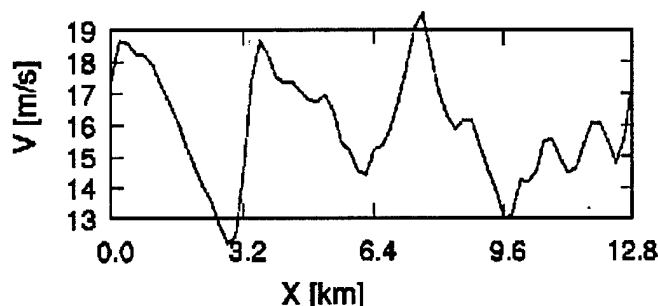
Fig. 4: Variation of the mean horizontal wind velocity component parallel to the direction of the wind streaks at a height of 16 m along the scan line A-B marked in Fig. 5.

SIMULATIONS OF ATMOSPHERIC BOUNDARY LAYER ROLLS

The atmospheric boundary layer rolls visible on the S*R image have been simulated by using a modified version of a 3-dimensional, time dependent, non-hydrostatic model described in [5]. The equations governing the resolved-scale motions are the three-dimensional, spatially averaged, incompressible Boussinesq equations conserving mass, momentum, liquid water potential temperature, and total moisture content.

On March 24, 1993, during the ARKTIS 1993 experiment [3], meteorological measurements were carried out in the Greenland Sea from a research aircraft. Thus the meteorological parameters needed for the model calculations are known. On that day, cold and stably stratified air blew off the Arctic ice pack over the warm West-Spitsbergen current. Due to an air-sea temperature difference of about -30 K, the initially very shallow boundary layer rapidly changed with respect to depth, temperature and moisture with increasing distance from the ice edge. The wind direction was about 10° and the wind speed within the boundary layer increased from about 10 m/s at the ice edge to 17 m/s in the area marked A-B in Figure 2. Near the top of the boundary layer, the wind decreased and exhibited a vertical shear which increased downstream.

Inserting the measured meteorological parameters in the 3-dimensional atmospheric model we have calculated the horizontal wind speed at the lowest grid level (16 m) in the direction parallel to the direction of the wind streaks at the location A-B marked in Figure 2. The variation of this wind velocity component along a line perpendicular to the wind streaks at a distance of 140 km downstream from the ice edge is plotted in Fig. 4. Comparing the plots of Figure 3 and Figure 4 we see that the SAR derived and simulated wind speeds agree quite well [13].

CONCLUSIONS

The present investigation shows that SAR imagery acquired over the sea can yield valuable information on atmospheric boundary layer rolls over the ocean. The orientation and spacing (wavelength) of the rolls can be extracted from SAR images. By using a wind scatterometer model also the variation of the sea surface wind velocity associated with the atmospheric rolls can be extracted from SAR images. ERS SAR images acquired over the ocean are also well suited for validating atmospheric models of atmospheric boundary layer rolls.

ACKNOWLEDGMENT

REFERENCES

[1] W. Alpers and B. Brümmer, "Atmospheric boundary layer rolls observed by the synthetic aperture radar aboard the ERS-1 satellite", J. Geophys. Res., 99, 1994, pp. 12613-12621.

[2] Y. Miura, "Aspect ratios of longitudinal rolls and convection cells observed during cold air outbreaks", J. Atmos. Sci., 1986, pp. 43, 26-39.

[3] B. Brümmer, "Boundary-layer modification in wintertime cold-air outbreaks from the Arctic sea ice", Boundary-Layer Meteorol., 80, 1996, pp. 109-125.

[4] A. Stoffelen and D.L.T. Anderson, "ERS-1 scatterometer data characteristics and wind retrieval skill", Proceedings of the First ERS-1 Symposium, Cannes, France, March 1993, ESA publication ESA SP-359, 1993, pp. 41-47.

[5] G. Müller and A. Chlond, "Three-dimensional numerical study of cell broadening during cold-air outbreaks", Boundary-Layer Meteorol., 81, 1996, pp. 298-323.

COAST WATCH'95 : Upper Ocean Features from ERS SAR Imagery

O. M Johannessen*, E .Korsbakken, H. A. Espedal, V. Jensen, A. D. Jenkins and J .A Johannessen**

Nansen Environmental and Remote
Sensing Center, Edvard Griegs vei 3a, N-5037 Solheimsviken, Bergen, Norway;
Phone: +47-55 29 72 88, Fax: +47-55 20 00 50
email: Ola.Johannessen@nrsc.no, WWW: http://www.nrsc.no:8001/
*Also at Geophysical Institute, University of Bergen, Norway.

**ESTEC, European Space Agency, P.O. Box 299, 2200 AG Noordwijk, The Netherlands
phone:+31 71 56 55 959, fax:+31 71 56 55 675, email: jjohanne@.estec.esa.nl

ABSTRACT

In order to quantify the mesoscale upper ocean and atmospheric boundary layer processes, a tandem ERS-1/2 ESA AO experiment was carried out off the south-western coast of Norway during September 1995. A unique integrated data set was collected, including SAR coverage (148 scenes) in the ERS-1/2 tandem mode, an extensive set of oceanographic and meteorological variables from the R/V Håkon Mosby of the University of Bergen, met-ocean parameters from state-of-the-art metocean buoys, and natural slick sampling with two radio-controlled "mini research vessels". Also ATSR and NOAHH AVHRR data was obtained during the experiment.

Analysis from this comprehensive integrated experiment is reported (in this paper and references), in particular a brief examination of a) coastal jet and currents, b) surface slicks and c) wind front. Features in the SAR images are discussed in terms of ABL stratification, coastal wind field retrieval, surface slick detection and in situ measurements of oceanographical and meteorological parameters. We have also focused on advantages of ERS-1 and ERS-2 tandem operation, and synergetic use of different spaceborne sensors in coastal applications.

Figure 1 The experimental area, showing SAR coverage in gray (including both descending and ascending orbits), the location of moorings (M = metocean buoy, C1/C2 = current meter moorings), and ship track. The field experiment took place from 11 September to 1 October 1995.

INTRODUCTION

In order to advance in the understanding of, and to quantify the mesoscale upper ocean and atmospheric boundary layer processes, a tandem ERS-1/2 ESA AO experiment [1] was carried out in the Skagerak, off the south-west coast of Norway, during September 1995.The data collected represents a unique integrated data set, with SAR coverage in the ERS-1/2 tandem mode, ship-borne active/passive microwave observations, meteorological and oceanographic observations from a ship and moored instruments and in situ sampling of natural surface slicks. Fig.1 shows the experimental area. The ERS SAR coverage (Fig.1) shows that ample use was made of the tandem ERS-1/2 SAR imagery at 24-hour separation, and also ascending/descending ERS passes at 11-13-hour separation. There was also substantial cloud-free coverage by ERS ATSR and NOAA AVHRR infra-red sensors, giving good information on the ocean surface thermal structure.

The University of Bergen research vessel R/V Håkon Mosby was employed in the field program, to make in situ meteorological and oceanographic measurements.

The Norwegian Meteorological Institute also provided a special operational forecast service, for meteorology, sea state and currents and also diagnostic weather data from hindcast model.

An Aanderaa weather station provided wind, pressure, air temperature and humidity observations from the Håkon Mosby. The Naval Postgraduate School (NPS) weather station duplicated these observations, with additional observations of turbulent wind components using an ultrasonic anemometer and turbulent humidity fluctuations using an Ophir hygrometer. Surface-layer aerosol particle

size distribution in the range 0.3-200 µm was measured continuously, and regular rawindsonde launches were performed.

In situ measurements were made by the Environmental Research Institute of Michigan/University of Michigan team, using a rail-mounted system consisting of a C-band dual-polarized Doppler radar, C-band radiometer and video camera.

Temperature and salinity measurements down to seabed or maximum 200 m depth were made using a SeaSoar towed CTD (Conductivity Temperature Depth instrument). The current profile was measured from the bottom of the ship to the seabed or maximum 500 m depth with an Acoustic Doppler Current Profiler (ADCP).

The NPS metocean buoy measured two-dimensional wave spectra using a Hippy Datawell sensor. It also measured pressure, vector wind, air and sea temperature, humidity, turbulent fluctuations in wind, temperature and humidity, and aerosol particle size distribution. Two sub-surface current meter moorings were deployed, with Aanderaa current meters at 25 m, 50 m and 100 m depth and at 25 m above the sea bottom. Two remotely-controlled platforms "INTERFACE I and II" were deployed on September 13, 15, 17 and 18. Both were equipped with a rotating Teflon drum to take direct samples of the surface microlayer. INTERFACE II was also equipped with air and sea temperature sensors and a K-band radar.

COAST WATCH'95 DATA ANALYSIS

In the following sections we will give a brief analysis of a coastal current, for analysis of surface slicks and coastal wind fields se respectively [2] and [3]

COASTAL CURRENTS

Several of the SAR images from the COAST WATCH'95 show oceanic fronts which can be explained as the effect of current gradients. In Figure 2, A-D, taking advantage of the ERS-1, ERS-2 tandem operation, a series of four collocated SAR images from 27, 28 ,29 and 30 September are shown. However, these images show a very clear example of signature persistence and demonstrate the SAR capabilities due to a higher temporal sampling frequency of an area. A comparison of the strong front or jet in the four images reveals a westward movement for the jet structure within four days. The wind as obtained from R/V Håkon Mosby varies from 9 m/s SW (27.09) to 1.0 m/s NE (28.09); 8 m/s NW (29.09) and 3 m/s SE on the 30.09. An AVHRR image (Figure 2, F) from 30 September also clearly reveals the SST gradients in the same area as the prior SAR images, demonstrating the possibility of a synergetic use of different remote sensors to improve the spatial and temporal coverage and provide quantitative information about the ocean feature.

The west boundary of the jet like feature in the image from 27 September is crossed by R/V Håkon Mosby simultaneously with satellite overpass resulting in a unique record of meteorological and oceanographical parameters and corresponding backscatter coefficient over the jet, Figure 2 A (ship track inserted as white line) and Fig. 3. The SST measured by the thermistor (Fig. 3, bottom) established the surface layer to be 9°C in the jet (dark signature in the SAR image) and 13°C outside (west of) the strong gradient at the boundary. The salinity and density sections from the SeaSoar (not shown) also clearly
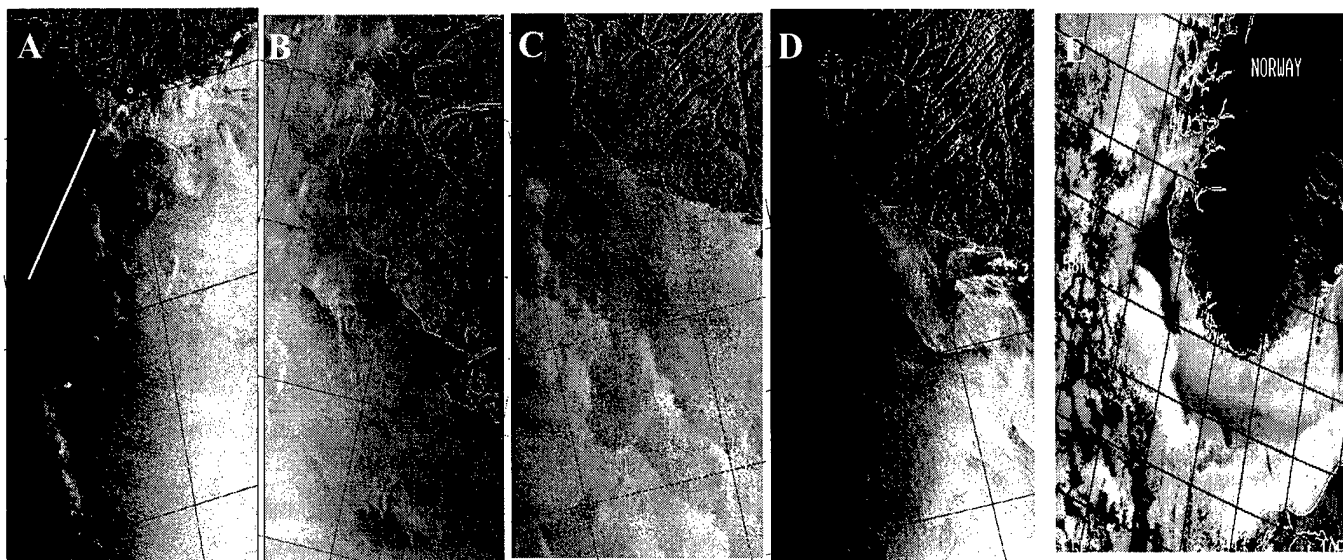
Figure 2 A-D is the mosaic of SAR images on 27 to 30 September 1995 Panel E shows a NOAA AVHRR thermal image from 30 September.
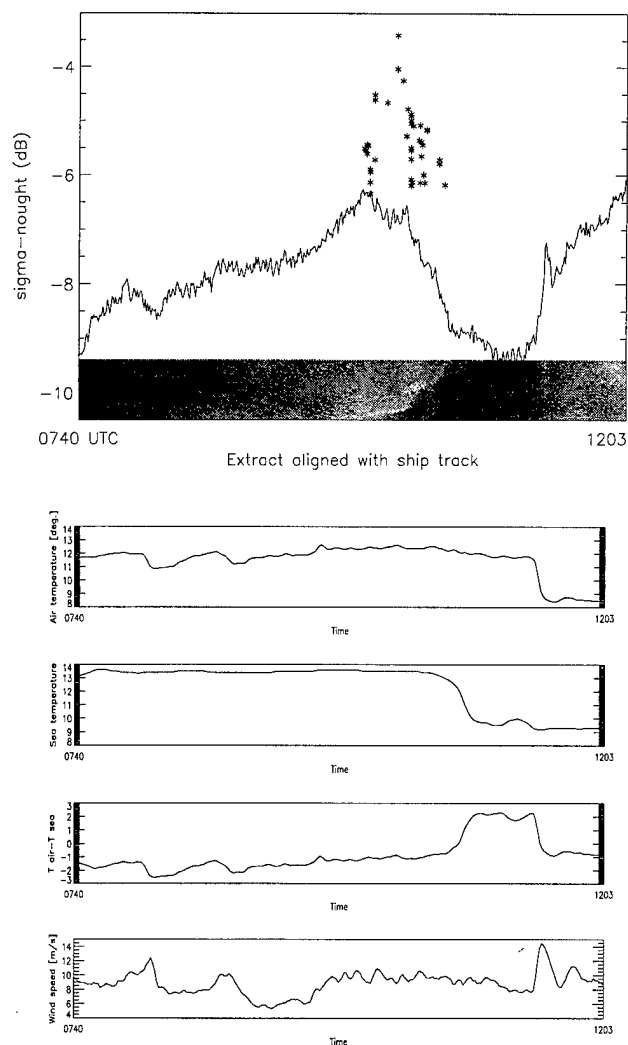
Figure 3 The upper panel shows the averaged backscatter coefficient profile (the peak σ_0 value at the shear for each line is indicated with an asterisk) and the corresponding sub-image along the ship track. The remaining four plots shows respectively air and sea temperature, air-sea temperature difference and finally the wind speed from R/V Håkon Mosby.

show the west boundary of the jet well collocated with the temperature structure. The cold water moves westwards in the jet at typical current speeds, measured by the ship-borne ADCP, to 60 cm/s. Sharp changes in the current were measured when the ship moved across the jet boundaries. The SAR backscatter and the surface met/ocean parameters shows clearly the western boundary of the jet, moreover the eastern boundary is somewhat interfered with a wind front. The dark signature of the jet is associated with a stable atmospheric condition. This suggest that the visibility of the jet is likely to be a result of the increased atmospheric stability as the air flows over the colder water, reducing the wind stress and thus the growth of short wind-waves.

However the backscatter peak (Fig. 3, top, plotted as asterisks) on the western side of the jet (the boundary zone) is probably caused by strong horizontal shear interacting with the short wind waves [4].

SUMMARY

During COAST WATCH'95 a unique integrated data set was collected, including extensive SAR coverage (148 scenes) in the ERS-1/2 tandem mode, an extensive set of oceanographic and meteorological variables from the R/V Håkon Mosby of the University of Bergen, met-ocean parameters from state-of-the-art met-ocean buoys, and natural slick sampling with two radio-controlled 'mini-research vessels'. Also ATSR and NOAA AVHRR data was obtained during the experiment.

Analysis from this comprehensive integrated experiment is reported, in particular a brief examination of; coastal jet, currents, surface slicks and coastal wind field.

In addition we have addressed the ERS-1 and ERS-2 tandem operation, and synergetic use of different spaceborne sensors in coastal applications. We anticipate that further studies will lead to improved algorithms and validation for retrieval of quantitative estimates of dominating geophysical parameters in the upper ocean and lower atmospheric boundary layer such as strength of current shear and convergence, and sub-synoptic wind field. Better quantitative interpretation of SAR images will furthermore lead to improved classification capabilities of natural film and oil spill.

REFERENCES

[1] Johannessen O. M. , J. A. Johannessen, A. D. Jenkins, K. Davidson, D. R. Lyzenga, R. Shuchman, P. Samuel, H. A. Espedal, J. Knulst, E. Dano and M. Reistad, 'COAST WATCH'95: ERS-1,2 SAR Applications of Mesoscale Upper Ocean and Atmospheric Boundary Layer Processes off the Coast of Norway'. In proceedings of IGARSS'96, Lincoln, Nebraska, USA, May 1996

[2] Espedal H. A. , O. M. Johannessen, J. A. Johannessen, E. Dano, D. Lyzenga and J. C. Knulst, "ERS-1/2 SAR detection of natural film on the ocean surface", 1997 (this issue)

[3] Korsbakken E, J. A. Johannessen and O. M Johannessen 'Coastal Wind Field Retrievals from ERS SAR Images' 1997 (this issue)

[4] Johannessen J. A. , R. A. Shuchman, G. Digarnes, D. R. Lyzenga, C. Wackerman, O. M Johannessen and P. W. Vachon, 'Coastal Ocean Fronts and Eddies imaged with ERS-1 Synthetic Apreture Radar', J. Geophys. Res., vol. 101, No. C3, pp. 6651-6667, 1996

ERS–1/2 SAR detection of natural film on the ocean surface.

H.A. Espedal, O.M. Johannessen,* J.A. Johannessen[1], E. Dano[2], D. Lyzenga[3]† J.C. Knulst[4]

Nansen Environmental and Remote Sensing Center, Edv.Griegsvei 3A, 5037 Solheimsviken, Norway
Phone: +47 55297288, Fax: +47 55200050, E-mail: Heidi.Espedal@nrsc.no

[1]ESA/ESTEC, P.O. Box 299, 2200 AG Noordwijk, The Netherlands.
Phone: +31 715655959, Fax: +31 715655675, E-mail: jjohanne@estert.jw.estec.esa.nl

[2]Dept. of Naval Architecture & Marine Engineering, University of Michigan, Ann Arbor, USA.
Phone: (313) 764-6470, Fax: (313) 936-8820, E-mail: ebd@engin.umich.edu

[3]Environmental Research Institute of Michigan, Ann Arbor, USA.
Phone: (313)994-1200 ext 2683, Fax: (313)994-5824, E-mail: lyzenga@erim.org

[4]Swedish Environmental Research Institute, Aneboda, Sweden.
Phone: +46 472 62075, Fax: +46 472 62004, E-mail: johan.knulst@ivl.se

ABSTRACT

Ocean mesoscale phenomena such as eddies and current convergence zones can often be seen in SAR images due to characteristic patterns caused by natural film induced damping of the waves. Such films have also been found to exert a significant effect on air–sea gas exchange, which may be important for the global scale climate system. Satellite synthetic aperture radar (SAR) may prove very useful to quantify the extent of natural film. To investigate the composition of these films and their effect on radar return, samples of the sea surface were taken simultaneously with ERS-1/2 SAR coverage of a fjord (the Korsfjord experiment), and later in coastal ocean areas (COASTWATCH'95). During COASTWATCH'95, simultaneous observations were made with a shipmounted C–band dual–polarized Doppler radar, and surface drifters were deployed to investigate the surface current variations in vicinity of the slicks. The dependence of the existence of slicks on wind speed is also investigated, and an estimate of natural film distribution during the experiment period given.

INTRODUCTION

Natural film on the ocean surface is formed from marine organisms or terrestial material delivered by runoff or atmospheric transport. The composition of natural films varies, but substances such as proteins, lipids, saccharides, organic acids, and metals associated with the organic matter, are usually present at higher concentrations than in the corresponding bulk water [1]. Sea surface films have been seen to influence energy dissipation in capillary waves [2;3], gas exchange rates [4] and marine aerosol formation [5]. Asher [6] has estimated that the impact of various hypothetical slick coverages on global air–sea CO_2 exchange is important. However, global spatial film quantification has so far not been done, and it is therefore difficult to know whether natural films really are extensive enough to be of importance in global change studies.

The spaceborne SAR, with its high spatial resolution (25m), may contribute significantly in global mapping of natural films at the ocean surface during moderate wind conditions. Damping of the capillary and short gravity waves by the film, which are sensed by radars via the Bragg backscatter, produce dark slick signatures in the ERS SAR imagery. So far, oil slicks [7] and artificial monomolecular films [8] are well documented in satellite and airborne SAR experiments respectively. In contrast, only one previous study exists in which the chemical components of natural films were sampled simultaneously with satellite SAR acquisition. This experiment was conducted under calm wind conditions in a Norwegian fjord [9] and showed that there exists a chemical difference between slicked and non–slicked areas in an ERS–1 SAR image.

The primary objective of the work reported here, was to extend the documentation of the composition of natural films and their effect on radar return, to include different coastal oceanographic and atmospheric conditions. This may in turn give new valuable insight into the geophysical processes responsible for accumulation of different natural films in coastal areas. Eventually this may also help develop satellite SAR as a tool in mapping the global extent, distribution and variability of natural films, to be used in e.g. climate studies. Knowledge of natural films are also important for SAR oil–spill detection systems, since these films are difficult to distinguish from oil in the SAR imagery.

---

*Also at Geophysical Institute, University of Bergen, Norway.
†Also at the University of Michigan, Ann Arbor, USA.

THE COASTWATCH'95 EXPERIMENT

A tandem ERS-1/2 ESA AO experiment was carried out off the south-western coast of Norway during the month of September 1995 [10]. The main objectives of this experiment were to investigate and quantify natural films, coastal jets, ocean fronts, wind velocity, wind fronts and rain showers from ERS-1/2 SAR. Information from the C–band (5.3GHz) VV-polarized SAR images in near real time were used to navigate the research vessel R/V Håkon Mosby to different SAR features of interest.

Extensive temporal and complete spatial satellite SAR coverage of the experiment region was possible due to the ERS-1/2 tandem mission. A total of 53 SAR scenes (each covering 100 x 100km) from the experiment region were analyzed during the field campaign from 11 September to 1 October 1995. In addition, 18 scenes covering the same region in the months before and after the experiment, were analyzed in this work.

A C–band (4.92GHz) continuous wave (CW) Doppler scatterometer with VV and HH polarization, was installed to acquire shipborne radar backscatter measurements during COASTWATCH'95. The radar cross section (RCS) and spectral statistics plots in this work were based upon a 35sec running average (equal to a distance of ~100m).

During the first part of the COASTWATCH'95 experiment surface slick material was collected using two remotely controlled surface slick samplers, INTER-FACE I (length 1.2m) and II (length 2m) [11]. They were both equipped with a rotating hydrophilic teflon drum [9]. The INTERFACE II was also fitted with a GPS receiver, temperature probes, an anemometer and a data logger. Bulk water samples were obtained at 20cm depth for comparison. The samples were analyzed for salinity, anions, fatty acids, alcanes, total organic carbon, cations and trace metals. Ultra violet (UV) and visual light (VIS) scans were made on all samples, and pH, specific conductivity and turbidity were determined.

QUANTIFICATION OF FILM COVERAGE

To investigate the dependence of observed slicks on wind speed and give an estimate of natural film distribution, 71 ERS-1/2 SAR images collected over the COASTWATCH'95 experiment region (in the period August-October 1995) were analyzed for slick signatures. It is by now a well documented fact that also oil spills, grease ice, convergent current zones, rain cells, internal waves, threshold wind speed ($\leq$2–3m/s), wind sheltering by land or large platforms and current wakes (created when ocean currents meet an obstacle such as a large platform) may cause dark areas in SAR imagery [12]. To discriminate between natural films and these similarly appearing features requires a direct analysis of the SAR image (shape, size, texture, gradients and backscatter reduction of the slick), and a contextual analysis (meteorological data, currents, bathymetry, platform and ship lane locations). In some cases, running SAR models such as the ERIM Ocean Model [13] or oil drift models, may give important additional information. In this work, the decision of whether a slick was caused by natural film was based on simple flow chart algorithms and experience in slick classification using SAR.

The results indicates that for increasing wind speeds, the percentage of film coverage in the SAR scenes expectedly decreases. Many of the 71 investigated SAR scenes have the approximate same % film coverage. The largest film coverages (up to 40%) are found for the lowest wind speeds, 2.5m/s (in these cases large homogeneous areas are classified as caused by low winds, while the surrounding inhomogeneous slick features including eddies are classified as caused by natural film). For 5 to 10m/s wind speed, the natural film coverage has sunken below 5% in all cases. For 12.5m/s and 15m/s, the coverage is below 1%. The backscatter values for slicks classified as natural film varied between -6dB and -26dB (noise floor).

DISCUSSION

For the Doppler radar, the average drop in vertically polarized radar cross section (RCS) when entering the slicks is 9.4dB (includes cases where no SAR or slick sampling were available). Low backscatter levels were observed to persist over time intervals ranging from tens of seconds to several minutes, depending on the width of the slick. The overall RCS varied with wind speed and other environmental parameters, but stayed in the range between -20 and -40dB (includes both slicked and non–slicked regions).

The chemical analysis of the samples showed that trace metals were generally enriched in the surface microlayer, especially in the slicked areas. Trace metal enrichment is related to particulate matter present in the films, and possibly associated with humic substances (measured as UV absorbance). Humic substances were also enriched in the surface microlayer. Concentrations of free fatty acids indicate that these are raised inside slicks, but also in one of the outside slick samples. In this outside slick case, the high wind speed (9-10m/s) predicts that much lower values should have been found. The sample is therefore believed to be contaminated (probably by biological fats/fish oil from fishing vessels). Most fatty acids originated from marine organisms (plankton and macro–algae), since there are very few high molecular weight fatty acids available. The latter might have indicated higher plant material from terrestial sources, that could have been introduced from land via fjords into coastal waters.

The typical drop in backscatter caused by the natu-

ral films varied between 2dB and 11dB. Increasing wind speeds expectedly lead to decreasing damping by natural film. The wide range of damping values, especially for low wind speeds, is probably due to varying film composition and thickness. Moreover, 27 SAR scenes were classified as showing no natural film (no damping). They all had a wind speed of 5m/s or more.

When comparing COASTWATCH'95 results with the slick sampling experiment carried out in Korsfjord south–west of Bergen, Norway [10], none of the surface microlayer samples seemed heavily impacted by mineral oil products, even though the fjord carried considerable ship traffic. Less, and smaller molecules of fatty acids were found during COASTWATCH'95 compared to the fjord case. The small fatty acid molecules are associated with marine organisms, while the larger come from terrestial sources. Moreover, the investigated slicks from COASTWATCH'95 were generally thinner than those studied in Korsfjord. This is most likely related to fetch lengths which are shorter in fjords than in coastal areas [14]. However, both experiments showed an approximate one order of magnitude increase of the concentration of fatty acids inside compared to outside slicks. For the Korsfjord case, the backscatter damping was slightly higher than found in COASTWATCH'95 cases. This is probably due to film thickness.

CONCLUSIONS

Generally, a correspondence was found between damping in ERS SAR images, C-band Doppler radar values and sea surface chemistry. Compared to an earlier fjord experiment, the investigated slicks were thinner and contained smaller fatty acid molecules, which indicated marine organisms. In the fjord, terrestial sources dominated the slicks. The thinner slicks in COASTWATCH'95 gave slightly lower damping (dB) in the SAR imagery compared to the fjord cases. Moreover, the damping caused by the slicks investigated in COASTWATCH'95 were higher for the Doppler radar, than in the ERS SAR imagery. This is probably due to the lower resolution of the ERS SAR, causing some resolution cells to contain returns from both slick and surrounding slick–free sea, thus reducing contrast. Using the Doppler radar data and surface drifters, we were also able to show that one geophysical process responsible for verified natural film accumulation, was convergence. Also a natural film discrimination algorithm was used to obtain estimates of natural film coverage under different wind conditions.

ACKNOWLEDGMENT

REFERENCES

1. Duce, R., et al., 1994, The sea-surface microlayer and its potential role in global change, *GESAMP WG34, XXIV/7*, A&M Univ. Press, College Station, TX.

2. Lucassen-Reynders, E., and J. Lucassen, 1969, Properties of capillary waves, *Adv. Colloid Interface Sci., 2,* 347-395.

3. Huhnerfuss, H., et al., 1987, Attenuation of wind waves by monomolecular sea slicks by the Marangoni effect, *J. Geophys. Res., 92,* 3961-3963.

4. Frew, N., et al., 1990, Impact of Phytoplankton–Generated Surfactants on Air–Sea Gas Exchange, *J. Geophys. Res., 95,* 3337–3352.

5. Gershey, R., 1983, Characterization of seawater organic matter carried by bubble-generated aerosols, *Limnol. Oceanogr., 28,* 309-319.

6. Asher, W., 1996, The Sea Surface Microlayer and its Effect on Global Air/Sea Gas Transfer, in *The Sea Surface and Global Change,* edited by Duce R., and P. Liss, in press, Cambridge University Press.

7. Wahl, T., et al., 1996, Radar satellites: A new tool for pollution monitoring in coastal waters, *Coastal Management, 24,* 61-71.

8. Huhnerfuss, H., et al., 1994, Classification of sea slicks by multifrequency radar techniques; New chemical insights and their geophysical implications, *J. Geophys. Res., 99,* 9835-9845.

9. Espedal, H.A., O.M. Johannessen and Johan C. Knulst, 1996, Satellite detection of natural film on the ocean surface, *Geophys. Res. Letters, 23,* 3151-3154.

10. Johannessen, O.M., et al., 1996, COASTWATCH-95: ERS-1/2 SAR Applications of Mesoscale Upper Ocean and Atmospheric Boundary Layer Processes off the Coast of Norway, *IGARSS'96, 11,* 1158-1161.

11. Knulst, J.C., 1996, Interfaces in aquatic ecosystems: Implications for transport and impact of anthropogenic compounds, *Doctoral Dissertation,* SE-LUNBDS/NBKE-96/1010+136, Lund Univ., Sweden.

12. Espedal, H., J.A. Johannessen and G. Digranes, 1994, Norwegian Surface Slick Report, *Tech. Rep. No. 81,* Nansen Environmental and Remote Sensing Center, Bergen, Norway.

13. Tanis, F.J., J. Bennett and D. Lyzenga, 1989, Physics of EOM, *Technical Report no. 028,* Environmental Research Inst. of Michigan, USA.

14. Wheeler, J.R., 1975, Formation and collapse of surface films, *Limnol. Oceanogr., 20,* 338-342.

Tilting Effect on the Derivation of Wind Speed from Satellite Altimeters

Paul A. Hwang[1], William J. Teague[1], Gregg A. Jacobs[1] and David W. Wang[2]
[1]Oceanography Division, Naval Research Laboratory, Stennis Space Center, MS, 39529 USA
[2]Computer Science Corp., Stennis Space Center, MS, 39529 USA
Phone: (601)6884708; Fax: (601)6884843; email: phwang@nrlssc.navy.mil

Abstract – The tilting effect (caused by water waves that are much longer than the radar waves) modifies the local radar incidence angle and introduces a strong attenuation of the radar backscattering return. It is shown that when this tilting effect is accounted for, the agreement of the wind speed derived from the altimeter with the buoy measurement of wind speed is significantly improved.

INTRODUCTION

Feasibility of deriving the wind speed at the sea surface from satellite altimeter data has been convincingly demonstrated during the past two decades with output from GEOS, SEASAT, GEOSAT and most recently TOPEX/POSEIDON missions. The basis for relating radar measurements to wind speed is that the radar backscattering intensity is dependent on the surface roughness and that in the ocean, the surface roughness is mainly caused by wind-generated surface waves. The measured radar intensity (the normalized radar cross section), σ_0, however, was found to differ significantly from theoretical calculations using equations derived from scattering processes (e.g., [1]) and measured physical properties of the surface roughness (e.g., [2]). Most puzzling of all, calculations consistently indicated that the sea surface detected by radars, with wavelengths on the order of a few centimeters, was "rougher" than those detected by optical instruments that depend on light with wavelengths in the sub-micrometer wavelength range (Fig. 1).
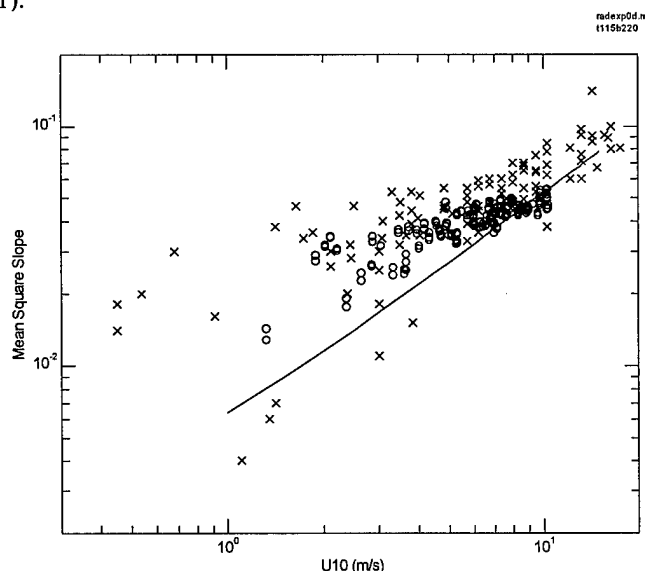
Fig. 1. Ku-band altimeter-derived mean square slopes. x: GEOS-3 [3], o: TOPEX data reported in this article, the solid curve representing the average of the optical measurements.

This perplexing result was not resolved in the past two decades since the advent of altimeter data. Up to this stage, the majority of wind speed algorithms are based on empirical or statistical analyses, most of them rely on the correlation of coincident and collocated databases of the satellite radar cross section and in-situ wind speed (e.g., [4-6]). One algorithm [7] relies completely on the independently derived statistical properties of the altimeter backscattering cross section and sea surface wind speed. The difference among these algorithms are relatively minor. It is shown that the tilting effect (caused by water waves that are much longer than the radar waves) modifies the local radar incidence angle. The change of local incident angle results in an exponential attenuation of the radar return. When this tilting effect is accounted for, the agreement of the wind speed derived from the altimeter with the buoy measurement is significantly improved.

TILTING EFFECT

A conceptual sketch to illustrate the tilting effect is shown in Fig.2 [8]. The sketch illustrates a train of plane waves (indicated by the parallel wave front) impinging on the water surface, corresponding to the scattering of the far-field radar waves from satellite altimeters. The scattered wave patterns from the water surface will vary according to the surface roughness conditions, been more directional and narrowly distributed from a smooth surface, as in patch 1. The primary direction of the scattering pattern is along the direction of specular reflection. Therefore, for surfaces of equivalent roughness, such as patches 2, 3 and 4, the scattering patterns are similar in the directional distribution (the beam width, determined by the surface roughness), but the primary direction of the scattering will vary depending on the orientation of the roughness patch. The backscattering intensities, that is, the scattering in the direction opposite to the incoming waves, for the three patches shown will be different. The modification of the local incident angle results in a reduced, or attenuated, radar return compared to the condition when the scattering is assumed to be on a flat surface such as depicted in patch 5. The concept illustrated in Fig. 2 forms the basis of this paper regarding the tilting effect on the altimeter scattering from the ocean surface.
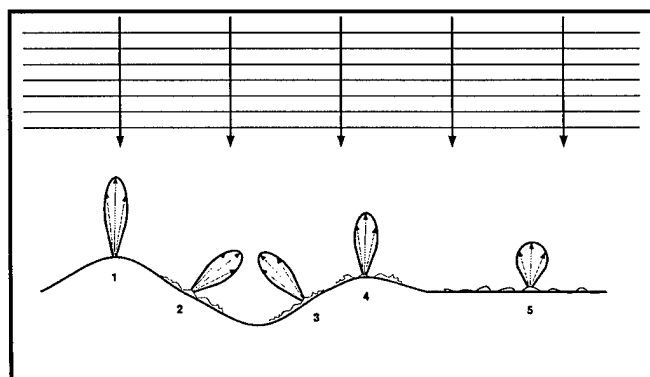
Fig. 2. A conceptual sketch illustrating the scattering of radar waves by surface roughness.

For monostatic radar applications, that is, projecting and receiving radar waves with the same antenna, backscattering properties are of most interest. The backscattering intensity is generally expressed as the normalized radar cross section (NRCS), σ_0. Many expressions of σ_0 have been presented in the literature. The major differences of their results are the assumptions of the surface roughness and the dielectric constant of sea water, which determines the refractive index of the sea surface. For radar altimeter applications, the expression given in [1] is frequently employed (assuming a Gaussian distribution of the scattering surface roughness)

$$\sigma_o(\theta_i) = \frac{|R(0)|^2}{s_f^2} \sec^4 \theta_i \exp\left(\frac{-\tan^2 \theta_i}{s_f^2}\right) , \quad (1)$$

where θ_i is the radar incidence angle, denoting the angle between the propagation direction of radar waves and the surface normal; $|R(0)|^2$ is the Fresnel reflection coefficient, characterizing the surface reflectivity; and s_f^2 is the filtered mean square slope, representing the portion of surface roughness elements with length scales greater than the diffraction limit. Eq. (1) corresponds to the zero-th order solution of the scattering of electromagnetic waves from a rough surface. With a normal incidence, $\theta_i=0$, (1) can be expressed as

$$\sigma_o(0) = \frac{|R(0)|^2}{s_f^2} . \quad (2)$$

Introducing the concept of local incident angle (e.g., [9-10]), (1) can be expressed as

$$\Sigma_o(\theta_i) = \int \frac{|R(0)|^2}{s_f^2} \sec^4(\theta_i + \theta) \exp\left(\frac{-\tan^2(\theta_i + \theta)}{s_f^2}\right) p(\theta)d\theta , \quad (3)$$

where θ is the slope of the long wave roughness (the tilting waves) that contributes to the modification of the local incidence angle, $p(\theta)$ is the probability density distribution (pdf) of the tilting waves, and Σ_0 is the expected radar cross section measured by the altimeter. For normal incidence, $\theta_i=0$, and (4) becomes

$$\Sigma_o(0) = \int \frac{|R(0)|^2}{s_f^2} \sec^4 \theta \exp\left(\frac{-\tan^2 \theta}{s_f^2}\right) p(\theta)d\theta . \quad (4)$$

Comparing (2) and (4), the analytical form of the attenuation factor, $\Delta\sigma_0$, due to the tilting effect can be assessed by the ratio of Σ_0 and σ_0

$$\Delta\sigma_0 = \frac{\Sigma_o(0)}{\sigma_0(0)} = \int \sec^4 \theta \exp\left(\frac{-\tan^2 \theta}{s_f^2}\right) p(\theta)d\theta . \quad (5)$$

Fig. 2 shows a comparison of computational results using (2), shown as dashed curve, and (5), shown as solid curve, with the TOPEX Ku-band altimeter data, shown as circles. The agreement with the altimeter data with the consideration of the tilting effect is significantly improved.
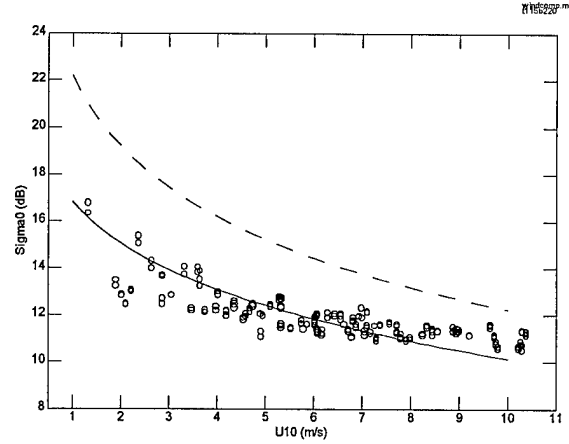
Fig. 3. Tilting effect on the altimeter cross section.

COMPARISON WITH BUOY MEASUREMENTS

Two different wind speed algorithms are developed in [8, 11] to account for the tilting effect. The first (Tilt-ALT) is an operational algorithm that calculate the wind speed directly from the altimeter cross section, and the second is a research algorithm (Tilt-Surface) that assumes a prior knowledge of the tilting slopes in order to correct the altimeter cross section (5). Comparison in term of the distributions of the wind speed difference between in-situ buoy data and altimeter measurements based on five different algorithms are presented in [11]: the two mentioned above plus the empirical algorithms of Brown et al. (B81) [4]; Modified Chelton and Wentz (MCW) [6]; and the statistical algorithm of Freilich and Challenor (F&C) [7]. Typically, the distributions of the first three empirical algorithms are quite similar. For example, one case study (Fig. 4) shows the following statistics: the rms difference and the correlation coefficient are (1.41 m/s, 0.81), (1.39 m/s, 0.81) and (1.51 m/s, 0.81), respectively for B81, MCW and F&C. The statistical properties of the wind speed difference based on the operational algorithm (Tilt-ALT) are very similar to the other three algorithms just discussed, the rms difference and the correlation coefficient are (1.49 m/s, 0.80). However, if the tilting slope can be accurately calculated, and the correction to the measured cross section applied properly, the distribution of wind speed difference is noticeably narrowed. The rms difference and the correlation coefficient improve significantly to (0.84 m/s, 0.96). Similar improvements are found with other data sets we have compiled in the Gulf of Mexico. Table 1 lists the rms differences and the correlation coefficients of the surface wind speed comparisons using the 5 algorithms just described. We may conclude from this comparison that the accuracy of the satellite altimeter is considerably better than we have previously accepted. If independent measurement of the tilting slope is available, the rms difference between the altimeter output and in-situ measurements will be reduced from the currently accepted magnitudes established by empirical algorithms. The improvement is approximately 40 percent based on the results shown in Table 1. And most significant of all, this conclusion is based on sound physical ground relating the altimeter backscattering and the surface slope properties, unlike the earlier operational algorithms that depend on

empirical formulae established from co-located buoy and
altimeter databases
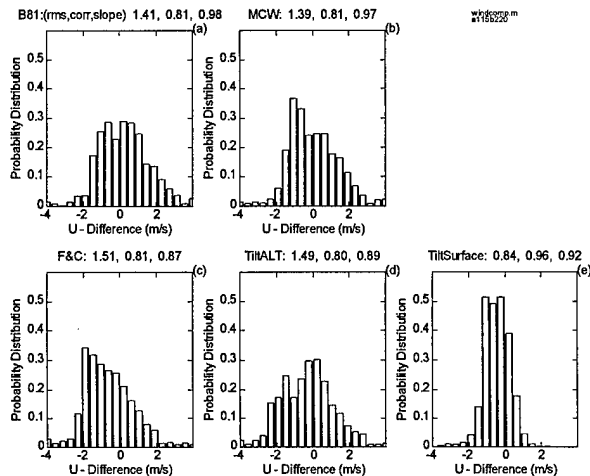
Fig. 4. The distributions of wind velocity differences (ALT -
Buoy) for the five algorithms discussed in this article. (a)
B81 [4]; (b) MCW [6]; (c) F&C [7]; (d) TiltALT [8], and (e)
TiltSurface [8].

Table 1. Comparison of the rms difference and correlation
coefficient of buoy winds and altimeter winds [11].

(a) RMS (m/s)

	B81	MCW	F&C	Tilt-ALT	Tilt-Surf
A115B220	1.41	1.39	1.51	1.49	0.84
A21B220	1.28	1.35	1.62	1.58	0.97
A46B203	1.75	1.74	1.79	1.83	1.07
A59B202	1.30	1.14	1.33	1.56	0.86
A46B236	1.30	1.36	1.46	1.41	0.80
A26B202	2.73	1.45	1.52	1.65	1.21

(b) Correlation Coefficient

	B81	MCW	F&C	Tilt-ALT	Tilt-Surf
A115B220	0.81	0.81	0.81	0.80	0.96
A21B220	0.90	0.90	0.90	0.89	0.97
A46B203	0.82	0.83	0.83	0.81	0.95
A59B202	0.92	0.93	0.93	0.91	0.98
A46B236	0.90	0.91	0.91	0.90	0.98
A26B202	0.65	0.88	0.87	0.80	0.91

CONCLUSIONS

In the course of studying the wind speed derivation from
satellite altimeters, it is found that the surface tilting effect is
a significant factor of consideration. The effect is especially
noticeable at lower wind velocities where differences of more
than 6 dB are found between the altimeter measurements and
the computations using the classical equation relating the
backscattering cross section and the surface roughness (2).
With the correction of the tilting effect in the cross section
measurement, the calculated wind speed is found to be in

much better agreement with the surface buoy measurement.
The improvement is on the order of 40 percent when
compared to the results derived from other statistical or
empirical algorithms including B81, MCW and F&C. This
result suggests that the theoretical frame work relating the
backscattering cross section and the surface roughness is
fundamentally sound when the tilting effect that modifies the
local incident angle is taken into account. It also indicates
that the accuracy of deriving wind speeds from altimeter
cross sections is potentially much better than we have
perceived, however, in order to achieve the full potential of
the altimeter wind sensing, independent measurement of the
sea surface slope component contributing to the tilting may
be needed.

REFERENCES

[1] Barrick, D. E., Rough surface scattering based on the
specular point theory, IEEE *Trans. Antenna. Propag.*,
AP-16, 449-454, 1968.

[2] Cox, C. S., and W. Munk, Statistics of the sea surface
derived from sun glitter, *J. Mar. Res.*, 13, 198-227,
1954.

[3] Brown, G. S., Quasi-specular scattering from the air-sea
interface, in *Surface Waves and Fluxes*, Vol. 2, eds. W.
Plant and G. Geernaert, Kluwer Academic, 1-40, 1990.

[4] Brown, G. S., H. R. Stanley, and N. A. Roy, The wind
speed measurement capability of spaceborne radar
altimeters, IEEE *J. Oceanic Eng.*, OE-6, 59-63, 1981.

[5] Chelton, D. B. and F. J. Wentz, Further development of
an improved altimeter wind speed algorithm, *J.
Geophys. Res.*, 91, 14250-14260, 1986.

[6] Witter, D.L., and D.B. Chelton, A Geosat altimeter
wind speed algorithm and a method for altimeter wind
speed algorithm development, *J. Geophys. Res.*, 96,
8853-8860, 1991.

[7] Freilich, M.H., and P.G. Challenor, A new approach for
determining fully empirical altimeter wind speed model
functions, *J. Geophys. Res.*, 99, 25051-25062, 1994.

[8] Hwang, P.A., D.W. Wang, W.J. Teague, and G. A.
Jacobs, Effect of surface tilting on altimeter wind
measurement, subm. *J. Geophys. Res.*, 1997.

[9] Valenzuela, G.R., Theories for the interaction of
electromagnetic and oceanic waves - a review, *Bound.-
Layer Meteorol.*, 13, 61--85, 1978.

[10] Wright, J.W., A new model for sea clutter, IEEE *Trans.
Anten. Propag.*, AP-16, 217-223, 1968.

[11] Hwang, P.A., W.J. Teague, G. A. Jacobs, and D.W.
Wang, A statistical comparison of wind speed, wave
height and wave period derived from satellite altimeters
and ocean buoys, subm. *J. Geophys. Res.*, 1997.

Automated hierarchical classification of SAR images

P.C. Smits, R. Vaccaro, and S. Dellepiane

University of Genoa - Department of Biophysical and Electronic Engineering
Via all'Opera Pia 11A - 16145 Genoa - Italy
Phone +39-10-3532662 Fax +39-10-3532134
E-mail: smits@dibe.unige.it, roby@dibe.unige.it, silvana@dibe.unige.it

Abstract - This paper faces the problem of achieving a satisfactory classification of SAR data, based on statistical methods as Maximum Likelihood. The proposed method performs a hierarchical classification, making an automatic feature selection, simulating the behaviour of a real exhaustive selection in the features space. The method, whose accuracies outperforms those obtainable with a classical ML one shot, uses a new statistical characterisation of classical features as sample mean and sample variance that exploits the spatial correlation between data.

INTRODUCTION

The supervised, statistical classification of Synthetic Aperture Radar (SAR) images has to deal with the difficulties involved in processing this kind of data, and often results in poor accuracies.

There are two important issues that relate to this problem. The first issue regards the low flexibility of the mathematical models which are used to describe the data to be classified. For instance, the statistical properties of the second order are often overlooked, and so the resulting models may be heavily simplified.

The second issue is of a more specific kind and regards one of the major problems in all supervised classification algorithms: the limited availability of training samples [1],[2]. Conventional classification technologies, as the classical ML one shot or KNN, often do not respond effectively to the rapid development in SAR technology: resolution increases, as does the amount of data, with the possibility to distinguish between an always growing number of particulars, while often the training areas remain small.

This paper offers a solution to these problems in the framework of an automated hierarchical classification methods.

METHOD

The proposed method follows a hierarchical approach [3], and provides decisional trees which are searched in the graph space using a branch function based on the Battacharyya distance [4]. The search of the decisional tree follows a top-down approach and is carried out by simulating the search strategy of the exhaustive classification algorithm in the feature space.

The simulation of the exhaustive search is done by observing the extraction strategy of the features and of the classes, which set the nodes of the tree, followed by the real exhaustive classification method. Two sets, the first empty and the second containing all the natural classes, are initialised at the first step. Then, the natural class which has the best separability measure as compared to the set formed by the remaining natural classes, is extracted from the second set. The chosen class is put in the set initially empty and the state of the two set is stored together with the feature selected to separate the class. The extraction and storing process continues until the set, initially full, is composed by only one class and all the others are put in the set initially empty. Finally, the configuration of the two sets is chosen which has the best separability compared to those of all the stored configurations. The winning configuration will form the state of two new nodes of the hierarchical tree. The method continues until each state of each node of the tree is formed by only one natural class.

The method provides a locally optimal classification result, reducing the computational complexity from the exponential level (real exhaustive search) to the quadratic level (proposed simulated exhaustive search). Moreover it performs an automatic selection in the features space. In the following, an estimate of the computational complexities, expressed as a function of the number of Battacharyya distances that have to be computed by the different algorithms, is presented.

We define the following quantities: C complexity, K total number of considered images, P total number of considered features, N total number of considered classes. The total number of features used is: K*P.

Real hierarchical exhaustive classification complexity

In this case we have that:
$$C = K \left[P \left(2^N \right) \right]$$

The behaviour of the function is exponential.

Simulated algorithm for hierarchical classification

The complexity of the algorithm is the following:

$$C = KP \sum_{t=0}^{N-2} \left[\sum_{i=0}^{N-t-2} \left[(N-t-i) - 1 \right] + (N-t-2) \right]$$

The double sum exploits the almost square behaviour of the complexity of algorithm.

Simulated algorithm for hierarchical classification with variable branch function

This is the computational complexity for a variation of the simulated algorithm. In this case, instead of computing the Battacharyya distance for all the natural classes contained in the set initially full a simplifying hypothesis is done. The mean and the standard deviation of the feature under examination are used to compute a distance measure based only on the difference between these quantities. The accuracy achievabile by this algorithm is lower than those of the simulated algorithm. This happens because the introduced simplification is equivalent to consider classes as characterised by rectangular probabilities densities. The computational complexity allowed by this variation is almost linear.

$$C = K \sum_{t=1}^{N-2} [(N - t - 1)(P + 2) - 1]$$

In Fig.1 a graph of the behaviour of the complexities of the different algorithms , considering one only image and one only feature, is shown. The complexity of the real exhaustive algorithm makes the problem intractable while, thanks to their reduced complexity, the two proposed algorithms are suitable to make tractable the hierarchical classification with automated feature selection.
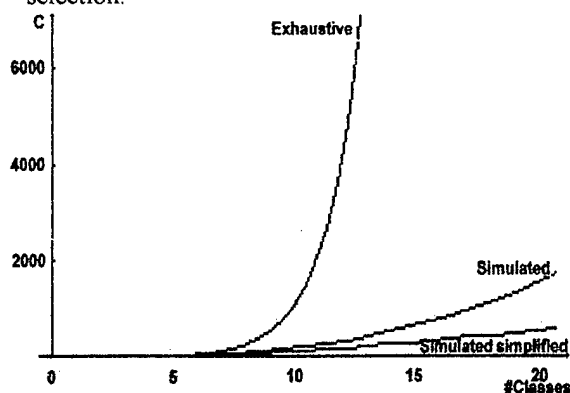
Fig.1. Behaviour of the complexities for the proposed algorithms.

An important issue of the statistical classification is that classical statistical feature estimators do not exploit the dependence among the samples of an acquired image. The textural information of an object is lost because of the simplified approach to classification.

We have developed estimators of the first and second statistical properties of features like sample mean and sample variance that exploit the correlation property. We have made the simplifying hypothesis of data with gaussian distribution.

In the following, the parametric estimators of the statistical properties of the first and the second order of the two features are shown.

Those features have been used by the hierarchical classifier developed both to compute the Battacharyya distance and to make the maximum likelihood classification.

This increase of information captured by the proposed method of features estimation makes an improvement of the classification accuracy.

Mean of the sample mean

The mean of the above sample mean is the same of the one estimated with the hypothesis of sample independence:

$$E\left\{\hat{\mu}\right\} = \frac{1}{N} \sum_{i=0}^{N-1} E\left\{x_i\right\} = \mu$$

Variance of the sample mean: The estimate of the variance of the sample mean is quite difficult because we don't use the hypothesis of data independence. The parametric expression of the variance of the sample mean is the following:

$$\text{var}\left\{\hat{\mu}\right\} = \frac{1}{N^2} \sum_{i=1}^{N-1} 2(N-i)\left[\frac{1}{N} \sum_{n=0}^{N-i-1} x_n' x_{n+i}'\right] + \frac{1}{N} \sum_{k=0}^{N-1} \left(x_k'\right)^2 \quad (1)$$

where x_i' are the samples of the signal with the estimated mean value subtracted, and: $i=1....N$.

As can be observed from (1), the number of calculations necessary for the estimate of the variance of the sample mean is onerous, but it can be reduced investigating the nature of the data. In fact, we have experimentally seen on our set of SAR images that after seven, at most ten samples, the spatial autocorrelation value is about zero. In (1), we have limited, the term which express the spatial autocorrelation to the meaningful values that we have estimated on our images.
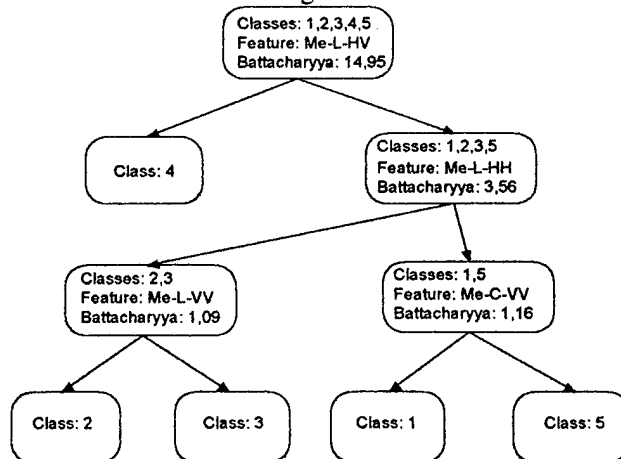
Fig. 2. Classification tree generated by the simulated hierarchical algorithm (Legend: ME-LHV=sample mean on L band with HVpolarization).

Mean of the sample variance

The mean of the sample variance made without the independence hypothesis has a difficult demonstration, similar to those found for the variance of the sample mean

1175

The new estimate of the mean of the sample variance is the following:

$$E\{\hat{\sigma}^2\} = \hat{\sigma}^2 - \frac{1}{N^2}\sum_{i=0}^{N-1}2(N-i)\left[\frac{1}{N}\sum_{n=0}^{N-i-1}x_n'x_{n+i}'\right] - \frac{1}{N^2}\sum_{n=0}^{N-1}x_n'^2$$

The reasoning made about possible simplifications related to the nature of the spatial correlation keeps the computation of the estimator effective.

Variance of the sample variance: The analytic estimate of the variance of the sample variance is very complex, because the demonstration requires the computation of 4th order moments. This estimator is still to develope. We suggest, for the moment, to use, when computing this quantity, the simplifying hypothesis of independent samples.

RESULTS AND CONCLUSIONS

The method for the hierarchical classification with automated features selection has been tested on different agricultural sites (Flevoland and Feltwell).

The classification results for the Feltwell sites are shown in Fig.3, while in Fig.2 the generated classification tree can be seen. In Fig 3, five different classes are present: sugar beets, stubble, bare soil, carrots and potatoes. We have contemporary used, for the classification six, one look, SAR data acquisitions of this site: HH, HV and HV polarised, in the L and C bands. For every image we have computed the intensity and the sample mean and sample variance features with the new

Fig. 3 Classification map of the Feltwell site.

estimators of their statistical properties of the first and the second order.

The space of the features, in which the algorithm made the feature selection, was set to 18 elements.

In Table 1 the classification accuracy achieved with these features is compared with that obtained with other classical methods.

Table I. Classification accuracy obtained on the Feltwell site. A: ML one shot; B: Simulated hierarchical; C: Simulated simplified hierarchical.

	A	B	C
1: Sugar Beets	58,63	70,83	18,75
2: Stubble	26,49	83,63	83,63
3: Bare Soil	72,62	87,79	90,18
4: Potatoes	93,15	96,73	96,72
5: Carrots	47,32	73,81	69,34
Tot.	59,64	82,56	71,7

It can be seen that the difference in quality is high. In fact the average accuracy improves of more than 20% if compared with the classical Maximum Likelihood one shot. The classification accuracy percentage is based on the training areas. We have always found, in our tests, the accuracy of the simulated algorithm to be the same of the really exhaustive algorithm, while that of the simulated simplified degrades of something, which is due to the hypothesis done. The discrimination power of the features with the new estimators is good. The sample mean, thanks to our statistical characterisation, obtains classification accuracies that exceed those obtained by work developed in the same field [5].

In conclusion, both from the theoretical and the practical point of view, the method represents a good solution to efficiently achieve accurate classification maps. The automated feature selection allows to find that configuration which performs better and thus which better reduces the confusion between classes. The proposed method prooved to be extremely suitable to be employed as an initial classification for higher level systems like, for instance, Markov Random Field based approaches.

REFERENCES

[1] B.M. Shahshahani, D. A. Landgrebe, "The effect of unlabeled samples in reducing the small sample size and mitigating the Huges Phenomenon", IEEE Transaction on Geoscience and Remote Sensing, vol.32, no. 5, Sept 1994.

[2] E.Rignot, R. Chellappa,"Maximum a posteriori classification of multifrequency, multilook, synthetic aperture radar intensity data" J.Opt.Soc.Am.A, Vol 10,No.4, April 1993

[3] L. Kanal, "Problem-Solving Models and Search Strategies for Pattern Recognition", IEEE Transaction on Pattern Analysis and Machine Intelligence, Vol. PAMI-1,No.2, April 1979

[4] B.Kim A.D.Landgrebe, "Hierarchical Classifier Design in High-Dimensional Numerous Class cases", IEEE Transaction on Geoscience and Remote Sensing, Vol. 29,No.4, July 1991.

[5] A. Freeman, J.Villasenor, J.D.Klein, P.Hoogeboom, J.Groot,"on the use of multifrequence and polarimetric radar backscatter features for classification of agricultural crops",Int.J.Remote Sensing,1994, Vol.15,no.9,1899-1912.

Identifying Classes in SAR Sea Ice Imagery Using Correlated Texture

Leen-Kiat Soh and Costas Tsatsoulis
Department of Electrical Engineering and Computer Science
The University of Kansas, Lawrence, KS 66046
Tel: (913)864-3041 Fax: (913)864-7789 Email: lksoh@ittc.ukans.edu

Abstract -- This paper presents a new technique in identifying classes in Synthetic Aperture Radar (SAR) sea ice imagery using correlated texture. First, we employ dynamic local thresholding to generate a histogram of thresholds. Then, we use a multi-resolution peak-detection method, a strategy used in digital image quantization field, to extract significant intensity thresholds from the histogram and provide an initial segmentation. Next, we compute correlated texture of the result and create a matrix of spatial, probabilistic relationships among the classes. Given the texture, we cluster the classes into different groups. The clustering concept is based on an innovative 'solidification' model that strives to obtain similar auto-correlated textural values for all groups. This process produces a second segmentation with the correct number of classes. We have tested our technique in more than 200 SAR sea ice imagery successfully. The entire process is fully automated and fast.

each group made up of several classes. This unsupervised discovery is the key to the automation of our design. The final segmentation of sea ice imagery is then achieved by thresholding the image using the maximum threshold value of each group.

Note that we propose a segmentation technique that identifies classes in SAR sea ice imagery as a pre-processor to classification. We believe a SAR image processing task be incremental and modular. To be incremental, a good segmentation process preempts a good classification result. To be modular, it allows us to incorporate expert geophysical knowledge and ancillary data into classification and not overburden the task of image segmentation. This two-tier strategy has been utilized in sea ice classification[3], land use mapping[6], drainage channel networks detection[5], integration of ancillary data[1][4], and other image processing tasks.

INTRODUCTION

In SAR sea ice research, the improvement in the image resolution and the increase in the number of satellites have rendered manual image analysis impractical. In addition, the analysis of natural scenes such as sea ice presents many unique problems. Sea ice features are not structured and cannot be represented consistently by structural rules or grammars. Also, in contrast to artificial objects, sea ice features do not obey strict positioning rules. Finally, the backscatter of sea ice types can vary greatly based on the geographic area, the season, the weather conditions[2][7][10]. Thus, approaches using pre-determined number of classes are not viable in performing segmentation of such imagery. This leads to the need of a data-driven method that automatically derives the number of segmentation classes from the image (or data) itself.

In this paper we present a methodology that integrates traditional image processing algorithms with a clustering process that employs correlated texture of the classes in the image. First, we analyze a sea ice image using multi-level dynamic local thresholding to generate a histogram of thresholds. Next, we apply a multi-resolution peak detection strategy to extract significant thresholds from the histogram. Given these significant thresholds, an initial segmentation is achieved. Further, we compute for each class a correlated texture, a vector that specifies the probability of another class being a neighbor to the class. Our clustering then uses an innovative solidification model to partition the threshold set into a number of groups, with

METHODOLOGY

Our underlying methodology is to use image processing to provide clues to describe a preliminary segmentation of the image and perform numerical clustering to refine and produce the final segmentation. This approach allows clustering to analyze only on selected information of the image, reducing the amount of computational work, and preventing irrelevant information from influencing its outcome. Moreover, the clustering module relieves the burden of determining the number of classes from the segmentation process. Hence the segmentation process can focus on low-level, syntactic image manipulation, leaving higher order tasks such as semantic interpretation to clustering.

Multi-Level Dynamic Local Thresholding
We have adapted the dynamic local thresholding technique from [3]. We assume an N-class image, instead of three, with N determined by our multi-resolution peak detection algorithm. First, we divide the image into overlapping regions and compute the histogram and its variance for each region. Only histograms with their variance values greater than an image dependent threshold are selected for further processing. The threshold is set to admit at least 25% of all histograms. This implicitly helps preserve global information. Second, given each qualified histogram, we approximate its binormal Gaussian mixture by computing its means and standard deviations using stochastic estimation in [11]. Third, given the parameters of the approximation process, we compute peak-to-valley

ratios to filter out mixtures that are not significantly bimodal. Further, we derive from these parameters the optimal threshold via the maximum likelihood method. As a result, we obtain a histogram of computed threshold values, from which significant thresholds are extracted.

Multi-Resolution Peak Detection

This feature extraction process assumes that each class of areas could have a range of intensities such that the representative thresholds found from these areas could be far apart from each other. Occupying the interval between each pair of these thresholds are other (residual) threshold values comprising the intensity difference. We have designed a multi-resolution peak detection technique that extracts significant jumps in the cumulative distribution function (CDF) of the histogram. Utilizing the cumulative distribution function to look for peaks has two advantages: 1) a peak's significance can be based on its surrounding values, and 2) noisy peaks can be ignored due to the use of windowing [9]. First, we generate, from the histogram, the cumulative distributed function. Second, we search for the starting windowing size, K, based on the range of the histogram. Second, we develop a resolution plane of peaks detected from the CDF when it is averaged using size K, $K-2$, ..., and 3. Note that peaks found at low resolutions (when the window size is large) are substantial since, for them to survive the averaging, they must have been significant in the original histogram. This is the *detection* objective. On the other hand, peaks found at higher resolutions are for the *localization* purpose. They define the exact location of a peak. This detction-localization approach has been used in most multi-resolution tasks[8]. Third, we track peaks through the resolution plane and obtain a set of significant thresholds. A preliminary segmentation is then generated by applying these thresholds to the image.

Numerical Clustering

From the preliminary segmentation, we obtain correlated texture for each class. A correlated textural value of a class i for a class j, $C(i,j)$, is the probability of a pixel labeled as class i having a neighboring pixel of class j. Thus, we have a vector of probabilities describing the relationship between each class and every other class. In our solidification model, a compact class i will have a high auto-correlated textural value, $C(i,i)$. On the other hand, a scattered class i, usually occupying the fringes of another class, j, will have a high $C(i,j)$. Given these two assumptions, we use a over-commitment clustering strategy that allows us to overshoot a target score—the strongest $C(i,i)$—by admitting the partial borderline class into a group and speeds up the process of clustering. First, we identify the strongest class, i.e., the class with the highest $C(i,i)$. Second, we scan the list, from top to bottom, of classes and combine them to form an aggregate of $C(i,i)$s to match the strongest class. Third, we scan from bottom to top. As a result, we obtain two clustering configurations. Fourth, we combine the two by resolving

conflicts, if any, between them. This produces a cluster of groups of classes with which we threshold the image for the final segmentation.

RESULTS

Fig. 1 shows one part of an ERS-1 SAR sea ice image, taken on December 1, at 73.1N, 130.7W. The lower portion of the figure depicts the classification result. Our technique found three classes: dark, gray, and bright. To reiterate, we do not attempt to label these classes but simply label them as segmentation classes useful for further classification. The technique is fast. The average computational time required to process a 1024x1024 image is less than 30 seconds on an SGI-IRIX 5.3 operating system. We have applied our technique to more than 200 SAR images and achieved satisfactory visual evaluation for more than 75% of them.

CONCLUSION

In conclusion, we have designed a fully automated and fast technique that identifies classes in SAR sea ice imagery. It integrates image segmentation and numerical clustering techniques as a two-tier process: the former to derive selected information; the later to perform numerical taxonomy on the information to discover classes. This data-driven methodology suits the image processing tasks of SAR sea ice imagery with dynamic characteristics. The technique is also fast and fully automated.

REFERENCES

[1] M. Ehlers, D. Greenlee, T. Smith, and J. L. Star, "Integration of Remote Sensing and GIS: Data and Data Access," Photo. Eng. Rem. Sen., vol. 57, 1991, pp. 669-676.

[2] A. J. Gow and W. B. Tucker III, "Sea Ice in the Polar Regions," Polar Oceanography, Part A: Physical Science, 1990, pp. 47-121.

[3] D. Haverkamp, L.-K. Soh, and C. Tsatsoulis, "A Comprehensive, Automated Approach to Determining Sea Ice Thickness from SAR Data," IEEE Trans. GARS, vol. 33, no. 1, 1995, pp. 46-57.

[4] C. F. Hutchinson, "Techniques for Combining Landsat and Ancillary Data for Digital Classification Improvement," Photo. Eng. Rem. Sen., vol. 48, 1982, pp. 123-130.

[5] C. Ichoku, A. Karnieli, A. Meisels, and J. Chorowicz, "Detection of Drainage Channel Networks on Digital Satellite Images," Int. J. Rem. Sen., vol. 17, no. 9, 1996, pp. 1659-1678.

[6] X. Li, "A Method to Improve Classification with Shape Information," Int. J. Remote Sensing, vol. 17, no. 8, 1996, pp. 1473-1481.

[7] R. G. Onstott, "SAR and Scatterometer Signatures of Sea Ice," Geophysical Monograph 68, Remote Sensing of Sea Ice, F. D. Carsy (Ed.), American Geophysical Union, 1992, pp. 73-104.

[8] A. Rosenfeld (ed.), Multiresolution Image Processing and Analysis, 1984, Berlin: Springer-Verlag.

[9] M. I. Sezan, "A Peak Detection Algorithm and Its Application to Histogram-Based Image Data Reduction," CVGIP, vol. 49, 1990, pp. 36-51.

[10] R. A. Shuchman and R. G. Onstott, "Remote Sensing of the Polar Regions," Polar Oceanography, Part A: Physical Science, 1990, pp. 123-169.

[11] T. Y. Young and G. Coraluppi, "Stochastic Estimation of a Mixture of Normal Density Functions Using an Information Criterion," IEEE Trans. IT, vol. 16, 1970, pp. 258-263.

Figure 1 The original ERS-1 SAR sea ice image and the result of our segmentation. Our technique has identified three segmentation classes in the image automatically.
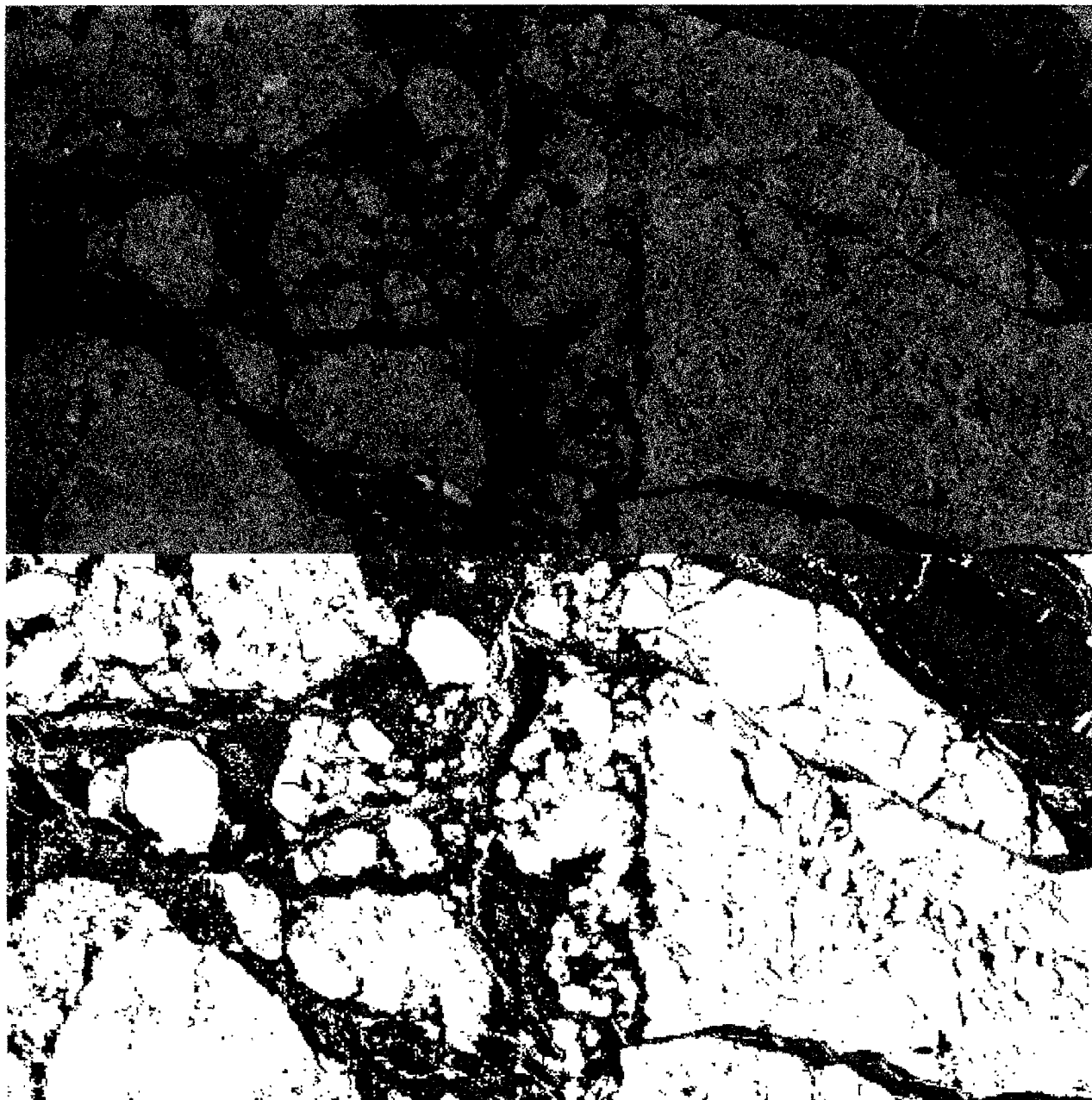
Use of SAR Image Texture in Terrain Classification

M. Craig Dobson, Leland Pierce, Josef Kellndorfer, Fawwaz Ulaby
The University of Michigan, Radiation Laboratory
Ann Arbor, MI 48109-2122 USA
Tel.: +1-313-647-1799, Fax: +1-313-647-2106, email: dobson@eecs.umich.edu

Abstract -- Classification is a common first step in the use of SAR data. Intensity of a pixel is generally used as a feature vector. This is complicated by coherent fading that yields multiplicative noise. Consequently, the first statistical moment of intensity (over some local window) is often used as a feature vector instead. In some cases this leads to unacceptably high rates of misclassification. The 2nd statistical moment also can be used to distinguish categories but is dependent on the composite effects of the sensor (N of looks), the mean backscatter (via multiplicative noise) and the true spatial variance in average backscatter relative to SAR resolution. Thus, using variance measures as feature vectors can lead to increased classification accuracy. However, such measures ignore the observation that the variance for many terrain categories is not stationary and indeed may not be isotropic. Further improvement in classification can be realized by quantifying the translational variance in backscatter using scale-dependent geostatistical measures such as semi-variance and lacunarity that characterize the spatial structure of image intensity. Simulated SAR data are used to understand the effects of system parameters (such as number of looks and spatial resolution) and target conditions (such as probability of occurance and stationarity) on geostatistical measures of texture. ERS-1 and JERS-1 SAR data demonstrate the use of these techniques in terrain characterization. These statistics also give measures of heterogeneity of interest to ecologists.

INTRODUCTION

In general, there are four types of intensity variations within a radar image that must be considered in terrain classification from SAR data: (1) variations in average intensity from one terrain type to another (i.e., such as between bare soil and forest), (2) variations within a given terrain category related to the spatial variance in geometrical attributes of the surface or overlying vegetation (i.e., such as between tree plantations of differing ages), (3) variations within a given terrain type due to temporal variance (such as those resulting from changes in dielectric properties of the scene i.e., soil moisture or snow cover), and (4) random variation due to fading at the pixel level. For purposes of terrain classification, single-date classifications are typically based upon the pixel means and variations (2-4) become noise. Multi-temporal approaches extend this to explicit treatment of variation (3). Both commonly use spatial filtering to mitigate the noise contributed by fading. In this study we examine geostatistical techniques to quantify true spatial variance in scene properties in the presence of fading.

Local variance in backscatter arises from (1) coherent fading which is a multiplicative noise dependent upon the n-of-looks and (2) fine scale spatial variance in scene attributes, primarily vegetation structure and is dependent upon spatial resolution of the SAR relative to the patch size of vegetation. Two general methods can be used to define the joint PDF due to texture and fading: (1) a purely statistical approach and (2) an image-based spatial approach. In the statistical approach, the measured single-look scattering PDF is compared to the expected distributions for common clutter models such as the Rayleigh fading model, the log-normal distribution, the Weibull distribution, the Rice distribution and the k-distribution [1-3]. The Rayleigh model works well for many combinations of sensor parameters (frequency and polarization) and terrain category. However, some categories, such as forest and savanna woodlands, characterized by strong scattering elements are better characterized by models such as the Rice or log-normal distributions. Multiple forward scattering between the ground and the trunks (double-bounce) can dominate backscatter from forests particularly for hh-polarization at long wavelengths.

Statistical approaches assume random distributions of scattering elements within a given region. This assumption is valid in many situations particularly when the scattering elements are numerous and small relative to resolution and vegetation cover is actively managed to maintain uniformity (i.e., agriculture, rangeland and forest plantations), but natural vegetative covers often exhibit 'clumpiness' and gaps. Studies of SAR image texture [4] have largely ignored the spatial structure of texture.

GEOSTATISTICAL METHODS

Geostatistical techniques can be used to quantitatively characterize 'texture' with respect to both the variance and the spatial dependence of this variability. These measures test the assumption that the underlying attributes (scatterers in this case) are randomly distributed and

therefore characterized by a stationary PDF (i.e., translationally invariant). Importantly, these measures explicitly incorporate the scale dependence of the phenomenon and hence have the potential to describe the dependence of texture on image resolution. Two common being those (1) based upon the spatial autocorrelation function and (2) related to the fractal dimension.

The autocorrelation function can be calculated from the measured distributions and summarized in terms of the correlation length and the form of decay (i.e., exponential or Gaussian). A related approach is the semi-variogram [5] which describes the mean squared pair differences (semi-variance) as a function of spatial offset or lag, h. The semi-variogram function is defined as

$$\gamma(h) = (1/2N_h)\Sigma(z_i - z_{i+h})^2 \qquad (1)$$

where there are N pairs of observations, z, at distance h from the ith location. When z is translationally invariant, $\gamma(h)$ will be a constant (for h>0) related to the variance. For SAR data, the variance is a function of both sensor parameters (N of looks) and average target properties (mean backscatter) plus the true spatial variance in target properties. Spatially variant distributions asymptotically approach this value, or sill, at a log distance called the range. $\gamma(h)$ will oscillate for periodic patterns. Thus, it is not surprising that Miranda and Carr [6] found consistent differences in the values of the sill between terrain categories in SIR-B, ERS and JERS SAR data. They found consistent differences in the range which provides information on the spatial structure. The behavior of $\gamma(h)$ shows the degree of translational invariance in the fading/textural statistics. Miranda's analyses show a spatial periodicity of radar backscatter from open tropical vegetation and flooded vegetation, in particular, while dense tropical vegetation decorrelates quickly with distance.

This approach has been modified by Cressie and Hawkins [7] to be less sensitive to the skewing effect induced by large outliers in the distribution of z_n through the use of mean square-root pair difference (SRPD).

$$SRPD(h) = (1/N_h)\Sigma|z_i - z_{i+h}|^{0.5} \qquad (2)$$

This is significant for SAR data because the underlying statistics are exponentially distributed (assuming Rayleigh fading and square-law detection); and furthermore, the sample may contain one or more point targets of high return. SRPD has been applied to imagery [8], but not SAR data.

Another geostatistic to test stationarity is lacunarity, the term Mandelbrot [9] applied to describe the spatial distribution of gap sizes in self similar geometric structures. Lacunarity is a scale dependent measure of translational invariance that can operate using a windowing approach on 2-D images [10]. The lacunarity index has been developed for binary data and is calculated as a function of window size (scale). This index has been used for quantized orbital SAR data of the Pantanal region of Brazil [11] and the results were

compared to measures based upon the gray level co-occurrence matrix, GCLM [12]. They found the GCLM measures to be relatively insensitive to dramatic temporal changes in the texture of ERS-1 SAR imagery related to seasonal flooding, while the lacunarity index provided good textural discrimination.

This technique can be easily extended to scalar data

$$\Lambda(r) = (\sigma_z(r) / \mu_z(r))^2 + 1 \qquad (3)$$

where $\Lambda(r)$ is the lacunarity index for a window of dimension r, σ_z is the standard deviation of the Σz within the sliding window and μ_z is the mean Σz within the window over some region. $\Lambda(r)$ is maximum for r=1 and is proportional to the number of looks of the source data. As r becomes very large, $\Lambda(r)$ approaches unity. The rate of decay in $\Lambda(r)$ describes the 'granularity' in the texture. A constant rate of decay indicates a self-similar, fractal structure.

A textural variance index (TVI) has been defined for SAR data [4] that explicitly incorporates n-of-looks

$$TVI(r) = ((\sigma_z/\mu_z)^2-((4/\pi)-1)/N_r)/(1+((4/\pi)-1)/N_r)) \qquad (4)$$

where all terms are as previously defined and N is the number of independent looks. Assuming linear detection with N=1, $TVI=((\sigma_z/\mu_z)^2-1)/2$.

SAR RESULTS

Simulated SAR data (linear detection) was generated for various spatial patterns of two classes: 'A' is a tree-like class with a mean backscatter $\sigma°=-5dB$ and 'B' is an agricultural class with $\sigma°=-20dB$. The following patterns where generated: (1) random location with P(A)=(0, 0.1, 0.5, 0.9 and 1.0), (2) regular 'checkerboard' patterns with squares of side lengths 1, 2, 3, 4, 5 and 9 and (3) randomly located squares with P(A)=0.5 of side lengths 2, 3 and (4) a fractal 'Y' pattern. For each pattern, class names are assigned using the stated probabilities. Backscatter values are generated using the mean backscatter and assuming Rayleigy fading. The simulations are iterated for N=1, 2, 3, 4, 5 and 1,000.

The two measures based on the autocorrelation function are very similar in behavior and are highly dependent on N while lacunarity and TVI(r) quickly aopproach a limit for N>2 (see Fig.1). The dependencies of the geostatistical measures on spatial pattern and probability of class occurrence are shown in Fig.2 for N=1 with linear detection. All are found to be sensitive to pattern type, spatial scale and probability.

Orthorectified and coregistered composites of 6-look ERS and JERS SAR data from southwestern and northern Michigan are subsampled for various general land-cover classes. The average results are shown in Fig.3 for operations over windows with a spatial dimension of 675-m.
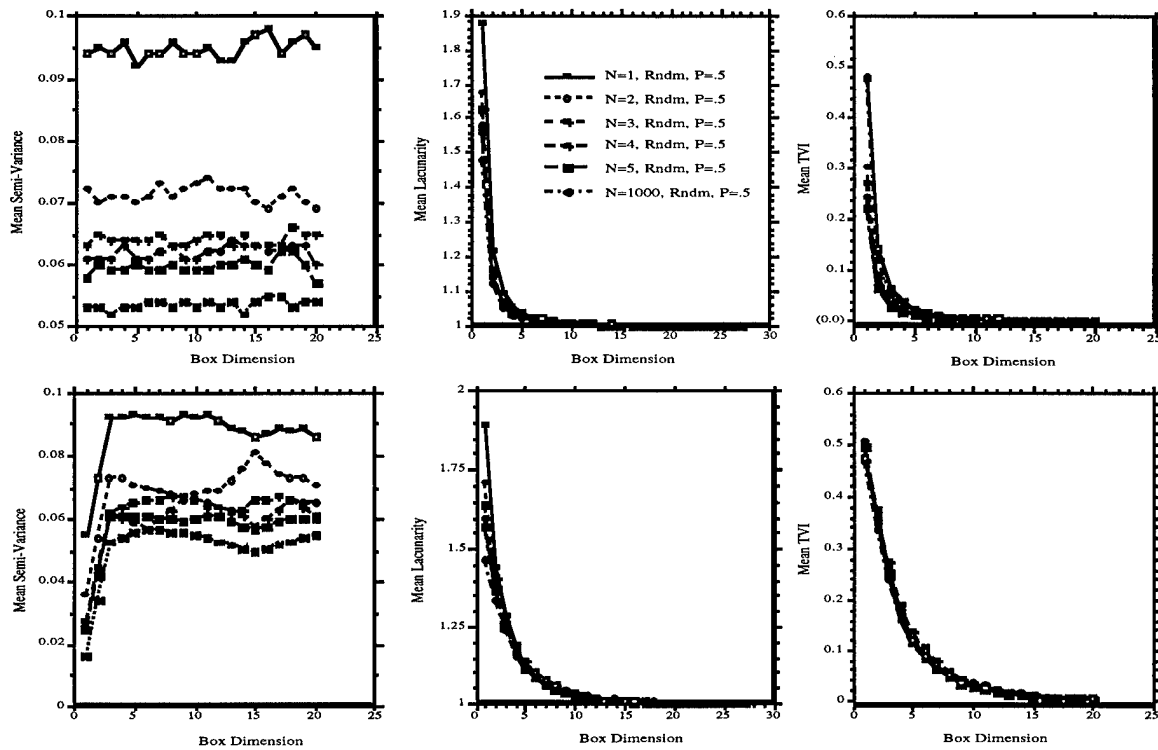
Figure 1. Effect of N of looks on geostatistical measures.
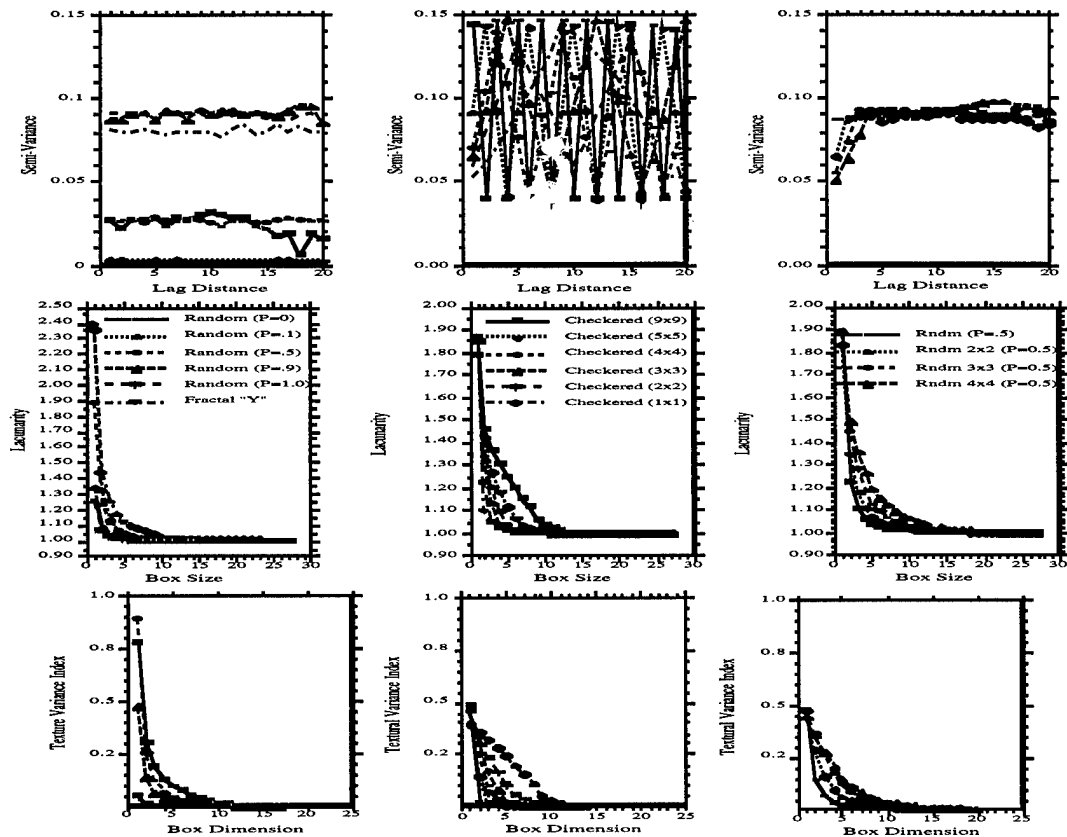
Figure 2. Effects of pattern, probability and spatial scale on geostatistical measures.

REFERENCES

[1] F.T. Ulaby and M.C. Dobson, Handbook of Radar Scattering Statistics for Terrain, Artech House, Inc., Dedham, MA, 1989.

[2] S.H. Yueh, et al., "K-Distribution and polarimetric radar clutter," in Polarimetric Remote Sensing, ed. by J.A. Kong, Elsevier, Amsterdam, pp. 237-276, 1990.

[3] S. Quegan and I. Rhodes, "Statistical models for polarimetric data: consequences, testing and validity," Int. J. Rem. Sens., 16:7:1183-1210, 1995.

[4] F.T. Ulaby, F. Kouyate, B. Briscoe, T.H.L. Williams, "Textural information in SAR images," IEEE Trans. Rem. Sens. Geosci., GE-24:235-245, 1986.

[5] A.G. Journel and C.J. Huijbregts, Mining Geostatistics, Academic Press, New York, NY, 1978.

[6] F.P. Miranda and J.R. Carr, "Application of the semivariogram textural classifier (STC) for vegetation discrimination using SIR-B data of the Guiana Shield, NW Brazil," Rem. Sens. Rev., 10:155-168, 1994.

[7] N. Cressie, D. Hawkins, "Robust est. of the variogram," J. Int. Assoc. Math. Geol., 12:115-125, 1980.

[8] R.M. Lark, "Description of image texture," Int. J. Rem. Sens., 17:11:2115-2133, 1996.

[9] B.B. Mandelbrot, The Fractal Geometry of Nature, Freeman, New York, NY, 1983.

[10] R.E. Plotnick, R.H. Gardner, R.V. O'Neill, "Lacunarity indices as measures of landscape texture", Landscape Ecol., 8:3:201-211, 1993.

[11] H. Kux and G. Henebry, "Multi-scale texture in SAR imagery: landscape dynamics of the Pantanal, Brazil," Proc. IGARSS'94, Pasadena, CA, 2:1069-1071.

[12] R.M. Haralick and L. G. Shapiro, Computer and Robot Vision, Vol. 1, Addison-Wesley, Reading, MA, 1992.
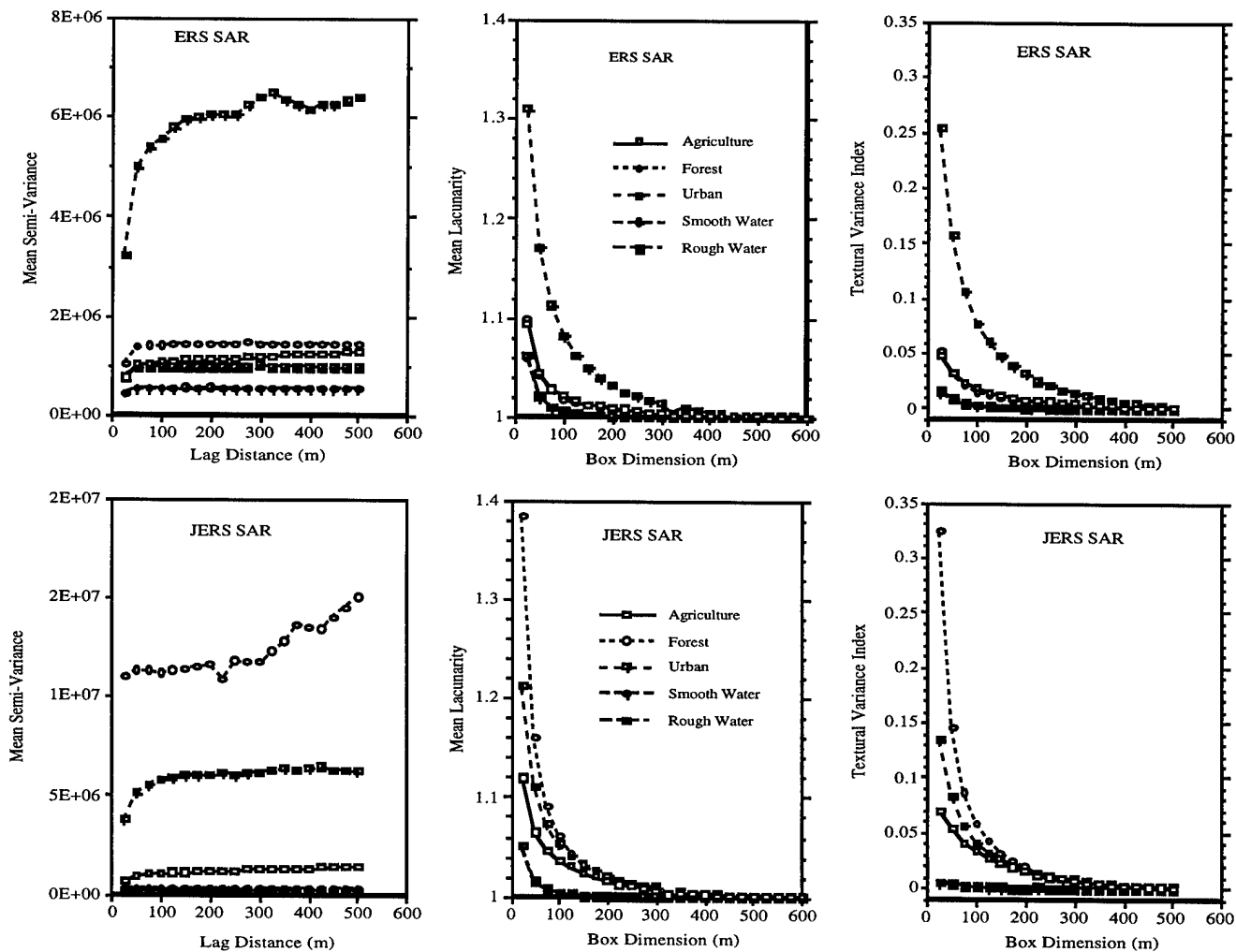
Figure 3. Application of geostatistical measures to ERS and JERS SAR data.

Fuzzy Clustering of Textured SAR Images Based on a Fractal Dimension Feature

L. Alparone[*], M. Barni[*], M. Betti[*], A. Garzelli[°]

[*]Dipartimento di Ingegneria Elettronica, University of Florence, via S. Marta, 3, I-50139 Firenze, Italy
Phone: +39-55-4796-372; Fax: +39-55-494569; E-mail: alparone@cosimo.die.unifi.it
[°]Dipartimento di Ingegneria dell'Informazione, University of Siena, via Roma, 56, I-56100 Siena, Italy
Phone: +39-577-263616; Fax: +39-577-263602; E-mail: garzelli@ing.unisi.it

Abstract -- Texture is an important feature to improve image segmentation. This paper describes a wavelet-based fuzzy clustering procedure which receives as input both the original image and a texture map based on a fractal model, derived from the wavelet transform of the image itself. This preliminary evaluation has shown the potential usefulness of the fractal signature for improving texture discrimination and enhancing segmentation results, and suggests this multi-scale approach for Remote Sensing image texture analysis.

INTRODUCTION

Clustering is a segmentation technique commonly used for Remote Sensing image interpretation. When ground truth is not available to provide samples to train a supervised classifier, segmentation is often accomplished by clustering, which requires little "a priori" information about the imaged scene. In particular, multi-resolution clustering methods generally provide better performance in discriminating different cover classes, when compared to *global* algorithms: the *wavelet* transform is a scale-space representation which yields uncorrelated data at different resolutions [1].

Segmentation success strongly relies on the dimensionality of the data set: in the case of mono-band, non-polarimetric SAR images, the local variation coefficient is the most useful feature, besides the signal itself. Due to the lack of features reflecting spatial correlation, however, a number of pixels may result to be mislabeled. In this case, additional features can be provided by textural measurements, based on the relation between signals backscattered from neighboring pixels [2].

A useful mathematical tool for describing many complex shapes found in natural scenes is provided by fractal geometry. The essential feature of fractals is their statistical *self-similarity*, i.e., invariance under changes of magnification. Many natural surfaces exhibit a fractal behavior within a certain range of scales. Such a behavior is well represented by the concept of *fractal dimension* [3], which can be related to an intuitive concept of surface "roughness". Since the effectiveness of the fractal model increases with resolution, it is particularly useful in the case of SAR images [4].

The most suited approach to computation of fractal dimension comes from power spectra: the ratio between powers at different scales is straightforwardly related to fractal dimension. In this work, we propose a method to obtain a fractal signature, based on the multi-scale image decomposition provided by the wavelet transform.

Fuzzy clustering is widely used for image segmentation [5]. In fact, fuzzy set theory provides a better representation for information in the cases in which clusters boundaries are vague. This often happens in Remote Sensing images, where situations such as cover class mixture are often found [6].

The *Fuzzy C-Means* algorithm, which is an iterative technique based on the minimization of generalized objective functions, was employed. Instead of performing clustering on the whole data set, the multi-resolution framework was used to reduce computation while preserving segmentation results.

This paper describes a complete wavelet-based fuzzy clustering procedure which receives as input both a SAR image and a texture map, built starting from a fractal model derived from the wavelet transform of the image itself. Trials were carried out on samples of true textures derived from SAR images coming from the X-SAR experiment.

FRACTAL ANALYSIS

The common feature used in most segmentation techniques is image *tone*, i.e., grey level throughout the entire scene. The other complementary aspect that characterizes a digital image is *texture*, which represents intrinsic spatial variability of grey level in the neighborhood of each pixel.

A fractal approach [6,7] started being used with promising results, since many natural surfaces exhibit a fractal behavior within a certain range of scales. Such behavior is summarized by the concept of *fractal dimension*, which can be related to our intuitive concept of surface "roughness" [3].

The most suitable mathematical model for random fractals found in nature is the *fractional Brownian motion* (FBM). Basically, a FBM surface function $V_H(x,y)$ is described by a random field having zero-mean Gaussian increments satisfying

$$E\{|V_H(x,y)-V_H(x+\Delta x,y+\Delta y)|\} = \|(\Delta x,\Delta y)\|^H \qquad (1)$$

where $\|.\|$ is the Euclidean norm, and $0 < H < 1$ is the Hurst, or *persistence* parameter, controlling the roughness of the

surface, with $H = 1$ corresponding to a smooth surface and $H = 0$ to a very rough texture. The fractal dimension D and the persistence parameter are related by: $D = 3 - H$.

Different approaches exist to compute D [4]. FBM can be characterized by a random-phase Fourier description obeying a generalized power density of the form:

$$P(\omega_1,\omega_2) = \frac{1}{\left[\sqrt{\omega_1^2+\omega_2^2}\right]^{\beta}} \qquad (2)$$

in which $\beta = 2H +2$. Thus, D can be computed through a linear regression on $log[P(\omega_1,\omega_2)]$ versus $log[(\omega_1^2,\omega_2^2)^{1/2}]$.

The above methods have already been used in remote sensing texture analysis [2,4], although, given the variability of fractal dimension with the computation algorithm, other methods have often been preferred. As it has been shown in [4], however, the power spectrum technique seems to yield very accurate estimates, and for this reason it has been chosen here, by exploiting the characteristics of the wavelet representation, which is well suited to evaluate self similarity. In fact, wavelets can be seen as a new analysis technique in time-frequency domain (space-frequency, in the 2D case) [1].

The wavelet representation allows to easily obtain fractal dimension D from power spectrum: since the detail signals are obtained by filtering and downsampling the original signal, the power spectrum of the output at resolution 2^j is given by:

$$P_{2^j}(\omega_1,\omega_2) = P(\omega_1,\omega_2) \cdot |\Psi(2^{-j}\omega_1,2^{-j}\omega_2)|^2 \qquad (3)$$

After sampling at a rate 2^j, and integrating at two different scales, the following relationship is obtained from (2):

$$\frac{P_{2^j}}{P_{2^{j+1}}} = 2^{2H} \qquad (4)$$

where P is the energy of the detail signals. The above result is independent of the specific scale 2^j, with $-1 \leq j \leq J$; a linear least square fit performed on (4) yields:

$$H = \frac{1}{(J+1)log4} \cdot log\frac{\prod_{j=-1}^{J-1} P_{2^{j+1}}}{\prod_{j=-1}^{J-1} P_{2^j}} \qquad (5)$$

which is used to obtain H, and thus fractal dimension D.

FUZZY CLUSTERING ALGORITHM

In a fuzzy clustering framework, each cluster is a fuzzy set, and each pixel in the image has a *membership value* associated to each cluster, ranging between 0 and 1, measuring "how much" the pixel belongs to that particular cluster [5].

There have been many different families of fuzzy clustering algorithms proposed in the last decade: the one used in this work is the *Fuzzy C-Means* algorithm (FCM), which is an iterative technique based on minimization of a generalized within-group sum of squares (WGSS) objective function [5].

Instead of performing clustering on the whole data set, a multiresolution framework can be exploited to reduce the computational burden while retaining segmentation results. First, an image pyramid is obtained by using the wavelet transform; the fuzzy clustering procedure is then implemented on the pyramid using a region growing method: given $J < 0$, FCM algorithm is first run on the coarsest image version; for each pixel, a test is carried out on the final membership values

$$max\{u_{1k},u_{2k},...,u_{ck}\} \geq T \qquad (6)$$

where c is the number of clusters and T a prescribed threshold. If this condition is not met, the pixel is labelled as uncertain. Clustering is then repeated on all uncertain pixels at the lower level, higher resolution, approximation. This procedure is iterated downward until the bottom of the pyramid is reached, where all pixels remaining uncertain are labeled. Thus, cluster membership values can be used to split mixed regions into smaller regions at higher resolution levels. The clustering algorithm is described in Figure 1. Median post-filtering is used to obtain more homogeneous regions.
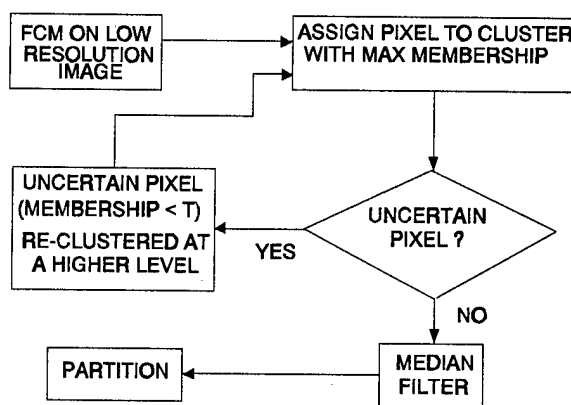
Figure 1. FCM algorithm implemented on the wavelet pyramid of the input image.

The method is very similar to the one proposed in [6], but implemented on a different pyramid structure, in which each layer represents a more precise approximation of the original image, thus providing better results than in [6].

The same algorithm that builds the pyramid also gives the fractal measure to be input to the clustering chain, together with the original data. There is no need for a separate processing, as it always happens for the commonly used methods for computing D.

RESULTS

X-SAR spaceborne system operates with vertical polarization, and incidence angles from 15° to 55°. From the images provided by such experiments, some texture patches, shown in Figure 2, have been extracted to test the performance of the clustering algorithm. These are mainly natural cover types, coming from different places around the world, with the exception of one showing an urban district.

The level J of wavelet decomposition was set equal to -5. In the FCM algorithm parameter T was empirically set to 0.985. The maps resulting from directly clustering the original mono-band images are shown in Figure 3. As it can be seen a large number of pixels were misclassified: the only tone intensity value is insufficient to discriminate among the different cover types. Thus, parameter H has been obtained for each of the four different textures in the two test images and assigned as an additional feature to each pixel of every subregion. Figure 4 shows the maps resulting from clustering the images with both features. By comparing such maps with those in Fig. 3, it can be seen that addition of the fractal signature has considerably improved segmentation accuracy. Correct classification rates of the maps in Fig. 4, relative to the texture patches of Fig. 2, are shown in Table 1.

Table 1 - Correct classification rates for the textures in Fig. 2.

	Correct Classification rates
Equatorial Forest	100 %
Mountainous Area	89.7 %
Urban District	99.8 %
Sandy Desert	99.9 %
Water Surface	100 %
Boreal Forest	98.1 %
Rocky Desert	98.8 %
Tundra	99.2 %

Figure 3. - Clustering maps obtained from images of Fig. 3, by using FCM based on image tone only.
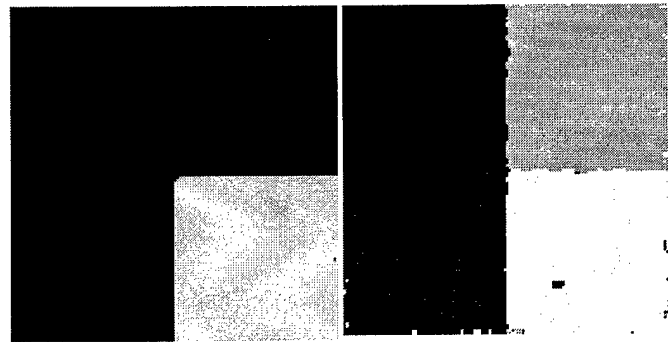
Figure 4. - Clustering maps obtained from images of Fig. 3, by using FCM based on tone and local fractal dimension.

(a)   (b)

Figure 2. Test images: clockwise from upper left: (a): equatorial forest (Amazonas, Brazil); mountainous area (Alps, Austria); urban district (Moscow, Russia); hot sandy desert (Sahara, Algeria). (b): water surface (Tropical Pacific Ocean); boreal forest (Black Forest, Germany); mid-latitude rocky desert (Gobi, Mongolia); tundra (Kamchatka).

REFERENCES

[1] S. G. Mallat, "A Theory for Multiresolution Signal Decomposition: the Wavelet Representation," *IEEE Trans. Pattern Anal. Machine Intell.*, vol. 11, no. 7, pp. 674-693, 1989.

[2] S. C. Liew, H. Lim, L. K. Kwoh, G. K. Tay, "Texture Analysis of SAR images," *Procs. IGARSS'95*, pp. 1412-1414, 1995.

[3] A. P. Pentland, "Fractal-Based Description of Natural Scenes," *IEEE Trans. Pattern Anal. Machine Intell.*, vol. 6, no. 6, pp. 661-674, 1984.

[4] C. V. Stewart, B. Moghaddam, K. J. Hintz, L. M. Novak, "Fractional Brownian Motion Models for Synthetic Aperture Radar Imagery Scene Segmentation," *Procs. of the IEEE*, vol. 81, no. 10, pp. 1511-1522, 1993.

[5] J. C. Bezdek, S. K. Pal, *Fuzzy Models for Pattern Recognition*, IEEE Press, 1992.

[6] M. N. Trivedi, J. C. Bezdek, "Low-Level Segmentation of Aerial images with Fuzzy Clustering", *IEEE Trans. Systems Man Cybern.*, vol. 16, no. 4, pp. 589-598, 1986.

[7] T. J. Dennis, N. G. Dessipris, "Fractal Modelling in Image Texture Analysis," *IEE Proc.~F*, vol. 136, no. 5, pp. 227-235, 1989.

Multiresolution Analysis and Processing of Synthetic Aperture Radar Images Using Wavelets

Seisuke Fukuda and Haruto Hirosawa
Institute of Space and Astronautical Science
3-1-1, Yoshino-dai, Sagamihara, Kanagawa 229, Japan
Tel: +81-427-51-3911(ext.2711) / Email: fukuda@atom.eng.isas.ac.jp

Abstract – This paper proposes new techniques of multiresolution analysis and processing of synthetic aperture radar (SAR) images using wavelets. Here, two works are presented; one is speckle reduction by reducing the amplitude of the detail images in wavelet subspaces, while preserving edges by releasing the amplitude reduction around edges, and the other is estimation of fractal dimension which is featuring 'roughness' of the 2-D surface, by wavelet-based multiresolution analysis combined with the fractal Brownian motion (fBm). Both methods have been satisfactorily applied to real SAR images, and are expected to be useful for SAR remote sensing.

Fig.1. A wavelet transform of an image; "approximated image" is the sub-image composed of the low frequency parts in both row and column derections (LL), and "detail images" are the remaining three images, containing high frequency components (LH, HL, and HH).

Fig.2. Windows for judgement of edge information.

INTRODUCTION

This paper presents new techniques of multiresolution analysis and processing of synthetic aperture radar (SAR) images using wavelets, and has two aims; one is speckle reduction, the other is estimation of fractal dimension.

For the last several years, the wavelet analysis has been applied to various fields, where the theoretical bases are given by the multiresolution analysis by Mallat [1] and the composition of compactly supported orthonormal wavelet bases by Daubechies [2]. The multiresolution analysis decomposes an input signal into low frequency sub-bands iteratively, and as a result, the pyramidal representation of the signal is constructed. The multiresolution analysis can be easily applied to 2-dimensional images by transforming in row and column directions separately. A wavelet transform of an image generates four sub-images with a quarter area; one "approximated image" and three "detail images" (see Fig.1). In this paper, we aim at speckle reduction and estimation of fractal dimension by processing or analysing detail images in each wavelet subspace.

SPECKLE REDUCTION

Algorithm

First, we propose a new method of reducing speckle in SAR images by reducing the range of the pixel power (the "wavelet coefficient" in [1]) of detail images in each wavelet subspace [3,4]. In detail images, information on edges of the original image appears with the following properties:

- The LH image: information on the edges in vertical and 45° directions,
- The HL image: information on the edges in horizontal and 45° directions,

- The HH image: information on the edges in 45° directions.

If we reduce the power range of entire detail images, we will smooth not only speckle but also edges, and consequently, unacceptable square ghosts will appear around edges. Then, we propose the following algorithm:

I. Classify each pixel of detail images as *high level* or *low level* using the threshold T.

II. Reduce the power of the *low level* pixels to $\alpha\%$.

III. Consider a 3×3 window around the *high level* pixels, and define *high area* in the window for each detail image as Fig.2. If the *high area* in the window contains at least one *high level* pixel, let the power of the central pixel of the window to keep its original value, judging that it has edge information.

IV. Regard the pixel, which is not judged in III to be with edge information, as speckle component, and reduce the power of it to $\beta\%$.

An output image is reconstructed from the processed detail images in each wavelet subspace. Identification of the pixels with edge information in III is following the appearance property of edge information.

Simulations and Application to SAR Images

We have evaluated performance characteristics of the method through simulations and application to a SAR

TABLE I. Comparison of smoothing capability.

		ENL				
Original		4.06				
Proposed method	level	1	2	3	4	5
	Haar(D2)	10.78	18.71	22.96	24.35	24.75
	D4	10.80	18.84	22.92	24.32	24.72
Local statistics (3 × 3)		25.41				

Image. Concerning the parameters in the algorithm, we have set $T = 128$, $\alpha = 40$, $\beta = 50$. We have employed the Daubechies wavelet [2]; D2 and D4. D2 is known to be equivalent to the Haar basis.

TABLE I shows the comparison of the smoothing capability between the proposed method and the local statistics method by Lee [5]. The value in the table is equivalent number of looks (ENL) given by

$$\text{ENL} = \mu^2/\sigma^2, \tag{1}$$

where μ and σ are the average value and the standard deviation, respectively, of the power. The original image is 4 look one simulated a homogeneous area; size 256×256, grayscale levels 256, average power 50. We see from TABLE I that the smoothing capability of the proposed method, when the wavelet subspace level is 5 or so, is almost comparable to that of the local statistics method. We also see that smoothing characteristics seem to be insensible to the difference of the basis, Haar or D4.

Fig.3 shows 3-dimensional representation of the pixel power by which we have tried to evaluate the edge preservation characteristics of the proposed method. The edge in the output of the proposed method using the Haar basis when the wavelet subspace level is 5, seems to be preserved more sharply than that in the output of the local statistics method. This indicates that the algorithm described above, works efficiently. The edge in the D4 basis case is a little degraded compared with that in the Haar basis case. From this result, it is deduced that a wavelet basis with a shorter tap is useful in preserving edges.

Fig.4 shows an example of a real SAR image processed by the proposed method. The original SAR image is 4 look one, obtained by NASA/JPL AIRSAR. The scene is an agricultural field in Flevoland, the Netherlands. The frequency band is L, and the polarization is HH. Examing the figure, we see that the proposed method succeeds both in smoothing speckle and in preserving edges, and also succeeds in attaining visually-natural appearance. The performance of the proposed method for this scene seems superior to that of the local statistics method.

ESTIMATION OF FRACTAL DIMENSION

Method

Some natural scenes can be considered to be statistically self-similar, while they are not self-similar in the strict
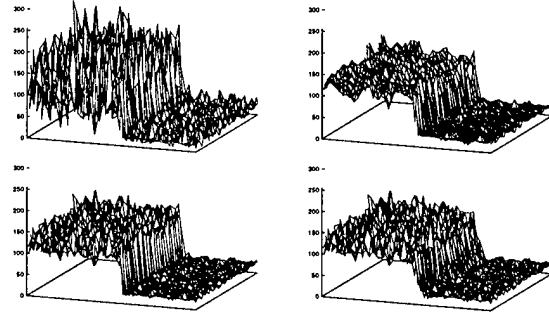
Fig.3. Comparison of the performance at an edge; upper left – original speckle pattern (4look), upper right – local statistics (3 × 3), lower left – proposed (Haar, 5level), lower right – proposed (D4, 5level).
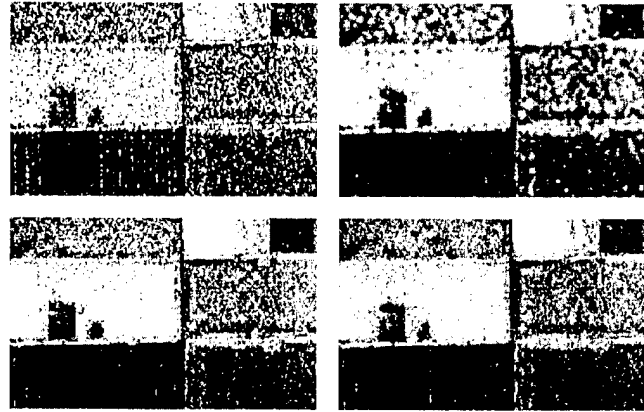
Fig.4. Filtering of a SAR image; upper left – original (4look), upper right – local statistics (3×3), lower left – proposed (Haar, 5level), lower right – proposed (D4, 5level).

mathematical sense. When such a 3-D surface regarded as 'statistically fractal' is imaged by SAR, fractal dimension of the image is featuring roughness of the surface. Here, we present that fractal dimension of a SAR image can be estimated by wavelet-based multiresolution analysis.

Fractional Brownian motion (fBm) is known to be a typical model of statistically fractal. It is a nonstationary zero-mean Gaussian random process, and defined as [6]

$$B_H(t) =$$
$$\frac{\left[\int_{-\infty}^{0} \left(|t-s|^{H-\frac{1}{2}} - |s|^{H-\frac{1}{2}}\right) dB(s) + \int_{0}^{t} |t-s|^{H-\frac{1}{2}} dB(s)\right]}{\Gamma(H+1/2)}, \tag{2}$$

where $B(t)$ is an ordinary Brownian motion and H is the self-similar parameter $(0 < H < 1)$. The parameter H is directly related to the fractal dimension D by

$$D = E + 1 - H, \tag{3}$$

where E is the topological dimension.

Flandrin showed that the self-similar parameter H of a 1-dimensional signal can be estimated by wavelet analysis [7]. In [7], the variance of the detail signal at the j-th wavelet subspace level is given by

$$\log_2\left(\mathrm{var}\left(d_j[n]\right)\right) = (2H + 1)j + \mathrm{const.} \qquad (4)$$

Hence, we can easily acquire the parameter H (and the related fractal dimension D) from the slope of this variance plotted as a function of wavelet subspace level j in a log plot.

For wavelet-based estimation of fractal dimension of SAR images, we have to extend (4) to the 2-dimensional case. Now we asuume that 2-dimensional fBm has characteristics of fBm in both x- and y- directions. As the detail signal of 2-dimensional wavelet transform, we consider $d_j^{HH}[n,m]$, the detail image containing high frequency components of an input image in both x- and y- directions (i.e., the HH image in Fig.1). Then, we have [8]

$$\log_2\left(\mathrm{var}\left(d_j^{HH}[n,m]\right)\right) = 2(H + 1)j + \mathrm{const.} \qquad (5)$$

Using (5), we can obtain the self-similar parameter H of a 2-dimensional image in the same way as the 1-dimensional case, while the slope of the log plot varies from $2H + 1$ to $2(H + 1)$.

Application to Multi-Parameter SAR Images

We have estimated the fractal dimension of multifrequency, multipolarization, 4look AIRSAR images using (5). The scene is Raco area in U.S.A. The frequency band is C, L, P, and the polarization is HH, HV, VV. We have also estimated the fractal dimension of speckle reduced images by the above-mensioned method, to examine the relation between fractal dimension and speckle.

Since the SAR image using here is a discrete data, we should estimate the fractal dimension from the slope of the log plot at coarse wavelet subspace levels [7]. So we have obtained the fractal dimension by linear regression at 3 points; $j = 6, 7, 8$.

TABLE II shows the estimated fractal dimension of each SAR image. We see from this table that the fractal dimension of the SAR images depends upon observation parameters; the fractal dimension seems to be large in order L, P, C band concerning the frequency, and in order HV, HH, VV concerning the polarization. From this result, we can infer that the manner of describing roughness of the surface differs with frequency and polarization, though the order may be restricted to images used here. Another noticeable result is that the fractal demension of the speckle reduced images is almost equal to that of the original images; fractal dimension of SAR images seems to be independent of speckle. Consequently, we may regard fractal dimension of speckle reduced images as that of original images straightforwardly.

TABLE II. Relation between observation parameter and fractal dimension

Frequency	C Band			
Polarization	HH	HV	VV	
Original Image	2.3513	2.5323	2.2863	...
Speckle reduced.	2.3519	2.5338	2.2868	

L Band			P Band		
HH	HV	VV	HH	HV	VV
2.9214	2.9817	2.8968	2.6388	2.7078	2.5740
2.9215	2.9862	2.8983	2.6387	2.7066	2.5749

From the results, we think that fractal dimension could be used as an efficient quantity for segmentation of multifrequency, multipolarization SAR images.

SUMMARY

We have introduced new wavelet-based multiresolution methods for speckle reduction and estimation of fractal dimension. The methods have been satisfactorily applied to SAR images. We will treat classification/segmentation of multifrequency, multipolarization SAR images using estimated fractal dimension in a future study.

REFERENCE

[1] S. G. Mallat, "A theory for multiresolution signal decomposition: the wavelet representation," IEEE Trans. Pattern Anal. and Machi. Intell., vol.11, pp.674–693, July 1989.

[2] I. Daubechies, "Orthonormal bases of compactly supported wavelets," Comm. Pure Applied Math., vol.41, pp.909–996, Nov. 1988.

[3] S. Fukuda and H. Hirosawa, "Wavelet-based speckle reduction in synthetic aperture radar images," Electronics and Communications in Japan: Part 3 (in press) [Trans. of IEICE, vol.J79-A, pp.1994–2001, Dec. 1996 (In Japanese)].

[4] S. Fukuda and H. Hirosawa, "Suppresion of speckle in synthetic aperture radar images using wavelet," submitted to Int. J. Remote Sensing.

[5] J. S. Lee, "Speckle analysis and smoothing of synthetic aperture radar images," Comput. Graphics and Image Process., vol.17, pp.24–32, Sept. 1981.

[6] B. B. Mandelbrot and J. W. Van Ness, "Fractional Brownian motions, fractional noises and applications," SIAM Rev., vol.10, pp.422–437, Oct. 1968.

[7] P. Flandrin, "Wavelet analysis and synthesis of fractional Brownian motion," IEEE Trans. Inform. Theory, vol.38, pp.910–917, Mar. 1992.

[8] S. Fukuda and H. Hirosawa, "An estimation of fractal dimension of multi-parameter SAR images using wavelets," Technical Rep. of IEICE, SANE96-95, Feb. 1997 (In Japanese).

Trends on Information Processing for Remote Sensing

C. H. Chen

University of Massachusetts Dartmouth
Electrical and Computer Engineering Dept.
North Dartmouth, MA 02747-2300 USA
Tel (508)999-8475; Fax (508)999-8489; Email: cchen@umassd.edu

Abstract - There has been greatly increased activity in the last twelve years on the use of information processing techniques on remote sensing problems including signal/image processing, compression, segmentation, feature extraction, pattern recognition, neural networks, etc. The past progress is reviewed from which a trend is developed. The trend shows a further emphasis on using neural networks and wavelet transforms for remote sensing.

REVIEW OF PAST PROGRESS

This review is based mainly on a small set of selected publications on the IEEE Trans. on Geoscience and Remote Sensing from 1986 to 1997. A major progress has been made on the use of statistical and contextual pattern recognition [15,16,18,23,28], feature extraction [1,3,7,25,36], principal component analysis [19, 22], SAR image filtering & edge detection [20, 21,32, 33], image/signal compression [4,6,17, 30,40], image registration [31,37], fuzzy method [38], AI & knowledge based systems [24,26,27, 39]. The interest in using neural network since early 90s has not been decreased [2,5,8,9,10,13, 14,29,34,35,41] because of the many capabilities offered by the neural nets. However neural nets have not been able to replace existing techniques and much more study or exploration of neural nets in remote sensing is needed.

THE TRENDS

It is always risky to predict future from limited past. However remote sensing encompasses many different problem areas with a variety of data involved. Neural nets offer some universal properties suitable for many such problems. Also the nerual net potential has not been fully known. So a continued and strong interest is expected. We have noted another trend in the use of wavelet transforms which also have mnay different capabilities [11,12,40]. As an example, Fig. 1 shows a popular SAR image studied by many researchers. Fig. 2 shows the wavelet representation reesult. Figs. 3 and 4 are wavelet transform segmentation results without feature selection [11] and with channel selection [12] respectively. . The result in [12] making use of the physical properties of the SAR image data is better than that in [11]. An important advanatge of the wavelet domain analysis is that the procedure is again universal and it can be computationally very efficient. We believe that wavelet analysis is another emerging approach in information processing for remote sensing. It should be emphasized that the opinion given in this paper is **strictly** that of the author.

REFERENCES

[1] H. Anys and D.C. He, "Evaluation of textural and multipolarization radar features for crop classification", T-GE vol. 33, Sep 95.

[2] J.A. Benediktsson, et al., "Neural network approaches versus statistical methods in classification of multisource remote sensing data", T-GE vol. 28, Jul 90.

[3] J.A. Benediktsson, et al.," Classification and feature extraction of AVIRIS data", T-GE vol. 33, Sep 95.

[4] C.Y. Chang, et al., "Spatial compression of seasat SAR imagery", T-GE vol. 26, Sep 88.

[5] C.H. Chen and A. Jozwik, "A sample set condensation algorithm for the class sensitive artificial neural network", Pattern Recognition Letters, vol. 17, July 1996.

[6] T.M. Chen, et al., "Information content analysis of Landsat image data for compression", T-GE vol 25, Jul 87.

[7] C.C.T. Chen and D.A. Landgrebe, "A spectral feature design system for the HIRIS/MODIS era", T-GE vol. 27, Nov 89.

[8] D.T. Davis et al., "Solving inverse problems by Bayesian iterative inversion of a forward model with applications to parameter

mapping using SMMR remote sensing data", T-GE vol. 33, Sep 95.

[9] M.S. Dawson and A.K. Fung, "Neural networks and their applications to parameter retrieval and classification", T-GE Newsletter, Sep 93.

[10] M.S. Dawson, et al., "A robust statistical-based estimator for soil moisture retrieval from radar measurements", T-GE Jan 97.

[11] L.J. Du, et al., "Segmentation of SAR images using the wavelet transform", IJIMST vol. 4, 1992.

[12] Y. Du, "Wavelet analysis for SAR image segmentation using Bhattacharyya distance for channel selection", MSEE thesis, UMass Dartmouth, May 1997.

[13] Y. Hara, et al., "Application of neural networks to radar image classification", T-GE vol. 32, Jan 94.

[14] P.D. Heermann and N. Khazenie, "Classification of multispectral remote sensing data using a back-propagation neural network", T-GE vol. 30, Jan 92,

[15] B. Jeon and D.A. Landgrebe, "Classification with spatio-temporal interpixel class dependency contexts", T-GE vol. 30, Jul 92.

[16] Y. Jhung and P.H. Swain, "Bayesian contextual classification based on modified M-estimates and Markov random fields", T-GE vol. 34, Jan 96

[17] R. Kwok and W.T.K. Johnson, "Block adaptive quantization of Magellan SAR data", T-GE vol. 27, Jul 89.

[18] C. Lee and D.A. Landgrebe, "Fast likelihood classification", T-GE Jul 91.

[19] J.B. Lee et al., "Enhancement of high spectral resolution remote sensing data by a noise adjusted principal component analysis", T-GE vol. 28, May 90.

[20] J.S. Lee and J. Jurkevich, "Segmentation of SAR images", T-GE, vol. 27, Nov 89.

[21] J.S. Lee, et al., "Speckle reduction in multipolarization, multifrequency SAR imagery", T-GE vol. 29, Jul 91.

[22] J.S. Lee and K. Hoppel, "Principal components transformation of multifrequency polarimetric SAR imagery", T-GE vol. 30, Jul 92.

[23] B. Kim and D.A. Landgrebe, "hierarchical classifier design in high-dimensional numerous class cases", T-GE vol. 29, 1991.

[24] D.M. McKeown, Jr., "The role of artificial intelligence in the integration of remotely

sensed data with geographic information systems", T-GE vol. 25, May 87.

[25] J.F. Parrot and H. Taud, "Detection and classification of circular structures on spot images", T-GE vol. 30, Sep 92.

[26] L.E. Pierce, et al., "Knowledge-based classification of polarimetric SAR images", T-GE vol. 32, Sept 94.

[27] J. Qian, et al., "DENESYS-an expert system for automatic extraction of drianage networks from digital elevation data", T-GE vol. 28, Jan 90

[28] E. Rignot, et al., "Unsupervised segmentation of polarimetric SAR data using the covariance matrix", T-GE Jul 92.

[29] S.B. Serpico and F. Roli, "Classification of multi-sensor remote-sensing images by structured neural networks", T-GE May 95

[30] A.S. Spanias, et al."Transform methods for seismic data compression", T-GE May 91

[31] J. Ton and A.K. Jain, "Registering Landsat images by point matching", T-GE, Sep 89.

[32] R. Touzi, et al., "A statistical and geometrical edge detector for SAR images", T-GE vol. 26, Nov 88.

[33] R. Touzi and A. Lopes, "The principle of speckle filtering in polarimetric SAR imagery", T-GE, Sep 94.

[34] L. Tsang, et al., "Inversion of snow parameters from passive microwave remote sensing measurements by a neural network trained with a multiple scattering model", T-GE vol. 30, Sep 92.

[35] Y.C. Tzeng, et al., "A dynamic learning neural network for remote sensing applications", T-GE vol. 32, Sep 94.

[36] F.T. Ulaby, et al., "Texture information in SAR images", T-GE, vol. 24, Mar 86.

[37] A.D. Ventura, et al., "Image registration by recognition of corresponding structures", T-GE vol. 28, May 90.

[38] F. Wang, "Fuzzy supervised classification of remote sensing images", T-GE Mar 90.

[39] F. Wang, "Integrating GIS's and remote sensing image analysis systems by unifying knowledge representation schemes", T-GE vol. 29, July 1991.

[40] S.A. Werness, et al., "Experiments with wavelets for compression of SAR data", T-GE Jan. 94

[41] T. Yoshida and S. Omatu, "Neural network approach to land cover mapping", T-GE vol. 32, Sep 94.
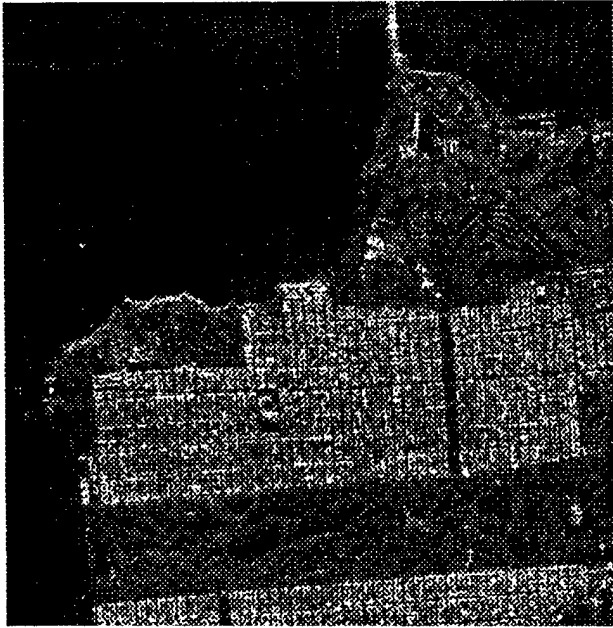
Figure 1. Polarimetric SAR HH Channel image of San
Francisco Bay area (512 by 512)
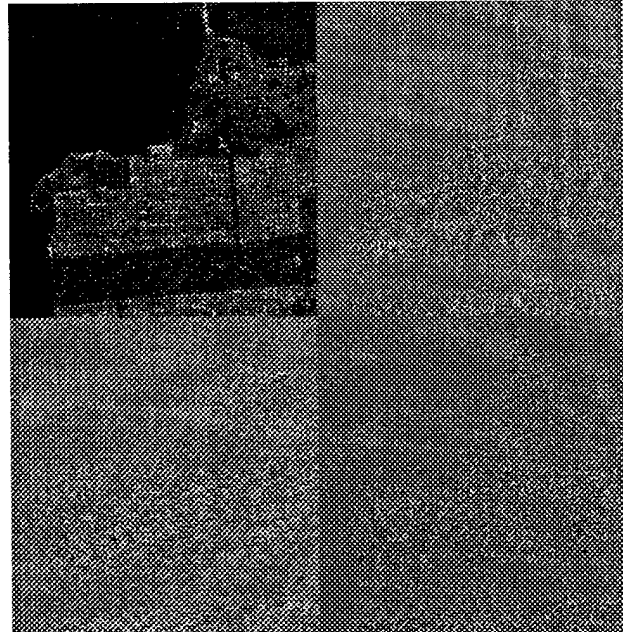
Figure 2. Wavelet representation of the polarimetric
SAR HH Channel image of San Francisco Bay
area in the 1st level (512 by 512)
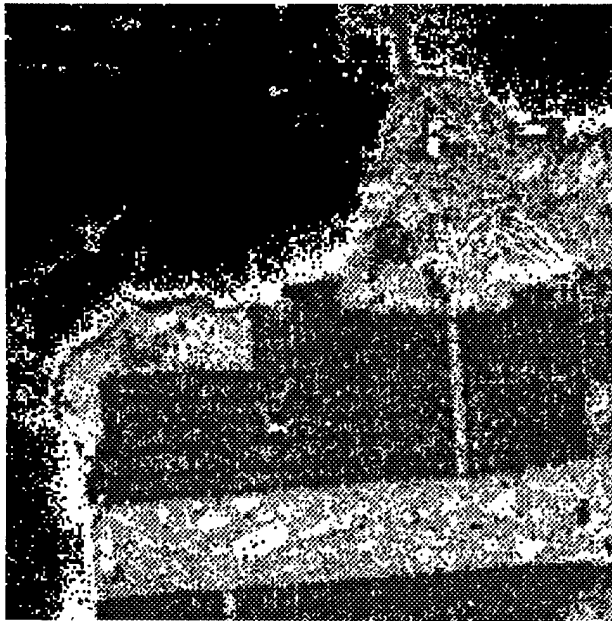
Figure 3. Segmentation of the polarimetric SAR imagery
using non-feature extraction representation in the
wavelet domain. (256 by 256)
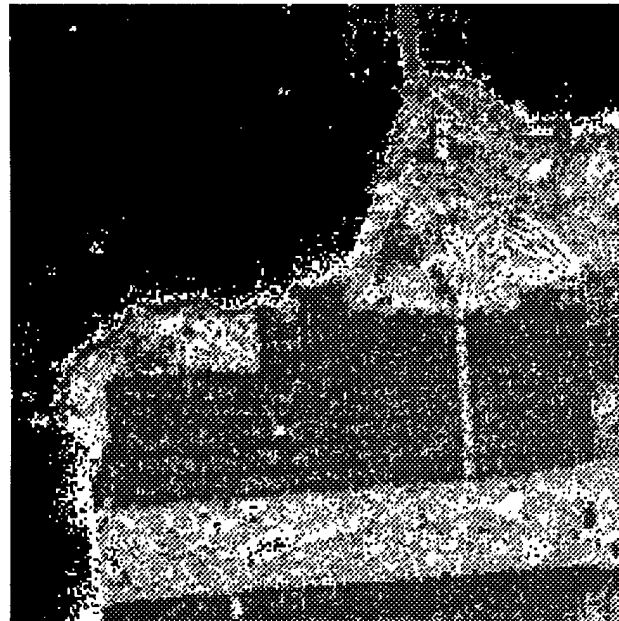
Figure 4. Segmentation of the polarimetric SAR
imagery using the combination representation
of approximation and detail channels in the
wavelet domain. (256 by 256)

ARTIFICIAL NEURAL NETWORK-BASED INVERSION TECHNIQUE FOR EXTRACTING OCEAN SURFACE WAVE SPECTRA FROM SAR IMAGES

Dayalan Kasilingam* and Jian Shi**

*Centre for Remote Imaging, Sensing and Processing
National University of Singapore
Lower Kent Ridge Rd.
Singapore, 119260.
Tel: (65) 771-5173; FAX: (65) 775-7717; e-mail: crsdpk@leonis.nus.sg

**Department of Electrical and Computer Engineering
University of Massachusetts, Dartmouth
North Dartmouth, MA 02747.
Tel: (508) 999 8480; Fax: (508) 999-8485; e-mail: jshi@umassd.edu

Abstract: An artificial neural network (ANN) based nonlinear technique for inverting the SAR image spectrum of ocean surface waves is developed. In this technique, a multi-layer perceptron (MLP) is used to perform the inversion process. The MLP is trained using simulated SAR and wave spectra. The training process utilizes the standard error-backpropagation technique. The results indicate that the method works well over a large range of wind and wave conditions. The error in the inversion process was found to increase in the higher sea states. The technique works best if the network is used within the range over which it was trained. It is noted that this technique may be used independent of SAR imaging models, by training the network with coincident and co-located measurements of SAR and wave spectra.

INTRODUCTION

Satellite-borne synthetic aperture radar (SAR) imaging systems have the potential for synoptically measuring the ocean surface wave spectra on a global scale. The capability to quantitatively monitor ocean surfaces wave spectra from SAR images would serve a critical need in oceanography. The SAR image is a map of the complex radar reflectivity from the ocean surface [1]. The amplitude and phase of the radar reflectivity are modulated by the surface waves. Information about the surface waves is imparted onto the backscattered signal through complex interaction processes. In SAR systems, there are additional motion effects that also influence the image information content. The mapping of the ocean surface waves onto the SAR image is inherently nonlinear. Thus, extracting useful quantitative information about surface waves requires accurate and efficient nonlinear inversion techniques.

ANN are ideally suited for applications where the input to output relationship is either unknown or too complex to describe analytically. They simply require a sufficiently large and variable data set consisting of measurements of the input parameters and the corresponding measurements of the output parameters. The ANN can then be trained to learn the mapping process between the input and the output. This type of inversion has been used in other applications in remote sensing [2].

In this paper, an ANN-based technique is developed for the extraction of ocean surface wave spectra from SAR image spectra. Simulated wave and SAR spectra are used as the input and the output, respectively, to train the ANN. It has to be noted that the inversion process is specific to the SAR imaging model used to simulate the training data. However, the technique may also be used independent of imaging models, by training the network with coincident and co-located measurements of SAR and wave spectra.

METHODOLOGY

The forward process that describes the nonlinear relationship between the SAR image spectrum and the wave spectrum is well understood. Since the nonlinear models that relate the SAR image spectrum to the wave spectrum are known, simulations of these models may be used to train an ANN to perform the nonlinear inversion process. During the training phase, the SAR image spectrum will be used as the input and the wave spectrum (orbital velocity or slope) will be used as the output.

In the simulations, the SAR image is generated using the Kasilingam and Shemdin model [1]. This model uses the modulated normalized radar cross-section (NRCS) and the orbital velocities of the surface waves as inputs. The NRCS is

described by the composite surface model [3]. In the composite surface model, the backscatter is shown to be due to the resonant interaction between the electromagnetic wave and short scale surface waves of comparable wavelength which is known as the Bragg wavelength. The NRCS of a small scale facet is proportional to the short scale roughness determined at the Bragg wavelength. The longer waves influence the scattering process by tilting and hydrodynamically modulating the short scale waves. A modified form of the Pierson Moskowitz model [4] is used to generate random realizations of ocean surface waves.

An artificial neural network is a highly parallel distributed information processing array of elementary processing elements connected to each other [5]. A multi-layered perceptron (MLP) is such an array consisting of several cascaded layers of elements. The layers consist of input and output layers and one or many hidden layers. Each layer consists of one or more elements. The signals flow from the input layer and pass through the hidden layers and terminate at the output layer.

The network is trained to produce the proper nonlinear mapping process sequentially using samples of input/output conditions. After each training set is presented to the network the strengths of the interconnections are modified so as to produce the desirable input/output relationship. The modifications are driven by the error between the output of the network and the desired output. The back-propagation method is the most widely used training scheme for training a layered perceptron.

RESULTS AND DISCUSSION

Fig. 1 shows the normalized error for three different networks. 1500 SAR images were simulated for wind seas, over the wind speed region 5-15 m/s. The wind direction was varied uniformly. The *(R/V)* ratio is 20 s. The wave and image spectra used for the training consisted of 64×64 spectral values. The input and output layers, each had that many units. All three networks had two hidden layers. Each layer in networks 1, 2 and 3 had 50, 30 and 20 units each, respectively. Each network was trained for 1 million cycles. Network 1 learns the fastest and has the smallest final error. This is because it has more weights and hence can describe the mapping process more accurately. However, the final error between the three networks does not vary significantly.
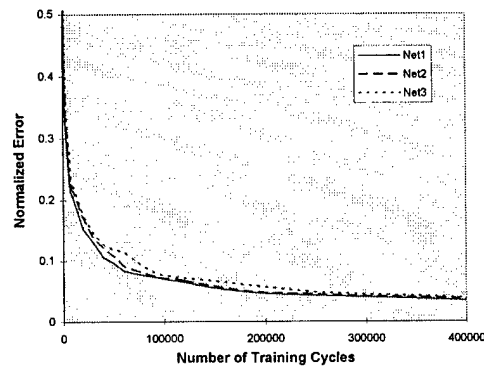
Figure 1 - The normalized training error as a function of the training cycle for three different networks.

Fig. 2 shows the results when network 2 is used to invert a SAR image at a wind speed of 5 m/s in the range direction ($\phi_0 = 90°$). Figures 2(b) and 2(c) show the actual and the inverted two-dimensional wave spectra. Figure 2(a) is the two-dimensional SAR image spectrum which was used as the input to the network. In this case, velocity bunching is negligible, since most of the waves are travelling in the range direction. Even though velocity bunching is small, the imaging process is still nonlinear because of the nonlinearities in the tilt modulation. The output of the network appears to be in good agreement with the actual wave spectrum used to generate the SAR image.
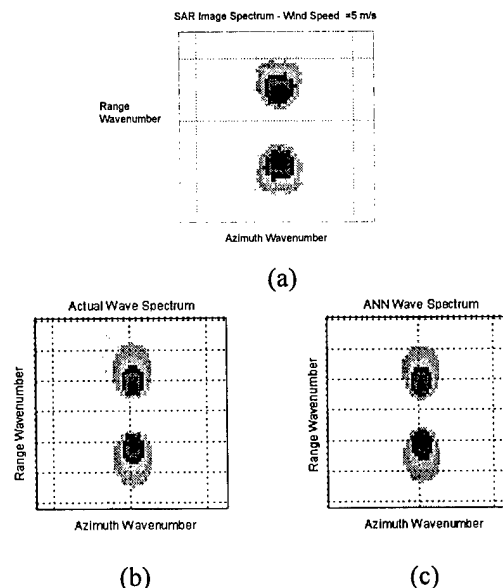
Figure 2 - Inversion of range travelling waves at a wind speed of 5 m/s - (a) SAR image spectrum, (b) wave orbital velocity spectrum and (c) ANN output.

Figure 3 shows the results for the inversion of a SAR image at a wind speed of 5 m/s for $\phi_0 = 45°$. In this case, the image content is determined by both velocity bunching and tilt modulation. There is coupling between the different modulation processes because of the nonlinearities in both mechanisms. Tilt modulation is dependent on the wave slopes and velocity bunching is dependent on the wave orbital velocities. Even though in linear wave theory, these quantities are related, the nonlinear coupling of the two modulation mechanisms results in a rather convoluted mapping process. Estimating the wave spectrum requires the de-coupling of these two processes. Again, the outputs of the network appears to be in good agreement with the actual wave spectra used to generate the SAR images. It appears that the inversion technique is able to de-couple the different modulation mechanisms to produce accurate estimates of the wave spectrum.

SAR Image Spectrum - Wind Speed =5 m/s

Range Wavenumber

Azimuth Wavenumber

(a)

Actual Wave Spectrum

Range Wavenumber

Azimuth Wavenumber

(b)

ANN Wave Spectrum

Range Wavenumber

Azimuth Wavenumber

(c)
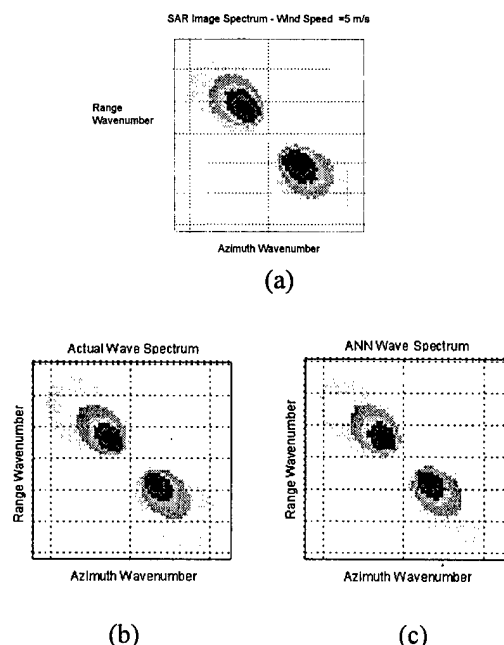
Figure 3 - Inversion of waves travelling at 45° to range at a wind speed of 5 m/s - (a) SAR image spectrum, (b) wave orbital velocity spectrum and (c) ANN output.

Figure 4 shows the normalized testing error when network 2 was tested with independent SAR image spectra at various wind speeds. The normalized error is largest at the extremes of the wind speed range. Note this network was trained with data samples in the 5-15 m/s wind speed range. Yet it appears to have acceptable error levels at wind speeds around 17 m/s. It is important to train the network with training samples that cover the wind speed range over which it is to be used.
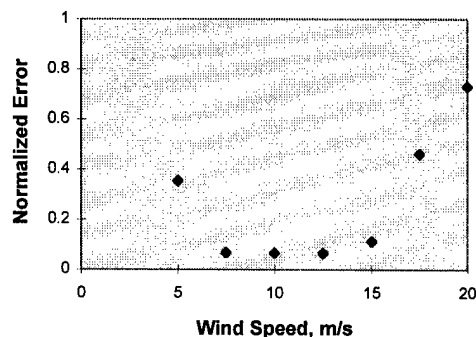
Figure 4 - The normalized testing error plotted as a function of wind speed. The network was trained with samples in the wind speed range 5-15 m/s.

CONCLUSION

The ANN-based inversion technique is able to accurately invert the SAR image spectrum to generate estimates of the wave orbital velocity spectrum. It is able to de-couple the different competing modulating processes. It is also shown that the inversion process is least accurate at the extremes of the wind speed range over which the network is trained. It is recommended that the network be trained with training samples that cover the wind speed range over which it is to be used.

REFERENCES

[1] Kasilingam, D.P. and O.H. Shemdin, J. Geophys. Res., 13837-13848, 1988.

[2] Tsang, L. et al, IEEE Trans. Geosci. Remote Sens., GE-30, 1015-1023, 1992.

[3] Kasilingam, D.P. and O.H. Shemdin, Intl. J. Remote Sens. 2079-2104, 1992.

[4] Pierson, W.J. and L. Moskowitz, J. Geophys. Res., 5181-5190, 1964.

[5] Hertz, J, A Krogh and R.G. Palmer, *Introduction to the Theory of Neural Computation*, Addison-Wesley, 1991.

Neural Computing for Seismic Principal Components Analysis

Kou-Yuan Huang
Department of Computer and Information Science
National Chiao Tung University, Hsinchu, Taiwan

Abstract -- The neural network of the unsupervised generalized Hebbian algorithm (GHA) is adopted to find the principal eigenvectors of a covariance matrix in different kinds of seismograms. The theorem about the effect of adding one extra point along the direction of the eigenvector is proposed to help the interpretations that more uniform data vectors along one principal eigenvector direction can enhance the eigenvalue. Diffraction pattern, fault pattern, bright spot pattern and real seismogram are in the experiments. From analyses the principal components can show the high amplitude, polarity reversal, and low frequency wavelet in the detection of seismic anamalies and can improve seismic interpretations.

INTRODUCTION

Given a set of random data $\bar{X}$ with dimension N and $E[\bar{X}]=\bar{0}$, we can compute the correlation matrix (covariance matrix) $Q=E[\bar{X}\bar{X}^T]$ and find the eigenvalues and the corresponding eigenvectors. This is the Karhunen-Loeve transformation [1] or the principal components analysis (PCA). The principal components analysis had been applied to seismic data set by Hagen (1981) [2] and Jones (1985) [3]. But they did not use the method of neural network. Here the neural network of the Sanger's unsupervised generalized Hebbian algorithm (GHA) [4, 5] is adopted to find the principal eigenvectors of a covariance matrix in different kinds of seismograms, the input data vectors are from horizontal and vertical directions respectively.

GENERALIZED HEBBIAN LEARNING RULE

The neural network of Sanger's learning rule is shown in Fig. 1. The network has a single weighting layer. The input N-dimensional column vector is $\bar{X}$, $E[\bar{X}]=\bar{0}$, the weight matrix W is MxN, and the output M-dimensional column vector is $\bar{Y}=W\bar{X}$ with M<N. The input data are fed into the net iteratively to find the principal eigenvectors of the correlation (covariance) matrix $Q=E[\bar{X}\bar{X}^T]$. The weight matrix W needs to be updated for each step.

Sanger (1989) had proved that the network converged from any initially random set of weights to find the principal eigenvectors of the input covariance matrix in decreasing eigenvalue order. And the algorithm was called the "Generalized Hebbian Algorithm" (GHA). The learning rule from Sanger (1989) is given by:

$$W_{ij}(t+1) = W_{ij}(t) + \eta(t) Y_i \left(X_j - \sum_{k=1}^{i} Y_k W_{kj} \right),$$

where j is the index of input, i is the index of output. or in matrix form as:

$$\Delta W(t) = \eta(t)(YX^T - LT[YY^T]W(t)),$$

where $\bar{X}=[X_1,X_2,...,X_N]^T$, $\bar{Y}=[Y_1,Y_2,...,Y_M]^T$, and LT[.] is the lower triangular matrix, i.e., all elements above the diagonal of its matrix argument are zeros. $\lim_{t\to\infty}\eta(t) = 0$ and $\sum_{t=0}^{t=\infty}\eta(t) = \infty$. The procedure is guaranteed to find the eigenvectors which we seek. The i-th eigenvector e_i is $W_{ij}, j=1,...,N$.

EFFECT OF ADDING ONE EXTRA POINT ALONG THE DIRECTION OF EIGENVECTOR

Because the Sanger's learning net updates the eigenvectors sequentially one sample by one sample, the theorem about the effect of adding one extra point along the direction of the eigenvector is proposed to help the interpretation that more data points along one principal eigenvector direction can enhance the eigenvalue. The theorem can help interpretations in the input data vectors of uniform wavelets and uniform neighboring traces.

Theorem 1 (Effect of adding one extra point along the direction of eigenvector of a covariance matrix):
Given a covariance matrix Q computed from N data and its eigenvalues λ_i and eigenvectors e_i, if adding one extra data vector (mean vector is removed) along the direction of eigenvector e_i, then (a) the new eigenvalue λ_i' is enhanced more than new eigenvalues λ_j' ($j \neq i$), (b) the new eigenvalue λ_i' is larger than the original eigenvalue λ_i if the square length of the extra data vector is larger than λ_i, otherwise λ_i' is less than λ_i.

Proof: The extra data vector (the mean vector is removed) is represented as $c e_i$, c is the length of the vector, $c \neq 0$. The set of the new eigenvalues and eigenvectors computed from the N+1 data is as follows.

New covariance matrix is $\frac{1}{N+1}[N\,Q + (c\,\mathbf{e}_i)(c\,\mathbf{e}_i)^T]$. For Q, its eigenvalues λ_i and eigenvectors $\mathbf{e}_i$ are given. For $\mathbf{e}_i\,\mathbf{e}_i^T$, because $\mathbf{e}_i\,\mathbf{e}_i^T\,\mathbf{e}_i = \mathbf{e}_i$, $\mathbf{e}_i^T\,\mathbf{e}_i = 1$, the eigenvector is $\mathbf{e}_i$. So the eigenvectors of the new covariance matrix are the same as those of Q.

For eigenvector $\mathbf{e}_i$, $\frac{1}{N+1}[NQ+(c\,\mathbf{e}_i)(c\,\mathbf{e}_i)^T]\mathbf{e}_i = \lambda_i'\,\mathbf{e}_i$.

$$\frac{N}{N+1}Q\mathbf{e}_i + \frac{1}{N+1}c^2\,\mathbf{e}_i(\mathbf{e}_i^T\,\mathbf{e}_i) = \lambda_i'\,\mathbf{e}_i.$$

$$\frac{N}{N+1}\lambda_i\,\mathbf{e}_i + \frac{1}{N+1}c^2\,\mathbf{e}_i = \lambda_i'\,\mathbf{e}_i, \quad \mathbf{e}_i^T\,\mathbf{e}_i = 1$$

$$(\frac{N}{N+1}\lambda_i + \frac{1}{N+1}c^2)\mathbf{e}_i = \lambda_i'\,\mathbf{e}_i. \quad \frac{N}{N+1}\lambda_i + \frac{1}{N+1}c^2 = \lambda_i' \quad (1)$$

$$\lambda_i + \frac{1}{N+1}(c^2 - \lambda_i) = \lambda_i' \quad (2)$$

From (2), if $c^2 > \lambda_i$, then $\lambda_i' > \lambda_i$. This proves (b).

For eigenvector $\mathbf{e}_j$ $(j \neq i)$, $\frac{1}{N+1}[N\,Q + (c\,\mathbf{e}_i)(c\,\mathbf{e}_i)^T]$

$$\mathbf{e}_j = \lambda_j'\,\mathbf{e}_j. \quad \frac{N}{N+1}\lambda_j\,\mathbf{e}_j = \lambda_j'\,\mathbf{e}_j, \quad \mathbf{e}_i^T\,\mathbf{e}_j = 0.$$

$$\frac{N}{N+1}\lambda_j = \lambda_j' \quad (3)$$

From (1) and (3), the new λ_i' is enhanced more than the new λ_j' $(j \neq i)$. This proves (a).

EXPERIMENTAL RESULTS

(I) Analysis of a fault

The seismogram in Fig. 2(a) shows a fault. The left hand side has 24 uniform traces and the right hand side has 8 uniform traces. The seismic trace has the 20 Hz zero-phase Ricker wavelet with reflection coefficient -0.2, 4 ms sampling interval, and 10 - 56 Hz Gaussian white band noise (mean=0, standard deviation=0.1). Fig. 2(b) shows the projection of each horizontal data vector on the 1st eigenvector. And Fig. 2(c) shows the projection of each horizontal data vector on the 2nd eigenvector.

(II) Filtering of diffraction pattern

The simulated horizontal geological layer with termination is shown in Fig. 3(a). The depth of the layer is 500 meters, the seismic P-wave velocity is 2,500 meter/sec., and the receiving station interval is 50 meters. The generated seismogram after normal moveout correction (NMO) has reflection and diffraction patterns in Fig. 3(b). The source signal is a 20 Hz zero-phase Ricker wavelet with reflection coefficient 0.2. The Gaussian white band noise are added to the seismogram. Fig. 3(c) shows that the diffraction seismic pattern is filtered from horizontal reflection layer in the projection of each horizontal input data vector on the first eigenvector.

(III) Analysis of bright spots

For the input data vector in the horizontal and vertical directions, the central part of bright spots can show the uniform property.

(IV) Application to real seismogram at Mississippi Canyon

(A) We use the input data vector in the horizontal direction to compute the principal eigenvectors of the covariance matrix in real seismogram at Mississippi Canyon in Fig. 4(a). Fig. 4(b) shows the 3 projection values. The central part of Fig. 4(c) reflects strong to the projection on the 1st eigenvector. The left part of Fig. 4(d) reflects strong to the projection on the 2nd eigenvector. A structure can be decomposed into several principal components.

(B) We use the input data vector in the vertical direction in Fig. 4(a). Fig. 5(a) shows the 3 projection components, the 1st projection component can show the high amplitude and polarity reversal. Fig. 5(b) shows the projection vector of each trace on the 1st eigenvector. The seismic traces at the central part of the seismogram show the uniform property.

REFERENCES

[1] Y. T. Chien and K. S. Fu, "On the generalized Karhunen-Loeve expansion," IEEE Trans. Information Theory, v.IT-13, pp.518-520, 1967.

[2] D. C. Hagen, The application of principal components analysis to seismic data sets, Proceedings of the 2nd International Symposium on Computer Aided Seismic Analysis and Discrimination, 1981, pp.98-101.

[3] I. F. Jones, Applications of Karhunen-Loeve transform in reflection seismology, Ph.D. thesis, The University of British Columbia, Vancouver, Canada, 1985.

[4] T. D. Sanger, Optimal unsupervised learning in a single-layer linear feedforward neural network, Neural Networks, Vol.2, pp.459-473, 1989.

[5] T. D. Sanger, An optimality principle for unsupervised learning, in D. S. Touretzky, ed. Advances in Neural Information Processing Systems, v.I, Morgan Kaufmann, San Mateo, 1989, pp.11-19.
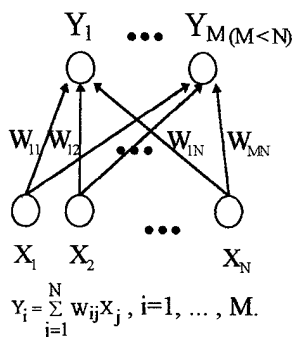
Fig.1.Sanger's neural net.

$$Y_i = \sum_{j=1}^{N} W_{ij} X_j, \ i=1, \ldots, M.$$
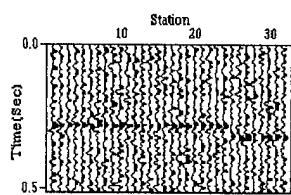
Fig.2(a).A fault (horizontal input). Fig.2(b). 1st projection. Fig.2(c). 2nd projection.
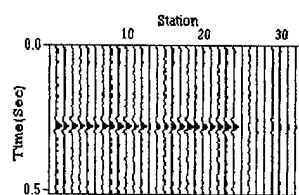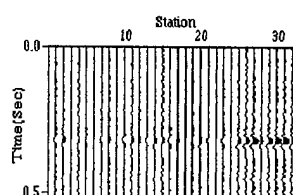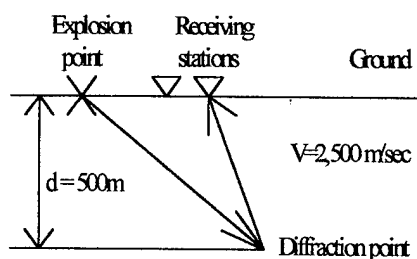
Fig. 3(a). Geological model.
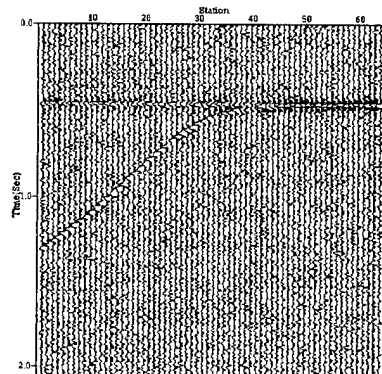
Fig.3(b).Reflection and diffraction.
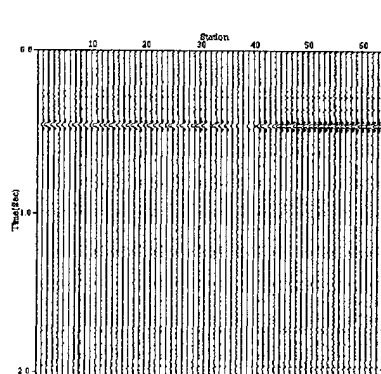
Fig.3(c).1st projection (horizontal input).
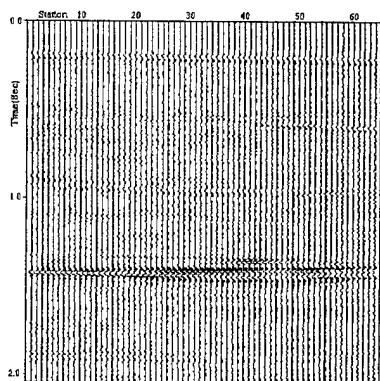
Fig. 4(a). Real seismogram.
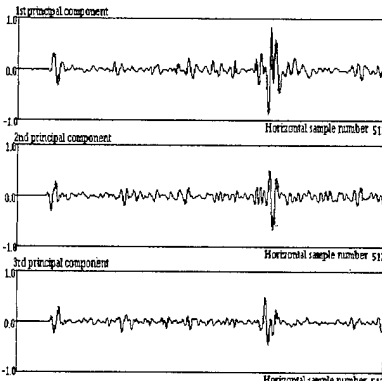
Fig.4(b).3 principal values (horizontal input).
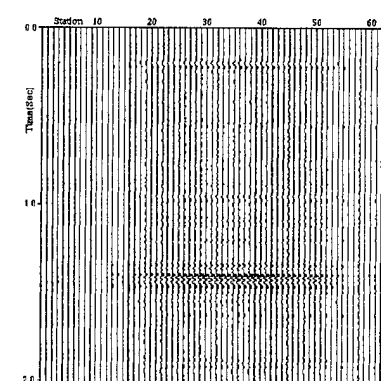
Fig. 4(c) 1st projection.
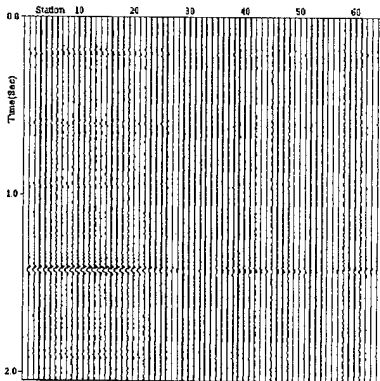
Fig.4(d). 2nd projection.
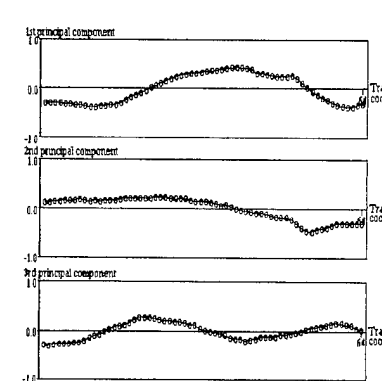
Fig.5(a).3 principal values (vertical input).
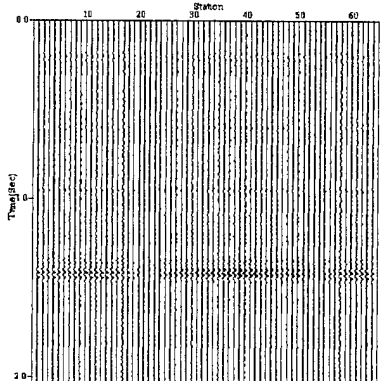
Fig.5(b). 1st projection.

1198

Filtering Effects on Polarimetric SAR Image Classification

K. S. Chen, Y.C. Tzeng[1], C.T. Chen, and J.S. Lee[2]
Center for Space and Remote Sensing Research
National Central University
Chung-Li, Taiwan
2Naval Research Laboratory, Code 20375-5351.
Washington D.C20375-5599., USA

Abstract

Feature extraction from SAR images is usually impeded by the presence of speckle noise. This becomes more serious in the case of polarimetric SAR system. A polarimetric filter recently proposed by Lee et al.[1] emphasizes not introducing additional cross-talk and statistical correlation between channels, preserving polarimetric information and not degrading the image quality. This paper exams its effects on the image classification by a supervised fuzzy dynamic learning neural network trained by a Kalman filter technique. Based on the available ground truth, the classification performance were evaluated using the original and filtered SAR images. Two independent test sites are selected for this purpose. The first case is a P-band JPL polarimetric SAR data over Les Landes for tree age classification. A total of 12 classes between 5 to 44 years of age were to be classified, along with a bare soil type. The second test site is over Flevoland of the Netherlands. This agricultural site consists of 11 landcover types. Again, the polarimetric SAR data were acquired with JPL P, L, C bands airsar system. For the first case, it was found that the overall classification accuracy was able to improve from 69% to about 86% with kappa coefficient up from 0.46 to 0.76. Substantial improvement was also confirmed for the second case. In particular, when classification was performed using only single frequency. This shows that the polarimetric information are well preserved. By visual inspection from classified map, the land cover boundaries were also delineated more clearly. As for fuzzy neural network performance, among the tested cases, the fuzzy index equal to 2 gets the best results.

1.0 Introduction

Polarimetric SAR is a powerful tool for terrain mapping and classification[2]. It stores target complete polarimetric responses from which the targets are discernible. Although polarimetric SAR needs a more complicated calibration procedure to maintain the polarization information and channel balance, and subsequently obtain absolute radar coefficients of target, when properly applied, identification and classification can be achieved to a highly acceptable degree. For parameter retrieval, care about absolute calibration should be taken.

Speckle reduction of polarimetric SAR imagery has been studied using several different approaches. Novak and Burl[4] derived the polarimetric whitening filter by optimally combining all elements of the polarimetric covariance matrix, and produced a single speckle reduced image. Lee et al. proposed two algorithms that produced speckle reduced HH, VV and HV images by using a multiplicative noise model and minimizing the mean square error. The off-diagonal terms were not filtered. Goze and Lopes generalized Lee's approach to include all element of the covariance matrix for one-look imagery. All these approaches exploited the degree of independence between HH, HV and VV channels. The statistical characteristics, such as correlation between channels, and polarimetric signature preservation, were not addressed[4]. This paper examines the impact of using this polarimetric speckle filtering on terrain classification. NASA/JPL polarimetric P-L-C-band SAR data is used for illustration.

2.0 A Fuzzy Neural Classifier

A new fuzzy classifier, FDL [3] was used to perform supervised classification to evaluate the filtering impacts. This classifier is based on the framework of dynamic learning NN[2] and makes use of c-means algorithm to determine the desired outputs, or class centers in such a way that the inputs may belong to several classes in a fuzzy fashion according to their membership values. The algorithm is simple, easily implemented, and yet, naturally integrates the features of neural net and fuzzy logic into one classifier. It has been shown that a fuzzy neural classifier is more robust in classification and indeed has pixel unmixing capability[3]. A neural network can be modelled as $Y=WX$, where X is input vectors, Y is output vectors, and W is network weights matrix. The determination and update of W in FDL network are summarized below. The more detail algorithm of FDL was referred in [3].

Step 1: for $k=1,2,....,C$, initialize network weights w_k^1

Step 2: for $j=1,2,...,N$

for $k=1,2,...,C$

assign $\mu_k^j = d_k^j$

Step 3: for $j=1,2,...,N$

    for $k=1,2,...,C$

    calculate Kalman gain g_k^j

    update network weights $w_k^{j+1} = w_k^j + g_k^j (\mu_k^j - w_k^j \underline{x}^j)$

Step 4: for $k=1,2,...,C$

    calculate class center $\underline{V}_k$

Step 5: for $j=1,2,...,N$

    for $k=1,2,...,C$

    calculate membership values μ_k^j

Step 6: if $e = \sum\limits_{j=1}^{N} \sum\limits_{k=1}^{C} \frac{1}{2} \left\| \mu_k^j - w_k^{N+1} \underline{x}^j \right\| < \varepsilon$ and $|\Delta U| < \delta$

then stop

else go to Step 3.

In above, C is number of class, N is total number of patterns for training and ΔU is the difference of matrix U whose dimension is $C \times N$ with elements μ_k^j, between two iterations. The calculations of class center and membership values are according to the c-means algorithm.

3.0 Test Sites and Data Processing

Two independent test data sets were used in this paper. Both were acquired by JPL multifrequency polarimetric AIRSA system. One site was over Landes, France, a forest area with tree age from 5 to 44 years old. Since the tree age classification is of interest, only P-band data were used. Another data set was acquired over Flevoland, The Nethelands, an agriculture area with total 13 classes to be classified. A combination of P, L, C band multipolarization data were used for this case. First, the data were filtered by the polarimetric SAR speckle filter[1]. The steps are as follows:

1) convert the stokes' matrix into covariance matrix for filtering:

$$
Z = \begin{bmatrix}
|HH|^2 & HH \cdot HV^* & HH \cdot VV^* \\
HH^* \cdot HV & |HV|^2 & HV \cdot VV^* \\
HH^* \cdot VV & HV^* \cdot VV & \|VV\|^2
\end{bmatrix} \quad (1)
$$

The diagonal terms can be characterized by multiplicative noise model. The off-diagonal complex terms are difficult to characterize, but their real and imagery parts can be approximated by an additive and multiplicative noise model.

2) To filter the whole covariance matrix, we use the span image to obtain filtering weight by applying the refined Lee filter with multiplicative noise model.

$$S = |HH|^2 + 2|HV|^2 + \|VV\|^2 \quad (2)$$

The the filtered pixel value with local statistics filter are

$$S = \bar{S} + k(S_z - \bar{S}) \quad (3)$$

and

$$k = \frac{var(S_z) - \bar{S}_z^2 \sigma_v^2}{var(S_z)(1 + \sigma_v^2)} \quad (4)$$

where the S_z is the pixel to be filtered, $\bar{S}$ is the local mean and $var(S_z)$ is the local variance. They are computed in an edge directed window.

Note that the gradient is determined by using four 3x3 edge masks. The window is selected based on the location of the center pixel on the side of similar pixel value.

3) For each pixel, the k value and the window number obtained from step 2) are used to filter the whole covariance matrix including the off-diagonal terms. The filtered covariance matrix is

$$Z = Z + k(Z - \bar{Z}) \quad (5)$$

where each element of $\bar{Z}$ is the local mean computed using the same sub-window.

4) The covariance matrix can be converted easily into the stokes' matrix in either uncompressed or JPL compressed format.

Now that, synthesizing the SAR image from Stokes* matrix of polarimetric SAR data into HH, HV, and VV polarized images is in order. Then, it is a common practice[2] to select the suitable training data and to test the classifier, with the available ground truth map. It is of interesting at this point to investigate the statistical properties of pre- and post-filtered data, in particular, the phase-difference and amplitude ratio between channels. Fig.1 shows the comparison of phase-difference(C-band HH-VV) distribution of pre- and post-filtered. The reduction of speckle noise is obviously shown. The amplitude ratio distributions were plotted in Fig.2. Again, the variance was greatly reduced making the ratio values concentrated around the mean. The correlation coefficient and phase angle were nearly unchanged stating the fact of preservation of polarimetric information using the polarimetric filter.

4.0 Results and Discussions

For the first case we illustrated the tree age classification from P-band data. Although optimum polarized channels may be extracted, only linear polarizations were used here. The tree ages were divided into 6 groups, 5-8, 8-11, 11-14, 15-19, 20-25, 33-44 years. A bare soil class was also identified although it was clearly distinguished from tree covers. After the filtering, the overall classification accuracy was up from 69% to 86.5% while Kappa coefficient was up from 0.46 to 0.766. The most distinct improvement is the 8-11

years class. For each class, the respective accuracy of each class was also observed. At this point, we have shown the effectiveness of our classifier and filter. It should be useful to illustrate the polarimetric filtering effects using the second test case, when compared to non-polarimetric filters, as shown below.
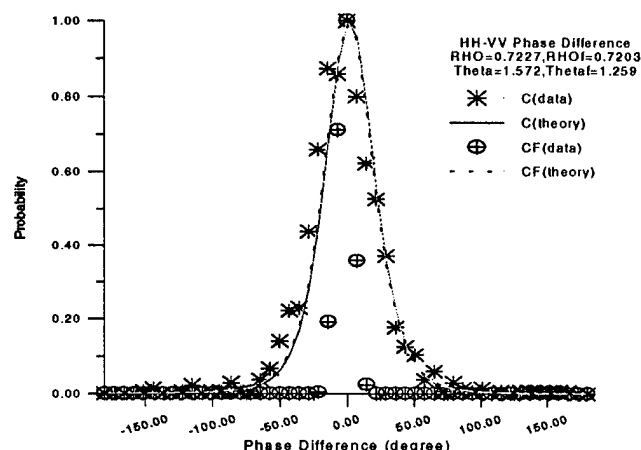
Fig.1 Phase difference (HH-VV) distributions of pre- and post-filtered data
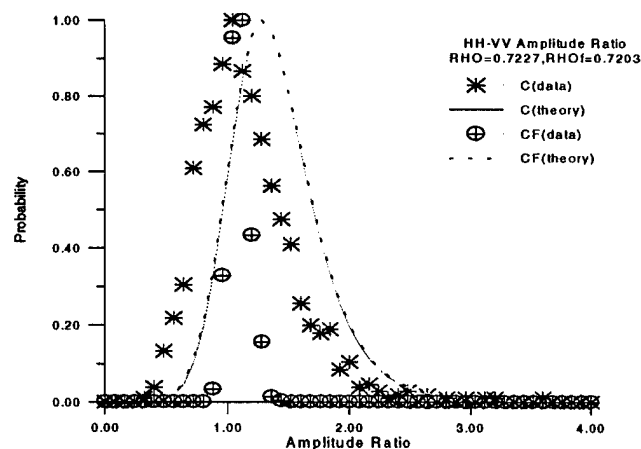
Fig.2 Amplitude ratio distribution of pre-and post-filtered data.

The Flevoland site was surveyed with total of 13 classes identified. Again only linear polarizations were extracted. For single frequency-multipolarization configuration, P-band(HH,HV,VV) gives best classification results with accuracy of 96%. If multifrequency-single polarization is chosen, HV-polarized (P-L-C) has accuracy of 92%. VV- and HH-polarized gave comparable results. For comparisons, the adaptive Lee filter, Gamma MAp filter were selected. No efforts was yet made to compare other polarimetric filters but should be of interests to do so in the future work. Table 1 and 2 gave the final compared results of multipolarization and multifrequency, respectively. Of all the comparisons, we find that the new polarimetric filtering give best classification results. It should be emphasized that the FDL indeed is a

high performance in SAR image classification in terms of learning speed and classification accuracy.

Table 1: Multipolarization classification

	Lee	Gam map	New filter
C	0.58(0.54)	0.58(0.54)	0.63(0.60)
L	0.81(0.79)	0.81(0.79)	0.82(0.80)
P	0.95(0.95)	0.94(0.94)	0.97(0.96)
HH,HV, VV-polarizations were used			

Table 2: Multifrequency classification

	Lee	Gam map	New filter
HH	0.78(0.76)	0.78(0.76)	0.79(0.77)
HV	0.89(0.88)	0.90(0.89)	0.92(0.91)
VV	0.79(0.77)	0.79(0.77)	0.80(0.78)
P,L,C-band were used			

5.0 Conclusions

Using a fuzzy neural network as image classifier, the effects of polarimetric filter on SAR image classification was evaluated using two independent data sets both acquired by JPL AIRSAR system. The new filter was developed by Lee based on his earlier adaptive version. When compared to regular filters, it is clearly demonstrated that the new filter removes effectively the speckle noise while perseveres polarimetric information more effectively. This definitely improves the image classification accuracy.

6.0 References

[1] Lee, J. S, et al., Polarimetric SAR speckle filtering and its impact on classification,' *Proc. IGARSS97*, 1997.

[2] Chen, K.S., W.P. Huang, D.W. Tsay and F. Amar, 1996, ' classification of multifrequency polarimetric SAR image using a dynamic learning neural network,' *I.E.E.E. Transactions on Geoscience and Remote Sensing*, 34(3), 814-820.

[3] Tzeng Y.C. and Chen,K.S., A fuzzy neural network for SAR Image Classification,' Accepted to *I.E.E.E. Transactions on Geoscience and Remote Sensing*, 1997

[4] Novak, L.M. and M.C. Burl, 'Optimal speckle reduction in polarimetric SAR imagery, ' *IEEE Trans. Aerosp. Elec. Syst.*, vol. 26, pp. 293-305, 1990

Training of neural networks for classification of imbalanced remote-sensing data

S.B. Serpico and L. Bruzzone

Dept. of Biophysical and Electronic Engineering - D.I.B.E.
University of Genoa, Via Opera Pia, 11a, I-16145 Genova (Italy)
Phone: +39-10-3532752; Fax.: +39-10-3532134; E-mail: vulcano@dibe.unige.it, lore@dibe.unige.it

Abstract -- The multilayer perceptron is currently one of the most widely used neural models for the classification of remote-sensing images. Unfortunately, training of multilayer perceptron using data with very different a-priori class probabilities (imbalanced data) is very slow. This paper describes a three-phase learning technique aimed at speeding up the training of multilayer perceptrons when applied to imbalanced data. The results, obtained on remote-sensing data acquired with a passive multispectral scanner, confirm the validity of the proposed technique.

INTRODUCTION

The multilayer perceptron (MLP), trained by the backpropagation algorithm [1], is one of the most widely used neural models for the classification of remote-sensing data [2]. If properly trained, it provides approximations to the posterior class probabilities, given the feature vectors of the samples to be classified [3], which can be used to apply the optimal Bayes decision rule [4]. The major problems related to this classifier are the duration and the reliability of the training process, in particular, when the process is performed in "batch mode" on imbalanced data (i.e., when the a-priori probabilities of the various classes considered are very different from one another). Such problems are encountered in many remote-sensing applications.

In literature, several techniques aimed at speeding up the training of MLPs have been proposed [1,5]. However, only few authors have addressed the problem of training an MLP in presence of imbalanced data sets [6,7]. Anand et al. [6] proposed a technique suited to two-class cases aimed at reducing the training time for MLPs. The same authors extended the use of this technique to multiclass cases [7]. However, these techniques do not allow the output of the networks to be considered an approximation of the posterior class probabilities optimized in accordance to a given criterion.

This paper describes a three-phase learning technique for speeding up the training process of an MLP when it is applied to imbalanced data. Such a technique allows to train MLPs so to obtain an estimate of the a-posteriori class probabilities by minimization of the mean squared error (MSE). Experiments are carried out on remote-sensing data acquired by a passive multispectral scanner on an agricultural area.

TRAINING MLPS WITH IMBALANCED DATA

Let us assume to use a neural network with one hidden layer and sigmoidal non-linearities; let us consider a problem with M classes and assume that the number of samples from each class is in proportion of the a-priori probability of class membership. The class ω_d is the dominant one, i.e., the number n_d of samples of this class is larger than the number n_p of samples of the other classes ($n_d >> n_p$, $\forall\, p \neq d$). In order to make the network output provide an approximation to the a-posteriori probability $P(\omega_l/x)$ of the class ω_l, given the feature vector x of a sample, optimized with respect to the MSE, we use the error back-propagation (EBP) training algorithm and the MSE as a cost function [3]:

$$E = \sum_{l=1}^{M} E_l = \sum_{l=1}^{M} \frac{1}{nM} \sum_{k=1}^{M} \sum_{i=1}^{n_l} \left(t_k^{(l)} - o_k\left(x_i^{(l)}\right) \right)^2 \qquad (1)$$

where n_l is the number of samples of class ω_l; $t_k^{(l)}$ is the target for the k-th output of the network for the samples of the l-th class; $o_k\left(x_i^{(l)}\right)$ is the k-th output of the network when the i-th sample of the l-th class has been presented to the input; E_l is the contribution of the class ω_l to the MSE. In order to obtain approximations to the posterior class probabilities, the sum of the outputs of the network should be normalized to 1 [3].

Let us recall the reasons why training with imbalanced data sets is slow. As shown in [6] in a similar situation, at the beginning of the training phase, the gradient of the mean squared error (∇E) calculated with respect to the network weights is dominated by the contribution related to the dominant class ω_d $\left(\|\nabla E_p\| << \|\nabla E_d\|, \forall\, p \neq d \right)$. Since, at the beginning of the training phase, the contribution of minority classes to the direction of the gradient E of the error is negligible, the mean squared error of some of such classes may increase and approach its upper limit. Consequently, training may become slow.

THE THREE-PHASE TECHNIQUE PROPOSED

The proposed technique divides the training process into three phases so that convergence can be reached while avoiding a sharp increase in E_p related to minority classes.

In the first phase, it exploits a modified cost function that "simulates" the training in presence of classes with the same a-priori probabilities. Then, in the second phase, this cost

function is gradually modified from that of the first phase to the standard MSE criterion. Finally, in the third phase, the training is completed according to the standard MSE criterion.

In the following we report a detailed description of each of the three phases.

Phase 1: The EBP algorithm is applied to the following modified cost:

$$E' = \sum_{l=1}^{M} E'_l = \sum_{l=1}^{M} q_l E_l, \quad q_l = \frac{n_d}{n_l} \quad (2)$$

Thanks to the modification to the cost function, the mean values $\left\| \nabla E'_l \right\|$ of all the contributions E'_l to E' are about equal, so that the contribution of minority classes to $\left\| \nabla E' \right\|$ is not negligible any more (a similar proof as that of Theorem 3 in [6] can be provided). This balance among contributions (which is natural for training with data evenly distributed among all different classes) helps to avoid slow convergence. This phase is stopped when the following condition is satisfied:

$$E'_l \le \frac{n_d}{n} \cdot T \quad (l = 1, \dots, M; \ T << 1). \quad (3)$$

This ensures that both the overall MSE (see (1)) and the following class-related MSEs will be smaller than or equal to T:

$$MSE_l = \frac{1}{n_l} \sum_{j=1}^{n_l} \left(t^{(l)} - o\left(x_j^{(l)} \right) \right)^2 = \frac{n}{n_l} E_l \le T. \quad (4)$$

Phase 2: Unfortunately, the output of the network obtained in this way does not represent an approximation to the a-posteriori probability $P(\omega_l/x)$, due to the cost modification introduced into Phase 1 (see (2)). We can then use the network weights obtained at the end of the first phase as the initial weights of the second training phase. This phase is aimed at gradually modify the cost from E' to the standard MSE criterion in order to avoid a discontinuous change in the cost function that could generate oscillatory phenomena. This is carried out in S steps by gradually modifying the q_l coefficients of (2) according to the algorithm that is described below.

Initialization: The initial values of the coefficients (i.e., q_l^0) are assumed equal to the values of q_l in the first phase:

$$q_l^0 = q_l \quad (l = 1, \dots, M). \quad (5)$$

Step j: at step j $(j=1, \dots, S-1)$ the values of the coefficients q_l^j are updated as follows:

$$q_l^j = \begin{cases} q_l^{j-1} - \dfrac{(n_d/n_m - 1)}{S} & \text{if } \left[q_l^{j-1} - \dfrac{(n_d/n_m - 1)}{S} \right] \ge 1 \\[4mm] 1 & \text{if } \left[q_l^{j-1} - \dfrac{(n_d/n_m - 1)}{S} \right] < 1 \end{cases} \quad (6)$$

where n_m is the number of samples of the most minoritary class ω_m. Each step is carried out by training the network with the EBP algorithm until the convergence criterion, that evaluates the stability of the cost, is verified.

Phase 3: It corresponds to the S-th step of the algorithm defined for Phase 2. The training is performed with the standard MSE as cost function since all the coefficients q_l^S are equal to 1. Consequently, the network output may be used directly as an approximation to $P(\omega_l/x)$.

EXPERIMENTAL RESULTS

In our experiments, we considered a data set referred to an agricultural area near the village of Feltwell (U.K.). We selected a section (250×350 pixels) of a scene acquired by a multispectral optical sensor (a Daedalus 1278 Airborne Thematic Mapper (ATM) with eleven spectral bands). We considered only the six spectral bands of the ATM that correspond to the bands provided by the Thematic Mapper sensor installed on Landsat satellites (with exception for the thermal band). Each pixel of the multispectral image was considered as an input pattern. The six bands utilized were associated with each pixel to form the "feature vector" that was used as input to the neural classifier.

For our experiments, we considered the following agricultural classes: wheat, sugar beets, potatoes, carrots, and stubble. The training-set pixels were obtained by sampling the related fields. In order to assess the advantages of the proposed technique in presence of classes with low a-priori probabilities, we reduced the probabilities of occurrence for the wheat and the potatoes classes. This was accomplished by further subsampling the fields of such classes. Table 1 shows the numbers of samples obtained in the resulting training set.

For each experiment, we defined a fully-connected MLP (with 6, 10, and 5 units in the input, hidden and output layers, respectively) and compared the numbers of iterations required by the standard EBP algorithm with the MSE criterion and the proposed three-phase technique. The same learning rate ($\eta=0.01$) was used for both training techniques (and for all phases of the proposed technique). The final convergence criterion was also the same for both training techniques, and was given by fixing the number of misclassified samples below which training can be stopped (i.e., 4.5% of the training samples). The convergence criterion to stop the first phase of the proposed technique was given by fixing the value of the threshold T to 0.3. Concerning the second phase, S was chosen equal to 15.

Five experiments were carried out on the above data set, starting from the same five randomly generated sets of weights for both the standard and the proposed techniques. Results are given in Table 2. As can be noticed, the proposed method allowed notable speed-ups (an average of about 49 times). An alternative evaluation of speed-ups can be computed by neglecting the experiments which provided the best and the worst speeding-ups, and by averaging the speed-ups obtained in the other three experiments. Also according

1203

to this evaluation, the speed-up provided by the proposed three-phase technique (i.e., about 15 times) can be considered significant.

DISCUSSIONS AND CONCLUSIONS

In this paper, a technique to speed up the training of MLPs with imbalanced remote-sensing data sets has been presented, and compared with the standard EBP algorithm. For the remote-sensing data sets considered, several experiments were carried out, starting from the same randomly generated set of weights for both the standard and the proposed techniques. Results pointed out that the proposed method allowed notable speed-ups for all randomly-generated weights considered.

The problem of the training of MLPs in presence of imbalanced data was also faced in [6], for two-class cases, and in [7] for multiclass cases. For a comparison, we may note that the extension from two-class to multiclass cases required the definition of as many networks as the number of classes. In addition, the outputs of MLPs trained by the techniques described in such papers cannot be used directly to implement the Bayes decision rule for a minimum error classification.

ACKNOWLEDGMENTS

REFERENCES

[1] Hertz, J., A. Krogh, and R.G. Palmer, Introduction to the Theory of Neural Computation, Addison Wesley, The Advance Book Program, Reading, MA, 1991.

[2] Paola, J.D., and R.A. Schowengerdt, "A detailed comparison of backpropagation neural network and maximum-likelihood classifiers for urban land use classification," IEEE Transactions on Geoscience and Remote Sensing, vol. 33, pp.981-996, 1995.

[3] Richard, M.D., and R.P. Lippmann, "Neural network classifiers estimate bayesian a posteriori probabilities," Neural Computation, vol. 3, pp.461-483, 1991.

[4] K. Fukunaga, Introduction to statistical pattern recognition, 2nd ed., New York: Academic Press, Inc., 1990.

[5] Vogl, T.P., J.K. Mangis, A.K. Rigler, W. T. Zink and D.L. Alkon , "Accelerating the convergence of the back-propagation method," Biological Cybernetics, vol. 59, pp. 257-263, 1998.

[6] Anand, R., K. G. Mehrotra, C.K. Mohan, and S. Ranka , "An improved algorithm for neural network classification of imbalanced training sets," IEEE Transactions on Neural Networks, vol. 4, pp. 962-969, 1993.

[7] Anand, R., K. G. Mehrotra, C.K. Mohan, and S. Ranka, "Efficient classification for multiclass problem using modular neural networks," IEEE Transactions on Neural Networks, vol. 6, pp. 117-124, 1995.

Table 1. Classes and related number of pixels in the considered training set.

Class	Number of pixels	A-priori probability
Wheat	90	0.06
Sugar Beets	728	0.51
Potatoes	90	0.06
Carrots	319	0.23
Stubble	191	0.14

Table 2. Numbers of iterations required to reach an overall classification error less or equal to 4.5% (i.e., 64 misclassified samples) for the five experiments carried out. The speed-ups provided by the proposed technique are reported.

Experiment	Standard EBP	Proposed technique	Speed-up provided by the proposed technique
1	5851	552	10.6
2	129258	676	191.2
3	7246	587	12.3
4	4581	578	7.9
5	12637	541	23.4
Average	31915	587	49.1

Land Use Analysis of Remote Sensing Data by Kohonen Nets

Yoshikazu Nogami, Yoichi Jyo, Michifumi Yoshioka and Sigeru Omatu
Department of Computer and Systems Science,
College of Engineering, Osaka Prefecture University,
Sakai, Osaka 593, JAPAN
TEL: +81-722-52-1161 ext. 2288, FAX: +81-722-57-1788
E-mail: nogami@sig.cs.osakafu-u.ac.jp

Abstract -- The neural network approach by the back-propagation method (BPM) to land-use has been discussed in recent years. Using such a method, the accuracy depends on a training data set which has been selected manually. It takes much time to select a suitable training data set. In this paper, as a preprocessing of classifications we use the Kohonen feature map (KFM) and the competitive learning (CL) to get the better training data set. As a first step, the KFM that takes the Landsat TM data as input is adopted to form a rough classification of the wide area based on the observed data. In the next step, the CL whose inputs are the weights of the KFM node data is carried out to determine the category of each node of the KFM. The first weight set of the CL is a set on weights at four corners of the KFM. The combination of the two neural network techniques enables us to determine the rough land-use of an object region automatically. After that, the classification results by the KFM and the CL are further classified into more fine items by using the BPM. Finally, the classification results have been compared with other methods.

INTRODUCTION

Remotely sensed multi-spectral data have been used for many kinds of applications, for example, land-use analysis, the estimated crop, the water pollution, etc. It is important to analyze the data sampled form a satellite since we can observe the artificial and natural changes of the phenomenon in cycles, and investigate the wide range data of the earth surface at the same time. These could not be certainly obtained by the ground truth. We have classified the multi-spectral TM data observed from Landsat-5 by neural network approaches. The neural network trained by the BPM is also applied to non-Gaussian distributed data so long as we can choose a fine training data set. But the choice of the training data set is difficult even if well-organized ground truth were performed. Since a pixel does not consist of only typical class. The remotely sensed data are separated in many clusters even if they belong to the same class, since, shadow of the neighboring buildings or cloud may cause the different spatial phenomena for the same object. Therefore, it is difficult to choose a good training data set from the target image data. To overcome the problem, some researchers have employed the preprocessor before performing the classification. The preprocessor by the KFM was used to perform rough classification of the input data. A training data set from classification result by the KFM is chosen, and improved the classification accuracy.

However, how the remotely sensed data has been influenced by the KFM has not been demonstrated quantitatively. The KFM does not need a training data set and can automatically make a topology preserved map of the input data on its competitive plane. Therefore, we consider that the competitive units represent the small cluster of the input data. In this paper, we propose a new approach using the competitive weight vectors as the training data set. Using the weight vectors enables us to find the good training data set more easily than the random sampling. It is illustrated that the approach to the real remotely sensed data produces an excellent computational result.

PROPOSED METHOD

The proposal method has two stages. As a first step, the KFM that inputs the Landsat TM data is adopted to form a rough classification of the wide area based on the observed data. In the next step, the CL that inputs the weight of the KFM node data is carried out to determine the category of each node of the KFM. The first weight set of the CL is a corner weight set of the KFM nodes. We can select easily and more accurate supervisor data from classified data by the KFM and the CL for BPM.

Landsat TM Data

In this paper, we use TM band data observed from LANDSAT-5. The TM image is composed of seven bands, i.e., six of them, namely, band-1, 2, 3, 4, 5, and 7, are in the visible and near infrared portions of the spectrum, and band-6 senses

infracted data. The special resolution of the TM band is about 30 square meters per pixel, except for of band-6 of 120 square meters. We use three bands, namely, band-3, 4, and 5.

The target area of this work is located around Sakai City in Osaka, Japan, sampled on August 20th, 1995. The size of the images is 512 x 512 pixels and contains four classes, namely, W (water area), C (city, road area), T (town, suburb area), and G (wood, lawn area).

Kohonen Feature Map (KFM)

As shown in Fig.1, the KFM preprocessor is a two-layered network, one is an input layer and another is a competitive layer. The number of input unit is specified by the dimension of the input patterns likewise that of the BPM classifier. The competitive layer is organized as a two-dimensional grid. The two layers are fully interconnected via u_{ij}, as each input unit is connected to all of the competitive units where u_{ij} denotes the connection weight vector between the j-th element of the input pattern and the competitive unit i.

We also call the u_{ij} as a competitive weight vector. For example, when an input pattern $x_{ip} = [x_{1p}, x_{2p}, x_{3p}]$ is presented to the input layer, the winner unit c is chosen by using a competitive learning rule:

$$u_c \geq u_j \quad \Lambda \quad \forall j \tag{1}$$

where

$$u_i = \sum_i x_{ip} \cdot w_{ij} , \tag{2}$$

Next, the weight vector in the nearest neighbor of the winner unit c is updated to chose on the input

Fig.1 The structure of network

pattern p. The weight updating is given by the following algorithm:

$$u_{ij}^{new} = u_{ij}^{old} + \Delta u_{ij} \quad \Lambda \quad j \in N_c , \tag{3}$$

$$\Delta u_{ij} = \eta_t \left(x_{ip} - u_{ij}^{old} \right), \tag{4}$$

$$\eta_t = \eta_0 \left(1 - \frac{t}{T} \right), \tag{5}$$

where t and T denote a current training epoch and its total number, respectively.

The neighbor N_c is the square grid around the winner unit c.

$$N_c = (2d_t + 1) \times (2d_t + 1), \tag{6}$$

$$d_t = d_0 \left[1 - \frac{t}{T} \right], \tag{7}$$

After training, we can get the topology preserved map, from the space of input patterns to the competitive plane. When an input pattern is presented, we can make sure that the topographic map uniformly covers the distribution of input patterns by checking the response from the closest competitive unit.

Competitive Learning (CL)

The competitive learning is an unsupervised neural network. The structure of the network is consists of two layers; one is an input layer and another is a competitive layer. In general the initial weights of network are set randomly. But in this study, the first weight set of the CL is a corner weight set of the KFM nodes, shown A B C D nodes in Fig.1, to converge the network. Since the KFM is learned by using the neighbor N_c, the feature map is made up so that the similar weight vectors gather in the neighborhood. As the result the weight vectors of Feature map unit are distinct each other.

The CL needs a precision classification. Each of the KFM weight vectors is close. The inputs of a KFM node vector into the CL are very severe to classify. As the weight vector of the KFM nodes does not input directly into the CL input node, we code the input data by using coarse coding as preprocessing. Coarse coding can be considered as a kind of interpolation. One uses n units which are distributed (usually, but not necessary) uniformly in an interval. This means that every node i is assigned as a fixed location z_m. When coding the numerical value w_{ij}, the output of node m at location z_m is given by a Gaussian response function (other forms are also possible):

$$w_{ijm}(w_{ij}) = e^{\frac{-(w_{ij} - z_m)^2}{\sigma^2}}, \tag{8}$$
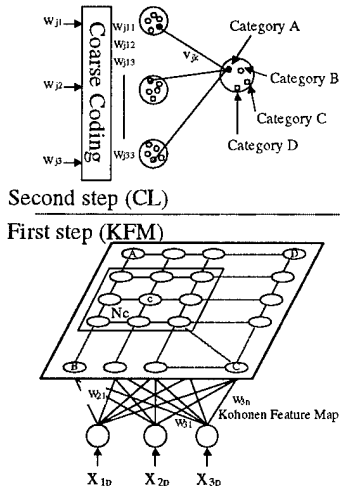
```
A A C C C C C C
A A C C C C C C
A C C C C C C C
B C C C C C C C
B B C C D D D D
B B B D D D D D
B B B D D D D D
B B B D D D D D
```

Fig.2 The category of Feature map units after CL

where σ is a parameter characterizing the width of the curve.

During learning, an input pattern is presented to the input layer and using a competitive learning rule we choose the winner unit c:

$$u_c \geq u_j \quad \Lambda \ \forall j , \tag{9}$$

where

$$u_j = \sum_j w_{ij} \cdot v_{jk} , \tag{10}$$

$$v_{jk}^{new} = v_{jk}^{old} + \Delta v_{jk} , \tag{11}$$

$$\Delta v_{jk} = \eta_t \left(w_{ijm} - v_{jk}^{old} \right), \tag{12}$$

SIMULATION RESULTS

We show the structure of this method in Fig.1. The lower network is the KFM. The upper network is the CL. The KFM has two layers. We look a suitable parameter of these networks in learning speed and from accuracy point of view, the Feature map has two-dimensional 8 x 8 nodes, the learning late η is 0.2, the number of learning times T is 80,000 and the initial size of neighbor d_0 is 5. The CL has 4-competitve nodes, the learning late η is 0.02 and the number of learning times is 12,000.

At the second stage, the CL is carried out. The conclusion of the CL is shown in Fig.2. This figure shows which the category of the KFM units belong to. These units in same category are close each other.

Fig.3 shows the 4-classification result by the unsupervised learning using the KFM and the CL. We can select easier and more accurately the same supervisor data from this figure than from the original data. The accuracy of this method shows in Table.1. This table shows that proposed method is effective to give us finer supervised data set.

CONCLUSIONS

The KFM and the CL method indicates that it is difficult to select the supervisor data set from original data, but it is easier and finer to select supervisor data set from roughly preclassified data

Fig.3 The classification results

Table.1 Comparison of classification accuracy

Method	C	W	B	D G	L G	T
Only BPM (%)	90	94	100	96	94	90
KFM+CL +BPM(%)	96	96	100	100	98	94

set. The second advantage of this method is the ability to classify roughly even unknown data.

A problem of this method is that this method cannot classify into 4-categories. But if we need to more detail classification, we can use it again for more divided category. Now I am considering the method to classify into more than 5-category.

REFERENCES

[1] Hiroshi Murai, Sigeru Omatu: "Principal Analysis for Remotely Sended Data Classified by Kohonen's Feature Mapping Preprocessor and Multi-Layered Neural Network Classifier", Trans. of IEICE, Vol. E78-B, No.12, 1995.

[2] Yoshikazu Nogami, Yoichi Jyo, Sigeru Omatu: "Remote sensing data analysis by neural network:, ISCIE'96, pp221-222, 1996.

[3] J. Dayhoff: "NEURAL NETWORK ARCHITE-CTURES: An Introduction", New York, Van Nostrand Reinhold, 1990.

[4] H. Bischof, W. Schneider, and A. J. Pinz: "Multi-spectral Classification of Landsat-Images Using Neural Networks", IEEE Trans on geoscience and remote sending, Vol.30, pp. 482-490, May 1992.

[5] Philip D.Heermann and Nahid Khazenie: "C-lassification of Multispectral Remote Sensing Data Using a Back-Propagation Neural Net-work", IEEE Trans. on geoscience and remo-te sensing, Vol.30, No.1, pp. 81-88, January 1992.

Wind Reconstruction from ERS-1 Scatterometer Data Using Neural Network

Y. C. Tzeng, and K. S. Chen*
Department of Electronics Engineering
National Lien-Ho College of Techonlogy and Commerce
Miao-Li, Taiwan, R.O.C.
*Center for Space and Remote Sensing Research
National Central University
Chung-Li, Taiwan, R.O.C.

Abstract -- A dynamic learning neural network is adopted to relate the normalized radar backscattering coefficient σ° to the wind vector. By given the average wind speed and wind direction and their standard deviations, a set of test wind vector fields are simulated. The corresponding σ° values are calculated according to the well known empirical model named CMOD-4. To improve the accuracy of the estimated wind direction, spatial information is considered in the reconstruction process. Thereafter, the neural network is iteratively trained by the input-output pairs generated from the test wind fields. Finally, the wind parameters are reconstructed upon applying σ° values to the well trained neural network. Experimental results indicate that neural network is an effective tool for wind reconstruction.

INTRODUCTION

In the 1990s, several satellite scatterometers are dedicated to Earth and ocean observation such as the ERS-1 advanced micromave imager (AMI) [1] and the NASA scatterometer (NSCAT) [2]. As shown in Fig. 1, the ERS-1 scatterometers are microwave radar capable of measuring ocean surface wind speed and direction. It provides three radar images of the ocean surface with a spatial resolution of 50*km* and a swath width of 500*km*. The three images are acquired by the three different antennas: the mid-beam, looking to the right side of the satellite, perpendicular to the ERS-1 ground track, the fore-beam, looking forward at 45° azimuth projection angle, with respect to the mid-beam, and the aft-beam, looking backwards at 45° azimuth projection angle, with respect to the mid-beam. The relationship between the normalized radar cross section σ° measured by the scatterometers and the wind vector can be established by using a geophysical model function. It is known that the wind field estimate is not unique but is identifiable from scatterometer measurements. Conventional approach to wind estimate involves formulating a cost function from the scatterometer measurements and then minimizing it to obtain estimates of wind field. Local minima are usually appear due to the nature of geophysical model function. This leads to the so called aliasing or ambiguity. Since dealiasing or ambiguity removal relies on the information not contained in measurements, it is not pursed here. In this paper, we are primarily concern with the inversion of the geophysical model function. Because it is nonlinear and the exact character of the nonlinear behavior may not be known *a priori*, this paper suggests a highly flexible, yet accurate, alternative approach to retrieve the wind vector by making use of the neural network techniques. In the next section, the detail experimental procedures are listed. The experimental results are shown in the following section. Finally, some conclusions are drawn.

EXPERIMENTAL PROCEDURES

Wind Field Generation

According to the simulation model [3], the wind vector field is assumed to be an expression of the form

$$u(x,y) = \sum_{k_x=0}^{n} \sum_{k_y=0}^{m} U(k_x,k_y)\exp\left[i\left(\frac{2\pi}{L_x}k_x x + \frac{2\pi}{L_y}k_y y\right)\right] \quad (1)$$

$$v(x,y) = \sum_{k_x=0}^{n} \sum_{k_y=0}^{m} V(k_x,k_y)\exp\left[i\left(\frac{2\pi}{L_x}k_x x + \frac{2\pi}{L_y}k_y y\right)\right] \quad (2)$$

where the coefficients $U(k_x,k_y)$ and $V(k_x,k_y)$ should satisfy the following conditions

Fig. 1 ERS-1 scatterometer Geometry

$$\frac{k_x}{L_x}U(k_x,k_y)+\frac{k_y}{L_y}V(k_x,k_y)=0 \qquad (3)$$

$$i\frac{k_x}{L_x}V(k_x,k_y)-i\frac{k_y}{L_y}V(k_x,k_y)=C(k_x,k_y) \qquad (4)$$

The coefficients $C(k_x,k_y)$ that can be chosen arbitrarily are complex numbers of absolute value

$$\left|C(k_x,k_y)\right|^2=\frac{\alpha}{\pi\left(k_x^2+k_y^2\right)^{1/2}} \qquad (5)$$

for some $\alpha > 0$ and phase $\exp[i\tau(k_x,k_y)]$ where $\tau(k_x,k_y)$ is a random variable uniformly distributed in $[0, 2\pi]$. By given the average wind speed and wind direction and their standard deviations, a set of test wind vector fields are generated For the case of ERS-1, we set $m=19$ and $n=19$, having a grid of size of $D_x(=25\text{Km})$ x $D_y(=25\text{Km})$ with patch size of $L_x(=475\text{Km})$ x $L_y(=475\text{Km})$. Fig. 2a shows an example of the simulated wind vector field whose mean wind speed is 10 (m/s), mean wind direction is 22.5 (deg), and standard deviations is 2 (m/s).

Wind Field Reconstruction

The corresponding $\sigma°$ values which simulate the aft-beam, the mid-beam, and the fore-beam of the ERS-1 scatterometer returns are calculated according to the well known empirical model named CMOD-4. The relationship between $\sigma°$ and wind vector are given by

$$\sigma°=b_0\left[1+b_1\cos\varphi+b_3\tanh(b_2)\cos 2\varphi\right]^{1.6} \qquad (6)$$

where φ is the wind direction and the coefficients b_0, b_1, b_2, and b_3 are functions of the wind speed and incident angle. A dynamic learning neural network [4] is adopted to relate $\sigma°$ and wind vector. To improve the accuracy of the estimated wind direction, spatial information is considered in the reconstruction process. Therefore, the neural network is constructed to have twenty eight input nodes, the three $\sigma°$ returns at each cell of a 3×3 window and the incident angle of the mid-beam, and two output nodes, the wind speed and wind direction. Thereafter, the neural network is iteratively trained by the input-output pairs generated from the test wind fields. Finally, the wind parameters are reconstructed upon applying the $\sigma°$ values to the well trained neural network. A very satisfactory result is obtained. Fig. 2b shows an example of the reconstructed wind vector field with mean wind speed of 10.17 (m/s), mean wind direction of 23.68 (deg), and standard deviations of 2.01 (m/s). In the following section, we shall apply the measured $\sigma°$ values acquired by the ERS-1 scatterometers to the well trained neural network to retrieve the wind speeds and wind directions.
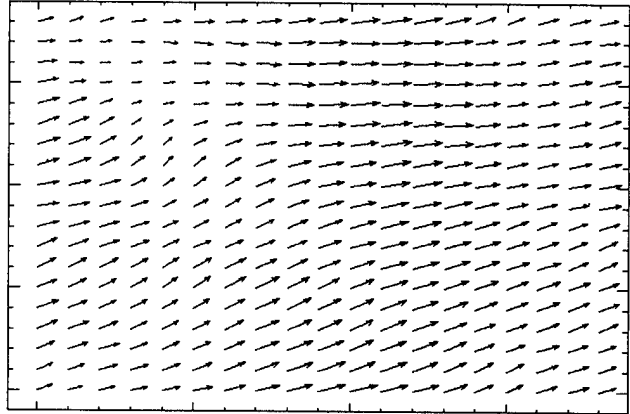
wind speed = 10 m/s

a. simulated wind vector field
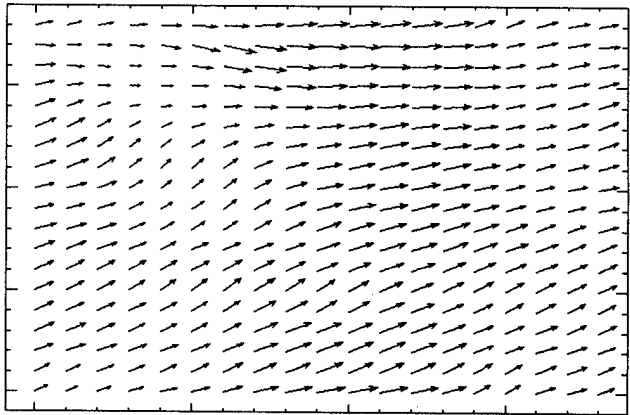
wind speed = 10 m/s

b. reconstructed wind vector field

Fig. 2 An example of a wind vector field whose mean wind speed is 10 (m/s), mean wind direction is 22.5 (deg), and standard deviations is 2 (m/s)

EXPERIMENTAL RESULTS

Due to the absence of ground truth, we compare our results with the wind field reported by ECMWF. First, from the wind speeds and wind directions reconstructed by the neural network and some related parameters, we can gain three $\sigma°$ values of ERS-1 scatterometers using the model CMOD-4. Similarly, from the wind fields reconstructed by ECMWF, we can acquire three $\sigma°$ values using CMOD-4. Finally, the differences between these two sets of $\sigma°$ and measured $\sigma°$ are calculated. In addition, since we take spatial context into account, the grid mesh of a wind field becomes 17 x 17. An example of the results for a data set labeled 1F14292-38 are shown in Fig. 3. The axis represents 289 cells (17 x 17) and the y axis represents the $\sigma°$ in real values.
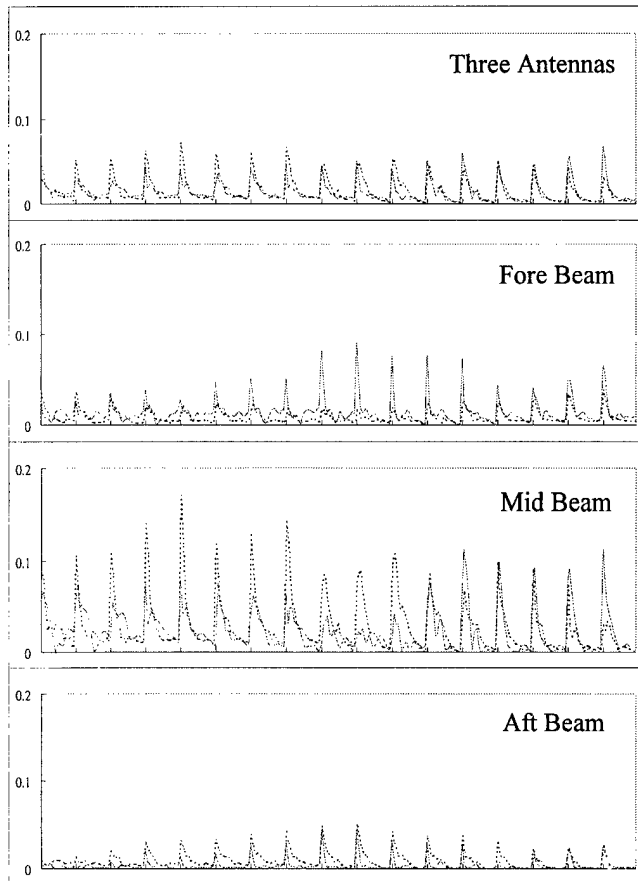
Fig. 3 The difference between σ° reconstructed by DLNN and measured σ° is plotted in solid line; and the difference between σ° reconstructed by ECMWF and measured σ° is plotted in dot line.

CONCLUSIONS

From, the above experimental results, a very satisfactory result is obtained. Results indicate that neural network is an effective tool for wind reconstruction. It is also seen that the use of neural network to remove the ambiguity is also applicable and reliable.

REFERENCES

[1] Attema E. P. W., "The Active Microwave Instrument on-board the ERS-1 satellite," *Proceedings of the IEEE*, vol. 79, pp. 791-799, 1991.

[2] Naderi F. M., M. H. Freilich, and D. G. Long, "Spaceborne radar measurement of wind velocity over the ocean - An overview of the NSCAT scatterometer system," *Proceedings of the IEEE*, vol. 79, pp. 850-866, 1991.

[3] Bartoloni A., C. D'Amelio, and F. Zirilli, "Wind reconstruction from Ku-band of C-band scatterometer data," *Journal of Geophysical Research*, vol. 91, pp. 5153-5158, 1986.

[4] Tzeng Y. C., K. S. Chen, W. L. Kao, and A. K. Fung, "A dynamic learning neural network for remote sensing applications, " *IEEE Transaction on Geoscience and Remote Sensing*, vol. 32, pp. 1096-1102, 1994.

The Application of Artificial Neural Networks and Standard Statistical Methods to SAR Image Classification

Barbara M G Ghinelli and John C Bennett

University of Sheffield, Department of Electronic & Electrical Engineering, Mappin Street, Sheffield S1 3JD, UK
+44(0)114-22-25582, Fax: +44(0)114-272-2097, B.Ghinelli@iee.org
+44(0)114-22-25839, Fax: +44(0)114-272-2097, J.C.Bennett@Sheffield.ac.uk

Abstract -- In order to fully utilise SAR techniques, it is important to employ classification schemes which can discriminate between surface cover types having closely related statistics. A hybrid method, consisting of statistical textural measures and radial basis function (RBF) neural networks, is proposed for this problem. Imagery obtained for areas of South American rain forest are employed for this study and standard statistical techniques are used as a benchmark for comparison.

A supervised method for training the RBF neural network hidden layer and parameters (e.g. centres, width, etc.) is proposed, based on a minimum-classification-error criterion. This modified RBF network has been applied to the forest data and has been found to outperform standard statistical techniques and the conventional RBF with k-means (or other similar) training method for hidden layer parameters in these classification tasks.

INTRODUCTION

Satellite-borne synthetic aperture radar now provides regular, quantitative, all weather images of the Earth and microwave remote sensing is proving an essential tool for Earth Observation. So far, the majority of approaches have been limited to distinguishing between image classes with quite different statistics. It is therefore important to address the problem of classifying surface cover types having closely-related statistics.

Recent years have seen an increase in the application of artificial neural networks (ANNs) to radar imaging and encouraging results have been reported [1,2,3]. ANNs are able to process a large amount of input information in parallel and generate categorical or generalised output. They can adaptively learn to build non-linear input-output mapping structures specific to a particular problem. Radial basis functions are non-linear layered feedforward neural networks which are capable of implementing arbitrary non-linear transformations of the input space with consistent computational efficiency and learning speed. This paper proposes a new implementation of RBF networks which differs from conventional approaches [4-5]. It adopts a minimum-classification-error criterion to train the hidden layer parameters of the network in a supervised manner. The technique is applied to a series of SAREX images obtained from the banks of the River Tapajos in the Tapajos National

Park. The Grey-Level Co-occurrence Matrix [6-7] is used to reduce the data by extracting 12 textural features from 3 different data sets, each of 300 image sections selected from the original SAREX data. The probability density functions of the resulting features are computed for each set of images and the complexity of the data is assessed by means of the probability of error between each corresponding feature. The same data is used as input to a logistic regression classifier [8] which provides a benchmark comparison for the ANN. Finally, the radial basis function neural networks, with both conventional and newly implemented training procedures, are applied to the two sets of images whose statistical features are highly overlapping and the performances of the various methods are compared.

EXTRACTION OF TEXTURAL FEATURES

Grey-level Co-occurrence matrices (GLCMs) describe texture by means of computational processing for various angular relationships and distances between neighbouring resolution cell pairs of a given image. Haralick et al. [6] assumed that texture-context information is specified by the matrix of relative frequencies P_{ij} with which two neighbouring resolution cells separated by distance d, positioned at an angle a, occur on the image, one with grey tone i and the other one with grey tone j.

The GLCM technique was implemented in Fortran software, which was fully tested and applied to 3 sets of 300 128x128 images selected from the original SAREX data of the Tapajos National Park. Each set represented a different surface cover: the lower level forest near the river Tapajos [Fig.1(a)], the Terra Firme forest [Fig.1(b)] and non forest data [Fig.1(c)] (for convenience, hereafter described respectively as set1, set2 and set3).

For each image, twelve textural features were generated according to the equations defined by Haralick. For subsequent processing, the correlation between features was calculated, together with the pdf of each feature. These distributions were plotted and compared for each corresponding feature of the 3 image sets. The misclassification percentage of each pair of pdfs was calculated as the probability of error between the two distributions. This gave an approximate measure of the classification accuracy that could be achieved by standard statistical techniques.
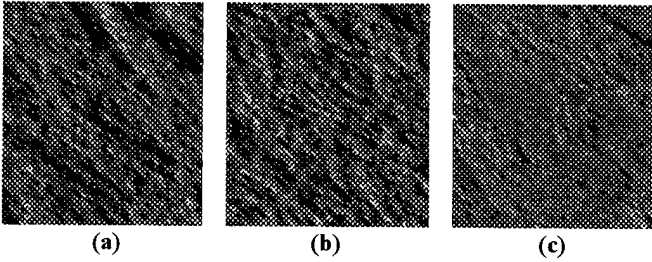
Fig.1. - Typical images respectively representing the three data sets: (a) the lower level forest; (b) the Terra Firme forest and (c) the non-forest data.

It was observed that the pdfs of set1 and set2 were highly overlapping, but each differed significantly from the pdfs of set 3. As an example, the probabilities of error between the SA distributions of set1/set2 , set1/set3 and set2/set3 are respectively: 51.8%, 21.8% and 23.9%.

LOGISTIC REGRESSION ANALYSIS

Logistic regression (LR) is a multivariate technique for directly estimating the probability of an event occurring and in this application, the 12 sets of features of each image class were used as the independent variables of the LR model of the SPSS Windows package. As expected, in accordance with the probability of error results, set1/set3, and set2/set3 could be perfectly distinguished, unlike set1/set2 that only provided 79.3% and 80.7% classification accuracy on training and test data respectively.

The Wald statistics option was selected from the SPSS LR command window, in order to assess the contribution of each feature to the correct classification percentage of the data. The resulting values were very close to those already calculated with the probability of error, for example the SA feature gave 49%, 78% and 76% accuracy on the training data for set1/set2, set1/set3, and set2/set3 respectively, thus demonstrating the reliability of the LR method. The Wald statistic had also been used to select the most meaningful features for the classification of the two sets of forest data, since some of the 12 features could mislead the classification performance if not relevant with this investigation.

RADIAL BASIS FUNCTION NEURAL NETWORKS

Radial basis functions are feedforward neural networks with an input layer, a single hidden layer and an output layer. The input layer is made up of source nodes (sensory units). The hidden layer consists of a number of RBF nodes, with simple kernel functions. Each layer is fully connected to the following one. The input data does not go through complex and time consuming multi-hidden layer expansions, therefore RBF networks result in great training speed and application flexibility. Each hidden node evaluates a radial

basis function on the incoming input and the classifier output is simply a weighted linear summation of these functions.

The network can be configured with one radial basis function centre at each training data point. However, to minimise the complexity of the network it is convenient to reduce the number of centres. For this purpose, a variety of approaches have being developed [4,5]. The *K-means clustering algorithm* was applied to the two data sets of the South American rain forest, in order to select the centres of the radial basis functions, and their width was fixed. The output layer used a single perceptron and its weights were calculated using the iterative least mean square algorithm

The network was trained for 50 cycles with 70 hidden nodes and the width was set to be 60% of the minimum distance between the basis function centres. This network classified the training data with 81.7% accuracy, but only gave 66.4% classification accuracy for test data.

A NEW SUPERVISED RBF NEURAL NETWORK

The accuracy of RBF networks can be improved if supervised learning of the function centres is used. A new supervised algorithm was developed. This uses a minimum-classification-error criterion to select the best centres directly from the input data and determines the optimum weights of the output layer by means of Wiener-Hopf simultaneous equations.

The algorithm starts with only one hidden unit. The training sample that gives the minimum classification error is selected as the first centre of the RBF network. Then, at each subsequent cycle an unpicked sample, c_u, is selected as a new centre, $c(n+1)$, and added to the network, if it, together with the previously selected centres, c_p, gives the best performance. When overlearning occurs, the performance of the network stops improving, as shown in Fig.2. In this way the algorithm also finds the optimal number of centres that the RBF network should contain. This algorithm can be mathematically expressed as in (1), when applied to N data samples, x_p, whose desired output, d_p, can be either 1 or 0.
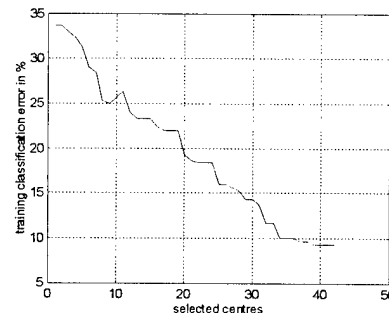
Fig.2 - The curve of classification error vs number of selected centres during training.

At step $n + 1$, for $n = 0,1,...,N$ and $K = n+1$:

$$c(n+1) = \arg\min_{u \in \{N\} - \{n\}} \sum_{j=1}^{N} \left\| d_j - \varphi\left[\sum_{p=0}^{n} w_p(n+1) * \Phi_p(x_j, c_p, \sigma) + \right.\right.$$

$$\left.\left. + w_{n+1}(n+1) * \Phi_{n+1}(x_j, c_u, \sigma) - \lambda\right]\right\| \quad (1)$$

where, $w_0(n+1)$ is the bias weight, $\Phi_0(\cdot) = 1$, $w_p(n+1)$, for $p = 1,2,...,(n+1)$, is the *pth* output weight, using c_p and c_u and finally $\varphi[\cdot]$ is a unit function, so that:

$$\varphi[\cdot] = \begin{cases} 1 & \text{if } [\cdot] > 0 \\ 0 & \text{otherwise} \end{cases}$$

The initial width, σ, and threshold, λ, used in the above method, are both set to 0.5. Once the RBF centres have been selected, the width and threshold can be varied in order to find their optimal values.

The newly developed RBF software was applied to the two sets of forest data of the Tapajos Park. The resulting optimal RBF network consisted of 39 hidden units and a width fixed at 0.5. It consistently outperformed both common RBF networks and traditional statistical techniques, achieving 90.7% and 87.4% classification accuracy on training and test data respectively. Furthermore, the similarity of these two values shows a very good generalisation ability, which makes this network very reliable.

The classification performances of the above described statistical and neural network techniques are summarised in Table 1.

Table 1 - Comparison of the results for the three classification techniques employed

Classification Method	Training Data Classification Accuracy	Test Data Classification Accuracy
LR	79.3%	80.7%
K-means RBF	81.7%	66.4%
New RBF	90.7%	87.4%

CONCLUSIONS

This paper has introduced a new approach to the classification of imagery with closely related statistics. Both standard statistical techniques and neural networks have been applied to two sets of forest data and one set of non-forest data. Logistic regression, the statistical technique, gave a high accuracy on the classification of forest data and non-forest data, but it only gave average results for the two sets of forest data. However, this result could be consistently

improved by means of a newly developed RBF network. This new RBF algorithm trains the network in a supervised manner by means of a minimum-classification error criteria. Also, it was found that image textural information is an appropriate classification measure in this application. In particular, the GLCM technique extracted meaningful textural features used as inputs to the network classifier, reducing in this way the dimensionality of the problem.

Future work will involve the use of this classification system to sets of high resolution imagery acquired by means of the ground based polarimetric SAR , developed in the Communications and Radar Group at Sheffield University. These imagery will represent a crop in three different stages of growth and the ability of the network classifier to distinguish between the three different conditions will be assessed.

ACKNOWLEDGMENTS

REFERENCES

[1] C. J. Oliver; R.G. White; "Real-Time SAR change detection using Neural Networks," Proc. of SPIE - The International Society for Optical Engineering, vol. 1348, pp. 40-50, 1990.

[2] J. V. Geaga; T.C. Le; C. T. Saller; "Neural net spectral pattern recognition," Proc. of SPIE - The International Society for Optical Engineering, vol. 1766, pp. 609-18, 1992.

[3] C. M. Bachmann, S.A. Musman; A. Schultz; "Classification of simulated radar imagery using Lateral Inhibition Neural Networks," Neural Networks for Signal Processing II, Proc. of the IEEE-SP Workshop; pp. 279-88, 1992.

[4] Christopher M. Bishop; "Neural Networks for Pattern Recognition," Oxford University Press, pp. 165-191, 1995.

[5] John Moody, Christian J.Darken; "Fast Learning in Networks of Locally-Tuned Processing Units," Neural Computation 1; pp. 281-294; 1989

[6] R. M. Haralick; "Textural Features for Image Classification," IEEE Trans. on Systems, Man and Cybernetics, vol. SMC-3, NO. 6, pp. 610-620, November 1973.

[7] R. C. Gonzalez; P. Wintz; "Digital image processing," Reading, Mass.: Addison-Wesley, chap. 5, pp. 414-417, November 1987.

[8] David W. Hosmer, "Applied Logistic Regression," New York; Chichester; Wiley, c1989.

First Airborne Tests with the new VHF SAR CARABAS II

A. Gustavsson, B. Flood, P.-O. Frölind, H. Hellsten, T. Jonsson,
B. Larsson, G. Stenström, and L.M.H. Ulander
Defence Research Establishment (FOA)
P.O. Box 1165, S-581 11 Linköping, Sweden
Phone: + 46 13 31 80 00, Fax: + 46 13 31 81 00, E-mail: andgus@lin.foa.se

Abstract -- The first airborne experiment with a new upgraded VHF SAR system was carried out in October 1996. A very flat island was selected as the test area to minimize the influence from the topography and facilitate the calibration and system analyses. Data acquired over the area with this new sensor, CARABAS II, have successfully been processed. The major problem encountered concerns large paired-echo sidelobes. To improve the image quality, a careful system analysis has been carried out to obtain correction coefficients for the signal processing to compensate the overall amplitude and phase ripple. The results presently available indicate resolution figures somewhat lower compared to the theoretical values. It is believed that the main explanation for the found performance degradation is insufficient information of the antenna characteristics and the measures currently taken for the radio frequency interference filtering.

INTRODUCTION

A unique airborne SAR system, CARABAS (Coherent All RAdio BAnd Sensing), has been developed at FOA. It is designed for operation in the lowest part of the VHF-band (20-90 MHz), using horizontal polarisation, and provides a spatial resolution of wavelength. The longer wavelengths adopted give the system a potential to penetrate the surface top layers and hence retrieve information in foliage and below ground. This opens new applications for imaging radar.

The first generation of the system, CARABAS I, has been available since 1992. Radar data have been gathered for environments ranging from rain forests to deserts, most often simultaneously with other airborne SAR sensors. The results indicate that a VHF SAR sensor combines a low two-way attenuation value with a low foliage backscatter coefficient, also for very dense forests [1, 2]. This is favourable in many applications, e.g. highlighting concealed targets or increasing the non-saturated interval in biomass estimation.

The reduced clutter levels are obtained at moderate resolutions (or ultimately in the order of the wavelength), which implies that the surveillance capability is higher for a VHF system. Man-made targets are detected by resonant reflectors, or equivalently by their reflectivity strength, rather than detection by shape against a severe clutter background as for high resolution UHF and microwave SAR systems. The resonance effects means also that VHF is a countermeasure against stealth-designed objects. The handling and dissemination of data are in general a bottleneck independently of the sensor system. A VHF SAR to screen large areas, combined with some high resolution SAR or optical imaging instrument for classification of detected potential targets, is thus an attractive reconnaissance concept.

Realization of a new upgraded VHF SAR sensor, CARABAS II, was approved based on the promising results obtained with the first airborne testbed. The used frequency interval is the same for the CARABAS II sensor, i.e. 20-90 MHz. These figures are still about ten times lower than comparable airborne experimental systems in operation or under development in USA, Russia, Germany, Ukraine and South Africa.

The upgraded sensor has been developed as a joint project between FOA and Ericsson Microwave Systems AB (EMW). The hardware was fully assembled in 1996. A final approval of the airworthiness for the redesigned antenna arrangement was given, and the first airborne radar imaging test took place in October 1996. This initial test will here be summarized and some processed CARABAS II images presented.

CARABAS II

The main modifications in CARABAS II include a new antenna design with improved gain pattern and a delay line for beam pointing, dual 14-bit 2 MHz receivers to double the instantaneous bandwidth with an increased dynamic range, and finally a new digital waveform generation [3]. Large time-bandwidth transmit signals will increase the duty factor for high altitude operations and the long signal duration enables narrow transmit notches for frequency cohabitation. Linear FM and uniform/non-uniform stepped frequency waveforms are examples that can be defined and downloaded into the signal memory in a flexible manner. In parallel to the hardware development, a new processing scheme, local backprojection, has been derived and is currently being implemented on a multi-processor system to improve the overall computation performance [3].

The design goals for the new antenna concept developed were to maintain a dipole character of the radiation pattern and the VSWR below 3:1 over the frequency range 20-90 MHz. The realization found and optimized is a loaded wire conical antenna [4]. The conical structure was chosen since it has a natural broadband behaviour. Furthermore, the antenna should not exceed the dimensions of a 4.9 m long and 0.2 diameter tube. The size limits stem from aerodynamic restrictions found from simulations with the antenna carried in the nose of a small business jet aircraft, a Sabreliner.

THE TEST SITE

The test area used for the initial imaging trials was the northern part of an island, Visingsö, located in a fairly large fresh water lake in southern Sweden. The island is approximately 14 km long, oriented south-west to north-east, and between 600 m to 3 km wide. The site was selected since it exhibits environments appropriate for calibration and system analyses. Visingsö is very flat, i.e. effects from the topography are negligible. The area consists mainly of agricultural land with houses, farming buildings and some isolated clumps of trees. One major forested part is found in the middle section of the island. Thus an area predominantly very smooth for CARABAS wavelengths. Furthermore, a calm water surface on the opposite side of the aircraft reduces any remaining influence from the right/left separation ambiguity. Four 5 m trihedrals were deployed within the test area at different distances in range, on open fields and on a local airfield. See also Fig. 1.
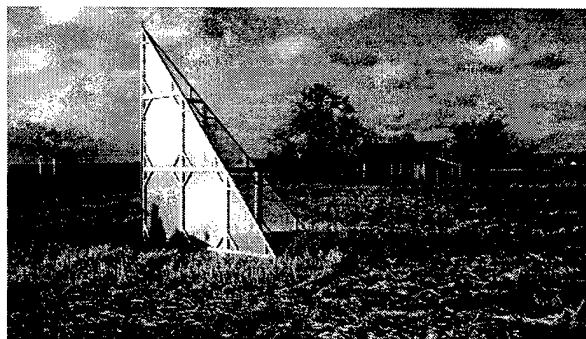
Fig. 1. A 5 m trihedral corner reflector set up in the open on the island Visingsö. The agricultural landscape is very flat with many small houses and farming buildings. Two large white poles, giving support to wind-power stations, can barely be seen in the distant to the far left.

Four SAR registrations were carried out from an altitude of about 2 100 m. The aircraft heading specified was along an east-west line, with the broadside illumination of the island pointing from the north. Restrictions on altitude and synthetic aperture length were imposed during this first flight mission due to severe interference on the aircraft radio caused by the radar transmission, and this also limited the tests with different signal waveforms. The interference problem has later on been solved by introducing a filter in the transmitter unit.

The base station for the differential GPS system, used to collect data for the motion compensation processing, was deployed at a dedicated position on the island also found in the Swedish Land Survey reference system. Close to the experiment, the island was imaged by aerial photography to facilitate the interpretation and analysis of the CARABAS II radar images. Moreover, the northern part has also been mapped by the SAR sensors available during the second SIR-C/X-SAR mission in October 1994. For SIR-C, the polarizations HH and VV were co-registered for both C-band and L-band. Fig. 2 shows SIR-C images of Visingsö.
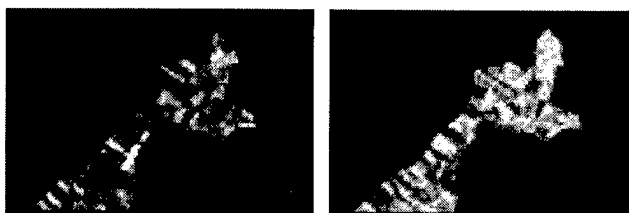
Fig. 2. Northern part of the Visingsö island from the SIR-C instrument, L-band to the left and C-band to the right. The illumination is opposite to the CARABAS II registrations, i.e. from the bottom or south (courtesy: NASA/JPL).

EXAMPLES OF IMAGERY

It has been possible to process SAR images based on this first acquired set of radar raw data. Preliminary analyses have shown that the system provides SAR data with uniform quality across the full 70 MHz bandwidth, which was not the case with CARABAS I. The antenna gain pattern is smoother and no Doppler aliazing occurs. Leakage problems in the switching network has been noticed and initially a slightly higher system noise than expected was measured. Degradation from paired-echo sidelobes due to periodic amplitude/phase ripple was also found, cf. Fig. 3. The full transmitted bandwidth is realized by a stepped frequency waveform and the ripple is introduced when the individual sub-bands are resampled and aligned to reconstruct the full spectrum in the pulse compression. The measured resolution figures are somewhat lower compared to the theoretical values and will require a refined characterization of the amplitude and phase behaviour in the system over the full frequency band.

Fig. 3. Example of an early output from the SAR processing of the Visingsö data set. The paired-echo effect is clearly visible for major scatterers and generates false bright spots in range centred around the true response. The three very bright pixel locations correspond to wind-power stations.

The impact and sensitivity from the ripple have recently been studied in detail, including dedicated measurements on the radar units in the laboratory, to find appropriate correction procedures in the signal processing where applicable, and hence improve the image quality [5].

Fig. 4 shows the result when a correction scheme has been included in the processing, giving a considerable improvement in the image quality. In comparison with the microwave images in Fig. 2, the cultivated fields are almost invisible for the long CARABAS wavelengths, except for ditches or fences with an orientation not too far from the azimuth direction. Typical man-made targets give a strong return, e.g. houses, farming buildings, wind-power stations but also power cables with an appropriate orientation. Large-scaled natural objects, like trees, are also visible in the images. The shoreline is depicted depending on its steepness and the integrated aperture angle.

SUMMARY

The first field campaign with CARABAS II has been carried out and the gathered raw data had a quality good enough to generate radar images. The preliminary results indicate resolution figures somewhat lower compared to the theoretical values. It is believed that the main explanation for the found performance degradation is insufficient information of the antenna characteristics and the measures currently taken for the radio frequency interference filtering.

The large amount of data that now easily can be collected with the system emphasizes the need of developing models for VHF radar backscattering. Some of this work have started, focusing on forest backscatter mechanisms.

REFERENCES

[1] B.T. Binder, M.F. Toups, S. Ayasli, and E.M. Adams, "SAR Foliage Penetration Phenomenology of Tropical Rain Forest and Northern U.S. Forest," Proc. IEEE International Radar Conference, Alexandria, VA, 8-11 May 1995, pp. 158-163.

[2] A. Gustavsson, et al., "The Experimental Airborne VHF SAR Sensor CARABAS. A Status Report," Proc. IGARSS´96, Lincoln, NE, 27-31 May 1996, pp. 1877-1880.

[3] H. Hellsten, L.M.H. Ulander, A. Gustavsson, and B. Larsson, "Development of VHF CARABAS II SAR," Proc. Radar Sensor Technology, Orlando, FL, 8-9 April 1996, pp. 48-60.

[4] J. Westerling and L.G. Andersson, "Design of a Broadband Loaded Antenna Element for Use in a VHF-UWB Airborne Radar," to be presented at Antenn 97, Göteborg, Sweden, 27-29 May 1997, (9 pages).

[5] L.M.H. Ulander, et al., "Analysis of CARABAS VHF SAR Data from BALTASAR-96," to be presented at IGARSS'97.
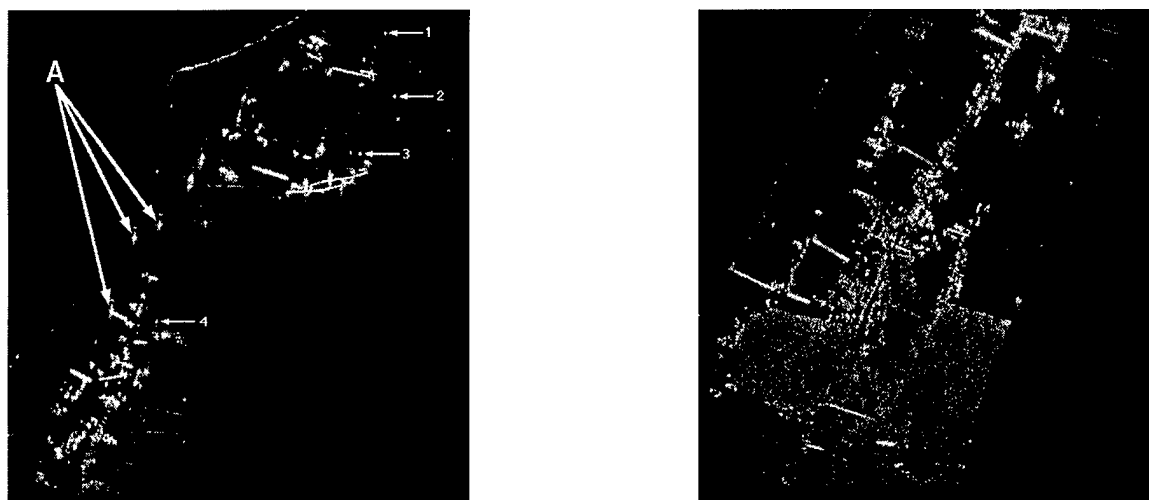
Fig. 4. CARABAS II images of the northern half of Visingsö, each covering about 16 sqkm. The northernmost part (left) has been processed using the frequencies 29-45 MHz. The incidence angle varies between 54°-73° and the aperture angle is 77° at the centre. The adjacent image to the south (right) has also been processed between 29-45 MHz and the corresponding angles are 73°-79° and 48°, respectively. On the southernmost image the major forested area on the island can be identified as the large grey area in the lower part. The numbered arrows show the location of the trihedrals, where 3 corresponds to Fig. 1 with the small house to the left. The label A pinpoints the wind-power stations. The measured resolution figures from the trihedral responses are approximately 10 m in range and 4 m in azimuth, respectively.

RADARSAT-1 Background Mission for a Global SAR Coverage

Ahmed Mahmood
Canadian Space Agency
6767 route de l'aeroport, Saint-Hubert, Quebec, Canada J3Y 8Y9
Tel: (514) 926-4432, Fax: (514) 926-4433, E-mail: Ahmed.Mahmood@space.gc.ca

Abstract -- RADARSAT-1 Background Mission is the first attempt ever to acquire uniform global synthetic aperture radar (SAR) data in various seasons and imaging modes. A multi-mode global coverage is made possible by making use of the flexible imaging parameters of the satellite and its real-time as well as on-board recording capabilities. Synoptic, continental scale coverages alongwith local time-sensitive and application-specific data collections are planned. All data acquired under Background Mission are archived and, like the archives of any other RADARSAT-1 data, are accessible to the user community for its scientific and operational needs. RADARSAT-1 Background Mission started with the commencement of normal satellite operations in April 1996. This article reports on the progress made so far in the first two coverages of the world, one with the ScanSAR Wide and the other with the Standard 7 imaging beams of RADARSAT-1 SAR.

INTRODUCTION

Canada's RADARSAT-1 is the first synthetic aperture radar (SAR)-bearing remote sensing satellite with variable imaging parameters that result in ground resolution from less than 10 metres to about 100 metres and imaging swath width range of 50 km to 500 km. These parameters are therefore ideal for broad regional studies of the Earth's features as well as for localized viewing of ground targets. The satellite's orbital characteristics, operational modes, on-board tape recorder and ground data receiving stations, described in detail elsewhere [1] and [2], make it possible to image most of the globe. A global coverage mission, called Background Mission [3], was therefore started to make use of the multiple advantages associated with RADARSAT-1 imager. The mission has several objectives.

One of the objectives is to accomplish a rapid overview of the Earth using wide coverage ScanSAR beams. The data sets can be used to demonstrate the value of RADARSAT mission for remote sensing applications. The other objective is to provide a global stereo data base. Over the past several years, radargrammetry has emerged as a rigorous science and has been used to produce maps, digital map products and digital elevation models with satellite SAR data. The global stereo acquisitions ensure that data are available to cartographers and value-added companies that may wish to supply these products.

A final rationale for Background Mission is to create a data bank of time-sensitive, application-specific acquisitions of the regions of the world where RADARSAT-1 has a high potential of use in view of its orbit pattern and multi-mode imaging capabilities. Examples of time-sensitivity are ocean phenomena, flooding, volcanism, seismicity, etc., where a time series analysis of data is considered valuable for studies like prediction modelling and weather changes. These data are primarily for research purposes.

The final phase of RADARSAT-1 Background Mission coverage will emphasize monitoring of global dynamic phenomena and will cover special geophysical elements. The areas of interest are world's major flood plains for seasonal mapping of flooding, changes in river courses and other fluvio-morphological processes; converging plate margins characterized by young mountain chains and strong seismic and volcanic activity causing geohazards; island arc system coastal zones; and rain forests where the all-weather imaging capabilities of RADARSAT-1 are particularly well suited to support science objectives of environmental monitoring and verification of international protocols regarding sustainable development and biodiversity. This coverage will also result into special data sets for agriculture, forestry and mapping applications.

Contrary to other spaceborne radars, the variable incidence angle and ground resolution obtained with RADARSAT-1 permit the user to select the imaging parameters adapted to the local topography and the purpose for which data are collected. Therefore, the selective data bank will also include those regions of the world which may be missed during the earlier, more general ScanSAR and Standard beam coverages due to shadowing, layovers, low ground resolutions and untimeliness of the acquisition.

COVERAGE

Several Background Mission coverages are planned for the entire operational life of RADARSAT-1. The following is a brief definition and acquisition status of the coverages undertaken so far.

Continental and Polar ScanSAR Coverage

The first is a wide area, four-season ScanSAR Wide B coverage of world's continents, continental shelves and polecaps, which is expected to result in sufficient contingency data sets early in the RADARSAT mission. The synoptic view of the Earth in different seasons should provide the maximum contrast of terrestrial vegetation over most of the world. It should furnish the separation of the small vegetation signal from the large landform background.

Initially, the coverage was carried out with real-time acquisitions over North America within the reception masks of the two Canadian receiving stations at Gatineau (Quebec) and Prince Albert (Saskatchewan), but as the on-board tape recorder and, later, the international network of receiving stations at West Freugh

(U.K.), Tromso (Norway) and Singapore became operational, a worldwide ScanSAR coverage was made possible. Fig. 1 represents the total coverage reached so far. This includes complete summer coverages of North America and Australia and autumn coverage of Europe (see table 1). Globally, the world coverage is 51% complete. This ScanSAR coverage can serve in future to create regional or continental mosaics, and with this in mind a minimum of 15% to 20% overlap between adjacent swaths was maintained wherever possible.

Continental Stereo Coverage

This coverage is undertaken in fulfilment of RADARSAT mission requirement for providing a global stereo data set of the world's landmass by means of two different Standard beams. The first coverage in the stereo pair is carried out with Standard 7 beam of RADARSAT-1. Coverage with Standard 7 beam is undertaken first in order to secure quickly the advantages associated with this beam. Because of its shallow incidence angle, Standard 7 causes least geometric distortion of image data. Generally speaking, there is better thematic information to be obtained at shallower incidence angles. The choice of other beam in the stereo pair will fall on the RADARSAT Standard 2 in view of parallax requirements in the pair as well as the lower susceptibility of this beam to shadowing in areas of high relief.

After completing the ScanSAR Wide B coverage of North America and Europe, the real-time Standard 7 coverage of these continents started in late summer and has continued since then. Globally this coverage is 21% complete (Fig. 2 and table 1). Certain areas in these continents have been already fully covered. These are Greenland, western Europe, and Canada excluding the High Arctic regions.

Table 1.   Summary of Background Mission coverage

Region	ScanSAR Wide B (% completion)	Standard 7 (%completion)
North America	100	80
Europe	100	63
Africa	37	1
Australia	100	2
Indochina and Indonesia	67	20
Total world	51	21

CONCLUDING REMARKS

As RADARSAT-1 starts the second year of its operations, the priority for Background Mission is to acquire rapidly one complete ScanSAR coverage of the world by means of the on-board tape recorder. Following the completion of the first global ScanSAR coverage, regional coverages in different seasons will start.

The Standard 7 coverage will continue in the real-time data receiving station masks. As more and more international receiving stations are brought on line to provide real-time imaging opportunities, Background Mission acquisitions will be accelerated. Until such time, the mission will have to rely on the on-board tape recorder, which is a limited resource shared among all the different RADARSAT-1 data users.

Background Mission is a major undertaking which is likely to last the entire operational life of the RADARSAT-1 satellite and is expected to generate a data wealth which can be exploited in future for various scientific, economic and operational purposes.

ACKNOWLEDGMENTS

Thanks are due to Dr. Surendra Parashar of RADARSAT Program, Canadian Space Agency, for his review of the paper.

REFERENCES

[1] S. Parashar, E. Langham, J. McNally, and S. Ahmed, "RADARSAT mission requirements and concept," Canadian J. Remote Sensing, vol. 19, no. 4, pp. 280-288, November-December 1993.

[2] A. Mahmood, S. Carboni, J. Muller, and S. Parashar, "Potential use of RADARSAT in geological remote sensing," Proceedings of the Eleventh Thematic Conf. Geological Remote Sensing Las Vegas, Nevada, pp. I-475-I-484, 27-29 February. 1996.

[3] A. Mahmood and S. Parashar, "RADARSAT Background Mission," RADARSAT for Ice and Oceans, Early Experience and Data Access, The 6th Workshop of the Canadian Ice Working Group, 3p, November 19-21, 1996.
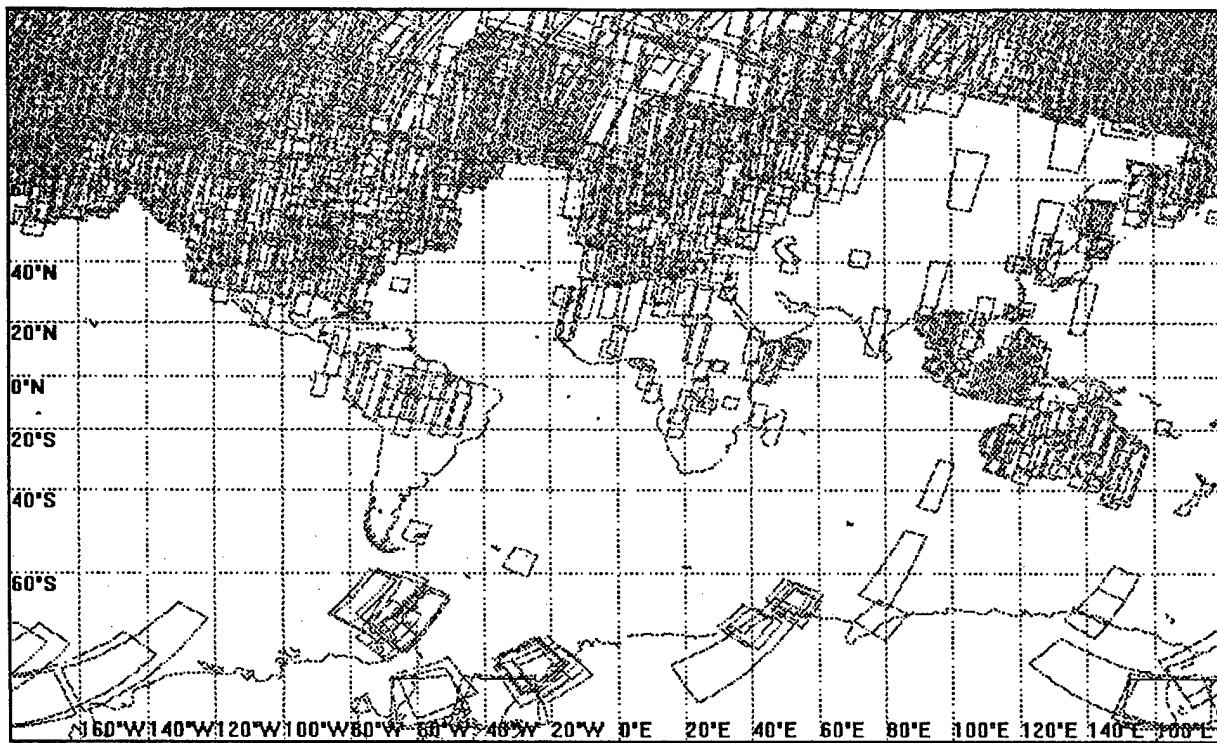
Fig. 1. World ScanSAR Wide B Coverage
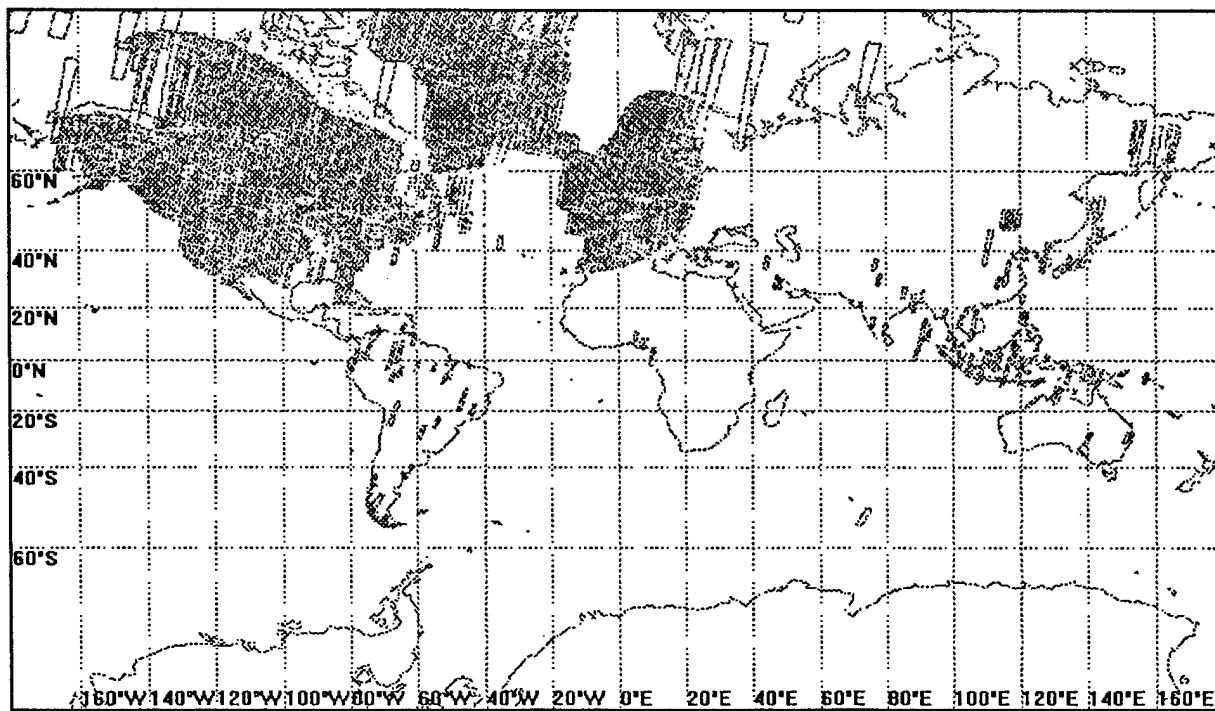
Fig. 2. World Standard 7 Coverage

The MODIS BRDF/Albedo Product: Prototyping Albedo Retrieval Using AVHRR and GOES

A. Strahler,[1] R. d'Entremont,[2] W. Wanner Lucht,[1] B. Hu,[1] X. Li,[1] and C. Barker Schaaf[1]

[1]Center for Remote Sensing, Boston University,
725 Commonwealth Avenue, Boston, MA 02215 USA
Voice: +1 617 353 5984, Fax: +1 617 353 3200
E-mails: alan, wanner, baoxin, lix, and schaaf @bu.edu

[2]Atmospheric and Environmental Research, Inc.
840 Memorial Drive, Cambridge, MA 02139 USA
Voice: +1 617 377 2983, Fax: +1 617 377 9638
E-mail: rpd@aer.com

Abstract*— Directional data acquired by both the MODerate resolution Imaging Spectroradiometer (MODIS) and the Multiangle Imaging Spectroradiometer (MISR) on NASA's Earth Observing System (EOS) will be used to produce a global bidirectional reflectance distribution function (BRDF) and albedo product once every 16 days. The product will be derived using the kernel-driven semiempirical Ambrals BRDF model, utilizing five variants of kernel functions characterizing isotropic, volume and surface scattering. The BRDF and the albedos of each land surface pixel will be modeled at a one kilometer spatial resolution in seven spectral bands spanning the visible and the near-infrared.

As a prototyping activity, we assembled a 16-day sequence of AVHRR GAC 1-km data in red and near-infrared bands and GOES 1-km data in the visible band and applied the Ambrals model to fit BRDFs and calculate albedos for the New England region of the USA. The resulting fine-resolution albedo map shows strong spatial detail primarily related to the land covers of the region. Urban and suburban regions show BRDFs dominated by geometric-optical scattering, while multiple scattering is more important in BRDFs fitted to forested areas.

INTRODUCTION

The earth's surface scatters radiation anisotropically in many wavelength regimes. The Bidirectional Reflectance Distribution Function (BRDF) specifies the behavior of surface scattering as a function of illumination and view angles at a particular wavelength. The albedo of a surface describes the ratio of radiant energy scattered upward and away from the surface in all directions to the downwelling irradiance incident upon the surface. Like the BRDF, albedo is spectrally dependent. If the BRDF is known, the albedo can be derived given knowledge of the atmospheric state.

As a part of the Earth Observing System, we will provide a global BRDF/Albedo product using the MODIS and MISR instruments on the EOS AM-1 platform, scheduled for launch in mid-1998. The purpose of the MODIS/MISR BRDF/Albedo product is (1) to describe the anisotropic reflectance of the earth's surface at a fine spatial and temporal scale by fitting models of the bidirectional reflectance distribution function to angular observations; and (2) to provide two surface albedo measures, "black-sky" albedo, or directional-hemispherical reflectance, and "white-sky" albedo, or bihemispherical reflectance, that allow quantification of the balance in upwelling and downwelling surface energy fluxes also at fine spatial and temporal scales.

Albedo is a fundamental parameter for global climate modeling, since it is a function that drives much of the energy flux at the land boundary layer. Black- and white-sky albedos, as pure surface properties, can be used with any atmospheric specification to provide true surface albedo as an input to regional and global climate models. Fine-grained global maps of land surface albedo will be extremely useful to regional climate modelers, and, given the way that our algorithm specifies BRDF and albedo, such maps can be easily collapsed to the coarser resolutions that global climate models can ingest directly.

This paper presents some brief results of a recent study [1] to retrieve surface BRDF and albedo measures using existing sources of satellite data in the pre-MODIS/MISR era. These include the Advanced Very High Resolution Radiometer (AVHRR) in visible and near-infrared bands (0.565-0.695 μm, 0.75-0.97 μm) and the GOES (Geostationary Operational Environmental Satellite) Imager visible band (0.52-0.72 μm). Here we present results for AVHRR red and GOES visible bands only.

RESEARCH DESCRIPTION

The remotely sensed database for this study consisted of AVHRR (NOAA-14) HRPT and GOES-8 observations for the New England region of the northeastern United States (40.6° N to 44.2° N lat., 74.6° W to 69.7° W long.) during late August to mid-September, 1995. AVHRR data, consisting of 15 usable scenes during the 17-day period September 2–18, were (1) radiometrically calibrated using data of Rao

and Chen [2]; (2) initially mapped to a 0.75 km (east-west) by 1.1 km (north-south) grid using orbital ephemeris information; then (3) reregistered using first-order polynomials with a residual error of about 0.4 km. To assure cloud-free data, eight tests were performed using the full range of AVHRR channels to remove cloud-contaminated pixels [3]. These included an adjacency test to remove pixels adjacent to clouds and shadows.

GOES Imager data from the visible band were acquired hourly for 1315-2015 UTC from August 25 through September 6. Calibration was based on an estimate of 16 percent loss in responsivity from May 1994 to September 1995 (M. Weinreb, personal communication to R. d'Entremont). Data were cloud-cleared using the temporal differencing technique of d'Entremont et al. [4] and registered to the New England grid. Fig. 1* maps the number of looks available in the dataset for combined AVHRR red and GOES visible bands. Nearly all pixels have at least seven cloud-free looks, a number deemed sufficient for inversion and fitting of a BRDF model.

Both AVHRR and GOES data were atmospherically corrected using MODTRAN [5] and 6S [6] radiative transfer codes driven by surface visibility observations from within the region.

The MODIS-MISR BRDF/Albedo product fits BRDFs to each pixel using the Ambrals model [7]. Here, the BRDF is modeled as a weighted sum of a constant and two trigonometric functions of view zenith, illumination zenith, and relative azimuth angles. The functions are referred to as "kernels." One kernel is derived from approximations to volume-scattering radiative transfer models, while the other is derived from surface-scattering theory. For the current work, we employ two choices of volume-scattering kernels (Ross-thin and Ross-thick) and two choices of surface-scattering kernels (Li-sparse and Li-dense) [7]. From the four possible combinations, the algorithm uses the combination associated with the lowest root mean squared (RMS) error as fitted to the available observations. Outputs include the kernel pair selected and three weights—a constant, representing the weight of isotropic scattering, and two values that describe the weights assigned to each kernel for the least squares solution. Thus, it is the weights of the physically-based kernels that are retrieved, not a set of physical parameters governing the scattering of the surface.

An important consideration in fitting a BRDF model is the angular sampling presented by the observations at hand in both viewing and illumination hemispheres. MISR and MODIS are along-track and across-track sensors, respectively, and so draw on different angular information sources in fitting the BRDF model. Together they can provide a good sample of the viewing hemisphere [8]. With its across-track scanning, the AVHRR instrument is a good analogue for MODIS. Like

MISR, the GOES Imager provides an additional angular dimension, but it is a very different one from MISR. In contrast to the sensors aboard platforms with sun-synchronous orbits, which view the earth with the sun in about the same position each day, the GOES Imager's geostationary orbit images every location from a constant viewing position in the hemisphere, but at many different sun positions. Thus the combination is likely to provide an information content similar to that anticipated for MISR and MODIS.

To explore the relative importance of surface and volume scattering in fitting the directional observations of each pixel, it is possible to calculate and plot a normalized difference between volume and surface scattering weights, termed the NDFI [1]:

$$NDFI = \frac{F_{vol} - F_{surf}}{F_{vol} + F_{surf}}$$

Fig. 2 presents a map of this parameter for the New England scene. In this case, the kernel choice is forced as Ross-thick/-Li-sparse.

The map shows definite geographic patterns that appear to be related to the nature of the surface covers within subregions. The metropolitan areas of Boston, Providence and New York show strongly negative values, indicating the dominance of surface scattering in these regions. These landscapes include many structures that are better modeled by the principles of geometric optics used to derive the Li-sparse kernel than by the principles of volume scattering used to derive the Ross-thick kernel. The dominance of the geometric-optical kernel also extends along major rivers and coastal lowland regions where development is intensive. Positive NDFI values indicate volume scattering, and dominate in areas where forest covers are more or less continuous. These are largely hilly and highland areas where farmlands abandoned early in the century have reverted to a mix of deciduous and conifer forests.

Fig. 3 presents an image of white-sky albedo (bihemispherical reflectance). These values are derived by double numerical integration of each BRDF over all view and illumination angles, and represent the spectral albedo for the case of isotropic illumination (white sky). Urban and suburban regions show albedos that are consistently higher than other regions. The abundance of manmade materials, many of which are brighter in the red band than vegetation, probably accounts for this difference. Hilly and highland areas again contrast with the lowland regions, but with lower albedos. The Adirondack Mountain region, with its many areas of mature forest, is particularly noticeable for its low albedo.

In preparation for the release of our BRDF/Albedo product, we have carried out extensive studies on the accuracies of retrievals of BRDF and albedo given the limitations of (1) angular sampling from earth orbit; (2) the presence of noise in the data; and (3) errors in atmospheric correction of radiances [8]. Although these studies cannot be summarized here, they

---

*Figures are presented in black and white in camera-ready copy, but are shown in color on CD-ROM.

1221

lead us to conclude that the albedo retrievals shown in Fig. 3 are probably accurate to within 10 percent of their true values. Similarly, we conclude that the errors in parameter retrievals on which Fig. 2 is based are probably somewhat higher, producing an uncertainly on the order of about 15 percent.

CONCLUSION

The merging of AVHRR and GOES data has provided the opportunity to test the MODIS/MISR BRDF/Albedo product algorithm on a real dataset with many of the same characteristics that will be encountered with MODIS and MISR data. The result has been the accurate retrieval of both kernel weights, which provide an index to the dominant physical scattering mechanism of the surface, and white-sky albedo, which is a surface property of keen interest in global and regional climate modeling and studies of surface energy balance. These results confirm the appropriateness and utility of the Ambrals algorithm for application to data from the coming EOS era.

REFERENCES

[1] R. P. d'Entremont, Meteorological Applications of Surface Bidirectional Reflectance Distribution Functions Retrieved from Satellite Data. Ph.D thesis, Boston University, Boston, MA, June 1997.

[2] C. R. N. Rao and J. Chen, "Post-Launch Calibration of the Visible and Near-Infrared Channels of the NOAA-14 Spacecraft," Int. Jour. Remote Sens., vol. 17, pp. 2743–2747, 1996.

[3] G. B. Gustafson, R. P. d'Entremont, and R. G. Isaacs, Support of Environmental Requirements for Cloud Analysis and Archive (SERCAA): Final Report. USAF Phillips Laboratory Technical Report PL-TR-96-2224, Hanscom AFB, MA, 71 pp., 1996.

[4] R. P. d'Entremont, G. B. Gustafson, and B. T. Pearson, "Analysis of geostationary satellite imagery using a temporal differencing technique," Proc., 7th Conf. Satellite Meteorol. Oceanog., Amer. Meteorol. Soc., Monterey, CA, pp. 243-246, 6-10 June 1994.

[5] A. Berk, L. S. Bernstein, and D. C. Robertson, MODTRAN: A Moderate Resolution Model for LOWTRAN 7. USAF Phillips Laboratory Technical Report GL-TR-89-0122, Hanscom AFB MA, 1989.

[6] E. Vermote, D. Tanre, J. L. Deuze, M. Herman, and J. J. Morcrette, Second Simulation of the Satellite Signal in the Solar Spectrum (6S), 6S User Guide. NASA Goddard Space Flight Center, Code 923, Greenbelt MD 20771, 183 pp., 1994.

[7] W. Wanner, X. Li, and A. H. Strahler, "On the derivation of kernels for kernel-driven models of bidirectional reflectance," Jour. Geophys. Res., vol. 100, No. D10, pp. 21077-21089, 1995.

[8] Strahler, A. H., et al., MODIS BRDF/Albedo Product: Algorithm Theoretical Basis Document Version 4.0. MODIS Science Team Report, 1996.
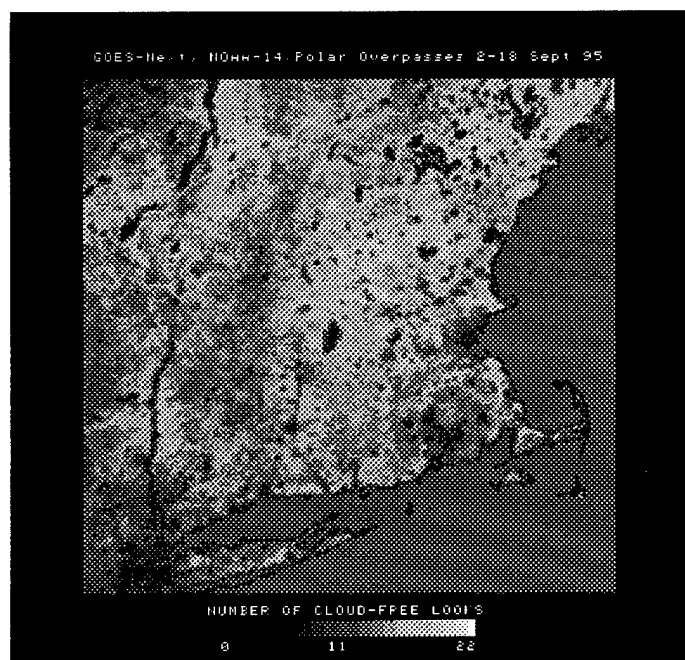
Fig. 1. Map of number of cloud-free looks, New England, combined AVHRR and GOES data.
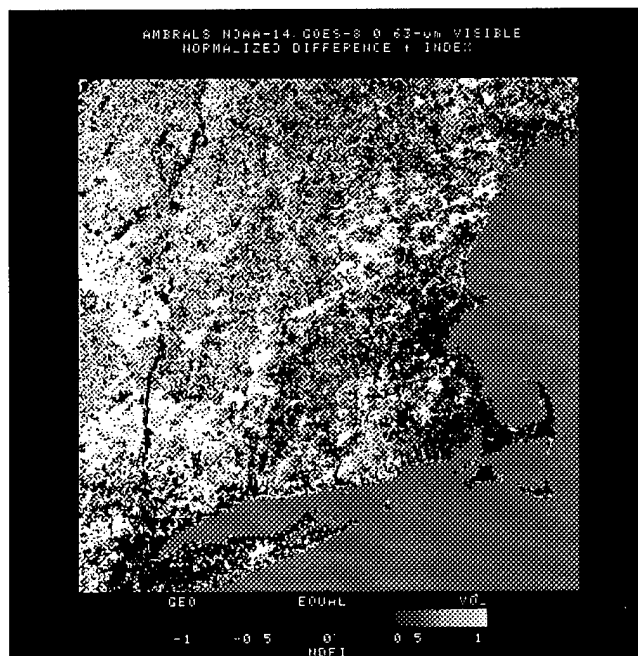
Fig. 2. Map of NDFI values.

1222

Fig. 3. Red-visible white-sky albedo (bihemispherical reflectance) for New England from AVHRR and GOES data.

A cost-effective, airborne video system
for producing rectified, geo-referenced digital images

Martti Kemppinen and Tuomo Auer
Helsinki University of Technology, Laboratory of Space Technology
P.O. Box 3000, 02015 HUT, Finland
Phone: +358-9-451 2370, Fax:+358-9-451 2898, Email: kemppinen@ava.hut.fi

Abstract - - Optical images provide a useful reference for passive microwave radiometer data. The images need not have state-of the-art spatial resolution, but they should include positioning data and be producted and manipulated with ease. The paper introduces the HUT pushbroom video imager consisting of a video camera, frame grabber, controlling PC and optional attitude-DGPS. System calibration and pixel geopositioning are discussed, and an example image is presented.

INTRODUCTION

This paper focuses on finding a sound method to provide optical reference images for microwave radiometer data. Optical images are traditionally used as a reference for the localization and interpretation of airborne microwave radiometer data. This is because of their superior spatial resolution and natural-look output, which is very familiar to a human observer. As a consequence of the spread of relatively cheap and accurate DGPS receivers during the 90's, the localization task is no longer relevant. Furthermore, the scene properties can nowadays often be retrieved more efficiently from GIS-databases, hence reducing the need for optical reference images for interpretating scene properties. However, there are a lot of scene types whose properties vary continuously, for example, sea ice, snow cover and river flood areas, and therefore need simultaneously measured reference data to properly support the microwave measurements. In addition to ground truth measurements, the optical reference images still have an important role in these applications.

Due to the coarse spatial resolution of passive microwave instruments, the optical reference images need not possess state-of the-art spatial resolution. In a snow application, for example, the discrimination of snow-covered and snow-free areas may suffice, while in a typical sea ice application, ice types, cracks and ridges should be distinguished. Our rough estimation is that, depending on the application, the optical image pixel size should be 1/2-1/20 of the radiometer footprint width. This means that the spatial resolution of a VHS video format, 240 horizontal pixels, is typically good enough, while some applications may require S-VHS (420 h. pixels) or DV (Digital Video, 550 h. pixels) resolution. It should be noted that oversized spatial resolution requirements lead not only to higher apparatus cost but also to more expensive and much slower image processing and data storage. Hence, the system requirements should be considered carefully.

IMAGE PRODUCTION METHODS

The highest quality optical images are still produced with the conventional aerial photogrammetry technology that is based on high-end optics, metric cameras and film. The single images are shot with ≈60% overlap to be able to determine the exterior orientation of all of these images employing the bundle block adjustment method. If the scene were flat, the single images could be composed into a mosaic right after the bundle block adjustment. Since it is not, an orthorectification process should be executed with the help of an external elevation model or by detecting more congruent points in consecutive images, preferably prior to the bundle block adjustment [1]. Even if no orthorectification is made, these image mosaics usually become too expensive for microwave radiometer reference purposes, unless the organization already happens to possess aerial photogrammetry capabilities.

For remote sensing purposes, alternative, cheaper methods have been developed. Typically, the very expensive metric cameras have been replaced with relatively cheap video cameras, whose output can be digitized in real time, and the orthorectification is omitted. A good example is the PC-controlled video camera system of the Technical Research Centre of Finland. It has been successfully used by a Finnish forest company, Enso, to inventory the forest resources of Malaysia. In their system [2], frames are digitized with 60% along-track and 20% across track overlap from a flight altitude of 2000 m. For the bundle block adjustment, a few common points are manually detected from consecutive images and the camera position is estimated with GPS data. No orthorectification is performed. The video camera is a 2/3" 3-CCD S-VHS camera with 16 mm focal length optics, and the system yields 1m × 1m spatial resolution on ground.

Another typical possibility is not to use the bundle block adjustment at all, but to rectify the single images employing congruent points with a map or other orthorectified reference, and compose the rectified single images into a mosaic.

The pushbroom video method

The pushbroom concept is familiar from satellite imagers, e.g. Spot HRV, but to the knowledge of the authors, the proto-

type version of DLR MERES system [3], was the only optical airborne implementation, until we adopted their idea for further development.

Generally, a pushbroom imager covers the image area with the progressive motion of the platform, and an array of n detectors that simultaneously measure the radiation of an entire cross-track line. In our pushbroom video system, we employ a regular surveillance CCD color video camera, but exploit only a few horizontal lines (a line block) from the very center of the image for image production, see Fig.1.
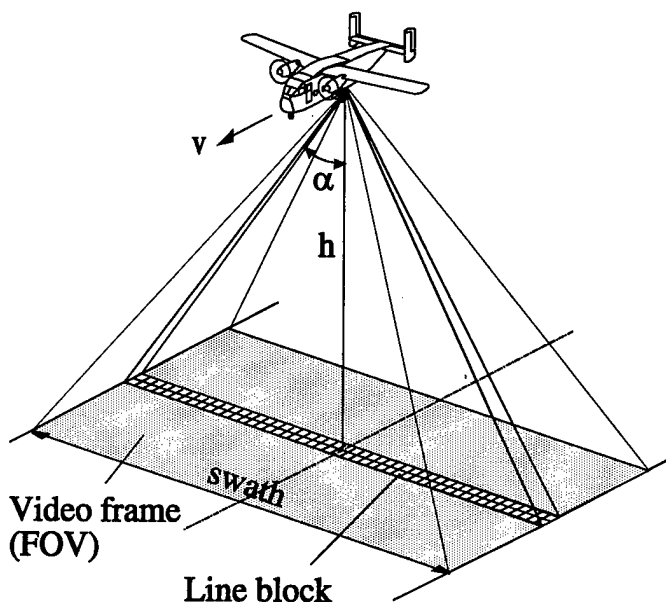
Fig. 1 HUT pushbroom imaging geometry

The major benefit of the pushbroom method is that the image becomes inherently orthorectified in the along-track direction, as all the lines are (almost) orthogonally measured. Moreover, no (manual) search for congruent points in consecutive frames is needed due to the automatic imaging process, hence dramatically reducing the post-processing time, effort and cost. The major drawback is that no image content based method—like bundle block adjustment—is used to determine the exterior orientation of the consecutive line blocks. Due to the platform perturbation motion, this leads to somewhat warped and inconsistent orientation of consecutive line blocks, even if the platform position and orientation were measured and the line orientations computationally compensated for (passive stabilization). However, since the platform perturbation motion is typically smooth and slow compared to the line acquisition rate, the image quality remains good enough for microwave radiometer data interpretation, even if no computational stabilization is performed at all.

THE HUT PUSHBROOM VIDEO SYSTEM

Fig. 2 presents a block diagram of the HUT (Helsinki University of Technology) pushroom video system. The actual hardware configuration is more complicated, because it is a subsystem of our 93 GHz imaging radiometer [4].
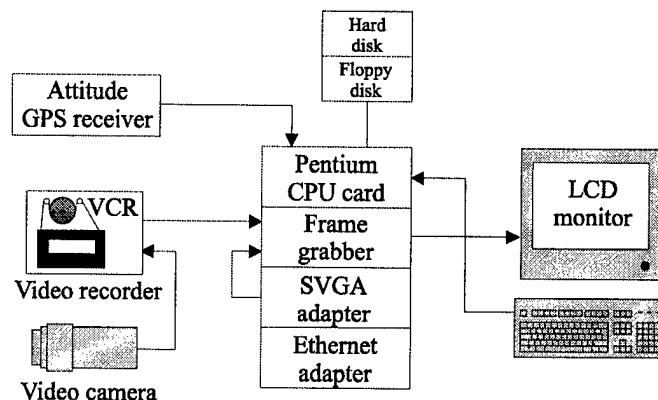
Fig. 2 HUT pushbroom imager block diagram.

The scene is observed by a regular 1/2" CCD surveillance video camera, which has a "pirate" C-mount lens with 4.8 mm focal length and 66.8° across-track view. For redundancy, the PAL video signal is fed through a VHS video recorder before entering the frame grabber card. The frame grabber continuously and independently digitizes the video signal and displays a live video image on the LCD color monitor. When the platform has flown forward the length of one line block, the CPU freezes the digitization, and the pixels of the line block are read from the frame grabber buffer and saved on the hard disk. Each line consists of 284 pixels. The line block contains a preset number of extra lines, which are also saved to provide an appropriate marginal for the passive stabilization. The passive stabilization requires the platform position and orientation data, which are recorded in the header of each line block in real time, but not used until the passive stabilization execution in the post-processing phase. Unfortunately, the attitude-DGPS subsystem of the HUT pushbroom imager is not yet operational. In non-turbulent weather and weak transverse wind, however, good results can be obtained without any stabilization, see Fig.3 recorded at Oulu, Finland on March 1997 on 300m altitude, resulting in 396m image width.

Geometrical calibration of the system

Since a camera lens, CCD cell alignment, signal processing and frame digitizing are never geometrically perfect, the whole system must be calibrated. This is especially true with our cost-effective apparatus set. We performed the calibration by attaching the camera housing to an optical bench, and carefully aligning a 1m wide calibration scale (see Fig.4) in the middle of the mechanical center axis of the camera assembly.

Fig. 3 HUT pushbroom image of an agricultural area (above), and the respective map (below).

After grabbing and saving a video frame, the correspondence of the pixel ordinal and the metric scale was detected from the frame, and expressed mathematically employing first and third degree polynomial fit. The calibration revealed a considerable, decreasing offset towards the right (max. 10 pixels) and a slight constant offset downwards (2 pixels). The nonlinearity introduced by the relatively wide-angle lens was surprisingly small, the maximum deviation from the linear relation being 1.5 pixels. Hence, the simpler linear correction relation was chosen. The lens projection center was detected by the virtual cross-section of two steel beam edges, whose start and end were adjusted to coincide on the video monitor, and the distance from the center to the target was measured.

Fig. 4 Pushbroom camera calibration target.

Image geopositioning and rectification

Reference [5] introduces a Cartesian Local Coordinate System (LCS), in which the HUT pushbroom images will be expressed after the attitude-DGPS subsystem becomes operational. The LCS is spanned by a target line start point A (LCS origin) and end point B, which lies on the LCS y-axis. Both A and B are given in the WGS-84 coordinate system, but [5] presents the transformation formulas to express the platform position (read in WGS-84), pixel locations, camera calibration and the passive stabilization maneuvers in the LCS. Once the final pixel locations are computed in the LCS, they can be easily transformed to WGS-84 employing the formulas of [5]. The use of the two coordinate systems makes the operation and pixel coordinate computing clear and easy, and ensures

result compatibility with GIP (Geographic Image Processing) systems. Moreover, it offers a straightforward method for large area mapping: if a large area is covered by multiple overflights over parallel lines A_1B_1, A_2B_2, ..., A_nB_n with, say, 10% overlap, all the pixels can be expressed in WGS-84 with a good accuracy, and merged easily in a GIP system to automatically produce an accurate optical image of a large area.

CONCLUSION

The current version of the HUT pushbroom imager is capable of qualitative images in non-turbulent weather. An attitude-DGPS system is to be installed to geolocate each pixel to an accuracy of a few meters, and to computationally compensate for the platform perturbation motion. Large area mapping will also be tested. After completing these tests, a stand-alone system is to be built to achieve higher image quality and up to 768 pixels/line instead of the current 284 pixels/line.

REFERENCES

[1] C. C. Slama (editor-in-chief), Manual of Photogrammetry, fourth edition, American Society of Photogrammetry, 1980.

[2] M. Holm, S. Väätäinen, M. Rantasuo, E.-A. Herland et al., "PC-based System for Capturing of Airborne Video Imagery and Creation of Digital Aerial Mosaics," Digest Third International Airborne Remote Sensing Conference and Exhibition, Copenhagen, Denmark, July 1997.

[3] K. Grüner, G. Kalisch, H. Schreiber, P. Sliwinski, B. Vowinkel, "A new passive microwave line scanner for airborne measurements of maritime oil pollutions," IEEE-MTT-S International Microwave Symposium, Albuquerque, NM, USA, June 1992.

[4] M. Kemppinen, T. Auer, I. Mononen, M. Hallikainen, "Advanced Airplane Version of the HUT 93 Ghz Imaging Radiometer," Digest IGARSS'96, pp. 484-486, Lincoln, USA 1996.

[5] M. Kemppinen, "Real-time geopositioning of airborne imaging radiometer and pushbroom video data," Helsinki University of Technology, Laboratory of Space Technology., Report 29, unpublished.

A Test Site Network for EOS-MODIS Global Land Cover Classification Based on Representativeness Criteria

Douglas M. Muchoney
John Hodges
Andrew Hyman
Alan Strahler

Center for Remote Sensing, Boston University
675 Commonwealth Avenue
Boston, MA 02215 USA
Phone: 617-353-1049/Fax: 617-353-3200/email: muchoney@bu.edu

Abstract -- The land remote sensing communities require a database of global training, testing and validation sites to generate reliable maps of land cover based on the new generation of Earth Observing System (EOS) sensors. The MODIS (Moderate Resolution Imaging Spectroradiometer) land cover products to be produced by Boston University include global maps produced on a quarterly basis using the International Geosphere Biosphere Programme (IGBP) land cover classification system, and quarterly change detection products, all at 1km resolution. Given the large data volume, area and high temporal frequency, it is critical that we develop a database of global sites that can be used to train classifiers, test algorithms and validate products. Global site selection is driven by data and analytical costs, the need to use sites where there is a wealth of existing data, and the diverse needs of global research. Thus, the site network must be representative of a number of meteorological, climatological, ecological, geographical and biological criteria. A primary objective of the research presented here is to evaluate the effectiveness and representativeness of the existing site network based on physical and biological gradients.

GLOBAL SAMPLING OBJECTIVES

A number of programs have produced global maps of land cover and surface parameters. ISLSCP, the International Satellite Land Surface Climatology Project, has produced a global set of surface parameters to support global climate modeling [1],[2]), while the IGBP is producing a global map of land cover [3],[4]. These efforts are based primarily on NOAA Advanced Very High Resolution Radiometer (AVHRR) data. With the launch of EOS-AM in 1997, Boston University will begin producing global land cover and land cover change products based on a complex suite of MODIS-derived data including nadir-adjusted reflectance, vegetation index (VI), and a characterization of the surface bidirectional reflectance distribution function (BRDF)[5].

MODIS land cover in turn, will be used to assign surface parameters for global models. With the current and projected capabilities to map land cover globally there is a requirement for a network of global sites to provide data for testing algorithms, training classifiers and validating map products.

The objectives of developing a global site network for MODIS land cover and other MODIS land products including snow/ice, fire, leaf area index (LAI), fraction of photosynthetically active radiation (FPAR), surface temperature and vegetation index (VI) are the testing of algorithms in terms of efficiency, feature selection and robustness, and accuracy assessment and validation of products. Land cover has the additional requirement of training supervised neural network and/or decision tree classifiers[5], [6]. Sampling specifications include that the sampling be spatially independent. A critical criterion is that the scheme must capture the intrinsic variability of the global landscape. That is, we need to ensure that the suite of training site represents well the range of biogeophysical, climatological and physical parameters, as well as inter-class variability that will be encountered in such global applications.

Constraints to global sampling are imposed by limitations in remotely sensed and ancillary data, both for developing sampling schemes and extracting training and validation data. Remotely sensed data may not be of appropriate spectral, spatial and radiometric resolutions. Data acquisition and processing costs may be prohibitive and data temporality may impact the utility of existing data. From an operational standpoint, site accessibility, information management and classification, and information standardization are problematic. Data availability, type, temporality, and problems in certainty of feature extraction mean that training may be less than optimal, and may potentially introduce error into training and validation.

GLOBAL SAMPLING APPROACHES

Sampling criteria include that global sampling approaches must not be unique nor optimized for specific classification systems, remotely sensed data nor analytical approaches. There are several approaches that are possible for developing a global site network that meet our criteria. Systematic, non-aligned sampling frames have the benefit of being classification-free, unbiased and independent of prior knowledge. They are non-optimal, however, and do not take advantage of knowledge about the population to be sampled.

Remote sensing classification-based sampling is dependent on a previous classification system and its mapping based on remote sensing. Sampling can be stratified by class, with *n* samples allocated per class and/or stratified based on proportional allocation by area. While this type of sampling can be optimized for the particular classification system, remote sensing data or analytical approach, it will be biased for other systems and data. Since land cover is generally a manifestation of a complex suite of biogeophysical and climatological parameters coupled with anthropogenic factors, a gradient approach can be used to ensure that the complete range of biogeophysical variables are being globally sampled. This is a stratification based on environmental gradients.

Our approach is to use a coarse-filter design for representativeness sampling using gradient section (gradsect) analysis, a tool which has been applied to sampling representativeness based on ecological criteria [7]. Datasets selected for analysis comprise soil, precipitation and atmosphere, surface energy and surface reflectance data.

ANALYSIS

We used ISLSCP [1],[2], Legates and Wilcox, and Lemans and Cramer [8] data based on one-degree (360 x 180), half-degree (360 x 720) and tenth-degree (2160 by 1080) grids to estimate the percent of each gradient category captured by area by the site network. 221 site locations were compiled from a number of sources as candidate sites for MODIS Land Team. While the site list is incomplete and preliminary, it provides a reasonable estimate of the distribution and representativeness of existing sites.

Comparative data on life zones and land cover are monthly composited FASIR AVHRR normalized difference vegetation index (NDVI) -based land cover [6], Holdridge Life Zones and aggregated Holdridge Life Zones classifications [8] and SiB ISLSCP vegetation cover [1],[2]. Soil date are soil texture and depth derived for ISLSCP from global FAO soils. Precipitation and atmospheric data included percent cloudiness and mean monthly corrected

precipitation. Temperature data are mean monthly temperature [8]. Surface energy data used are the monthly mean net shortwave radiation for 1988 from ISLSCP. Surface reflectance data are monthly composited FASIR NDVI for 1988, ISLSCP 1988 FPAR, LAI and surface albedo [1],[2].

Our approach was to partition each gradient into a reasonable number of classes using thresholds and clustering. The purpose of clustering was data reduction, pattern analysis and generation of a comparable number of gradient categories. Clustering rather than intersection allows for a natural organization of gradient classes and reduces the number of potential categories that would result from intersecting such a large number of datasets, each with a large number of internal categories.

Data were clustered into 25 clusters using an isoclass clustering algorithm. The percent of the 25 gradient categories that were captured by the sample sites was calculated to give an indication of how well the overall sampling plan captured each of the gradients. We then calculated the ratio of site area to gradient category unit area as an indicator the sampling ratio by gradient category (stratum). Summary statistics of mean, variance, minimum and maximum values for areal coverage within the various partitions of each gradient provide an overall estimate of how well the site network captures the variation on the gradient.

RESULTS AND CONCLUSIONS

Table 1 provides the summary statistics of the ratio of sites per unit gradient category area for a subset of the gradients that we analyzed. By comparing the number of sites in each gradient category with the area per gradient category, we get an understanding of how well overall gradients, as well as gradient elements, are represented by the test site network. Results indicate that while some classes are well represented, others are not. For example, six of ten gradients had one or more partitions that went unsampled.

Since some datasets were derived from identical and/or similar data, coupled with general spatial autocorrelation and correlation of related biophysical parameters (eg. LAI, FPAR and NDVI), the analysis does not represent the full benefit of stratifying sampling based on biogeophysical and climatological data. Other data are not yet available or may be over-generalized at one-degree, half-degree and tenth-degree grid cell representation. The site selection itself is preliminary and sites were also generalized to grid cells. This may both under and over-represent how well the site network is represents global gradients.

Table 1. Statistics for percent sampled area within gradient categories.

statistic\gradient	LAI	FPAR	NDVI	SiB	precip	sw_net	holdridge	soil_texture	soil_depth	elevation
gradient partitions	25	25	25	14	25	25	14	7	25	25
mean	2.85	2.54	2.17	3.03	2.58	3.12	1.65	2.10	2.00	1.80
variance	1.54	1.86	1.56	3.42	1.62	3.09	3.51	0.97	1.88	1.14
minimum	0.03	0.00	0.00	0.03	0.16	0.00	0.00	0.03	0.00	0.00
maximum	6.49	5.73	5.96	5.41	6.94	10.80	2.70	3.45	7.11	4.35

Although this analysis was based on coarse spatial resolution data, it provides a template for developing a more effective set of sites for characterizing and monitoring global land cover given the present limits to more comprehensive systems. While the use of biogeophysical and climatological data can improve sample design, sampling must also include current data on landscape processes and anthropogenic impacts which are the core of the MODIS land cover characterization and change detection activities. Representativeness criteria provide a means of sampling that is not tied to specific classification systems, remotely sensed data and analytical procedures, yet emphasizes the primary independent variables that determine land cover. Problems of gradient correlation should be minimized by future data products, both of ancillary and MODIS-derived data.

REFERENCES

[1] C.Justice, D.A.Dazlich and D.A.Randall, "A global 1° by 1° NDVI data set for climate studies, Part 2: The generation of global fields of terrestrial biophysical parameters from the NDVI", Int. J. Remote Sensing 15: 3529-3545,1994.

[2] B.W.Meeson, F.E.Corprew, J.M.P.McManus, D.M.Myers, J.W.Closs, K.-J. Sun, D.J. Sunday and P.J. Sellers, "Global Data Sets for Land-Atmosphere Models, Volumes 1-5", Internat. Satellite Land Surface Climatol. Project, Initiave I, NASA Goddard DAAC Science Data Series, 5 CD-ROM disks,1995.

[3] A. Belward, and T.R. Loveland, "The IGBP 1km Land Cover Project". In Proceedings of the 21st Annual Conference of the Remote Sensing Society, Southampton, UK, pp. 1099-1106,1995.

[4] IGBP-DIS, "The IGBP-DIS Global 1 Km Land Cover Data Set: A Validation Strategy", A. Belward, (ed.), IGBP-DIS, Universite de Paris, Paris, France, 1995.

[5] A.H. Strahler, J. Townshend, D. Muchoney, J. Borak, M. Friedl, S. Gopal A. Hyman, A. Moody and E. Lambin, "MODIS Land Cover and Land-Cover Change Algorithm Theoretical Basis Document (ATBD), Version 4.1". Boston: Boston University, 102 pp., 1996.

[6] S. Gopal, C. Woodcock and A.H. Strahler, "Fuzzy ARTMAP classification of global land cover from AVHRR data set". Proceedings of the 1996 International Geoscience and Remote Sensing Symposium, Lincoln, Nebraska, May 27-31, Vol. 1, pp. 538-540, 1996.

[7] B.G. Mackey, M.F.Hutchinson, J.P. MacMahon and P.M. Fleming, "Assessing Representativeness of Places for Conservation Reservation and Heritage Listing", Environmental Management Vol.12(4), pp.501-514,1988.

[8] US Environmental Protection Agency/US Department of Commerce, "Global Ecosystems Database, Version 0.1, Database Documentation", 1991.

First in-flight results from POLDER/ADEOS over the terrestrial biosphere

Marc Leroy and Olivier Hautecoeur

CESBIO (Centre d'Etudes Spatiales de la Biosphère)
Unité Mixte de Recherches CNES-CNRS-UPS
18, avenue Edouard Belin, 31401 Toulouse Cedex 4, France

Abstract -- This paper presents the objectives of the POLDER program for land surface monitoring and provides a description of the first products acquired over terrestrial surfaces - top of atmosphere and surface reflectances on various targets, and composites of surface reflectances over large areas.

INTRODUCTION

POLDER (POLarization and Directionality of the Earth's Reflectances) is a new spatial instrument devoted to the global observation of the polarization and directionality of solar radiation reflected by the Earth surface-atmosphere system (Deschamps et al., 1994). It allows a near-daily coverage of the Earth in several spectal bands from 443 nm up to 910 nm at a resolution of about 7 km. It was launched on the Japanese ADEOS platform in August 1996. The original capabilities of POLDER, compared to other current and planned spaceborne instruments are (i) its polarized reflectance measurements in the visible and near-infrared part of the solar spectrum, and (ii) its capability to measure a surface target reflectance from up to 14 viewing directions during a single satellite pass. The scientific objectives of this instrument concern the fields of aerosol cycling, cloud-radiation interactions, Earth radiation budget, ocean primary productivity and continental biosphere dynamics.

OBJECTIVES OF POLDER FOR LAND SURFACE MONITORING

For land surfaces, the objectives are to identify precisely the major biomes on the surface of the planet, and to be able to detect changes in their composition or mapping, due either to anthropogenic or climatic causes. They are also to permit the understanding and modeling of the general functioning of the terrestrial biosphere system, i.e., vegetation growth, maturity, and decay, at regional or global scales. The description of the continental phases of the carbon and hydrological cycles is intimately related to the description of the general functioning of the biosphere. Finally, land monitoring provides boundary conditions in General Circulation Models (GCM) to describe accurately the exchanges of mass, momentum and energy at the biosphere-atmosphere interface.

Monitoring of terrestrial vegetation at global or regional scales requires accurate and frequent measurements of surface reflectance. The key improvement brought by POLDER in this context is to provide, at high temporal repetitiveness, measurements of surface reflectance brought to the same directional standard and corrected for atmospheric effects (Leroy et al., 1997).

Another important aspect is that, after compositing of satellite measurements, POLDER provides the land surface BRDF at regional and global scales. Several science products take advantage of this new signature.

Albedo.
The BRDF measurements permit an estimate of spectral hemispherical reflectances. This is an important step forward for the estimation of daily surface albedo, which plays a key role in water and energy exchanges between surface and atmosphere.

Classifications.
The directional signature may be thought of as additional channels, which add to the more conventional spectral and temporal information. Demonstrations that species discrimination is enhanced with directional signatures have been made at local scale, in particular on boreal forest covers (Bicheron et al., 1997).

Biophysical parameters.
An alternative way of using a directional signature is to invert it in terms of biophysical parameters, such as LAI (Leaf Area Index), fAPAR (fraction of absorbed PAR), or vegetation cover, using a BRDF model. The accumulation of directional data in short periods of time permitted by the POLDER concept can be used for that purpose (Bicheron et al., this issue). In the context of model inversion, the hot spot effect, - the signal enhancement when the sun and view directions coincide, is of particular interest, and can easily be seen with POLDER (Bréon et al., 1997).

Wetland mapping.
Another interesting particular geometry is the specular direction, for which the signal is a function of the surface wetness. This is particularly interesting for the monitoring of large wetland areas (Vanderbilt et al., 1997).

FIRST IN-FLIGHT RESULTS

Although the validation plan of the land surface products is still in an early phase, some preliminary results are available.

1) A quite clear (cloud-free) orbit segment acquired on the Europe-North Africa area was acquired on September 16, 1996. The results show that very clean BRDF signatures are

acquired over the 7 km resolution pixels. Several single orbit Top of Atmosphere BRDF signatures were analysed over specific test areas in Europe-Africa : agricultural sites (Orthez and Chartres test areas of the MARS project), forest sites (Fontainebeau, Landes), mountainous sites (Observatoire Midi-Pyrénées), urban sites (Paris), and a desert site (Algerian Sahara). Directional signatures have a very smooth aspect, with little noise like high frequency components (Figure 1); they differ distincly with species. A strong signal enhancement is seen in the neighborhood of the hot spot direction over most vegetated areas (not on desert areas). In the case of the Chartres area, seen exactly under the hot spot viewing direction, there is a factor 1.5 - 2 between forward scattering and hot spot reflectances (Figure 1). Strong directional effects, species dependent, are also apparent when mapping the Europe-Africa segment with a selection of different given viewing directions, for example the first and the last viewing directions seen by any pixel. Moreover we

have shown that estimating the NDVI with the first or last available directions result in errors of 10-20 % compared to the NDVI estimated with the most nadir available direction.

2) BRDF signatures were examined at level 2 (after cloud screening and correction of Rayleigh scattering and gas absorption) over several test sites in the USA : Maricopa (agricultural crops), the FIFE site in Kansas (grasslands), and the Jornada site in New-Mexico (steppes). A collection of such signatures, covering various parts of directional space, were obtained during the period Oct. 30 - Nov. 11. The results show that the signatures acquired at different days are consistent with each other and show a good level of symetry relative to the principal plane (Figure 2). A strong enhancement in the backscattering direction is a prominent characteristic seen in all BRDF signatures. In addition, a hole-type feature is seen in the forward scattering space for the FIFE site.

3) A composite product (level 3) was created on the USA area. It contains, per pixel, at 4 spectral bands (443 nm, 670 nm, 765 nm, 865 nm), the 3 directional parameters of a linear

Figure 1. Top : location in directional space of viewing directions for the agricultural site of Chartres, on September 16, 1996. Bottom : Top of atmosphere reflectance in several spectral bands, as a function of $\theta_v \cos\phi$ (θ_v viewing zenith angle, ϕ azimuth between view and sun directions).
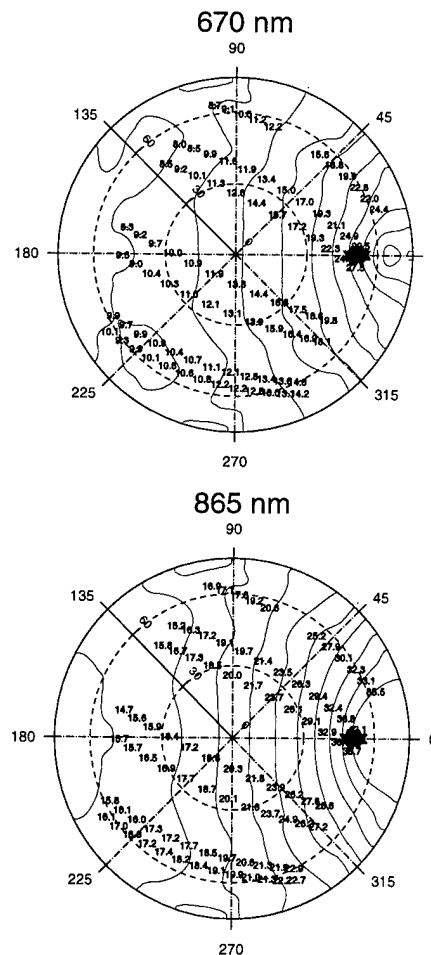
Figure 2. Surface BRDF acquired on the agricultural site of Maricopa farm, using data from Oct. 30 to Nov. 11, 1996, at 670 nm and 865 nm.

Directional parameters – 865 nm
November 1996, 1st decade

1st parameter

0.4

0.3

0.2

2nd parameter

0.1

0.05

0

3rd parameter

0.8

0.6

0.4

CESBIO / CNES / NASDA
non calibrated data / non validated product
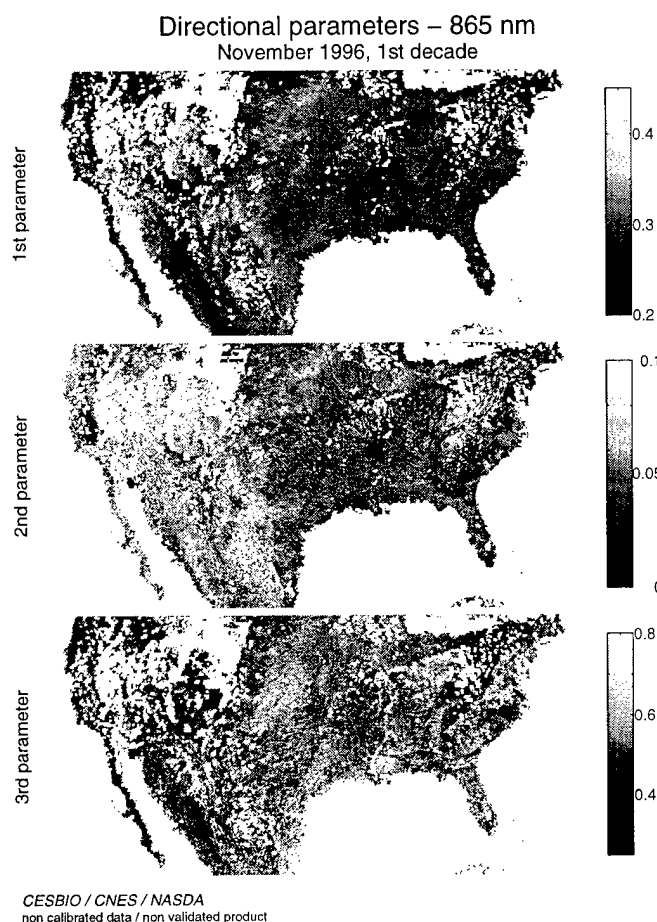
Figure 3. Mapping of the 3 parameters of the BRDF model adjusted against data from Oct. 30 to Nov. 11, 1996, over the USA area. White areas are detected as cloudy during the whole period.

BRDF model (Roujean et al., 1992) adjusted on the level 2 BRDF data acquired during the period Nov. 30 - Dec. 11. According to the model, the first parameter represents the reflectance seen at nadir with a sun at zenith, the second the backscattering effects due to shadows, and the third the volume scattering effects. The mapping of each of these 3 directional parameters show that consistent signatures are found (it is not just noise), with an information apparently uncorrelated between the 3 directions (Figure 3). From the directional parameters, we derived at each wavelength a mapping of the hemispherical reflectance, and from the hemispherical reflectances at 670 and 865 nm, a mapping of the NDVI, thus in principle nicely corrected for sun and view directional effects.

CONCLUSION

The first results appear promising. Current work consists in analyzing the efficiency of cloud detection algorithms using synoptic meteorological network data, and the efficiency of atmospheric correction using sunphotometer AERONET

network. Detailed analysis of the compositing process operated at level 3 is under way on the South Africa area. In particular, a comparison is carried out between POLDER level 3 data and Global Vegetation Index data from AVHRR on this area. Preliminary results show that the temporal evolution of reflectances in the visible and near infrared is significantly smoother in the case of POLDER data, in agreement with expectations.

REFERENCES

[1] Bicheron, P., M. Leroy, O. Hautecoeur, et F.M. Bréon, "Enhanced discrimination of boreal forest covers with directional reflectances from the airborne POLDER instrument", *JGR*, accepted, 1997.

[2] Bréon, F.M., V. Vanderbilt, M. Leroy, et al., 'Evidence of hot spot directional signature from airborne POLDER measurements', *IEEE TGARSS* , 35, 479-484, 1997.

[3] Deschamps, P.Y., F.M. Bréon, M. Leroy, et al., 1994, 'The POLDER mission: Instrument characteristics and scientific objectives', *IEEE TGARSS*, 32, pp. 598-615, 1994.

[4] Leroy, M., J.L. Deuzé, F.M. Bréon, et al. ' Retrieval of atmospheric properties and surface bidirectional reflectances over the land from POLDER/ADEOS ', *JGR-Atmosphère*, in press, 1997.

[5] Roujean J.L., M. Leroy, and P.Y. Deschamps, 'A bidirectional reflectance model of the Earth's surface for the correction of remote sensing data', *JGR*, 97, no D18, pp. 20,455-20,468, 1992.

[6] Vanderbilt, V.C., G. Perry, J.A. Stearn, et al., ' Discrimination of wetland and non-wetland community types with multi-spectral, multi-angle, polarized POLDER data', *IEEE TGARSS*, to be submitted, 1997.

Application of the TES Algorithm to TIMS Data Acquired in HAPEX-Sahel

Thomas Schmugge
USDA Hydrology Lab, Beltsville, MD 20705, USA
Tel:301-504-8554, FAX:301-504-8931, email: schmugge@hydrolab.arsusda.gov
Simon Hook
Jet Propulsion Laboratory, Pasadena, CA 91109 USA
César Coll
Department of Physics, University of Valencia, Spain

ABSTRACT --In 1992 Thermal Infrared Multispectral Scanner (TIMS) data were acquired from the NASA C-130 aircraft over the Sahel, Africa as part of the Hydrological and Atmospheric Pilot Experiment in the Sahel (HAPEX). The TIMS instrument measures the radiation from the surface modified by the atmosphere in 6 channels located between 8 and 12.5 μm. These airborne TIMS data provide a surrogate for data that will be available globally with the launch of the Advanced Spaceborne Thermal emission Reflectance Radiometer (ASTER) in 1998 on the first AM Earth Observation System platform and were used to test the Temperature Emissivity Separation (TES) Algorithm being developed for ASTER. This method relies on an empirical relationship observed between the range of emissivities and the minimum value for the 6 TIMS channels. HAPEX is an international land-surface-atmosphere observation program that was undertaken in western Niger, in the west African Sahel region. The TES algorithm was applied to scenes of about 1000 scans for both the east and west central sites with the interesting results on 2 and 4 September. The spectral behaviors of Tiger Bush, bare soil and millet sites were studied. There was up to a 10 K difference in the brightness temperature over the 6 channels for the bare soil site. Channels 1 to 3 (8.2 to 9.4 μm) were 10 K cooler than the longer wavelength channels (9.6 to 12.5 μm) which is characteristic of soils rich in quartz. While for tiger bush site there was less than 0.5 K difference observed. In terms of emissivity, channel 5 showed very little spatial variation in emissivity and the short wavelength channels observed substantial regions with emissivities of less than 0.8. As expected there was little spectral difference in emissivity observed for vegetated pixels,, less than 0.01, and the average amplitude was 0.97. The extracted vegetation temperature was close to the air temperature. Our results indicated a large sensitivity to the values used for the atmospheric corrections, which in our case was done using MODTRAN 3.5 and nearby radiosoundings of the atmosphere.

INTRODUCTION

HAPEX-Sahel (Hydrological and Atmospheric Pilot Experiment in the Sahel)[1] is an international land-surface-atmosphere observation program that was undertaken in western Niger, in the west African Sahel region. The overall aims were to improve our understanding of the role of the Sahel on the general circulation, in particular the effects of the large interannual fluctuations of land surface conditions in this region and, in turn, to seek relationships between the general circulation and the persistent droughts that have affected the Sahel during the last 25 years. The field program obtained measurements of atmospheric, surface and certain sub-surface processes in a 1deg x1deg area that incorporates many of the major land surface types found throughout the Sahel.

In order to obtain data for this large area, an extensive measurement program was undertaken including field, aircraft, and satellite remote sensing measurements, mainly between mid 1990 and late 1992. An intensive operations period was undertaken for 8 weeks from mid to late growing season of 1992. The aim of HAPEX-Sahel was to make simultaneous measurements of relevant variables at the micro and meso scales. HAPEX-Sahel faced several particular challenges. The heterogeneity of surface types and seasonal variation in the region are much greater than in the areas studied in any previous measurement campaign of this type. To address this aspect of the problem an extensive remote sensing program was used to extend the field measurements to the entire region, i.e to the meso-scale.. This was performed by a suite of sensors on the C-130 aircraft. These included a microwave radiometer for soil moisture observations, a visible and near IR scanner for vegetation and albedo data and a thermal infrared scanner (TIMS) for surface temperature and emissivity.

TIMS

The data we present here were obtained with the TIMS sensor on board the NASA C-130 during the 1992 HAPEX aircraft campaign. TIMS has six channels in the thermal infrared (8 - 12 μm) region of the electromagnetic spectrum. The instantaneous field of view is 2.5 mrad[2]. Thus from an altitude of 600 m the pixel size is 1.5 m. At this altitude with a ground speed of about 75m/sec the separation between scans is 3 m at the fastest scan rate. Thus the instrument is under scanning.

The radiance at the aircraft is given by

$$L_j(\text{surf}) = (L_j(\text{a/c}) - L_j(\text{atm}\uparrow)) / \tau_i \qquad (1)$$

where the values of τ_j and L_j (atm$\uparrow$) can be calculated from MODTRAN [3] using the radiosonde data [4] taken within one

hour of the overflight. The atmospheric corrections for the cooler surfaces, e.g. vegetated, are, typically, <1 C while for the bare soil the corrections are 2 to 4 C even at this low altitude. The remaining problem is to relate these radiances to the surface emissivity in the 6 channels without direct knowledge of the temperature, T_{grd} using the relation:

$$L_j(surf) = \epsilon_j BB_j(T_{grd}) + (1 - \epsilon_j) \cdot L_j(atm\downarrow) \qquad (2)$$

where:

$$BB_j(T) = \frac{C_1}{\lambda_j^5 \pi \left[\exp\left(\frac{C_2}{\lambda_j T}\right) - 1 \right]}$$

is the Planck equation for the radiation from a black body.

TEMPERATURE/EMISSIVITY RECOVERY

Equation 2 indicates that if the radiance is measured in n spectral channels, there will be n+1 unknowns: n emissivities (one per channel) and a single unknown surface temperature. The set of equations described by a set of radiance measurements in n spectral channels is thus under determined, and additional information is needed in order to extract either the temperature or emissivity information. This has led to the development of a variety of techniques which differ according to the assumptions that they make. Several techniques have been developed which work better in areas where there is a wide variation in surface emissivity. These include normalized emissivity and alpha emissivity techniques [5]. Recently, a new technique was proposed by Gillespie et al. [6] which incorporate the advantages of these techniques and is termed Temperature Emissivity Separation (TES). This algorithm is planned for use with data from the Advanced Spaceborne Thermal Emission Reflectance Radiometer (ASTER) scheduled for launch on the first AM-1 Earth Observing Platform in 1998 [7]. The following description of the TES algorithm is summarized from Gillespie et al. [6]. The estimated kinetic temperature, T, is taken to be the maximum T estimated from the radiances for the n spectral channels calculated from (2). The emissivity value (ϵ) used in (2) is set to 0.97 so that typical surface types, vegetation, snow, water, soil and rock, will all be within ± 0.03 of the chosen value. The relative emissivities, β_j, are found by ratioing the acquired radiance data, corrected for atmospheric effects to the average of all channels:

$$\beta_j = \frac{L_j \overline{BB}}{\overline{L\ BB(T)_j}} \qquad (3)$$

In principle β_j may range widely. However, since the emissivities are generally restricted to 0.7-1.0 the ratioed values are restricted to 0.7-1.4. The β_j values provide a temperature independent index which can be matched against β_j values calculated from

laboratory/field measurements of natural materials. In the TES method the maximum-minimum difference (MMD=max(β_j)-min(β_j)) or contrast is related to the minimum emissivity. From laboratory measurements of emissivities [8] the relationship between ϵ_{min} and MMD was found to be [6]:

$$\epsilon_{min} = 0.994 - 0.687 * MMD^{0.737} . \qquad (4)$$

and can be used to calculate the emissivities from the β spectrum:

$$\epsilon_j = \beta_j \left(\frac{\epsilon_{min}}{min(\beta_j)} \right) \qquad (5)$$

The β_j are determined from the measured surface radiances L. From these ϵ_j a new temperature can be obtained and the process repeated until the results. Convergence usually occurs after 2 or 3 iterations.

RESULTS

The radiances for 3 selected targets in the scene for the east central site were obtained from the images. The sites were: a fully vegetated section of the tiger bush, a bare soil and highly vegetated section of a milled field. The brightness temperatures (T_B) before and after atmospheric correction are presented in Fig. 1. These results are from line 2 on September 4, 1992. They show about a 10 K range of T_B for the bare soil field after
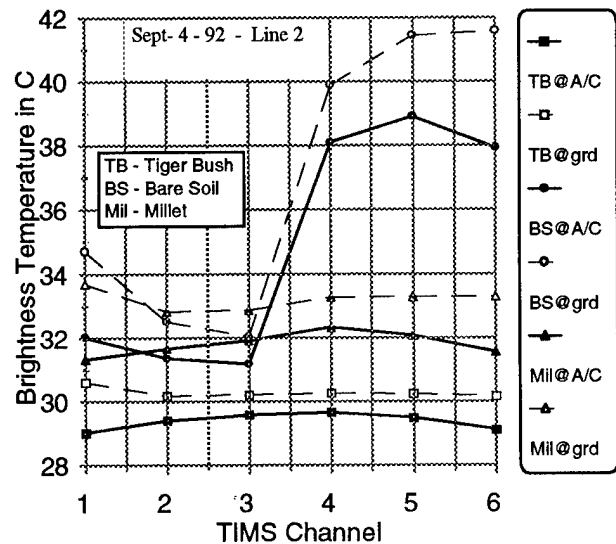
Figure 1. T_B values for 3 targets at the east central site. The solid symbols are the values at the aircraft and the open symbols are the values at the ground.
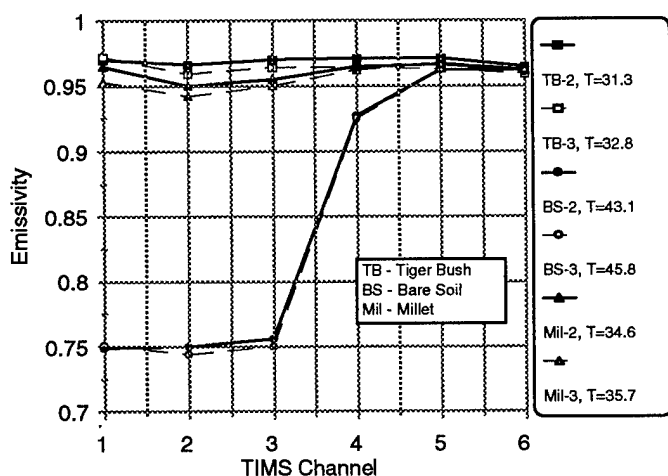
Figure 2. Comparison of derived emissivities for lines 2 and 3 on September 4. The values of the derived temperature are given in the legend. The solid symbols are for line 2 and the open are for line 3.

correction and less 0.5 K range for the tiger bush. The millet shows a little more spectral variation because of the possibility of some bare soil showing. Note, that even for a 600 m flight altitude the atmospheric correction was up to 2 K for the bare soil and about 0.5 K for the tiger bush. The same area was over flown on line 3 about 20 minutes later with similar results except that the temperatures were about 1 or 2 degrees warmer.

The TES derived emissivities for these 3 sites are presented in Fig. 2 for both the passes. The solid symbols are the results from line 2 and the open symbols with the dashed lines are for line 3. There is excellent agreement between the two lines. Especially for the bare soil case, where the emissivities for channels 1,2, and 3 are about 0.75 in both lines. There is a little more difference for the two vegetation targets especially for the millet field and for the shorter wavelength channels. Note that there are observation differences for the 2 lines; for line 2 the targets were in the northern half of the swath while for line 3 they were in the southern half of the swath. Recall that at the 600 m altitude the scene in under scanned so that only about half of the area is actually seen. So that even if cover the same areas on both lines, slightly different pieces of the terrain may be seen. Thus for the millet field we may be responding to slightly different amounts of bare soil for the millet target on the two flight lines.

DISCUSSION and CONCLUSIONS

A version of the TES algorithm was implemented and tested on several 1000-scan TIMS scenes for the East and West Central sites in the HAPEX Sahel experiment. The scenes were from 5 different flight lines on 2 and 4 September 1992 from an altitude

of 600 m. There is excellent reproducibility when the same area is seen in different lines on the same day. However there are differences when the same area is seen on the two days especially for the low emissivity values. Some of these differences may be due to soil moisture differences which were observed on the two days. There was very little emissivity variation observed for TIMS channel 5 over the scenes, this was partially due to the noise in the MMD values. This limits the high values of emissivity obtained with the TES algorithm, e.g. over vegetation. Since channels 1 and 6 of TIMS were seen to have the largest noise, we implemented the TES algorithm using only center 4 channels of TIMS with some what better results. The resulting temperatures for the vegetated areas are in good agreement with the air temperature at the time of the flight.

REFERENCES

[1] Prince, S.D. et al., 1995. Geographical, Biological, and Remote Sensing Aspects of the Hydrologic Atmospheric Pilot Experiment in the Sahel (HAPEX-Sahel). Rem. Sens Environm, vol. 51, pp. 215-234.

[2] Palluconi, F,& Meeks, GR (1985) Thermal infrared multispectral scanner (TIMS): an investigator's guide to TIMS data; NASA, JPL Publ 85-32, Pasadena, June 1985.

[3] Kniezys, FX, Shettle, EP, Abreu, LW, Chetwynd, JH, Anderson, GP, Gallery, WO, Selby, JEA, & Clough SA (1988) User Guide to Lowtran 7, Air Force Geophysics Laboratory Report No AFGL-TR-88-0177, Hanscom AFB, Massachusetts 01731.

[4] Bessemoulin, P. And Trauille, O., 1994. Documentation for Radio-sounding data collected by CNRM in Hamdallay, Niger. HAPEX-Sahel Information System CD-ROM.

[5] Kealy, P.S. and Hook, S.J., 1993. Separating Temperature and Emissivity in Thermal Infrared Multispectral Scanner Data: Implications for Recovering Land Surface Temperatures. IEEE Trans GRS, vol. 31, pp. 1155-1164.

[6] Gillespie, A. R., Rokugawa, S., Hook, S. J. Matsunaga, T. and A. B. Kahle, 1996. Temperature/Emissivity Separation Algorithm Theoretical Basis Document, vers. 2.1.

[7] Fujisada,H., 1994. Overview of the ASTER instrument on the EOS-AM1 platform. Proc. SPIE, Vol. 2268, pp 14-36.

[8] Salisbury, J.W. and D. M. D'Aria, 1992. Emissivity of Terrestrial Materials in the 8 - 14 μm Atmospheric Window. Remote Sens. Environ., vol. 42, pp. 83-106, 1992.

ASTER OBSERVATIONS FOR THE MONITORING OF LAND SURFACE FLUXES

Thomas Schmugge

USDA Hydrology Laboratory, Beltsville MD 20705, USA

Tel: 301-504-8554, FAX: 301-504-8932, email: schmugge@hydrolab.arsusda.gov

ABSTRACT -- This paper presents a review of how data from the Advanced Spaceborne Thermal Emission radiometer (ASTER) can be used to estimate the energy fluxes from the land surface. The basic concepts of the energy balance at the land surface are presented along with an example of how remotely sensed surface brightness temperatures can be used to estimate the sensible heat. The example is from the Monsoon 90 experiment conducted over an arid watershed in the state of Arizona in the United States.

INTRODUCTION

The monitoring of the land surface fluxes at regional spatial scales is recognized as important for applications such as the modeling of atmospheric behavior and the monitoring of water resources. When one looks at a thermal infrared image, it is clear that the large variations in surface brightness temperatures, T_B, which are seen arise from differences in the surface energy balance for the land surfaces. Recall that T_B is a measure of the emitted radiation from the surface is directly related to the temperature of the surface and its emissivity. The temperature contrasts seen between fields with different vegetation conditions imply a different partition of the incoming solar energy into latent and sensible heat components. Cooler temperatures usually indicate that there is sufficient moisture available so that most of the incoming energy goes into latent heat or evaporation, while hotter temperatures indicate that most of the incoming energy goes into the sensible or convective heating of the atmosphere. However there is another aspect of the problem of determining the surface fluxes which arises due to the differences in the heat transfer coefficients arising from the various types of vegetation and their heights. Thus a 20 m tall pine forests can be just as cool as a well-watered field but transpiring much less becaue of its greater heat transfer capability. The problem is to quantify these fluxes in terms of the remotely sensed T_B and other observables from the Advanced Spaceborne Thermal Emission Radiometer, ASTER, to be flown on NASA's Earth Observing System (EOS) first spacecraft to be launched in 1998.. There is a long history on the use of T_B to monitor these surface fluxes [1,2,3] and in this paper we will describe the contributions remotely sensed data from ASTER can make towards quantifying these fluxes.

SURFACE ENERGY BALANCE

To estimate the land surface fluxes it is necessary to determine:
1) The energy driving forces, i.e. the incident solar energy (insolation), surface albedo and resulting net radiation;
2) The moisture availability or status in the soil and the vegetation/soil interaction; and
3) The capacity of the atmosphere to absorb the flux, which depends on surface air temperature, vapor pressure gradients, and surface winds.

There has been considerable work recently on methods for estimating factors relating to the first two items from remotely sensed data. It is possible to estimate from remotely sensed data the surface parameters related to the soil/vegetation system (leaf area indices and surface soil moisture), radiation forcing components (essentially incident solar radiation and albedo) and indicators of the surface response to them (surface temperature). However there is no remote sensing method for estimating the surface atmospheric parameters. Therefore conventional surface measurements will be required for this factor.

To understand better how ASTER observations can contribute to the determination of the surface fluxes, let us consider the basic energy and moisture balance equations. In the absence of advection or precipitation the energy balance at the land surface is given by:

$$R_n + G + H + LE = 0 \qquad (1)$$

where R_n is the net radiation, G the soil heat flux, H the sensible heat flux and LE the latent heat or moisture flux into the atmosphere. The net radiation is the sum of the incoming and outgoing short and long wave radiation fluxes:

$$R_n = (1 - \alpha) \cdot R_s + (1 - \epsilon) \cdot R_{L\downarrow} - \epsilon \sigma T^4 \qquad (2)$$

where α is the surface albedo, R_s is the incoming solar radiation, $R_{L\downarrow}$ is the incoming long-wave radiation, ϵ the surface emissivity and T the surface temperature in Kelvins.

There has been considerable progress in estimating R_s and α from geostationary satellite data. The basis of the method is that the major modulator of surface insolation is cloudiness. The information contained in the satellite radiances is interpreted in terms of scattering, reflection and absorption parameters which are subsequently used in radiative transfer model calculations for the atmosphere [4]. The albedo α, can also be estimated from these data. $R_{L\downarrow}$ can be estimated from the atmospheric sounders or empirically from surface conditions. The surface temperature T can be estimated from the thermal channels of ASTER. The surface albedo can also be estimated from multi-spectral data such as that which will be available form the VNIR channels of

ASTER. So it would appear that the components of the radiation flux in (2) can be estimated reasonably well using remotely sensed data and a review of the procedures is given in [5].

The difficulty arises then in determining the surface fluxes in (1), both the sensible and ground heat flux involve temperature gradients; one in the soil and the other in the atmosphere. The latent heat flux involves the vapor pressure gradient. Thus for the ground heat flux we have:

$$G = \lambda dT_{soil} / dz \qquad (3)$$

where λ is thermal conductivity of the soil. While the soil temperature gradient can not be determined from remotely sensed data the temperature profile can be modeled with sufficient accuracy to estimate G. There is a reasonable empirical relationship between the ratio G/R_n and vegetation indices such as and NDVI.

The sensible heat flux into the atmosphere is:

$$H = \rho c_p \cdot (T_{aero} - T_a) / r_a \qquad (4)$$

where ρ is the air density, c_p is the specific heat of air at constant pressure, T_{aero} is the aerodynamic temperature in the canopy, T_a is the air temperature just above the canopy, and r_a is the aerodynamic resistance. The latter, r_a, is a rather complex function of various geometrical factors such as roughness lengths, displacement heights, etc., and the wind speed and is usually empirically determined. T_{aero} is the temperature of the source for the convective heat transfer and can be determined from the profiles of temperature and windspeed in the boundary layer. For an aerodynamically smooth surface, T_{aero} and T_B are equivalent since such a surface is the source for both the radiative and convective or sensible heat fluxes. However for most natural surfaces, T_{aero} and T_B are not equivalent as demonstrated by Hall et al.,[6] working with data from FIFE. This difference between T_{aero} and T_B is thoroughly discussed in the recent paper by Norman et al. [7].

The latent heat flux into the atmosphere is given by:

$$LE = \rho c_p \cdot (e_a - e_s) / \gamma \cdot (r_a + r_s) \qquad (5)$$

where γ is the psychrometric constant, e_a is the atmospheric vapor pressure in the boundary layer, e_s is the saturation vapor pressure at the temperature T, and r_s is the stomatal resistance to water vapor transport. To get around the absence of these temperature and vapor pressure gradients in the soil and lower atmosphere 1-D models have been developed of the heat transfer in the soil and from the land surface into the atmosphere [8]. These models use the remotely sensed surface temperature as a boundary condition and model parameters are varied to obtain the best fit between the predicted and observed surface temperatures.

From (1) to (5), we see that the available energy (Rn - G) is partitioned into latent and sensible heat components. The approach that is frequently used is to estimate the H using the remotely sensed surface brightness temperature (T_B) in (4) and to determine LE as a remainder term. This is the approach we will consider here.

Equation (4) implicitly assumes that the canopy is a thin layer with a single temperature, which is clearly not the case for a vertically developed canopy exhibiting variations in temperature. While both T_{aero} and T_B result from contributions of the surface temperatures of the canopy elements, they do so in different ways and as a result are not equivalent. The problem is that T_{aero} in (4) being the effective temperature for the canopy heat transfer process is not a measurable quantity and is not equal to T_B. The thermal radiation observed by a radiometer originates from the soil and the vegetation elements having various temperatures and orientations which leads to variations in T_B with viewing angle. If the classical value of r_a is used in (4) with T_B, it is found to give poor agreement with observed fluxes [6]. However Stewart et al. [9] have shown that if an additional resistance, r_r, is added the agreement improves substantially. This additional resistance is necessary because T_B is larger than T_{aero} and is needed to account for the increased resistance to heat flow compare to that for the momentum flux.

RESULTS

In view of these difficulties in determining the appropriate surface resistance for heat transfer, it is clear that at the present time it may not be possible to estimate H from remotely sensed observations alone. However if we have a reference point where flux measurements are made it is possible to determine the spatial variation of H from TIR data. One example this approach is available from the Monsoon'90 experiment [10] conducted over the arid Walnut Gulch watershed in Arizona during the summer (Monsoon season) of 1990. A summary of the conditions from that experiment is given in Fig. 1, which presents box plots of the surface air temperature and surface radiation temperature for 8 sites over the watershed. The data are for 3 days which represent a range of conditions. The TIR radiation temperatures (T_{surf}) are from the NS001 sensor on board the NASA C-130 aircraft. The bandpass for the TIR channel is approximately 10 to 12 μm. The data are from 2 flight lines at an altitude of 2400m above the ground, yielding a pixel size of 6.3 m. The data were acquired between 10:00 and 10:30 local standard time, i.e., close to the time of the ASTER overflights. The temperatures were corrected for atmospheric effects using radiosoundings launched at the site., and the results were found to agree with ground radiometer measurements to within 1 K . The boxes show the median and range of T_{surf} and T_{air} values for each day. The air temperatures were relatively consistent for the 3 days about 25 C while the surface temperatures show considerable variation resulting form differences in the soil moisture status for the 3 days. Conditions were very dry on day 213 (Aug 1, 1990, $<T_{surf}>$ = 37 C) and quite wet on day 216 (Aug 4, 1990, $<T_{surf}>$ = 31 C) following up to 50 mm of rain on the previous 3 days. Note the narrow range of T_{surf} on this day. There were intermediate, and more variable, moisture conditions on day 221 (Aug 9, 1990, $<T_{surf}>$ = 33 C). The average sensible heat flux (H) for the 8 sites is given at the
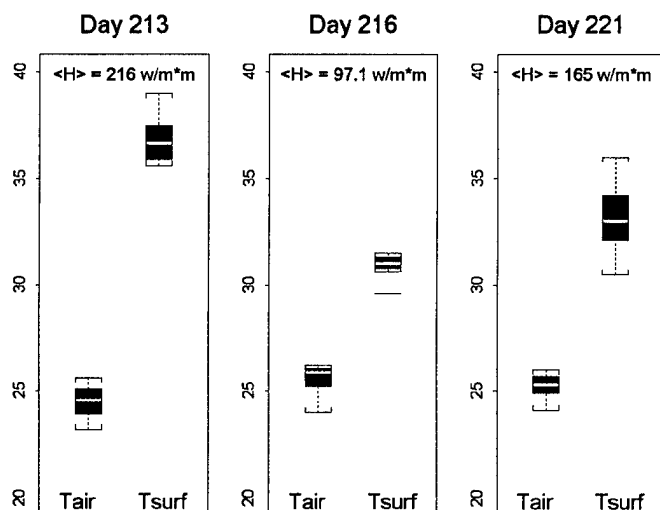
Figure 1. Boxplot of flux and temperature data from Monsoon 90 experiment. The vertical axis is in degrees C.

top for each day. It is clear that the magnitude of H is proportional to the difference between the average T_{surf} and the average T_{air} values. Maps of these surface temperatures were used with an average value of r_h derived from measured values of H, T_B, and T_{air} at the 8 ground flux stations. The spatial variations of T_B were used to derive the spatial variation of H over the watershed. The reader is referred to [10] for the details of the procedures and the maps of the sensible heat flux.

CONCLUSIONS

In this paper we have reviewed the physics of the energy balance at the land surface and the factors that can be accessed through remote sensing. These include the incoming solar radiation, R_s, and the surface albedo , α, from the VNIR channels of ASTER. The longwave radiation components, R_{Li} and $\epsilon\sigma T^4$, can be estimated from temperature sounding instruments. The primary contribution that ASTER can make to surface flux determinations will be through the thermal infrared channels. The problems with estimating the sensible heat flux were discussed and an example from the Monsoon 90 experiment was presented. By making use of a reference flux site a map of the spatial variation of H was generated from the T_B map and the range of values is in agreement with ground observations. These results indicate that at the present it may not be possible to determine the surface energy fluxes from remotely sensed data alone but that the spatial variation can be determined from T_B maps.

REFERENCES

[1]   Jackson, R.D., Reginato, R.J. and Idso, S.B.(1977). Wheat canopy temperature: a practical tool for evaluation water requirements. Water Resources Res. 13:81-86.

[2]   Price, J.C.(1982). On the use of satellite data to infer surface fluxes at meteorological scales. J. Appl. Meteorol. 21:1111-1122.

[3]   Soer, G.J.R. (1980). Estimation of regional evapotranspiration and soil moisture conditions using remotely sensed crop surface temperatures. Rem. Sens. Env. 9:27-45.

[4]   Dedieu, G., Deschamps, P.Y., and Kerr, Y.H.(1987). Satellite estimation of solar irradiance at the surface of the earth and of surface albedo using a physical model applied to Meteosat data, J.Clim. App. Meteorol. 26:79-87.

[5]   Suttles, J.T. and Ohring, G., Editors(1986). Surface radiation budget for climate applications. NASA Ref. Pub. 1169.

[6]   Hall, F.G., Huemmrich, K.F., Goetz, S.J., Sellers, P.J. and Nickeson, J.E. (1992). Satellite Remote Sensing of Surface Energy Balance: Success, Failures and Unresolved Issues in FIFE. J. Geophys. Res., 97:19061-19089.

[7]   Norman, J.M., Divakarla, M. and Goel, N.S. (1995). Algorithms for Extracting Information from Remote Thermal-IR Observations of the Earth's Surface. Remote Sensing Environment, 51:157-168.

[8]   Shuttleworth, W.J., (1991). Evaporation Models in Hydrology, Chapter 6 in Land Surface Evaporation: Measurement and Parameterization edited by T.J. Schmugge and J.-C. Andre, Springer-Verlag NewYork Inc.

[9]   Stewart, J.B., Kustas, W.P., Humes, K.S., Nichols, W.D., Moran, M.S. and DeBruin, H.A.R. (1994). Sensible Heat Flux - Radiometric Surface Temperature Relationship for Semiarid Areas. J. Appl. Meteor., 33:1110-1117.

[10] Humes, K.S., Kustas, W.P. and D.C. Goodrich, 1997. Spatially Distributed Sensible Heat Flux over a Semi-Arid Watershed. Part 1: Use of Radiometric Surface Temperature and a Spatially Uniform Resistance. J. of Appl. Meteorol., 36:281-292

Application of High Resolution Side-looking MSS Data
to Heat Island Potential in Urban Area

Akira Hoyano and Akinaru IINO

Tokyo Institute of Technology

4259 Nagatusta-cho, Midori-ku, Yokohama 226, Japan

Tel: +81-45-924-5501 / Fax: +81-45-924-5519 / Email: hoyano@depe.titech.ac.jp

Abstract -- We employed side-looking airborne MSS data with high resolution to investigate the actual conditions of surface temperature distributions in urban area with the complex ground surface form. In addition, airborne MSS and GIS data were used to calculate the HIP of various types of residential regions, and results verified its effectiveness for monitoring urban land use change and thermal environment.

INTRODUCTION

Urban climates have recently been characterized by the heat island phenomenon which considers various changes in land cover conditions and also the increase of artificial heat sources. Such information is vital for urban development planning because it can be used to obtain an accurate prediction method for estimating an urban thermal environment.

We proposed a new index based on sensible heat flux, called the "heat island potential (HIP)," which is defined to express the thermal characteristics of each type of region contained in an urban area, i.e., spatial forms and materials[1]. The actual conditions to be considered by the HIP were determined using downward-looking and side-looking airborne multi-spectral scanner (MSS) data with high resolution.

SIDE-LOOKING AIRBORNE MSS IMAGE

Methodology for observations

Airborne MSS observations provide useful data for measuring the surface temperature distribution of an urban area with the complex ground surface form, and in general, only downward-looking airborne MSS observations have been considered. Here, however, we employ downward-looking and side-looking observations to measure the all surface temperature distribution of various types of residential regions located in a suburban area which was under development.

The conditions used for obtaining airborne MSS observations are as follows:

1) The angle of the MSS sensor could be adjusted to view the horizontal and vertical surfaces of buildings (Fig. 1).

2) To investigate the influence of building walls on the HIP, we used time-series airborne MSS images that were obtained on a winter day with a clear sky.

3) Kawasaki, Japan, was selected for representing various land cover conditions. MSS observation conditions are summarized in Table 1.

Observation results

Figure 2 presents typical data showing infrared (IR) thermal images obtained by side-looking airborne MSS observations of two types of residential regions containing wooden buildings or reinforced concrete (RC) buildings. Aspects of these images with about 2m resolution which show complex form on ground
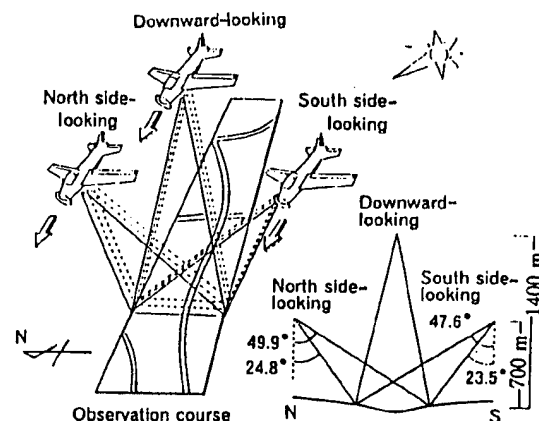
Fig.1 Flight course and look angles of airborne MSS observation.

Table 1   MSS observation conditions

Date	February 26, 1992
Time	8:31-8:51, 12:28-12:46, 17:10-17:41
Location	Kawasaki, Japan
Sensor	Multi-spectral scanner
IFOV	2.5 mrad
Bands used for analysis	Visible 0.61-0.69 μ m Near infrared 0.80-1.0 μ m Thermal infrared 8-11 μ m

surface, depend on the look angle of the observation. In case of Daytime, the north side-looking images are obviously darker (lower temperature) than the south side-looking images. Sunset side-looking images show that surface temperature of building walls is the highest because of heating loss.

HIP IN RESIDENTIAL AREAS

Methodology for HIP calculation

The observed downward- and side-looking IR thermal images were used to determine the HIP of each type of considered residential region. The following assumptions were used:
1) It is assumed that the emissivity of all surfaces is 1.0, i.e., the radiant and surface temperatures are considered to be equal.
2) It is assumed that the surface temperature of trees, which could not be measured by the MSS sensor, is equal to the air temperature, and that the area of a group of trees is equal to the area it projects onto the ground.

The HIP index was subsequently determined using

$$HIP = \frac{\int_{all\ urban\ surfaces} (T_s - \bar{T}_a)\ dS}{A} \qquad (1)$$

and calculated by following equation using remote sensing data and GIS data.
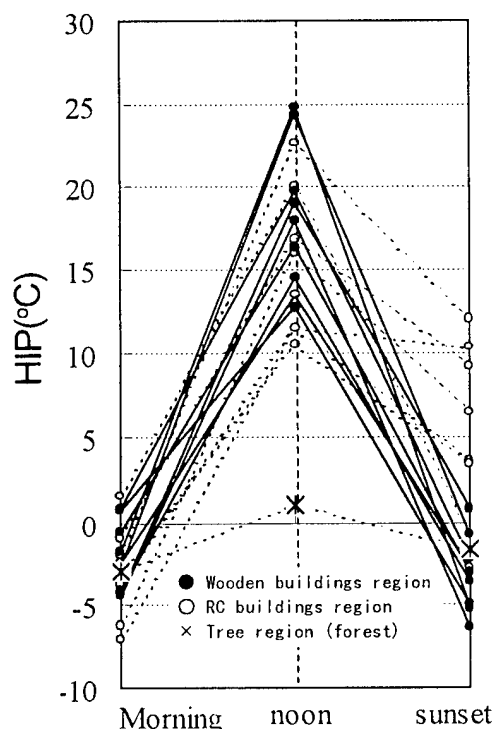
Fig.3 Durnal change of HIP on winter day with a clear sky.

$$HIP = \frac{(T_{sh} - \bar{T}_a)S_h + (T_{sv} - \bar{T}_a)S_v}{A} \qquad (2)$$

where HIP is the heat island potential (°C), T_{sh} is the average temperature of a horizontal plate (°C), T_{sv} the average temperature of a vertical plate (°C), T_a the air temperature (°C), S_h the total area of horizontal plate (m²), and S_v the total area of vertical plate (m²).

Because the sensible heat flux and HIP correlate well, the HIP functions as an index for expressing an urban region's characteristics using the difference between the temperature of the atmosphere and that of all urban surfaces within it, with such characteristics being determined by the land use and land cover conditions of each region.

Diurnal change of the HIP for various land cover regions

The HIP index of various land cover regions was calculated using MSS thermal images obtained on a clear day in winter at morning, noon, and sunset. As shown in Figure 3, the daytime HIP of the tree regions only ranges from -3 to 1°C, with this range in temperature being almost equal to that of air temperature.

On the other hand, the HIP of various regions containing wooden and RC buildings significantly varies with observation time, i.e., at morning it ranges from -7 to 2°C, and also many regions have a HIP less than 0°C due to the increase in the air temperature. These values naturally increase from morning to noon, reaching a maximum of 24°C, then decrease from noon to sunset. Note that at sunset the wooden building regions have similar HIP values as the tree regions, although in comparison, those for the RC building regions are much higher. One RC building region showed a constant HIP value of 12°C from noon to sunset. This result is thought to have been caused by these buildings storing solar radiation during the day and emitting building heat from their walls and windows.

Effect of land cover conditions on diurnal changes of the HIP

The development status of a region was described using two indices: "the vegetation cover ratio," which indicates the degree of tree destruction due to urban development, and "the floor area ratio" (ratio of total floor area to a region's area) of a region's wooden buildings (including steel structure buildings) or RC buildings, which indicates heat capacity of each type of building. We calculated the vegetation cover ratio using a map of vegetation cover which was made by analyzing downward-looking MSS data via the maximum likelihood method, while the floor area ratio was calculated using 1:2500-scale GIS data which provided the shape and area of each building.

1240
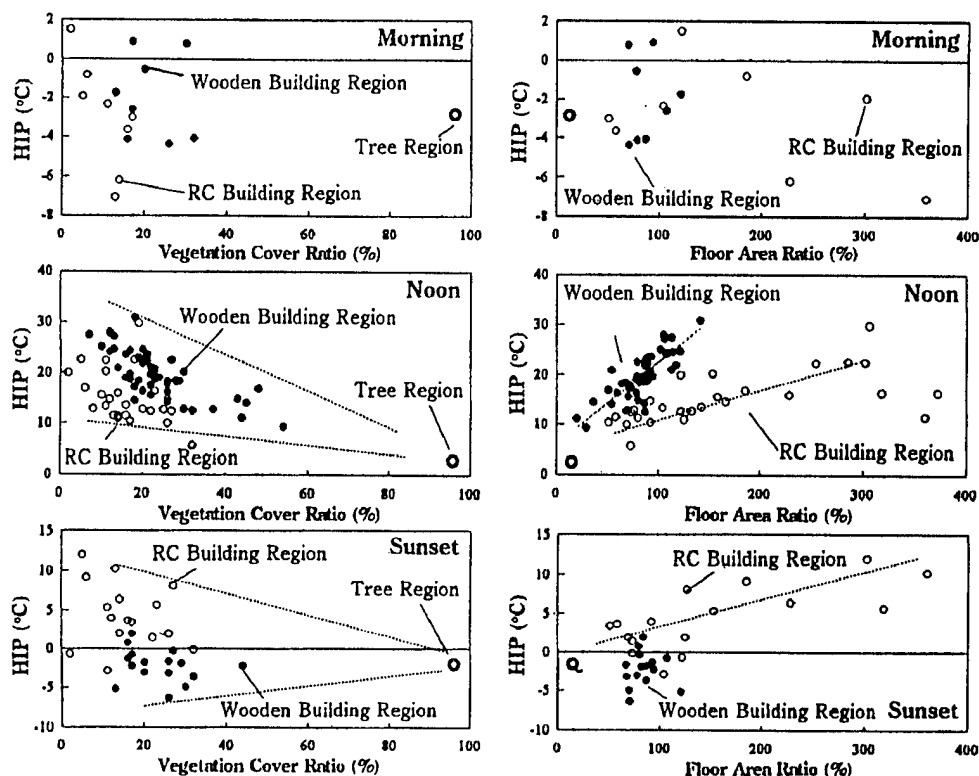
Fig.4 Relationship between the HIP and the vegetation cover/building area ratio for various land cover conditions at indicated times of the day.

Figure 4 shows resultant HIP values calculated at indicated times of the day versus the vegetation cover and floor area ratios of wooden, RC, and tree regions. At noon, the HIP of the tree regions is about 1°C, whereas that of other regions is greater than 10°C. In general, as a region's vegetation cover ratio decreases, its HIP increases. Also, the HIP values of wooden building regions are larger compared to those of RC building regions.

Note the sunset HIP values of wooden building regions are less than 0°C, while those of RC building regions are greater than 0°C. Moreover, increasing the floor area ratio of RC building regions causes the largest increase in HIP, with the HIP value for a floor area ratio of 300% being over 10°C. Since the diurnal change in HIP was found to appropriately vary with respect to the considered land cover conditions, this verifies that the HIP is an efficient index for indicating the thermal characteristics of each region.

CONCLUSIONS

A new index based on sensible heat flux was proposed, named the "heat island potential (HIP)," which can be employed in urban development planning to evaluate the urban thermal environment. The HIP of various residential regions was calculated using side-looking airborne MSS data, after which

the HIP was verified to be an effective index representing the thermal characteristics of each type of region.

ACKNOWLEDGEMENTS

REFERENCES

[1]Akinaru IINO and Akira HOYANO, Development of a method to predict the heat island potential using remote sensing and GIS data, Energy and Buildings 23, pp.199-205, 1996
[2]Akira HOYANO, Kazuhiro KOGA and Junichi YAMASHITA, Analysis for sensible heat flux in hillside development area by using side-looking airborne MSS data, J. Archi. Plann. Environ. Eng., AIJ, No.462, 49-58, Aug., 1994 (in Japanese).
[3]Akira HOYANO, Akinaru IINO, Kazuhiro KOGA and Hitomi SANO, Quantification of heat island potential of hillside development areas using side-looking airborne MSS data and its relationship to land cover conditions, J. Archit. Plann. Environ. Eng., AIJ, No.471, 29-37, May, 1995 (in Japanese).
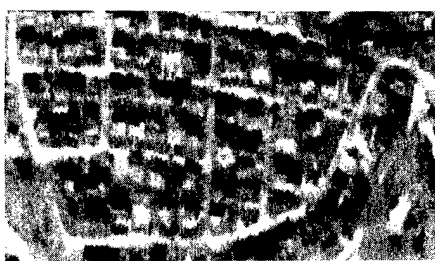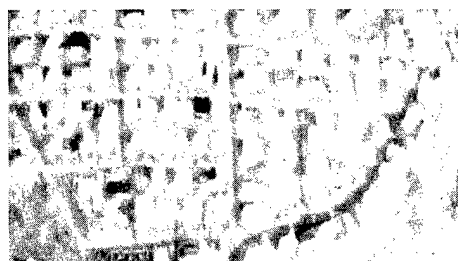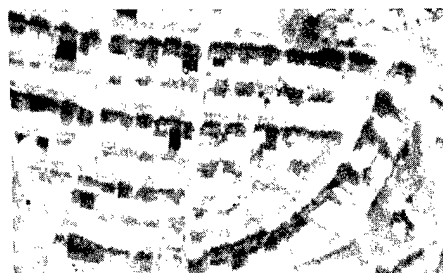
Morning (8:30)
Air temperature: 4.4°C

Noon(12:30)
Air temperature: 9.0°C

Sunset (17:30)
Air temperature: 7.6°C

(a) Wooden building region
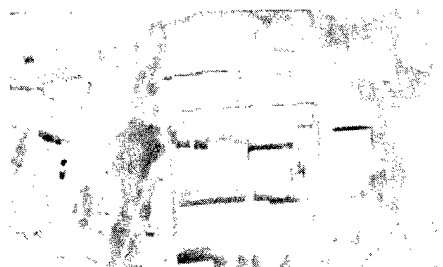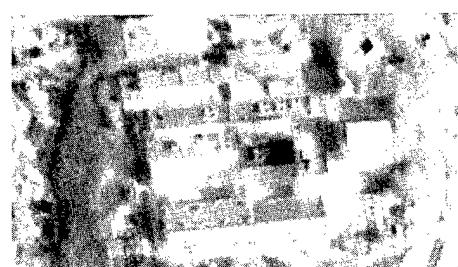
Morning (8:30)
Air temperature: 4.4°C

Noon(12:30)
Air temperature: 9.0°C

Sunset (17:30)
Air temperature: 7.6°C

(b) RC building region

upper: North side-looking
lower: South side-looking
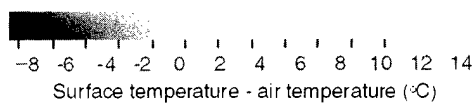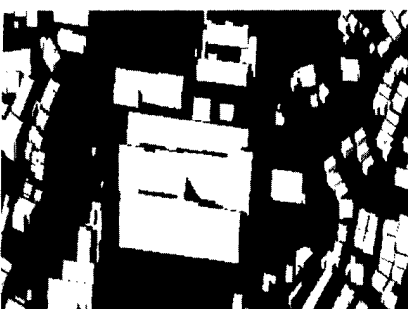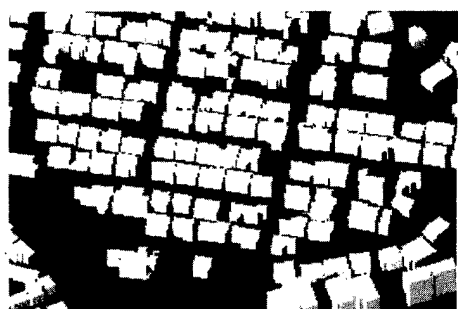
Wooden building region

RC building region

(c) GIS data

−8 −6 −4 −2 0 2 4 6 8 10 12 14
Surface temperature - air temperature (°C)

Fig.2
Side-looking IR images and GIS
data of both Wooden and RC
buildings regions

1242

Derivative Analysis of Hyperspectral Data for Detecting Spectral Features

Fuan Tsai, William Philpot
Cornell University
453 Hollister Hall, Cornell University, Ithaca, NY 14853 USA
Tel: +1-607-255-0801/Fax: +1-607-255-4662/Email:ft11@cornell.edu, wdp2@cornell.edu

Abstract -- A derivative algorithm was adapted to deal with spectral data acquired in narrow, continuous bands as truly spectrally continuous data. An investigation on intelligently detecting spectral features from a synthetic spectrum and a laboratory vegetation spectrum demonstrated the use of derivative algorithm in extraction of subtle information at different spectral scales of interest.

INTRODUCTION

Methods for traditional multispectral analysis in remote sensing are usually derived from established methods in multivariate statistics [5][15]. When higher resolution, spectrally continuous remote sensing data become available, researchers in remote sensing tended to select suitable bands to optimize the existing algorithms of multispectral data analysis [6], or to generate new algorithms based on traditional multispectral concepts [2][11][12]. In typical multispectral analysis, each spectral band is considered as an independent variable--a reasonable assumption for multispectral data but not really appropriate for hyperspectral data. Only a few researchers have manipulated data as truly spectrally continuous data [3], although there are methods that are commonly used in spectroscopy for dealing with continuous data.

Not all methods used in spectroscopy can be directly adapted to remote sensing analysis because there are inherent differences between these two types of data [18]. Among the techniques developed in spectroscopy, derivative analysis is particularly promising for use with remote sensing data. Derivatives not only emphasize subtle spectral details, they also minimize illumination and atmospheric effects [4][13]. Thus, derivatives are well-suited to extracting spectral features relating to specified target properties.

The purpose of this study was to develop a "finite divided difference approximation" derivative procedure that treats hyperspectral data as truly continuous data and to use the derivative algorithm to extract subtle spectral features.

METHODS

Derivatives are very sensitive to noise. Therefore, before computing derivatives, smoothing or otherwise minimizing random noise might be necessary. Savitzky and Golay provided a simplified least-square-fitting procedure for simultaneously smoothing and differentiating a spectrum in [16]. Corrections and modifications to the Savitzky-Golay convolution procedure were provided by other researchers in [10] and [17]. The Savitzky-Golay procedure implicitly assumes that random noise has similar characteristics through the spectrum and can be handled by an invariant procedure over the spectrum. Kawata and Minami [8] argued that, since random noise usually varies over the spectrum, polynomial curve-fitting might alter the signal waveform instead of eliminating the noise. They presented an alternative based on minimizing the mean-squared errors. Another commonly used smoothing algorithm is the mean-filter algorithm, which simply computes the mean value of samples within a local smoothing window and use it as the new value of the midpoint of the window. When spectral features are broad and the noise is relatively high frequency comparing to the real spectral features, there should be little significant difference among the three methods. In such a case, mean-filter is preferred because it is straight forward and requires the least time of computation.

Derivatives were estimated using finite divided difference approximation algorithm with a finite band separation, $\Delta\lambda$. The first order derivative is calculated by:

$$\frac{ds}{d\lambda}\bigg|_i \approx \frac{s(\lambda_j) - s(\lambda_i)}{\Delta\lambda} \qquad (1)$$

where $\Delta\lambda$ is the separation between adjacent bands--i.e., $\Delta\lambda = \lambda_j - \lambda_i$. In general, the n-th order derivative can be represented as:

$$\frac{d^n s}{d\lambda^n}\bigg|_j = \frac{d}{d\lambda}\left(\frac{d^{(n-1)}s}{d\lambda^{(n-1)}}\right) = \ldots \approx \frac{s(\lambda_{i+n}) - \ldots + s(\lambda_i)}{(\Delta\lambda)^n} = \frac{\sum_{k=i}^{i+n} C_k s(\lambda_k)}{(\Delta\lambda)^n} \qquad (2)$$

where $j=(2i+n)/2$, if $2i+n$ is even, or $j=(2i+n+1)/2$, if $(2i+n)$ is odd; this indicates that if the resultant derivative falls between sampling points, it is assigned to the next larger wavelength or wave number. The coefficients, C_k, are calculated using an iteration scheme.

Applying derivatives to spectra may cause some side effects. For example, as the band separation, $\Delta\lambda$, increases, the magnitude of derivatives will be depressed because the derivatives are normalized by a power of $\Delta\lambda$ as shown in (2). However, this effect may not be necessarily disadvantageous.

It is possible to mimic different spectral scales by selecting suitable band separations for filtering spectral features smaller than $\Delta\lambda$ and enhancing features at the scale of $\Delta\lambda$. This quasi-smoothing effect overcomes the imperfection of inverted Gaussian procedures provided in [1], which neglected the scale effect and implied the detection of spectral positions is independent to bandwidth and sampling intervals. The application of this effect is demonstrated in the following example.

Fig.1 The synthetic spectrum composed of five Gaussian features whose characteristics are described in Tb.1.

DERIVATIVES IN DETECTING SPECTRAL FEATURES

According to Huguenin and Johns in [7], derivatives can be used to detect absorption band positions from reflectance spectra. The criteria for determining the occurrence of an absorption band position is that the fifth derivative is zero, the fourth derivative is positive and the second derivative is negative. If applying the finite approximation derivative algorithm, the finite band separation can be a potential source of error. Spectral features smaller than $\Delta\lambda$ will be lost. On the other hand, spectral features larger than $\Delta\lambda$ should remain detectable for the derivative algorithm. To test this hypothesis, a synthetic spectrum was created to evaluate the performance of the developed derivative algorithm in detecting the original peak positions of sub-spectra that compose the synthetic spectrum. The spectrum consists of five overlapping Gaussian features, each with a different mean, peak strength and half-width (full width at half maximum, FWHM) values described in Tb.1 and shown in Fig.1. Each Gaussian band can be represented as:

$$f(k)=h*exp[-0.5*(k-k_0)^2/\sigma^2] \qquad (3)$$

where h is the peak strength, k_0 is the position of mean center and σ is the standard deviation of the distribution function. In this case, the value of σ can be determined by the pre-determined half-width,$W=2*(2*ln2)^{1/2}/\sigma$.

Two of the five constituent bands (the second and the fourth) are much smaller in amplitude and width than the other three. They can be considered as artifacts and assume that the central peak is the primary feature of interest. Further assume that the critical factor for detecting the occurrence of an peak position is the zero-crossing of the fifth derivative. It is hoped that the developed algorithm can successfully detect
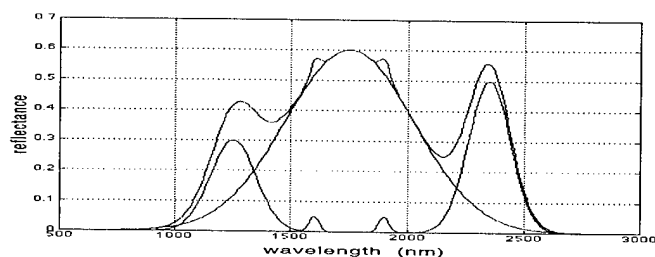
Tb.1 Parameters of Gaussian features to construct a spectrum

Feature	Peak Position	Peak Value(%)	Half Width
1	1,250	30	230
2	1,600	5	50
3	1,750	60	650
4	1,900	5	50
5	2,350	50	210

the three major peak positions from the composite spectrum. Fig.2 shows the results of fifth derivatives at band separation of 1, 5, 10, 15, 20, and 30 sampling intervals (1 sampling interval equals 10 nm). As shown in Tb.1, the two artifacts are 150 nm less and greater the feature centered at 1750 nm. In Fig.2, when band separations are smaller than or equal to the distance between the noise peak and its neighboring features ($\Delta\lambda$=10, 50, 100 and 150 nm), the zero-crossings occur almost exactly at the three central peak positions. However, as $\Delta\lambda$ approaches and exceeds the distance between artifact centers and its neighbors, the derivative results gradually change to a simpler smoother curve. This indicates that the effects of artifacts on the derivative first diminishes and then disappears.As a result, in Fig.2, the derivative at 20 sampling intervals (200 nm) loses both "noise" positions, but the major peak position is still identified.

In real application, this band decomposition algorithm can be very helpful in extracting spectral features from complex laboratory or remote sensing data. Fig.3 shows a portion of a soybean leaf fluorescence spectrum at excitation wavelength of 337 nm [14] and its 2nd, 4th and 5th derivatives. The derivatives were computed at $\Delta\lambda$=16 nm (8 sampling intervals) after smoothing with mean-filter. Applying the criteria of band decomposition, the peak at 600 nm was identified with ease. A second feature, one which was arguable in the original spectrum, was located around 530 nm. This could be the shoulder of blue-green fluorescence emission

Fig.2 Fifth derivatives of the synthetic spectrum at different $\Delta\lambda$.
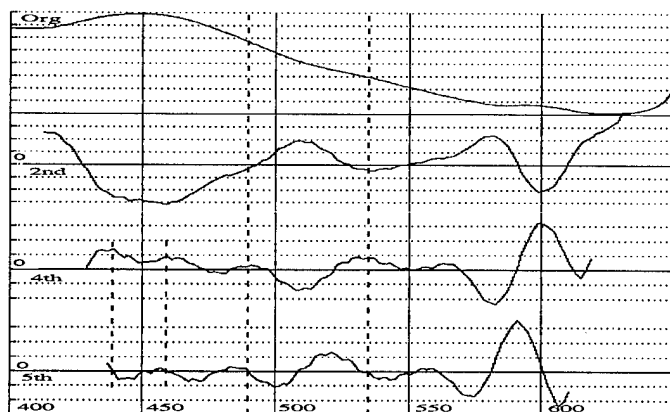
Fig.3 Fluorescence spectrum of a soybean leaf at excitation of 337 nm and its derivatives.

occurs at 525 nm as stated in [9]. There is ambiguity in detecting the band position at 450nm. There are three zero-crossings near 450 nm. All of them fulfill the criteria of the occurrence of an band position. However, if the criteria are modified such that 5th derivative is zero, the 4th is positive and at or near a local maximum (i.e., within the range defined by FWHM), and the 2nd is negative and at or near a local minimum, the interpretation changes. Applying these expanded criteria to the result in Fig.3, the possibility of a band peak at 490 nm is now excluded because its 2nd derivative is beyond the FWHM of the local minimum. The occurrence of band position at 450 nm is no longer sustained either, because the 4th derivative is in a local minimum. Instead, both 440 nm and 460 nm would be considered as potential positions, although there is no evidence in the fluorescence literature supporting the presence of more than one peak around 450 nm. The ambiguity probably results from an improper selection of band separation or bandwidth. According to Fig.3, if the band separation is increased, the local minimum at 450 nm in the 4th derivative is expected to disappear and the two local peak peaks are expected to incorporate into one. Thus, 450 nm would be identified as a peak band position even according to the expanded criteria.

REFERENCES

[1] G. F. Bonham-Caeter, "Numerical Procedures and Computer Program for Fitting Inverted Gaussian Model to Vegetation Reflectance Data," Computers and Geoscience, 14:339-356, 1988.

[2] E. W. Chappelle, M. S. Kim, & J. E. I. McMurtey, "Ratio Analysis of Reflectance Spectra (RARS): an algorithm for the remote estimation of chlorophyll A, B and carotenoids in soybean leaves," Remote Sens. Environ., 39:239-247, 1992.

[3] T. H. Demetriades-Shah, M. D. Steven, & J. A. Clark, "High Resolution Derivative Spectra in Remote Sensing," Remote Sens. Environ., 33:55-64, 1990.

[4] K. Dick, & J. R. Miller, "Derivative Analysis Applied to High Resolution Optical Spectra of Freshwater Lakes," in the 14th Canadian Symposium on Remote Sensing, Calgary, Alberta, CA, 1991.

[5] R. O. Duda, & P. E. Hart, Pattern Classification and Scene Analysis, John Wiley & Sons, New York, 1973.

[6] J. P. Hoffbeck, & D. A., Landgrebe, "Classification of High Dimensional Multispectral Image Data," in the 4th Annual JPL Airborne Geoscience Workshop, Washington D.C., 1993.

[7] R. L. Huguenin, & J. L. Johns, "Intelligent Information Extraction from Reflectance Spectra: Absorption Band Position," J. Geophysical Research, 91(B9):9585-9598, 1986.

[8] S. Kawata, & S. Minami, "Adaptive Smoothing of Spectroscopic Data by A Linear Mean-Square Estimation," Applied Spectroscopy, 38(1):49-58, 1984.

[9] M. Lang, P. Siffel, Z. Braunová, & H. K. Lichtenthaler, "Investigations of the Blue-green Fluorescence Emission of Plant Leaves," Bot. Acta, 105:435-440, 1992.

[10] H. Madden, "Comments on The Savitzky-Golay Convolution Method for Least-Squares Fit Smoothing and Differentiation of Digital Data," Analytical Chemistry, 50(9):1383-1386.

[11] M. E. Martin, & J. D. Aber, "Measurements of Canopy Chemistry with 1992 AVIRIS Data at Blackhawk Island and Harvard Forest," in the 4th Annual JPL Airborne Geoscience Workshop, Washington D.C., 1993.

[12] J. Peñuelas, J. A. Gamon, A. L. Fredeen, J. Merino, & C. B. Field, "Reflectance Indices Associated With Physiological Changes in Nitrogen- and Water-limited Sunflower Leaves," Remote Sens. Environ., 48:135-146, 1994.

[13] W. D. Philpot, "The Derivative Ratio Algorithm: Avoiding Atmospheric Effects in Remote Sensing," IEEE Transactions on Geoscience & Remote Sensing, 29(3):350-357, 1991.

[14] W. Philpot, M. Duggin, R. Raba, & F. Tsai, "Analysis of Reflectance and Fluorescence Spectra for Atypical Features: Fluorescence in Yellow-green," J. Plant Physiol., 148:567-573, 1996.

[15] J. A. Richards, Remote Sensing Digital Image Analysis, 2nd ed., Springer-Verlag, New York, 1993.

[16] A. Savitzky, & M. J. E. Golay, "Smoothing and Differentiation of Data by Simplified Least Squares Procedure," Analytical Chemistry, 44:1906-1909, 1964.

[17] J. Steinier, Y. Termonia, & J. Deltour, "Comments on Smoothing and Differentiation of Data by Simplified Least Squares Procedure," Analytical Chemistry, 44(11):1906-1909, 1972.

[18] F. Tsai, "Derivative Analysis of Hyperspectral Data," Master Thesis, Cornell University, New York, 1996.

Reading SAR Data:
A New General Reader and a Proposed New Standard

Leland Pierce

The University of Michigan, Radiation Lab
Ann Arbor, MI 48109-2122 USA
Phone: +1-313-763-3157 FAX: +1-313-647-2106 email: lep@eecs.umich.edu

ABSTRACT

All recent scientific SAR data is formatted in compliance, more or less, with the CEOS standard developed recently. If this standard were followed meticulously by each organization that produces SAR data, a single program could read all of the data. However, there are small but significant differences in how each sensor's data is formatted and this has led to the need for a different program to read the data for each sensor, and even for each format from the same sensor. This makes using the data difficult for most users, as the first step is to read it in to some kind of image processing system, such as ERDAS, PCI, GRASS, KHOROS, etc.

The solution to this problem has been for data providers and commercial vendors to write tape readers for their customers. Unfortunately, many of these readers do not read all the ancillary data and do not allow easy porting for use with other image processing systems. A new general reader has been developed that solves all these problems. It uses simple text "format" files to define the data that is to be read in: variable name and type, location in file, and format. The reader writes a new file in a new format, as described later. A standard reader now reads from this new file, allowing the user to write interface code to read the data (ancillary and image) into the user's image processing system.

The new proposed format addresses the following issues: (1) a single file per image, with a single record-length per file; (2) Ancillary data in ASCII: KEYWORD = value ; comment; (3) Self-documenting via comments and strict syntax; (4) Self-reading, so that a program can inspect input file and generate code that can read in all data in input file; (5) Addition of new parameters is simple, and users can generate readers for the new format with the program in #4.

This code is written and works now.

1. INTRODUCTION

The previous version of this paper presented the design strategy, but the programs were not yet written. Now, the programs are written and they work well together. The design strategy is presented here as it has evolved since last year.

This paper presents a working solution to the problem of constantly writing new software to read in, and otherwise process, a SAR image every time a new format must be supported. The basic problem is that the CEOS standard for SAR data is not being meticulously followed, hence there is a new format to deal with whenever receiving data from a different sensor or different processing facility. Section 2 details the problems with the present standard, and section 3 presents a computer program that solves these problems in a way that requires no programming from the user. Section 4 gives a detailed example of a format-file that is used for that solution. Section 5 then goes on to propose a new standard that would be better for both data provider and data user. A detailed example of this new standard is given in section 6, followed by the conclusions in section 7.

2. PRESENT TROUBLES

To any SAR data user who uses data from different sensors or different processing facilities the problems with the present standard for this data is obvious: the formats are nearly identical, but not exactly. When they aren't exactly identical in areas that matter to the user, the solution involves writing a custom computer program for each format type. In our lab this has quickly become a prohibitive time sink with 2 or 3 new formats every year. The solution presented here is a code-generator: a program that writes the source code for another program.

But back to the problems: how serious are they? It all depends on the kind of processing required: which parameters you need. Some example problems include: (1) one needs the *resolution* of a pixel, not *spacing*, to estimate the number of looks applied, and it's not there; (2) one needs a calibration constant for calculating an absolutely-calibrated image, for comparison with other images, and that constant is zero or missing. The kinds of problems encountered so far are summarized below:

1. missing data (zero or not supplied at all)
2. wrong data (the value is wrong or inconsistent)
3. data with different meanings (eg.: one facility uses sensor resolution, while another uses image resolution)
4. data in different places and/or different formats (eg.: date formats)

5. data is not in the same form as in another format. Requires writing a program to calculate required parameter(s).
6. poorly-defined parameters (eg.: polynomial coefficients for doppler centroid do not give a clue as to the polynomial equation they go with.)

3. SOLUTION

The proposed solution to most of these problems involves the user writing a simple ASCII "format-file" for each file-type, describing what to read, where to read it, and the format. This can take care of problem #4 above. The format file also allows one to assign default values and to do arbitrary processing of the values to produce new ones. This will solve problems #3 and #5, and can solve #1, #2, and #6 under most circumstances. To solve problem #6 and sometimes #1, one must resort to asking the data provider for more information. This is usually very difficult since the question usually involves something rather detailed or esoteric. Often, things that are missing or wrong are predictable for a particular format (from a particular sensor and processing facility) and so default values can be used instead. The data with different meanings is also a constant for a particular file-type and so can usually be transformed so that it has a standard meaning as desired by the user. However, there still may be unresolvable problems that the "format-file" approach cannnot solve, eg.: no calibration constant. But since this "format-file" scheme solves most problems it saves lots of time and is still worth using in most cases.

Each format file that a user writes specifies how to read in ancillary and image data as provided by a particular processing facility in one among several formats that are specific to the sensor involved. For example, four format files would be written in order to read data from: (1) ERS-1 as provided by Gatineau (Canada) in MLD format, (2) ERS-1 as provided by DLR (Germany) in PRI format, (3) SIR-C as provided by JPL (USA) in SLC format, (4) X-SAR as provided by DLR (Germany) in SSC format. Each is different, each has its own quirks, but these quirks are predictable for each and can be encoded in the format files that the user must write.

These format files are detailed enough so that a computer program is generated from them. The new program is capable of reading the data as specified in the format file. There are two main reasons for this method:

1. The generated code can easily be customized to work with different image processing packages. This is through the use of a few standardized calls to subroutines/functions that are package-specific. When compiling the program one merely links using the library appropriate for the image processing package of choice,

2. The resultant data sets, from disparate sensors and processors, can all have the exact same set of ancillary data. This is due to the translation and calculation abilities built in to the format file specification. For instance: All the dates can be MM-DD-YYYY, all the distances can be meters, all the calibration constants can be multiplicative as applied, etc.

Both of these are major advantages when one must write code to perform further processing. For example, our lab uses six different orthorectification programs for six different SAR formats. This is a nightmare of wasted effort in writing and maintaining them. One orthorectifier is all that should be needed with this new data reader and re-formatter.

The file produced using this data reader is in a new format which is described below. It is felt that this format is more flexible than the present one and that it is flexible enough to represent all SAR data in the forseeable future.

4. EXCERPT FROM EXAMPLE FORMAT-FILE

```
% format file for: Gatineau ERS-1/MLD
file_type: DEFAULT="format",LOCAL
int_format: DEFAULT="2s-complement",LOCAL
int_byte_order: DEFAULT=[4,3,2,1],LOCAL
%
voldesc: RECORD-ID=5:5,"BIU8",192;6:6,
    "BIU8",192;7:7,"BIU8",18;8:8,"BIU8",18
%
tapeID:  READ="voldesc",45:60,"A32"
sensor:  READ="voldesc",61:76,"A16"
%CCODE=if(strncmp(sensor,"ERS",3) !=0 ) {
%CCODE=    printf("Error: Expecting ERS
              sensor, got: %s\n",sensor);
%CCODE=    return(error); }
totpix:  READ="imop_fdesc",249:256,"I8"
totlin:  READ="imop_fdesc",237:244,"I8"
%
% Now the image data:
imgbfr:  DATA="image",193:$,"BIU2"
```

5. PROPOSED NEW FORMAT

The new standard for SAR format files is described here. What are the requirements of this new standard? The most basic requirement is that it be used by the data providers. I formulated the following list with that in mind, as well as ease of use by the data users:

1. One file per image (can be multi-channel).

2. All records in file same length.

3. All ancillary data in ASCII at start of file:
   KEYWORD = value ; comment

4. Self-Documenting:
   • parameters clearly defined with comments
   • parameter types unambiguous via syntax rules

5. Self-Reading: Developed code that can examine any file and output the source code for a program that will read in the file. As in the general reader for present CEOS-SAR data, the same customization to a user's own image processing system is available.

6. Must have a set of parameters (and definitions) that all data providers agree to that would be mandatory for all data sets. Optional parameters for different types of sensors can be defined as well.

7. Addition of new parameters by the data providers is as simple as adding the parameter name, value and comment. Users can then read the "new format" after creating a reader for it by running the program in #5.

Each of these is easy to accomplish by the data providers, and will allow for increased ease-of-use by the end-users. Becasue SAR is still in rapid development there are constantly new requirements in the ancillary data that no standardizing committee could hope to keep up with. That is why the present standard (CEOS-2) has a special record that is to be used for anything extra that the data provider thinks is important. The new standard proposed here makes the entire header area like this special record so that there is nothing special about new ancillary data: making it special just makes it more work to write a program to read it in. So all ancillary data is in the top of the file, in the same format, as given in point #3 above. Adding new keywords is easy for the data provider, since the ordering of the keywords and thier positions is completely arbitrary. Old programs that don't read these new keywords still work, since they effectively ignore any data that they weren't told to read. All common scalar, vector, and matrix data types are supported and have a unique syntax so that their data-types are unambiguous. Various required keywords specify important details concerning the image data such as data-type and byte-ordering. All capabilities in the old format are preserved in this new format, such as geocoding line-by-line, since vectors of arbitrary length are a supported ancillary data type. The ASCII header can be displayed at the terminal very simply, since all that is needed is a translation from the end-of-keyword character used in the data file to the end-of-line character used by the computer. The image itself no longer has any header or trailer in each line so that it is very simple to read it in with standard programs. Also, a record of image data on the tape is one line in the image, allowing the user to easily extract a subset while reading the tape, if necessary.

Lastly, because it is strongly typed, the data file can be used as a template by a code-generator to produce a new tape-reading program that will read in all of the ancillary data, thus alleviating the end-user of the task of writing a new tape reader for each new format. On the processing facility side, there is another program which can read a data file, but generate code to *write* a data file of that kind. With all this in hand, the user will never again need a hard-copy of the tape format describing fields byte-by-byte.

6. EXCERPT FROM EXAMPLE NEW FORMAT

Note that many of the comments have been deleted in an effort to save space for this article.

```
%START-OF-HEADER
RECORD_LENGTH= 512
FILE_FORMAT="CEOS-3 SAR"
NHEADER_RECORDS= 30
% Example fmt for CEOS-3 SAR Image Data.
%
NUMBER_OF_IMAGE_LINES=512 % No. of lines
% (y-dir) in the image for a single band.
% (NOT #records)
NUMBER_OF_IMAGE_PIXELS=512 %No. of pixels
% (x-dir) in the image for a single band.
%
DATA_TYPE="signed integer"
DATA_NUMBERS_PER_PIXEL=1
DATA_BYTES_PER_NUMBER=1
DATA_INTEGER_FORMAT="2s-complement"
DATA_BAND_INTERLEAVING="pixel"
%
SENSOR_NAME="SRL-1, SIR-C"
DATA_FORMAT_CODE="MLD"
DATA_FORMAT_NAME="Multi-Look Detected"
ACQUISITION_DATE="01-13-1960" %dd-mm-yyyy
ACQUSITION_TIME="13:45:23.023"
                         % hh:mm:ss.xxx
RESOLUTION_AZIMUTH=30.  % Resolution in
%              azimuth direction, meters.
RESOLUTION_SLANT_RANGE=30.  % Resolution
%         in slant range direction, meters.
```

7. CONCLUSIONS

Two new programs have been written that can help both SAR data users and providers to save time and do their work better. The first program can read several format-files, describing different formats of CEOS-SAR data files, and create a program that will distinguish between the different formats and will read them in, so that both the ancillary data and the image data are in a uniform format for use by other processing programs. The second program is really a set of programs that allows a user and data provider to read and write a new format that is flexible and powerful enough to satisfy all data formatting needs for SAR data in the forseeable future. This set of programs alleviates the need for users or providers to ever write a format-reader or format-writer ever again. These programs are available to any non-commercial user. Just email the author for more information.

Standard Data Products from the MODIS Science Team

Laurence E. Fishtahler
Computer Sciences Corporation
Terrestrial Information Systems Branch / Code 922
Goddard Space Flight Center
Greenbelt, Maryland 20771
301-286-8518
larryf@ltpmail.gsfc.nasa.gov

INTRODUCTION

The Moderate Resolution Imaging Spectroradiometer (MODIS) instrument will view the Earth in 36 spectral bands ranging from 0.4 to 1.4 micrometers with spatial resolution from 250 to 1,000 meters. Its first flight will be onboard the EOS-AM1 spacecraft scheduled for launch in mid '98 into a near-polar 10:30 AM descending sun-synchronous orbit. In this orbit MODIS will provide global coverage every two days. Science instrument data will be brought to Goddard Space Flight Center for conversion from raw counts to TOA radiances supplemented with geolocation, view angle, and sun angle information.

The MODIS Science Team consists of more than thirty members, divided into four discipline groups: Atmosphere, Land, Ocean, and Calibration. The MODIS Science Team is developing algorithms to routinely produce the following Standard Data Products: Cloud Mask, Aerosol Concentration and Optical Properties, Cloud Properties, Vegetation and Land-Surface Cover (including Surface Reflectance, Vegetation Indices, Land Cover Type, FPAR/LAI, and Net Productivity), Snow and Sea-ice Cover and Reflectance, Land and Ocean Surface Temperature, Ocean Color, Chlorophyll-a Concentration and Chlorophyll Florescence.

This paper identifies information resources associated with the MODIS Standard Data Products. It is drawn from the version of a WWW Page, (http://ltpwww.gsfc.nasa.gov/ MODIS/ IGARSS_97/MODIS_SDP.html), and related WWW Pages that were current at the time for submission for this conference; this WWW Page ("MODIS_SDP") will be updated with new information as the MODIS data products and their file formats are finalized. An attempt will be made to update "MODIS_SDP" with references to the most useful WWW Pages created by other related EOS organizations.

THE MODIS INSTRUMENT

MODIS is a key instrument on the EOS AM-1 spacecraft. The MODIS Team has a WWW Page (http://ltpwww.gsfc. nasa.gov/MODIS/MODIS.html) that provides an overview of the MODIS organization and provides links to a wealth of MODIS related information.

The MODIS instrument technical specifications are summarized in Table 1, and in the "Technical Specifications" WWW Page linked to the "MODIS" page. The AM-1 Spacecraft Project has a WWW Page (http://fpd-b8-0001. gsfc.nasa.gov/421/421proj.htm#EOS AM-1 MISSION) that provides information related to the AM-1 spacecraft.

THE MODIS SCIENCE TEAM'S PRODUCTS

The MODIS Science Team is composed of more than thirty lead scientists specializing in four disciplines: instrument calibration and characterization, land, ocean, and atmosphere. Each of these scientists is responsible for developing algorithms that are used in the production of the MODIS Standard Data Products. These Standard Data Products are listed in Table 2, and in the "SDP Catalog" WWW Page linked to the "MODIS_SDP" WWW Page (http://ltpwww. gsfc.nasa.gov/MODIS/IGARSS_97/SDP_Catalog.html). For the calibrated radiances, the geolocation, and each of the geophysical parameters that comprise these products, the MODIS Science team has developed an Algorithm Theoretical Basis Document; these are available for distribution via the "ATBD" WWW Page (http://eospso.gsfc.nasa.gov/atbd/ modistables.html). The ATBD provides the science rationale and heritage for the computation of the related parameters; it is the best place to start for an "in depth" understanding.

The following WWW Page references provide summary information for the Calibration, Land, Ocean, and Atmosphere disciplines; additional information can be found in the "SDP Catalog" WWW Page. Each MODIS Discipline Group's WWW Page identifies its science team members (and provide links to their WWW Pages), and provides discipline related information.
MODIS Calibration Discipline:
http://modarch.gsfc.nasa.gov/MODIS/modcal.html
MODIS Land Discipline:
http://modarch.gsfc.nasa.gov/ MODIS/modland.html
MODIS Ocean Discipline:
http://modarch.gsfc.nasa.gov/MODIS/modocean.html
MODIS Atmosphere Discipline:
http://modarch.gsfc.nasa.gov/MODIS/modatm.html

TABLE 1

Scan Rate:	20.3 rpm, cross track		
Swath Dimensions:	2330 km (cross track) by 10 km (along track at nadir)		
Telescope:	17.78 cm diam. off-axis, afocal (collimated), with intermediate field stop		
Quantization:	12 bits		
Spatial Resolution:	250 m (bands 1-2), 500 m (bands 3-7), 1000m (bands 8-36)		

Primary Use	Band	Bandwidth	Spectral Radiance	Required SNR
Land/Cloud	1	620 - 670	21.8	128
Boundaries	2	841 - 876	24.7	201
Land/Cloud	3	459 - 479	35.3	243
Properties	4	545 - 565	29.0	228
	5	1230 - 1250	5.4	74
	6	1628 - 1652	7.3	275
	7	2105 - 2155	1.0	110
Ocean Color	8	405 - 420	44.9	880
Phytoplankton	9	438 - 448	41.9	838
Biogeochemistry	10	483 - 493	32.1	802
	11	526 - 536	27.9	754
	12	546 - 556	21.0	750
	13	662 - 672	9.5	910
	14	673 - 683	8.7	1087
	15	743 - 753	10.2	586
	16	862 - 877	6.2	516
Atmospheric	17	890 - 920	10.0	167
Water Vapor	18	931 - 941	3.6	57
	19	915 - 965	15.0	250
				Required NE(Delta-T)
	20	3.660 - 3.840	0.45	0.05
	21	3.929 - 3.989	2.38	2.00
	22	3.929 - 3.989	0.67	0.07
	23	4.020 - 4.080	0.79	0.07
Atmospheric	24	4.433 - 4.498	0.17	0.25
Temperature	25	4.482 - 4.549	0.59	0.25
Cirrus Clouds	26	1.360 - 1.390	6.00	SNR: 150
Water Vapor	27	6.535 - 6.895	1.16	0.25
	28	7.175 - 7.475	2.18	0.25
	29	8.400 - 8.700	9.58	0.05
Ozone	30	9.580 - 9.880	3.69	0.25
Surface/Cloud	31	10.780 - 11.280	9.55	0.05
Temperature	32	11.770 - 12.270	8.94	0.05
Cloud Top	33	13.185 - 13.485	4.52	0.25
Altitude	34	13.485 - 13.785	3.76	0.25
	35	13.785 - 14.085	3.11	0.25
	36	14.085 - 14.385	2.08	0.35

Bands 1 to 19 are in nm   Bands 20 to 36 are in um   Spectral Radiance values are in W/m^2-um-sr

TABLE 2

MOD01	Level-1A: Instrument Counts	MOD10	Snow Cover
MOD02	Level-1B:Calibrated Radiance	MOD33	Gridded Snow Cover
MOD03	Geolocation Fields	MOD29	Sea Ice Extent
MOD04	Aerosol Product (ocean/land)	MOD42	Gridded Sea Ice
MOD05	Near IR Precipitable Water	MOD18	Water-leaving Radiance
MOD06	Cloud Properties	MOD19	Pigment Conc., CZCS
MOD07	Ozone: Total Burden	MOD20	Chlorophyll Fluorescence
MOD08	Atmos. Stability (Lifted Indx)	MOD21	Chlorophyll_a Concentration
MOD30	Temp. and Moisture Profiles	MOD22	Photosynthetic. Avail. Rad.
MOD35	Cloud/Surface Classific Mask	MOD23	Ocean Suspended-solids Conc
MOD38	Water Vapor (Thermal IR)	MOD24	Organic Matter Concentration
		MOD25	Coccolith Concentration
MOD09	Land Surface Reflectance	MOD26	Ocean Attenuation Coef.
MOD11	Land Surface Temperature	MOD27	Ocean Productivity
MOD12	Land Cover	MOD28	Sea Surface Temperature
MOD13	Vegetation Indices	MOD31	Phycoerythrin Concentration
MOD14	Thermal Anomalies (Fire)	MOD32	Ocean Calibration (Match-up)
MOD15	Leaf Area Index & FPAR	MOD36	Absorption Coefficient Total
MOD17	Photosynthetic Activity/NPP	MOD37	Ocean Aerosol Radiance
MOD43	BRDF and Albedo	MOD39	Clear Water Epsilon

THE MODIS SWATH AND GRID

EOSDIS has defined a "data level" scheme for data products from its spaceborne instruments. Levels 1 and 2 relate directly to the "pixel" data values generated by the MODIS instrument. Level 3 data have been composited (spatially and temporally) onto a geographically defined grid. Each of the disciplines is developing grids (both equal area and equal angle) scaled appropriately for their geophysical parameters; see their WWW Pages for more information as it is available.

DATA PRODUCT DISTRIBUTION

The MODIS Standard Data Products will be distributed by the EOSDIS Distributed Active Archive Centers, DAACs. The MODIS Snow and Ice Data Products will be distributed by the National Snow and Ice Data Center (see: http://www-nsidc.colorado.edu/NASA/GUIDE/). The MODIS Land Data Products will be distributed by the Land Processes DAAC (see: http://edcwww.cr.usgs.gov/landdaac/landdaac.html). The MODIS Oceans and Atmospheres Data Products will be distributed by the Goddard Space Flight Center's DAAC (see: http://daac.gsfc.nasa.gov/DAAC_DOCS/gdaac_home.html).

MODIS DATA FORMATS

All of the MODIS Standard Data Products will be distributed (via the EOSDIS) in the HDF data format. HDF is developed and maintained by the National Center for Supercomputing Applications (see http://hdf.ncsa.uiuc.edu). This data format facilitates the interoperability of data over many computing systems. In addition, the EOSDIS has defined classes of HDF files, "HDF-EOS," for which EOSDIS-specific services will be provided. The best way to learn about HDF-EOS is to start with the EOSDIS Information Architecture WWW Page (http://spsosun.gsfc.nasa.gov//InfoArch.html), and follow the links to the HDF-EOS WWW Pages. MODIS will be compatible with HDF-EOS Swath and Grid. Specific formats for the MODIS Products will be available through the "SDP Catalog" WWW Page when they are finalized.

CONCLUDING REMARK

Because the development of the MODIS Standard Data Products is an ongoing effort, the best way to get current information is to monitor the WWW Pages indicated above. Other sites that may be of interest include the EOSDIS Home Page (http://eospso.gsfc.nasa.gov/eos_homepage/eosdis.html), the EOSDIS Project Home Page (http://spsosun.gsfc.nasa.gov/EOSDIS_main.html), and the EOS Project Science Office Home Page (http://spsosun.gsfc.nasa.gov/eosdata.html), and the pages linked to them.

ACKNOWLEDGMENTS

Towards a Common Language in Satellite Data Management:
A New Processing Level Nomenclature:

Garik Gutman and Alexander Ignatov
Office of Research and Applications
NOAA/NESDIS/ERA12,WWB 712,
Washington, DC 20233, USA,
Tel. (301) 7638042, Fax (301) 7638108, ggutman@nesdis.noaa.gov

Abstract -- This paper represents an attempt to standardize the terminology used in satellite data processing and utilization from raw sensor counts to end products. The proposed processing level nomenclature (PLN) and the flow structure are based on our experience with the Advanced Very High Resolution Radiometer (AVHRR) data production and are intended to complement and enhance the PLN currently used for the Earth Observing System (EOS) datasets. The proposed four-level structure is designed considering two major groups: 1) data producers and 2) data users. The A and B levels of the structure are primarily oriented to serve the first group, consisting mostly of remote sensing specialists, whereas the C and D levels fit better the purposes of scientists in the second group (e.g. weather-climate numerical modelers) that are interested in end products but not in remote sensing methodology. A simple PLN is proposed to facilitate communication between producers and users of satellite data.

INTRODUCTION

Scientists working with satellite data can be roughly subdivided into two major categories: 1) **data producers**, consisting of remote sensing specialists who develop methods to retrieve geophysical variables from reflected and emitted radiances received by satellite sensor and 2) **data users**, working on environmental applications, such as agriculture, weather-climate modeling, ecology, etc. The requirements of these two groups differ because of the nature of their research.

Data production is a complex multi-level task, which usually includes navigation, mapping, radiometric calibration, pixel classification, and retrieving geophysical variables. For volume compression, data are sampled and composited, and the residual noise is supressed by interpolation and smoothing. Thus, remote sensing researchers, working on improving procedures to retrieve geophysical variables, are either data producers or contribute to this category. They require data at a particular processing stage (raw counts or calibrated radiances, before or after cloud detection, composited or at the original temporal resolution, etc.) so that they can test applications of new techniques. Auxiliary information, that is mandatory for technique development, e.g. sun elevation, satellite ephemeri and viewing geometry, cloud detection flags, etc., should be included as part of data. Which of the procedures are applied, how rigorously, and in what order depends on the

scientific and technical capabilities within each particular data processing group, and is also dictated by users' needs.

The data producers should be distinguished from the **"end product users"** who are interested in complete fields of geophysical variables after all necessary remote sensing procedures have been applied. They usually want interpolated and/or smoothed fields, or even just the statistical structure of these fields. Much of the information from satellite processing (original radiances, satellite geometry, etc.) is not required and can be omitted. Yet, sometimes data users have no choice but to start over from a certain processing stage, maybe even from raw data, and go through several procedures to obtain what they need, which could be prohibitively expensive. Our experience is that numerical modelers would prefer not to spend time and resources on processing satellite data.

A generic PLN exists for EOS data products, presenting a sequence of levels moving in one direction, so that some of the existing products/procedures are not readily identified in this PLN. The current paper proposes a modification to account for procedures that are currently in practice and do not readily comply with the sequential structure of the EOS PLN. We propose its enhancement in three ways: 1) subdivide the levels into remote sensing processing to retrieve geophysical variables and preparation of complete fields of these variables, 2) identify the processing steps applied and the path through the steps taken to the final product, and 3) make data products self-explanatory in terms of space/time scale. Our goal is to move towards a potential unification (standardization) of the existing schemes and nomenclatures in order to facilitate the interaction between data producers and users.

EXISTING CLASSIFICATIONS

The levels of data defined by EOS [1] are: level 0 - reconstructed unprocessed instrument data at full space-time resolution; level 1A - reconstructed unprocessed instrument data at full resolution, time-referenced, and annotated with ancillary information, including radiometric and geometric calibration coefficients and georeferencing parameters (i.e. platform ephemeri) computed and appended, but not applied to the level 0 data; level 1B - level 1A data processed to sensor units; level 2 - derived geophysical variables at the same resolution and location as the level 1 source data; level 3 - variables mapped on unform space-time grid scales (i.e.

spatially and/or temporally resampled from levels 1 and 2 products, which may have included averaging and compositing); level 4 - model output or results from analysis of lower level data, i.e. variables derived from multiple measurements.

The World Climate Research Program (WCRP) follows the Global Atmospheric Research Program (GARP) data-level categories [2], which are subdivided into three general levels: 1) primary instruments readings expressed in appropriate physical units and referred to earth coordinates, but requiring conversion to geophysical parameters; 2) retrieved geophysical parameters after appropriate quality assurance and reformatting; 3) analysis or fields prepared from level 2 data. This categorization has been used by WCRP elements, such as Tropical Ocean and Global Atmosphere (TOGA), Global Energy and Water Cycle Experiment (GEWEX), International Satellite Cloud Climatology Project (ISCCP), and others, either as is or with slightly modified definitions. For example, TOGA PLN for level 3 lists "homogeneous data fields derived from level 2 by an analysis technique" [3].

ISCCP uses a three-level PLN, denoting them, as A, B, and C [4]. Level A are raw satellite image data. B1 is data sampled in time and spatially averaged, B2 is further spatial sampling, B3 is the primary global radiance dataset, with normalization and calibration results appended. C1 is reduced space and time resolution data after application of cloud flags, and C2 is monthly statistics of C1.

Committee on Earth Observations Satellites (CEOS) classifies data products "by the sort of processing used in their generation and, to a lesser extent, the sort of uses to which these products might be put" [5]. CEOS PLN has a five-level structure similar to the EOS PLN. The VEGETATION and POLDER programs' data productions conform with CEOS PLN, but do not list the fifth CEOS-defined level, probably leaving the production of complete (interpolated/smoothed) geophysical fields to data users [6,7].

The European Space Research Institute (ESRIN) of the European Space Agency (ESA) uses a two-level PLN, but splits the level 2 products into three sublevels 2A, 2B, 2S [8]. Further processing is being developed on experimental basis, such as objective analysis of sea surface temperature data, which is analogous to level 4 in CEOS PLN.

The above brief review suggests that there are commonalities as well as minor differences in the existing PLNs, varying in the number of levels and their content. Level 4 in the above PLNs reflects the use of the data products by numerical modelers. However, often the users request datasets even if the remote sensing processing was not fully accomplished, e.g. without atmospheric or surface anisotropy corrections. Therefore, indication of the processing steps used to produce a dataset is needed. Also, a space-time resolution notifier would be useful addition.

PROPOSED PLN

The proposed PLN is based on the major common features described above, taking into consideration data use for developing processing methods and for numerical modeling, and is enhanced twofold: 1) to identify the processing path in addition to the final step, and 2) to indicate dataset's space-time resolution. A more complete description of the PLN with flow charts is given in [9]. To identify the time and space resolution, we propose a flexible mnemonics: TS where T can be H, D, P, W, Dk, M, Y for hourly, daily, pentadly, weekly, dekadal, monthly, and yearly, respectively, and S can be 1, 8, 15, 100, 250 representing 1-, 8-, 15-, 100- and 250-km resolutions (there is, however, some room for removing the ambiguity between scales given in km or degrees).

A-level: the original readings received from satellite sensor. The output from the A-level processing is the raw data with calibration and navigation appended. Details of this level pre-processing are described by Users Guides.

B-level: calibration, cloud and quality flags generation, atmospheric and surface anisotropy correction, derivation of geophysical variables. The B-level data are mostly remote sensing oriented, hence they should include auxiliary information, such as observation-illumination geometry, calibration coefficients, cloud and quality control flags, etc., that would allow tests and development of alternative methods to improve the quality of data products. B1 - the input from the A-level, i.e. raw data with navigation/calibration information appended but not applied (commonly known at NOAA as the 1B-level). B2 - data mapped into a regular space/time grid (i.e. sampled from the original resolution). B3 - data sampled further (space and/or time), such as composites. Thus, the three stages at their "zero" step provide users with BX.0 data (X=1,2,3): B1.0 (orbits), B2.0 (maps), B3.0 (composite maps). Any of them may be used as a starting point for further processing. BX.0 data product is, in effect, the A-level output, which is either retained as is (B1.0), or spatially/temporally sampled and mapped (B2.0), or presented as composite maps (B3.0). The processing steps that can be done at all BX stages (X=1,2,3) are discussed below.

The steps that comprise the B-level processing are denoted as BX.Y (Y=1,..., 5) and consists of calibration (BX.1), cloud identification (BX.2), atmospheric corrections (BX.3), surface anisotropy corrections (BX.4) and transformaton to geophysical variables (BX.5). Note that the "cloud flags" generated at BX.2 are not applied but *appended* to BX.1. The BX.3-5, on the other hand, can be made by means of look-up tables so that the whole image, independently of the cloud flags, is transformed with efficient use of computer time. The flags are, thus, carried over through BX.3-5 steps.

Thus, the B-level product is proposed to be presented as BX.Y/TS, where X=1,2,3 and Y=1,2,3,4,5, denoting the stage

and the step, respectively, and TS denoting the time/space resolution as described above.

C-level: complete fields of the variables produced by spatial/temporal averaging, interpolation, and smoothing, using the B-data as input. This data level is intended for numerical modelers, who need satellite-derived products for initialization and validation of models and who usually prefer to bypass the remote sensing processing. For those modelers, who desire to work with the original point measurements at full time-space resolution without any C-level processing, the B-level data products are readily available.

At this level, all auxiliary information is omitted, cloud and other quality flags have been applied and complete fields of the variables are produced by spatial/temporal averaging, interpolation, and smoothing, to fill in the data gaps and to filter out residual noise caused by the imperfections in the original data and the B-level processing. Some of the signal, however, may be lost as a result of these procedures, but this is the cost of having complete fields ready for use in models.

The C-level data has the same X.Y/TS structure as the B-level: CX.Y/TS. Note that TS values may vary from those in the B-level due to the procedures used.

D-level: integral and statistical characteristics of C-level data, e.g. climatology. The D-level is intented for use by researchers that are interested only in the descriptive statistics of a particular dataset to complement some other statistics. They would not need the whole time series or the full maps but require some integral and statistical characteristics. Such D-level products are of immediate use in climate analysis with practically no additional data processing involved. Combining the C- and D-level data can be utilized for monitoring purposes [10]. The X.Y/TS structure applies to the D-product as well.

It is important to notice that the above scheme identifies the final processing step only. The result, however, does depend on the path that lead to the final product. For instance, compositing with further atmospheric correction yields different results from compositing of atmospherically corrected data. Therefore, the path should be an integral part of the nomenclature. For brevity, one can operate with the final product index/notifier. We propose that a path index be appended to the dataset header.

Summarizing, note that the A-level in the proposed PLN is similar to EOS level 1, the B-level encompasses EOS levels 2-and 3, and the C-level has much in common with EOS level 4. EOS' and other existing PLNs, however, do not account for a possibility of moving first from stage to stage within a step (e.g., composites of the original counts are not readily classified) and do not clearly distinguish the remote sensing processing from applications to numerical modeling. The proposed PLN can potentially serve as an enhancement to the current EOS' PLN and lead to unification of all the available data production schemes and nomenclatures.

CONCLUSIONS

The proposed PLN is based on our experience with AVHRR data processing. It can be further developed, elaborated and adjusted to the existing EOS PLN notations (A,B,C,D could be replaced with 1,2,3,4 with possible adjustments). Our goal was to make a first step in unifying many existing systems, while enhancing the current EOS PLN. It would be beneficial for both the remote sensing and numerical modeling communities to develop a consensus on this matter. The proposed system facilitates understanding of the data product, pointing to the missing parts in developing the final product. As an exercise, the reader may want to use the proposed PLN to find proper notations for the products that are being generated or are under investigation in their group.

ACKNOWLDEGMENT

REFERENCES

[1] The EOS Reference Handbook, 1993.

[2] Scientific plan for GCIP,WCRP, WMO/TD-461,67, 1992.

[3] Scientific plan for TOGA, WCRP, WMO/TD-3, 64, 1985.

[4] ISCCP: Description of reduced resolution radiance data, WCRP, WMO/TD- 58, 1985.

[5] Auxiliary data in the CEOS community: Reference Guidelines Document, 1994.

[6] O.Arino, J.-M.Melinotte,A.Buongiorno and G.Pittella, "ESA/ESRIN software demonstration: AVHRR data production and access from acquisition to delivery". Proc.of ISPRS, Val d'Isere, Physical Measurement and Signatures in Remote Sensing, 17-21 January, 1994.

[7] G. Saint, "VEGETATION onboard SPOT 4. Mission specifications. LERTS, 1992.

[8] CNES-NASDA Research Announcement "POLDER on ADEOS"

[9] G. Gutman, D. Tarpley, A. Ignatov, and S. Olson, "The enhanced NOAA global land dataset from the Advanced Very High Resolution Radiometer". Bull. Amer. Met. Soc., 76, 1141-1156, 1995.

[10] G.Gutman and A. Ignatov, "Global land monitoring from AVHRR: potential and limitations". Int. J. Rem. Sensing, 16, 2301-2309, 1995.

Innovations in Response to Floods of Data

Daniel C Ziskin
NASA Goddard Space Flight Center Distributed Active Acrchive Center
George Mason Univ. Center for Earth Observations and Space Research (CEOSR)

Paul Chan
NASA Goddard Space Flight Center Distributed Active Acrchive Center
NASA/GSFC code 902.2 Greenbelt MD 20771
Tel:301-614-5264/Fax:301-614-5268/Email:ziskin@daac.gsfc.nasa.gov

ABSTRACT --The good news is that the Earth Science community will not be data-starved in the Earth Observing System (EOS) era. The bad news is that techniques to cope with enormous volumes of Earth Science data have not yet met the challenge. Coping with data involves processes such as becoming familiar with a data center's inventory, searching for appropriate data, and retrieving only the data that are needed. The Center for Earth Observations and Space Research (CEOSR) of George Mason University, in partnership with the NASA Goddard Distributed Active Archive Center (DAAC), have developed some innovations to reduce barriers that users may experience in accessing Earth Science data. The techniques are extensions of two fundamental concepts: Data distribution must become responsive to data users' needs, and statistical summaries of data stored as metadata can provide a basis for content-based data selection.

INTRODUCTION

Science is a competitive process. There are systematic rewards (including funding) to researchers who published unique analysis of data. An undesirable consequence of this competition is that it provided an advantage to researches who had access to data over those who did not. Because data producers lacked an incentive to widely distribute data to their competitors, attempts to standardize data distribution have not been fully supported.

We are now entering an era in which researchers are encouraged to publish both their analysis and the data themselves. For example, EOS instrument teams are funded to create hundreds of data products [1]. Most aspects of the EOS data stream, from the "raw" level 0 data through to highly processed assimilated data products are intended to be publicly available. This includes the algorithms themselves and even the experimental test data products. This re-alignment of resources toward data production and distribution should generate an unprecedented amount of data. Users should easily be able to find the data they need (or discover their existence). And the distribution of the data from the EOS system to the researcher's system should be efficient.

Unfortunately this success story will not be achievable using present paradigms of data management. Why not? There is too much data and too many users. There is too much data for users to select from, so meaningful choices will be difficult. Today's user asks "Are there any observations of Z?". In contrast, the user of EOS data will ask "Should I be using observations of Z produced by instrument X or instrument Y?". And there will be users from such diverse perspectives, levels of expertise, and technical capability that the distribution of a "one-size-fits-all" product will fail.

An artifact of the system's enormous scale is that it is being optimized for ease of data production. Unless significant attention is paid to post-production customization, the quantity and diversity of users will over-tax the distribution process. The system will be at risk if it is being scaled to support relatively few users to customize (i.e. reformat, subset, resample, etc.) their data during distribution. The risk is due to the cost of processing a custom order as a "special case". Too many special cases would shut down such a system. The system which protects itself by not catering to the user (i.e. no customization) would have few users. Since the target audience of the system will demand customization, the emphasis must shift to accommodate it. The flexibility to customize the data must be built into the distribution system. The Center for Earth Observations and Space Research (CEOSR) of George Mason University, in partnership with the Goddard DAAC, are developing some innovations to reduce barriers that users may experience in accessing Earth Science data. The innovations stem from asking two fundamental questions: "Who is the user?" and "What are the data?".

WHO IS THE USER?

The task of distributing data is simplified if either the user community is well-defined or the data are so valuable that users will surmount any barrier to their use. In the EOS era, neither of these criteria will be satisfied. A consequence of NASA's ambitious Mission to Planet Earth (which EOS is part of) is the stimulation of use of Earth science data beyond

its conventional users. It will be a challenge to respond to such a diverse user community and impossible to anticipate the novel ways Earth Science data will be utilized in the future.

A proposed solution to this obstacle is to further de-centralize the distribution of EOS data [2]. The de-centralization should be accomplished within a "federated" framework, where each node of data distribution serves its users and maintains a commitment to inter-operability with the other members of the federation. Furthermore, care should be taken in establishing the members of this federation, so that each of the various communities of data users are identified and served. This would remove the burden of trying to serve all users from the centralized system, and simultaneous give the federated data centers a clear conception of its customers.

WHAT ARE THE DATA?

The data volumes are expanding from several distinct trickles into a flood. If we rely on current methods of providing access, the vast majority of the information inherent in the data will go under-utilized. Because of the overwhelming volume, users themselves will invent methods to limit the amount of data they need to analyze. Such techniques might include limiting the temporal or geographic scope of their research or using degraded resolution data. These scenarios constitute under-utilization since the science has potentially been compromised by the constraints of data management.

A more science-enabling approach would be to provide access to summaries of the available data. This is the concept behind traditional browse images. However, without sophisticated automated searches (i.e. artificial intelligence) and enhanced network connections, paging through image after image may frustrate the user before enough data have been sorted through. A more efficient summary could be provided statistically. To summarize the content would distill much of the scientific value out of the data, and may be an adequate way to search through massive volumes. If users can search the summary statistics of the data, they can potentially order a smaller volume of the actual data archived. CEOSR is developing an interface demonstrating this principle which appears promising [3].

CONCLUSION

The centralized data center which attempts to satisfy all users with non-customized data products will fail to serve users in the EOS era. There will be too much data and the user community will be too diverse. Data centers can succeed if they recognize that they should be targeting specific communities. These data centers should then support each community it expects to serve either by integrating itself into

the user network (perhaps through partnerships with universities). To each supported community, the data center must act as if it existed to support that particular flavor of research. Emphasis should be placed on effective searching through "floods of data" and customized data delivery.

REFERENCES

[1]SW Wharton and MF Myers, Eds., 1997 MTPE EOS Data Product Handbook,Vol 1, Goddard Space Flight Center, National Aeronautics and Space Administration, Washington, DC.

[2]M Kafatos, et al,The GMU ECS Federated Client-Server Architecture, Contract ECS-00010, 1994. http://www.ceosr.gmu.edu/indy-study/indy-study.html.

[3]M Kafatos, Z Li, R Yang, P Hertz, D King, XS Wang, H Weir, H Wolf, D Ziskin, 1997, The Virtual Domain Application Data Center: Serving Interdisciplinary Earth Scientists, Ninth Annual Conference on Scientific and Statistical Database Management, Evergreen State College, Olympia, Washington.

A Catalog-Browse System with Quick-Look Images for SPOT, ERS and RADARSAT Data Archives

Leong Keong KWOH
Centre for Remote Imaging, Sensing and Processing
National University of Singapore, Lower Kent Ridge Road
Singapore 119260, Republic of Singapore
Tel : (65) 772 3220, Fax : (65) 775 7717
e-mail : crsklk@leonis.nus.edu.sg

Abstract -- To allow for easy access to CRISP's data archive of SPOT, ERS and RADARSAT, a WWW catalog browse system has been developed. Besides descriptive (meta) data, quicklook images are also available for viewing. The database for the catalog browse system is updated daily and automatically by the system. The system is implemented with: (1) standard HTML fill-out forms for communication between users' browsers and CRISP's Web server, and (2) Common Gateway Interface (CGI) and 'C' programs for communication between CRISP's Web server and CRISP's database.

INTRODUCTION

The Centre for Remote Imaging, Sensing and Processing (CRISP), Singapore, operates a ground station which has been actively acquiring data from SPOT and ERS satellites since September 1995, and RADARSAT satellite since November 1996. To date, there are about 50,000 scenes of SPOT images, 9000 scenes of ERS images and 350 scenes of RADARSAT images in the archive. A common problem of ground stations is how to disseminate information on data availability to potential users, both locally and internationally. Recent advances and popularity of Internet World Wide Web (WWW) has made it possible to effectively and economically provide a solution to this problem. In CRISP, a WWW Catalog Browse System has been put in operation since October 1995. This system can be accessed at http://www.crisp.nus.edu.sg.

WWW CATALOG BROWSE SYSTEM

The WWW catalog browse system was developed in-house and has evolved from a very simple system initially to a highly friendly system today.

To keep the design simple and flexible, we choose to have a separate suite of software modules for each of the satellites. This approach allowes us to adapt to the peculiar requirements of each satellite, e.g., RADARSAT does not have standard predefined frames like SPOT and ERS but have many beam modes.

When a user first accesses the system, he will be asked to choose from a list of the three satellites. By clicking on any one of them, the system will load a Java Applet, shown in Fig. 1, with a map of South East Asia and CRISP's coverage. The user can zoom in and out of the map and when he is satisfied with his area of interest, he will click the submit button which will load up a page with standard HTML fill-out forms. For user who do not have a Java enabled browser, we have an alternative page where the area of interest is keyed-in from the keyboard.

From the HTML fill-out forms, the user will be able to enter other search criteria such as start and end dates, satellite numbers, cloud covers etc. A click on the submit button will send these search criteria to CRISP's Web server. These criteria will be passed using the common gateway interface (CGI) to the search software which are implement
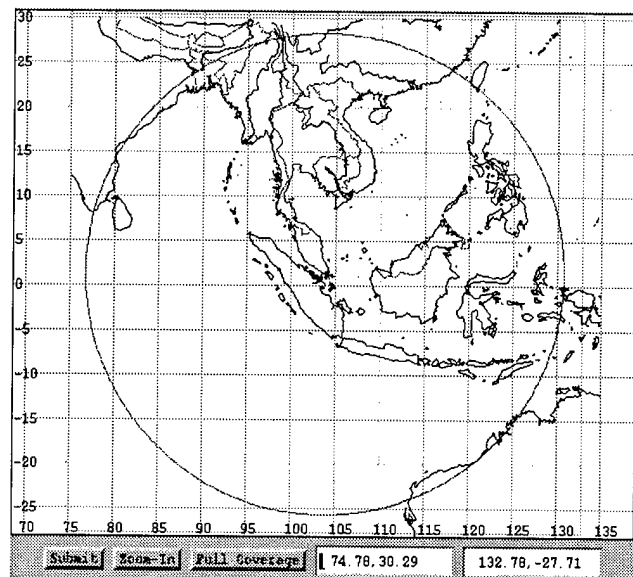
Fig. 1 - Java Applet for Selection of Area of Interest

in 'C'. The search software then interacts with CRISP's database and returns a list of scenes that satisfy the user's criteria.

The scenes returned by CRISP's database are then plotted onto a raster map according to their geographic coverages and presented to the user for his selection (Fig. 2). Usually there are many overlapping scenes over any location, so when the user click on any point on the map, a list of scenes will be returned. When one of these scenes is clicked, the system will present a quicklook image of the scene, a small location map and descriptive data for the scene. The quicklook image is kept small to speed up user's browse session. The user may click on the small quicklook to obtain an enlarged version of the quicklook (Fig. 3).

There are two additional convenient features to help searching. The first is a link to the preceding and succeeding scenes of the satellite pass. The second is the 'shift along track' (SAT) feature. The SAT feature was implemented because in many cases, the area of interest will not coincide conveniently with the standard scenes of SPOT or ERS.

USER FRIENDLINESS

We have taken great care to make the system user friendly. With a Java enabled browser, a user will be able to perform the whole catalog search by only clicking the mouse button. He will not need to reach-out for his keyboard. The size of data files and image files that need to be passed over

Fig.2 - Scenes Satisfying Search Criteria

the internet are also kept relatively small so that the waiting time for data downloading will not be too long.

CATALOG DATABASE

The catalog database consists of the descriptive database and the quicklook image database. For the descriptive database of SPOT, we followed SPOT Image's Standard Catalog Information Exchange (SCIE) record structure where each record of 218 bytes will contain all the useful information about a given SPOT scene. The quicklook images are stored in standard JPEG format. For convenience, we store each SPOT pass in separate directory and name the quicklook images according to the 21-character SPOT scene ID. The link between the descriptive record and the quicklook filename is maintained with a separate file. This file has two fields, a field containing the scene ID and another field containing the full filename of the quicklook image, including its absolute path. With this implementation, we can move the quicklook imagery to any directory or filesystem and also name the quicklook images in any manner. The database scene records are pre-sorted in reverse chronological order of scene acquisition time so that the most recent scene will be the first record presented.

For ERS data, there is no standard catalog format, so we have to define one ourselves. Following SPOT's scene ID concept, we defined a 24 character ID for each ERS scene. The ID basically is a concatenation of the satellite number, the orbit number, the frame number, the date and time of imagery. The orbit and frame numbers are actually redundant but was kept for convenience. The scene ID will uniquely define the ERS scene. The quicklook images are stored in similar manner as that for SPOT, in standard JPEG format and named according to the 24 character ID, and a separate file to link the descriptive data records to the quicklook images.

For RADARSAT, we had to adapt a different approach because RADARSAT data does not have standard framing convention. RADARSAT scenes are defined by satellite number, date and time of acquisition. We still maintain a descriptive database and a quicklook database. For the descriptive database, each record now defines a segment which can contain many scenes. For the quicklook images, we break the segments up into many scenes. The link file now is more complicated as it has to link many quicklook images to one descriptive record. Each time a scene is requested, two quicklook images will usually be read, then joined and trimmed to the required scene length before being presented to the user.
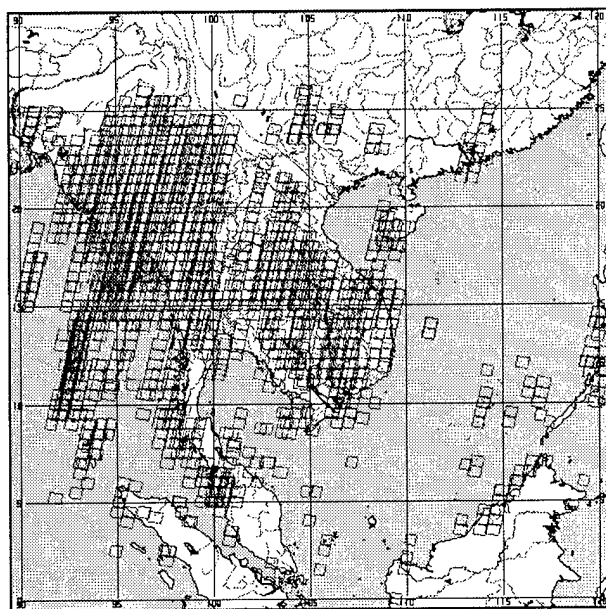
CATALOG UPDATING

We have also put in place an operator friendly system for updating the catalog. Every time a satellite pass has been acquired and processed (quicklook generated and cloud cover assessment done), the required descriptive records and quicklook images will be generated and moved to its destination directory. Another program, which is activated by the system twice daily, will automatically updates the descriptive database and the link file. Should the descriptive database or the link file be corrupted, the same program can also be used to rebuilt the database from scratch easily.

SECURITY

We allow all users access to our system. We are however concerned about data corruption and misuse. To protect our catalog, we keep the actual filesystems and directories of our descriptive and quicklook image database separate from the working directories which is visible by WWW browsers. The CGI based searching programs, which are complied executables, will make a copy of the user requested quicklook image from the original directory to a temporary directory which is visible by WWW browsers. This temporary directory is automatically cleaned up daily.

CONCLUSIONS

The simplicity and flexibility of WWW has allowed us to developed a low cost, but effective and user friendly catalog browse system accessible via the internet. The system is also used by CRISP's production operators as a quality control tool. It will be continually upgraded to improve its user friendliness and functionality.

REFERENCES

[1] "The Common Gateway Interface Specification", http://hoohoo.ncsa.uiuc.edu/cgi.

[2] "HTML Forms", http://www.w3.org/pub/WWW/MarkUp/html3/forms.html.

[3] "Record Structure for the Standard Catalog Information Exchange", SPOT Document: S4-CI-C/E-1625-SI, 5 Aug 1993.

```
K-J      : 266339 Date : 970101 Time : 040247
SPOT No: 2  HRV  : 1   Mode : X  SAT : 3

Latitude/longitude
Upper Left      :    5.6654/ 100.0625
Upper Right     :    5.5664/ 100.6957
Scene Centre    :    5.3520/ 100.3125
Lower Left      :    5.1354/  99.9407
Lower Right     :    5.0368/ 100.5735

Cloud Cover  : AAAAAAAA  Max : A     Avg : A

Scene Orient : 009.1 Incident Angle : +24.4
Sun Azimuth  : 146.6 Sun Elevation  : +55.5

Revolution Num : 067
```
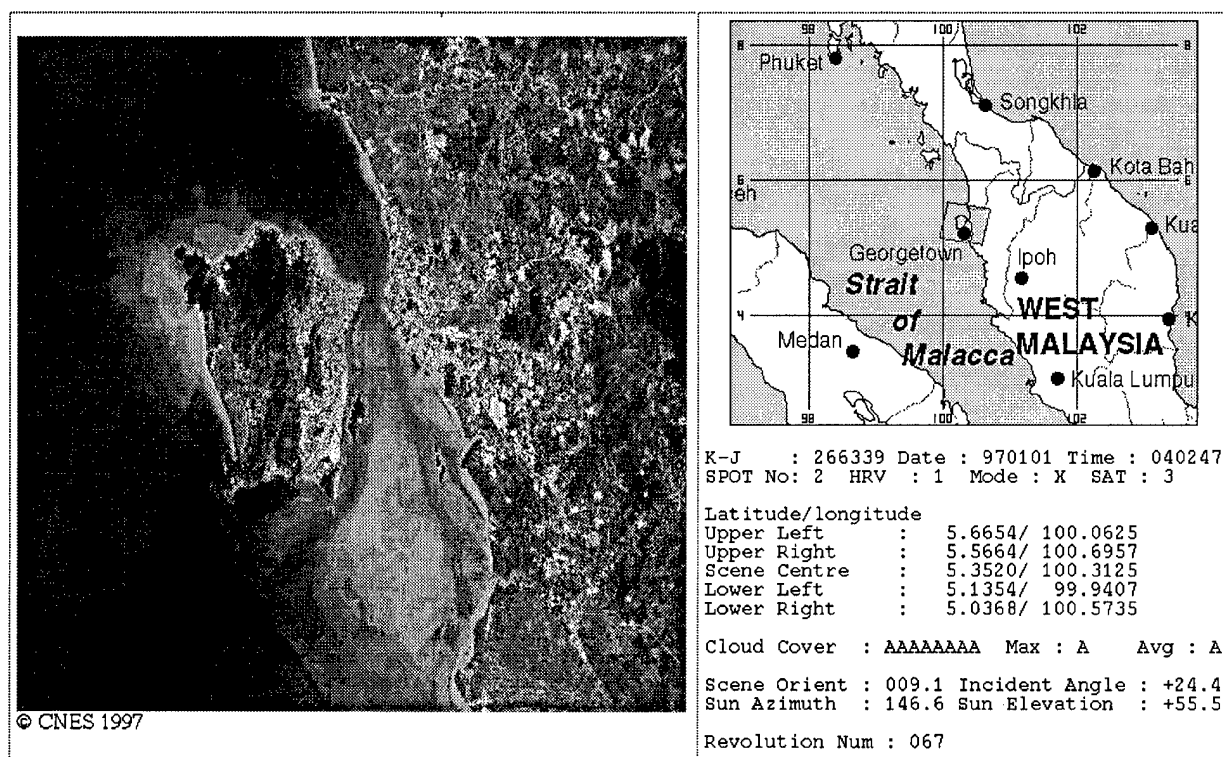
Fig. 3 - Quicklook Imae, Location Map and Descriptive Data

Estimating Hydrological Parameters with Multifrequency SAR Data

S. Paloscia, G. Macelloni, P. Pampaloni and S. Sigismondi
Istituto di Ricerca sulle Onde Elettromagnetiche - CNR
Via Panciatichi 64 - 50127 Firenze, Italy
Fax: +39 55 4235 290, Ph.: +39 55 4235 205, E-mail: microrad@iroe.fi.cnr.it

Abstract -- This paper presents an overview of the results obtained on Montespertoli area from the different SAR missions. An analysis of the sensitivity of radar backscattering to some parameters which are of primary importance in modelling the geophysical processes of the hydrological cycle has been carried out. In particular the effects of surface roughness and soil moisture on microwave backscattering have been investigated.

INTRODUCTION

The operational capability of remote sensing for monitoring hydrological parameters in large watersheds is not yet fully explored and extensive research is being carried out to evaluate the potential of microwave sensors and to assess the achievable accuracies of measurements.

The test site of Montespertoli, located south of Florence, Italy, was imaged several times between 1991 and 1994, at different incidence angles by different SAR systems: the C-band ERS-1, the L-band JERS-1, and the multifrequency polarimetric AIRSAR and SIR-C/X-SAR (Table I). Since SAR images were collected in different seasons: spring, summer and fall, a wide range of soil moisture conditions has been investigated. Weather was in fact dry in summer when vegetation was well developed; on the contrary the average soil moisture was rather high both in April (15-18%) and October (generally higher than 20%) when most agricultural fields were bare or covered with small vegetation. The area was equipped with two trihedral corner reflectors of 180 cm and one of 240 cm, deployed parallel to flight line. In addition few 'extended homogeneous targets' had been specifically prepared, to be used as cross reference between flights. Ground truth measurements included: soil moisture, roughness, and dielectric characteristics, soil erosion features, crop maps, and vegetation parameters [1].

The measured quantities taken into consideration are the full polarimetric features at L- and C-bands and the backscattering coefficient $\sigma°$ at VV polarization at X band.

The effects of surface roughness and soil moisture on microwave backscattering have been analysed using SAR data collected on various surface types. A fairly good correlation with soil moisture of bare or scarcely vegetaed fields has been found both at L- and C-bands and $\theta = 23°\text{-}26°$, where the influence of surface roughness and vegetation cover is minimized. However, the quality of SAR images at θ close to the nadir is affected by a relatively poor spatial resolution which makes it difficult the exact identification of field borders. The correlation appreciably increases up to 90% if soil moisture is estimated, in different times, on the same area including many fields. In the range of observed roughness the highest correlation to the height standard deviation of the surface was found at L-band $\theta \approx 35°$ [2]. Experimental data have been compared with the Integral Equation Model [3] implemented for single scattering.

Tab I: Processed SAR data on Montespertoli area

Sensors	Frequency Pol.	Theta	Ground Resol (m)	Dates
MAC'91	C, L, P Quad-pol	20° 35° 50°	12.2x6.6	22/6/91 29/6/91 14/7/91
ERS-1	C VV	23°	30x26.3	29/5/92 07/8/92 24/4/94
JERS-1	L HH	35°	18x24.6	24/6/92 14/4/94
SIR-C X-SAR	C, L Quad-pol X VV	20° 60°	25 x 20	April Oct. 1994

EXPERIMENTAL RESULTS

Sensitivity to soil moisture

Fairly good empirical correlations between the co-polar backscattering coefficient at L-band and the gravimetric soil moisture of the first 5 cm layer have been obtained both at 35° and 25° incidence angles using the whole SAR data set, including AIRSAR data collected in 1991 and SIR-C data collected in April and October 1994. As an example, in figure 1 $\sigma°_{HH}$ measured at L-band, $\theta= 26°$ is represented as a function of the gravimetric SMC (0-5 cm) of a certain number of bare or scarcely vegetated (leaf area index, LAI <1 and plant water content, PWC ≤0.5 kg/m²) fields. Although at this so steep incidence angle the effect of soil roughness is minimized, by separating two classes of roughness with height standard
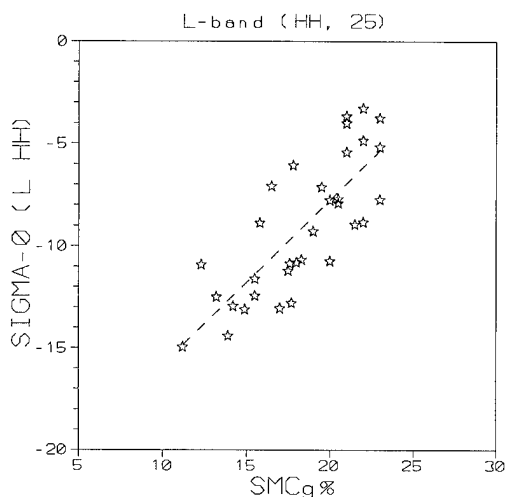
Figure 1 - σ°_{HH} at L-band, $\theta = 25^\circ$ (AIRSAR + SIR-C) as a function of SMC of bare and scarcely vegetated (plant water content < 1 Kg/m²) fields.

Figure 3a - σ°_{HH} at L-band, $\theta=26^\circ$ (continuous line) and SMC (dashed line) of an area of about 20 bare fields as a function of time.

deviation $s \le 2$ cm and $s > 2$ cm respectively, the spread of data decreases and the correlation improves. The correlation coefficient r^2, which is equal to 0.62 when the soils are considered all together, goes up to $r^2 = 0.71$ if only the smooth soils are taken into account and decreases to 0.45 for rough soils. At $\theta=35^\circ$ the correlation is obviously worse and the correlation coefficient for the same dat set becomes $r^2=0.44$. At C-band a direct comparison between ERS-1 and SIR-C data (VV pol, $\theta=23^\circ$-25°) showed a poor sensitivity to soil moisture content of bare fields (Fig.2) with a correlation coefficient

rather low ($r^2=0.4$).

One of the problems in measuring the soil moisture field by field is represented by the spatial variations of roughness, texture, vegetation characteristics which strongly affect the backscatter and determine a heavy scatter of data. For this reason the correlation between the backscatter coefficient and the soil moisture can be sensibly increased if variations in time of the same area are considered rather than variations in space of different fields. Subsequently an average value both of σ° and SMC was computed for a rather flat and homogeneous

Figure 2 - σ°_{VV} at C-band, $\theta = 23^\circ$ (ERS-1 + SIR-C), as a function of SMC of bare and scarcely vegetated (plant water content < 1 Kg/m²) fields.
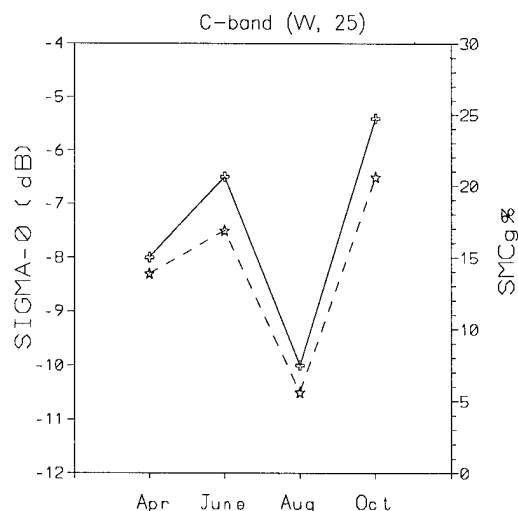
Figure 3b - σ°_{VV} at C- band, $\theta = 23^\circ$ (ERS-1 + SIR-C) (continuous line) and SMC (dashed line) of an area comprising 20 bare or scarcely vegetated fields.

zone along the Pesa river, inside the larger agricultural area, at different dates corresponding to AIRSAR (June and July), SIR-C and ERS-1 flights [4]. In the diagram of figure 3 the average values of $\sigma°_{HH}$ and SMC are represented as a function of time (months) at $\theta \approx 25°$ for L-band (a) and C-band (b). It can be noticed that the agreement between the $\sigma°$ and SMC appears very good at both frequencies. If these two quantities are directly related to each other, the correlation becomes surprisingly good and the correlation coefficients increase up to 0.9.

Sensitivity to surface roughness

From the analysis of our experimental database which includes data from P to X band, at various polarization and incidence angles, the highest sensitivity to soil roughness, at least in the investigated range of height standard deviations, has been noticed at L-band, copol, and $\theta = 35° - 50°$ [2].

A comparison of experimental data with theory has been carried out considering direct relations between the backscattering coefficient and the surface roughness and soil moisture content. Since the degree of roughness of a surface is defined in terms of electromagnetic wavelength, a typical parameter used to investigate the variations of the backscattering coefficient with roughness is the product (ks) of the height standard deviation s with the wave number k ($k = 2\pi/\lambda$, λ = electromagnetic wavelength).

Experimental data have been compared with the Integral Equation Model [3] implemented for single scattering. In the model the dielectric constant of soil was simulated by using a polynomial fit [5], we assumed a soil with a mean value of texture (70% sand and 30% silt+clay), moisture SMC=15% and an exponential autocorrelation function with correlation length lc ranging between 4 and 10 cm. Fig. 4 shows that the model (continuous lines) reproduces quite well the data up to ks = 2 where multiple scattering effects can be neglected. It should be noted that, whereas at L-band $\sigma°$ gradually increases with ks, at C-band the saturation confirms that the same surface may appear rougher at C- than at L-band.

FINAL REMARKS

The analysis carried out on Montespertoli site using multi-frequency, multitemporal SAR data indicates that in the scale of surface roughness typical of agricultural areas, a co-polar L-band sensor observing at two incidence angles (close to 20° and 35°/50°) gives the highest information content for estimating soil moisture and surface roughness. At the observation parameters of ERS-1 the sensitivity to soil parameters on a spatial scale is rather low. However, considering data collected at different dates on the same area, the correlation and sensitivity to soil moisture is significant. Finally, a good agreement has been found between experimental data and simulations with the Integral Equation Model.
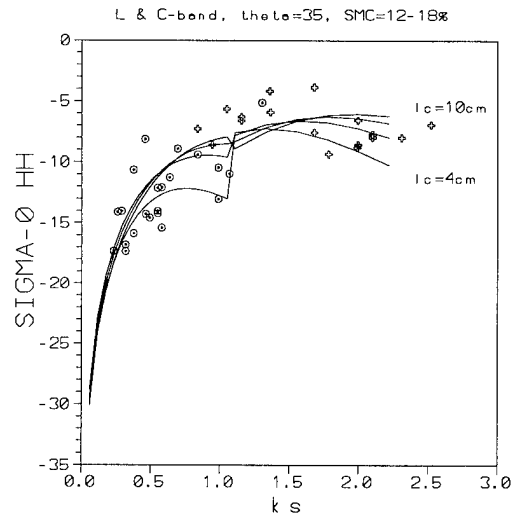
Figure 4 - Experimental data of $\sigma°_{HH}$ at C (crosses) and L (points) bands as a function of ks. Lines refer to the IEM implemented for four different values of lc (4, 6, 8 and 10 cm).

REFERENCES

[1] S.Baronti, F.Del Frate, S.Paloscia, P.Pampaloni and D.Solimini, 1995, SAR polarimetric features of agricultural areas, *Int. J. Remote Sensing*, 16, 2639-2656.

[2] P.Coppo, G. Macelloni, P. Pampaloni, S. Paloscia and S. Sigismondi, 1996, The SIR-C/X-SAR experiment: the sensitivity of microwave backscattering to surface roughness of bare soils, *Proc. Int. Geosci Remote Sensing Symp. (IGARSS'96)*, Lincoln, Nebraska, 2131-2133.

[3] Fung A.K., 1994, Microwave scattering and emission models and their applications Artech House Inc., Boston

[4] P.Pampaloni, G.Macelloni, S.Paloscia, S.Sigismondi, 1997, ERS-1 sensitivity to hydrological parameters: a comparison with SIR-C and AIRSAR data, Proc. of 3rd ERS Symposium, Florence 17-21 March 1997

[5] Hallikainen M.T., Ulaby F., Dobson M.C., El Rayes M.A., Lin Ku Wu, 1985, Microwave dielectric behavior of wet soils - Part I: Empirical models and experimental observations", *IEEE Trans. Geosci. Remote Sensing*, vol. GE-23, pp. 25-33

Profile Soil Moisture Estimation Using the Modified IEM

Jeffrey P. Walker[1], Peter A. Troch[2], Marco Mancini[3], Garry R. Willgoose[1] and Jetse D. Kalma[1]

[1]Department of Civil, Surveying and Environmental Engineering, The University of Newcastle, Callaghan, 2308, AUSTRALIA
[2]Laboratory of Hydrology and Water Management, University of Gent, Coupure Links 653, 9000 Gent, BELGIUM
[3]Polimi, Dipartimento di Ingegneria Idraulica, Ambientale e del Rilevamento Piazzo Leonardo da Vinci 32, I-20133 Milano, ITALY
Tel: +61 49 216073, Fax: +61 49 216991, email: cejpw@cc.newcastle.edu.au

Abstract - A variable transition rate factor is proposed for the modified IEM, such that it uses a variable dielectric profile down to the radar observation depth. A theoretical observation depth model is also proposed. It is shown that radar observation depth calculated by this model agrees with values noted in literature, and that backscattering simulations using the variable transition rate factor compare well with data collected in the European Microwave Signature Laboratory (EMSL) experiments.

INTRODUCTION

Soil moisture in the root zone is a key parameter in meteorology, hydrology and agriculture. The significance of soil moisture is its role in the partitioning of energy at the ground surface into sensible and latent heat exchange with the atmosphere, and the partitioning of precipitation into infiltration and runoff [1, 2]. As remote sensing observations only respond to the soil moisture in a thin surface layer, observations of surface soil moisture must be related to the complete soil moisture profile in the unsaturated zone, to be of use for climatic, hydrologic and agricultural studies [3].

The problem of relating surface soil moisture to that of the profile has been studied for the past two decades. Four approaches have been adopted: regression, knowledge-based, inversion, and combinations of remotely sensed data with soil water balance models [4].

A recent attempt to relate passive microwave observations of surface soil moisture to that of the profile has been made, where a radio-brightness temperature model and coupled soil heat and moisture transfer model have been combined in the context of a Kalman filter [1]. In order to extend this approach to radar observations, the backscattering equations must be related to the complete soil moisture profile. Using a series of separate regression relationships between soil moisture and backscattering coefficient for different depths of soil, an empirical method of relating a single backscattering observation to the soil moisture profile in the top 10 cm layer has been presented [5]. Apart from this, all empirical and semi-empirical backscattering models have been related to a single soil moisture value in the top 2-5 cm. Furthermore, until recently all theoretical backscattering models have been formulated as a function of the dielectric constant of the soil

at the air-soil interface, and have not accounted for the effects of volume scattering in the soil.

A modification to the theoretical backscattering IEM (Integral Equation Model) was proposed by [6], to account for volume scattering from a drying profile. This modification was made by replacing the Fresnel reflection coefficients with a modified set of reflection coefficients, which incorporate a dielectric profile. In so doing, an exponential dielectric profile model was used, in which the relative dielectric constant (ε_r) as a function of depth (z) is given by:

$$\varepsilon_r(z) = 1 + \left(\varepsilon_{r_\infty} - 1\right)\frac{\exp(mz)}{1 + \exp(mz)} \tag{1}$$

The inputs to this dielectric model are the transition rate factor m (which controls the rate of change of ε_r with depth) and the dielectric constant at depth $z=\infty$ (ε_{r_∞}). By (1), the relative dielectric constant starts from 1 in air and gradually changes to ε_{r_∞} at the rate m. It has been suggested that a value for m equal to about 12 cm^{-1} is appropriate, and this was shown to be an improvement in the simulation of backscattering when compared to the IEM [6].

However, a value of $m=12$ cm^{-1} suggests that the modified IEM may only be used to relate backscattering observations over a profile depth of around 3 mm. This limits application of the model, as a variable dielectric profile over a depth of 3 mm does not provide any additional information on the soil moisture profile than the surface scattering models. Furthermore, various authors have noted that radar observation depth is of the order of a few tenths of a wavelength [2], and varies as a function of soil conditions and radar configuration.

This paper presents a variation on the modified IEM, such that it uses a variable dielectric profile down to the radar observation depth, by using a variable transition rate factor. In order to estimate the radar observation depth, an observation depth model is required.

A radar penetration depth relationship has been proposed by [7]. This relationship defines penetration depth, as the depth at which the transmitted power in the soil has diminished to the proportion $1/e$ (ie. 37%). However, if the transmitted wave has lost 63% of its power to penetrate to this depth, it is unlikely to provide a detectable contribution to backscattering upon return to the surface from this depth.

Hence, this relationship does not correspond with the observation depth of the radar. Therefore a theoretical radar observation depth model which accounts for soil moisture, observation frequency, incidence angle and wave polarisation is proposed.

Fig. 1: Diagrammatic illustration of observation depth model.

VARIABLE TRANSITION RATE FACTOR

As m governs the depth over which a varying dielectric profile is imposed on the theoretical backscattering model, through the modified reflection coefficients, it is proposed that m should be a function of the observation depth. The proposed method for specifying m and ε_{r_∞} in the modified IEM is as follows. (i) Estimate the observation depth d for the given observation conditions; (ii) Evaluate from (1) an appropriate value of m such that $\varepsilon_r(z) = \varepsilon_{r_\infty}$ at $z = d$; (iii) As the radar can only "see" as deep as the observation depth, the value given to ε_{r_∞} in the model should be the value at depth d.

OBSERVATION DEPTH RELATIONSHIP

As no quantitative relationships for radar observation depth which account for soil moisture could be found in literature, we propose a theoretical amplitude attenuation model. This model compares the amplitude of the volume scattered wave with that of the surface scattered wave, as illustrated in Fig 1. The theoretical basis for this model is that when the amplitude of the volume scattered wave (E_{vol}) falls below some proportion of the surface scattered wave amplitude (E_{sur}), it is no longer making a detectable contribution to the total backscattering from the dielectric medium. Hence, the maximum depth from which a volume scattered wave is returned to the surface such that it just satisfies an imposed limit of E_{vol}/E_{sur}, may be considered as the observation depth (d).

The model treats the soil as consisting of two dielectric layers, with the intermediate boundary representing a dielectric discontinuity in the soil. Using the Fresnel reflection (R) and transmission (T) coefficients (functions of soil dielectric constant, incidence angle and wave polarisation) and the incident wave amplitude (E_i), the reflected (E_{sur}) and transmitted (E_t) wave amplitudes are evaluated at the soil surface. The amplitude of the transmitted wave is then attenuated by an amplitude attenuation factor (a) [8], as it passes through the surface layer to the dielectric discontinuity. Upon reaching this discontinuity, the attenuated wave (E_t') is reflected. The reflected wave (E_r) arrives back at the surface with further attenuated amplitude (E_r'), where it again undergoes transmission and reflection. The amplitude of this transmitted wave (E_{vol}) is then compared with that for the surface reflected wave (E_{sur}), and the layer thickness altered
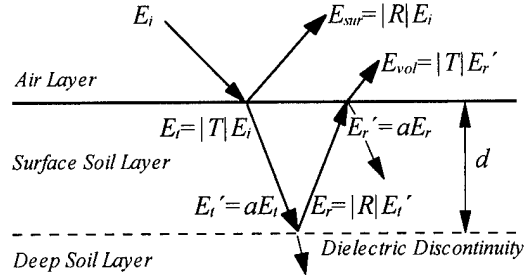
until the imposed ratio between the surface scattered and volume scattered waves is achieved.

A major weakness of the above model is the assumption of a homogeneous specular reflecting surface at the layer interfaces. However, the volume scattered waves may be expected equally in all directions, as volume scattering is caused by dielectric discontinuities whose spatial locations are random [7]. Therefore, if the soil surface is lambertian, evaluation of the observation depth using the specular model will yield the same results.

A difficulty associated with evaluating this observation depth model is the specification of an appropriate limit on the ratio of volume scattered wave amplitude to surface scattered wave amplitude. This problem is addressed through an error analysis of the backscattering equation [9]

$$\frac{E_{vol}}{E_{sur}} = \partial\sigma° \frac{\ln 10}{20} \qquad (2),$$

by considering the sensitivity of the backscattering coefficient ($\partial\sigma°$) to soil moisture and calibration accuracy of the sensor. In the first case, for a 2% change in soil moisture, there can be between 0.15 to 1 dB change in backscattering coefficient [10]. For the latter case, the literature suggests an absolute radiometric calibration accuracy between 1 and 2 dB [11]. Therefore, calibration accuracy appears to govern the observable influence of volume scattering at the present time. Hence a backscattering sensitivity of about 1.5 dB is appropriate, yielding a ratio of volume to surface scattering of 0.17.

APPLICATION OF THE MODELS

Both the observation depth model and variable transition rate factor have been tested using data collected in the European Microwave Signature Laboratory (EMSL) experiments [3]. Simulations for the modified IEM with variable transition factor are also compared with the IEM and modified IEM for m=12 cm^{-1}.

Fig. 2 indicates that the proposed observation depth model gives values which correspond with those suggested in literature, while Fig. 3 indicates that the modified IEM with a
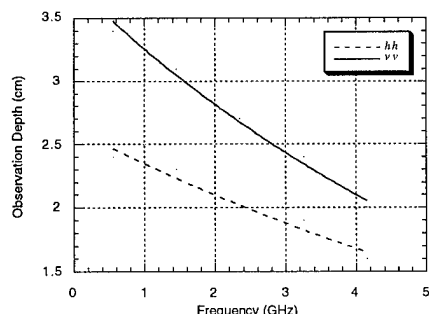
Fig. 2: Observation depth for vv and hh polarisation at an incidence angle of 23° and average volumetric soil moisture of 9%.

variable transition rate factor yields good results when compared to EMSL data. Furthermore, the simulations of backscattering coefficient at low frequencies are an improvement on those from the IEM and the modified IEM with $m=12$ cm^{-1}, for this particular data set.

CONCLUSIONS

The comparisons of backscattering simulations using the modified IEM with a variable transition rate factor show good agreement with the EMSL data. We conclude that by using the modified IEM with a variable transition rate factor, soil moisture profiles to a depth of 3.5 cm may be determined at low frequencies. Furthermore, the theoretical model presented for estimating radar observation depth gives comparable results to those suggested in literature.
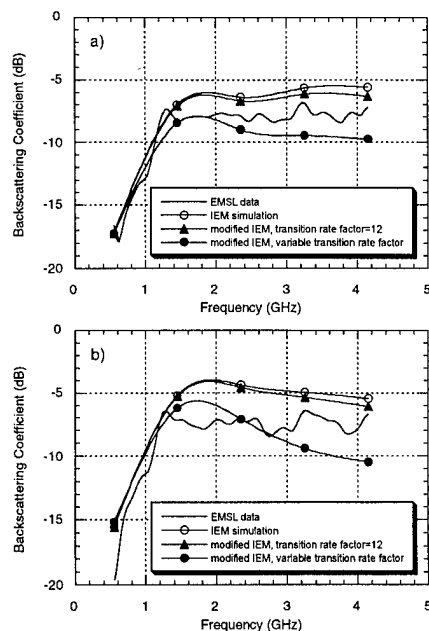
Fig. 3: Comparison of backscattering simulations with EMSL data for correlation length of 60 mm, rms roughness height of 25 mm, incidence angle of 23° and; a) hh polarisation, b) vv polarisation.

REFERENCES

[1] D. Entekhabi, H. Nakamura, and E. G. Njoku, "Solving the inverse problem for soil moisture and temperature profiles by sequential assimilation of multifrequency remotely sensed observations," *IEEE Trans. Geosci. Remote Sensing*, vol. 32, pp. 438-448, 1994.

[2] T. J. Jackson, T. J. Schmugge, and E. T. Engman, "Remote sensing applications to hydrology: soil moisture," *J. Hydrol. Sci.*, vol. 41, pp. 517-530, 1996.

[3] M. Mancini, F. Vandersteene, P. A. Troch, O. Bolognani, G. Terzaghi, G. D'Urso, et al., "Experimental setup at the EMSL for retrieval of soil moisture profiles using multifrequency polarimetric data," presented at International Geoscience and Remote Sensing Symposium, Firenze, Italy, 1995.

[4] K. G. Kostov and T. J. Jackson, "Estimating profile soil moisture from surface layer measurements - A review," presented at The International Society for Optical Engineering, Orlando, Florida, 1993.

[5] L. Bruckler, H. Witono, and P. Stengel, "Near surface soil moisture estimation from microwave measurements," *Remote Sens. Environ.*, vol. 26, pp. 101-121, 1988.

[6] A. K. Fung, M. S. Dawson, K. S. Chen, A. Y. Hsu, E. T. Engman, P. O. O'Neill, et al., "A modified IEM model for scattering from soil surfaces with application to soil moisture sensing," presented at International Geoscience and Remote Sensing Symposium, Nebraska, USA, 1996.

[7] F. T. Ulaby, R. K. Moore, and A. K. Fung, *Microwave remote sensing, active and passive, Volume II: Radar remote sensing and surface scattering and emission theory*. Norwood, MA: Atech House, Inc., 1982.

[8] F. T. Ulaby, R. K. Moore, and A. K. Fung, *Microwave remote sensing, active and passive, Volume I: Microwave remote sensing fundamentals and radiometry*. Norwood, MA: Artech House, Inc., 1981.

[9] A. K. Fung, *Microwave scattering and emission models and their applications*. London: Artech House, 1994.

[10] E. Altese, O. Bolognani, M. Mancini, and P. A. Troch, "Retrieving soil moisture over bare soil from ERS 1 synthetic aperture radar data: Sensitivity analysis based on a theoretical surface scattering model and field data," *Water Resour. Res.*, vol. 32, pp. 653-661, 1996.

[11] M. Zink, P. Olivier, and A. Freeman, "Cross-calibration between airborne SAR sensors," *IEEE Trans. Geosci. Remote Sensing*, vol. 31, pp. 237-245, 1993.

Examination of Soil Moisture Retrieval Using SIR-C Radar Data and a Distributed Hydrological Model

A.Y. Hsu
SSAI, Code 974, NASA/GSFC, Greenbelt, MD 20771 USA
Tel: 301-286-8909, Fax: 301-286-1758, E-mail:hsu@hydro.gsfc.nasa.gov

P.E. O'Neill
Hydrological Sciences Branch/974, Laboratory for Hydrospheric Processes
NASA/Goddard Space Flight Center, Greenbelt, MD 20771 USA
Tel: 301-286-8237, Fax: 301-286-1758, E-mail: peggy@hydro4.gsfc.nasa.gov

E.F. Wood, M. Zion
Department of Civil Engineering, Princeton University, Princeton, NJ 08544 USA
Tel: 609-258-4675, Fax: 609-258-1270, E-mail: efwood@pucc.princeton.edu

INTRODUCTION

A major objective of soil moisture-related hydrological research during NASA's SIR-C/X-SAR mission was to determine and compare soil moisture patterns within humid watersheds using SAR data, ground-based measurements, and hydrologic modeling. Currently available soil moisture inversion methods using active microwave data are only accurate when applied to bare and slightly vegetated surfaces [1]. Moreover, as the surface dries down, the number of pixels that can provide estimated soil moisture by these radar inversion methods decreases, leading to less accuracy and confidence in the retrieved soil moisture fields at the watershed scale. The impact of these errors in microwave-derived soil moisture on hydrological modeling of vegetated watersheds has yet to be addressed.

In this study a coupled water and energy balance model operating within a topographic framework is used to predict surface soil moisture for both bare and vegetated areas. In the first model run, the hydrological model is initialized using a standard baseflow approach, while in the second model run, soil moisture values derived from SIR-C radar data are used for initialization. The results, which compare favorably with ground measurements, demonstrate the utility of combining radar-derived surface soil moisture information with basin-scale hydrological modeling.

SIR-C WASHITA '94 EXPERIMENT

The Little Washita River watershed is situated in southwest Oklahoma in the Great Plains region of the United States and covers an area of approximately 600 km². Two intensive field measurement campaigns were conducted in the watershed in 1994 coincident with the two Shuttle Radar Laboratory (SRL) missions in April and October. During the SRL-1 experiment (April 5-18, 1994), field conditions were initially dry, became wet as a result of a heavy rainstorm on the afternoon of 4/10/94 and morning of 4/11/94, and then gradually dried down throughout the remainder of the experimental period (a change in volumetric soil moisture of 15%). In contrast, during the SRL-2 experiment, most of the watershed remained dry except for localized rainfall in the northwest and north central part of the watershed. Thus, this study has focused on data collected during SRL-1 because of the favorable hydrologic conditions in the watershed at that time.

HYDROLOGICAL MODELING

The model used in this study is known as TOPLATS for TOPMODEL-based Land surface-Atmosphere Transfer Scheme [2]. It assumes that subsurface moisture flows are driven by topographic gradients as described by the soil-topographic index with diffusion formulation for vertical moisture movement, and uses Brooks-Corey equations to relate soil moisture, matrix potential, and unsaturated hydraulic conductivity [3]. The unsaturated soil column is divided into two layers: a 5-cm thin upper layer and a deeper transmission zone; vegetation roots can be distributed between both layers. Canopy interception storage is included in the flux calculations for vegetated pixels. Meteorological forcings used in the model include available energy (net radiation minus ground heat flux), air temperature, relative humidity, wind, and precipitation. Previous work with a statistical version of the Princeton TOPLATS model using data from the Washita '92 experiment with the passive microwave ESTAR aircraft sensor demonstrated that initializing the hydrological model with surface soil moisture estimated from microwave remote sensing produced more accurate surface soil moisture fields compared to a more traditional initialization via baseflow analysis [4].

ANALYSES AND CONCLUSIONS

During the Washita '94 experiment, radiation and

meteorological data were measured at 43 Micronet sites across the Little Washita River watershed, and rainfall data were interpolated from NEXRAD radar measurements. To demonstrate the usefulness of satellite radar data in characterizing the spatial and temporal variability of soil moisture, the '92 analysis was repeated using the SIR-C data from SRL-1 in April, 1994 and a fully distributed version of the TOPLATS model. In the first set of model runs, the hydrological model is initialized using standard streamflow/water table methodology on April 5 and allowed to run for the next thirteen days based on the meteorological forcings. In the second set of model runs, the model is started on April 5 as before but then is re-initialized on April 12 using surface soil moisture fields retrieved from the SIR-C radar data following the Shi modified IEM inversion approach [1]. The first SIR-C data take over the Little Washita on April 11 occurred during an active rain event and was therefore discarded for soil moisture intialization purposes in favor of the next data take on April 12. The model is then allowed to run through April 18 as before based on the meteorological inputs. In watershed areas not covered by the SIR-C data take on April 12, the surface soil moisture fields as calculated by the baseflow model are used (i.e., only those pixels with a SIR-C response and an IEM-derivable soil moisture are re-initialized). Those pixels without a Shi-IEM solution are primarily moderate vegetation and trees.

In both model runs, soil moisture values for the 0-5 cm surface layer were generated on an hourly basis and could be used for comparison with the ground measurements of soil moisture collected in 10-15 test fields distributed throughout the watershed. Fig. 1 shows surface soil moisture images for six days during the SRL-1 mission produced by the model after the SIR-C initialization on April 12. The drydown of the watershed after the rainfall event is very obvious. The top central part of the watershed is covered by every multi-polarization data take during SRL-1 mission. The moisture patterns of this area simulated by TOPLATS resemble those derived from SIR-C data using Shi's approach (see Fig. 10 of [5]), but without pixels of no estimation due to vegetation.

Fig. 2 is a plot comparing the two different model initialization schemes with the ground measurements of surface soil moisture superimposed; all values are watershed averages of the 0-5 cm surface layer. The model run using the standard baseflow initialization produces estimates of soil moisture which are consistently wetter than the model output with the SIR-C initialization, and only match the ground measurements on the day immediately after the rainfall. The model using the Shi SIR-C soil moisture from April 12 initially underestimates soil moisture, but then matches the ground measurements quite well during the subsequent drydown.

The underestimation of soil moisture by the Shi approach has been documented before [1] and is likely due to the absence of vegetation effects in the modeling. Thus, an area of ongoing work is the improvement of radar soil moisture retrieval methods for vegetated areas, in particular the incorporation of vegetation effects in the IEM modeling approach, and documentation of the subsequent improvement in hydrological model performance at the basin scale.

REFERENCES

1. J. Shi, J. Wang, A. Hsu, P. O'Neill and E. Engman, "Estimation of bare surface soil moisture and surface roughness parameters using L-band SIR-C image data," IEEE Trans. Geosci. Remote Sensing, in press.
2. J. Famiglietti and E. Wood, 1994, "Multi-scale modeling of spatially variable water and energy balance processes," Water Resources Research, vol. 30, pp. 3061-3078.
3. C. Peters-Lidard, M. Zion and E. Wood, "A soil vegetation-atmosphere transfer scheme for modeling spatially variable water and energy balance processes," J. Geophys. Res., in review.
4. O'Neill, P., A. Hsu, T. Jackson, E. Wood, and M. Zion, 1997, "Investigation of the accuracy of soil moisture inversion using microwave data and its impact on watershed hydrological modeling," Proc. Applic. of Rem. Sens. in Hydrology, NHRI, Greenbelt, MD, Oct. 1996, pp. 211-226.
5. J. Wang, A. Hsu, J. Shi, P. O'Neill, and E. Engman, 1997, "A comparison of soil moisture retrieval models using SIR-C measurements over the Little Washita River watershed," Remote Sens. Environ., vol. 55, pp. 308-320.

Fig. 2. Comparison of Hydrological Model Initialization Schemes. Daily measured watershed average soil moisture is represented by the x's.
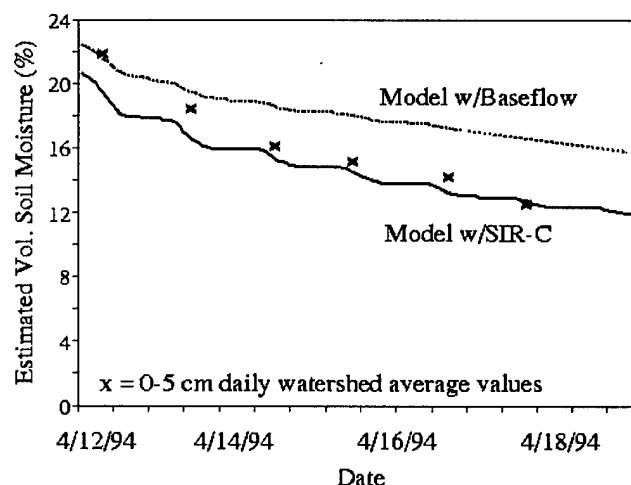
Fig. 1: WASHITA '94 SIR-C INITIALIZATION

April 12

April 16

April 13

April 17

April 15

April 18

Vol. Soil Moisture (%)

8   12   16   20   24   28   >32
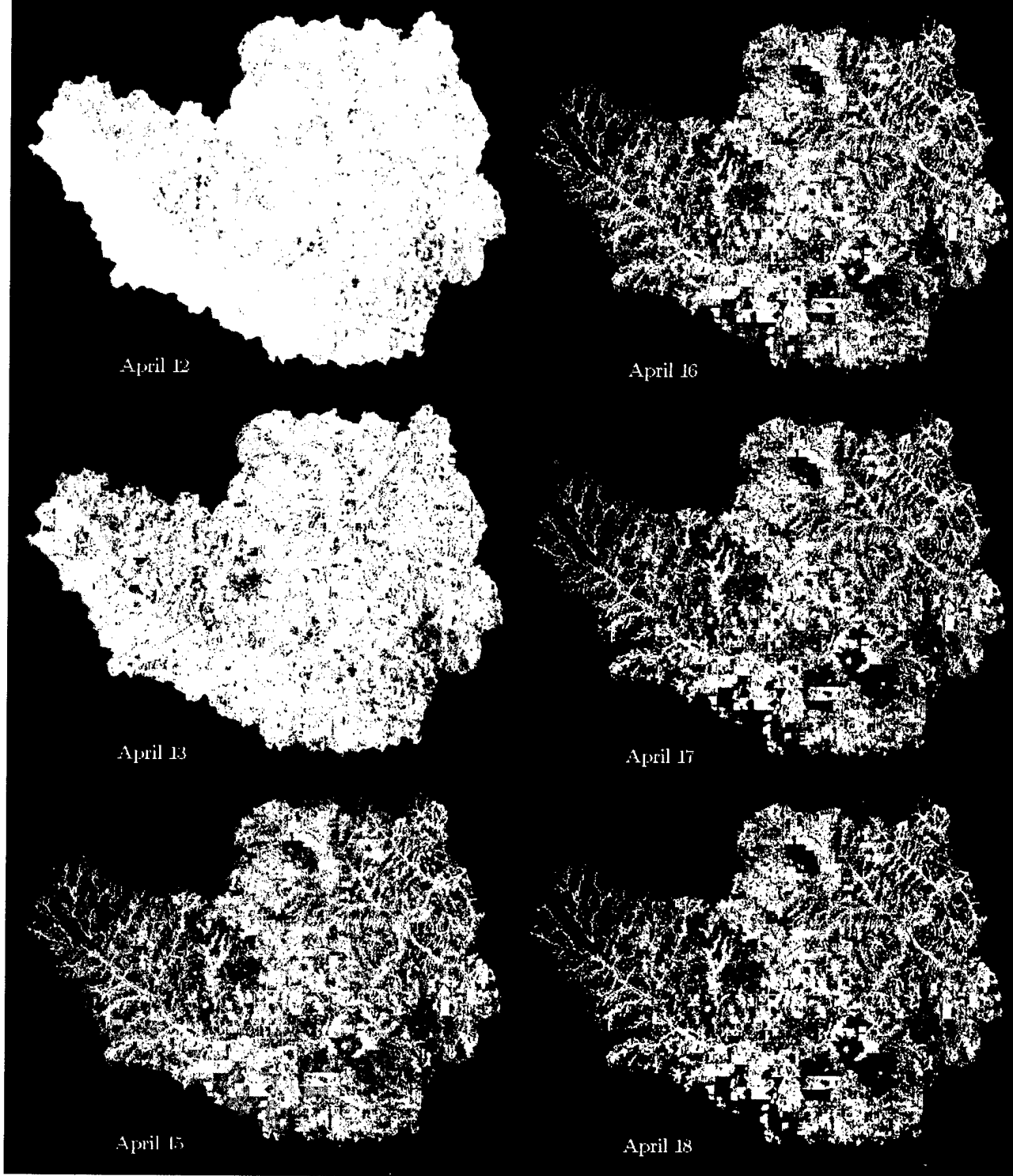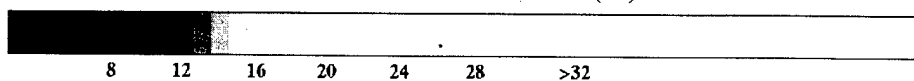
Estimation of Soil Moisture for Vegetated Surfaces Using Multi-Temporal L-band SAR Measurements

Jiancheng Shi
Institute for Computational Earth System Science
University of California, Santa Barbara
Tel: 805-893-8116, Fax: 805-893-2578, E-mail: shi@icess.ucsb.edu

G. Sun, A. Hsu, J. Wang, P.O'Neill, J. Ranson and E. T. Engman
NASA Goddard Space Flight Center, Greenbelt, MD

Abstract - This paper demonstrates the technique to estimate ground surface and vegetation scattering components, based on the backscattering model and the radar decomposition theory, under configuration of multi-temporal L-band polarimetric SAR measurement. This technique can be used to estimate soil moisture of vegetated surface.

INTRODUCTION

Soil moisture is a key parameter in numerous environmental studies, including hydrology, meteorology, and agriculture. It plays an important role in interactions between the land surface and the atmosphere, as well as in the partitioning of precipitation into runoff and ground water storage. In spite of its importance, soil moisture has not found a widespread application in the modeling of hydrological and biogeochemical processes and related ecosystem dynamics, in part because soil moisture is a difficult parameter to measure on a large area, cost-effective, and routine basis.

In attempting to use active microwave remote sensors to estimate soil moisture, we are facing two major problems: effects of surface roughness and vegetation cover. Recently, several algorithms have been developed for measuring bare surface soil moisture quantitatively using dual-polarization L-band SAR image data [1,2] or three-polarization SAR measurements [3]. All of these algorithms use weighted combinations of different polarization signatures to minimize the effect of surface roughness so that soil moisture can be directly inferred from SAR image data. However, the effect of vegetation cover has not been included in the currently available algorithms. It is clear that the presence of vegetation will cause an under-estimation of soil moisture and an over-estimation of surface roughness when we apply the algorithm for bare surface soil moisture to vegetated regions.

In this study, we take one step further to estimate soil moisture accurately for vegetated surfaces using a multi-temporal L-band polarimetric SAR approach. An algorithm has been developed to reduce the vegetation effect on the estimation of soil moisture based on a radar backscattering model and decomposition theory. We will demonstrate the physical principles and development of this algorithm.

BASIC PRINCIPLE OF THE ALGORITHM

A backscattering model [4] for a vegetated surface can be written as

$$\sigma_t^{pp}(\theta) = \sigma_v^{pp}(\theta) + \sigma_{sv}^{pp}(\theta) + \sigma_s^{pp}(\theta)L_{pp}^2 \qquad (1)$$

where $L_{pp}^2 = \exp\left(-2k_e^{pp}d\sec(\theta)\right)$ is the double pass attenuation factor. κ_e is the volume extinction coefficient which depends on the polarization configuration pp (for HH or VV). d is the thickness of the vegetation layer and θ is the radar incidence angle. The subscripts t, v, s, and sv are for total, volume, surface, and surface-volume interaction terms. The direct volume scattering and the surface-volume interaction scattering terms in (1) can be written as

$$\sigma_{sv}^{pp}(\theta) = 0.5\eta_{pp}\left(1 - L_{pp}^2\right)/\kappa_e^{pp} \qquad (2)$$

and

$$\sigma_{sv}^{pp}(\theta) = 2\eta_{pp}dR_{pp}L_{pp}^2 \qquad (3)$$

where η is the volume scattering coefficient depending also on the polarization. R is the surface reflectivity.

Both the volume extinction and scattering coefficients are strongly dependent on density, shape, size, and orientation of scatterers, as well as canopy thickness. It is extremely difficult to estimate the surface scattering components or soil moisture from a limited set of SAR measurements.

Recently, a technique called "Decomposition Theory" has been developed based on the covariance matrix of the scattering terms for polarimetric data [5,6]. A polarimetric SAR backscatter measurement, by using eigenvalues and eigenvectors of the covariance matrix, can be decomposed into three components based on the scattering types: (1) odd number of reflections, (2) even number of reflections, and (3) cross-polarized (diffuse) scattering power. For azimuthally symmetric and reciprocal targets, it can be written as [6]

$$\mathbf{T} = \lambda_1 \mathbf{K}_1 \mathbf{K}_1^{*T} + \lambda_2 \mathbf{K}_2 \mathbf{K}_2^{*T} + \lambda_3 \mathbf{K}_3 \mathbf{K}_3^{*T} \qquad (4)$$

where λ and $\mathbf{K}$ are eigenvalues and eigenvectors. * is a conjugate operator for a complex number, and T is a transpose operator for a vector. The subscripts 1, 2, and 3 represent the decomposed odd, even, and diffuse components, respectively. This decomposition technique allows us to estimate the single and double reflection components of the backscattering coefficients for VV and HH polarization. By comparison with backscattering components in (1) and (4), we can approximately write

$$\sigma_1^{pp}(\theta) \approx \sigma_v^{pp}(\theta) + \sigma_s^{pp}(\theta) L_{pp}^2 \qquad (5)$$

$$\sigma_2^{pp}(\theta) \approx \sigma_{sv}^{pp}(\theta) \qquad (6)$$

where subscript numbers 1 and 2 represent the single and double reflection components.

ALGORITHM DEVELOPMENT FOR MULTI-TEMPORAL L-BAND SAR CONFIGURATION

Since the temporal variability of surface roughness and vegetation cover are much smaller than that of soil moisture, we can reasonably assume that both surface roughness and vegetation cover remain approximately constant at time intervals from a few days to a week unless there is human activity. A change in SAR measurements between repeat passes at this temporal scale will most likely result from a change in ground dielectric properties or soil moisture. Under this assumption, from two repeat-pass polarimetric SAR measurements we can write

$$\sigma_1^{pp1} - \sigma_1^{pp2} = (\sigma_s^{pp1} - \sigma_s^{pp2}) L_{pp}^2$$

$$= \sigma_s^{pp1}(1 - \sigma_s^{pp2}/\sigma_s^{pp1}) L_{pp}^2 \qquad (7)$$

and

$$\sigma_2^{pp2}/\sigma_2^{pp1} = R_{pp2}/R_{pp1} \qquad (8)$$

where the number after pp in both superscript and subscript represents the first or second SAR measurement. At L-band the surface roughness parameter RMS height is small in comparison to the incident wavelength, so we can approximate the polarization amplitude as that in the small perturbation model α_{pp} , which depends only on the surface dielectric constant ε_s and incidence angle θ. α_{pp} is given by:

$$|\alpha_{hh}|^2 = \left[\frac{(\varepsilon_s - 1)}{(\cos\theta + \sqrt{\varepsilon_s - \sin^2\theta})^2} \right]^2 = R_{hh} \qquad (9)$$

$$|\alpha_{vv}|^2 = \left[\frac{(\varepsilon_s - 1)(\sin^2\theta - \varepsilon_s(1 + \sin^2\theta))}{(\cos\theta + \sqrt{\varepsilon_s - \sin^2\theta})^2} \right]^2 \qquad (10)$$

As we can see from (9), the polarization amplitude is exactly same as the surface reflectivity for HH polarization. Under the assumption that surface roughness does not change between the two SAR measurements, we have

$$\sigma_s^{hh2}/\sigma_s^{hh1} = |\alpha_{hh2}|^2/|\alpha_{hh1}|^2 = R_{hh2}/R_{hh1} \qquad (11)$$

Furthermore, using (7), (8) and (11), we obtain

$$\sigma_s^{hh1} L_{hh}^2 = (\sigma_1^{hh1} - \sigma_1^{hh2})/(1 - \sigma_2^{hh2}/\sigma_2^{hh1}) \qquad (12)$$

and

$$\sigma_v^{hh} = (\sigma_1^{hh2} - \sigma_1^{hh1}\sigma_2^{hh2}/\sigma_2^{hh1})/(1 - \sigma_2^{hh2}/\sigma_2^{hh1}) \quad (13)$$

Therefore, we can decompose or directly estimate the volume and surface scattering components by (12) and (13) for HH polarization measurements.

Furthermore, because both R_{vv} and $|\alpha_{vv}|^2$ are only a function of the surface dielectric constant and incidence angle, it is easy to carry out the relationship

$$|\alpha_{vv2}|^2/|\alpha_{vv1}|^2 = a(\theta)(R_{vv2}/R_{vv1})^{b(\theta)} \qquad (14)$$

1270

at a given incidence angle as shown in Figure 1. a and b are coefficients depending only on the incidence angle.

It follows that we can also decompose VV polarization:

$$\sigma_s^{vv1} L_{vv}^2 = \left(\sigma_1^{vv1} - \sigma_1^{vv2}\right) / \left(1 - a(\theta)(\sigma_2^{vv2}/\sigma_2^{vv1})^{b(\theta)}\right) \quad (15)$$

and

$$\sigma_v^{vv} = \left(\sigma_1^{vv2} - \sigma_1^{vv1} a(\theta)(\sigma_2^{vv2}/\sigma_2^{vv1})^{b(\theta)}\right)$$

$$/ \left(1 - a(\theta)(\sigma_2^{vv2}/\sigma_2^{vv1})^{b(\theta)}\right) \quad (16)$$

Similarly, we can derive the surface backscattering components for the second SAR measurements, that is, $\sigma_s^{hh2} L_{hh}^2$ and $\sigma_s^{vv2} L_{vv}^2$. In this way, we can directly decompose or estimate both the volume and surface backscattering contributions in VV and HH polarization without knowing any vegetation information.

From the above technique, we can now obtain an estimation of the surface backscattering components for both VV and HH polarization and for both temporal SAR measurements. However, we still need to estimate the attenuation effect at different polarizations. Using the IEM model [7], we simulated a wide range of surface dielectric and roughness conditions. We found that the surface backscattering coefficients are highly correlated and the relationship can be written as

$$\log 10(\sqrt{\sigma_s^{hh}} + \sqrt{\sigma_s^{vv}} = a(\theta)\log 10(\sigma_s^{hh} + \sigma_s^{vv})$$

$$+b(\theta)\log 10(\sigma_s^{hh}) + c(\theta)\log 10(\sigma_s^{hh}/\sigma_s^{vv}) \quad (17)$$

The a, b, and c again are coefficients determined from regression analyses and only depending on the incidence angle. The maximum standard error for this relation is only 0.1 dB. Using the estimated surface and volume scattering components and (17), we can further estimate the attenuation factor and the surface backscattering coefficients which can be applied to the bare surface soil moisture algorithm.

REFERENCES

[1] P. C. Dubois, J. J. Van Zyl, and E. T. Engman, Measuring soil moisture with imaging radar, *IEEE Trans. Geosci. and Remote Sens.*, vol. 33, no. 4, pp. 195-926, 1995.

[2] J. Shi, J. Wang, A. Hsu, P. O'Neill, and E. T. Engman, Estimation of bare surface soil moisture and surface roughness parameters using L-band SAR image data, In press, *IEEE Transactions on Geoscience and Remote Sensing, 1997.*

[3] Y. Oh, K. Sarabandi, and F. T. Ulaby. An empirical model and inversion technique for radar scattering from bare soil surface, *IEEE Trans. Geosci. Remote Sens.*, vol. 30, no. 2, pp 370-381, 1992.

[4] G. Sun and D.S. Simonett, Simulation of L-band HH radar backscattering for coniferous forest stands: a comparison with SIR-B data, Int. J. of R. S., vol. 9 (5), pp 907-925, 1988.

[5] S. R. Cloude, Uniqueness of target decomposition theorems in radar polarimetry, in *Direct and inverse methods in radar polarimetry: Part 1*, Kluwer Academic Publishers, Dordrecht, pp. 266-296, 1992

[6] J. J. van Zyl, Application of Cloude's target decomposition theorem to polarimetric imaging radar data, *Submitted to PIERS Progress in electromagnetics research symposium*, 1993.

[7] A. K. Fung, Z. Li, and K. S. Chen. Backscattering from a randomly rough dielectric surface, *IEEE Trans. Geosci. Remote Sens.*, vol 30, no 2, pp 356-369, 1992.
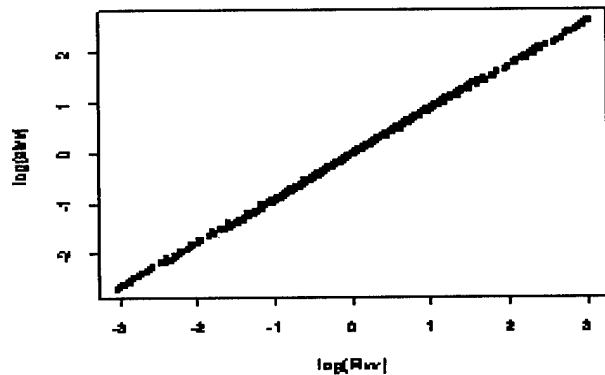
Figure 1. The calculated R_{vv2}/R_{vv1} as x-axis and $|\alpha_{vv2}|^2/|\alpha_{vv2}|^2$ as y-axis at 40° incidence for a soil moisture range of 2% to 50% by volume and all possible soil moisture changes from positive to negative.

On the Retrieval of Soil Moisture from SAR Data over Bare Soils

G. Pasquariello (1), G. Satalino (1), F. Mattia (2), D. Casarano (3),
F. Posa (3), J.C. Souyris (4), T. Le Toan (4)

(1) IESI-CNR, via Amendola 166/5, 70126 Bari (Italy)
tel.+39 80 5481612, fax. +39 80 5484311, e-mail: Pasquariello@iesi.ba.cnr.it
(2) ITIS-CNR, c/o CGS-ASI, Loc. Terlecchia, 75100 Matera (Italy)
(3) Dipartimento Interateneo di Fisica, via Amendola 173, 70100 Bari (Italy)
(4) CESBIO, 18 av. Edouard Belin bpi 2801, 31401 Toulouse Cedex 4, (France)

Abstract - The purpose of this paper is to investigate the possibility of estimating soil moisture content from single angle and single frequency SAR data. To reach this objective, a priori information such as profile height std is assumed. An inversion technique based on a neural approach trained with the IEM model is presented and its performances are discussed. Two sources of errors in the final estimates are analyzed. Errors due to the limited input information and errors due to possible failures of IEM in predicting scattering from natural surfaces.

INTRODUCTION

Over the last few years, the potential of SAR data for estimating soil moisture has been extensively investigated. Previous works have demonstrated that soil roughness plays a major role in the surface scattering, even though the understanding of the roughness effect is still incomplete. The main problem is related to the statistical properties of natural surfaces. The roughness state is traditionally assumed to be a bidimensional stationary Gaussian processes with an associated autocorrelation function (ACF). However, the analysis of a large number of surface profiles acquired over several European test sites have shown a wide spread in the estimated classical roughness parameters (i.e. profile height std and correlation length), as well as non stationary effects such as the dependence of the correlation length estimate on the measured profile length.

The purpose of the paper is to assess the feasibility of retrieving soil moisture content over bare fields by using SAR data currently or in the near future available on a continuous basis, i.e. ERS2 (*VV, 23°, 5.3 GHz*), JERS1 (*HH, 35°, 1.275 GHz*) and the forthcoming ASAR on board of ENVISAT (*HH, VV, HV, 15°-45°, 5.3 GHz*). In fact, the physical quantity taken into account is the relative dielectric constant (ε') which may be easily related to the soil moisture content by means of well assessed semiempirical expressions.

The retrieval technique under use is based on a neural approach. Neural networks (NN) are candidate in applications that need to approximate an unknown function f starting from the knowledge of a set of input output couples $(x_i, f(x_i))$. Although previous works (see for example [1]) aimed at finding the best network configuration to invert a given e.m. model exist, little work was done to assess inversion performances using realistic data set characterized by a wide variability of the geophysical parameters.

In this paper, we train a neural network with backscattering coefficients simulated by means of the Integral Equation Method (IEM) model [2] which requires as input surface parameters: the profile height std (s), the appropriate roughness ACF along with its correlation length (l) and the relative dielectric constant (ε').

Ranges of input parameters are derived from ground measurement campaigns. The simulated configurations are: 1) single frequency (either 5.3 GHz or 1.3 GHz), single polarization (*VV* or *HH*, respectively) and single incident angle (23°); 2) single frequency (5.3 GHz), double polarization (*VV* and *HH*) and single incident angle (23°). In order to reduce the problem complexity we assume the knowledge of profile height std (s). To prepare for the use of ASAR data, a further configuration has been considered: 3) single frequency (5.3 GHz), double polarization (*VV* and *HH*) and double incident angle (23°,45°).

The analysis focuses on two different aspects. In a first step, the inversion performances are tested on data sets generated by IEM. In this way, we can quantitatively assess the achievable accuracy in ε' estimation as a function of the different SAR configurations, under the hypothesis that IEM describes the e.m. forward problem without any error. In a second step, we assess the robustness of the inversion with respect to possible IEM failures. More precisely, an independent data set obtained by means of a Monte Carlo (MC) simulation of backscattering from surfaces showing self similar properties [3] fed the NN and the impact on ε' estimation is assessed.

The next section describes the inversion technique. Subsequently, the results concerning the inversion of IEM as well as of MC simulated data are presented and discussed. Finally, conclusive remarks are given.

INVERSION METHOD

The algorithmic complexity for retrieving geophysical quantities is proportional to the number of parameters to be estimated, to the number of input physical variables and to the complexity of the model used for describing the direct forward problem.

Y_i being the measured values, the inversion task can be regarded as an optimization problem such as the minimization of the difference between the measured values and the data T_i predicted by the direct forward model M. In other words, the set of parameters to be estimated p_i, can be obtained by minimizing the cost function:

$$C\left(p_i\right) = \left\| Y_i - T_i\left(M, p_i\right) \right\|$$

Neural networks are candidate as a tool in applications which need to approximate a function f only known by a set of values $\{x_i, f(x_i)\}$. In fact a network W, finds a root mean square approximation $\left(f^* = f^*(W)\right)$ of f that minimizes:

$$\left\| f - f^* \right\| = \int_{R^n} \left| f(x) - f^*(x, W) \right|^2 dx$$

In general, neural network utilization requires two phases: the training phase and the test phase performed on independent data sets.

In this paper, the inversion is performed by using a Multi Layer Perceptron (MLP) trained by BackPropagation (BP) algorithm. After the appropriate training phase, for each input configuration, the network computes the real part of the relative dielectric constant ($Re(\varepsilon')$) as output. In this way, the inverted ε' has been approximated only by its real part assuming the imaginary part negligible. Fit between MLP outputs and targets is evaluated by the root mean square (rms) of the error. To get good function approximations in the root mean square sense, it is necessary to have a representative training data set. In our case, the IEM model has been used to generate the required training data set. A preliminary phase aimed at assessing the model sensitivity to physical inputs is useful to adapt the training set density to the direct model sensitivity. The input NN configurations under consideration are:

1) single incident angle (23°), single polarization (VV), single frequency (5.3 GHz), and roughness s. It has been denominated: C 1p+s;
2) single incident angle (23°), single polarization (HH), single frequency (1.3 GHz), and roughness s (denominated: L 1p+s);
3) single incident angle (23°), double polarization (HH, VV), single frequency (5.3 GHz) (denominated C 2p);
4) single incident angle (23°), double polarization (HH, VV), single frequency (5.3 GHz) and roughness s (denominated C 2p+s) ;
5) double incidence angle (23°, 45°), double polarization (HH, VV), single frequency (5.3 GHz) (denominated C 2p+2θ);

The ranges considered in the training phase are:
s (cm) = [0.6,2.4]; l (cm) = [10.0,24.0];
ε^r = [3.0 + i 0.1, 20.0 + i 5.0]. The previous ranges being fixed, two different ACF have been considered: exponential ACF and hybrid ACF (intermediate case between exponential and Gaussian ACF). In summary, a set of 10 different NN (5 different input configurations and 2 different ACFs) have been realized.

RESULTS AND DISCUSSION

As a first step, the achievable accuracy in the dielectric constant estimates as a function of different SAR configuration has been investigated. IEM has been used to generate a set of test data which have been fed to the NN. Table 1 shows the obtained results. The NN performances are summarized by the obtained rms error between estimated and actual values. Inversion performances are almost the same for the configurations C 1p+s and C 2p. In addition, there is no clear improvement using the L 1p+s configuration. However, other results (here not included) show that using both HH and VV polarization at L band clearly improves the accuracy figure with respect to the same configuration at C band. Moreover, as can be seen from table 1, there is an improvement going from C 2p to C 2p+s. Same trend is obtained for L band. However, the smallest error is achieved with the C 2p+2θ configuration. This means that the multi angle information is valuable for inversion purposes. Moreover, the NN is not sensitive to the changes of the ACF. This is due to the fact that the IEM sensitivity on ε^r is almost constant whatever the shape of the ACF (i.e. the roughness spectrum). To summarize, the maximum estimate percentage error on $Re(\varepsilon^r)$ is in the order of 12% when using either a C/L 1p+s or C 2p configuration. Considering the case of C 2p+s the maximum estimated percentage error may reduce to 6% whereas in the case of C 2p+2θ it may reduce to 1%.

Table 1: Inversion of IEM data

Configuration	ACF	rms on Re(ε^r)
C 1p + s	exp.	2.4
L 1p + s	exp.	2.1
C 2p	exp.	2.5
C 2p + s	exp.	1.2
C 2p + 2 θ	exp.	0.31
C 1p + s	hyb. (l_G=0.3 l)	2.4
C 2p	hyb. (l_G=0.3 l)	2.0

It should be stressed that such figures refer to the ideal case where the IEM predicts σ_0 without errors.

As a second step, in order to assess the inversion sensitivity on forward error models, an independent data set obtained by means of a MC simulation of backscattering [3] from surfaces with multiscale roughness has been fed to the NN. Surfaces were generated using bidimensional fractional Brownian motion processes with Hurst exponent $H=0.4$ and different height profile std. According to experimental ground measurements, such surface statistics may be considered as more realistic for natural roughness. For this reason, it is expected that the MC simulated data set may represent a meaningful test for assessing the NN performances when attempting the inversion of real data. In [3], a comparison between IEM and MC simulated data is carried out. As a general result, a poor agreement was found. When using a hybrid ACF, a better agreement at 23° was obtained setting $l_G=0.6$ l. Here, the input configuration is the C 1p+s. The s values have been measured over 1.7 m long profiles extracted from the self similar simulated surfaces. Table 2 shows the obtained results. In this case, to better understand the trend, the actual and estimated values are compared for each value of s in input. In the case of exponential ACF, the NN, no matter what the profile std is, gives a reliable ε' estimate only for its lowest values. An opposite situation is found when using the hybrid ACF. The NN gives an almost constant estimate for ε^r which is closer to its highest values. Although in this case the IEM model was in better agreement with MC simulated data, the inversion results are worse. This is due to the fact that when using an hybrid ACF with lG= 0.6 l, the model sensitivity to correlation length increases producing a worse estimate of ε^r.

CONCLUSION

In this work, the feasibility of estimating relative dielectric constants by using single angle (23°) and single frequency data has been investigated. Providing a priori information in terms of profile height std, a MLP network trained by BP algorithm has been found able to invert the IEM model with an accuracy on the ε^r estimate of 12%. It has been shown

Table 2: Inversion of backscattering data obtained by means of MC simulation

MLP input s (cm)	MLP output exp. ACF Re(ε^r)	MLP output hyb. ACF Re(ε^r).	Expected Re(ε^r)
2.5	6.38	16.	6.5
2.	6.09	15.9	6.5
1.5	6.17	15.8	6.5
1.	6.48	15.5	6.5
2.5	7.56	16.	12.5
2.	7.32	16.2	12.5
1.5	7.27	16.2	12.5
1.	9.8	16.1	12.5
2.5	8.09	15.8	18.5
2.	7.88	16.33	18.5
1.5	7.86	16.52	18.5
1.	10.42	16.52	18.5
2.5	8.44	16.7	24.5
2.	8.25	16.4	24.5
1.5	8.27	16.7	24.5
1.	10.84	16.8	24.5

that some improvements may be obtained by adding a second polarization although the most valuable information to improve the accuracy on ε^r estimate is the multi angle capability. Furthermore, an attempt to assess the expected accuracy in the ε^r estimates when dealing with real data has been carried out. In this case, the sensitivity of the inversion performances with respect to errors made in modeling the e.m. forward problem has been investigated. To achieve this goal, an independent data set obtained by means of a Monte Carlo simulation of backscattering from self similar surfaces has been fed to the NN and the output results have been analyzed. As a general conclusion, the inversion procedure has been found very sensitive to forward model errors which need to be improved by adapting realistic description of natural soil surfaces.

REFERENCES

[1] K. S. Chen, W. L. Kao, and Y. C. Tzeng, "Retrieval of surface parameters using dynamic learning neural network", Int. J. Remote Sensing, Vol. 16. No 5, 1995, pp. 801-809.

[2] A.K. Fung, "Microwave Scattering and Emission Models and their Applications," Artech House, Boston-London, 1994.

[3] D. Casarano, F. Posa, F. Mattia, G. De Carolis, J. C. Souyris, T. Le Toan, and G. Pasquariello, " Monte Carlo Simulation of Backscattering from Natural Surfaces", Proc. IGARSS'97, Singapore, 1997.

Passive Microwave Signatures of the Melting Layer in Stratiform Clouds

P. Bauer
German Aerospace Research Establishment, Space Systems Analysis Division,
Linder Hoehe, 51170 Koeln, Germany
(+49) 2203 - 601 - 2995 / (+49) 2203 - 68309 / peterb@dv.kp.dlr.de

J.P.V. Poiares Baptista and M. de Iulis
European Space Agency /ESTEC, Electromagnetics Division,
Keplerlaan 1, 2200 AG Noordwijk, Netherlands
(+31) 71565 - 4319 / (+31) 71565 - 4999 / pedro@xe.estec.esa.nl

Abstract -- A study was carried out in order to estimate the effect of melting particles on brightness temperatures at microwave frequencies between 10.7 and 85.5 GHz. A meteorological model framework was set up to determine the melting stage of various frozen particles below the freezing layer. Different approaches for calculating the effective permittivity of mixed particles were compared. The resulting extinction coefficients, single scattering albedos, and asymmetry parameters indicate a maximum effect when a water matrix with air/ice inclusions is assumed. Extreme local differences of 20-25% between the optical parameters employing either a Marshall-Palmer or a Gamma-type dropsize distribution occur. When radiative transfer calculations are carried out, maximum deviations of >20 K at low frequencies are observed. Neglecting the melting effect may lead to severe overestimations of surface rainrates by up to 100% in stratiform conditions.

METEOROLOGICAL MODEL

The meteorological part is based on the work of [1] with the major model assumptions: (1) mass conservation of individual particles and (2) stationary conditions, i.e. a constant in- and outflow of mass. Particle interaction processes, for example, aggregation and breakup as well as the condensation of water vapor on particles are neglected. As an input for the meteorological model the density of the snow particles above the freezing level (FL) as well as the rainrate and the number density of the rain below the melting region have to be defined. A more detailed model description in this context is given in [2].

PARTICLE DIELECTRIC PROPERTIES

In the most common approach, a dielectric mixing formulation has to be applied once for mixing air and ice and then for mixing air/ice with water [3]. Here, the generalized Maxwell-Garnet [4] formula for ellipsoidal inclusions with equally probable shapes was used for either the mixture of air/ice with water or vice versa. [5] derived a new approach to combine both configurations of water-in-air/ice and air/ice-in-water matrices as a function of the volume ice fraction to obtain the effective permittivity of the matrix-inclusion combination based on the Fourier transform numerical method. In contrast to the air/ice-in-water approach a smooth transition between those stages dominated by either frozen or melted particle components is provided. For this purpose, an error function is employed to describe the weight of the contribution of either ice/air inclusions in a water matrix or vice versa.

PARTICLE OPTICAL PROPERTIES

Calculations were carried out for profiles of three different rainrates, i.e. 1, 5, 10 mm/h (only results for 5 mm/h are shown here), employing a Marshall-Palmer dropsize distribution. The environmental temperature was set to 273 K. The spectra were integrated between radii of $r = 0.1$ mm and $r = 10$ mm with a stepwidth of $\Delta r = 0.1$ mm. The volume extinction coefficient, σ_{ext}, the single scattering albedo, ω_o, and the asymmetry parameter, g, were then calculated in 1 m steps between 100 m above and 1000 m below FL.

When the air/ice-in-water mixture is analyzed, a very distinct increase of extinction is observed with the onset of melting at all frequencies (Fig. 1a). The extinction maximum is located at 100 m below FL at 10.7 GHz and is shifted toward lower altitudes as a function of frequency. This maximum is easily explained by the strong increase of the refractive index once water has formed on the particle's surface. The relative increase is stronger at lower frequencies because the refractive index gradient increases with decreasing frequency due to melting.

The single scattering albedo shows the opposite behavior (Fig. 1b). Since ice particles are effective scatterers at microwave wavelengths, ω_o shows values between 0.6 at 10.7 GHz and 0.98 at 85.5 GHz which are almost independent on rainrate above the 0°-isotherm. Below FL the water matrix causes a very strong and abrupt drop of ω_o. The locations of minimum values are at those altitudes where the maximum values of volume extinction occur.

When the effective permittivity is calculated using the weighted approach, the optical parameters behave quite differently (Fig. 2a). The weighted mixing causes a rather smooth transition between the two phases. The distinct increase of extinction with a maximum between 100-200 m below FL is only observed at lower frequencies. The weigthing produces scattering efficiencies which approach the properties of water drops at lower altitudes which causes a downward shift of the relative minimum values of ω_o (Fig. 2b). Although the principal shape of the curves is similar, the difference of magnitudes indicate a considerable effect of the chosen mixing formula on the integrated optical properties.

SENSITIVITY TO DROPLET SPECTRUM

The simulations of σ_{ext}, ω_o, and g, were carried out using the same constraints as described above but comparing different droplet spectra. Here, we used the exponential form of the Marshall - Palmer dropsize distribution (MPDSD) and the Gamma dropsize distribution (GDSD). The most obvious features are large negative differences (-25%) of extinction coefficients associated with large positive differences (12%) of single scattering albedos right below the FL. These are caused by the lower number of small particles of the GDSD. Using the GDSD less small particles are completely melted so that total extinction is smaller. Total scattering is larger than given by the MPDSD because the effective radius of scattering particles is generally bigger. This effect is equalized when all small particles are melted in both cases. Then the differences remain within ± 5%.

RADIATIVE TRANSFER CALCULATIONS

Plane-parallel simulations of radiances emitted by stratiform clouds at the frequencies of the Special Sensor Microwave / Imager (SSM/I) and Tropical Rainfall Measuring Mission (TRMM) Microwave Imager (TMI) and a zenith angle of 52.8° were carried out. In order to estimate the relative effect of melting particles on the emission, the simulations were compared to profiles assuming all frozen particles to be completely melted at all altitudes below FL. A set of 565 model atmospheres obtained from radiosonde measurements were used and realistic random variations of the relevant background parameters were introduced, i.e. vertical cloud extent, rainrates, and liquid water content of non-precipitating drops coexisting with precipitating particles.

At 10.7 GHz there is clear evidence of the effect of melting particles on the emission when an ice-in-water mixture is assumed. Then, for large particles such as melting snow with dielectric properties close to water the relative effect of the melting layer may exceeds 60 K at horizontal polariza-

tion. However, the assumption of a constant ice-in-water configuration may not hold for snow because the high amount of air inclusions and the large surface area of snow crystals will cause the water to be rather well mixed with air and ice right after the onset of melting [6]. Then, the implementation the weighted average of the air/ice-in-water and water-in-air/ice mixtures leads to much lesser but still remarkable relative brightness temperature increases at lower frequencies.

RAIN RETRIEVALS

Fig. 3 shows results of rain retrievals when applied to the above described data sets excluding or including a melting layer (using the air/ice-in-water mixture). Two algorithms submitted to the Algorithm Intercomparison Project No.3 were selected, i.e. the technique of Ferraro (FE-3) and Ferriday (FR-1) (compiled by [7]). The general performance shows that at those rainrates where the clouds have moderate optical depths, i.e. R ∈ [1, 10 mm/h], an overestimation is observed when a melting layer is present compared to the two-layer structure. Then, maximum deviations of 10 mm/h may occur which decrease with increasing rainrate due to the obscuration by cloud layers on top of the melting layer.

REFERENCES

[1] A.W. Dissanayake and N.J. McEwan, „Radar and attenuation properties and bright band". IEE Conf. Publ., vol. 169-2, pp. 125-129, 1978.

[2] P. Bauer and J.P.V. Poiares Baptista, „On the effect of the melting layer on the microwave emission of clouds". Submitted to J. Atmos. Sci., 1997.

[3] W. Klassen, „Radar observations and simulation of the melting layer of precipitation. J. Atmos. Sci., vol. 34, pp. 3741-3753, 1988.

[4] J.C. Maxwell Garnett, „Colors in metal glasses and in metallic films. Philos. Trans. Roy. Soc. London, Ser. A, vol. 203, pp. 385-420, 1904.

[5] R. Meneghini and L. Liao, „Comparisons of cross sections for melting hydrometeors as derived from dielectric mixing formulas and a numerical method. J. Appl. Meteor., vol. 35, pp. 1658-1670, 1990.

[6] C.A. Knight, „Observations of the morphology of melting snow". J. Atmos. Sci., vol. 36, pp. 1123-1130, 1979.

[7] E.E. Ebert, and M. Manton, „Global Precipitation Climatology Project (GPCP), Summary report of the Third Algorithm Intercomparison Project (AIP-3). WMO/TD No. 714, World Climate Research Programme (WCRP), 1995.
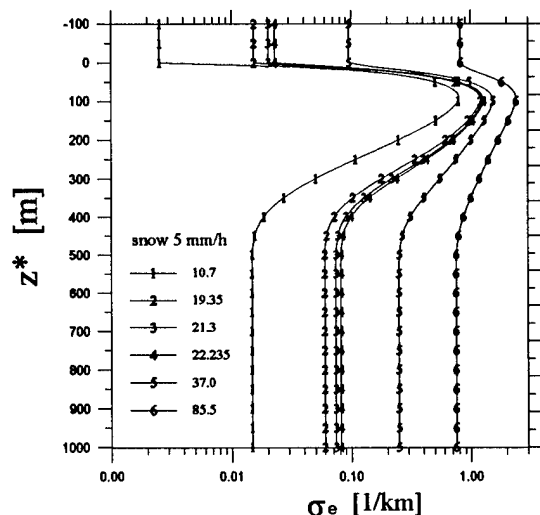
Fig. 1a: Extinction coefficient for ice-in-water mixture.
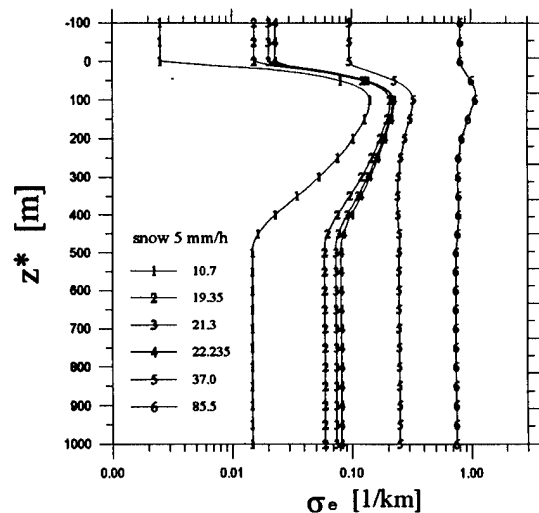
Fig. 2a: see Fig. 1a for weighted mixture.
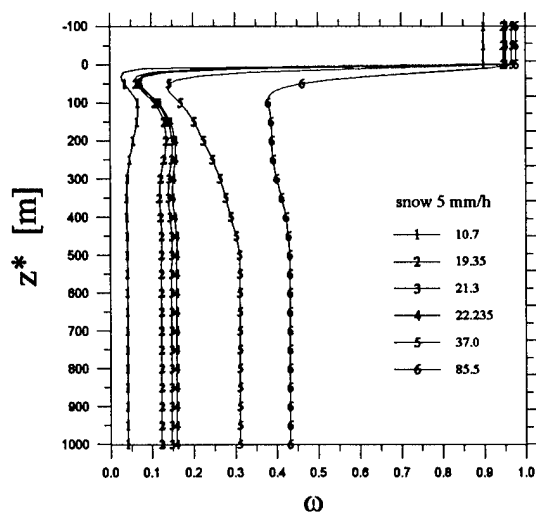
Fig. 1b: see Fig. 1a for single scattering albedo.
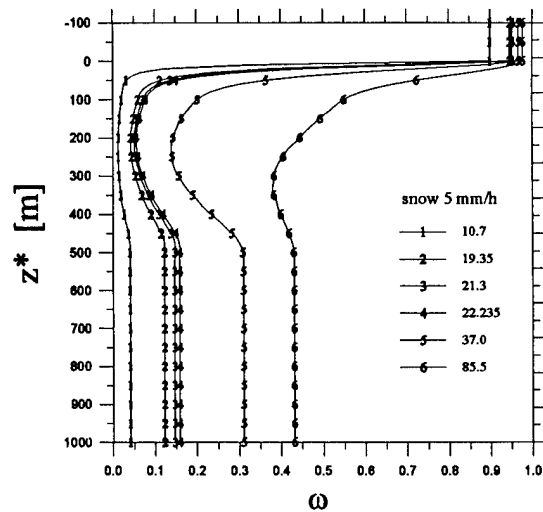
Fig. 2b: see Fig. 1b for weighted mixture.
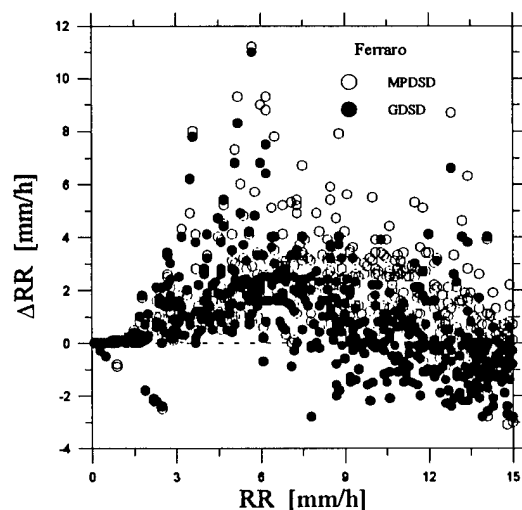
Fig. 3a: Relative melting effect on FE-3-rain retrievals.
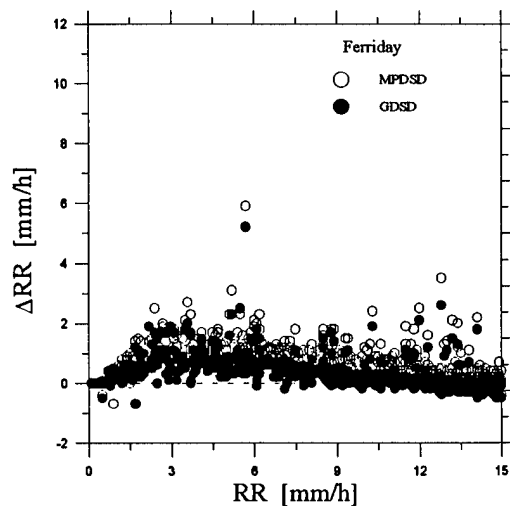
Fig. 3b: see Fig. 3a for FR-1.

ULTRAWIDEBAND RADAR DETECTION OF BURIED OBJECTS

David J Daniels

ERA Technology

Cleeve Road, Leatherhead, Surrey KT22 7SA, United Kingdom

Tel ++ 1 372 367 084 Fax ++1 372 367 081 E-mail david.daniels@era.co.uk

Abstract -- Most commercially available ground probing radars operate in the time domain while the design of a proportion of such radars is based on frequency modulation techniques. This paper briefly considers the two approaches and some of the aspects that define their respective performance. The paper includes a selection of applications to illustrate current capability: detection of explosive mines, detection of the victims of avalanches and archaeological artefacts.

INTRODUCTION

As a result of the development of ultra-wideband radar technology over the last twenty years, practical ultra-wideband radar systems have been demonstrated for numerous applications, most notably surface penetrating radar. During this time, the capabilities of ultra-wideband radar have been the subject of considerable research that has resulted in an improved understanding of the special characteristics of ultra-wideband radar signals and their interaction with targets and target environments[1,2,3,4]. This paper considers some, but not all, of the characteristics that are important to radar system design. Ultra-wideband radars use a variety of modulation methods such as impulse, FMCW, step frequency, phase coded, etc., but all share the common feature of operation at very high percentage bandwidths, that is, greater than 25% and often 100%.

Although on first consideration frequency domain radars should offer a superior sensitivity to time domain radars, because of their lower receiver bandwidth and hence thermal noise, the range sidelobes of the radiated spectrum may result in an equivalent or worse sensitivity.

The output from most ultra-wideband radar systems can be compared as a time domain representation of the waveform. Almost all types of radar can be assessed not just by their signal to noise and signal to clutter ratio but also by comparing their comparative inherent sensitivity. One approach is to compare the range sidelobes of the signal transmitted by candidate radar designs. Such a process reveals the characteristics that define radar performance. An example is given in Figure 1 in which the range sidelobes of three radiated waveforms are compared. The standard for comparison is a single monocycle (lower), the two other types of waveform are a typical impulse radar wavelet (middle) and the time domain equivalent of a stepped frequency radar signal (upper). As would be expected, the frequency content of the radiated signal and the way in which the spectral shaping of the stepped frequency output is carried out, is critical to maintain a low level of range sidelobes.
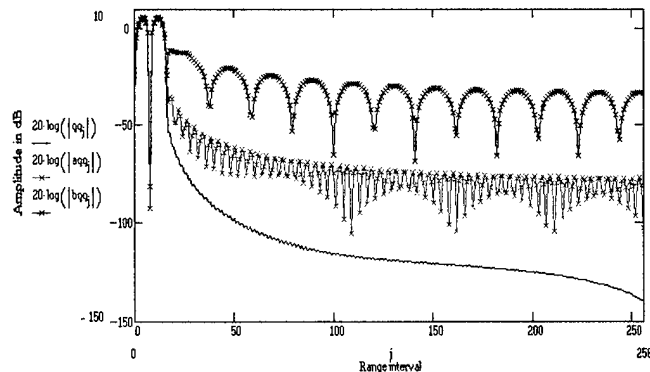
Fig 1 Comparison of range sidelobe level for three cases

It is quite clear that for the stepped frequency radar to achieve a comparable performance to the impulse radar it must transmit an equivalent spectral content. Where the envelope of the spectrum of the signal radiated by the stepped frequency radar is characterised by sudden transitions in the frequency domain, then the amplitude of the time domain range sidelobes of the latter are increased and system performance is degraded. This effect is shown in Fig. 2 where the ratio of the first range sidelobe to the main signal is plotted as a function of the ratio of the lowest frequency cut-off to the centre frequency.

It should be noted that the spectral characteristics of the radiated signal are not only a function of the radar transmitter and receiver but also the transmission characteristics of the antenna and the latter need to be included in any assessment.
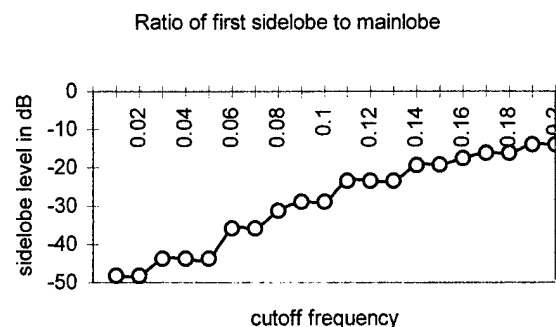
Fig 2 First sidelobe level as a function of relative LF cut-off

ANTENNAS

In the wideband case the radar antennas are considered in terms of their transfer function rather than their gains or effective apertures. In many cases a separate transmit and receive antenna is used hence their transfer functions may not be identical. The type of antenna that is used with an ultra-wideband radar has an important role in defining the performance of the radar.

The types of antenna that are useful to the designer of ultra-wideband radar fall into two groups, dispersive antennas and non-dispersive antennas. However, in principle, all antennas are dispersive to some extent. Examples of dispersive antennas that have been used in ultra-wideband radar are the exponential spiral, the Archimedean spiral, the logarithmic planar antenna, the Vivaldi antenna, slot antennas and the exponential horn. The impulse response of this class of antennas is extended and generally results in a 'chirp' waveform if the input is an impulse. Examples of non-dispersive antennas are the TEM horn, the bicone, the bow-tie, the resistive, lumped element loaded antenna and the continuously resistively loaded antenna. Element antennas are characterised by linear polarisation, low directivity and relatively limited bandwidth unless either end loading or distributed loading techniques are employed, in which case bandwidth is increased at the expense of radiation efficiency.

Horn antennas have found most use with FMCW ultra-wideband radars where the generally higher frequency of operation and relaxation of the requirement for a linear phase response permit the consideration of this class of antenna. FMCW ultra-wideband radars have used an offset paraboloid fed by a ridged horn. This arrangement was designed to focus the radiation into the ground at a slant angle to reduce the level of the reflection from the ground. Care needs to be taken in such arrangements to minimise the effect of back and side lobes from the feed antenna which can easily generate reflections from the ground surface.

Future developments in ultra wideband radar may be based on the use of arrays of antennas. There is the possibility of beam steering in a time domain radar by means of time control, although the inter-element time delay is limited to a maximum equivalent to the distance between each element. The use of timed transmitter arrays and inverse synthetic aperture processing of the signals from a receiver array offers the possibility of achieving considerably improved directionality over all the previous types of antennas discussed in this chapter. A 10 by 10 element array will have a two way peak sidelobe amplitude of -26 dB relative of the main lobe and beam steering up to 50 degrees is feasible. The ability to carry out beam forming by means of inverse synthetic aperture processing could be potentially valuable in many applications.

TIME DOMAIN RADARS

The most frequently used system design is that of the impulse radar and the majority of commercially available radar systems use short pulses or impulses. Considerable bandwidth is required to achieve adequate levels of resolution for an ultra-wideband radar and the resolution equivalent to a monocycle dictates a bandwidth of at least a decade. The majority of ultra-wideband radar systems have used impulses of radio frequency energy variously described as baseband, video, carrierless, impulse, monocycle or polycycle. A sequence of pulses typically of amplitude within the range between 20 V to 200 V and a pulse width within the range 200 ps to 15 ns is applied to the transmit antenna at intervals up to a few microseconds. The output from the receive antenna is applied to a sequential sampling receiver in the form of an ultra high speed sample and hold circuit. It is vital that the entire radar system exhibits a very high level of relative timing stability and a value of 10-20 ps is appropriate.

The high-speed sequential sampling approach used to acquire RF waveforms produces a low S/N ratio because the spectrum of the sampling pulse is a poor match for that of the received pulse. Alternative methods of data acquisition are based on high speed analogue to digital converters or the cross correlator receiver. The wideband cross-correlator receiver can use coherent processing and if required time dithered decoding. The cross-correlator is equivalent to a matched filter, but has more flexibility. The reference waveform can be matched to the transmitted waveform, or in the case of radar, to the complex signature of a particular target and can be changed in real time if needed.

FREQUENCY MODULATED CONTINUOUS WAVE

The main advantages of the FMCW radar are the wider dynamic range, lower noise figure and higher mean powers that can be radiated. In addition a much wider class of antenna is available for use by the designer. An FMCW radar transmits a continuously changing carrier frequency by means of a voltage controlled oscillator (VCO) over a chosen, frequency range on a repetitive basis. The received signal is mixed with a sample of the transmitted waveform and results in a difference frequency which is related to the phase of the received signal, hence its time delay and hence range of the target. The difference frequency or intermediate frequency (IF) must be derived from an I/Q mixer pair if the information equivalent to a time domain representation is required, as a single ended mixer only provides the modulus of the time domain waveform. The FMCW radar system is particularly sensitive to certain parameters. In particular it requires a high degree of linearity of frequency sweep with time to avoid spectral widening of the IF and hence degradation of system resolution.

STEPPED FREQUENCY RADAR

Any repetitive pulsed signal can be transformed to a frequency domain representation which will consist of a line spectra whose frequency spacing is related to the pulse repetition whose frequency spacing is related to the pulse repetition rate and envelope is related to the pulse shape. Hence a repetitive impulsive waveform can be synthesised by transmitting a sequential series or individual frequencies whose amplitude and phase are accurately known.

Two forms of the synthesised radar can be considered. The first and simplest system is a stepped frequency continuous wave

radar. The second form is more complex in that each individual frequency is appropriately weighted in amplitude and phase prior to transmission. Normally the radar is calibrated both to establish a reference plane for measurement as well as to reduce the effect of variations in the frequency characteristics of components and antennas.

The radar system will introduce additional phase shifts on the transmitted and received system. These will be caused by the electrical lengths of the signal paths to the antennas and the effective radiation phase centre of the antennas. This means that the phases of the transmitted and received signals will be different at each integer frequency and will require compensation. Evidently it is important that the recorded values of amplitude and phase at each frequency are accurately related. Any temporal variation in the system characteristics that degrades the system calibration will of course reduce the resolution and accuracy of measurement. In addition the repeatability of the frequency is important and must be such that the calibration remains valid. The main advantages of a stepped frequency continuous wave radar are its ability to adjust the range of frequencies of operation to suit the material and targets under investigation, a higher mean radiated power level per spectral line and the ability to integrate the received signal level hence improving the system sensitivity. The calibration of the radar does, of course, depend on stable system characteristics and antenna parameters that are invariant with front surface-antenna spacing. The synthesized pulse radar is a variant of the stepped frequency continuous wave radar in that the relative amplitudes and phases of the transmitted frequencies are adjusted on transmission in order to synthesize the desired pulse waveform. A significant advantage for this approach is that it is possible, within limits, to take account of the frequency characteristics of the antennas. For example, the low frequency cut-off point of an antenna can be compensated by weighting the amplitude of the low frequency spectral lines. However, the requirement to maintain an accurate phase relation between each of the spectral lines is difficult to achieve in real time. It is generally easier to carry out computation on down-converted and recorded data.

MINE DETECTION

Mines are weapons which are used in the military role to frustrate and slow down the manoeuvrability of enemy forces. Where mines have been used or scattered indiscriminately, the civilian population suffers the consequences of such irresponsibility.
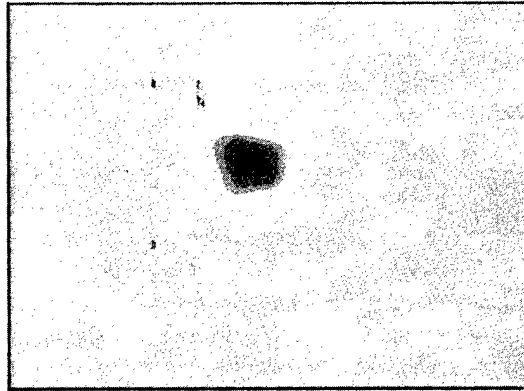
Fig 3 Radar plan image of plastic anti-tank mine. Scale 1.8m by 1.8m, depth 250 mm.

It is estimated that there are some 100 million uncleared mines in the world. Mines are still being laid at the rate of 2 million per annum and the rate of clearance is painfully slow. In Afghanistan it has been estimated that it would take 4300 years to clear mines manually from just 20% of the country. Starting from the Falklands War and over the last decade we have researched the capability of impulse radar to detect buried mines, particularly the non-metallic type and the radar image generated by the latest generation radar, from a typical plastic anti-tank mine, is shown in fig 3.

AVALANCHE VICTIMS

The difficulty of recovering skiers buried alive in avalanches has resulted in investigations as to the capability of ground probing. In March 1997 we carried out a series of measurements on volunteers buried in snow in ski stations in France. With the appropriate radar system it is possible to detect humans buried up to two metres in snow.

Fig 4 Test conditions for radar detection of victims of avalanches
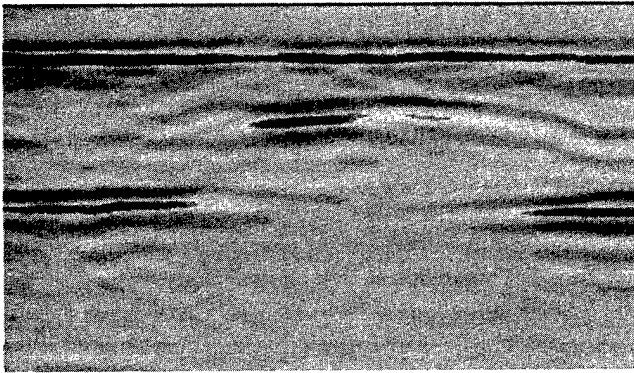
Fig 5 Radar image of volunteer buried metre deep in snow, horizontal scale 2m

Fig 7 Radar image of culverts under the Cellarium at Fountains Abbey, Yorkshire, UK. horizontal scale 4m

The test situation is shown in fig 4 and a radar image is shown in fig 5.

ARCHAEOLOGY

Fountains Abbey in North Yorkshire, founded in 1134 by the Cistercians, is an outstanding example of a mediaeval monastery. It stands in the valley of the River Skell and the existing ruins give a clear impression of life in one of England's greatest and best preserved abbeys. A photograph of the Abbey is shown in fig 6. Recently, and in collaboration with the University of York, Department of Electronics, ERA Technology carried out a survey of parts of the grounds of the Abbey. The radar image of the culverts under the Cellarium is shown in fig.7. The radar image in this particular case is unfocussed and therefore most of the reflections give rise to hyperbolic traces. This is particularly noticeable when caused by the corner reflectors formed by the river water surface and the masonry side wall of the culvert. Other hyperbolic reflectors can also be seen and these are caused by the masonry side supports of the culvert.

Fig 6 Photograph of Fountains Abbey Yorkshire UK

SUMMARY

The growing interest in ultra-wideband ground probing radar demonstrates the potential which is perceived for its application for non destructive testing, geophysical surveying, security, forensic and military applications. Continued technical improvements in antenna performance, receiver sensitivity and processing capability have resulted in compact, lightweight and portable equipment which provide higher quality images of the objects buried underground. The future challenges for the design engineers are to improve the signal to clutter performance, the true receiver dynamic range and the image quality and man-machine interface

ACKNOWLEDGEMENTS

REFERENCES

[1] J D Taylor (Ed), Introduction to Ultra-wideband radar systems, CRC Press, ISBN 0-8493-4440-9 1995
[2] I J LaHaie (Ed) Ultrawideband Radar, Proc. SPIE Jan 1992
[3] D J Daniels, Surface Penetrating Radar ,IEE,ISBN 0-85296-862-0, 1996
[4] A Al-Attar, D J Daniels, H F Scott, A novel method of suppressing clutter in very short range radars IEE Int. Conf. Radar-82, October 1982

Preliminary Field Results of an Ultra-Wideband (10-620 MHz) Stepped-Frequency Ground Penetrating Radar

Glen F. Stickley, David A. Noon, Mikhail Cherniakov and I. Dennis Longstaff
Department of Electrical & Computer Engineering
The University of Queensland, Qld 4072, Australia, and
Cooperative Research Centre for Sensor Signal and Information Processing (CSSIP)
Telephone: 61 7 3365 3645   Facsimile: 61 7 3365 3684   Email: stickley@elec.uq.edu.au

ABSTRACT -- We present the results from preliminary field trials using a newly developed ultra-wideband, stepped-frequency ground penetrating radar system. This system has been developed to improve the maximum penetration depth capability in ground penetrating radar (GPR) applications without degradation of resolving power. To achieve this, we have based our system on the stepped-frequency radar technique operating across the 10-620 MHz frequency band.

The stepped-frequency technique offers substantial benefits over existing time-domain (impulse) GPR systems. The main advantage of the technique is that it is relatively easy with current technologies to efficiently sample ultra-wideband signals with low speed analog-to-digital converters. Also, due to transmission of long duration waveforms, a high average transmitted power is much easier to obtain than for short-pulse and impulse waveforms. The stepped-frequency technique offers other potential advantages for GPR such as a variable dwell time on each frequency, and more flexibility in signal processing such as the ability to correct for system errors.

Our system can operate over multi-octave bands within the 10-620 MHz frequency range. The radar has the capability to employ a short range gate (~10ns duration) at each frequency step which can suppress unwanted strong signals (eg. direct wave between antennas) relative to weak reflections from deep targets. Field trials of the radar have demonstrated the effectiveness of gating and of the system as a whole.

INTRODUCTION

The stepped-frequency technique is an accepted technique amongst the radar community and has recently been looked to as a means of improving the penetration performance of ground penetrating radar (GPR) without sacrificing penetration. Currently available commercial GPRs almost exclusively use impulse transmitters with sampling head receivers. Such receivers are inherently inefficient as many

pulses must be transmitted to record a single range profile. In addition, the mean power available from the impulse transmitter is also limited by the low duty cycle.

The main disadvantage of stepped-frequency and other continuous wave techniques, is that strong signals either from leakage between the transmit and receive antennas or from shallow reflectors can mask weaker signals from deep reflectors.

A gated stepped-frequency GPR [1] attempts to combine the high average power and efficient sampling of stepped-frequency radar with the ability of impulse GPR to image deep (weak) targets despite the presence of shallow (strong) reflectors. As GPR deals with targets at very close ranges often only a few cycles of the carrier is contained in the gate.

Gating is applied at each frequency step and involves turning both the transmitter and receiver on and off at the same repetition rate but offset in time. Typical gating functions are shown in Fig.1.
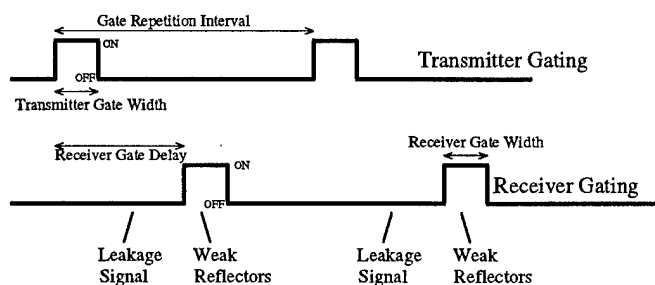
Figure 1- Typical gating functions applied to the transmit and receive gates. The receive gate is delayed relative to the transmit gate. The delay between the gates should be varied to match the return travel time to reflectors of interest.

SYSTEM

Our system is a stepped-frequency radar operating from 10 to 620MHz. The main body of the radar includes a synthesiser, quadrature receiver, digital signal processor and real-time display. To this various antenna subsystems incorporating transmit and receive amplifiers can be

connected. An earlier version of our system and laboratory testing of it have been described in [2].

Field results with this earlier version were limited by the antenna subsystem [2]. This paper reports results obtained with a redesigned antenna subsystem. The new antenna subsytem is linked to the main body of the radar only by fibre optic links (Fig.2). This innovation was tried as it was conjectured that the coaxial cables and power cables previously used to link to the antenna subsystem had become part of the radiating structure; and that it was this undesired radiation from the cables that was limiting field performance of the system. The new antenna subsystem is a prototype and does not include the high power transmit amplifier or as low noise a receiver as the previous antenna subsystem.
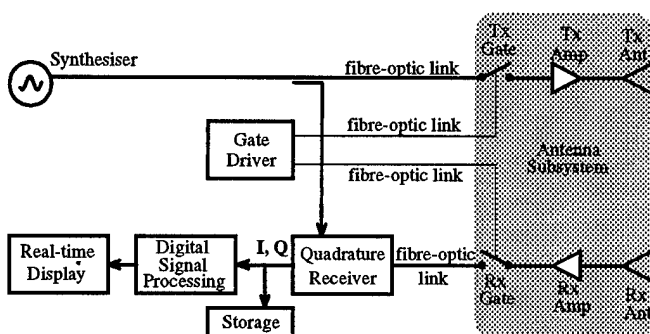
Figure 2- Simplified block diagram of radar. The antenna subsystem, shaded region, is physically separate from the bulk of the radar. All interconnections between the antenna subsystem and the rest of the radar are by fibre-optics links.

FIELD RESULTS

The radar was trialed around a perched freshwater lake on a sand island. The position of the water table was fairly well known around the lake edge and the sand is relatively uniform with low attenuation. The submerged water table should provide a strong though sometimes broken interface reflector.

To demonstrate the gating three surveys were taken along one survey path. The surveys started near the lake edge and moving directly away from the lake up a gently sloping bank. One survey was taken in ungated mode, the second in gated mode and the third with the system alternating between gated and ungated modes. In the display of all images a range gain curve has been applied. The gated and ungated data have been scaled so that a reflector centred in the range gate would have the same strength in both. The images are created using the synthesised real bipolar waveform. Hot colors indicate positive swings of the waveform and cool colors indicate negative swings.

Fig.3 shows the data taken in ungated mode. There are three strong signals, the direct wave between antennas, the
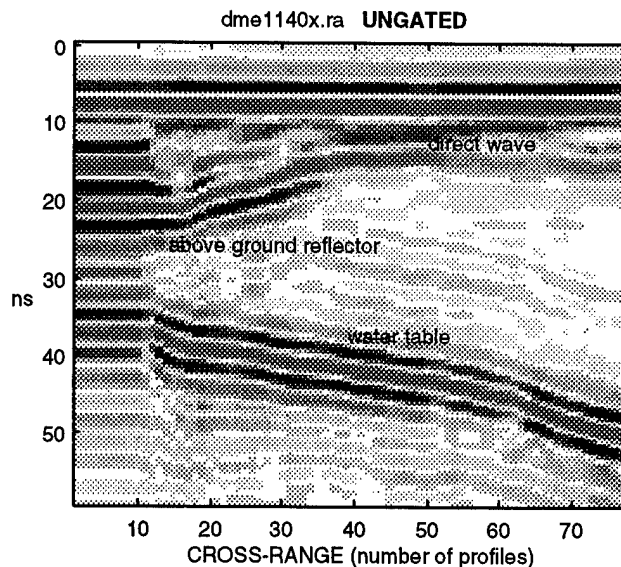
Figure 3- Ungated image of shallow water table.

reflection from the water table which recedes in depth from left to right in the image, and an above ground reflector. The water table is estimated (assuming that the water table is level with the surface of the lake) to be about 2.5m deep at the start of the survey and about 4m deep at the end. The water reflector at its deepest is about 20dB weaker than the direct wave.

Fig.4 shows the data taken in gated mode. The direct wave has been completely eliminated. The air reflector overlaps the receive gap slightly and hence is still present though much weak in the image.

Fig.5 show data taken with the radar alternately between gated and ungated mode. This image clearly demonstrates
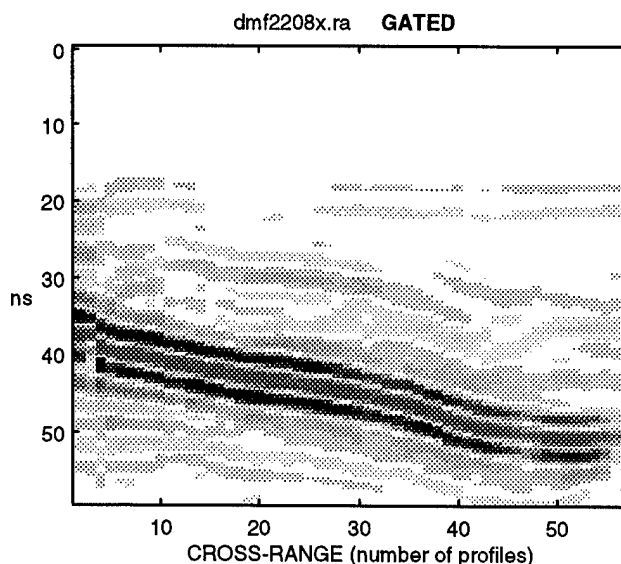
Figure 4- Gated image of shallow water table

1283

dmf4643x.ra GATED and UNGATED
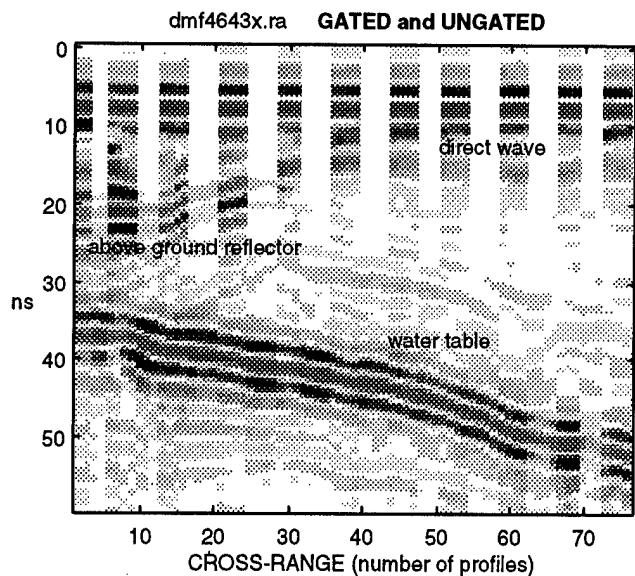
Figure 5- Image of the shallow water table with radar alternatively in gated and ungated mode. The gated and ungated data have been scaled so that a reflector centred in the range gate would have the same power in both.

dnc4739x.ra long continuous run GATED

Figure 6-..The above image is the result of a 120m survey conducted above a much deeper water table. The variation in depth seen above is consistent the surface topography. The underlying water table is believed to be flat.

the effectiveness of gating.

An important criteria for gated stepped-frequency GPR is how much rejection of the strong targets gating can achieve. In the survey shown in Fig.5 data was also taken while the antennas were stationary on the ground. This showed that the direct wave was rejected >60dB relative to a target approximately centred in the gate. In this data set that level of rejection is sufficient to render the direct wave below the noise. Laboratory measurements with similar gating electronics have shown rejection of >80dB [2].

Fig.6 shows a long survey (approximately 120m) conducted over a much deeper section of water table. The image of the water table mirrors the surface topography over which the survey was conducted. This survey was conducted exclusively in gated mode. In ungated mode the water table reflection was below the sidelobes of the direct wave.

Although they were not used in the trials reported here we have also been able to significantly reduce the power of the direct arrival by using shields around the transmit and receive antennas. This is usually done with standard GPR antennas with centre frequencies of 100MHz or more.

CONCLUSIONS

The use of optical fibre connections to the antenna subsystem and redesign of the antennas has allowed excellent field results to be obtained. This supports the conjecture that the field performance of the system had previously been limited by radiation from the cables joining the antenna subsystem and the main body of the radar.

Gating has been shown to reject strong reflectors in favour of returns from weak reflectors. A rejection of at least 60dB was obtained in the field.

A new antenna subsytem is being constructed to incorporate the advances made in the optical fibre linked antenna subsystem with the high transmit power and the low noise receiver reported in [2].

REFERENCES

[1] S-E. Hamran, D.T. Gjessing, J. Hjelmstad, and E. Aarholt, "Ground penetrating synthetic pulse radar: dynamic range and modes of operation," Journal of Applied Geophysics, Vol. 33, pp. 7-14, 1995.

[2] G.F. Stickley, D.A. Noon, M. Cherniakov, and I.D. Longstaff, "Current development status of a gated stepped-frequency GPR," Proc. Of 6th International Conference on Ground Penetrating Radar, Sendai, Japan, 1996, pp. 311-315

Extraction of Discriminant Features from Impulse Radar Data for Classification of Buried Objects

H. Brunzell
Chalmers University of Technology
Dept. of Applied Electronics
S-412 96 Göteborg, Sweden
Telephone: +46 31 772 1786; Fax: +46 31 772 1782
Email: brunzell@ae.chalmers.se

Abstract— This paper deals with the problem of detecting and classifying buried objects. The application in mind when addressing this problem is the detection of buried landmines. Modern landmines are to a large extent made out of plastic and ceramic materials. This makes detection with traditional sensors such as metal detectors and magnetometers almost impossible. Another problem with these sensors is the high false alarm rate induced by metallic debris from exploded bomb shells. A sensor type that seems to have capability to overcome these problems is the impulse radar. The impulse radar can detect non-metallic objects buried in the ground. The large bandwidth of the radar also gives additional information that can be used for classification purposes. The classification abilities enable discrimination between mines and stones and metallic debris, thus reducing the false alarm rate. An important step towards good classification results is to extract a set of features from measured data. The present paper elaborates on properties that an admissible feature type must possess and shows that the choice of features should be related both to the type of measurements and the type of classifier used. A number of different feature types are finally evaluated using measured data from an impulse radar system.

1 INTRODUCTION

The problem of clearing minefields in post-war zones has received much attention lately. According to the International Committee of the Red Cross about 100 million landmines are buried in 62 countries around the world. The clearing has traditionally been done using metal detectors, magnetometers or simply by probing the ground using a long stick. The probing is obviously a dangerous method, while the problem with the two above mentioned sensors is that they rely on a metal content of the mine. However, modern landmines are to a large extent made of non-metallic materials such as ceramics and plastics. Another problem is that the ground in a post-war zone is most likely contaminated with metallic debris from exploded bomb shells. This will give rise to a lot of false alarms using the metal detecting sensors. A way to overcome these problems seems to be to use an impulse radar as sensor. The impulse radar can not only detect non-metallic objects, but its large bandwidth also gives information that can be used for target discrimination (classification). If the system can discriminate a metal fragment from a mine, then the false alarm rate can be reduced. To enable a reliable classification, the essential information must be extracted from the measured signals. This essential information is condensed into a vector of so called *features*. The features should be "close" for measurements made on one object, while they at the same time should differ as much as possible from features extracted from measurements on other objects. It is also desirable that the features have certain invariance properties, such as time-shift invariance. This is due to that an unknown burial depth of an object will give rise to an unknown time delay, this time delay should not affect the feature set. Further feature properties are stated in Section 2, together with a list of possible feature types. These feature types are evaluated in Section 3 using real data from an impulse radar system. Finally, the results and conclusions of the evaluation are found in Section 4.

2 FEATURE EXTRACTION

Feature extraction is the process of mapping measurements to a number of figures, *features*, that in some sense represents the measurements. In the present paper the goal is to classify measurements to one class, out of a number of possible classes. The features should thus extract the information in the measurements that is essential for determining the class belonging. The feature extraction

can be divided into two steps. The first step is a mapping (often non-linear) into a number of *admissible* features. The type of mapping is to a large extent determined by the type of measurements, and what type of corruption of the measurements that can be expected. The present paper introduces a number of different mappings, or feature types, that for different reasons were expected to work for the type of signals considered here. The second step of the feature extraction process is to reduce the number of features as much as possible. In this step only linear transformations will be considered. The choice of transformation in this step should be related to the classification rule used. The ideal is of course if the transformation is selected such that the classification error is minimized. The exact classification error, however, is very difficult to use as an optimality criterion. In [1], a method that uses an estimate of the upper bound of the classification error as optimality criterion was presented and found to perform well. The present paper will focus on the first step though, i.e., how to find suitable feature types for a specific type of signals. The particular application considered here will impose a number of conditions that any feature extraction method must fulfill. The most important conditions are formulated below. Assume that a signal $f(t)$ is mapped to a feature vector $\mathbf{y}$ as $f(t) \xrightarrow{FE} \mathbf{y}$.

(a) $f(t-\tau) \xrightarrow{FE} \mathbf{y}$. Invariance to time-shifts. Time shifts occur due to different burial depths and varying antenna height.

(b) $f(at) \xrightarrow{FE} \mathbf{y}$. Invariance to time-scalings. Occur due to different propagation speeds in different soils.

(c) $f(t) + \gamma f(t-\tau) \xrightarrow{FE} \mathbf{y}$. Insensitive to multiple reflections.

(d) $f(t) + n(t) \xrightarrow{FE} \mathbf{y}$. Insensitive to additive noise, e.g., measurement noise.

3 PRESENTATION OF DIFFERENT FEATURE TYPES

This section will briefly describe a number of feature extraction methods that satisfy some of the conditions above. For a more complete description see [1].

Fourier spectrum — An estimate of the spectrum of the measurements is used as feature. Smoothing is employed to reduce the variance of the estimate. Satisfies property (a) and partly (c).

Fourier-Mellin transform — The Mellin transform is invariant to time-scaling. By combining it with the Fourier transform we can also obtain invariance to time-shifts, [2]. The Fourier-Mellin transform thus satisfies (a),

(b) and partly (c). Unfortunately, it is very sensitive to noise (condition (d)).

Cepstrum — Defined as the inverse Fourier transform of the logarithmed spectrum. Satisfies (a) and partly (c).

Bispectrum — Also called third order spectrum. Is a function of two variables. In [3] it was proposed to use line integrals of the bispectrum as features. Features obtained this way satisfy (a), (b) and partly (c) and (d).

Discrete wavelet transform — Expands the function in an ON-basis, where the basis functions are translated and scaled versions of a single function called the "mother wavelet". Extremely sensitive to time-shifts. To overcome this problem, the measurements are aligned in time before the transformation.

Pole estimation using ESPRIT — Models the signal as a sum of damped exponential and estimates the parameters of that model, i.e., pole-frequencies and dampings, [4].

Histogram — Estimate of the amplitude distribution of a signal. Satisfies (a) and (b), but does probably not provide enough discriminant information.

Time samples — Signals are time aligned to satisfy (a). Does not satisfy (b) thru (d). Included in this list mostly for reference.

4 RESULTS AND CONCLUSIONS

The data for the evaluation of the different feature types presented above are collected using an impulse radar system at Sweden's Defence Research Establishment (FOA) in Linköping, Sweden. The impulse radar antenna consists of two crossed dipole elements, one for transmit and one for receive. The radar transmits pulses of 0.3 ns length and samples the received return at a sampling frequency of 20 GHz with 14 bits amplitude resolution. The antenna is mounted on a positioning system above a sand container. Five different object are buried in the sand container at 10 cm depth. The objects are a metal sphere, a metal cylinder, a plastic mine dummy, a concrete filled plastic shell and a stone. For each object, 72 measurements are made with the antenna in different positions within a radius of 20 cm from the object. The measurements are mapped to features using the methods presented above and then the feature dimension is reduced to 10 using the method of [1]. An exception to this is made for the bispectrum features where the feature dimension is 20, and for the poles estimated using ESPRIT, where 5 poles are estimated. The features are classified using a Bayes classifier, with the assumption of normal distributed features. The classification error is estimated in two ways. A lower bound, $\hat{\varepsilon}_l$, is estimated using the same data set both for training and classification. An upper bound, $\hat{\varepsilon}_u$, is also estimated using a method called

leave-one-out, [5]. The upper bound is more relevant since this is the error one can expect when using independent data sets for training and classification (cross validation). The results from the evaluation are presented in Table 1.

Feature Type	$\hat{\varepsilon}_l$	$\hat{\varepsilon}_u$
Fourier Spectrum	1.39	12.22
Fourier-Mellin	35.00	47.78
Cepstrum	3.61	18.33
Bispectrum	3.06	16.67
Wavelet Transform	0.83	18.06
ESPRIT	51.94	55.00
Histogram	42.78	61.67
Time Samples	1.39	31.94

Table 1: Estimates of upper and lower bounds of classification errors for different feature types (in %)

The feature type giving the lowest error rate is the Fourier spectrum, with an upper bound of 12.22%. Three other methods also perform well, namely the cepstrum, bispectrum and wavelet features with error rates around 17–18%. The poor performance of the Fourier-Mellin transform is probably due to its high noise sensitivity. The ESPRIT method is also quite sensitive to noise, but the main problem is how to compare poles estimated from two different signals. As an example, consider the case when we have a signal with, say, 5 poles. If we now estimate the three most dominant poles of that signal, measured with different noise realizations, we will not always select the three same poles as being dominant. This causes problems for the classifier, and the figures obtained in Table 1 can probably be improved by assessing this problem. The high error rate of the histogram features is most likely due to that they simply not contain enough discriminant information. Time samples, finally, give an error rate of almost 32%. It is interesting to note that an adequate feature extraction method can reduce the error rate by more than a factor 2, compared to using the time samples directly. One should, of course, not forget that a poor feature extraction method can actually increase the error rate. The final conclusion is that it is of utmost importance to select the feature extraction method with great care. For the application considered in the present paper, four different methods were found to perform well (Fourier spectrum, Cepstrum, Bispectrum and Wavelets). These methods will be further investigated in future work, and attempts to reduce the effect of their shortcomings will be made.

References

[1] H. Brunzell. Detection and classification of buried objects using impulse radar measurements. Technical Report No. 243L, Department of Applied Electronics, Chalmers University of Technology, 1996.

[2] P.E. Zwicke and I. Kiss Jr. A new implementation of the Mellin transform and its application to radar classification of ships. *IEEE Transactions on pattern analysis and machine intelligence*, PAMI-5(2):191–199, March 1983.

[3] V. Chandran and S.L. Elgar. Pattern recognition using invariants defined from high order spectra - one-dimensional inputs. *IEEE Transactions on signal processing*, 1993.

[4] R. Roy and T. Kailath. ESPRIT-Estimation of signal parameters via rotational invariance techniques. *IEEE Transactions on Acoustics, Speech and Signal Processing*, 37(7):984–995, July 1989.

[5] K. Fukunaga. *Introduction to Statistical Pattern Recognition*. Academic Press, San Diego, sec. edition, 1990.

Radar Detection Of Near-Surface Buried
Metallic Reflectors In Wet Soil

Kevin O'Neill
U.S. Army Cold Regions Research and Engineering Laboratory (CRREL)
72 Lyme Rd   Hanover, NH 03755 USA
603-646-4312   koneill@crrel.usace.army.mil

For ground penetrating radar (GPR) sensing, with antennas positioned safely or conveniently above the surface, one must contend with the ground surface reflection as well as reflections from targets sought below it. Employing low enough frequencies to penetrate moist soil means resolution that will often not allow one to distinguish the surface from target return. New measurements at CRREL were analyzed using innovative methods to sucessfully reveal buried mine and mine-like targets in wet, rocky soil. With broad band short pulse illumination, one method used a simple model that predicted the expected waveforms when surface and target echoes interacted. The other method treated the same cases but proceeds from the observation that the total overlapping surface plus target return is distended in time relative to a reflection from the surface alone. By processing to define and isolate cumulative energy return over time, one could distinguish cases in which targets lay just below the surface. Both methods were successful with moist loamy soil. Performance of the second approach was also good in an extreme case, when seasonal effects were exploited.

INTRODUCTION

A fundamental problem in GPR sensing resides in the conflict between the need for good ground penetration and the desire for tolerable resolution. This translates into a question of frequency content. Lower frequencies penetrate wet ground more effectively with fewer scattering losses. At the same time, we desire higher frequencies for sufficient resolution. In this study, we assume that the sensing platform must have some (~ 2m or more) standoff from the ground surface, either for safety, to avoid disturbing the surface, or for ease of coverage. Thus the measured return will inevitably contain a ground surface reflection, particularly if, as in this study, we consider normal incidence. A reflector about one subsurface wavelength below the surface will generally produce a reflection that is difficult to separate from the ground surface return. The two returns will overlap in the time domain, with equivalent loss of discrimination in the frequency domain ([1],[2]). Viewing the scene from off-normal incidence does not entirely do away with the problem [3].

The problem is illustrated in Figure 1 which shows a ground surface reflection, above two depictions of returns from ground with a subsurface reflector. In each of these figures the trailing content is amplified by a factor of four with a ramp weighted transition zone between early and late time [2]. The reflector in this case is simply an assumed imperfectly reflecting interface below the surface layer with

reflection coefficient of about -0.4. As shown below, this provided a reasonable rough approximation of the relative magnitude of response from some buried metallic reflectors.. The top waveform is a measured signal, taken to correspond to the source wavelet used for computation of the lower two waveforms (center frequency 500 MHz ~ 600 MHz). We note that 1) over the three cases the signal is relatively unchanged in early time, which contains essentially only the ground surface reflection. Even with the late time amplification, early time contains the "brightest" part of the signal. Further amplification to detect trailing signal would likely bring up noise and false alarms. Thus in general one cannot search for near surface targets merely by looking for bright spots in radar records obtained over a surface area. 2) Even with a reflector at 20 cm depth it is not possible to distinguish separate reflections from surface and reflector, as needed for typical deconvolution operations. 3) The waveforms corresponding to different depths of reflector are distinct, being essentially interference patterns between surface and subsurface reflections. 4) When a reflector is just below the surface, the returned signal is distended in time relative to the source wavelet.

TWO METHODS FOR TARGET DISCRIMINATION

Waveform Recognition
As a first line of attack, we take inspiration from our modeling studies which suggest that, however obscured by other reflections, the returns contributed by our targets resemble the waveforms from a simple interface. As illustrated below, fine geometrical detail in the target tends to have only a higher order effect on the results. Using either the simple layer model or any more sophisticated treatment, one can compute a theoretical reference set of waveforms corresponding to reflectors at different possible depths, as in the lower two figures above. To evaluate the source of a measured signal, one determines which reference waveform correlates best with it. We use the simple interface model here, measuring soil moisture at about 16% by volume, corresponding to a dielectric constant of about 8, with frequency dependent lossiness corresponding to the volume fraction of water. An effective target reflection coefficient of about -0.4 was again assumed for top of the target.

Figure 2 shows the results of applying this system to three measurements: The top applies to reflections from a moist soil with no subsurface target other than natural rock clutter.

The middle and bottom (respectively) are from a 15 cm diamter metallic mine and a 30 cm diameter model of an anti-tank mine, both buried at 10 cm depth.
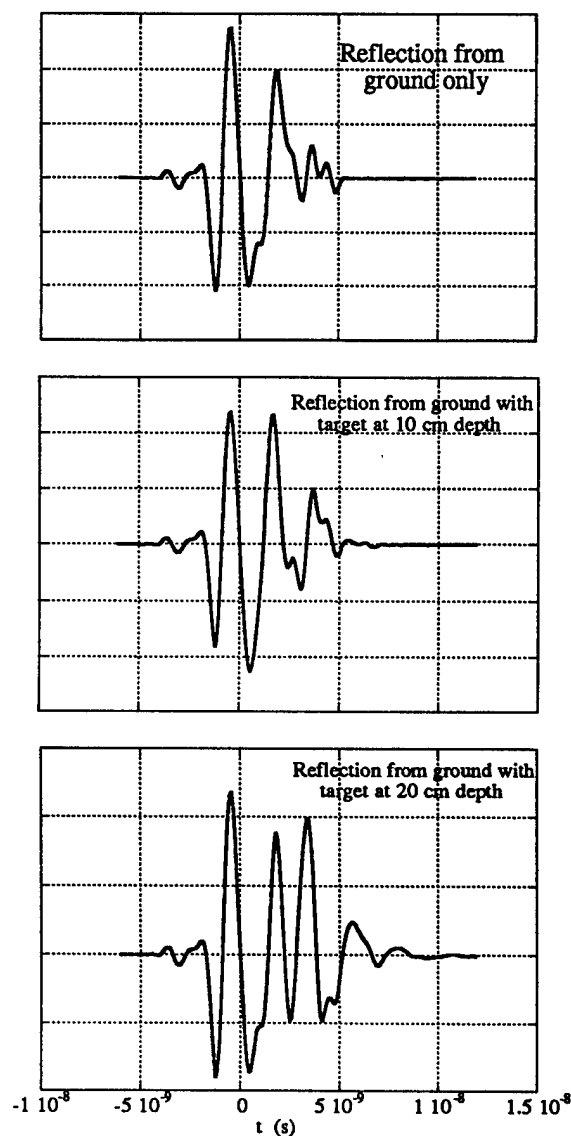
Figure 1. Wavelet reflected from ground surface without subsurface reflector (top) and with subsurface reflectors (middle and bottom). t denotes time.

The signal reflected from ground alone correlates approximately 100% for depth $d \sim 0$. That is, it virtually perfectly matches a theoretical return based on the assumption that reflection comes from the surface only. For the 15 cm mine one sees a significantly lower correlation for $d \sim 0$, and a peak correlation corresponding to a 10 cm deep target. For the anti-tank mine model the correlation with surface return alone is quite low, and the peak correlation matches the correct depth quite closely. In effect, the modeling/ signal processing allows us to recover some of the

resolution that is lost when we must resort to relatively low frequencies.

Energy Distention

Another approach depends less on any particular scattering model, but works simply from the realization that a the surface return will be distended by a shallow buried scatterer.
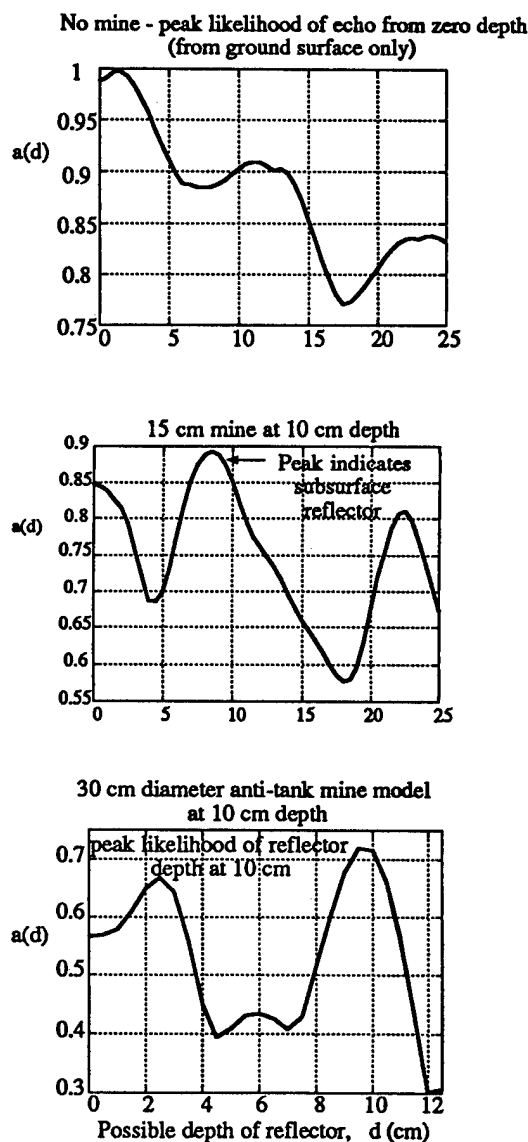
Figure 2. Computed correlation of measured with reference waveforms (a) as a function of depth (d).

By squaring and smoothing signals like those in Figure 1, each normalized to have unit energy, one obtains a record of "energy" accumulation through time. Figure 3 shows the results of such procedures, applied to reflections from the

1289

moist soil without a buried target, and from the same soil containing alternative metallic targets of comparable size. The same radar system was used as produced the pulse at the top of Figure 1. When there is no subsurface target the returned energy accumulates relatively quickly. Otherwise we note a characteristic delay in the approach to 100% arrival. That delay is not significantly dependent on target details. While both are axisymmetric, the mine is relatively smooth with a simple central cylindrical rise. The alternator contains a drive wheel with protruding rod, and other features reminiscent of various more complex mine morphologies. In either case the presence of the target is clear, by virtue of the trajectory of energy arrival. Similar experiments with other shapes and sizes of target at other depths proved likewise successful.

Measured arrival of reflected energy vs time
for 10 cm burial of 15 cm mine (solid line)
and car alternator (dashed)
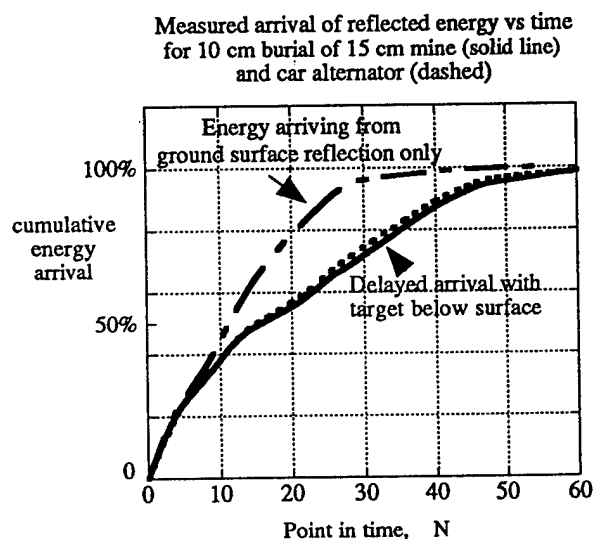
Figure 3. Time trajectories of cumulative energy arrival

It has been noted that GPR techniques fared quite poorly in locating buried unexploded ordnance in recent advanced technology demonstrations. This has been ascribed in part to wet clay soil at the survey site [4]. Clays can have electrically active particles, and can retain much more water than other soils, with commensurately greater reflectivity and lossiness. To investigate this together with seasonal effects, test plots were constructed with an extremely wet clayey soil (moisture content in excess of 40% by volume), at the US Army Cold Regions Research and Engineering Laboratory, in Hanover, NH, USA. Metallic targets of the general size and shape of anti-tank mines (30 to 35 cm across) were buried at $d \sim 13$ cm, and radar reflections were measured under both frozen and unfrozen conditions. Figure 4 shows results along survey transects in which the radar was above the target on the left side of the figure, then was moved away producing the scans on the right. N_{85} represents the time point within the trailing signal content at which the cumulative energy return of the signal segment reaches 85% of its ultimate value (cf Figure 3). The target is essentially invisible in the wet

clay, but shows very clearly in the pattern of N_{85} when the soil is frozen.
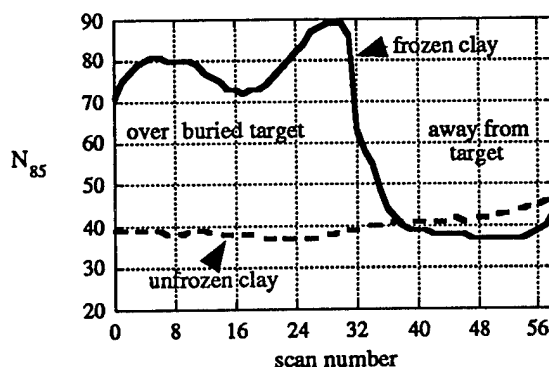
Figure 4. Point of 85% cumulative energy arrival (N_{85}) as a function of scan number for buried anti-tank mine models, when clayey soil is frozen or unfrozen.

CONCLUSION

In seeking to discriminate near-surface metallic targets on the order of the subsurface incident wavelength in size, the methods pursued here were successful in applications in moist soil of mixed type. Signal processing with or without modeling was required to interpret radar returns; one could not simply look for bright spots in the record. In the extreme case of very wet clay, it appears that returns from mine-like targets can still be distinguished from overlapping surface reflections, under frozen conditions. We anticipate improvement against some of the near false alarms (eg secondary peaks in Figure 2) by improvement of the reference signal set, either through more sophisticated modeling or incorporation of field data.

REFERENCES

[1] L. Riek, R.K. Crane, and K. O'Neill, "A signal processing algorithm for the extraction of thin freshwater-ice thickness from short pulse radar data," IEEE Trans. Geosci. Rem. Sens., 28: 137-145, 1990.

[2] K. O'Neill, "Radar sensing of surface layers," in press, IEEE Trans. Geosci. Remote Sensing, 1997.

[3] K. O'Neill, R.F. Lussky, and K.D. Paulsen, "Scattering from a metallic object embedded near the randomly rough surface of a lossy dielectric," IEEE Trans.Geosci. Remote Sensing, 34: 367-376, 1996.

[4] Institute for Defense Analysis, Evaluation of Individual Demonstrator Performance at the Unexploded Ordnance Advanced Technology Demonstration Program at Jefferson Proving Ground (Phase I), US Army Environmental Center, SFIM-AEC-ET-CR-95033., 1995.

A Comparison of Sea Ice Type, Sea Ice Temperature, and Snow Thickness Distributions in the Arctic Seasonal Ice Zones with the DMSP SSM/I

Karen St.Germain[1], Donald J. Cavalieri[2] and Thorsten Markus[2,3]

[1] Remote Sensing Division, Code 7223
Naval Research Laboratory, Washington DC 20375-5351
(202)767-3443; (202)767-9194 FAX; ksaint@ultraimg.nrl.navy.mil

[2] Laboratory for Hydrospheric Processes, Code 971
NASA Goddard Space Flight Center, Greenbelt, MD; (301)286-2444; (301)286-0240 FAX;
don@cavalieri.gsfc.nasa.gov

[3] Research Associate at the Joint Center of Earth System Science (JCESS)
University of Maryland at College Park, College Park, MD

INTRODUCTION

Global climate studies have shown that sea ice is a critical component in the global climate system through its effect on the ocean and atmosphere, and on the earth's radiation balance. Polar energy studies have further shown that the distribution of thin ice and open water largely controls the distribution of surface heat exchange between the ocean and atmosphere within the winter Arctic ice pack. The thickness of the ice, the depth of snow on the ice, and the temperature profile of the snow/ice composite are all important parameters in calculating surface heat fluxes. In recent years, researchers have used various combinations of DMSP SSMI channels to independently estimate the thin ice type (which is related to ice thickness), the thin ice temperature, and the depth of snow on the ice. In each case validation efforts provided encouraging results, but taken individually each algorithm gives only one piece of the information necessary to compute the energy fluxes through the ice and snow. In this paper we present a comparison of the results from each of these algorithms to provide a more comprehensive picture of the seasonal ice zone using passive microwave observations.

THE ALGORITHMS

The three algorithms used in this study were developed to operate on the brightness temperatures available from the DMSP SSM/I sensor. In addition, we make use of surface temperature estimates generated by Massom and Comiso from AVHRR radiances [1].

The thin ice algorithm [2] uses the 19.4 GHz vertical and horizontal, and the 37.0 GHz vertical channels of the SSMI to obtain an improved measure of ice concentration and to determine the distribution of new, young, and first-year ice types in seasonal sea ice zones. This algorithm was validated by high resolution AVHRR imagery and aircraft observations. The ice temperature algorithm [3], makes use of the radiances at 19.4 GHz vertical polarization as well as the ice type and corrected concentration output from the thin ice algorithm to determine the physical temperature of the surface. By assuming that the physical temperature of any open water within the satellite footprint is at the freezing point, the physical temperature of the ice can be calculated. The temperature algorithm was validated with surface temperature estimates from AVHRR and air temperature observations from Point Barrow and Gambell Stations. The snow thickness algorithm uses the ice concentration information and the 37 and 19.4 GHz horizontal polarization radiance data to estimate snow depth [4]. The validation for this algorithm was provided by in situ observations over similar ice in the sea ice around Antarctica.

COMPARISON OF ALGORITHM PRODUCTS

The initial comparison of products was made for April 4, 1988 in the Bering Sea. Ice type retrievals for the area of interest are shown in Figure 1.

To focus our comparisons in this initial study, we limited ourselves to a small area around St. Lawrence Island. Ice type, ice temperature, and snow depth are shown in Figures 2, 3, and 4 respectively.
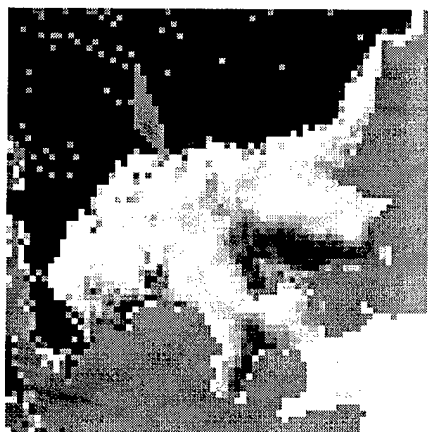
Figure 1. Ice type, in the Bering Sea, on a linear gray scale. The brighter areas contain thicker first year ice while darker areas contain thinner ice. Black areas are open water, and solid gray areas indicate either land or missing data. The gray area at the bottom left in the image is western Alaska. The white area in the bottom right is the thick first year ice in the Chukchi Sea. A large refrozen polynya is visible to the west and south of St. Lawrence island.
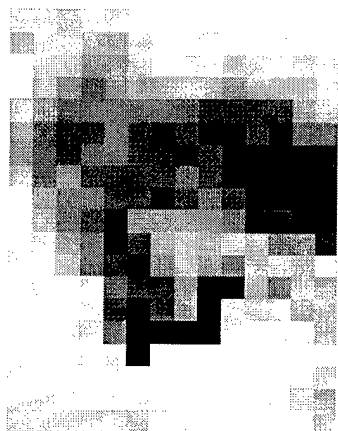
Figure 2. Ice type for the study area in the immediate vicinity of St. Lawrence Island, shown in black. The gray scale is the same as the scale in Figure 1.
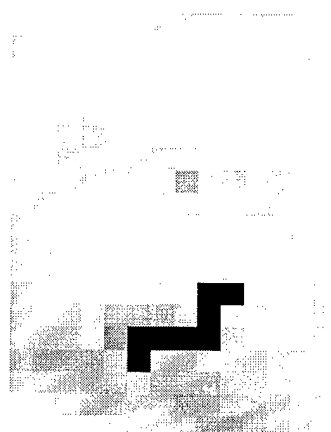
Figure 3. Ice temperature derived from the SSMI radiances for the study region. The scale ranges from 240K (black) to 275K (white), where the darkest gray in the image corresponds to 260K. Again, St. Lawrence Island is masked in black.
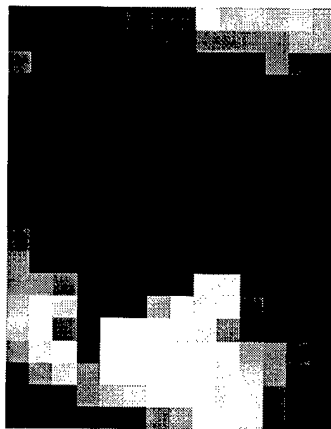
Figure 4. Snow depth derived from the SSMI radiances. The scale ranges from 0 (black) to 7 cm (white). To differentiate it from regions with no snow, St. Lawrence Island is shown in solid gray, at the same position as in the previous two figures.

DISCUSSION

The data presented in image format in the figures above are represented in scatter plot form below. Figure 5 reveals that there is relationship between the snow depth and the ice type, as expected. The thicker first year ice, which has been transported through the Bering Strait from the Chukchi Sea, has significantly thicker snow cover than the thinner first year ice types grown in the Bering Sea.
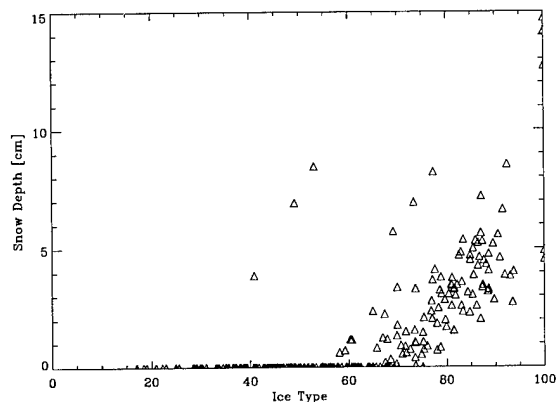
Figure 5. Snow Depth versus Ice type for the focus region around St. Lawrence Island.

The relationship between snow thickness and SSMI retrieved temperature is shown in Figure 6. For thin to thick first-year ice types, corresponding to ice types between 60 and 100, there is an inverse relationship between snow depth and temperature. Because the greater snow depth occurs on the thicker ice, we expect that the retrieved temperature should be colder where the thicker snow exists.
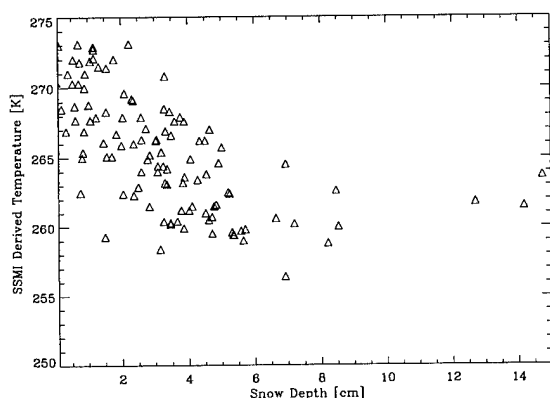
Figure 6. SSMI derived temperature vs. SSMI derived snow depth.

A similar plot for the AVHRR derived skin temperature is shown in Figure 7. We note that although the cluster shape is similar to Figure 6, the dynamic range of temperatures is larger for the SSMI than for the AVHRR. This is consistent with our expectation that the AVHRR retrieved temperature should be very close to the air temperature for snow covered ice.

Again, in these scatter plots we consider only the thin to thick first year ice, corresponding to ice types between 60 and 100. We do this because the AVHRR derived temperatures appear to be quite a bit colder

than expected over the new ice reasons. This may be due to vapor plumes rising from these areas that have gone undetected. Accordingly, we have deferred discussion of the thinner ice regions until we have a better understanding of the potential errors in both the microwave and infrared derived temperatures.
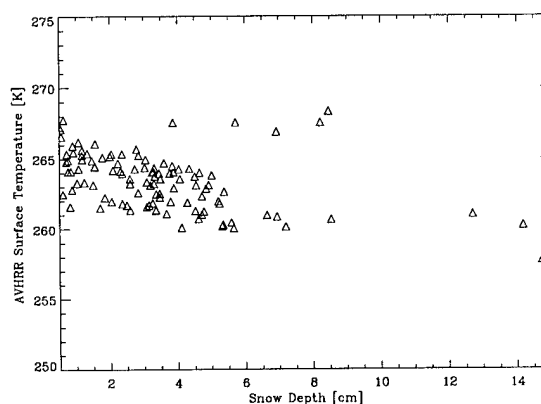
Figure 7. AVHRR derived temperature vs. SSMI derived snow depth.

CONCLUSION

The authors have initiated an effort to examine the relationship between the parameters derived from the SSMI radiances. At the present time, the algorithms examined appear to generate products that are consistent with physical expectations. In the absence of additional ground truth observations, this is an important error check.

[1] R. Massom and J. C. Comiso, "The classification of Arctic sea ice types and the determination of surface temperature using advanced very high resolution radiometer data", J. Geophys. Res., vol. 99, pp. 5201-5218, 1994.

[2] D. J. Cavalieri, "A microwave technique for mapping thin sea ice", J. Geophys. Res., vol. 99, pp. 12561-12572, 1994.

[3] K. M. St.Germain and D. J. Cavalieri, "A microwave technique for mapping ice temperature in the Arctic seasonal sea ice zone", IEEE Trans. On Geosci. And Remote Sens., accepted, 1997.

[4] T. Markus and D. J. Cavalieri, "Snow depth distribution over sea ice in the Southern Ocean from satellite passive microwave data", American Geophysical Union, Antarctic Research Series, submitted, 1997.

RESULTS OF SATELLITE AND IN-SITU REMOTE SENSING MEASUREMENT AND MODELING STUDIES OF ARCTIC SEA ICE WHICH SUPPORT THE MONITORING OF CHANGES IN THE GLOBAL CLIMATE

Robert G. Onstott
Center for Earth Sciences / Advanced Concepts Division
Environmental Research Institute of Michigan
P.O. Box 134001, Ann Arbor, MI 48113-4001
Phone: (313)994-1200 FAX:(313)994-5824 Email: Onstott@erim.org

Abstract - Coordinated satellite, *in situ* monitoring, and theoretical modeling studies of Arctic Sea Ice have been supported by both the Office of Naval Research and the National Aeronautic and Space Administration over the last 2 decades. Application of the results from these efforts is being applied to the monitoring of changes in the global climate. Two geophysical parameters are now retrieved on an operational basis: the extent of ice covered waters, and the fraction of multiyear ice, first year ice and open water. Efforts are on-going to increase the number of ice type categories and to invert signal statistics (e.g., emission and backscatter) to ice thickness. Knowledge of the distribution of ice thickness is critical to improving the ability to directly measure a geophysical response in the polar regions due to small changes in the global climate.

INTRODUCTION

Snow, ice, ocean, and clouds are key variables in the global climate system. They influence the global heat budget through feedback mechanisms which influence the exchange of heat, moisture, and momentum between the surface and atmosphere [1]. Sea ice covers the surface of the polar oceans and insulates the warm ocean below from a cold atmosphere. Sea ice is observed in thickness of less than a millimeter to that greater than 40 m. Because it lies at the boundary between the two large systems (atmosphere and ocean) its impact is considerable. Satellite remote sensing has the important role of providing time sequential observation of the polar pack and its margins which are necessary in describing key ice behavior and properties. This information may be used immediately to update predictive forecasting models [2], or archived and studied in support of climate change assessments.

There is considerable interest in the temporal variability of global sea ice in both the Antarctic and Arctic. The heat flux from the oceans into the atmosphere depends on sea ice thickness. Climate change model experiments have been conducted for a doubling of CO_2. Important changes in the distribution of sea ice thickness are noted. Based on the model results it is shown that sea ice properties are very sensitive to a changing environment, hence are an important indicator of climate change. Trends in ice thickness over the Arctic Ocean as a whole have been suggested to be an especially sensitive indicator of global change.

In general, it is believed that estimates of the ice thickness distribution, fraction of the various ice types, total mass of sea ice, mean ice thickness, production of new ice in the polar regions, and flux of ice out of the polar regions are needed to fully describe important sea ice processes [3].

In this paper, various aspects of the ability to perform the inversion of SAR backscatter to ice thickness is presented. What will be described is the information that may be retrieved based on a single image, from a temporal sequence of image data where feature tracking is possible, and when supplemented by ancillary data. The robustness of the signal inversion is demonstrated by examining the variance in the microwave response of the various ice forms based on example satellite SAR data, in-situ microwave scattering measurement results, forward model predictions, and the classified image products.

APPROACH

The Office of Naval Research and the National Aeronautics and Space Administration have sponsored a number of activities to improve our ability to retrieve geophysical properties of sea ice that are of interest. These include field, laboratory, and modeling investigations. *In situ* physical and electromagnetic property information have been obtained in tandem, often in conjunction with aircraft or satellite observations. A select set of results from these studies are presented here.

DISCUSSION

To improve the ability to retrieve ice property information it is important to document the transformation from open water to ice, and then the aging process. During the first year, level ice may attain a maximum thickness of about 2 meters. Ice which has survived the summer melt season,

called multiyear ice, may attain thicknesses greater than 3 m. Pressure in the pack ice may cause buckling of the pack ice sheets and result in deformed ice. A transfer function which relates ice form and radar scattering coefficient was assembled using *in situ* microwave observations. A similar transfer function has been shown to be true for the European Space Agency synthetic aperture radar and is shown in Fig. 1. Important characteristics are that (1) open water is separable, in most cases, from ice, (2) that new ice produces a backscatter that is considerably weaker than young and old ice, (3) that a peak in the first year ice behavior occurs at the transition of grey to grey-white ice, (4) that as the first year ice continues to age its backscatter cross-section decays, (5) that the backscatter intensity increases with increasing degree of deformation, and (6) that multiyear ice produces the strongest backscatter for level ice, but less than that produced by wind roughened water (e.g. speeds greater than about 8 m/s).

The detection of open water and thin ice areas is important because of the transfer of heat from a warm ocean to a cold atmosphere. The majority of heat transfer is associated with these two cases. It is therefore important to understand how the backscattering coefficient changes with increasing ice thickness during the evolution process. Laboratory investigations conducted in outdoor and indoor tanks have allowed detailed studies to be conducted of this transformation process. Perturbations considered include variations in ambient temperature, solar conditions, and wave action. An example response is shown in Fig.2 for a frequency of 5.3 GHz, and three incidence angles. An important attribute of this response is that for quiescent conditions and an electromagnetic wavelength of 6 cm, that the backscatter slowly decays to a minimum at about 9 cm, if the ice remains free of snow.

Figure 2. Backscatter response with increasing ice thickness based on laboratory study results at 5.3 GHz.

As shown in Fig. 1 the relationship between ice form and a backscatter intensity is not purely monotonic. Difficulty may arise when attempting to discriminate between newly formed ice and the older first year ice. A study was conducted to demonstrate how temporal observations may be used to assist with this problem. In this study case, a Beaufort Sea lead is observed for over a one month period during spring. In Fig. 3, a set of image chips show that the lead area in which new ice is produced is the most electromagnetically dynamic part of the scene.

Figure 1. Relationship between RSC and ice form based on ERS SAR in Beaufort Sea during spring.
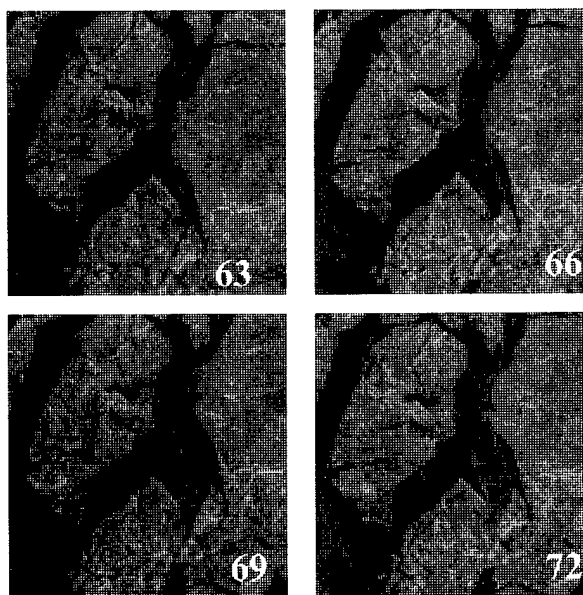
Figure 3. ERS-1 SAR observations of a lead was conducted of a lead in the Beaufort Sea during spring. Day of Year are indicated on each figure.

1295

The change in scattering coefficient for the lead, multiyear ice, and first year ice is also shown as a function of Day of Year in Fig. 4. During the study period, three areas opened in which new ice was produced. The time history for each of these area is included. The signatures of the newly formed ice is at an intensity below that of the surrounding first year ice. During the aging process, the signature of the lead and first year ice become similar in intensity level. The time during which this is true is short, however, because the lead signature is in transition to a level between that of typical first year ice and multiyear ice [4]. This transition takes about a week, during which the ice has grown to about 35 cm.

As first year ice ages, two processes are found to contribute to the change in properties which are able to be sensed remotely: the snow-ice interface, and the upper ice sheet dielectric properties. When first year ice transitions from 1.3 m ice to 1.8 meter ice, it is found that the ice sheet has experience further desalination and the ice-snow interface has become more smooth due to continuous metamorphism at the snow-ice interface. This is sufficient to account for a 2-3 dB difference in backscatter for these two ice thickness categories for level ice as shown in Fig. 5.

The ability to invert multiyear ice backscatter intensity to information associated with its thickness and physical properties has been examined. A relationship is found to exist between the properties of the low density portion of an ice sheet and the total ice thickness. This association is shown in Fig. 6.

REFERENCES

[1] Dickenson, R.E., G.A. Meehl, and W.M. Washington, "Ice-Albedo Feedback in a CO_2-Doubling Simulation," **Climate Change**, 10, 241-248, 1987.

[2] Thomas, R.H., Polar Research from Satellites, Joint Oceanographic Institutions, Inc., Washington, D.C., 1991.

[3] Thorndike et al., 1992.

[4] Onstott, R.G., "Study of the temporal nature of arctic leads during spring using ERS-1 SAR," Proc. ESA ERS Symposium, Florence, Italy, March, 1997.
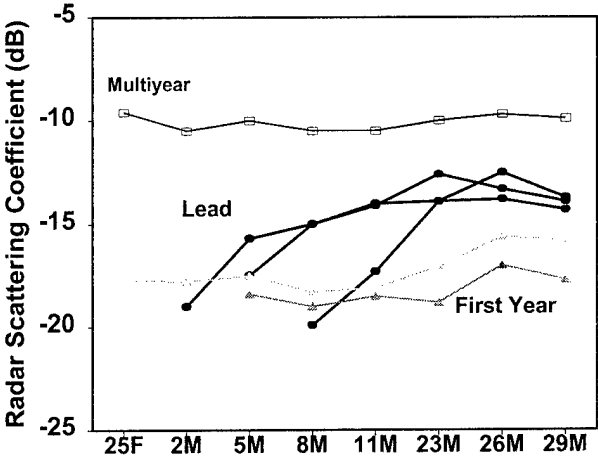
Figure 4   Change in radar scattering coefficient of lead, multiyear, and first year ice.
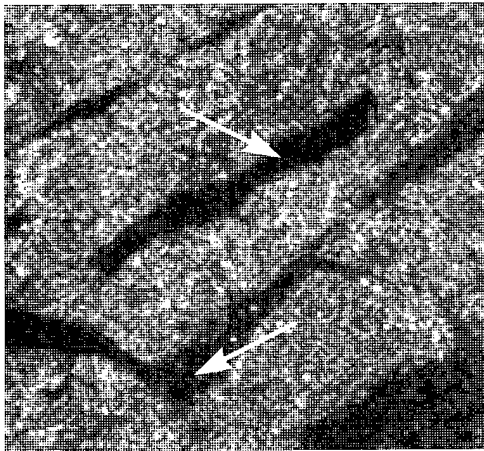
Figure 5.   Thick and medium first year ice during spring.
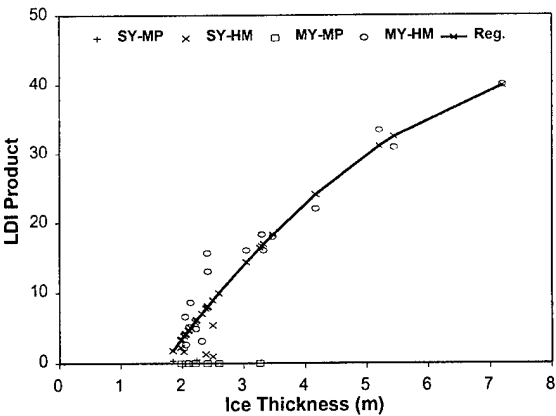
Figure 6. Relationship between the thickness of multiyear ice and the properties of the upper most portion of the ice sheet.

1296

SeaSat Scatterometer Observations of Sea Ice

Calvin T. Swift
Knowles Engineering Building
University of Massachusetts
Amherst, MA 01003
Telephone: (413) 545-2136
Facsimile: (413) 545-4652
Email: klemyk@ecs.umass.edu

Abstract -- SeaSat I Scatterometer data collected over the Beaufort Sea are analyzed and compared with a simple theoretical model that includes surface roughness and volume scattering. The values of the root-mean-square surface slope of roughness and the volume scattering albedo are adjusted to fit the data. With qualifications imposed on the theoretical assumptions, the data are well-modeled by the two parameters, and the sensor offers a means to monitor the statistical properties of sea ice in existing satellite scatterometers experiments, such as the European Remote Sensing Satellite and the NSCAT on the Japanese ADEOS I Spacecraft.

I INTRODUCTION

The SeaSat A was launched in 1978, and carried the first civilian wide-swath radar which collected back scattering data over the polar regions. This radar was named the SeaSat A Satellite Scatterometer (SASS). Reporting of SASS sea-ice results has been rather sparse for several reasons. First of all, SeaSat was an oceanographic satellite, and most of the resources of the experiment team were driven toward assessing the performance of the instrument to measure ocean windspeed and direction. Second, the satellite failed before Arctic field verification experiments could be undertaken. Third, the variable angle of incidence of the SASS complicates the interpretation of data over sea ice. The latter problem causes serious difficulties in data interpretation because the normalized radar cross-section naturally decreases with viewing angle and varies with surface roughness, distribution of volume scatterers, surface melt water and free-water content, to name a few parameters. On the other hand, the backscatter from the ocean depends only on surface windspeed and direction, and empirical curves were developed for each angle of incidence using aircraft data prior to the launch of the satellite. In this paper, the SASS data are presented for each incidence angle and is interpreted in terms of a simple theory of surface and volume scattering which contains only two parameters.

II THEORETICAL CONSIDERATIONS

It has been shown [1], [2] that the effective normalized radar cross-section (NRCS) of a medium that contributes both surface and volume scatter is given by the formula

$$\sigma_M^o = \sigma_s^o + \left(\frac{n\sigma_B}{\alpha_a}\right)\cos\theta_p \qquad (1)$$
$$= \sigma_p^o + \sigma_V^o$$

σ_M^o = the measured effective NRCS (nondimensional);

θ_p = the angle incidence;

t = power transmission coefficient at $\theta = \theta_p$;

n = the number density of subsurface scatterers (cm^{-3});

σ_B = backscatter cross-section per particle (cm^2);

α_a = the bulk volume attenuation coefficient (cm-1);

σ_S^o = the NRCS of the rough surface (dimensionless);

σ_V^o = the NRCS of the volume scatterer (dimensionless);

The volume scatterers will either consist of brine pockets or voids in sea ice. Furthermore, the volume scattering from multi-year sea ice will be much greater than that from first-year sea ice because the attenuation coefficient α_a of first-year sea ice is large. Indeed, it is so large that we will assume that there is negligible volume scattering from first sea ice. If there is only surface scattering, and if we can model the sea-ice surface as an ensemble of reflecting facets having a Gaussian distribution of slopes, then the process can be described in terms of a geometric optics solution. The problem has been studied in depth by Barrick [3] and others. They derive the following formula for σ_s^o:

$$\sigma_s^o = \frac{r(0)e^{-\tan^2\theta_p/2S^2}}{2S^2\cos^4\theta_p} \qquad (2)$$

where r(0) is the power reflection coefficient and S is the rms surface slope.

Although there are several quantities that contribute to the volume scattering process, this problem, like the surface scatter problem, reduces to only one parameter,

$$\eta = \frac{n\sigma_B(0)}{\alpha_a}, \qquad (3)$$

which we can identify as the scattering albedo.

III ANALYSIS OF DATA

The general area that was selected for the analysis is bounded by Banks island, Canada, and Point Barrow, Alaska, and was selected in order to provide land reference points to accurately locate ice features for kinematics, using the Synthetic Aperture Radar (SAR). A total of five orbits were selected during initial freeze up during the month of October 1978, just prior to the failure of the satellite. Orbit 1409 corresponds to the data collected on 3 October, 1978, and orbit 1452 passed over the same area on 6 October, 1978, in accordance with the three-day repeat cycles of the satellite. In addition, three other orbits - 1395 (2 October), 1438 (5 October) and 1481 (8 October) - were also analyzed to observe temporal changes in the ice growth.

The SASS was a dual-polarized precision radar, operating at 14.6 GHz center frequency. A data swath was developed by projecting four fan beams boresighted 45° to the subsatellite track and using Doppler filters to discriminate resolution cells in the long dimension of the fan beam, resulting in 500 km swaths on either side of the spacecraft. The swaths were formed by twelve cells (or channels) with the angle of incidence nominally varying between 23° and 65°

Figure 1 shows the normalized measured backscattering coefficient σ_M^o vs. longitude for orbits 1395, 1438, and 1481 at the rather steep incidence angle of 65°. The signatures of the multi year pack ice, the ice edge and wind roughened open water are clearly evident in the figure.

The most striking similarity between the data taken six days apart is the temporal stability of the multi-year ice signature. After six days, the overall change in the backscatter can be measured in tenths of decibels, even though the polarization alternates between vertical and horizontal. It is of further interest to note that the backscatter from the multi-year ice is relatively high, even at incidence angles of 65°, and that there are small but highly correlated spatial oscillations in the backscatter signature. We note that there are observed differences near the ice edge which may be associated with changing ice-ocean dynamics.

The average radar backscatter from first-year sea ice is plotted as a function of viewing angle in Figure 2. Also shown are plots of the theoretical values of the NRCS for slopes $2S^2 = 0.10$ and $2S^2 = 0.20$ and $\sigma_V^o = 0$. Since the instrument errors are of the order of a few tenths of a decibel, the error bars shown represent the geophysical variability of the average, which is more of a systematic variation than a random one. It therefore seems reasonable to conclude that there is a highly variable scale of roughness changes associated with the formation of first-year ice, which is consistent with known observations. Since the variability exceeds the instrument error, we may also conclude that spaceborne scatterometers with near nadir viewing capability will be able to monitor changes in the surface roughness of first-year

Figure 1: Measured values of the SASS normalized radar cross-section as a function of longitude for orbits 1395, 1438 and 1481. The incidence angle is 65°. The polarization was vertical for orbits 1395 and 1481, and horizontal for orbit 1438.
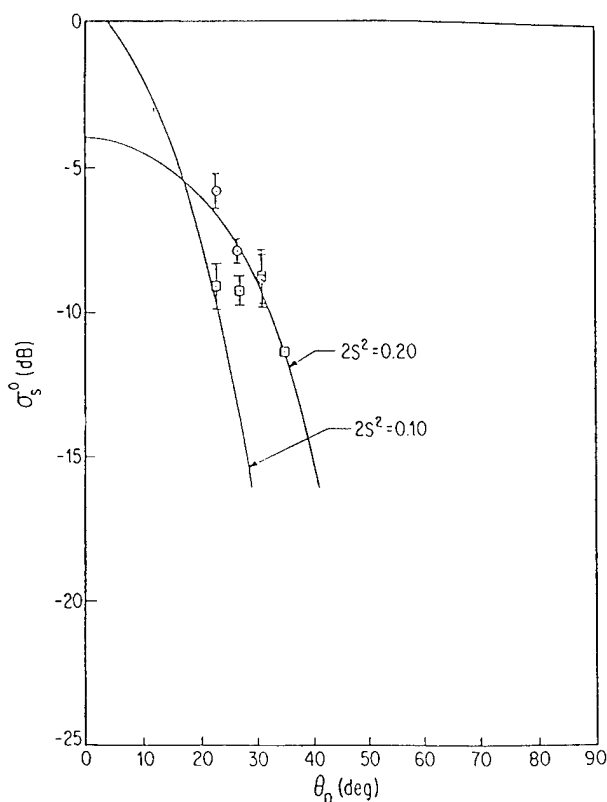
Figure 2: Experimental averages of the normalized radar cross-section of first-year sea ice versus angle. Two theoretical curves are shown to bracket the observations.

sea ice. It is of interest to discuss the experimental point at $\theta_p = 23°$, which exceeds the theoretical value of radar backscattering from a rough surface. Although this could be attributed to increased roughness or errors in the assumptions in the theory, such as the validity of geometric optics and a Gaussian slope distribution, we should point out that the numerical value of $r(0)$ was based upon an assumed dielectric constant of 3.2 with no loss. This gives a value of $r(0) = -11.0$ dB. On the other hand, if we assume that the dielectric constant is 3.8, the calculated values of the reflection coefficient become $r(0) = -10$ dB, and the theory begins to agree with the mean experimental observation. Thus, the spaceborne radar instrument technology has advanced to the point where the dielectric properties of the sea ice must be better defined to take full advantage of the capability of the sensor.

Figure 3 shows the average NRCS plotted as a function of incidence angle for multi-year sea ice for orbit 1409. Here, the data represents the average of many more values than were available for display of the results for first-year sea ice. We also note a generally smaller measurement variability, which in some cases begins to approach the noise levels of the instrument. Also
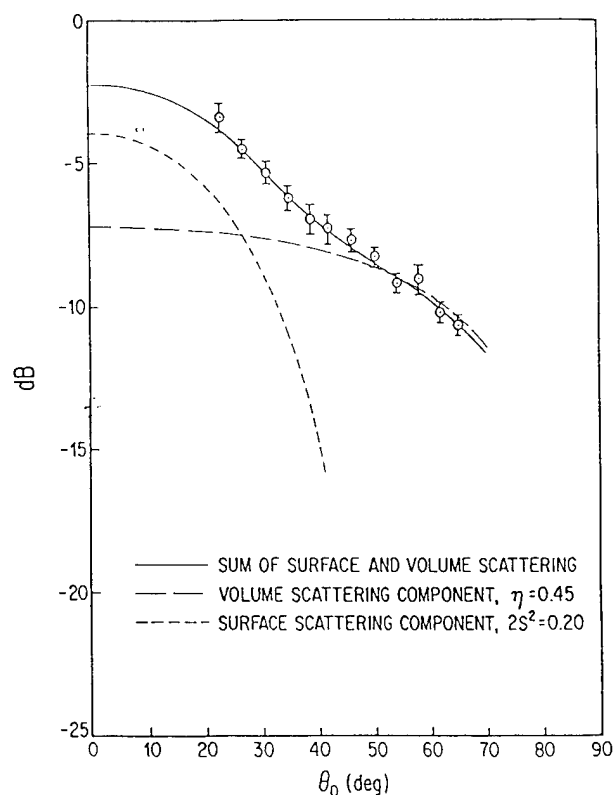
Figure 3.   Experimental averages of the normalized backscatter coefficient versus viewing angle for orbit 1409 over multi-year ice. Shown are the theoretical surface and volume scattering curves that give good fit to the data.

shown in the figure are theoretical values of scattering from a rough surface assuming a surface slope of $2S^2 = 0.20$ and that for volume scattering only with an assumed albedo of $\eta = 0.45$. The solid line through the data points represents the incoherent sum of the two theoretical values. We caution that there is good agreement between theory and experiment only because we are forcing the agreement to be good. That is, the values of the slope and albedo were chosen to achieve a good fit. Said another way, the scatterometer is being used as a sensor to derive two measurable sea-ice parameters. The confidence level can only be established by weaving a surface-truth expedition into future satellite programs. However, it is of value to note that the problem contains only two unknown parameters, which limits the validation requirements.

IV CONCLUDING REMARKS

SeaSat scatterometer data collected over sea ice was presented and interpreted in terms of a first-order theory that describes effects of backscattering from a rough surface and an ensemble of volume scatterers. Under the reasonable assumption that the backscatter from first-year sea ice is dominated by surface roughness, the theory indicates that the rms tilt angle varies from approximately 15° to 25°. Consistent with the geometric optics model, the backscatter from first-year sea ice significantly decreases with increasing angle of incidence. On the other hand, the data collected over multi-year ice is very strong as a function of incidence angle, which supports the first-order theory of volume scattering. Furthermore, the multi-year return remains relatively constant with time except near the ice edge and is independent of polarization.

Consistent with operational aircraft data, the scatterometer can detect the multi-year pack, thin smooth ice, and the ice edge. In addition, the instrument has the potential of monitoring surface roughness and the distribution of volume scatterers. With additional tuning of the SASS calibration, it may be possible to actually produce maps of the scattering albedo and other properties of the volume scatterers as more scatterometer frequencies become available. In this connection, it may be of interest to compare C-band backscattering measurements from ERS-1 with the Ku-band results of the ADEOS I NSCAT.

V REFERENCES

[1]   Ulaby, F.T., R.K. Moore and A.K. Fung, "Microwave Remote Sensing," Vol. III, Ch. 20, Artech House, 1986.

[2]   Swift, C.T., P.E. Hayes, J.S. Herd, W.L. Jones and V.E. Delnore, "Airborne Microwave Measurements of the Southern Greenland Ice Sheet," *J. Geophys. Res.*, 90, B2, 1983-1994, 1985.

[3]   Barrick, D.E., "Rough Surfaces," Chapter 9, *Radar Cross-Section Handbook* (G.T. Ruck, Ed.), 1970.

Antarctic Surface Temperatures using Satellite Infrared Data from 1979 Through 1995

Josefino C. Comiso and Larry Stock
Laboratory for Hydrospheric Processes, Code 971,
NASA/Goddard Space Flight Center, Greenbelt, MD, U.S.A. 20771
Telephone: 301-286-9135; FAX: 301-286-1761; E-mail: comiso@joey.gsfc.nasa.gov

ABSTRACT -- The large scale spatial and temporal variations of surface ice temperature over the Antarctic region are studied using infrared data derived from the Nimbus-7 Temperature Humidity Infrared Radiometer (THIR) from 1979 through 1985 and from the NOAA Advanced Very High Resolution Radiometer (AVHRR) from 1984 through 1995. Enhanced techniques suitable for the polar regions for cloud masking and atmospheric correction were used before converting radiances to surface temperatures. The observed spatial distribution of surface temperature is highly correlated with surface ice sheet topography and agrees well with ice station temperatures with 2K to 4K standard deviations. The average surface ice temperature over the entire continent fluctuates by about 30K from summer to winter while that over the Antarctic Plateau varies by about 45K. Interannual fluctuations of the coldest temperatures are observed to be as large as 15K. Also, the interannual variations in surface temperatures are highest at the Antarctic Plateau and the ice shelves (e.g., Ross and Ronne) with a periodic cycle of about 5 years and standard deviations of about 11K and 9K, respectively. Despite large temporal variability, however, especially in some regions, a regression analysis that includes removal of the seasonal cycle shows no apparent trend in temperature during the period 1979 through 1995.

INTRODUCTION

Surface air temperatures from ice stations in the Antarctic region have been observed to be highly variable [1,2,3]. Also, in many areas, significant positive trends are observed whereas in some other areas negative trends are apparent. The effect of a rising temperature can be alarming, especially since the West Antarctic Ice Sheet is on the average about -5K in the summer. It is also known that an early signal of a potential increase in global temperatures induced by greenhouse effects may be observed in the polar regions [4,5]. Station data may be separated into manned data and unmanned (stand alone) data. The quality control of the manned data is usually very good since the necessary maintenance and attention are provided to assure that the thermistors used for temperature measurements are working properly. For unmanned stations, however, the data sets are less consistent and gaps in the data record usually occur due to constant malfunction of the sensor. Unmanned stations have been used to supplement the small number of manned stations to obtain a better general overview of the continent. But considering the large extent of the ice sheet and it's varying topography, the available number of ice stations, some of which are clustered together in the same general areas do not provide good spatial coverage of the entire continent. Surface temperature information over sea ice around the continent is even more limited since most of the information is derived from buoy and/or ship data.

In this study, satellite infrared data are used to produce surface temperature maps and to study large scale spatial and temporal variability of surface temperatures in the polar open ocean, sea ice, and continental ice sheet. Thermal infrared systems operate during both day and night thereby providing continuous coverage except that clouds are persistent in the region. Since clouds are usually difficult to discriminate from snow covered surfaces, non-conventional means of masking them has to be implemented but errors due to masking limitations are sometimes not negligible. However, the technique may be the only way to obtain spatially coherent and synoptic measurements of surface temperatures in the region.

INFRARED DATA, CLOUD MASKING AND RETRIEVAL TECHNIQUES

The Advanced Very High Resolution Radiometer (AVHRR) aboard NOAA satellites is a cross track scanner operating at the following wavelengths: 0.58-0.68 μm (channel 1), 0.73-1.1 μm (channel 2), 3.5-3.9 μm (channel 3), 10.3-11.3 μm (channel 4) and 11.5-12.5 μm. At nadir, the resolution of the Local Area Coverage (LAC) data is about 1 km^2, but since the LAC data record is not complete, we use global area coverage (GAC) data in this study. GAC data have an effective resolution of 5 by 3 km^2 and are constructed as follows. Along the 2048-pixel scan line, the radiances from 4 successive spots are averaged while the next spot is skipped. Also, only every third scan line is recorded while skipping two scan lines. We also use data from the 11.5 μm channel of THIR data which has a resolution of 6.7 by 6.7 km. Some techniques for retrieving surface temperatures from AVHRR and THIR have been reported [5,7,8,9].

The accuracy in the retrieval of surface skin temperatures from satellite infrared data depends strongly on success in cloud masking. Clouds over open ocean are usually identifiable because of the large contrast in the albedo or emissivity of clouds and ocean. Clouds over sea ice and the ice sheets in the polar regions are more difficult to mask because of the presence of cold snow cover that substantially reduce the contrast in the albedo and emissivity of clouds and the surface.

With AVHRR data, cloud masking is usually done by thresholding techniques utilizing the visible channels or differences between channels 3 and 4 and/or channels 4 and 5. In the polar regions, the use of visible channels is limited because of long winter nights. Also, channels 3 and 4 are most effective only during day while channels 4 and 5 do not provide good consistency. Another technique, which we call daily differencing method and previously used for THIR [6], takes the difference of daily data and uses a threshold, based on enhancements due to movements of clouds over a one day period, to separate cloud covered areas from cloud free areas. The best method we have come up with is a combination of the use of channels 3 and 4 data and the daily differencing method using channel 4 data. Our masking technique is also applied separately to open ocean, sea ice, and ice sheet surfaces, each of which requires different thresholds.

Fig. 1a and 1b show an AVHRR orbital data over the Antarctic region at channel 1 and channel 4, respectively, and indicates where the cloud patterns are located. Fig. 1c shows the result of applying our technique with areas in black identified as cloud covered areas. The technique is reasonably effective in masking much of the cloud cover identified by inspection from channels 1 and 2 but some residuals remain. Because of large data gaps after masking, weekly averages are used as the basic product. The results presented in this study are from monthly average maps which show less effect of residual clouds, better spatial coherence and more consistency than the weekly average maps.

To correct for atmospheric attenuation, a slightly modified split window algorithm [10, 11] was used taking into consideration the zenith angle dependency of the air masses. Comparison of results with surface air temperatures in the Antarctic is shown in Figure 2 using data collected in stations monitored by the British Antarctic Survey (BAS). The correlation is high at 0.93 but the standard deviation is around 3K. Comparisons of AVHRR data with other Antarctic stations yielded similar results. The relatively high standard deviations may be partly due to mismatches in measurement sampling time and sizes of the sampling area. Also, the accuracy requirements for sea ice and ice sheet surface temperatures are not as high as over the ocean because of much larger natural fluctuations in temperature over the former.
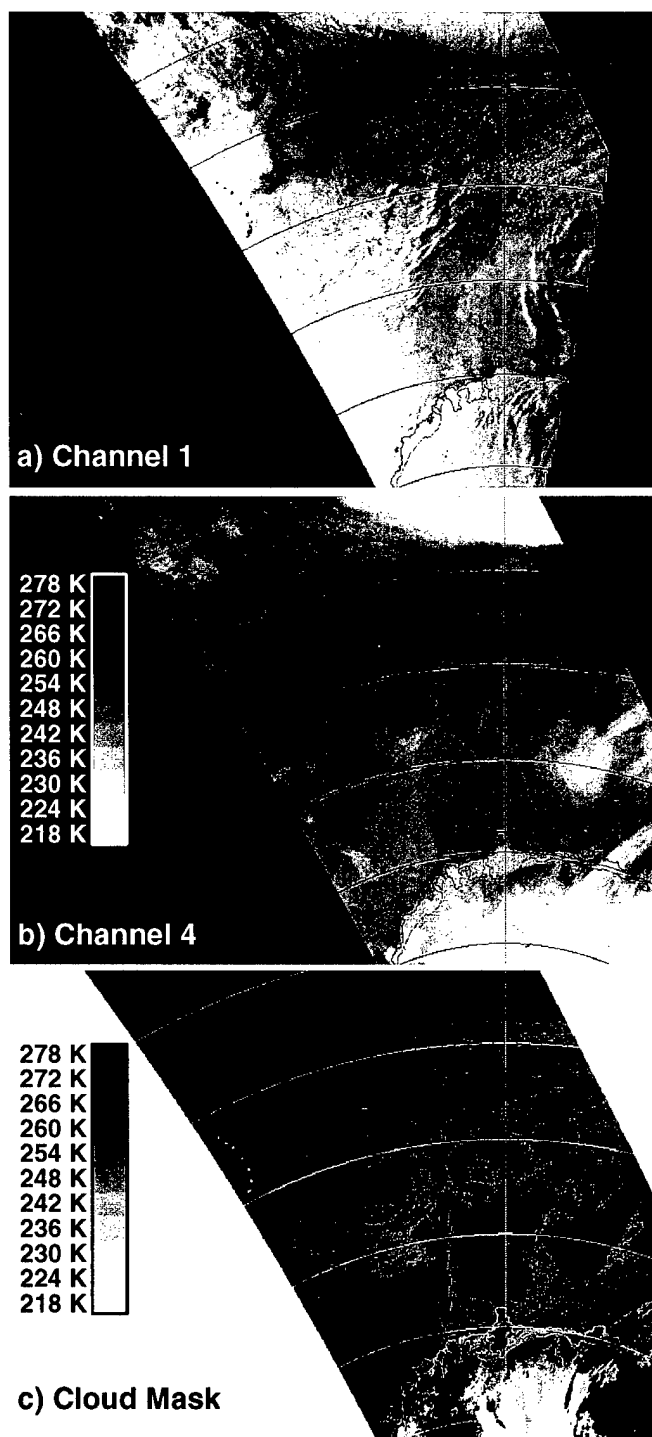
Figure 1. Orbital GAC AVHRR data showing (a) channel 1; (b) channel 4; and (c) channel 4 but with cloud mask (in black).

BAS Station Data
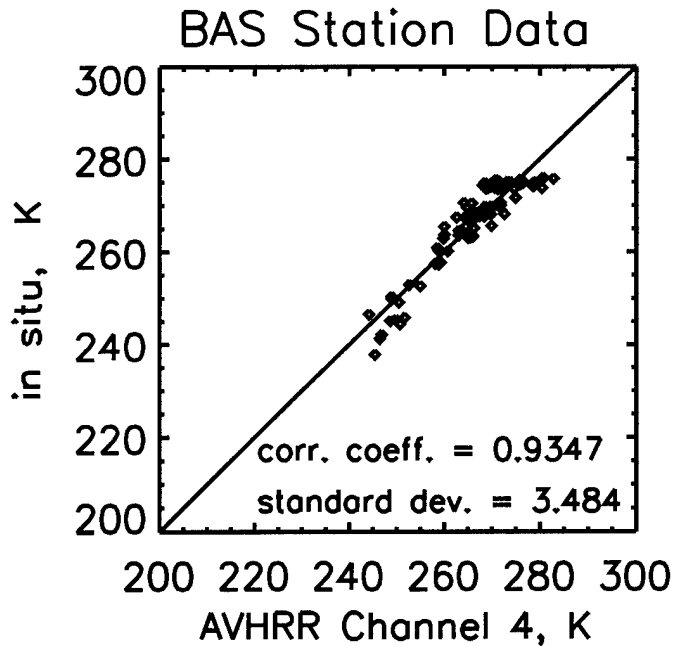
Figure 2. Comparison of surface ice temperatures derived from AVHRR with those from the British Antarctic Survey stations.

The night (ascending) data were analyzed separately from day (descending) data in order to optimize accuracy. The separation of day from night data offers the flexibility of making refinements associated with diurnal changes in the albedo and emissivity of cloud covered and cloud free surfaces. Also, it allows for studies of polar processes occurring during the day and be able to contrast them with those occurring during night. For example, large differences in spatial distribution of surface temperatures are apparent in the night and day data shown in Figs. 3a and 3b, respectively. In the Antarctic plateau, the temperature difference between night and day can be as high as 15K during the summer. Also, the high correlation of temperature with topography is better understood by having night data separated from day data.

SURFACE TEMPERATURES OF THE ANTARCTIC REGION

Fig. 4 shows a sequence of monthly maps in the Antarctic region during a winter month (i.e, July) from 1984 to 1994. The sequence illustrates in detail the interannual variability of surface temperatures in parts of the Antarctic region. Some years appear considerably colder than other years, especially in the Antarctic plateau. Yearly shifts in the general location of cold spots are also apparent but a general pattern* is not evident. Some other details are missing because of the 6K interval in the coded black and white

images. When coded at 2K interval and using color coded images, the maps show temperature distributions that follow closely the contours along the Transantarctic mountains and major Antarctic glaciers. The Ronne and the Ross ice shelf regions are also sites of considerable interannual variability.

The THIR and AVHRR data sets were combined to study long term effects. In this study, the THIR data set presented in Comiso (1984) was slightly altered over open ocean region to incorporate an improved cloud masking used for AVHRR data over the ocean. Data from open ocean
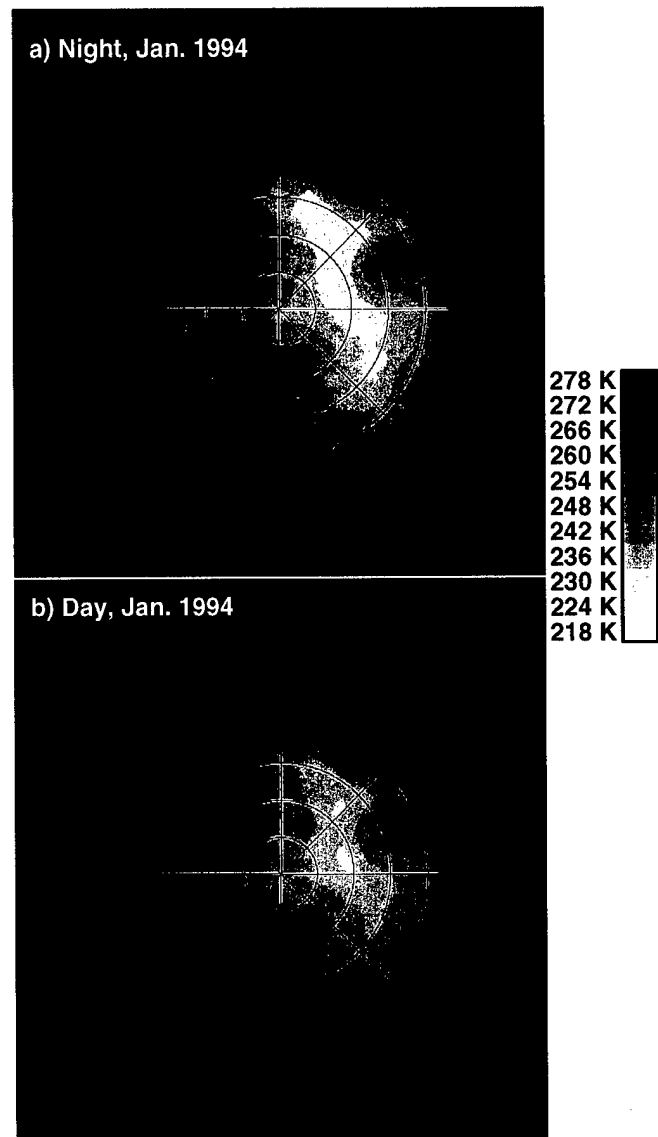
Figure 3. Weekly averages of surface ice temperature using (a) night data and (b) day data.

occur in the Antarctic plateau where temperatures in one year can be 15 K lower than average. ·

CONCLUSIONS

Satellite infrared data provides detailed spatial distribution of surface temperatures in the polar regions. While the error in the determination may be higher than desired (about 3K
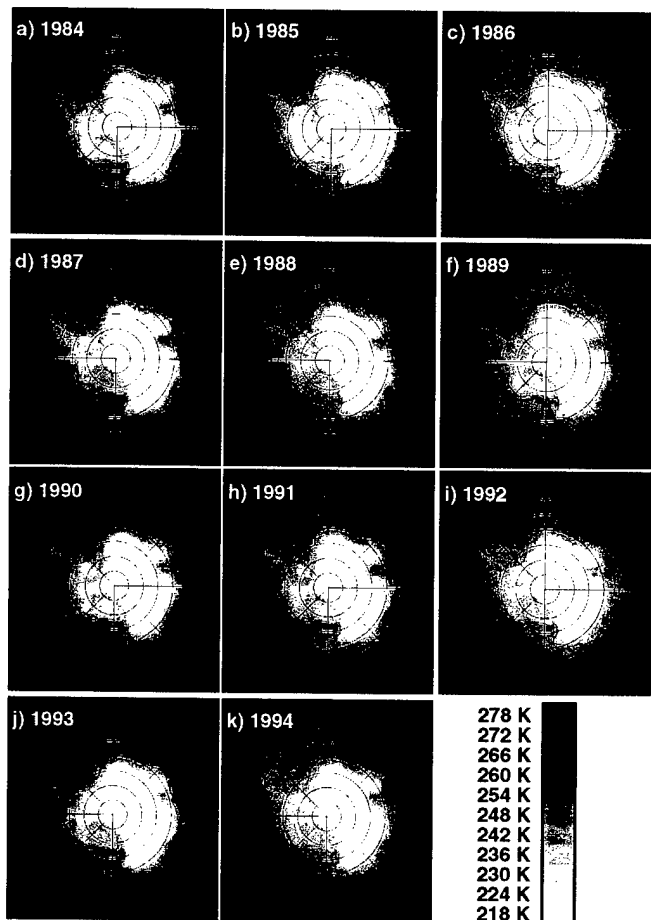
Figure 4. July monthly averages of surface ice temperatures from 1984 through 1994.

(>55°S), sea ice, and the ice sheet were processed separately and the average temperatures over these three surfaces are presented in Fig. 5. The interannual variations over the ocean is not apparent from the graph because of the scaling which makes it difficult to identify expected changes of less than 1K. The relatively constant values, however, is encouraging since it indicates that cloud masking is effective and consistently made. Variations over sea ice is more apparent and is as high as 5K during some years. Spatial variations of temperatures from the continent to the ice edge are however much higher. Interannual variations over the continent is substantially larger (than sea ice and ocean) during both summer and winter. The largest fluctuations

Figure 5. Average temperatures in the open ocean (>55oS), sea ice, and continental ice sheet in (a) summer (January) from 1979 through 1994 and (b) winter (July) from 1979 through 1994.

1303

on the average), the data provides a means to map many distinct features in the continent and within the sea ice margins. The historical data set also show interannual fluctuations that are small over the ocean, significant over the sea ice, and large over the ice sheets. Some cyclic dips in temperatures are apparent in the data and appears to have a period of about 5 years. Accuracies may be improved with better cloud masking techniques and perhaps better resolution.

REFERENCES:

[1] J.C. King, "Recent climate variability in the Antarctic peninsula," in Proceedings of the 5th Conference Climate Variations, Denver, Oct. 14-18, 1991, Boston:AMS, 1991, pp. 354-357.

[2] J. Weatherly, J.E. Walsh, and H.J. Zwally, "Antarctic sea ice variations and seasonal air temperature relationships, " J. Geophy. Res., vol. 96, pp. 15,119-15,130, August 1991.

[3] S. S. Jacobs, and J.C. Comiso, A Climate Anomaly in the Amundsen and Bellingshausen Seas, J. Climate, 10(4), 697-711,1997.

[4] M.I. Budyko, "Polar ice and climate," in Proceedings of the symposium on the arctic Heat Budget and Atmospheric Circulation, ed. By J.O. Fletcher, RM 5233-NSF, Rand Corporation, Santa Monica, CA, 3-21, 1966.

[5] S. Manabe , M.J. Spelman, and R.J. Stoufer, "Transient responses of a coupled ocean-atmosphere model to gradual changes of atmospheric CO_2. Part II: seasonal response," J. Climate, vol. 5, 105-126, February 1992

[6] J.C. Comiso, Surface Temperatures in the Polar Regions using Nimbus-7 THIR, J. Geophys. Res., 99(C3), 5181-5200, March 1994.

[7] Massom, R. and J.C. Comiso, Sea ice classification and surface temperature determination using Advanced Very High Resolution Radiometer Satellite Data, J. Geophys. Res.,99(C3), 5201-5218, March 1994.

[8] J. Key and and M. Haefliger, "Arctic ice surface temperature retrieval from AVHRR thermal channels, " J. Geophys. Res., vol. 97, pp. 5885-5893, 1993.

[9] R. Lindsay, and D. Rothrock, "Surface temperature and albedo distributions of Arctic sea ice from AVHRR," Ann. Of Glaciology., vol. 17, pp. 391-396, 1993.

[10] E.P. McClain, "Multiple atmospheric-window techniques for satellite sea surface temperatures, in Oceanography from Space, ed. By J.F. R. Gower, New York: Plenum, pp. 73-85, 1981.

[11] R.L. Bernstein, "Sea surface temperature estimation using the NOAA-6 satellite advanced very high resolution radiometer, J. Geophys. Res., vol. 87, pp. 9455-9465, November 1982.

Modeling and Interpretation of Ultra-Wideband Microwave Scattering Measurements of Simulated Sea Ice

P. Kanagaratnam and S.P. Gogineni
The University of Kansas, Radar Systems and Remote Sensing Laboratory
2291 Irving Hill Road, Lawrence, KS 66045, USA
913/864-7736 (T) - 913/864-7789 (F) - pkanagar@rsl.ukans.edu

K. Jezek
Byrd Polar Research Center, The Ohio State University, 1090 Carmack Road, Columbus, OH 43210, USA
614/292-7973 (T) - 614/292-4697 (F) - jezek@iceberg.mps.ohio-state.edu

Abstract - An ultra-wideband radar and a plane-wave antenna operating over a frequency range from 500 MHz to 18 GHz were used to measure the scattering response of bare saline ice, snow-covered ice and pancake ice at the US Army Cold Regions Research and Engineering Laboratory (CRREL) during the 1994 and 1995 winter seasons. Measurements were made at incidence angles between 0° and 50° with VV polarization. To estimate the scattering coefficient as a function of frequency, we had to extract the wideband response of the target. We used the Thomson's Multiple Windows technique to estimate the high-resolution spectrum and to extract the wideband response of the signal.

At 0°, the scattering from bare ice stayed fairly constant with about 1- to 2-dB variation across the 2- to 18-GHz frequency range. This indicates that the coherent component dominates over this frequency range. For pancake ice, the scattering increased from 21 to 29 dB with increasing frequency, which indicates an increasing contribution from the incoherent component with increasing frequency. In contrast, the scattering from snow-covered ice decreased from 25 to 19 dB with increasing frequency, which indicates a decreasing contribution from the coherent component at the higher frequencies. At 30° incidence angle, the scattering increased as a function of frequency, which is an indication of dominant incoherent scattering. The angular response of the scattering coefficients obtained using the plane-wave system show that surface scattering dominates at least until 30° for all the ice types. The results were compared with some simple models.

INTRODUCTION

An ultra-wideband radar and a plane-wave antenna [1] have been used to measure the high-resolution scattering response of bare saline ice, snow-covered ice and pancake ice during the winter seasons of 1994 and 1995 at the US Army Cold Regions Research and Engineering Laboratory (CRREL) during the 1994 and 1995 winter seasons. The objectives of these experiments were to study various mechanisms for simulating roughness and to understand scattering mechanisms better.

These backscatter measurements were made at 2 to 18 GHz and 0.5 to 16.5 GHz during the 1994 and 1995 experiments, respectively, and were made for incidence angles ranging from 0° to 55°. These broadband measurements provide a vigorous test for models at many frequencies using a single system instead of many single-frequency systems.

In this paper, we will present the signal processing techniques, the experimental results and model predictions of the backscatter measurements.

SIGNAL PROCESSING AND RESULTS

The primary parameter to be extracted from our measurements is the backscattering coefficient of the simulated sea ice as a function of the incidence angle and frequency. The radar equation for the plane-wave system is

$$\sigma^o = \frac{P_r \sigma_{cal}}{P_{cal} A_{ill}}$$

where σ^o is the backscattering coefficient of the ice,

P_r is the power returned from the ice,

P_{cal} is the return power from calibration target,

σ_{cal} is the radar cross section of the calibration target, and

A_{ill} is the area illuminated by the antenna.

The equation above does not include the range term since the fields do not decay as a function of range for plane waves.

To extract the scattering coefficient of the ice, we need to determine first the return power as a function of frequency. To do this, we windowed and inverse Fourier transformed the frequency-domain data to obtain the impulse response. The signal is then range gated to isolate the target return from the spurious reflections. A Fourier transform is then performed to obtain the return power as a function of frequency.

To determine the location of our target, we need first to obtain the high-resolution spectrum of our data. In the estimation of a spectrum, there are a variety of windows that we can choose to minimize leakage. Unfortunately most conventional windows that have good leakage resistance usually suffer from poor resolution. David J. Thomson [2] introduced a technique of estimating high-resolution spectra using multiple windows. These windows are optimum in the sense of maximizing the concentration of signal energy within a specified bandwidth, W. The windows are discrete prolate

spheroidal sequences (DPSS, also known as Slepian sequences) that satisfy a Toeplitz matrix eigenvalue equation given by

$$\sum_{m=0}^{N-1}\frac{\sin 2\pi W(n-m)}{\pi(n-m)}v_m^{(k)}(N,W) = \lambda_k(N,W)v_n^{(k)}(N,W)$$

where N is the number of data points,

W is the bandwidth, which is in the order of $1/N$,

k is the column number,

$v^{(k)}$ are the eigenvectors that correspond to the windows to be used to maximize the energy concentration within the specified bandwidth, W, and

λ_k are the eigenvalues that give us an estimate of the leakage that the data set incurs for the window, $v^{(k)}$.

Only the first $K=2NW-1$ terms with the largest eigenvalues are used to minimize leakage due to the higher order windows.

The complex spectrum, $S(t)$ (t is the travel time), can be estimated as follows

$$X_k(t) = IFFT\{x(f) \times v^{(k)}\}$$

$$S(t) = \frac{1}{K}\sum_{k=0}^{K-1}\frac{1}{\lambda_k}X_k(t)$$

where $x(f)$ is the raw data, and $X_k(t)$ is the individual spectrum estimate corresponding to the data window, $v^{(k)}$.

The Fourier transform of the Thomson windows were used to range gate the signal, thus providing us with an accurate representation of the return power as a function of frequency. The ringing due to the filter transient response was reduced by using the correction technique described in [3]. The correction factor was obtained by simulating an impulse function with a flat frequency response within the passband of our filter. The Fourier transform of this filtered impulse function gave us an estimate of the error due to the transient response. The target response was then divided by this correction factor to give us a more accurate representation of its frequency response.

As a first cut, the scattering response for bare ice and snow-covered ice were compared with some simple models. For bare ice, we used Fung and Eom's model [4] to determine the coherent contribution and the small perturbation model [5] for the incoherent components. The Rayleigh model [5] has been used to determine the backscatter due to snow volume.

Fig. 1a and 1b shows the angular response of bare and snow-covered saline ice and pancake ice at C band and Ku bands, respectively. From the plots, we can see that scattering for pancake ice is higher than bare ice for angles greater than zero. The results indicate there is more incoherent scattering from pancake ice because of its rougher surface. The volume contribution due to the 2-cm-deep snow cover is almost negligible. The slightly higher contribution from snow cover could be due to surface scattering. We can also see for the three ice types that surface scattering may dominate, at least until 30°, because of scattering coefficient falloff with angle.

Fig. 2a and 2b shows the frequency response of bare and snow-covered saline ice and pancake ice at 0° and 30°. At 0°, we see that scattering from pancake ice increased with

frequency. The scattering level increased from 21 to 29 dB as the frequency was increased from 2 to 15 GHz. From Fig. 2a, we can infer that, at the initial frequency of 2 GHz, the incoherent components dominated for pancake ice and, as the frequency was increased, we got an increase in scattering from the incoherent components. As for snow-covered ice, we observed that the scattering decreased from 25 to 19 dB as the frequency was increased from 3.5 to 16.5 GHz. From the model prediction, we see there is little contribution from snow volume. The higher scattering at the initial frequencies could be due to wet snow at the snow-ice interface. As the frequency increased, we got a decrease in scattering from the coherent component and an increase in scattering from the incoherent components. For the bare ice, there was no significant change in the scattering level across the frequency range. The model prediction for bare ice is dominated by the coherent contribution with negligible contribution from the incoherent components.

At 30°, the scattering level for bare ice and snow-covered ice increased by about 12 dB with increasing frequency. The model indicates that this increase corresponds to an increase in incoherent scattering. The scattering from pancake ice also exhibits similar behavior but with a higher scattering level due to its rougher surface.

CONCLUSIONS

An ultra-wideband radar and a plane-wave antenna were used to measure the high-resolution scattering response of bare saline ice, snow-covered ice and pancake ice. We developed signal processing techniques using Thomson's Multiple Windows to estimate the high-resolution spectrum and to extract the wideband response of the signal. The results of our experiment and the first-cut model prediction indicate that the backscattered signal from saline ice is dominated by contributions from the ice surface across the measured frequency range at angles less than 30°.

REFERENCES

[1] Gogineni, S.P., K. Jezek, L. Peters, J. Young, S. Beaven, and E. Nassar, "Application of plane waves for accurate measurement of microwave scattering from geophysical surfaces," *IEEE Trans. on Geosci. & Rem. Sens.*, vol. 33, no. 3, pp. 627-633, 1995.

[2] Thomson, D.J., "Spectrum estimation and harmonic analysis," *Proc. of the IEEE*, vol.70, pp.1055-1096, 1982.

[3] Higgins, R.J., *Digital Signal Processing in VLSI*, Englewood Cliffs NJ: Prentice Hall, 1990.

[4] Fung, A.K. and H.J. Eom, "Coherent scattering of a spherical wave from an irregular surface," *IEEE Trans. on Antennas and Prop.*, vol. AP-31, pp. 68-72, Jan 1983.

[5] Ulaby, F.T., R.K. Moore, and A.K. Fung, *Microwave Remote Sensing: Active and Passive,* vol. II, Norwood MA: Artech House, 1982.
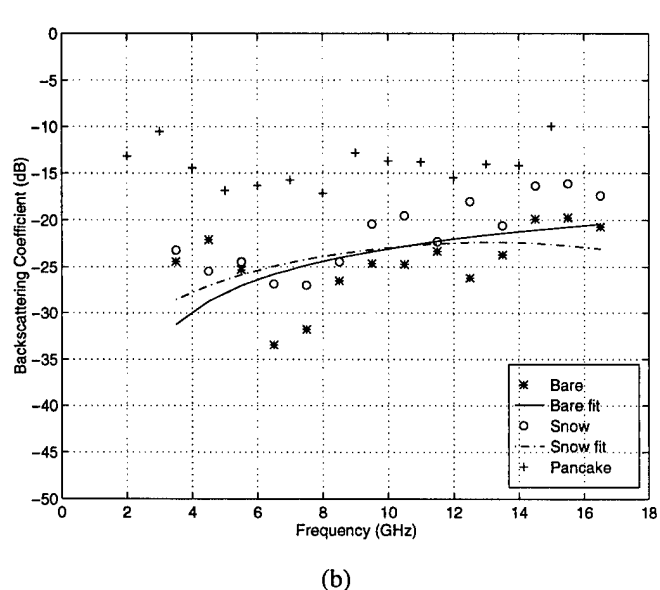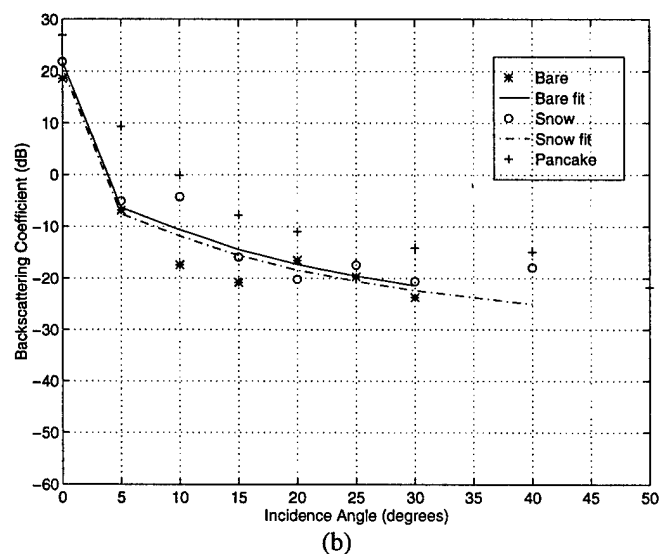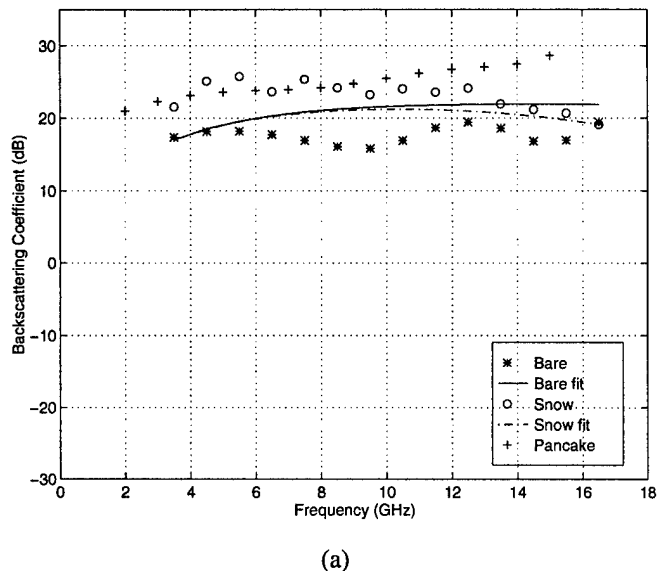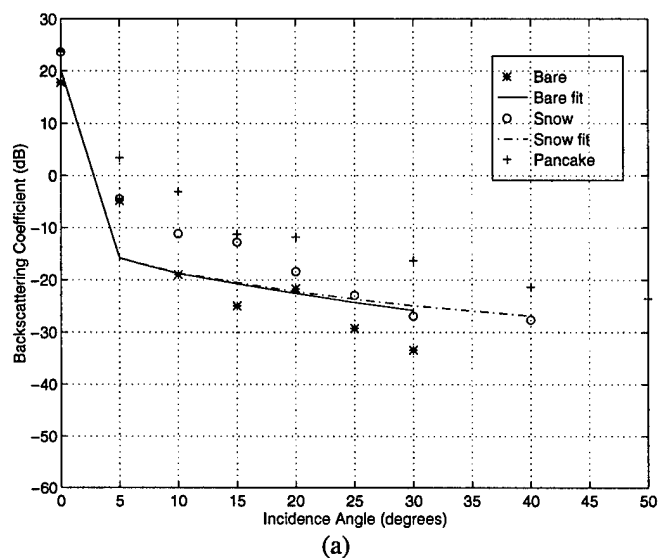
Fig. 1 Angular response of bare, snow-covered, and pancake ice at (a) C band and (b) Ku band.

Fig. 2 Frequency response of bare, snow-covered, and pancake ice at (a) 0° and (b) 30°.

MODELING INTERPRETATION OF ACTIVE AND PASSIVE MEASUREMENTS FROM SEA ICE

Adrian K. Fung and Saibun Tjuatja

Wave Scattering Research Center, Department of Electrical Engineering
University of Texas at Arlington, Box 19016, U.S.A.

Phone: (817) 272-3422   Fax: (817) 273-3443   Email: eefung@uta.edu

Abstract-- A combined surface-volume scattering model based on the radiative transfer formulation for an inhomogeneous layer above an inhomogeneous half space is developed using a dense medium phase function. This phase function gives the scattering properties of coherent scattering from a group of randomly positioned scatterers within a unit volume. For a bare saline ice or a snow-covered saline ice at C and X bands, backscattering at small angles of incidence is dominated by the air-ice or snow-ice interface. At large angles of incidence, volume scattering by ice, or snow and ice, is noticeable especially at higher frequencies. When the model is applied to passive measurements emission is found to be dominated by ice in the low frequency region. The presence of a snow cover enhances emission in the low frequency region and gradually turns into a darkening effect when frequency exceeds 35 GHz. At 94 and 140 GHz emission is dominated by snow. As frequency increases, the effect of group scattering lowers the rate of increase in albedo and permits a larger difference between like and cross polarized backscattering in active sensing and slows down the rate of decrease in emissivity in passive sensing.

INTRODUCTION

Snow and sea ice media are known to be dense because there may be more than one scatterer within the distance of a wavelength and because the volume fraction of scatterers may be more than half of a percent. When the wavelength is much larger than the size of the scatterer, the effect of a dense medium is usually not very significant in active scattering because the change in the level of scattering is close to or within experimental error. The optical depth of snow is small at long wavelength and generally it is the snow-ice boundary that is dominating backscattering from a snow-covered saline ice. However, at large angles of incidence ($\theta > 40^0$) volume scattering contributions from snow will be appreciable and the effect of a dense medium is to decrease the albedo value relative to the prediction based on a sparse medium theory.

In emission from a dense medium the effect of a decrease in albedo is most noticeable especially beyond 35 GHz. The darkening effect by snow in the 35–140 GHz range is much less than what is predicted by the classical radiative transfer model. Without including this dense medium effect, it will be impossible to account for the frequency behavior at these frequencies.

SCATTERING AND EMISSION MODELS

The model geometry is shown in Fig. 1 where the lower half space is saline ice. Note that the snow layer is an electrically dense inhomogeneous medium. The radiative transfer equation is solved within the inhomogeneous layers subject to the boundary conditions at the upper, and lower randomly rough boundaries. Unlike the conventional far field phase matrix, the dense medium phase matrix which accounts for close spacing between scatterers and first-order coherent interaction is utilized in the transfer equation. The formulation of the dense medium phase matrix is given in the following subsection. To account for the rough interface scattering effects, the IEM surface scattering model [1] is integrated into the snow layer scattering and emission models via the generalized boundary relation. In addition to the effects of boundary roughness, the generalized boundary relation also accounts for the coupling effects between an inhomogeneous layer and its rough boundaries. Detailed formulation of the generalized boundary relation is given in [1]. Thus, the snow layer scattering and emission models account for volume scattering, surface scattering by the interfaces, and surface-volume interactions simultaneously.

Dense Medium Phase Matrix

The phase matrix for dense medium is given by [2]

$$\bar{P} = \langle |\Psi|^2 \rangle_n \bar{S} = \langle |\Psi|^2 \rangle_n \begin{bmatrix} S_{VV} & S_{VH} \\ S_{HV} & S_{HH} \end{bmatrix} = \begin{bmatrix} P_{VV} & P_{VH} \\ P_{HV} & P_{HH} \end{bmatrix} \quad (1)$$

where $\langle |\Psi|^2 \rangle_n$ is the dense medium coherent phase correction factor needed to account for the first order coherent interaction between scatterers. This phase factor $\langle |\Psi|^2 \rangle_n$ is given by

$$\langle |\Psi|^2 \rangle_n = \frac{1 - e^{-k_{si}^2 \sigma^2}}{d^3} + \frac{e^{-k_{si}^2 \sigma^2}}{d^3} \sum_{q=1}^{\infty} \frac{(k_{si}^2 \sigma^2)^q}{q!} \cdot$$

$$\left[\left(\sqrt{\frac{\pi}{q}} \left(\frac{l}{d} \right) \right)^3 \exp\left(\frac{-k_{si}^2 \sigma^2}{4q} \right) - a(k_x)a(k_y)a(k_z) \right]$$

(2)

where $k_{si} = |\vec{k}_s - \vec{k}_i| = |\hat{x}k_x + \hat{y}k_y + \hat{z}k_z|$; $\vec{k}_s$ and $\vec{k}_i$ are the propagation vectors in the scattered and the incident directions respectively; σ is the standard deviation of the scatterer position from its central position in a uniform three-dimen-

sional array which defines the central locations of all scatterers; d is the mean distance between adjacent central locations; and l is the correlation length of the position deviation of one scatterer from its central position to that of the other scatterer; and

$$a(k_r) = \sqrt{\frac{\pi}{q}}\left(\frac{l}{d}\right)\exp\left(\frac{-k_r^2 l^2}{4q}\right)\text{Re}\left\{\text{erf}\left(\frac{(qd/l)+jk_r l}{2\sqrt{q}}\right)\right\}. \quad (3)$$

σ, l, and d are determined by the physical properties of the inhomogeneous medium, such as scatterer size and volume fraction. The average distance between scatterers is related to the scatterer volume fraction v_f and scatterer radius a by

$$d = a\left(\frac{4\pi}{3v_f}\right)^{1/3} \quad (4)$$

In (1), $\bar{S}$ is the phase matrix of a single scatterer which includes amplitude correction due to close spacing of scatterers in a dense medium. Detailed derivation of $\bar{S}$ is provided in [1].

COMPARISONS WITH DATA

Backscattering From a Snow-Covered Ice

Comparisons between model calculations and laboratory measurements over bare and cold, snow-covered saline ice are carried out. Ice surface roughness parameters are determined from model comparisons with data from bare ice and then used in model for predicting scattering from snow-covered ice at the same frequency for both VV and HH polarizations at 5.3 and 10 GHz. For this case coherent phase effect is not seen because many randomly located scatterers are within a wavelength thus destroying coherent phase effect. At 95 GHz and 140 GHz [3] only snow is seen by the radar. Fig. 2 and Fig. 3 give the comparisons of like and cross polarizations. Here the coherent phase effect is strong allowing a wider spacing between like and cross polarizations than predicted by conventional transfer theory [3]. Since natural ice particles in the snow layer are irregular in shape and different in size, and are randomly oriented as well, σ, the standard deviation of the variations from mean position, should be larger at 95 GHz than 140 GHz. In this case, we select $\sigma = 0.55d$ at 95 and $0.50d$ at 140 GHz. The correlation length l of snow samples has been reported in the literature [4] and is found to be within 0.05 mm (for fine snow grain sample) and 0.3 mm (for coarse snow grain sample). In the model predictions, l is chosen to be 0.12 mm for ice particles of radius 0.24 mm, and 0.11 mm for particles of radius 0.22 mm.

Emission From Snow Covered Sea Ice

Reference physical model parameters used in the emission calculations are listed in Table 1. The electrical parameters for snow and sea ice were determined using the formulas and tables provided in [5]. The model predictions at 6.7, 10, 18.7, 37, and 90 GHz using the physical parameters listed in Table 1 and reported in [6] agree well with the data provided in [6] at all frequencies. Note that model predictions show a higher emissivity (brightness temperature) of the snow-covered sea ice at 37 GHz than at 6.7 GHz. This increase is due to emission from snow with albedo lowered by the dense medium phase factor. The emissivity decreases at a rate much lower than predicted by conventioal radiative transfer theory as frequency increases further from 37 GHz to 90 GHz. This frequency behavior is consistent with the effect of the coherent phase factor (Fig. 4).

In the analysis of snow cover effects on sea ice emission, we assumed that the sea ice parameters are fixed. Fig. 4 shows the emissivity of sea ice with dry snow cover at 10, 37, and 90 GHz. As snow volumetric water content decreases, the total emissivity decreases due to an increase in snow albedo. Also, The separation between V and H polarizations decreases as snow volumetric water content decreases. Fig 5 shows a comparison between model and data at 90 GHz. The emission level remains quite high relative to 37 GHz for this particular data set because the snow is wet which further reduces albedo.

Table 1: Reference Parameters For Snow Covered Sea Ice

Physical Parameters	
Snow Layer:	
Layer thickness	8 cm
Scatterer radius (ice particle)	0.5 mm
Scatterer volume fraction	30%
Volumetric water content	1%
First Year Sea Ice:	
Layer thickness	60 cm
Scatterer radius (brine pocket)	0.1 mm
Scatterer volume fraction	1%

SUMMARY

A snow-covered sea ice model which partially accounts for dense medium effects was applied to data interpretation. Model predictions agree well with field measurements reported in [6]. Model predictions show a higher sea ice emissivity at 37 GHz than at 6.7 GHz. The emissivity decreases as frequency increases from 37 GHz to 90 GHz. A decrease in the snow cover volumetric water content causes a decrease in the emissivity of the snow-covered sea ice. As the snow grain size increases from 0.5 mm to 1.0 mm, the snow layer albedo increases resulting a decrease in total emissivity. In active sensing the separation between like and cross polarization is most sensitive to the coherent phase effect which leads to a wider separation between the two polarizations.

REFERENCES

[1] A.K.Fung, *Microwave Scattering And Emission Models*

And Their Applications, Artech House, MA, 1994.

[2] H.T.Chuah, S.Tjuatja, A.K.Fung, and J.W.Bredow, "A phase matrix for a dense discrete random medium: evaluation of volume scattering coefficient," IEEE Trans. GRS Vol. 34., No. 5, pp. 1137-1143, 1996.

[3] Ulaby, F.T.,Haddock, T.F.,Austin, R.T., and Kuga, Y., "Millimeter-wave radar scattering from snow: Comparison of theory with experimental observation," *Radio Science*, vol. 26, pp. 343-351, 1991.

[4] Vallese, F., and Kong, J.A. "Correlation function studies for snow and ice," *J. Appl. Phys.*, vol. 52, pp. 4921-4925, 1981.F.T.Ulaby, R.K.Moore, and A.K.Fung, *Microwave Remote Sensing*, Vol. 3, Appendix E, pp. 2017-2019, Artech House, Norwood, MA, 1986.

[5] F.T.Ulaby, R.K.Moore, and A.K.Fung, *Microwave Remote Sensing*, Vol. 3, Appendix E, pp. 2017-2019, Artech House, Norwood, MA, 1986.

[6] T.C.Grenfell, J.C.Comiso, M.A.Lange, H.Eicken, M.R.Wensnahan, "Passive microwave observations of the Weddell Sea during austral winter and early spring," *J. Geophy. Res.*,Vol. 99, No. C5, pp. 9995-10010, May 15, 1994.
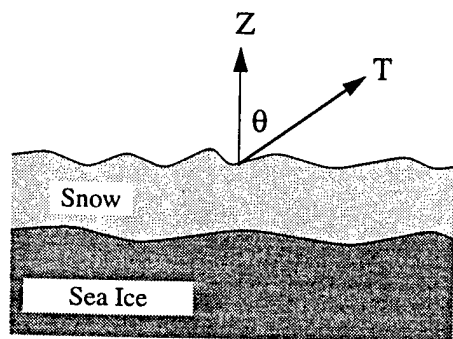
Figure 1. Geometry of the snow layer model.
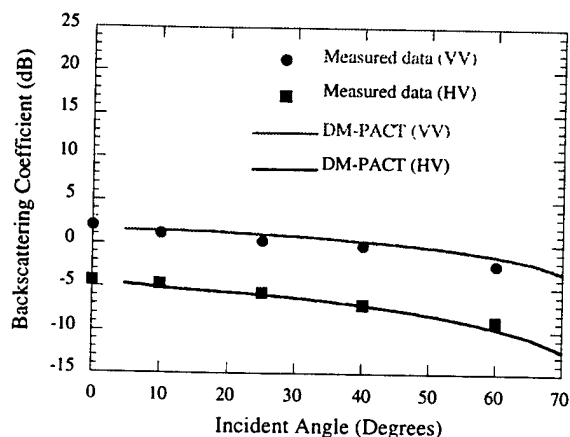
Figure 2. Backscattering from dry snow layer over soil at 95 GHz.
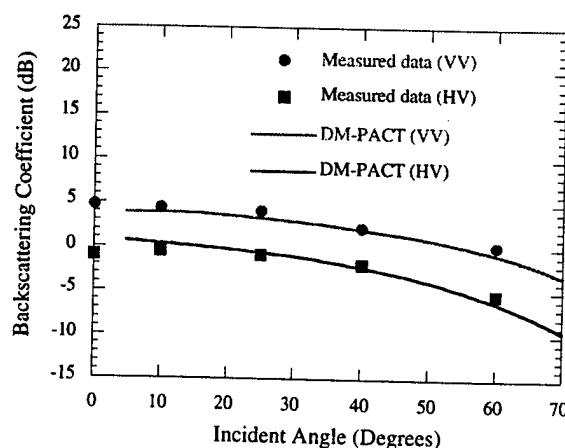
Figure 3. Backscattering from dry snow layer over soil at 140 GHz.
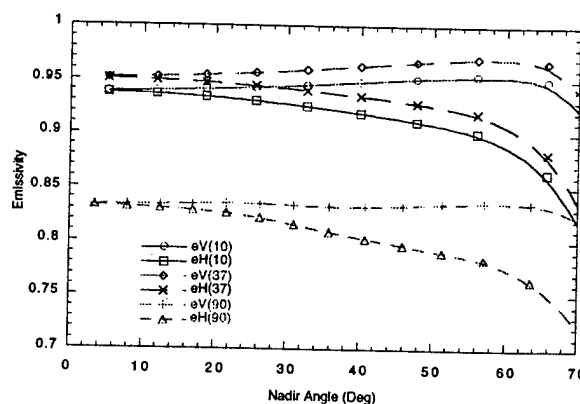
Figure 4. Emissivity of a snow-covered sea ice with dry snow cover.
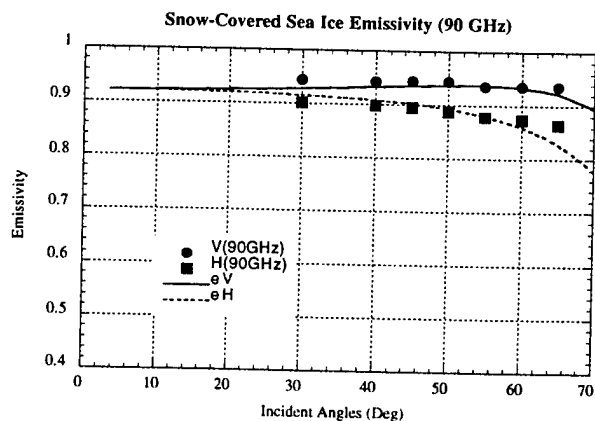
Figure 5. Emissivity of a snow-covered sea ice with wet snow cover.

The influence of the atmosphere on the remote sensing of sea ice using passive microwave radiometers

Christoph Oelke

International ACSYS Project Office
Norwegian Polar Institute, P.O. box 5072 Majorstua, N-0301 Oslo, Norway
Tel: +47 22 95 96 13, Fax: +47 22 95 96 01, e-mail: oelke@npolar.no

Abstract – The effects of weather systems on sea-ice concentration retrievals using passive microwaves are investigated because significant errors in estimating short-time variations and climatological concentration trends occur due to clouds and water vapor. For the assessment of these weather effects, the atmospheric parameters *integrated water vapor content* (W) and *cloud liquid water path* (LWP) are derived from radiosonde ascents measured in the pack-ice area of the Weddell Sea/Antarctica in 1992. Using a microwave radiative transfer model and typical surface emissivities, brightness temperatures are calculated from the radiosonde ascents. The first-year, multiyear and total sea-ice concentrations are calculated using the NASA team sea-ice algorithm for the SSM/I radiometer (*Special Sensor Microwave/Imager*). Thus the ice concentration changes depending on surface composition (open ocean, first-year ice, multiyear ice) and the values of LWP and W are modelled. Modelled atmospheric effects and measured sea-ice concentration changes, the latter being derived from SSM/I radiometer data, are in good agreement both geographically and quantitatively in areas with large frontal cloud structures, as identified using infrared satellite data. A method is presented for a large-scale estimation of the necessary parameters LWP and W over sea ice. Using these results the derived sea-ice concentrations can be corrected for the modelled atmospheric effects.

INTRODUCTION

Since the launch of the ESMR (*Electrically Scanning Microwave Radiometer*) in 1972 it has been possible to derive the approximate coverage of the polar oceans with sea ice from the measured radiance. The use of data from multichannel instruments – SMMR (*Scanning Multichannel Microwave Radiometer*) and SSM/I (*Special Sensor Microwave/Imager*), launched in 1978 and 1987 – also allowed the determination of different sea-ice types. But more precise identification of even small concentration changes is important in order to detect long-term climatic variability of sea-ice extent, concentration or type. Comparison with surface field measurements indicates that current algorithms which determine sea-ice concentration from passive microwave observations need to be improved, especially for Southern Ocean sea ice. Here the effects of weather systems on the derivation of sea-ice concentration are investigated for the most widely used NASA-Team algorithm [1]. Through the use of brightness temperature (T_B) ratios calculating its parameters polarization ratio

PR (1) and gradient ratio GR (2) the algorithm is almost insensitive to surface temperature variations.

$$PR = [T_B(19V) - T_B(19H)]/[T_B(19V) + T_B(19H)] \quad (1)$$
$$GR = [T_B(37V) - T_B(19V)]/[T_B(37V) + T_B(19V)] \quad (2)$$

However, due to the presence of atmospheric cloud liquid water, $T_B(37V)$ is stronger increased than $T_B(19V)$ while water vapor affects T_B at 19 GHz (closer to the absorption line at 22.3 GHz) stronger than at 37 GHz. Thus PR and GR are modified for conditions different from average, for which specific algorithm tie-point T_B were selected.

MODEL INPUT DATA

For the comparison with satellite data, brightness temperatures at the top of the atmosphere and at radiometer frequencies and polarizations are simulated using a microwave radiative transfer model [2, 7]. Surface emissivities were chosen for the Weddell Sea [6] and were kept fixed for the whole variety of atmospheric conditions allowing an assessment of the atmospheric effects. Typical atmospheric conditions and their variability over sea ice are taken into account using 155 radiosonde ascents, launched from the icebreaker *R. V. Polarstern* in winter 1992 over sea ice in the Weddell Sea/Antarctica. Since radiosonde observations do not contain direct information on cloud liquid water content, the profile of cloud liquid water is parameterized from the measured profiles of temperature and humidity using a modified adiabatic approach [2]. Profiles of *liquid water content* (LWC) and their integral value, the *liquid water path* (LWP), were verified with synoptic observations from *R. V. Polarstern*. Water vapor density (ρ_w) and its integral value, the *integrated water vapor content* (W) is calculated directly from the ascent measurements (Fig. 1). By using measured polar atmospheric conditions, especially a realistic cloud position, height and liquid water distribution, more realistic effects on derived sea-ice concentration are expected compared with previous approaches, e.g. [3].

MODEL RESULTS

The modelled effects of atmospheric cloud liquid water and water vapor are directly obvious in PR-GR space (Fig. 2). The radiosonde values (dots) depart characteristically from the sides of the sea-ice retrieval triangle which represent the pure surface types (first-year ice (A), older ice (B), open water (OW), and fractions thereof) without atmospheric influence. Water vapor and cloud liquid water decrease PR while the latter strongly increases GR.
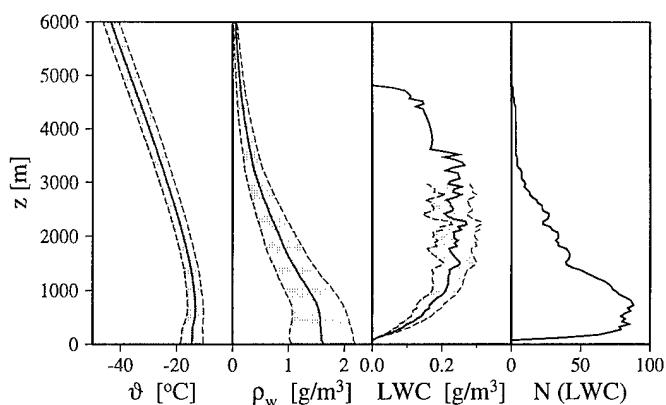
Figure 1: Average and standard deviation (for N ≥ 10) of temperature (ϑ), water vapor density (ρ_w) and cloud liquid water content (LWC) profiles for the used radiosonde ascents from the Weddell Sea. The right part shows the distribution of parameterized layers with water clouds.

These two different behaviors are most obvious at low concentrations (near the OW-point). The scatter within the clusters of points (each representing the atmospheric data set) is caused by varying cloud parameters and water vapor profiles (see [5] for details). Using the NASA-Team algorithm, curves of sea-ice concentration changes (dC) with LWP (Fig. 3a, c) and with W (Fig. 3b, d) are calculated by regression. The first-year ice concentrations (C_F) on the abscissas contain weather errors and thus can even be calculated as more than 100 % or less than 0 %. The abscissas of Fig. 3 can be identified as the line OW–A in Fig. 2, with C_F ranging from 0 % to 100 %. While LWP and W increase C_T by the same order of magnitude (Fig. 3c, d), the LWP effect on C_F can be up to six times as large (Fig. 3a, b).

Detailed comparison with previously published weather effects for the SMMR radiometer sea-ice algorithm, and

Figure 3: Modelled weather effects on first-year concentration, dC_F (a, b), and total concentration, dC_T (c, d) due to LWP (a, c) and W (b, d); units are kg m^{-2}.

for different sea-ice emissivities in other polar regions can be found in [6]. Changes of C_T predicted by the SSM/I radiometer algorithm are twice as large as those obtained from the older SMMR radiometer algorithm, resulting mainly from the larger water vapor effect at SSM/I frequencies. The weather effects for future MIMR (*Multifrequency Imaging Microwave Radiometer*) radiometer data will be in between those from SMMR and SSM/I.

SATELLITE DATA

The modelled atmospheric effects on sea-ice concentration retrieval are now used to correct satellite derived concentrations in the Weddell Sea where the radiosondes were launched and where ground-based observations exist. As an estimate of the atmospheric parameters, W and LWP (3) are computed over ice using open-water algorithms [7].

$$LWP = b_0 + b_1 \ln(280 - T_B(22V)) + b_2 \ln(280 - T_B(37V)) \tag{3}$$

The b_i are regression coefficients. A large change in satellite-derived ice concentration within a short period of time (less than one day) is supposed to be mainly the result of

Figure 2: Modelled atmospheric effects of W and LWP in *PR-GR* space for different compositions of sea-ice types (A, B) and open water (OW). Lines of total concentration are drawn in intervals of 10 % for scale.

a)

SSM/I
24.07.92 p.m.
- 24.07.92 a.m.

dLWP [kg/m²]

-0.5 -0.4 -0.3 -0.2 -0.1 0 0.1 0.2 0.3 0.4 0.5

b)

SSM/I
24.07.92 p.m.
- 24.07.92 a.m.

b')

SSM/I
24.07.92 p.m.
- 24.07.92 a.m.
corrected

dC_F [%]

-50 -40 -30 -20 -10 0 10 20 30 40 50
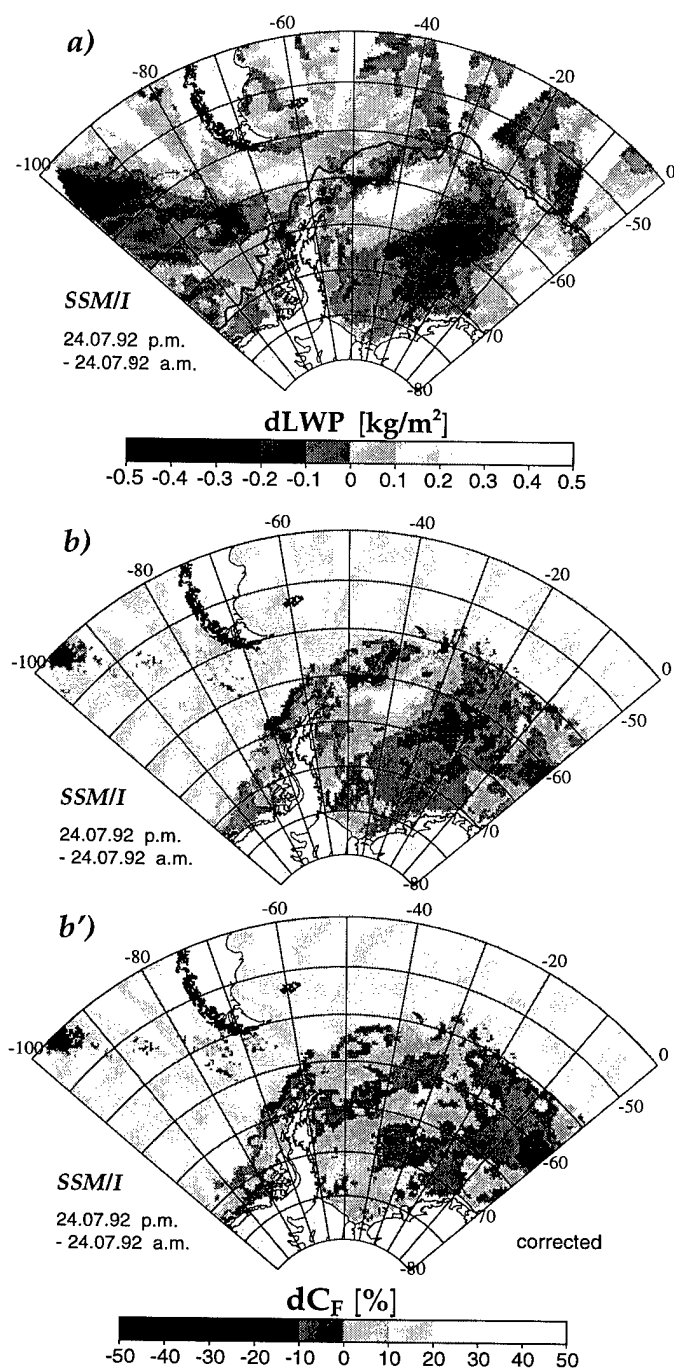
Figure 4: Difference plots (p.m. − a.m.) of SSM/I-derived LWP over ocean *and* sea ice (a), C_F (b) and corrected C_F (b') in the Weddell Sea/Antarctica for 24 July 1992.

fast-moving atmospheric disturbances and not the effect of real concentration changes, which can vary typically up to 3 % per day [4]. Therefore, the change of LWP (Fig. 4a) and W within 12 hours is computed as the difference between the values of evening (p.m.) and morning (a.m.) satellite overflights. The strongest LWP increase occurs in a region where a frontal cloud band passes the northwest-

ern Weddell ice pack, as detected using *Advanced Very High Resolution Radiometer* (AVHRR) infrared images. By applying the very similar modelled effects of LWP and W (Fig. 3) to satellite derived concentrations (here C_F) it is possible to reduce the concentration change between p.m. and a.m. values (formerly up to 50 %) significantly, as seen in the example of 24 July 1992 (Fig. 4b, b').

CONCLUSIONS

The model study for first-year sea ice areas indicates an increase of total sea-ice concentration of 10–15 % and an increase of first-year concentration of up to 60 % for high values of atmospheric cloud liquid water and water vapor, while a decrease of multiyear concentration of up to −50 % is calculated. Very similar effects have been observed for satellite derived sea-ice concentrations. If these concentrations, affected by disturbances on time scales of less than one day, remain uncorrected, a positive bias would result for C_F and C_T, and a negative bias for C_M. The correction of weather effects is important in order to identify climate-induced sea-ice concentration trends, especially if data from more than one radiometer are used. On the other hand, a climatological increase of LWP or W would incorrectly imply a higher total ice concentration with higher first-year and lower old-ice fraction. Further work must be done in order to separate weather and surface emissivity effects for cyclones passing the ice pack. Important parameters for the emissivity are crystal structure, salinity and free water content of an accumulating snow layer on the ice.

REFERENCES

[1] Cavalieri, D.J., et al., "Aircraft active and passive microwave validation of sea ice concentration from the DMSP SSM/I", J. Geophys. Res., 96, 21989–22008, 1991.

[2] Karstens, U., Simmer, C., and Ruprecht, E., "Remote sensing of cloud liquid water", Meteorology and Atmospheric Physics, 54, 157–171, 1994.

[3] Maslanik, J.A., "Effects of weather on the retrieval of sea ice concentration and ice type from passive microwave data", Int. J. Remote Sensing, 13, 34–57, 1992.

[4] Maslanik, J.A., Fowler, C., Heinrichs, J., Barry, R.G., and Emery, W.J., "Remotely-sensed and simulated variability of Arctic sea-ice concentrations in response to atmospheric synoptic systems", Int. J. Remote Sensing, 16, 3325–3342, 1995.

[5] Oelke, C., "The influence of the atmosphere on the remote sensing of sea ice using passive microwave radiometers" (in German), Reports on Polar Research, 208, 1–117, 1996.

[6] Oelke, C., "Atmospheric signatures in sea-ice concentration estimates from passive microwaves: modelled and observed", Int. J. Remote Sensing, 18, 1113–1136, 1997.

[7] Simmer, C., "Satellite remote sensing of hydrological parameters of the atmosphere with microwaves" (in German), Hamburg: Verlag Dr. Kovač, 1994.

Analysis of sea ice thickness and mass estimation with a spaceborne laser altimeter

J.-P. Luntama, S. Koponen, M. Hallikainen
Helsinki University of Technology, Laboratory of Space Technology
P.O.Box 3000, FIN-02015 Espoo, Finland
Tel: +358-9-451 2372
Fax: +358-9-451 2898
Email: Luntama@avanet.hut.fi

Abstract - Sea ice is one of the most important components of the Earth's cryosphere. It modifies the sea-air heat and momentum exchanges, Earth's radiation budget and affects the global heat and freshwater circulation. None of the existing satellite instruments can provide detailed measurements of the sea ice topography and elevation, that is necessary for the study of the sea ice mass balance.

This paper presents the results of an analysis that was made for the European Space Agency concerning the feasibility of a spaceborne laser altimeter for sea ice measurement. The analysis indicates that a laser altimeter with a spatial resolution of 50 m - 100 m can be used to globally measure sea ice thickness and estimate sea ice mass with an accuracy exceeding the accuracy of the present spaceborne measurement techniques.

INTRODUCTION

Sea ice is one of the most important components of the Earth's cryosphere as it continuously modifies the sea-air heat and momentum exchanges in the high latitude areas. The high albedo of sea ice plays a significant role in the Earth's radiation budget by reflecting the solar radiation and thus providing a positive feedback on the global temperature change. In a case of a global temperature decreasing the increasing area of the sea ice coverage would amplify the phenomena. Sea ice advection combined with ocean currents is an important factor in the global heat and fresh water circulation.

The mass budget of sea ice is not well known in spite of the fact that the areas covered by sea ice are well mapped. The main reason for this is that the present spaceborne remote sensing instruments do not provide adequate spatial resolution for the detailed mapping of sea ice topography.

Satellite altimetry has become one of the most important techniques to observe the ocean circulation. Radar altimetry from satellites has been used for more than a decade and is now one of the main data sources for studies of ice sheet topography and ocean currents. Radar altimetry has been tested for sea ice, but the technique is not yet mature for the observation of the sea ice topography and thickness. One of the problems of a spaceborne radar altimeter is the large footprint that averages out almost all deformations of the sea ice topography.

A spaceborne laser altimeter, with sufficient accuracy and resolution, has potentially the capability to provide topographic data which are needed for the ice thickness and mass balance studies.

SEA ICE THICKNESS MEASUREMENT

The ice thickness can be estimated from altimeter data by measuring the freeboard, which is the mean height of the ice floes above the sea level. For example, for 2 m thick sea ice the freeboard is typically 20 - 30 cm, depending on the density of the ice, the snow cover on the ice and the water content of the ice.

A factor R relating the sea ice draft and the freeboard can be calculated from the freeboard height by applying the Archimedes' law, the mean ice and snow density and the near-surface water density,

$$R = \frac{\rho_m}{\rho_w - \rho_m}, \qquad (1)$$

where ρ_m is the mean density of sea ice and snow and ρ_w is the density of near-surface water [1].

The accuracy with which R can be determined is crucial for the determination of ice thickness. From field experiments in the Arctic, where both freeboard and draft were observed directly, good correlation between freeboard distribution and draft distribution were found using a value of 7.8 for R [2]. However, the value for R can vary considerably depending of the thickness of the snow cover on the ice and ice type [2,3].

The sea ice thickness H can be calculated from R and freeboard height estimates by

$$H = A + B = (R+1)B, \qquad (2)$$

where A is the draft of the sea ice and B is the measured freeboard height.

This method is very sensitive to the freeboard height measurement error, because the factor R can be rather large. For example, the range accuracy of a state of the art spaceborne laser altimeter system is estimated to be about 6 cm [4]. This results in about 54 cm error in the sea ice thickness measurement. Thus the performance of a spaceborne laser altimeter is not sufficient to resolve sea ice thickness variability in areas of thin first year ice.

SIMULATION OF SPACEBORNE MEASURE-MENT

The main difference between a spaceborne laser altimeter and an airborne one from the data user point of view is the size of the footprint. The diameter of an airborne laser altimeter footprint is small (diameter < 1 m) compared to sea ice topography features. Based on the general sampling theory this means that the target is oversampled. When a spaceborne laser altimeter measures surface topography, only the average heights of the 50 - 100 m footprints (diameter between half-power points) are obtained. This can considered as subsampling of the measured target and a severe loss of target features.

In this study airborne laser altimeter data has been used to simulate the performance of a spaceborne instrument. Simulation has been performed by averaging airborne laser altimeter data from the Bay of Bothnia and the Arctic Sea regions near Greenland to create footprints of 50 m and 100 m of diameter. A Gaussian shape for the footprint energy distribution function has been used. These averaged profiles provide similar topographic information from the sea ice surface than a spaceborne laser altimeter would.

To study the statistical data produced by a spaceborne laser altimeter we have combined the averaged profiles to create 50x50 km target areas for the Bay of Bothnia and for the Arctic Sea region. The measurement of a satellite laser altimeter has been simulated by taking short random topography samples from the target areas. This simulates the operations of a laser altimeter with varying cloud coverage over the target areas. The percentage of successful laser measurements has been assumed to be normally distributed. The number of hits for a target area has been selected to equal the number of satellite passes over target areas at different latitudes and during different cloud conditions.

PROBABILITY DENSITY FUNCTION

Probability density function (PDF) is calculated by classifying each laser altimeter measurement to a height bin and dividing the number of hits in each bin by the total number of measurements. The height of the bin is defined to be the midpoint of the bin. This procedure is visualized in Fig. 1.

The advantage of the PDF is that the height measurement error related to a single altimeter range measurement can be reduced by averaging several samples within one height bin as

$$\Delta h_{pdf} = \frac{1}{\sqrt{n_{bin}}} \Delta r_{range}. \qquad (3)$$

where Δh_{pdf} is the error of the averaged result (also representing the confidence of that bin), Δr_{range} is the error of single range measurement, and n_{bin} is the number of averaged measurements.
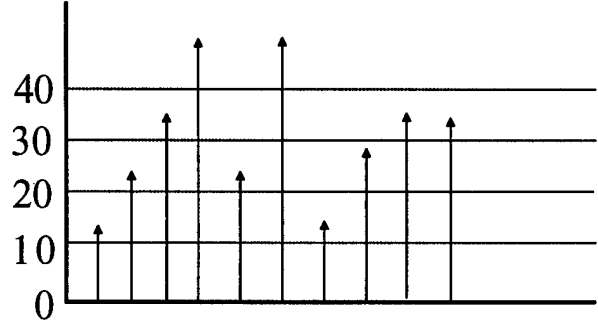
Fig. 1. *Procedure used to calculate ice height PDF.*

ICE VOLUME AND MASS ESTIMATION USING PDF

A very good mach between the PDFs of the sea ice freeboard and draft has been shown in [1]. This means that the sea ice volume distribution can be estimated from the PDF of the freeboard over the target area as

$$V = \sum_{i=1}^{k} A_T H(i)p(i), \qquad (4)$$

where V = freeboard volume
A_T = area of the measurement target
$H(i)$ = average height of bin i
$p(i)$ = probability of bin i
k = total number of bins.

The error in the sea ice volume estimate ΔV based on the PDF can be analyzed by using the total differentiating method. If the target area error is assumed to be 0 and all height measurement errors are included into a single error term ΔH_{bin}, the freeboard volume error can be calculated from the equation

$$\Delta V = A_T \left[\Delta H_{bin} \sum_{i=1}^{k} p(i) + \sum_{i=1}^{k} H(i) \Delta p(i) \right], \qquad (5)$$

where $\sum_{i=1}^{k} p(i)$ (sum of all probabilities) must be 1. Thus

$$\Delta V = A_T \Delta H_{bin} + A_T \sum_{i=1}^{k} H(i) \Delta p(i). \qquad (6)$$

$\Delta p(i)$, the probability of the erroneous samples in bin i, can be calculated from the measurement error, bin height and number of measurements in the bin as

$$\Delta p(i) = p(i) \cdot (\text{area fraction of erroneous samples} \qquad (7)$$
$$\text{in that bin}).$$

Fig. 2 presents the freeboard volume estimation error as a function of the bin height for a simulated 50x50 km target area of multiyear sea ice at the latitude of 80° N. The four

curves represent percentages of the measurements prevented by the cloud coverage when the satellite has passed over the target area. The total data collection time for the target area has been selected to be one month, and the number of satellite passes over the target area has been calculated accordingly. The satellite has been assumed to be on a 650 km dawn-dusk sun-synchronous orbit. The RMS freeboard height measurement error of the laser altimeter system has been assumed to be 16 cm (sum of the laser altimeter range resolution and the sea level determination error).

The results in the Fig. 2 indicate that the error in the freeboard volume estimate can be kept small with a proper selection of the PDF bin height even when cloud coverage prevents 90 % of the measurements from the target area. This indicates that the performance of a laser altimeter is not affected by the cloud coverage as severely as generally is considered.
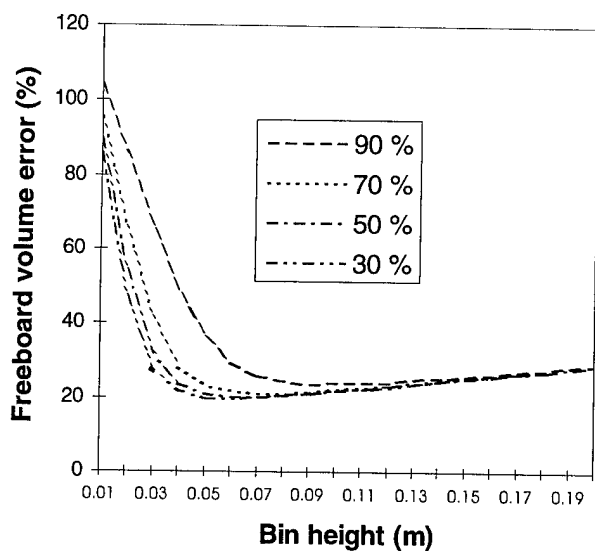
Fig. 2. *The error of the freeboard volume estimate in 50x50 km area as a function of the PDF bin height and for different cloud coverage probabilities for a multiyear sea ice in the Arctic region. A 50 m laser altimeter footprint diameter and 140 Hz measurement rate has been used in the simulation.*

If the freeboard to draft ratio R and the sea ice mean density ρ in the target area are known, the total ice mass M can be calculated from V with the equation

$$M = V(R+1)\rho . \qquad (8)$$

The errors in the sea ice mean density and in the ratio R introduce errors to the mass estimate. Most observed values for first-year sea ice density are in the range of 910-920 kg/m^3. For multiyear sea ice the density is usually between 910-915 kg/m^3 [2]. The value for R can vary between 4 and 9 depending on the ice thickness, ice density, and thickness and density

of the snow cover on top of the ice. The density of sea water also has an effect on the value of R.

Due to the additional error sources, the error in the ice mass estimate is larger than in the freeboard volume estimate. The analysis of the mass estimation error has not been completed yet, as some additional data on the seasonal and regional variation of the R is required.

CONCLUSIONS

This simulation indicates that a spaceborne laser altimeter can produce fairly accurate sea ice freeboard volume estimates even in very cloudy conditions. By PDF conversion and suitable selection of the PDF bin height a good accuracy of the freeboard volume estimate can be maintained even when the number of samples from the target area is severely reduced.

The accuracy of the ice mass estimate depends on the knowledge of the freeboard-draft ratio and sea ice mean density for the area and the season. Errors in these parameters may reduce the usefulness of the freeboard height measurement based sea ice mass estimation. However, a quantitative analysis of the sea ice mass estimation error requires better knowledge of the regional and seasonal behavior of the sea ice, than that presently available.

ACKNOWLEDGMENT

REFERENCES

[1] J. C. Comiso, P. Wadhams, W. B. Ktabill, R. N. Swift, J. P. Crawford and W. B. Hibler III, "Top/bottom multisensor remote sensing of Arctic Sea ice," J. Geophys. Res., 96(C2), 2693 - 2709, 1991.

[2] P. Wadhams, W. Tucker, W. Krabill, R. Swift, J. Comiso, and N. Davis, "Relationship Between Sea Ice Freeboard and Draft in the Arctic Basin, and Implications for Ice Thickness Monitoring," Journal of Geophys. Res., vol. 97, pp. 20325-20334. 1992 b.

[3] G.A. Maykut, and N. Untersteiner, "Some Results from a Time-dependent Thermodynamic Model of Arctic Sea Ice", Journal of Geophysical Research, vol. 76, pp. 1550-1575, 1971.

[4] J-P. Luntama, S. Sandven, A. Ullrich, A. Tveito, P. Månsson, K. Lundahl, M. Hallikainen, and S. Koponen, "Mission Study of an Ice Topography Observation System, Final Report, ESTEC Contract No 11613/95/NL/CN, 1996.

WAVE-BREAKING EFFECTS IN RADAR SIGNATURES FROM 2-DIMENSIONAL MODELLING OF THE HI-RES-1 RIP FEATURE

S. R. Chubb, A. L. Cooper, R. A. Fusina, R. W. Jansen
Remote Sensing Division
Naval Research Laboratory Washington, D. C. 20375-5351,U. S. A.
Telephone: 202.767.5270, FAX: 202.767.3303, EMAIL: chubb@ccf.nrl.navy.mil

Abstract -- Full-spectral modelling of a two-dimensional current structure is used to understand the role of wave-current interaction and wave-breaking (WB) effects in the Radar Signatures of the Rip-like sub-mesoscale feature that were observed during the First High Resolution Remote Sensing (HI-RES-1) experiment. It is found that the large variations in radar cross-section (RCS) in the neighborhood of the cusp-like features within the Rip can be reproduced with or without incorporation of wave-breaking (WB) effects. However, when WB effects are not included, consistent with previous models that have used 1-dimensional current structures, in regions away from these cusp-like structures, the composite scattering (CB) model significantly underpredicts the magnitude of the signature. As a consequence, somewhat surprisingly, <u>within the Rip</u> , the CB model *over-predicts* the magnitude of the cusp signature relative to the signature from the Rip in non-cusp-like regions. By including WB effects, this deficiency is overcome, and good agreement is obtained. The resulting agreement occurs when the WB effect is based on an estimate of the local critical crest acceleration Ω_c=0.4 g (g=9.8 m/s^2) that accompanies the onset of wave-breaking. This value for Ω_c is in good agreement with independently measured values obtained in wave-tank and field experiments. Incorporation of WB effects also eliminates a non-physical dependence on look-angle that occurs when the CB model alone is used.

INTRODUCTION

From full spectral modelling of surface waves, considerable progress[1,2,3] has been made in simulating radar signatures of the Rip-like sub-mesoscale feature that was observed during the First High Resolution Remote Sensing[4] (HI-RES-1) experiment. During this experiment, a meandering, sinusoidally-shaped region of large radar return, ranging between 10 and 15 dB in relative variation, was observed at a current convergence front[4,6], located at the boundary between Shelf water and the Gulf Stream near Cape Hatteras, NC. Quantitative agreement was obtained for the magnitude of this signature, based on two, independent models of the surface currents[1,2,3], and application of full-spectrum wave-current interaction calculations of surface wave spectra and the composite backscatter (CB) model, but only after additional effects from wave-breaking (WB) were included in an approximate manner through an improved version of the radar backscatter model. These earlier studies involved one-dimensional models of the surface currents, which were represented either as a simple current convergence[1] or as a current convergence in the presence of a shear[2,3]. As a consequence, the resulting estimates are applicable to regions where the effects of changes in the direction of the Rip are not pronounced. In the calculations presented in this paper, a more sophisticated, sinusoidally-varying, 2-dimensional model of the surface current structure is used that provides a more reliable representation of the underlying structure in regions where the direction of the Rip changes. Very good agreement with experiment is obtained for the magnitude of the signature (~11-17 dB) across and within the Rip, but only when the effects of wave breaking are included. In particular, it is found that when the CB model is used alone, within the Rip, the cross-section varies over a considerably larger range (6-16 dB) than is observed experimentally and also exhibits a non-physical dependence on look-angle that was not observed. When WB effects are included, these deficiencies are eliminated, and it is found that the location of maximal and minimal cross- section, and the manner in which cross-section varies within the meander all agree well with the experimentally derived imagery.

METHOD

Previous simulations[1-3] of RCS of the HI-RES-1 Rip feature have been based on wave-current interaction calculations of wave height spectra F, as a function of two-dimensional wave-vector $\mathbf{k}$, at locations $\mathbf{r}$ on the ocean surface. In these calculations, F is derived from the intrinsic angular wave fequency $\omega_0(k)$ ($\equiv (gk+T/\rho k^3)^{1/2}$, $k \equiv |\mathbf{k}|$, ρ=density of sea water,$T \equiv$surface tension) and wave action density $N(\mathbf{r},\mathbf{k},t) \equiv \omega_0(\mathbf{k})/k$ F, using either one (y-dependent) component[1] V, or both (U, and V) components[2,3] of the current, with the important simplifying assumption that the only spatial dependence in the currents occur in one direction: $V \equiv V(\mathbf{y})$, and[2,3] $U \equiv U(\mathbf{y})$. From these calculations of F, simulations of RCS were derived from the CB model, and two extensions of the CB model that incorporate WB effects.

Because these currents only included a dependence on y, it was not possible from these calculations to infer information about the behavior of the RCS in regions where strong spatial variation in the Rip occurs in both the x- and y-directions. To investigate this point, we have employed a different model, in which V=0, and $U= U(x,y)$ is modelled from

$$U(\mathbf{x}, \mathbf{y}) = -\frac{\delta U}{2} \tanh[\frac{x - x_o \sin(\frac{2\pi y}{\lambda})}{\delta x}]. \qquad 1$$

Here, the values for $\delta U=.6$ m/s and $\delta x=30$ m are used to mimic the convergence , observed [4] during HI-RES-1, that was used previously[1-3], while the values $x_o=300$ m, and $\lambda=1500$ m were inferred radar imagery[4,5,6]. Using this current model, N is derived from

$$\nabla_{\mathbf{k}}\omega \bullet \nabla_{\mathbf{r}}N - \mathbf{k_x}[\frac{\partial U}{\partial x}\frac{\partial N}{\partial k_x} + \frac{\partial U}{\partial y}\frac{\partial N}{\partial k_y}] = -\beta\frac{N}{N_o}(N-N_o) ,$$

where $\omega=\omega_o + k_x U$, and β and N_o , respectively, are the Plant wind growth rate and Bjerkaas-Riedel equilbrium wave action that were used previously [1-3].

As before[2,3], RCS values were determined from F, using the CB model, avoiding the small slope approximation[3] that was used in [1]. WB effects were investigated, using the LWBC approach[2,3], in which the RCS is derived probabilistically, by combining the CB model RCS (suitably weighted so that it applies in locations where breaking does not occur) with an approximate Feature model of a breaking wave, using the probabilities $P(r)$ and $(1-P(r))$ for wave-breaking to occur and not occur at r. Specifically, the RCS is derived from

$$\sigma^{sp}_{tot} = (1 - P(r))\sigma^{sp}_{CS} + P(r)\sigma^{sp}_{WB} , \qquad 2$$

where $P(r)$ and σ^{sp}_{wb} , respectively, are inferred from crest acceleration Ω and wave-height variance values that are derived from F. To determine $P(r$), it is necessary to establish a critical value $\Omega=\Omega_c$ of the crest acceleration, beyond which breaking is assumed to occur with 100% certainty. As in [2,3], this was accomplished by performing a number of calculations involving different values of Ω_c and finding a particular value that maximizes the variation in RCS across the Rip. The resulting value $\Omega_c = 0.4$ g is very close to the value ($\Omega_c = 0.38$ g) that was obtained previously [2,3] and agrees with independently measured values that have been obtained in wave-tank and field measuremnets. Additional details of the LWBC procedure are presented in [3].

RESULTS

Fig. 1 shows plots of the RCS with (Fig. 1B) and without (Fig. 1A) WB when the radar is pointed across the Rip. The signature (S) of the Rip appears as the meandering sinusoidally-varying region of large RCS-variation found in the center of each plot. The largest RCS-variations ($\sim$15-18 dB) are found in the locally vertical regions of large variation located in the "cusp-like" positions (marked by arrows) within the S in both plots. The smallest variations in RCS within the S in each case are found in the "non-cusp-like" regions (also marked by arrows). In the non-WB case (Fig. 1A) , this minimal RCS-variation (within the non-cusp-like

(A) **Radar Looking Across Rip**
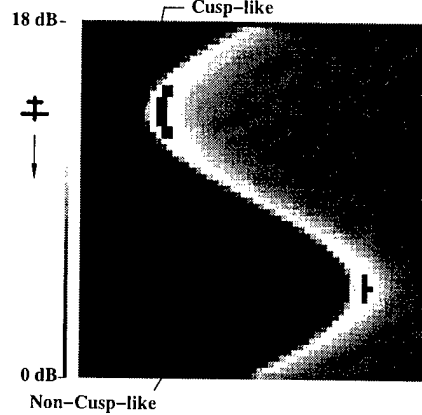
Without Wave-Breaking

(B) **Radar Looking Across Rip**
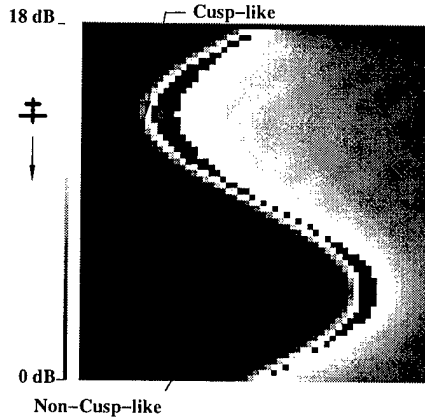
With Wave-Breaking

Fig. 1: Simulated RCS values, looking across Rip, without (A) and with (B) Wave-Breaking, in dB (as marked) relative to the minimum value associated with each plot. The schematic of the airplane is used to indicate the flight path in each plot. "Cusp-like" ("non-cusp-like") regions (marked by arrows) refer to regions where the signature is strongly (weakly) dependent on 2-dimensional variations in position within the Rip.

portion of the S) , relative to the minimal RCS value (found far from S) is ~6 dB; while in the cusp-like region, the comparable RCS-variation is 16 dB. Although experimentally[6], in comparable "cusp-like" regions, large ~15 dB variations in RCS were observed, variations in RCS of ~10 dB were observed in the "non-cusp-like" regions. As a result, when the CB model is used alone, a considerably larger range of variation (~10 dB) in RCS is obtained within the Rip than was observed. Considerable improvement (as can be seen in Fig. 1B) is obtained when the WB effect is

1318

included. For this case, we find that in the "cusp-like" and

(A) Radar Looking Along Rip

Without Wave–Breaking

(B) Radar Looking Along Rip
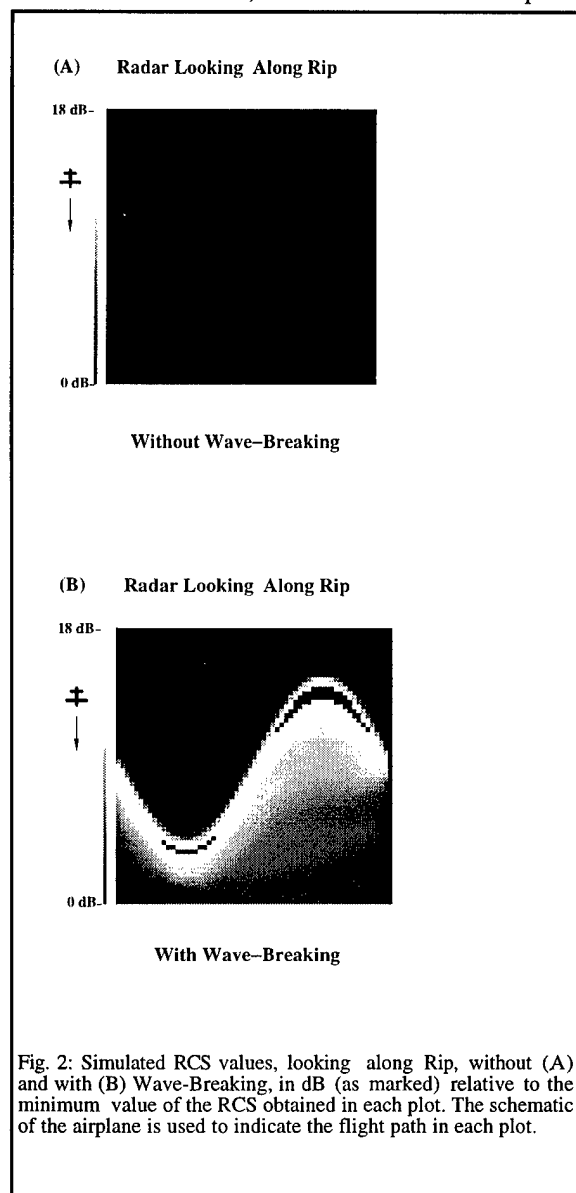
With Wave–Breaking

Fig. 2: Simulated RCS values, looking along Rip, without (A) and with (B) Wave-Breaking, in dB (as marked) relative to the minimum value of the RCS obtained in each plot. The schematic of the airplane is used to indicate the flight path in each plot.

"non-cusp-like" regions, respectively, the RCS varies by ~17 and ~12 dB. Thus, by including 2-dimensionally-varying currents, it is found that when the radar is pointed across the rip, significant (~15-18 dB) variations in RCS are obtained in the "cusp-like" regions of the Rip, regardless of whether or not WB effects are included, and this variation in RCS is significantly larger than the comparable variation that is obtained in "non-cusp-like" regions. Both of these trends agree with experimental observation. However, without WB, the range (~6-16 dB) of variation in RCS-values within the S is considerably larger than is observed experimentally. By incorporating WB, it is found that this deficiency is eliminated and quantitative agreement is obtained.

The presence of WB effects does not significantly increase the magnitude of the simulated signatures in the cusp-like regions. This is somewhat surprising since in the earlier 1-dimensional calculaltions, when WB is not included, the signature is underpredicted by 5 dB. In fact, in the non-cusp regions, the signature is underpredicted by 5 dB in the CB case, suggesting that the signature in these regions more closely approximates the comparable 1-dimensional results. A possible reason for the enhanced return in the cusp region is that the shear (defined by the gradient of U in the y-direction) behaves differently there than in the non-cusp region.

WB effects are also found to be important in our ability to simulate the look angle dependence. In particular, it is found that without WB effects, the RCS exhibits a sensitivity with respect to changes in look-angle that was not found experimentally, while when WB effects are included, this deficiency is eliminated. This effect is illustrated in Figs. 2 (A,B), where simulated plots of RCS are shown when the radar is pointed along the Rip (i.e., perpendicularly to the dominant current convergence). From this plot, it is seen that the signature effectively disappears in simulations that do not incorporate the WB effect, while for cases in which WB is included, the signature closely resembles the comparable signature that is obtained when the radar is pointed across the Rip.

ACKNOWLEDGMENT

REFERENCES

[1]R. W. Jansen, T. L. Ainsworth, R. A. Fusina, S. R. Chubb, and G. R. Valenzuela, IGARSS'94 Digest, vol 1, 460 (1994).

[2]R. W. Jansen, C. Y. Shen, S. R. Chubb, A. L. Cooper, and T. E. Evans, "Subsurface, Surface, and Radar Modeling of a Gulf-Stream Current Convergence," J. Geophys. Res., in press (1997).

[3]S. R. Chubb, A. L. Cooper, R. W. Jansen, and C. Y. Shen, IGARSS'96 Digest, vol 2, 902 (1996).

[4]G. O. Marmorino and C. L. Trump, J. Geophys. Res.,99, C4, 7627 (1994).Mied, R.P., et al., 1992 NRL Review, 181-183, (1992).

[5]R.A. Fusina, A.L. Cooper, and S.R. Chubb, J Comp Phys, in press (1997).

[6] F. Askari, EOS, 73, #A3/supplement, 247 (1992). F. Askari, unpublished.

Intercomparison and Validation of Bathymetry Radar Imaging Models

H. Greidanus, C. Calkoen[2], I. Hennings[3], R. Romeiser[4], J. Vogelzang[5], G.J. Wensink[2]
TNO Physics and Electronics Laboratory
P.O. Box 96864, 2509 JG Den Haag, The Netherlands
tel: +31-70-3740441, fax +31-70-3280961, e-mail greidanus@fel.tno.nl
2: ARGOSS; 3: GEOMAR; 4: UHSO; 5: RWS-RIKZ

Abstract -- Multi-frequency airborne SAR data over a submerged reef, with very large associated surface current variations, are compared with model calculations, using a wide variety in models and parametrizations. It is concluded that all models still underestimate the measured contrasts, that detailed differences in models cannot be validated due to speckle and non-bathymetric features, and that L-band is more suited for bathymetry applications than C- or X-band.

INTRODUCTION

In the presence of a current, submerged topographic features of the sea bed produce contrasts in radar images. These contrasts can be quantitatively understood and modeled, based on hydrodynamics and electromagnetic scattering theory. The, at present, generally accepted modeling includes the three steps of (1) surface current modulation by the bathymetry, (2) modulation of the (small) wave spectrum by wave-current interaction, and (3) radar backscattering by the sea surface which is characterized by the (modulated) wave spectrum. The ability to perform such a quantitative modeling makes it possible to extract quantitative bathymetric information from radar images; techniques for this purpose are presently being developed and put to use, based on inversion of the forward modeling.

Nevertheless, as the physics are too complex for a full description, the modeling contains numerous assumptions, approximations and parametrizations. In the past, the validity of the modeling has been explored and partly established; mostly, however, in relatively simple situations. As a consequence, the models have a limited accuracy and a limited range of validity, which are actually not very well known or described. When radar data are being used for practical purposes such as bathymetry extraction, the models applied need to be correct, or at least their limitations need to be well known.

This article reviews a test case for the models which is more extreme than previous cases. It concerns a submerged reef near the island of Heligoland, Germany. The bottom topography is dominated by a series of parallel reefs with very steep slopes, with depths ranging from 4 to 20 m, resulting in very large surface current variations. On the basis of the measured bathymetry and hydrometeo conditions, radar contrasts are computed by several different models; these are compared with airborne SAR imagery.

DATA

The data used for this study were originally collected in the framework of the SAXON-FPN experiment. Three data categories were used: radar data, bathymetry, and hydrometeo data. The radar data were taken on November 14, 1990, by the L-, C-, X-band SAR on board a P-3 aircraft operated by the Naval Air Development Center (Warminster, PA). The aircraft flew a northbound track looking west at 2.4 km altitude. The data were processed by ERIM (Ann Arbor, MI) to 6 x 6 km² scenes at a multi-look ground resolution of 4.8 m. The image was georeferenced by using prominent features on the Heligoland coast. A 2 x 2 km² depth map of the test site was constructed at 30 m resolution and 5 m sampling, by combining a digitized chart measured in 1970 with depth measurements from two surveys, in 1989 and 1991. (The stony nature of the reefs makes them not very dynamic.) The locally measured hydrometeo conditions indicated a wind (at 10 m height) of 9 m/s, direction 200° and waves of 1.1 m significant height, direction 260°. Both the SAR image and the depth map were rotated by 45° in order to have the reef direction coincide with one of the sampling axes.

MODELS

A regional tidal model was run on a 400 m grid size, with 10 m/s wind. Based on this coarse-grid flow field and the detailed depth map, a depth averaged flow field was calculated using the shallow water equations. The resulting flow field is, as expected, nearly one-dimensional, with the variations occurring in the direction perpendicular to the reefs. The depth averaged flow field was then converted to a surface flow field with a parametric model designed for flow over trenches.

This surface flow field was input to the various radar imaging models. All these models are based on weak hydrodynamic interaction theory (e.g. [1,2] and references therein), but differ in dimension, equilibrium wave spectrum, relaxation rate, source function, backscatter model, and algorithmic and numerical implementation. With the models, the radar contrasts along three cross-cuts perpendicular to the reefs were calculated, in L-HH, L-VV, C-VV and X-VV, corresponding to the available SAR data.
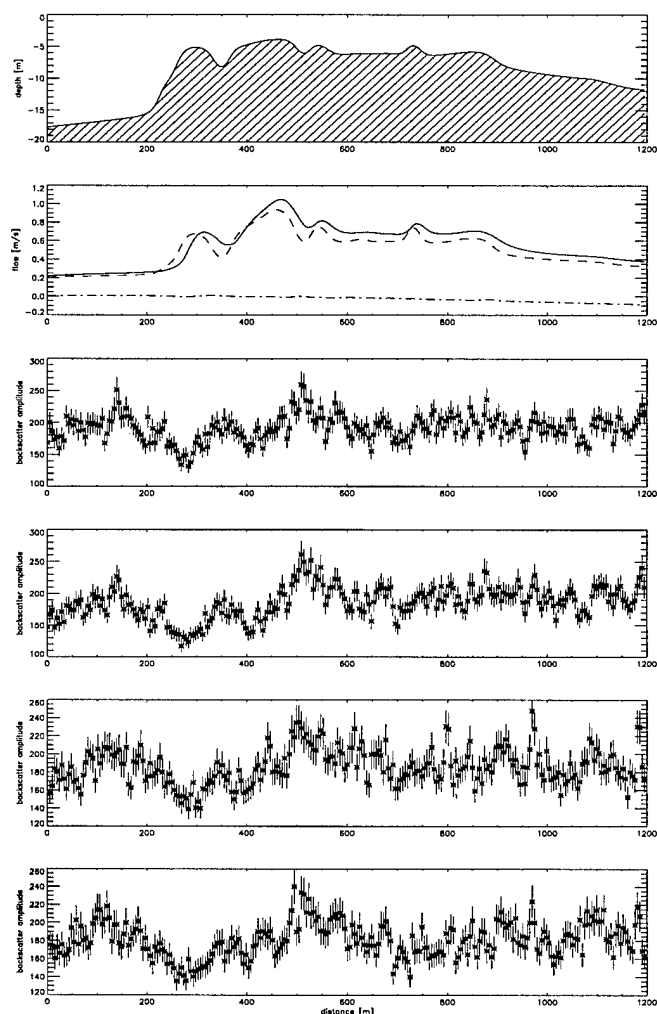
Figure 1. Cross-cuts perpendicular to the reef. Top: bathymetry. Second plot: surface flow along-track (drawn) and depth-averaged flow, along track (dash) and across-track (dot-dash). Next four: L-VV, L-HH, C-VV and X-VV with error bars based on estimated speckle level.

RESULTS AND DISCUSSION

The SAR images clearly show the bathymetry, in the form of bright/dark lines parallel to the submerged reefs. On all images the presence of surface waves is clearly visible; on the C- and X-band images also wind rows can be seen. Before extracting backscatter cross-cuts, the surface waves were suppressed by applying filtering in the Fourier domain. In order to reduce the speckle, the cross-cuts taken from the images were laterally averaged over 20 pixels.

One cross-cut is presented in this paper. The bathymetry, current, and radar contrasts are presented in Fig. 1. Some model results for L- and X-band are shown in Figs. 2 and 3. An overview of the features of the models used to produce these figures is given in Table 1.

It can be seen that all models give rather similar results, the main difference being the magnitude of the contrasts. The models with two-scale backscatter and the one with fitted relaxation rate have larger contrasts than the ones with Bragg backscatter. The low contrasts in model 'R' are a consequence of the relaxation rate used. However, even the models that show the highest contrasts still fall short of the observed contrasts, the effect being stronger in X-band than in L-band. This is in accordance with existing literature. Most of the features in the models correspond well with observed features, however, not always with similar relative magnitude; indeed, the models correspond more closely to each other than with the observations. Only model 'TB' at X-band behaves differently; here, the use of a Bragg model in combination with an equilibrium spectrum of which the Bragg wave intensity is a function of friction velocity, leads to a model cross-cut that is dominated by the dependency of the Bragg backscatter on the local wind speed. This is not realistic; the use of a two-scale model in this case (model 'TC') does not show this effect and gives better results. For L-band, contrasts in HH are observed to be larger than in VV, though the effect is small; this is also reflected by the two models that have a polarization dependence. A number of observed features is not reflected in the models, and this effect is more pronounced in X-band; these features are attributed to waves, wind rows, etc., also upon inspection of the images. In spite of the Fourier filtering to suppress the waves, these features are obviously still present at a level comparable to the bathymetric signatures, even over these steep reefs.

CONCLUSIONS

Based on the full study, which contained the two other cross-cuts and model runs covering a much broader range in modeling alternatives than shown here, the following conclusions were drawn (in addition to the points discussed before):

• The similarity in the results of the various, partly independent, models points to a basic robustness of the modeling principles;

• The use of a linear source function leads to much too high positive modulations;

• Velocity bunching and shoaling are not important effects (even in this case);

• Bragg backscatter leads to much too low contrasts. However, in case the radar look direction is more or less aligned with the current gradient, the use of an adjustable relaxation rate can compensate for this;

• Detailed differences between models cannot be judged due to the presence of speckle and features of non-bathymetric origin, even after spending considerable effort in reducing these;

• L-band imagery is more suited for bathymetry applications than C- or X-band, as the latter are more influenced by the atmosphere and can be less well modeled.
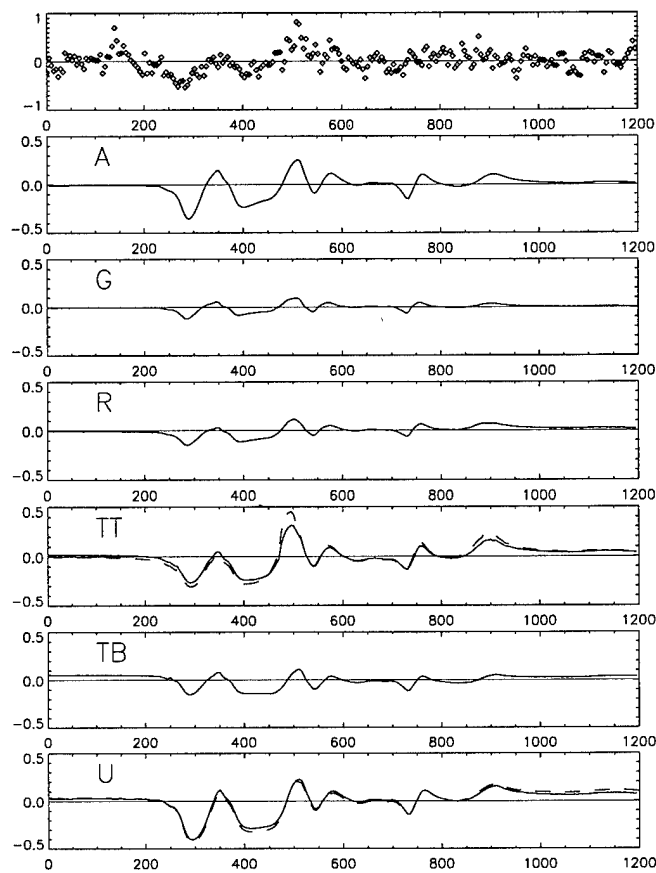
Figure 2. L-band VV intercomparison. Top: measurements. The other six plots are model results, ref. Table 1. Vertical axis is linear backscatter contrast $(\sigma^0/\langle\sigma^0\rangle - 1)$.

Figure 3. X-band VV intercomparison (as for Fig. 2).

Table 1. Overview of the different models as included in Figs. 2 and 3. "Dim" refers to the model dimension. Model 'G' is analytical and includes velocity bunching. Model 'R' includes shoaling. Model 'TC' has two-scale plus specular backscatter. All these models use a quadratic source function.

Model	Dim	Eql. spec	Relax. rate	Backscatt.
ARGOSS	1	Phillips	fitted	Bragg
GEOMAR	1	Phillips	Hughes [6]	Bragg
RWS	2	Apel [3]	H&S [7]	HSW [9]
TNO-C	1.5	VIERS [4]	Plant [8]	Composite
TNO-B	1.5	VIERS	Plant	Bragg
UHSO	2	RAW [5]	Plant	RAW

REFERENCES

[1] W. Alpers, and I. Hennings, "A theory of the imaging mechanism of underwater bottom topography by real and synthetic aperture radar", J. Geophys. Res. 89, 10529, 1984.

[2] J. Vogelzang, "The mapping of bottom topography with imaging radar", Int. J. Rem. Sens. 10, 1503, 1989.

[3] J.R. Apel, "An improved model of the ocean surface wave vector spectrum and its effects on radar backscatter", J. Geophys. Res. 99, 16,269, 1994.

[4] P.A.E.M. Janssen et al., "The VIERS-1 scatterometer model", unpublished.

[5] R. Romeiser, W. Alpers, and V. Wismann, "An improved composite surface model for the radar backscattering cross section of the ocean surface, 1", in press, 1997.

[6] B.A. Hughes, "The effect of internal waves on surface wind waves, 2", J. Geophys. Res. 83, 455, 1978.

[7] S.V. Hsiao, and O.H. Shemdin, "Measurements of wind velocity and pressure with a wave follower during MARSEN", J. Geophys. Res. 88, 9844, 1983.

[8] W.J. Plant, "A relationship between wind stress and wave slope", J. Geophys. Res. 87, 1,961, 1982.

[9] D. Holliday, G. St.-Cyr, and N.E. Woods, "A radar ocean imaging model for small to moderate incidence angles", Int. J. Rem. Sens. 7, 1809, 1986.

STRESS MODULATION ACCOUNT IN THE PROBLEM OF THE WAVE SPECTRUM TRANSFORMATION CAUSED BY NONUNIFORM CURRENTS

Yuri Trohkimovski
Space Research Institute, Profsoyusnayu 84/32, Moscow, 117810, Russia
ytrokh@mx.iki.rssi.ru

Abstract — The modulation of the momentum flux from turbulent wind flow to ocean surface caused by current gradient is considered. Simple estimation shows that the magnitude of such modulation can be up to 100-200% for strong internal waves (IW). Numerical technique is proposed to calculate stress modulation and simulations are made for periodical IW and solitons. Variable stress is used in the source function of the wave action balance equation and the modulation of X-band Bragg spectral density is calculate for typical IW soliton. Momentum flux modulation due to nonuniform current is to be incorporated in the theoretical models used for analysis and interpretation of ocean remote sensing from space.

BACKGROUND

Experimental results obtained in ground-, aircraft- and spacebased radar experiments indicate, that models for sea surface backscatter demand, as one of the elements, the account of the modulation of surface stress by gradients of surface currents. As was shown by Hara and Plant [1] the hydrodynamic modulation of short wind-wave spectra by long waves measured by microwave scatterometers is extremely large and we have to attribute this unexplained value to the variable wind shear stress. The same conclusion was done in the theoretical analysis by Smith [2]. It can be expected, that surface currents (including orbital motion of long gravity waves, internal waves in the coastal regions, fronts and streams in the ocean) modulate wind stress, and simple estimation shows that relative small amplitude of surface velocities can result to large modulation of momentum flux from the air flow to the sea surface.

The modeling of stress modulation due to current gradients is extremely difficult problem. There is no technique for simple and adequate account for the wind stress modulation by surface nonuniform currents. For example Monin-Obukhov theory for surface layer considers only horizontally uniform wind flow and doesn't predict anything about relaxation rates of the air turbulence to the equilibrium state and for that reason can not be applied to nonuniform conditions. Additional difficulty is connected with the fact, that one has to explain the modulation of momentum flux of large amplitude (100% or more) and the consideration based on small perturbation expansion (for example in Reynolds equation) is out of order. The lack of adequate theory for momentum flux in nonuniform marine boundary layer prohibits the quantitative analysis of aircraft or satellite radar images.

The results presented in this paper were obtained using new numerical model for turbulent momentum flux. This model can be referred to as "Random box model for turbulent momentum transfer". This model is in some sense a development of the "Transilient turbulence theory" by R. Stull [3].

SIMPLE ESTIMATION

First of all let us estimate the value of the stress modulation, that can be expected as the result from non-uniform current on sea surface. We suppose that both current and wind u are along x-axis. The magnitude of the current is equal to U_0 in the region $0 < x < L$ and is taken as 0 otherwise.

The thickness of new boundary layer, which develops over the region with nonzero current, can be estimated as: $\dfrac{u_* x}{<u>}$, where $<u>$ is the mean wind velocity in the surface layer, u_* is the friction velocity. Additional momentum in the new boundary layer is: $\Delta M \approx 0.5 \cdot \rho_a U_0 L^2 u_* / <u>$. Assuming that this increase of momentum is resulted from additional stress on sea surface $\Delta \tau$ we can estimate the same value ΔM as: $\Delta M \approx \Delta \tau \ L^2 / <u>$. Taking into account that stress is defined as $\tau = \rho_a u_*^2$, it is easy to estimate relative stress modulation:
$$\Delta \tau / \tau \approx 0.5 \cdot U_0 / u_* \ .$$

Hence, we have to compare the magnitude of surface current with friction velocity! For strong internal waves current amplitude U_0 is of about 0.5-0.7 m/s, friction velocity is of about 0.2-0.3 m/s and relative stress modulation might be up to 100-200%. The above estimation will be correct provided distance L is not to large.

RANDOM BOX MODEL FOR TURBULENT MOMENTUM TRANSFER

The model is a numerical model, which consider horizontal velocity as passive tracer similar to transilient turbulence theory by R. Stull [3]. In our model turbulent mixing is simulated by a rotation of boxes with different scales. The same rule is used for probability of rotation at all scales, for that reason the model obeys self-similar features. The probability of rotation is taken to be proportional to velocity gradient at the corresponding scale.

An assumption is made, that on the top and bottom boundaries the exchange of momentum is rapid. The minimum scale is taken as 0.2 m, the maximum scale is taken as 500 m. The model predicts logarithmic profile of mean wind velocity under uniform stationary conditions and the low -5/3 for wind speed fluctuations. Model predictions were checked for turbulent flows in channels and a good agreement was noted.

Nonuniform current on sea surface is accounted for as : 1) nonzeoro velocity is taken on the bottom boundary; 2) each horizontal layer is shifted in the horizontal direction with the mean velocity of air flow. The limitation of the model is small horizontal gradient of horizontal velocity, what is true for orbital velocity of long surface waves and for surface current induced by internal waves. There are no restrictions associated with large value of stress modulation, large amplitude of vertical gradient and rapid changes in horizontal velocity with time.

NUMERICAL RESULTS

Stress modulation. We have estimated stress modulation for relatively strong internal waves. Fig.1 shows results for cosine wave with current amplitude 0.2 m/s and period 600 m. Only one period is shown in the figure. Wind direction is from right to left in the figure. It was obtained stress modulation of about 100%. It is interesting to note, that model predicts nonlinear response to variable current on sea surface. Asymmetry of the modulated stress profile is obvious.

Fig.2 demonstrate results for internal wave soliton. The calculations were made in case when wind direction is from right to left and the internal wave propagates in the positive x-direction (from left to right). The stress modulation in case, when wind and IW are in the same direction, is a little smaller in the amplitude and has negative sign.

The contrast maximum is located between current velocity and strain rate maximum.

Fig.1

Distance, m
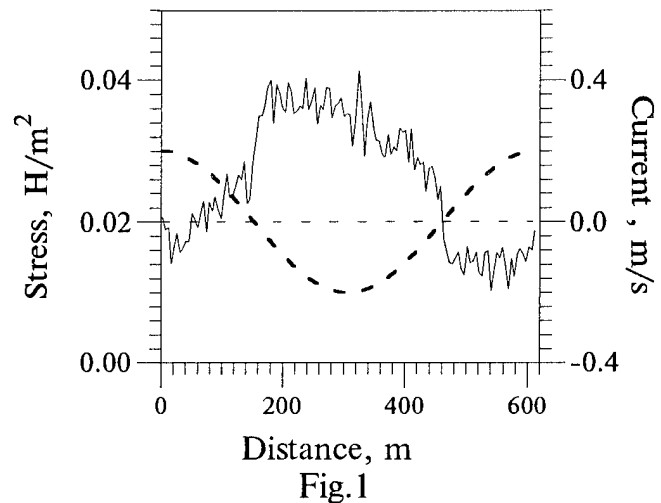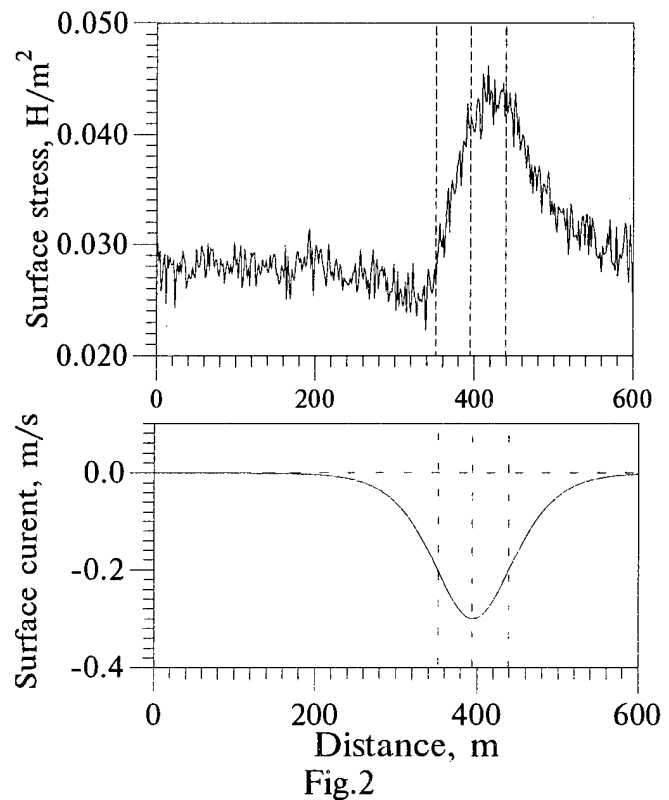
Fig.2

Radar Brag's wave modulation. Large magnitude of stress modulation demands to be accounted in models for radar images of internal waves. It seems reasonable to put variable friction velocity in the source function of the wave action balance equation. There are different forms of the source function; in

1324

this report we show only results based on the function proposed by Hughes [4].

Fig. 3 shows the modulation of X-band Bragg spectral density for the same parameters of IW soliton as is given in fig.2. Two results are given: dashed line - traditional wave action balance equation with source function by Hughes, solid line - the same equation with variable friction velocity in the source function. The difference is dramatically large.

Results, obtained for wind in the same direction as IW, are given in Fig.4. In this case we observe only negative contrast. This fact is well known from numerous radar observation.

Both examples indicate, that the account of variable stress results to significant increase in the contrast predicted by theory.
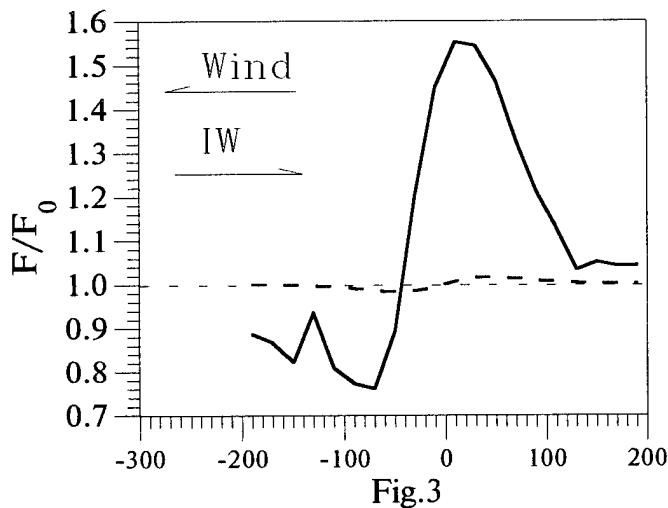
Fig.3
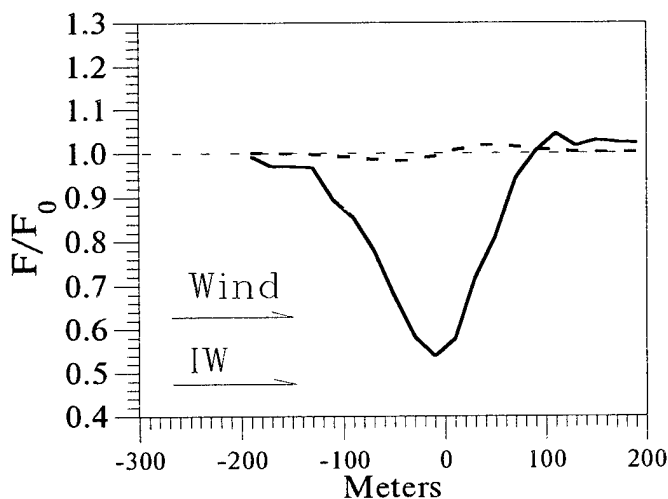
Fig.4

CONCLUSION

Momentum flux modulation due to nonuniform currents on sea surface is an important phenomena, which is to be incorporated in the theoretical model used for analysis and interpretation of ocean remote sensing from space. Simple estimation and numerical modeling demonstrate, that stress modulation for strong internal waves is of about 50-200%. Numerical model is developed and tested for periodical IW and solitons. The same model can be applied to the broad range of phenomenon: surface and internal waves, fronts, streams, surface manifestation of bottom topography.

ACNOWLEDGMENTS

REFERENCES

[1] Hara, T. and W. Plant, Hydrodynamic modulation of short wind-wave spectra by long waves and its measurements using microwave backscatter, J. Geophys. Res., 99(5), 9,767-9,784, 1994.

[2] Smith, J. A., Modulation of short wind waves by long waves, in *Surface Waves and Fluxes.* vol. I, *Remote Sensing,* edited by G. L. Geernaert and W. J. Plant, pp. 247-284, Kluwer Academic, Hingham, Mass., 1990.

[3] Stull, R.B., An introduction to boundary-layer meteorology, Kluver Academic Publishers,1988.

[4] Hughes, B.A., The effect of internal waves on surface wind waves, 2, Theoretical analysis, J. Geophys. Res., 83, 455-465, 1978.

On the Polarization-Dependent Signatures of Atmospheric and Oceanic Features in Radar Images of the Ocean Surface

Roland Romeiser
University of Hamburg, Institute of Oceanography
Troplowitzstr. 7, 22529 Hamburg, Germany
Phone: +49 40 4123 5430   Fax: +49 40 4123 5713   E-Mail: romeiser@ifm.uni-hamburg.de

Abstract -- Multi-polarization radar images of the ocean surface from various experimental campaigns suggest that the backscattered signal is more sensitive to wind field variations at vertical (VV) than at horizontal (HH) polarization. On the other hand, radar signatures of oceanic features like internal waves or underwater bottom topography are often better visible at HH. In this paper, a possible theoretical explanation for these phenomena is discussed. It is shown that polarization-dependent radar signatures are qualitatively consistent with predictions of a composite surface scattering model, where the ratio between modulation depths at HH and VV is determined by the intensity variations of ocean waves in different wave-number ranges. Using a simple scenario of wind and current variations, it is demonstrated that a pair of radar images with dominant oceanic and atmospheric signatures at HH and VV, respectively, can be basically obtained from the model.

INTRODUCTION

Aside from the well-known fact that the normalized radar backscattering cross section (NRCS) of the ocean is usually larger at vertical (VV) than at horizontal (HH) polarization, several experiments have shown that the backscattered signal appears to be also more strongly affected by spatial wind speed variations at VV than at HH, while signatures of oceanic features are often better visible at HH polarization.

Astonishing examples of this behavior have been obtained from a Russian airborne real aperture radar within the framework of the Joint US / Russia Internal Wave Remote Sensing Experiment (JUSREX-92) in the New York Bight [1,2]: Under stable atmospheric conditions, signatures of internal waves were clearly visible at both HH and VV polarization. However, under unstable atmospheric conditions, some pairs of images acquired simultaneously at HH and VV show dominant signatures of internal waves at HH but dominant signatures of wind variations at VV – the two images can look completely different. An example is shown in Fig. 1. The radar frequency was 13.3 GHz (K_u band), and the incidence angle was between 72° and 84° from nadir.

Common radar imaging models are not designed for such large incidence angles, thus they are not necessarily expected to be capable of reproducing the JUSREX images. However,
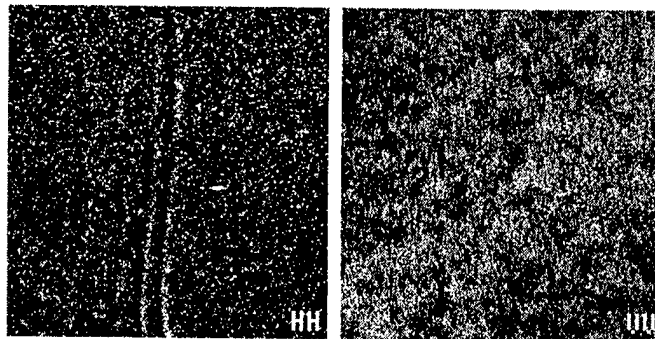
Fig. 1: Example of a pair of radar images acquired simultaneously at HH (left) and VV polarization (right) under unstable atmospheric conditions during JUSREX-92 (from [2]); radar look direction: from bottom to top, downwind.

as pointed out in [1], a similar dependence of radar signatures of oceanic and atmospheric features on polarization has also been observed at other radar frequencies and incidence angles, for which well-established and trustworthy backscattering models exist. It will be shown in this paper that the observed effects can be at least qualitatively explained within the framework of a two-dimensional composite surface scattering model based on Bragg scattering theory.

THEORY

It is generally accepted that the radar return from the ocean results – if no rain or other major atmospheric scatterers are present – from an interaction between the electromagnetic waves and the water surface. Thus both wind- and current-induced radar signatures must be associated with a modulation of the surface roughness, i.e., of the ocean wave spectrum. At moderate incidence angles between approx. 20° and 70°, the dominant backscattering mechanism is Bragg scattering, i.e., the backscattered power is proportional to the intensity of ocean waves of wavelength comparable to the electromagnetic wavelength [3]. Since these "Bragg" waves must be the same for all polarizations, it is not obvious why different radar signatures should be observed at HH and VV.

In addition to "ideal" Bragg scattering, a composite surface model accounts for the effect of tilt modulation of the Bragg scattering facets and hydrodynamic modulation of the Bragg wave intensity by all ocean waves which are long compared to the Bragg waves. The fact that the variation of the NRCS with the incidence angle – and thus with the surface slope – de-

pends on the polarization results in different contributions of the long waves to the NRCS at HH and VV.

In the composite surface model developed at the University of Hamburg [4], these contributions are represented by a number of second-order terms of the NRCS which depend on the mean square slopes of the ocean surface parallel and normal to the radar look direction. It is shown in [4] that, after some minor optimization, this model can reproduce the observed dependence of mean NRCS values on radar frequency, polarization, incidence angle, wind speed, and azimuthal radar look direction with respect to the wind direction quite well for wide ranges of these parameters.

Details of the composition of the NRCS according to the proposed model as well as the characteristics of theoretical radar signatures of underwater bottom topography in tidal waters are discussed in another paper [5]. For this analysis, modulated wave spectra are calculated by integrating the equations of weak hydrodynamic interaction theory (see, for example, [6]). It is shown that

- the relative contribution of the second-order terms of the NRCS increases with radar frequency and can, at higher frequencies like 10 GHz (X band), be comparable to the contribution of the zeroth-order Bragg scattering term;
- this contribution is, furthermore, larger at HH than at VV, particularly at large incidence angles;
- the inclusion of the second-order terms can lead to an increase of the modulation of the NRCS by surface current gradients by an order of magnitude, since waves at wavelengths in the decimeter to meter range are much more strongly modulated than the short ripples which act as Bragg waves at high frequencies;
- at high radar frequencies, large incidence angles, and low wind speeds, the theoretical modulation of the NRCS can be more than twice as strong at HH than at VV;
- finally, even current gradients normal to the radar look direction can modulate the NRCS significantly via its second-order terms, although no direct modulation of the Bragg waves takes place.

In contrast to current gradients over scales of several decameters or more, which modulate mainly waves of wavelengths in the decimeter to meter range, variations in the wind field over comparable scales will mainly affect the high-wavenumber range of the ocean wave spectrum, i.e. the Bragg wave range. Since all terms of the NRCS are proportional to the Bragg wave intensity, the theoretical effect of wind speed variations will exhibit a much less pronounced polarization dependence than the effect of current. This will be shown in the following section.

MODEL PREDICTIONS

Fig. 2a shows a typical surface current pattern as encountered over internal waves during JUSREX-92, where a typical phase speed of the internal wave is 0.7 m/s. Fig. 2b shows a
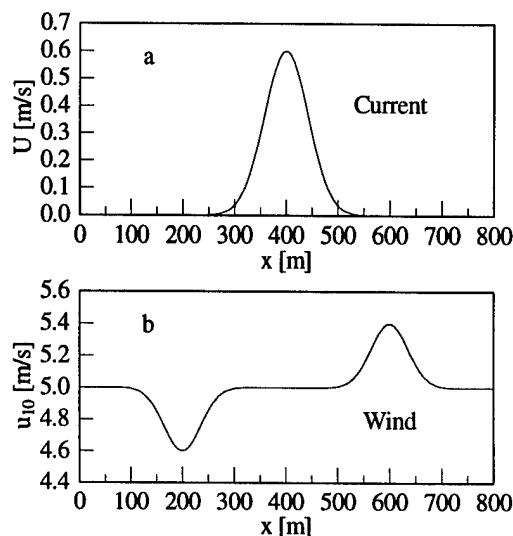
Fig. 2: Surface current (a) and wind speed (b) in x direction as function of x, as assumed for our model calculations.

wind pattern which has been chosen for the following comparison of current- and wind-induced effects. Both the current field (in combination with a constant 5 m/s wind blowing in various directions with respect to the current) and the wind field (in absence of any current) were fed separately into a numerical model for the computation of modulated wave spectra as described in [5]. The resulting two-dimensional spectra were converted into NRCS values for a frequency of 15 GHz, a large (but reasonable) incidence angle of 65°, and various azimuthal look directions, using the composite surface model described in [4]. The resulting "modulation ratio" for each scenario, i.e. the ratio between maximum and minimum NRCS values in each radar signature, is shown in Fig. 3.

Fig. 3a shows that the modulation associated with the current feature is always clearly larger at HH than at VV – particularly if the radar look direction is normal to the current gradient (90°, 270°), where practically no VV signatures are present (modulation ratio ≈ 1). The dependence of the radar signatures on the wind direction is found to be significant but only of minor importance for the problem considered here.

Fig. 3b shows the modulation of the Bragg waves (and, thus, of the zeroth-order term of the NRCS) by the current feature, which is practically negligible compared to the modulation of the total NRCS at HH polarization. In contrast to this, the modulation caused by the wind feature is almost the same for the total NRCS at HH and VV and for the Bragg waves, as shown in Fig. 3c.

DISCUSSION

The fact that radar signatures of oceanic features are better visible at HH than at VV polarization is consistent with model predictions. In contrast to this, the proposed composite surface model predicts polarization-independent signatures of atmospheric features, but it cannot explain stronger signatures
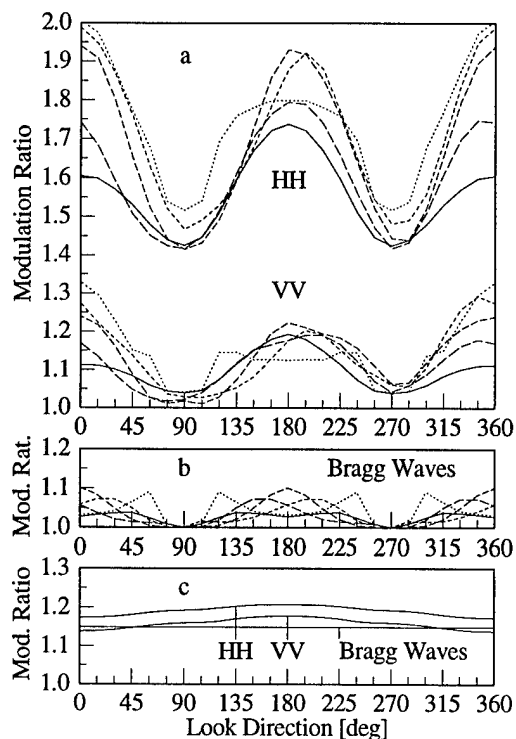
Fig. 3: Theoretical modulation ratios vs. azimuthal look direction; a) NRCS modulation at HH and VV for the current feature of Fig. 2a, b) corresponding Bragg wave modulation, c) NRCS and Bragg wave modulation for the wind feature of Fig. 2b; wind direction: solid – 0°, dashed – 45°, 90°, 135°, dotted – 180°, where 0° means "towards positive x".

at VV than at HH and may thus be not completely convincing in view of observations as encountered during JUSREX-92.

It is common practice, however, to set the greyscales of radar images such that the darkest and brightest pixels are mapped to black and to white, respectively. Images at HH and VV which look completely different after such procedures may have completely different dynamical ranges. Choosing appropriate current and wind conditions and radar parameters, it is in fact possible to obtain images from the proposed model which exhibit the observed phenomenon if they are displayed this way. In particular, the scenario of the images shown in Fig. 1, where the radar look direction is downwind and along an internal wave crest, is well suited for such model results.

Fig. 4 shows a pair of simulated images for a combination of the current of Fig. 2a and the wind of Fig. 2b blowing normal to the current. These conditions are close to the conditions corresponding to Fig. 1. Displayed in the aforementioned way, the images show a dominant internal wave signature at HH and dominant atmospheric signatures at VV.

It is not clear at the present stage of research whether this can really be considered a satisfactory explanation for the observed phenomena. However, the model results discussed in this work may give some valuable contribution to a better understanding of the involved physical and technical effects.
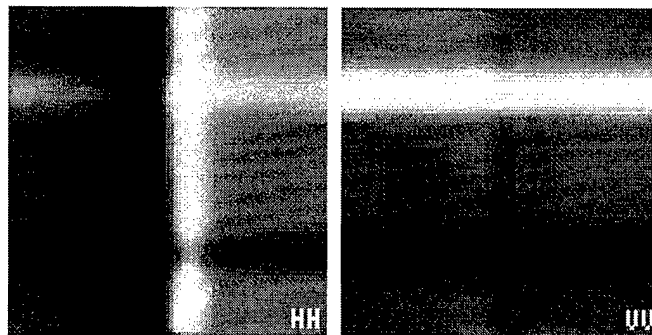
Fig. 4: Simulated radar images at HH (left) and VV polarization (right) of an oceanic current variation in x direction and a wind speed variation in y direction; radar look direction = y direction (i.e. from bottom to top); cf. Fig. 1.

ACKNOWLEDGMENTS

REFERENCES

[1] R.F. Gasparovic and V.S. Etkin, "An overview of the Joint US / Russia Internal Wave Remote Sensing Experiment", Digests IGARSS '94, vol. II, 1994, pp. 741-743.

[2] V.S. Etkin, Yu.G. Trokhimovski, V.V. Yakovlev, and R.F. Gasparovic, "Comparison analysis of Ku-band SLAR sea surface images at VV and HH polarizations obtained during the Joint US / Russia Internal Wave Remote Sensing Experiment", Digests IGARSS '94, vol. II, 1994, pp. 744-746.

[3] G.R. Valenzuela, "Theories for the interaction of electromagnetic and ocean waves – a review," Boundary Layer Meteorol., vol. 13, 1978, pp. 61-85.

[4] R. Romeiser, W. Alpers, and V. Wismann, "An improved composite surface model for the radar backscattering cross section of the ocean surface, 1. Theory of the model and optimization / validation by scatterometer data", J. Geophys. Res., in press, 1997.

[5] R. Romeiser and W. Alpers, "An improved composite surface model for the radar backscattering cross section of the ocean surface, 2. Model response to surface roughness variations and the radar imaging of underwater bottom topography", J. Geophys. Res., in press, 1997.

[6] W. Alpers and I. Hennings, "A theory of the imaging mechanism of underwater bottom topography by real and synthetic aperture radar", J. Geophys. Res., vol. 89, 1984, pp. 10,529-10,546.
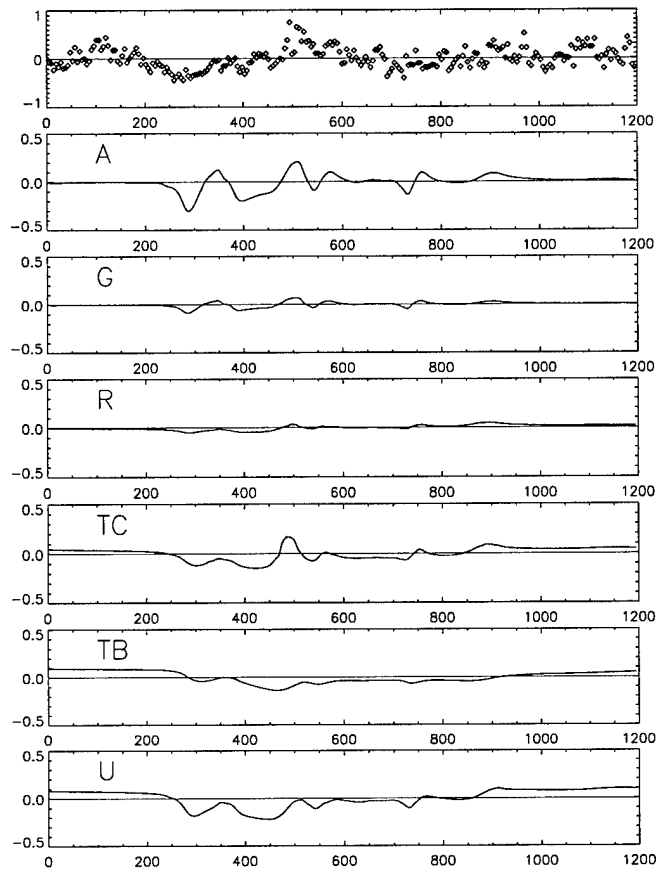
DYNAMICS AND STATISTICS OF INTENSE INTERNAL WAVES OVER A CONTINENTAL SLOPE

Tatjana Talipova and Efim Pelinovsky,
Institute of Applied Physics, 46 Uljanov Str., 603600, Nizhny Novgorod, Russia.
Fax: +(8312) 365976, Email: tata@appl.sci-nnov.ru
Peter E. Holloway
School of Geography and Oceanography, University College,
University of New South Wales, Australian Defence Force Academy,
Canberra ACT 2600 Australia.
Fax: 61 6 2688313, Email: p-holloway@adaf.oz.au

Abstract

Nonlinear effects are essential to internal waves because of to small speed of propagation, and nonlinear internal waves are recorded by remote sensing from space and direct measuring very often. In particular, the evolution of the semi-diurnal internal tide as it propagates across the Australian North West Shelf (NWS) leads to the formation of groups of solitons and hydraulic jumps. A numerical solution to the generalised Korteweg-de Vries (K-dV) equation, including quadratic and cubic nonlinearities, horizontal variability and dissipation, is used to model the evolution of an initially sinusoidal long internal wave, representing an internal tide. The model shows the development of shocks and solitons as it propagates shorewards over the continental slope and shelf. The inclusion of quadratic bottom friction in the model is investigated along with the dependence on initial wave amplitude and temporal and spatial variability in the coefficients of nonlinearity and dispersion. Friction is found to be important in limiting the amplitudes of the evolving waves. The model is run using observed hydrographic conditions from the NWS. Model results are compared to current meter and thermistor observations from the shelf-break region and demonstrate good agreement with wave amplitude and waveform. Measurements of current fluctuations due to internal waves obtained on the NWS have been analysed with the aim of calculating the probability of short-scale, large-amplitude internal waves. The exceedance probability has been calculated using Poisson statistics.

Extended Korteweg - de Vries Equation for an Internal Wave Field

The K-dV equation is well known as an appropriate physical model for the description of the nonlinear and dispersive properties of an internal wave field (Pelinovsky et al.,1994; Holloway et al, 1997). It is derived as a perturbation expansion and is valid to first order in wave amplitude and for long waves, i.e. it is assumed that $H/\lambda << 1$ and $a/H << 1$, where H is the local water depth, λ is a representative wavelength and a is a representative wave amplitude. For arbitrary vertical stratification of ocean density and background shear flow, the K-dV equation is written as

$$\frac{\partial \eta}{\partial t} + (c + \alpha \eta + \alpha_1 \eta^2)\frac{\partial \eta}{\partial x} + \beta \frac{\partial^3 \eta}{\partial x^3} = 0, \quad (1)$$

where $h(x, t)$ is the vertical displacement of the pycnocline, x is the horizontal co-ordinate, and t is tyme. The parameters α, β and c are coefficients of nonlinearity, dispersion and phase speed of long internal waves, respectively. They are determined by the background density and horizontal velocity profiles and are defined as (in the Boussinesq approximation)

$$\alpha = \frac{3}{2}\frac{\int (c - U)^2 (d\Phi / dz)^3 dz}{\int (c - U)(d\Phi / dz)^2 dz}$$

$$\beta = \frac{1}{2}\frac{\int (c - U)^2 \Phi^2 dz}{\int (c - U)(d\Phi / dz)^2 dz}, \quad (2)$$

where z is a vertical co-ordinate, positive upwards. The formula for α_1 is too complicated and omitted here. The phase speed of a linear long wave c and the vertical structure of vertical-displacement amplitude of a wave mode $\Phi(z)$ are determined by the solution of the eigenvalue problem

$$\frac{d}{dz}\left[(c - U)^2 \frac{d\Phi}{dz}\right] + N^2(z)\Phi = 0, \quad \Phi(0) = \Phi(H) = 0 \quad (3)$$

where $N(z)$ and $U(z)$ are the Brunt-Vaisala frequency and the background shear current and the value of $\Phi(z)$ is normalized by its maximal value. Then $\eta(x, t)$ is the isopycnal surface with maximum displacement.

Usually, for calculations of the coefficients of the K-dV equation only a single vertical profile of stratification is used assuming the density to be horizontally uniform. Analysis of Ivanov et al. (1992), made without shear flow for the deep water region of the Mediterranean, has shown that

the variability of the parameters c and β is related mainly to variability in water depth, but the nonlinear parameter is very sensitive to variations of the vertical stratification. The shelf/slope zone is generally characterized by large bottom slope and large variations in stratification and shear flow, and using mean stratification, can be inaccurate in the calculation of α, β and c. The analysis shows strong spatial variability in all coefficients which influence the variability of the internal wave field. Account must be taken of the horizontal variability of the ocean medium and accordingly the K-dV equation must be modified in the following way. If the horizontal variability is smooth the reflection of the wave energy from the shelf can be ignored and a solution can be sought for the vertical displacement of the pycnocline in the form $\eta(x, t)$, $\Phi(z, \varepsilon x)$, where Φ is again the vertical structure of the pycnocline displacement, found from (3), and the small parameter e characterizes the smoothness of the horizontal inhomogeneity of the ocean medium. Again using the asymptotic procedure the following equation (a generalized form of (1)) can be obtained,

$$\frac{\partial \xi}{\partial x} + \left(\frac{\alpha}{c^2\sqrt{Q}}\xi + \frac{\alpha_1}{c^2 Q}\xi^2\right)\frac{\partial \xi}{\partial s} + \frac{\beta}{c^4}\frac{\partial^3 \xi}{\partial s^3} +$$

$$+ \frac{kc}{\beta\sqrt{Q}}\xi|\xi| - \frac{v}{c^3}\frac{\partial^2 \xi}{\partial s^2} = 0 \qquad (4)$$

where

$$Q = \frac{c^2 \int\limits_{-H}^{0} (c - U)(d\Phi / dz)^2}{c_0^2 \int\limits_{-H}^{0} (c_0 - U_0)(d\Phi_0 / dz)^2} \qquad (5)$$

and values with index "o" are the values at any fixed point x_0. The substitutions s and x are:

$$s = \int\limits_{0}^{x} \frac{dx}{c(x)} - t \qquad (6a)$$

$$\xi = \eta \sqrt{Q(x)} \qquad (6b)$$

The propagation of an internal wave in the coastal zone is accompanied by energy losses due to the bottom friction and vertical and horizontal diffusion. In this paper, two forms of damping of the internal wave are considered. The first is related to the boundary-layer viscosity, where the turbulent boundary layer is parametrized by the empirical expression for the bottom friction stress in the Chezy form and the second is related to the viscosity of the fluid as a whole.,

The generalized K-dV equation (4) is the basic model used for the internal tide transformation on the NWS. Physically, the boundary problem of the spatial transformation of the internal wave which is periodical in

time is studied. Mathematically this is an initial value problem for equation (4), where the evolution coordinate is the spatial coordinate.

The example of the internal tide transformation on the North West Australian shelf is shown on the Figures 1-3. The initial form of internal wave is chosen as sinusoidal wave with amplitude 10 m on the depth 1300m on the continental slope. The effects of only quadratic nonlinearity and both of quadratic and cubic nonlinearity are shown on the Fig. 1. It is important for this shelf that as quadratic so as cubic nonlinear terms change their sign cross the break zone and the cubic effects are very significant where quadratic nonlinear coefficient is close to zero. Dashed line presents the wave form after internal tidal wave propagating shorewards over slope and shelf (the wave way is about 90 km) without cubic effects, only the quadratic nonlinearity is taken into account here. The solid line is corresponding the case when the cubic nonlinearity is included to the numerical scheme too. The great difference between lines allows us to speak about the great significance of the cubic nonlinear term effects for the internal wave transformation shorewards over the shelf.
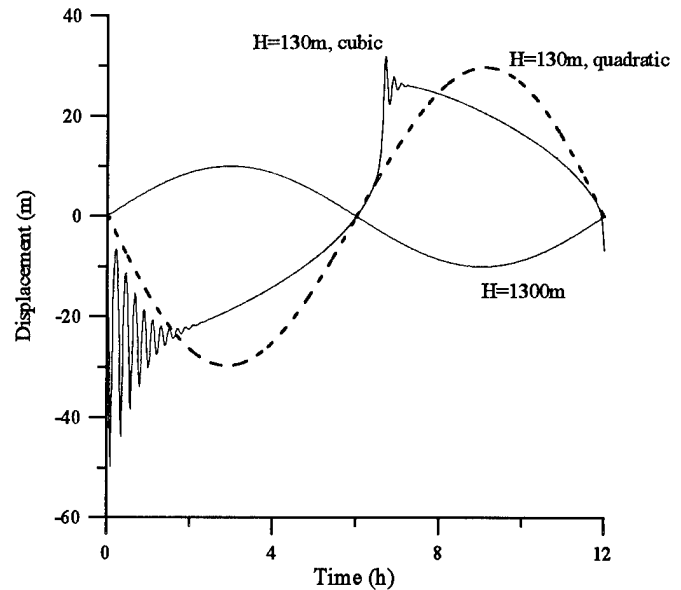
Fig. 1. The internal tidal wave form on the break zone with depth H=130m for the case when only quadratic nonlinearity is valid in the numerical scheme (dashed line) and for case when both of nonlinear terms are valid (solid line).

Figures 2 and 3 show the difference in the wave form in the shelf zone (the wave way is 113 km) between the case when we take into account only the quadratic nonlinear term (Fig. 2) and the case when we take both of terms (Fig. 3). The initial sinusoidal wave is transformed into soliton like wave group for the both cases. The small number of solitons on the Fig. 2 is due to the small quadratic nonlinear term in this

Fig. 3 is connected with the strong nonlinear effects (significant cubic nonlinear term) for internal waves in the shelf zone. The initial sinusoidal wave is shown on the all of figures.
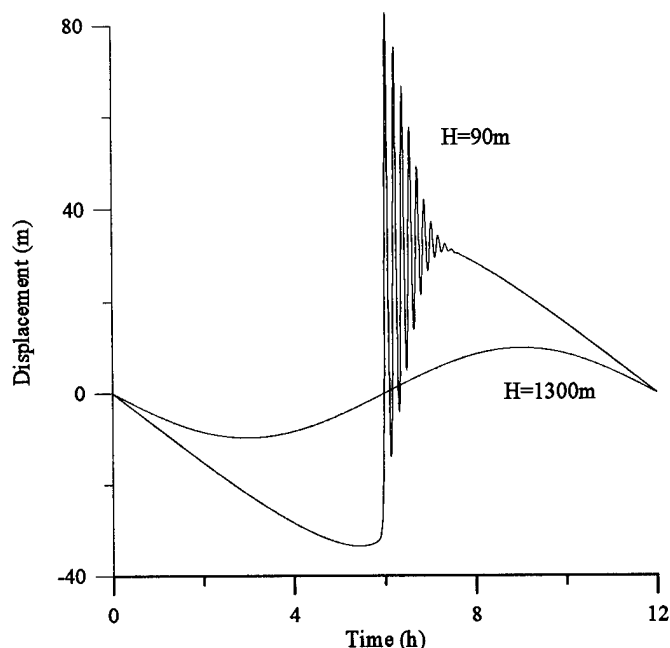
Fig.2 The internal tidal wave form on the shelf zone with depth H=90m for the case when only quadratic nonlinearity is valid in the numerical scheme.
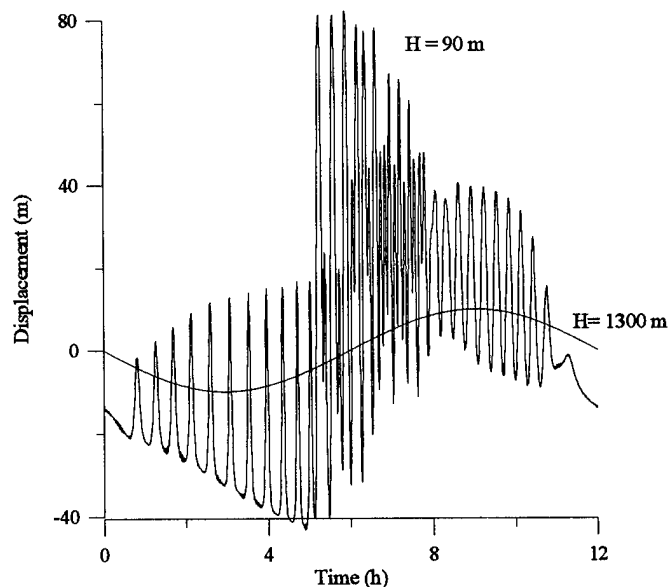
Fig.3 The internal tidal wave form on the shelf zone with depth H=90m for the case when both of quadratic and cubic nonlinearities are valid in the numerical scheme.

The results of the analysis of extreme characteristics of the internal wave field for NSW are summarised by Pelinovsky et al, 1995, and for other areas of the World Ocean (the Tropical part of Atlantic Ocean, the Levant (Mediterranean) sea), in the papers by Ivanov et al, 1993, 1994; Pelinovsky et al, 1995.

Acknowledgments

References

Ivanov V.A., Pelinovsky E.N., Talipova T.G. The Long-Time Prediction of Intense Internal Wave Heights in the Tropical Region of the Atlantic. J. Physical Oceanogr., 1993, v.23, No 9, 2136 - 2142.

Ivanov V.A., Pelinovsky E.N., Talipova T.G. Appearance Frequency of Internal Waves in the Mediterranean. - Oceanology, 1993, v.33, N. 2, 180 - 184.

Ivanov V.A., Pelinovsky E.N., Talipova T.G., Trojitskaya Yu.,I. The Geographical and Statistical Estimations of Nonlinear Parameters of Long Internal Waves near the Crimea Beach. Physical Oceanography, 1994, No 4, 9-17.

Holloway P. Internal hydraulic jumps and solitons at a shelf break region on the Australian North West Shelf. J. Geophys. Res., 1987, v. C95, 5405-5416.

Holloway P., Pelinovsky E., Talipova T. A Nonlinear Model of Internal Tide Transformation on the Australian North West Shelf, J. Physical Oceanography, 1997, v. 27, N. 6, 871 - 896..

Pelinovsky E.N., Stepanyants Yu.A., Talipova T.G. Modeling of Propagation of Nonlinear Internal Wave in Horizontal Inhomogeneous Ocean Izvestija Atmospheric and Oceanic Physics, 1994, v.30, No.1, 79-85.

Pelinovsky E., Holloway P., Talipova T. A statistical analysis of extreme events in current variations due to internal waves from the Australian North West Shelf. J. Geophys. Research}, 1995, v. 100, N. C12, 24,831 - 24,839.

Pelinovsky E., Talipova T., Ivanov V. Estimations of Nonlinear Properties of Internal Wave Field off the Israel Coast. Nonlinear Processes in Geophysics, 1995, v. 2, N. 2, 80 - 88.

Smyth N., Holloway P. Hydraulic jump and undular bore formation on a Shelf Break. J. Phys. Oceanogr., 1988, v. 18, 947-962.

Spectral Nonlinearities of the Gravity-Capillary Waves and their Effect on Sea Surface Radar Signatures

Petros J. Pavlakis
Hellenic National Centre For Marine Research
Ag. Kosmas - Hellenikon, GR. 16604 Athens - Greece
Phone:+301-9820212, Facsimile: +301-9833095, E-mail: ppavla@posidon.ncmr.ariadne-t.gr

Abstract -- To investigate the effect of the nonlinear wave-wave interactions, on the gravity-capillary spectral form, and to draw conclusions for the geophysical interpretation of sea surface SAR imagery, a numerical study has been carried out. Spectral anomalies, strongly susceptible to influences by oceanographic features (e.g. slicks or currents) are shown. These are narrow bands, of wind dependent energy depressions, related to the excitation of capillary waves. The more enhanced of them appear at the early stages of the spectrum development, in the neighborhood of 100 rad/m wave numbers. An opposite surface current or a slick accentuate them, while they become weaker at mature spectral stages, and by the induced wind drift current.

INTRODUCTION

In reducing the geophysical ambiguity, of the sea surface SAR imagery interpretation, the apprehension of the hydrodynamics dominating the still unclear gravity-capillary wave spectral region is important. For the currently in orbit SAR sensors, this region provides the constructive reinforcement of the backscattered electromagnetic field, due to the Bragg scatterering mechanism. Nevertheless a practical description of the gravity-capillary spectral form dynamics, is a prerequisite for optimum use and operational products, of coincident multiband SAR data, that will be the near-future of the spaceborne SAR surveillance.

Central of this description is the radiation equation (1), which yields in deep water the evolution in time t and space x, of the energy budget F, at each wave number k.

$$\partial F(k) / \partial t + (Cg+U)\nabla x\, F(k) = Sin + Snl - Sb - Sv \quad (1)$$

Here Cg stands for the wave group velocity and U for the velocity of the underlying current. Sin, Snl, Sb and Sv are source functions representing the wind forcing, the transferred energy among the waves by nonlinear resonant interactions, and the dissipation by breaking and viscosity respectively. In the gravity-capillary region, the spectral modification by nonlinear interactions is dominantly of second order (three-wave) [1]. This very short scale in time and fetch process, compared to that of four-wave interactions, is responsible for the excitation of capillary ripples, consuming energy from the short gravity waves. Therefore it bears a considerable effect on the gravity-capillary spectral form. Nevertheless in the open sea i.e. at large fetch and time scales, experimental data indicate [2], that the third order nonlinear interactions among four pure gravity waves, may also have a minor but measurable effect on the spectral form. In order to investigate the spectral shaping effect of these nonlinear mechanisms, a sequence of experimental computations have been attempted. Here numerical results, concerning the wind dependent development, of the gravity-capillary spectral region at its equilibrium state, are presented. The nonlinear features of the spectral form are discussed, as well as the influence of a surface current and of a monomolecular slick on them.

BRIEF DESCRIPTION OF THE NUMERICAL MODEL

Background in describing the source terms Sin, Sb and Sv was the theory of [3]. It assumes already initialized wave field, and employs the local balance between wind forcing and dissipation. Its key feature is the parameterization of Sb to account for the breaking dissipation, of both the gravity and capillary wave modes. In the present work the parameters of Sb were slightly adjusted to approximate the spectral slope derived by the empirical model of [4]. Following the consideration of [5], on the dynamic excitation of the capillary spectral tail, the second order nonlinear energy transfer Snl, has been numerically incorporated in (1), using the description given by [1]. The explosive type of short waves, that come almost instantaneously to the equilibrium level, permits for practical purposes to consider initially fetch limited waves. Thus starting with an initial spectral form, derived by the empirical model of [4], and assuming at the first run only three-wave interactions, (1) has been numerically integrated over the 1D wave number space up to 864 rad/m. The integration has been repeated, to cover a range of wind speeds from 3 to 15 m/sec. Stabilized spectral forms were reached after about 20 m of fetch. Consequently assuming unbounded sea and time limited waves, the resulted forms was used as initial conditions to study its modification, in time by the effect of four-wave nonlinear interaction. For the computation of the third order Snl the procedure given by [6], reduced in 1D was used, and the integration took place over the wave number space up to 157 rad/m. As minimum grid interval for both runs, the $\pi/2$ rad/m was selected. For the slick-covered sea surface, the theory given in [2] of wave damping due to monomolecular films was applied. In the case presented here, the rheological parameters of a SPAN film (sorbitane - mono -

Z- 9 - octadecen - 1 - oic acid ester) given in [7], were used in order to test the numerical results, against the open sea experimental radar backscattering data published by [7].

NUMERICAL RESULTS AND DISCUSSION

Fig.1, shows as a surface presentation, the development with the wind of a 20m-fetch gravity-capillary energy spectrum, derived by the first run. The spectral shapes are in closed approximation, to the spectra derived by measurements in tanks of large fetches, as those presented in [4]. In greater detail the spectra show, the high-frequency "roll-off" starting near 100 rad/m, the secondary high wave number maximum between 600 to 800 rad/m, that grows upwards from the "roll-off", and the wind-dependent growth of this secondary maximum, that rises rapidly at low wind speeds, but reaches saturation at higher ones (Fig.2).

One also feature is turned out here. This concerns the spectral disturbance at the beginning of the "roll-off", near 100 rad/m. It appears as a sequence of narrow-band energy depressions, implying that some wave numbers lose selectively higher amounts of energy, for the excitation of the capillary waves. The relatively high energy drop in these bands, and their constant spectral location in the region of the "Bragg scatterers" probed by the currently in orbit SAR sensors (e.g. 76-97 rad/m for ERS-C-Band SAR), give them a particular significance. It turns out, as shown on fig.2, that the strength of the energy drop in these bands is wind dependent. It is weaker at low, stronger at moderate, and weak again at higher wind speeds. This is attributed to the fact that at low wind speeds the capillary ripples are not well developed, and consume via (Snl) lower amounts of energy from the short gravity waves. When the capillary waves approach saturation, at moderate wind speeds, the amount of energy consumption increase drastically, and the spectral

Fig.2. Overshoot effects at a) k=100 rad/m b) k=138 rad/m.
c) Saturation of capillary maximum at k=740 rad/m.

energy drops at these bands, resulting to a kind of overshoot effect (Fig.2). At higher wind speeds, the consumed energy is balanced again by the wind input Sin.

Fig.3 and 4, show spectral forms at 5m/sec wind speed, for current free (early state), and wind induced current conditions (mature state). Note that at current conditions, the energy drop near 100 rad/m is reduced. Numerically it is due to the factor U in (1), that intensifies or reduces the shaping effect of the integration, depending on its sign with respect to Cg. The geophysical implication is that a C-Band SAR will "see" a wind-excited sea surface, brighter when the wind drift current is established, than when the wind starts to blow. On the contrary, an opposite U enhances the energy drop in this spectral region, thus it will make the influenced sea surface to show darker. Superimposed also on fig.3 and 4 are the resulted spectral forms, of the second

Fig.1. Modeled gravity-capillary energy spectrum development with the wind.
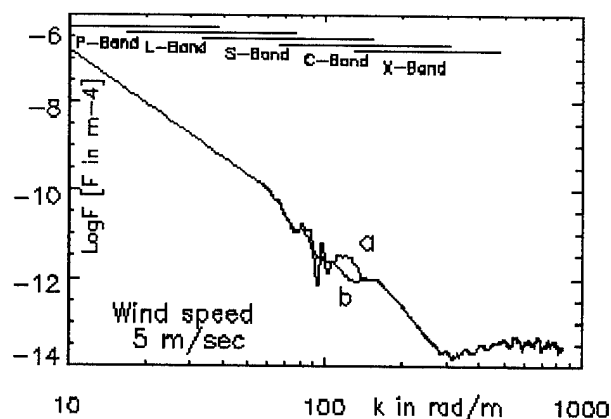
Fig.3. a) Gravity-capillary spectral form derived from the first run (three-wave interactions only), assuming current free conditions (early state). b) Effect of four-wave interactions after min. The Bragg wave spans for the several radar bands appear at the top.

1333
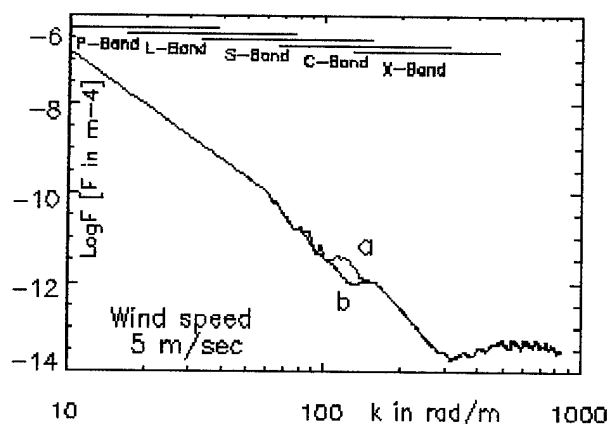
Fig.4. Same as in fig.3, but incorporating the effect of a 0.1 m/sec wind drift current (mature state).

Fig.6. Contrast curve of spectral forms a and c of fig.5. The radar backscattering data (triangles) are from [7].

integration run, for the effect of four-wave interactions. As it appears, this mechanism smoothes out gradually in time the sharp energy dispersions near 100 rad/m, refilling them with energy, from the neighboring spectral regions. Thus as the waves develop with time this spectral anomaly is modified to a broad shallow spectral trough, expanded slowly towards lower wave numbers, since the wind forcing bounds to some extent its expansion at high wave numbers. Geophysicaly it implies, that at large angles of incidence, an excited sea under moderate winds, may show brighter at extreme SAR bands (e.g. P and C-X), and darker at intermediate (e.g. S and/or L). However when a drift current is established, this effect will be reduced. The severe impact of a slick on the spectrum is shown on fig.5. Here aside to the spectrally broad wave damping, at high wave numbers (Marangoni effect), the energy drop at the nonlinear singularity near 100 rad/m is considerably increased. Thus since the amount of energy for the refilling process, via four-wave interactions is greater, it results to a faster expansion of the spectral trough

Fig.5. Effect of a SPAN slick on the spectrum. a) First run for clean sea. b) First run for slick-covered sea. c) Effect of four-wave interactions (second run).

towards lower wave numbers. The contrast curve, of this slick-modified spectrum to the clean-sea one, is presented in dB on fig.6, and it is in sound agreement with the published by [7], radar backscattering data over a SPAN slick.

REFERENCES

[1] K. van Gastel, "Nonlinear Interactions of Gravity-Capillary Waves: Lagrangian Theory and Effects on the Spectrum", J. Fluid Mech., 182, pp.449-523, 1987.

[2] W. Alpers and H. Huhnerfuss, "The damping of ocean waves by surface films: A new look at an old problem", J. Geophys. Res., 94, pp.6251-6265, 1989.

[3] M. A. Donelan and W. J. Pierson Jr., "Radar Scattering and Equilibrium Ranges in Wind-Generated Waves with Application to Scatterometry", J. Goephys. Res., 92, pp.4971-5029, 1987.

[4] J. R. Apel, "An Improved Model of the Ocean Surface Wave Vector Spectrum and its Effects on Radar Backscatter",J. Geoph. Res., 99, pp.16269-16291, 1994.

[5] K. M. Watson and J. B. Mcbride, "Excitation of capillary waves by longer waves", J. fluid Mech., 250, pp.103-119, 1993.

[6] D. Resio and W. Perrie, "A Numerical Study of Nonlinear Energy Fluxes due to Wave-Wave Interactions. Part 1. Methodology and Basic Results", J. fluid Mech., 223, pp.603-629, 1991.

[7] H. Huhnerfuss, A. Gericke, W. Alpers, R. Theis, V. Wismann and P. A. Lange, "Classification of sea slicks by multifrequency radar techniques: New chemical insights and their geophysical implications", J. Geophys. Res., 99, pp.9835-9845, 1994.

ACKNOWLEDGMENTS

Radar and Optical Measurements of Damping of Small-Scale Wind Waves in Artificial Slicks

S.A.Ermakov, E.M.Zuikova, I.A.Sergievskaya, Yu.B.Shchegolkov, S.V.Kijashko, A.G Luchinin
(Institute of Applied Physics, Russian Academy of Sciences, 46 Ulyanova St.,
603600, Nizhny Novgorod, Russia)
J.C.da Silva
(Dept. of Oceanography, University of Southampton, Southampton Oceanography
Centre, European Way, Southampton SO14 3ZH, UK)
N.Stapleton, and J.C.Scott
(Defence Research Agency, Winfrith Technology Centre, Winfrith Newburgh Dorset DT2 8XJ)

Abstract[1] — Damping of short centimetre-millimetre (cm-mm)-scale wind waves was studied during experiments conducted from a platform in the Black Sea. During the experiments artificial organic slicks were observed using Ka-band and X-band radars and using Optical Spectrum Analysers. Film sampling from the artificial slicks with small nylon nets was also performed and the film elasticity was later estimated from laboratory measurements of wave damping. One of the experiments was conducted during an ERS-2 satellite overpasss and the slick was imaged by the C-band ERS-2 SAR. It is shown that damping of mm-scale waves exceeds the damping of cm-dm-waves and exhibits a maximum at surface wavelengths about 5-7 mm. The maximum is assumed to be a manifestation of a new nonlinear mechanism of damping of "parasitic" capillary ripples generated on the slopes of decimetre (dm)-scale wind waves.

INTRODUCTION

It is well-known that organic films effectively damp short surface waves forming slicks on the sea surface. The problem of wave damping has a very long history and has been studied in a great number of papers (see, e.g. [1,2]). Nowadays the problem of wave damping is important, since marine slicks are often clearly discernible in radar satellite images of the sea surface and can therefore be used to detect and to characterize sea surface areas covered by films due to biological productivity or pollution.

Previous radar and optical measurements of damping of wind waves in slicks were carried out for dm-cm-scale waves larger than 2-3 cm (see, [3,4] and cited literature). For very short millimetre-scale surface waves the hydrodynamic theory of damping of freely propagating gravity-capillary waves (see, e.g. [5]) predicts that the damping effect should be weak even for highly elastic films. However, some

previous observations with Ka-band radars (see, [6]) indicate that wave damping is expected to be strong at wavelengths of about 10 mm and shorter.

Here optical and radar observations of damping of cm-mm-scale waves in organic slicks are presented. It is shown that the damping in the wavelength range of interest is very strong, and exceeds the damping for longer waves with maximum damping occurring at wavelengths of around 5-7 mm.

EXPERIMENT

Experiments with artificial slicks were carried out on the Black Sea from the Oceanographic Platform of the Marine Hydrophysical Institute in May-June, 1996. The Platform is located about 0.5 km to the south of the Crimean coast, the Platform coordinates are $34^0 1'$ E; $44^0 24'$ N. The water depth near the Platform is 30 metres. The following measuring apparatus was used in the experiments.

- Two Optical Spectrum Analysers (OSA) which measure the wavenumber spectrum of surface waves. The OSA instruments can be used to measure the surface wavenumber slope spectrum along an arbitrary surface wavevector direction. The wavelength range of the measured wind-wave spectrum at incidence angle of 60^0 was from 5.5 cm to about 50 cm for one of the OSA, and from 3.5 cm to 3.5mm for the other.

- A coherent Ka-band scatterometer (the radar wavelength is 0.8 cm, the incidence angle was 60^0)

- A coherent X-band scatterometer (the radar wavelength is 2.56cm, the incidence angle was varied from 18^0 to 23^0).

Both the scatterometers permit us to measure the power and the Doppler shift of backscattered signals.

Artificial slicks were created from a small rubber boat or from the Platform. The following surface-active substances were used: oleyl alcohol (OLA), oleic acid (OLE), sunflower oil (SO) and polymer Emkarox. The substances (except SO) before spreading on the sea surface were dissolved in pure alcohol (ethanol), the typical substance concentrations were about 10- 100 g/l.

Sampling of surfactants from the slicks after spreading was carried out from the boat with small nylon nets. The surfactants were washed out from the nets with pure alcohol and were kept in small containers. Then the dissolved surfactants were spread on water in the laboratory and the damping coefficient of standing surface waves at given frequencies was measured directly. The film elasticity parameter was estimated when comparing the measured relative damping coefficient with the theory [5]. Some estimates for the film elasticities obtained are given in the following Table together with environmental and instrument information. During 2nd June 1996 when ERS-2 imaged the Black Sea and the oceanographic platform about 3.5 litre of sunflower oil was poured on the sea surface around half an hour before the ERS-2 overpass. At the time of the ERS-2 image the slick dimensions were roughly 100-200 m. During the experiment the OSA operated at a fixed surface wavelength of 6.5 mm only.

Fig. 1. Contrast in the artificial slick experiment of 02.06.96

RESULTS

Wave damping in slicks can be characterized by the contrast K defined as a ratio of the wave spectrum F(k), where k is the surface wave wavenumber (or radar backscattered power assuming Bragg scattering) outside and inside a slick, i.e.

$$K(k) = F(non-slick)/F(slick) \qquad (1)$$

The contrasts observed on 2nd June by the OSA, Ka-band and X-band radars are shown in Fig. 1. The contrasts measured by the Ka-band and X-band radars are related to the surface wave energy at corresponding Bragg wavelengths (5mm and 3.3cm, respectively). For ERS-2 SAR (the Bragg wavelength is 7 cm) the contrast estimated from the image is about 2 which is comparable with that observed by the X-band radar.

Contrasts observed on 3rd June for the OLA I,II, OLE and Emkarox slicks are presented in Fig. 2. Due to some

technical reasons the look directions of the OSA and radars in the experiments were different and their footprints were not well colocated. Therefore, since the artificial slicks on 3rd June were quite small (dimensions of order 10m-30m) some of them passed outside or only partly through the footprints of some of the devices. Consequently, radar contrasts could be estimated reliably only for the OLE slick. The obtained optical contrasts are in good agreement with radar contrasts at the corresponding Bragg wavelengths. For highly elastic films of OLA, OLE and SO the contrasts observed for mm-scale waves are very strong, and from Fig.2, can be seen to exhibit maxima in the millimetre wavelength range.

DISCUSSION

The most remarkable peculiarity of the results shown in Fig. 2 is the occurrence of a strong maximum of wave damping at wavelengths of about 5-7mm for OLA and OLE slicks. The observed maximum cannot be explained in the terms of the hydrodynamic theory of damping of freely propagating surface waves, i.e. by the so-called Marangoni

TABLE. Experiments with artificial slicks

Date	Wind speed, diraction	Surfactant	Film elasticity (mN/m)	Device look direction
02.06.96	6m/s, 270^0	SO	50-60	C-band SAR OSA (90^0) Ka-band radar (45^0) X-band radar (90^0, inc.angle 23^0)
03.06.96	4.7m/s, 70^0	OLA I, OLA II OLE Emkarox	20-30 25 8	OSA (110^0) Ka-band radar (135^0) X-band radar (90^0, inc.angle 18^0)

Fig.2. Contrasts in the artificial slick experiment of 03.06.96

It has been shown earlier in laboratory experiments [8] that the ripples are generated by dm-cm-waves (wavelengths from about 3-5cm to 25-30cm. The wavelengths of these "parasiric" ripples range from about 5-6mm and shorter, and the ripple steepness depends strongly on the steepness of the short gravity waves. We thus hypothesize that the observed strong damping of mm-scale waves results from the damping of the short gravity (cm-dm) waves by the film. For the Emkarox slick the contrasts observed for mm-waves are smaller than for the OLA/OLE slicks. This is probably due to the fact that the elasticity of the Emkarox film was smaller and damping of cm-dm-waves in the Emkarox slick was therefore weak.

REFERENCES

[1] J.C. Scott, "Surface films in oceanography, in ONRL Workshop Proceedings- Role of surfactant films on the interfacial properties of the sea surface", ed. F.L.Herr, and J.Williams, ONR Rep.C-11-86, pp.187-213, U.S.Office of Naval Research, Arlington, Va, 1986.

[2] W. Alpers, and H.Huehnerfuss, "The damping of ocean waves by surface films: A new look at an old problem", J J.Geophys. Res., vol.94 (C5), pp.6251-6266, 1989.

[3] H. Huehnerfuss, A.Gerike, W. Alpers, R.Theis, and V.Wismann, Classification of sea slicks by multifrequency radar technique: New shemical insight and their geophysical implications, J Geophys. Res., vol.99, pp.9835-9845, 1994.

[4] S.A. Ermakov, S.G. Salashin, and A.R.Panchenko, "Film slicks on the sea surface and some mechanisms of their formation", Dyn. Atmos. Oceans, vol.16 (3-4), pp.279-304, 1992.

[5] E.N. Lucassen-Reynders, and J. Lucassen, "Properties of capillary waves", Adv.Colloid Interface Sci., vol.2, pp.347-395, 1969.

[6] S.A.Ermakov, L.V.Lubjako, and S.G. Salashin, Observations of film slicks and internal waves with Ka-band scatterometer, Proc.PORSEC-'92 (Conference for Pasific Ocean Environment & Probing). vol.2, pp.1151-1154, 1992.

[7] M.S. Longuet Higgins, "The generation of capillary waves by steep gravity waves", J.Fluid Mech., vol. 16, pp.138-159,1963.

[8] S.A.Ermakov, K.D.Ruvinsky, S.G.Salashin, and G.I. Freidman, "Experimental investigation of the generation of capillary-gravity ripples by strongly nonlinear waves on the surface of a deep fluid", Izv.Atmos.Ocean Phys., vol. 22, pp. 835-842, 1986.

mechanism, since maximum damping would be expected to occur at longer, centimetre-scale wavelengths (see, [2]).The observation that maximum damping occurs at millimetre-scale wavelengths suggests that nonlinear mechanisms must be important. This could explain why maximum damping is observed for millimetre-scale ripples. It is well known that large amplitude, short-gravity waves can produce on their leading slopes so-called "parasitic" ripples (see, e.g. [7]).

Producing ground deformation maps automatically: the DIAPASON concept

DIDIER MASSONNET
Centre National d'Etudes Spatiales
18 Avenue E. Belin, 31401 Toulouse cedex 04, France
Phone: (33) 5 61-27-34-18   Fax: (33) 5 61-27-31-67
Didier.Massonnet@cnes.fr

The use of radar interferometry has now been amply demonstrated. The limits of the technique are well understood, if not always predictable. In addition, the basic signal processing procedure seems to have reached a plateau.

Further improvements can only be achieved if the number of processed scenes and the variety of experiences in the people using the technique are greatly increased. This can be done only if the access to the interferometric technique is given to a large group of users who are not necessarily radar specialists and who use standard computers or workstations.

The architecture used at CNES for interferometric processing, called DIAPASON, has been designed to be user friendly and to require minimal work through the use of standard interfaces.

Initially designed for optimal signal processing and throughput, DIAPASON proved it could run automatically in the vast majority of cases. A first course session organized in 1996 for twelve geophysicists indicated that, in one week, they could learn to use the software and to perform trouble shooting when necessary. The software has been already distributed in several laboratories and countries for industrial as well as scientific use.

Here we describe the main features of the software and its conditions of use.

BACKGROUND

Initial attempts to perform interferometric processing began in 1985, using a single sample of SIR-B data typical of an orbit-crossing (a very specific situation), the results of a specially designed airborne experiment (FOCUS), or simulated data. At that time, the complexity of the processing schemes was not a problem within a very small team of experienced people. The computing time was not a problem given the scarcity of the data available.

The situation changed completely with the availability of ERS-1 data. In our view, radar interferometry was not "predictable" in such fields as scene coherence or phenomena observability. We were convinced that most of the answers had to be obtained experimentally by taking a high level of risk. On the other hand, radar processing with satellite data, whether form ERS-1/2, J-ERS1, SIR-C or RADARSAT, proved to be very homogenous, or at least much more homogenous than the samples of data mentioned above. Having decided to process tens or hundreds of scenes, we had to design a efficient procedure from the point of view of throughput (we have no exceptionally powerful computers) and from the point of view of labor load (there were never more than three people simultaneously involved in interferometry in our team).

DIAPASON is the result of these constraints, and came from "theoretical" thoughts (optimal signal processing scheme, best computer architecture for throughput) as well as empirical facts (analysis and reduction of task repetition in actual processing, filter optimization). The final software can process any satellite source indifferently and can be used by any user familiar with data processing, most of the time automatically.

DIAPASON ARCHITECTURAL CHOICES

The key idea is to remove everything which is already known from the fringes in order to keep them as a small signal, thus minimizing the need for unwrapping and enhancing details representing new information. Atmospheric artifacts were observed for the first time in this way. We pushed this idea up to the point of removing geophysical models which mimic ground displacements as well as we can. However, the main choice of DIAPASON is to assume the availability of DEM of the area being studied. An extremely useful assumption at five steps of DIAPASON, even if no DEM of the area exist!

1) The two radar images must be co-registered with a precision of a fraction of a pixel. The DEM and the orbits predict a deformation grid, which is compared to a sparse grid obtained from local correlation on actual images, which may fail at places but reveal actual datum. The comparison of the two grids allows to transfer exact datum to the predicted distortion grid, which becomes accurate down to a few hundredths of a pixel, both locally and globally.

2) One of the radar images must be registered in absolute geographic coordinates. We simulate a radar image whose

amplitude depends on the local topographic slope, which is then correlated with the observed image. The resulting precision is about half the size of a resolution cell in the topographic model used. This precision deteriorates over very flat terrain, but then the usefulness of the registration with the topography decreases.

3) DIAPASON applies a filter based on the local topographic slope during the interferometric fusion of the two images. This filter improves the results especially for the cases of steep relief and/or layover.

4) DIAPASON eliminates the topographic contribution by subtracting the fringe pattern calculated from the elevation model, removing any "predictable" fringes and leaving only those related to displacement and/or DEM improvement.

5) DIAPASON corrects the geometry of the interferogram into an orthogonal cartographic or geographic coordinates, so that users do not work in the distorted radar geometry.

FILE INTERFACE

The interfaces are critical for simplicity of use and optimal re-use of previous processing. DIAPASON is designed to define separately the information dealing with the sensor (for instance ERS-1), the DEM (for instance a UTM file on a specific area) or the data take (with a given starting time, sampling window and mean Doppler).

The corresponding files must be filled independently. For instance if we want to work with ERS1 and JERS1 on the same site, as we have done for the Northridge earthquake, we will use DIAPASON with different sensors and data takes files, but the same DEM file. In this regard, adding a new radar image to study a site where a lot of interferometry has already been done is really simple : a new data file must be created, which is almost the exact copy of a previous one, except for a few figures (the orbit number for instance, the starting time can be updated as well, but it is re-checked anyway by the process).

The current DEM structure accepts files in UTM, LAMBERT I, II or III, as well as latitude/longitude framing such as the one used in the DTED1 by USGS. Other descriptions of DEM (such as contour lines) must be first transcribed into one of the above possibilities. If no DEM is available, the user may describe a "fake" DEM (filled with zeroes for instance), which will still be very useful in the processing (orbital fringes removal, adaptive filtering for optimized interferometric fusion, better a priori co-registration, etc.). A fake DEM will also permit the final

result to be presented in the chosen geographic reference, even if the relief is, of course, not corrected.

Again, we advocate using any kind of preliminary information to improve the result and ease its interpretation. This information always exists: one may use an oversampled part of the world global DEM as an input.

In order to improve its flexibility, DIAPASON works from radar raw data as well as from complex data. Whenever possible, we prefer working from raw data although it requires the additional processing time. The specific parameters required may be used or generated blindly by users who are not radar specialists. Processing of one 100 by 100 km ERS scene typically takes one hour.

It is better than both images are processed identically. For instance, two radar images to be combined must share the same Doppler centroid, which should be set to the average of the optimal value found for each image. Another practical advantage is found when the study involves long segments. One the files of raw data are created, they are processed as a single data stream, which takes long for... the computer! Finally, raw data may cost less.

Being fully autonomous in interferometric processing implies being able to select one's scene of interest, which involves a number criteria, including the availability of images, their date and orbits. For example, events occurring at a specific time require an image both before and after the event. Slow, continuous ground movements need two acquisition dates separated by enough time to grow larger than the noise. The choice of scenes is influenced by local conditions. Seasonal effects such as snow are undesirable. If deciduous trees are present, it is better to work with scenes from the same time of year.

The choice of radar images depends crucially on the relative positions of the orbital trajectories and, of course, on the scenes available. As the number of possible interferometric pairs becomes large quickly when several scenes are available for the same site, CNES has developed software to help select useful pairs by considering computed orbits and catalogues of existing scenes. In practice, only the European Space Agency has made such information public and the selection program currently only handles data from ERS-1 and ERS-2. The program calculates which orbital tracks can see a given site, determines if radar images are available there, and computes the altitude of ambiguity for each potential pair. The final list of image pairs can be conditioned by logical criteria brought by the expertise of the final user. Among these, one can exclude pairs with an altitude of ambiguity lower than a specified value and/or pairs which do not span a specified date, etc.

Since the orbital files as well as the satellite activity files must be refreshed very often, we decided to make the data selection software, called ORBISCAN, available through electronic mail. It means that the potential user may interrogate a dedicated computer whose files are kept up to date. We plan to add J-ERS1 data to ORBISCAN soon.

Another specific tool allows the removal of residual orbital fringes. The user must just indicate how the fringe pattern should be modified at four selected points in the interferogram. The program then computes the proper orbital correction and, using the DEM again, creates the final differential interferogram.

An important point is that DIAPASON does not include a phase unwrapping tool. Unlike many other teams, we did not put emphasis on this aspect of interferometric processing because the "differential" philosophy of DIAPASON greatly reduces the use of phase unwrapping. Besides, we developed fringe simplification techniques which do not require prior phase unwrapping. However, if some phase unwrapping is needed at the end of the process, there exist many possibilities in the world which could be added to the DIAPASON process. That phase unwrapping works on the wrapped image alone without other interface is one more reason to keep phase unwrapping outside of the processing procedure.

Other auxiliary tools include interferogram enhancement and visualization, for which we will no go into details.

AVAILABILITY

DIAPASON can currently operate on VAX VMS workstations, for instance equipped with the DECa family of processors, as well as on UNIX stations such as SUN workstations. The software works best with a typical configuration of 64 Mbytes of core memory and a 4 Gbytes hard-disk.

The availability of the software depends on its use. For scientific applications, a license can be obtained at a cost typically equivalent to the cost of five ERS1 scenes. It has not been possible to make DIAPASON a freeware for legal reasons. We recommend following a dedicated course for optimal use.

For commercial applications, a more expensive license is available. It may include the right to re-sell the software within a more complete image processing package.

Several licenses of both types have been attributed. We expect the multiplication of users to be a continuous source of ideas for a better match between radar interferometry and its final users.

A Flexible System for the Generation of Interferometric SAR Products

Michael Eineder, Nico Adam

German Aerospace Research Establishment (DLR)

82234 Oberpfaffenhofen, Germany

Tel.: +49 8153 281396, Fax: +49 8153 281448 email: eineder@dfd.dlr.de

Abstract — With the increasing application of SAR interferometry the need for interferometric products is developing rapidly. While the algorithms for phase unwrapping are still being developed, upcoming missions like the Shuttle Radar Topography Mission are calling for stable and operational high throughput systems to generate continent wide Digital Elevation Maps (DEMs). At the German Remote Sensing Data Center (DFD) a modular interferometry system is being developed that bridges the aforementioned controversies. Due to the multithreaded architecture it takes full advantage of multiprocessor computers while it can run on small workstations as well. The system takes its flexibility from a modular concept: new input modules can easily connect to new SAR data sources, different phase unwrapping modules can be plugged in and compared. Subsets of the available modules comprise a pre–operational InSAR processor for ERS–1/2 Tandem data, while the overall system is also used as a development and research platform. The paper presents the architecture and the algorithms involved as well as throughput examples in the current configuration. Sample results from the field of differential interferometry and from topographic mapping experiments are presented.

INTRODUCTION

In the recent years InSAR technology that exploits the phase of SAR images developed rapidly. Starting originally with the generation of digital elevation models (DEM), todays applications in the field of differential interferometry range from detection of small surface changes of the earth to measurements of dielectric atmospheric effects. However, even if most processing steps are now well understood, the sheer amount of the data and even key processing steps like unwrapping the ambiguous phase make an operational InSAR system still an ambitious task.

DATA SOURCES AND DERIVED PRODUCTS

Most of the current InSAR data origin from ERS–1/2 sensors, especially the Tandem phase [7]. Environmental changes between the two interferometric data takes may limit the capabilities for DEM generation. However, the large number of repeats and the long temporal coverage since 1992 opens the field of surface change detection. Alone during the ERS tandem phase 110,000 [7] ERS frames have bee aquired that can be processed to interferometric products like

- coherence maps for qualitative surface change detection and land classification [5]

- unwrapped interferometric phase for DEM generation and differential interferometry

- surface slope maps derived from the interferometric phase

In 1999 the modified X–SAR sensor will fly as a part of the Shuttle Radar Topography Mission (SRTM) and acquire high quality single pass interferometric data between ± 60 degree latitude during an 11 day mission. The data will be processed to DEMs with a local error of 4 m and a global error of ca. 14 m.

THE DEM PROCESSING SYSTEM AT DFD

Fig. 1. shows the embedding of the InSAR System into the DEM Processing Chain at DFD as it is currently being developed. Input data is read from tape or transferred via highspeed network from the DFD robot archive. The GENEric System for Interferometric SAR (GENESIS) produces an unwrapped phase map and a coherence map, both in the radar slant range geometry. This phase map is later converted to a geocoded DEM using ground control points. DEMs from individual scenes are mosaicked to a large scale DEM with the DFD geocoding and mosaicking system GEMOS.
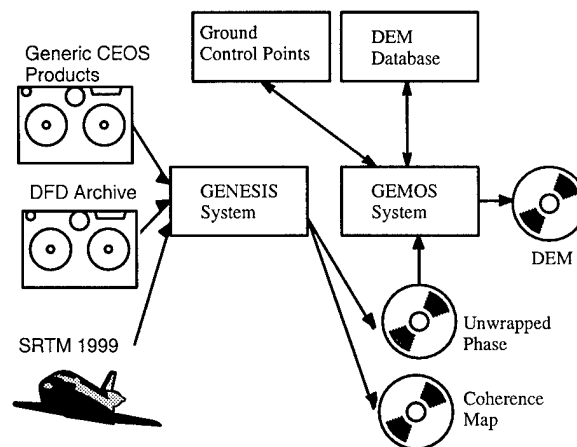
Fig 1. Structure of DEM Data Processing Chain

The following chapters will deal with the algorithms and system aspects in the interferometric processing system GENESIS.

GENESIS ALGORITHMS

Fig. 2. shows the algorithms currently involved. Some of the modules still origin from the work of M. Schwäbisch and D. Geudtner at DLR [10], [11]. The given computation times are for a ERS quarter scene (50 km x 50 km) on a SUN E4000 with 8 CPUs.
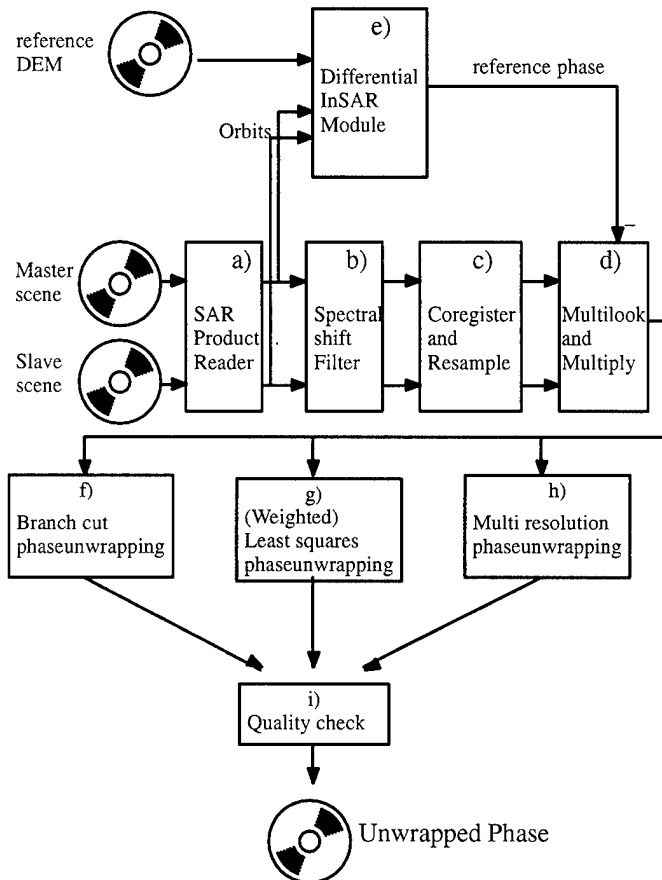
Fig 2. Interferometric processing steps

a) A data format specific SAR product reader extracts data and annotation from disk or Exabyte tape. For ERS products *precise orbit* state vectors from the DFD archive are used to coregister the scenes with an accuracy of a few pixels.

b) The following spectral shift filter improves coherence by filtering the data to common object spectrum in the range and azimuth domain. Nominally, a flat earth is assumed. When a coarse DEM is available which may even come from a first iteration step, a slope adaptive filtering may optionally be applied. See [1] for more details. The filtering process takes about 3.5 minutes CPU time.

c) After filtering, both data sets are coregistered. A bilinear transfer function is derived from the correlation results of 121 patches distributed over both images. The actual resampling is done with a cubic convolution kernel. For ERS data with a oversampling ratio of 18.96 MHz / 15.5 MHz a kernel of 4 x 4 points gives sufficient quality and computational speed: 50 seconds CPU time.

d) Now both data sets can be multilooked reducing resolution and phase noise. During multilooking the phase of the flat earth is subtracted which is estimated from the state vectors and a WGS84 ellipsoid or simply the signal spectrum if the precision of the state vectors is not sufficient.

e) For differential interferometry applications the virtual phase of a reference DEM can be calculated for the given orbits and subtracted from the SAR data phase. The remaining fringes can then be interpreted as terrain movement. The module uses the DEM to improve the orbit timing accuracy and for geocoding.

Usually only one of the phase unwrapping modules f)–h) is applied. Since the phase unwrapping problem is currently not solved satisfactory, several options are investigated and compared:

f) Branch cut algorithms – The phase is unwrapped avoiding branchcuts or adding/subtracting a fringe when crossing a branch cut [9]. The quality of the result depends strongly on the correctness of the branchcuts. Wrong branchcuts result in large errors (multiple cycles) along the unwrapping path. There are many different attempts to find the correct branch cuts. A very promising one based on network flow is currently being implemented and tested [6].

g) Least squares algorithms [8] find global and smooth solutions. A weighting process is required similar to branch cuts to discharge residues or curls in the gradient field. The typical errors are smooth and propagated over the scene. They can be visualized by subtracting the input phase and rewrapping the result. Execution time for weighted least squares phase unwrapping is ca. 10 minutes.

h) Another promising approach, the adaptive multi resolution phase unwrapping estimates the phase gradients in a more robust way on windows with varying size depending on the local data quality. Details can be found in [1], [2].

SYSTEM ASPECTS AND PERFORMANCE

The GENESIS software is coded in C++ for optimal performance and good maintainability. Tools for visualization and quality check are coded in IDL. Much effort was put into selection of the appropriate hardware and signal processing libraries. After benchmarking several systems and configurations a SUN E 4000 with 8 CPUs and 2 GB of RAM was selected. For FFTs, which dominate the computational load in SAR processing, "SUN Performance Library " was selected. A fast striped disk array holds the large intermediate data files.

The software scales automatically and distributes the load equally over all available CPUs using multithreading techniques. Typically 8 CPUs reduce the computation time by a factor of 7.5.

The current processing time for an ERS quarter scene starting from disk files including weighted least squares phase unwrapping is 15 minutes.

APPLICATION EXAMPLES

DEM Generation

The system is already used for preliminary DEM generation projects and validation tests.

Fig 3. shows the unwrapped phase map of the Fort Irwin area in California. The image was produced from two ERS data sets processed with DLR's precision chirp scaling processor [4]. The area covers 100 km x 100 km and was processed in 1 hour CPU time.

Fig 4. Unwrapped phase of Ft. Irwin area / US (raw data ©ESA)

Differential Interferometry
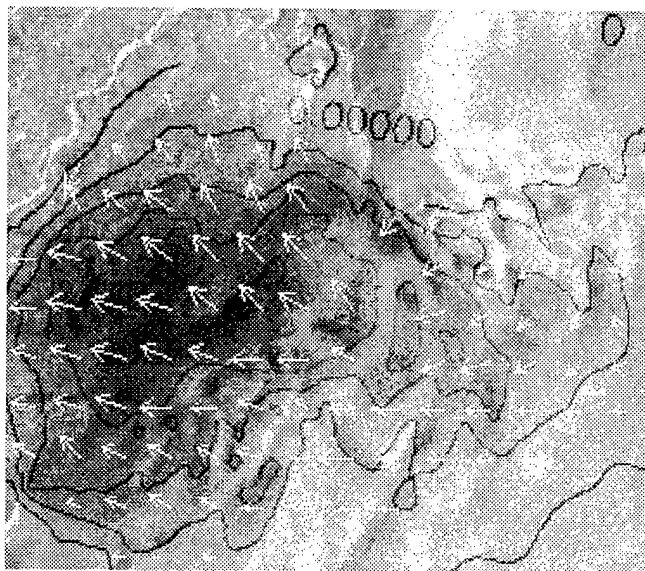
Fig 5. Ice flow on glacier Vatnajökull / Iceland (raw data ©ESA)

Fig 5. shows the motion field of the glacier Vatnajökull in Iceland. It was generated from two ERS tandem scenes acquired on 21./22. October 1996. The arrows represent the ice flow estimated along the sensor range direction, projected to the terrain slope vector. The longest arrows correspond to a speed of 40 centimeters per day.

REFERENCES

[1] R. Bamler, G. Davidson, "Multiresolution Signal Representation for Phase Unwrapping and Interferometric SAR Processing", IGARSS '97

[2] G.W. Davidson, R. Bamler, "Multiresolution phase unwrapping for SAR interferometry, submitted to IEEE TGRS, Dec. 1996.

[3] R. Bamler, N. Adam, G. W. Davidson, and D. Just, "Noise–induced slope distortion in 2–d phase unwrapping by linear estimators with application to SAR interferometry," submitted to IEEE Trans. Geoscience and Remote Sensing, Jan. 1996.

[4] H. Breit, B. Schättler, U. Steinbrecher, " A High Precision Workstation–Based Chirp Scaling SAR Processor", IGARSS'97.

[5] J. Askne Chalmers, G. Smith Chalmers, "Forest INSAR decorrelation and classification properties", published at the ESA FRINGE 96 workshop in Zürich, http://www.geo.unizh.ch/rsl/fringe96/papers/askne/

[6] Costantini M., "A phase unwrapping method based on network programming", published at the ESA FRINGE 96 workshop in Zürich, http://www.geo.unizh.ch/rsl/fringe96/participants/det ails/costantini.html

[7] G. Duchossois, G. Kohlhammer & P. Martin, Earth Observation Mission Management Office, ESA, Paris, "Completion of the ERS Tandem Mission", http://esapub.esrin.esa.it/eoq/eoq52/duch52.htm

[8] D. C. Ghiglia and L. A. Romero, "Robust two–dimensional weighted and unweighted phase unwrapping that uses fast transforms and iterative methods," J. Opt. Soc. Am. A, vol. 11, pp. 107–117, 1994.

[9] Goldstein, R.M., H.A. Zebker, and C.L. Werner. 1988. "Satellite Radar Interferometry: Two–Dimensional Phase Unwrapping," Radio Science, Vol. 23(4), pp. 713–720

[10] Schwäbisch, M., and D. Geudtner. 1995. "Improvement of Phase and Coherence Map Quality Using Azimuth Prefiltering: Examples from ERS–1 and X–SAR," Proceedings of IGARSS '95, Florence, Italy, pp. 205–207.

[11] M. Schwäbisch, "The Method of SAR Interferometry to Generate Digital Elevation Models", Doctoral Thesis Universität Stuttgart, DLR Forschungsbericht, 1995

Operational DEM generation by means of SAR interferometry

Einar-Arne Herland
VTT Automation, Remote sensing group
Otakaari 7 B
P.O.BOX 13002, FIN-02044 VTT, Finland
Tel: +358-9-4564799, Fax: +358-9-4566475
Einar-Arne.Herland@vtt.fi

Arto Vuorela
National Land Survey / Satellite Image Centre
P.O.BOX 84, FIN-00521 Helsinki, Finland
Arto.Vuorela@nls.fi

ABSTRACT

SAR images from the ERS Tandem Phase have been shown to be suitable for generation of digital elevation models by means of SAR interferometry. Based on previous work on SAR interferometry at VTT, a project has been started in Finland on the use of repeat-pass SAR interferometry for operational generation of digital elevation models. The project uses Northern Finland as a test area. This is an area covering approximately 100000 square kilometers between 66 and 70 degrees north. The dataset used is approx. 35 image pairs from the ERS Tandem mission, containing both ascending and descending passes. The area is moderately hilly, with relatively small amounts of areas causing radar overlay or shadowing. Most of the area is covered by boreal forests. An elevation model already exists for the area, as well as forest and land use maps. This makes the area very suitable as a test bed for operational DEM generation. Results indicate an elevation accuracy of 10 meters and a throughput of one image pair of 100 km by 100 km per day per operator.

INTRODUCTION

The National Land Survey, which is responsible for making and updating maps in Finland, has initiated a project on operational generation of digital elevation models (DEM) based on SAR interferometry. The data from the ERS Tandem Phase forms a particularly well suited data set for this purpose. The project is based on previous work on SAR interferometry at VTT Automation where the basic methods and software have been developed and tested ([1]).

Traditionally DEMs are generated from airborne optical stereo images. This is based on image correlation, either by automatic methods or a human operator. The process is quite slow and the data collection is expensive compared to satellite images. The existing height model in Finland is generated from digitized contour lines. The rasterized DEM is then generated by mathematical interpolation, which, depending on the method, introduces errors at hill tops and shore lines. The accuracy of a high quality DEM generated by this method is typically a few meters.

For certain areas a course DEM may already exist and other data may be available, e.g. water masks and land use maps. This kind of data is also useful when using INSAR through the relationship with interferometric coherence. One use of the software system developed in this project is to improve on low quality DEMs and to update old DEMs. Although the system is made as automatic as possible, the main emphasis is on the quality of the resulting DEM. This means that when the system is not able to decide on the unwrapping of a certain area, the human operator will be used to decide on how to proceed. Particular emphasis is therefore placed on the optimum use of the operator in order to optimize the DEM quality versus processing time.

When the system is completed in about half a year, it will be installed in the operational environment of the National Land Survey.

THE METHOD

The DEM generation for a certain area is defined as a project comprising the geographical coordinates and the projection together with the datum. This does in general comprise a number of SAR image pairs. The different processing steps for a single image pair are shown in Fig. 1.

Based on the precision orbit parameters available from ESA for the ERS satellites, the state vectors at the beginning of the two images are calculated with an in-house developed orbit propagator. Together with the header information from the SLCI-files, this forms the parameter set used for mapping from image to terrain and vice versa. When doing this positioning, the iterative algorithm presented in [3] is used.

The relative position of the images is then calculated from the orbit parameters. This is done for the corners of the images and is used as input to an image correlation routine for precision registration to subpixel accuracy. Based on this, a least mean square error fit is done to generate an interpolation grid for the slave image with respect to the master image. The master image is chosen to be the image with the larger incidence angle at near range in order to always maintain the same sign of the flat earth induced phase ramp.

Generation of image state vectors
Calculate relative image positions from the orbit parameters
Image registration by correlation
Slave image reinterpolation
Ellipsoid earth phase bias, phase to height conversion factors and local incidence angles
Fringe and coherence calculation
Phase unwrapping with operator assistance
Conversion of phase to height and generation of ortho DEM
DEM to map projection

Fig. 1. Processing chain for one complex image pair.

By means of the interpolation grid the slave image is then reinterpolated by means of a 4-point sinc-filter. The reinterpolated image is stored in a separate file and used in the subsequent processing.

The orbit parameters are used for calculating the ellipsoid earth induced phase bias. At the same time the baselines are calculated and converted into scaling factors for transforming the unwrapped phase into terrain elevation and the local incidence angles are calculated. Because all these parameters change relatively slowly throughout the image, a sparse grid is calculated and stored into separate files.

Calculation of interferometric fringes and coherence is done in three steps:

- azimuth common band filtering
- range common band filtering
- phase difference and coherence calculation

The azimuth common band filtering is done by means of FFTs using the doppler centroids from the SLCI image header a block at a time. The range common band filtering is done similarly using the calculated baseline values. The coherence is calculated after removal of the ellipsoid earth induced phase bias, but is not terrain corrected. The fringes are smoothed in azimuth and resampled with a factor of 5. This gives approximately equal pixel spacing in both directions. Before phase unwrapping the phases are smoothed by a 3 by 3 filter. The coherence is calculated using a window of 2 by 10 pixels in range and azimuth, respectively.

The method used for phase unwrapping is based on extraction of residuals from prefiltered fringe images ([2]) and direct integration of the unwrapped phase. After detection of inconsistent points ghost lines are generated. This is done by using the proximity of inconsistent points together with certain topological properties of the height curves connecting these points. When the algorithm does not succeed, the operator is asked to graphically connect the points. After this the interferometric phase is unwrapped by direct integration and the areas around inconsistent points and ghost lines are smoothed.

The unwrapped phase is transformed into elevation by means of the previously calculated scaling factors, and the local incidence angles are used to transform the height values into a ground range ortho image.

The final DEM is transformed into the desired projection by using the orbit parameters and height biases are removed by using ground control points if these are available.

RESULTS

The first version of the software also included a SAR processor for generating the complex images. This has later been changed so that the ESA supplied SLCI images are used as input data. Currently the system has been tested on two sets of SLCI images, one descending and one ascending pair, from March and April 1996. The area is located at about 69°N, and an existing DEM with 25 m pixel spacing is used as a refernce.

The orbit parameter based image registration is for both image pairs accurate to within 0.5 pixel in range, but in azimuth the accuracy is 0.5 pixel for one pair and 1.5 pixels for the other. This is thus insufficient for accurate registration, but it allows a very small search area to be used in the image correlation.

The baselines are 130 m for the descending pair and 70 m for the ascending one. The coherence is for both images around 0.5-0.8, and connection of inconsistent points by ghost lines succeeded without need for operator decisions.

Although relative positioning of the images succeeded with an accuracy of about 1-2 pixels, the absolute positioning is slightly worse in the range direction, about 4-5
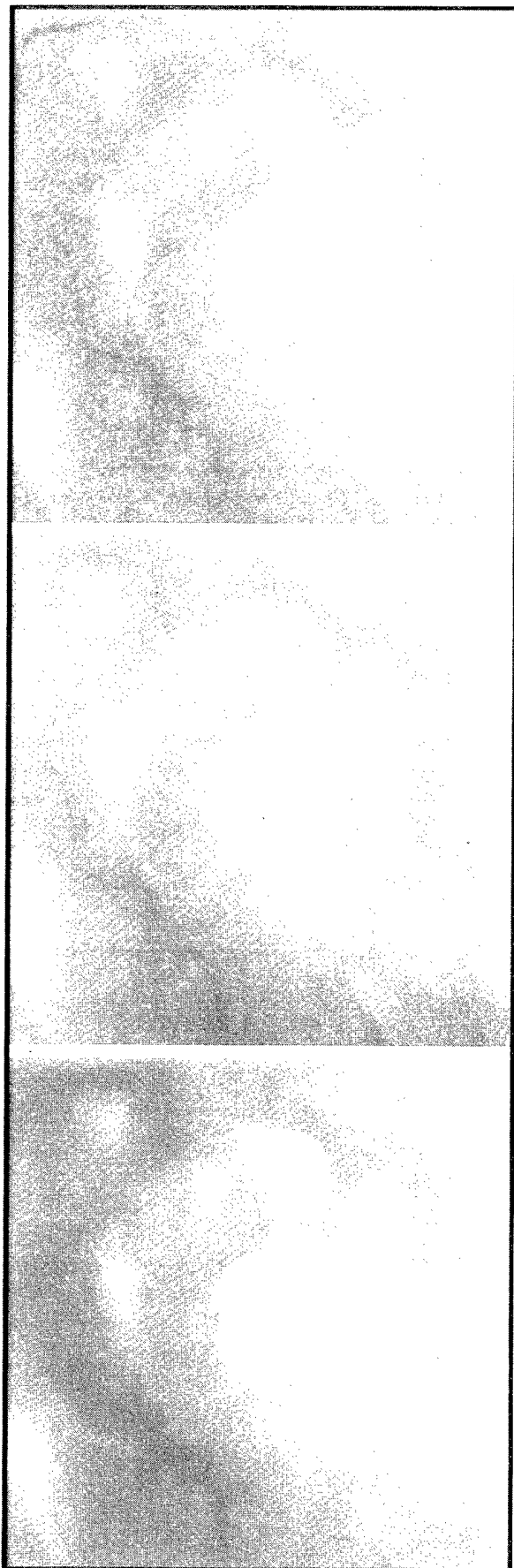
Fig.2. DEMs from ascending pass, descending pass and existing elevation model.

pixels. To find out whether this is a systematic effect, in case it can be removed, or whether it is inherent, will need a larger amount of test images.

For the ascending image pair, the ellipsoid earth phase bias seemed to be corrected with a high accuracy. For the descending pair, however, there seemed to be a residual across the 100 km by 100 km scene. Several control points will therefore be needed for large areas.

Fig. 2. shows the resulting DEMs. The image at the top is the rectified DEM from the ascending pair, the middle one from the descending pair, and the bottom image is the existing DEM. The general accuracy is between 10-15 m, and it is clearly seen that the accuracy of the lower baseline DEM is worse than for the higher baseline, as is to be expected from theory.

CONCLUSION

A first version of an operational DEM generation system based on SAR interferometry has been developed and tested. The test data indicated an accuracy of 10-15 m in elevation, and also showed that baselines above 100 m are preferable in order to achieve good accuracy.

ACKNOWLEDGMENT

REFERENCES

[1] E-A. Herland, "Sar interferometry with ERS-1 in forested areas", IGARSS'95, Firenze, Italy, pp. 202-204.

[2] J. Curlander, "Location of spaceborne SAR-imagery", IEEE Transactions on Geoscience and Remote Sensing, Vol. GE-20, No. 3, July 1982.

[3] P. Hartl, X. Wu, "Sar Interferometry: Experiences with various phase unwrapping methods", Proceedings of the seconf ERS-1 symposium, pp. 727-732, January 1994.

ERS SAR Interferometry: An Operational Evaluation
of the DTM Production

S. Dupont*, P. Nonin*, L. Renouard*, G. Pichon*, M. Berthod**

ISTAR*

Les Espaces de Sophia - Bât. F - 80, Route des Lucioles - 06560 Sophia Antipolis - France
Tél. +33 (0)4 93 95 72 44 - Fax. +33 (0)4 93 95 83 29
email: dupont@istar.fr, nonin@istar.fr, renouard@istar.fr, pichon@istar.fr

INRIA**

2004 Route des Lucioles - 06902 Sophia Antipolis Cedex - France
Tél. +33 (0)4 93 65 78 78 - Fax. +33 (0)4 93 65 76 43
email: berthod@sophia.inria.fr

Abstract – Spaceborne synthetic aperture radar (SAR) multi-pass interferometry is a technique based on the exploitation of the phase differences between two complex radar images taken from two slightly separated positions on different dates [4]. This measure contains not only geometric and topographic information, but also differential information covering land or atmospheric changes between the two scenes observed [3]. These atmospheric artifacts can be an obstacle to the production of digital terrain models (DTM) from multi-pass SAR interferometry [6, 7].

INTRODUCTION

Since 1991, ISTAR has developed, in association with CNES (French Space Agency), a DTM processing chain as an alternative to SPOT for DTM production [5]. Feasibility was demonstrated in 1993, a pre-operational software was set up in 94-95 and production tests on a large scale took place in 1996. Processing starts from raw images and includes DIAPASON software from CNES for interferogram generation. We then use three ISTAR modules, namely phase unwrapping, baseline registration with ground control points, and geocoding of the unwrapped phases, to get the DTM [1, 2]. To validate the chain on a large scale, multiple test sites were chosen. The complete surface exceeds 400,000 km^2. The results show large perturbations probably due to refractive index variations. These large perturbations introduce topographic elevation errors which can be an obstacle for DTM generation.

OBSERVATIONS

In all processed sites, we observed the presence of low frequency artifacts with a weak amplitude (between 0.3 and 0.5 phase cycles) and covering the whole image.

In a few processed images (about 10 %, although the weak number of processed images does not yield real statistics), we observed the presence of more localized phenomena, probably due to convective effects, with a higher amplitude (between 1 and 3 phase cycles)(Fig.1). They can hide a valley or a peak altogether). If they are detected, their small expanse allow them to be masked. We can then complete the masked area with exogenous information (DTM generated from digitized contour lines, for example). If they are not detected, their presence could have serious consequences in the generated DTM. In the worst case encountered (three phase cycles), altimetric errors can be 60 m for a 500 m baseline (altitude of ambiguity of 20 m), up to 300 m for a 100 m baseline (altitude of ambiguity of 100 m)!

For the main sites, the amplitudes of atmospheric effects were measured after the subtraction of a reference DTM to the InSAR DTM. The results are compiled in table 1. In this table, we can also find the mean and the maximal amplitudes of observed atmospheric phenomena in a number of phase cycles.

The results shown are as a whole more pessimistic than the ones already published. They were obtained in an industrial context for the production of DTM on a surface larger than 10 000 km^2 (the ground surface of an entire ERS scene). Consequently, they should not be compared to the published ones obtained over smaller surfaces.

In the case of 30 km × 30 km stamps, the high density of registration points, associated with a rather flexible modelization of interferometric geometry, can literally override the generated DTM to be combined with existing data. The flexibility of the model partially distorts the intrinsic results of SAR interferometry by compensating the effect of possible low frequency atmospheric phenomena on the reduced areas. The ensuing results can thus be compared to the result of an interpolation between ground control points, rather than to a true InSAR DTM production.

The results mentioned in this document show that the density of the ground control points is lower. Those points are used for orbital registration only. In addition, when segments are processed, the orbital constraints limit the model and have little chance of compensating atmospheric artifacts.

The ensuing results are of lower quality; however, they are more representative of what is expected from SAR interferometry, used in real production conditions for large surfaces.

Note: The division of unit images into small 30 km × 30 km stamps, registered separately, would not be a good solution. A set of tiny DTM would be obtained, tilted respective of one another and impossible to merge (each registration would, in its own way, compensate for atmospheric effects).

Tandem data may be used to limit ground incoherent differential effects but will not solve atmospheric problems due to their high temporal variability. Furthermore, the comparison of ascending and descending views has not yielded a more favorable time window which would minimize atmospheric artifacts.

SUMMARY AND CONCLUSIONS

Much more importantly than incoherent differential phenomena such as forests and rivers which remain very localized and visible on the coherence image, the coherent differential phenomena are the real problems. They are impossible to detect on a single interferogram and overlay sometimes the whole image. They can also represent several phase cycles locally. These important phase cycles have two consequences: they alter the registration of view parameters (DTM tilting) and are then converted to altitude (error amplitude depending on altitude of ambiguity).

These phemonena limit the use of multi-pass satellite InSAR DTM in an industrial context. The assumed "all-weather" aspect of radar images presented the InSAR DTM as a valid alternative to optical DTM, such as SPOT, on areas often covered with clouds. As explained in this document, these very clouds can also make radar interferometry useless.

To overcome these problems, only a confidence map can be envisaged [1]. This image is a linear combination of two interferograms normalized by their altitude of ambiguity which includes coherent differential effects only. The calculation, which can be combined with a quicklook type of processing, should allow ESA's ERS-1/ERS-2 archive to be purged until a simultaneous interferometric sensor becomes available.

REFERENCES

[1] S. Dupont, "Génération de modèles numériques de terrain par interférométrie ROS", *PhD Thesis*, to be published, 1997.

[2] S. Dupont, P. Nonin, L. Renouard, G. Pichon, F. Bignone, "Atmospheric artifacts in ERS DTM. ISTAR's experience over multiple sites and large areas", *Proc. of the 3rd ERS Symposium*, Firenze, 1997.

[3] D. Massonnet, K. Feigl, "Discrimination of geophysical phenomena in satellite interferograms", *Geophysical research letters*, No. 22, pp. 1537-1540, 1995.

[4] D. Massonnet, T. Rabaute, "Radar interferometry: limits and potential", *IEEE Trans. on Geoscience and Remote Sensing*, Vol. 31, No. 2, pp. 455-464, 1993.

[5] F. Perlant, D. Massonnet, "Different SPOT DEM applications for studies in SAR interferometry", *ISPRS Commission IV*, Washington, USA, 1992.

[6] H. Tarayre, "Atmospheric heterogeneities revealed by ERS-1 interferometry", to be published in *Geophysical Research Letters*.

[7] H. Zebker, P. Rosen, "Atmospheric artifacts in interferometric SAR surface deformation and topographic maps", submitted to *J. of Geophysical Research*.

Site (Ascending/ Descending)	Perpendicular baseline (m)	Altitude of ambiguity (m)	Elevation error Bias (m)	Elevation error Rms (m)	Atmospheric artifacts [mean/max] (phase cycle)
Angoulême (D)	700	13	0.2	4.9	[0.3/0.5]
Brittany (D)	560	18	1.2	5.2	[0.3/0.5]
Drum Hill (D)	255	40	0.4	10.7	[0.3/0.5]
Kununura (D)	465	20	-8.3	12.5	[0.5/1]
Death Valley (D)	181	55	7.7	14.6	[0.3/0.5]
Death Valley (A)	95	104	5.2	15.2	[0.3/0.5]
Luxemburg (D)	95	104	8.2	23.2	[0.3/0.5]
Brittany (D)	170	65	5.3	25.9	[0.5/2]
Kununura (D)	25	400	-17.9	98.9	[0.8/1.4]
Irish Canyon (D)	22	450	-146.6	370.5	[0.4/3]

Table 1: Statistics for several test sites.
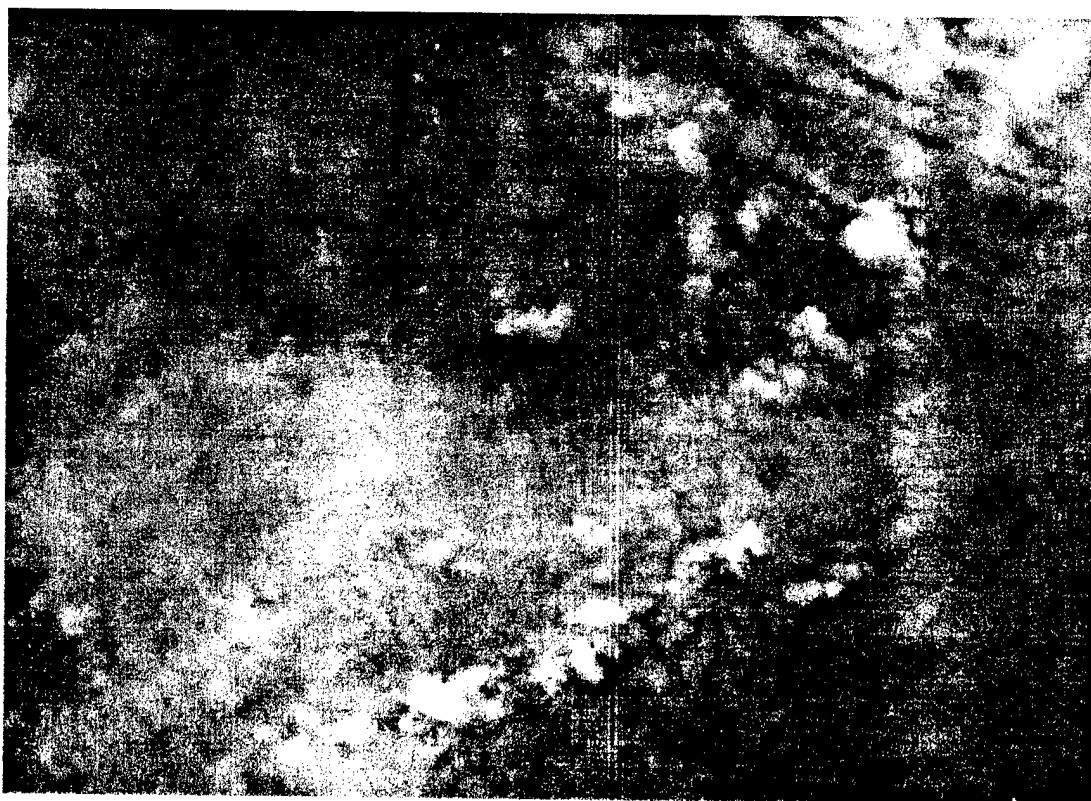
Figure 1: Example over Brittany test site: image of the difference between the InSAR DTM with a 65 m altitude of ambiguity and the InSAR DTM with a 18 m altitude of ambiguity in the master geometry. Amplitude of atmospheric artefacts is locally higher than 1.5 phase cycles. Ground dimensions are 50 km × 35 km.

MAP GENERATION UTILIZING IFSARE IMAGERY AND DIGITAL ELEVATION MODELS FROM THE INTERMAP STAR-3i SYSTEM

Michael E. Bullock
Intermap Technologies Inc.
Englewood, Colorado, USA

Garth Lawrence
Robert V. Dams
Intermap Technologies Ltd.
Ottawa, Ontario, Canada

Keith Tennant
Intermap Technologies Ltd.
Calgary, Alberta, Canada

ABSTRACT

In November of 1996, a new commercial venture, Intermap Technologies Inc. (Intermap), commenced operating the InterFerometric Synthetic Aperture Radar for terrain Elevation (IFSARE) system, developed by ERIM and NASA's Jet Propulsion Laboratory (JPL). The Defense Advanced Research Projects Agency (DARPA) had originally funded the IFSARE under an innovative program for developing new remote sensing technology for government and commercial applications. The IFSARE (now referred to as "STAR-3i") system is now being operated by Intermap for a wide variety of international commercial mapping applications including terrain mapping, resource exploration, resource management, and telecommunications and transportation planning. This paper presents an overview of the commercial applications of this X-Band IFSAR and Intermap's methodology in uniting this new technology with traditional remote sensing and mapping techniques. Technical improvements to the STAR-3i system that are currently in progress are also presented.

1.0 INTRODUCTION

1.1 GENESIS OF STAR-3i

Generation of large scale, highly accurate terrain and land cover maps for military, environmental and commercial applications has been a challenge for remote sensor system developers. The need is for rapid generation of accurate terrain elevations and associated land cover/use over large areas.
Operational and economic requirements requires all-weather, day or night operations, as well as a high speed collection and processing capability. To address these needs. DARPA, formerly known as the Advanced Research Projects Agency (ARPA), initiated a multiphase program intended to advance new technology from the conceptual stage through to a fully functional system with practical capabilities. The proposed solution was the single pass Interferometric Synthetic Aperture Radar (IFSAR). The U.S. Army Topographic Engineering Center (TEC) in Fort Belvoir, Va., because of their expertise, was chosen by DARPA to act as agent to oversee and evaluate this program.

In Phase I, a small scale IFSAR demonstration was performed in April 1992 followed by extensive proof of concept testing ending in April 1993. The feasibility experiments carried out in Phase I proved the capabilities of IFSAR and DARPA awarded the contract to design and build the interferometric radar and auxiliary data processor to the Environmental Research Institute of Michigan (ERIM). NASA's JPL

(Pasadena, California), had researched IFSAR on its DC-8 aircraft testbed (AIRSAR) for several years, and provided technical support to the contractor teams during Phase I. JPL was tasked to deliver the ground-based hardware and software for the image formation and Digital Terrain Elevation (DTE) processor necessary to produce the IFSAR output products. The ERIM designed IFSAR was installed in a Learjet aircraft and completed the integration and test phase of development late in 1994. Extensive evaluation of the system's operational capabilities were then carried out ending in late 1995. The product at the end of this highly successful development effort was the IFSARE system.

1.2 DARPA TECHNOLOGY TRANSFER PROGRAM

In response to DARPA's initial vision to utilize this new IFSARE mapping system in commercial applications, a new company, capable of realizing the potential of the technology, was established. This new company, Intermap Technologies Ltd., supplies complete information products and services to its clients. Intermap combines the resources and expertise of two partners:

- ERIM, who provide their valuable technical experience in radar imaging systems, and
- The Image Mapping Division of IITC Holdings Limited (formerly Intera Information Technologies), providing expertise in marketing, operation and management of remote sensing systems and the production of mapping products.

Intermap Technologies Inc., located in Englewood, Colorado, operates the IFSARE system, which is now referred to as the Intermap STAR-3i system. The STAR-3i aircraft is based in Denver.

On February 11, 1997, Undersecretary of Defense for Acquisition and Technology, Dr. Paul Kaminski, signed the DARPA transfer agreement, which transfers the ERIM-built IFSARE system to Intermap Technologies Inc. for world-wide commercial operations. The Department of Defense (DoD) still has access to the system for mapping and other applications. In times of U.S. national emergency (*e.g.*, natural disaster, peace-keeping,

military conflict, *etc.*), the DoD will have priority access to the IFSARE system.

2.0 STAR-3i SYSTEM DESCRIPTION

2.1 RADAR INTERFEROMETRY

Interferometric SAR is a technique that uses the relative phase difference between two coherent SAR images, obtained by two antennae separated by an across track baseline, to derive an estimate of the terrain surface height. The baseline length is an important design parameter since the height error diverges as the length approaches zero. Conversely, if the baseline length is too large, the returns from the two antennae become decorrelated, increasing the phase measurement error. The baseline length also affects the interferometer scale factor, which is the amount of phase shift for a given height change. Increasing the baseline length increases the height measurement accuracy (until the decorrelation limits performance) but decreases the ambiguity interval which causes the need for more phase unwrapping to occur, an often difficult operation. Decreasing the baseline length will have the opposite effect. Thus, an optimum baseline length exists. A block diagram of the basic process is illustrated in Figure 1 below.

In order to extract accurate height information from the airborne data, an interferogram must be created during the post-processing routine. Briefly, post-processing combines the highly accurate aircraft inertial navigation with airborne and ground-based GPS data to generate all the information necessary to align the raw radar data for proper focusing, and determine the location of the radar data with respect to local and global coordinate systems. Range compression, range curvature correction, range alignment, azimuth compression, depth of focus correction, and azimuth alignment are achieved, and result in two sets of two dimensional SAR imagery, one from each radar channel. The interferogram is created by combining the two complex SAR image data channels by multiplying one channel by the conjugate of the other on a pixel by pixel basis. The phase of the resulting complex samples is proportional to elevation and the magnitude is proportional to radar cross section. Inherent phase ambiguities present in the data are partially resolved in a process called phase unwrapping by comparison of the phases of adjacent pixels and from contextual

information (Zebker and Goldstein, 1986). For the placement of a pixel in three dimensional space, however, the absolute phase measured by the interferometer must be known. The elevations of control points in the area being mapped may be used to determine the absolute phase, thus resolving the remaining ambiguities. Madsen and Zebker have developed an alternate approach to obtain phase across the scene without the use of control points. Several references are available detailing height measurements from interferometric radar such as (Graham, 1974), (Madsen and Zebker, 1992), and (Adams *et al*, 1993).
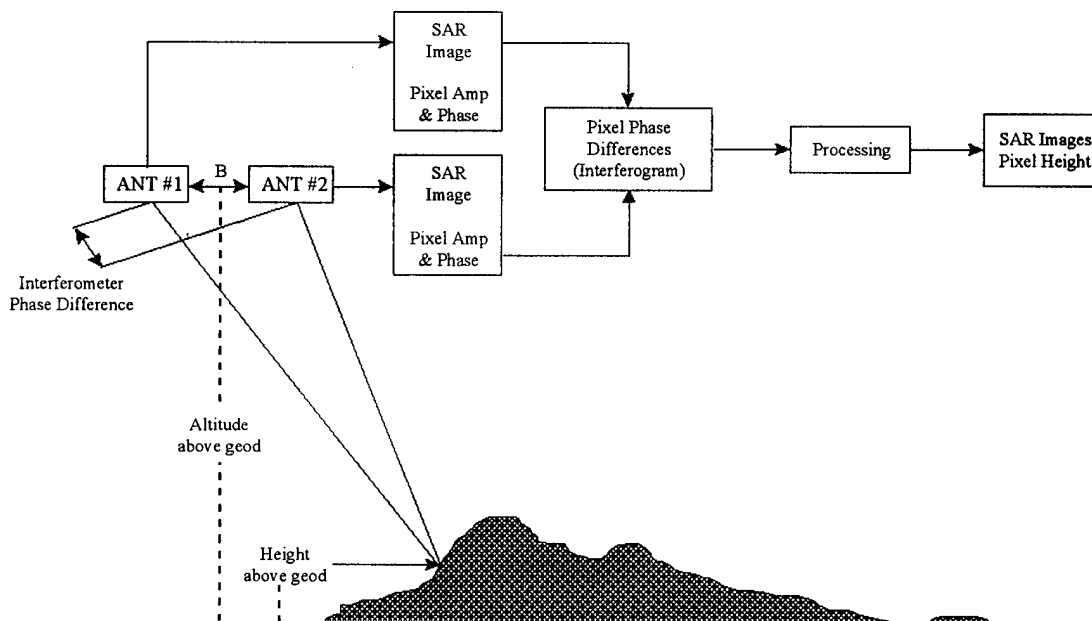
Figure 1. Basic IFSAR Process.

2.2 *THE STAR-3i SYSTEM*

The STAR-3i system is one implementation of an airborne single pass across track interferometric SAR. As in any implementation, the designers selected various compromises that determine the overall system performance. A major decision made by the ERIM design team was to limit the airborne system, which is referred to as the Interferometric Data Collection Sub-system (IDCS) to perform data acquisition functions only. Thus the IDCS has no processing, navigation or dynamic antenna control. The IDCS generates, amplifies and transmits a coded FM waveform and receives the returns. These raw return echoes and all motion data are recorded on high density digital tapes.

2.2.1 Coverage

Knowledge of the exact baseline length is critical to the performance of the interferometer. For this reason the STAR-3i antennae are welded to the antenna pedestal. This fact causes the coverage obtained to be dependent on the aircraft height above ground. As the aircraft height above ground decreases, so too does the ground coverage. The two critical parameters for the coverage are the far incidence angle and the antenna beam width, which are both constants for the STAR-3i. The combination of these two provides the swath coverage as illustrated in Figure 2
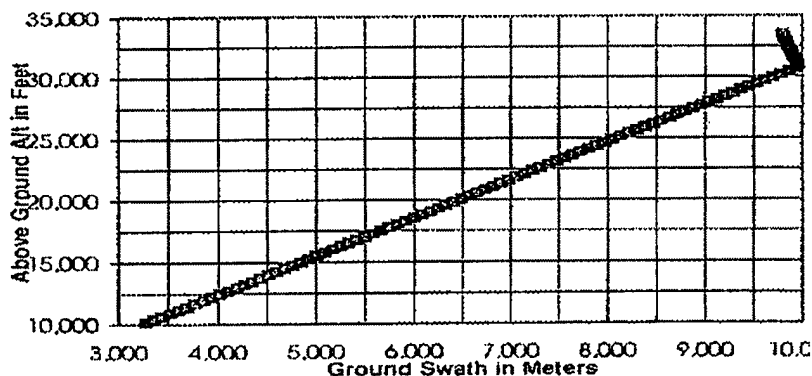
Figure 2. STAR-3i Ground Swath as a Function of Height (2.25 meter mode)

2.2.2 Resolution

The accepted parameter for determining a radar systems "resolution" performance is impulse response. Range impulse response is a function of the range bandwidth. Azimuth impulse response is a function of azimuth bandwidth, which is in turn a function of antenna azimuth beam width, aircraft speed and the number of azimuth looks processed. For the STAR-3i system, the impulse responses in range and azimuth are as follows:

- The 3 dB range impulse response is 2.5 meters. This resolution is represented by a 2.2 meter pixel in the slant plane.
- The azimuth impulse is processed to approximately 4 looks providing a 3 dB azimuth impulse response of nominally 3 meters. A single "look" of STAR-3i data has a nominal 0.75 meter resolution dependent on aircraft speed. The looks are used to reduce the presence of speckle in coherent image data.

The data is resampled (orthorectified) to provide nominal ground resolutions of 3 x 3 meter. However, through product resampling, the standard 3 meter pixel can be resampled to meet customer requirements.

2.2.3 Geometric Performance

The STAR-3i system has been verified for operation in Standard resolution (2.5 meter) mode and may be configured for two different data collection scenarios:

- Standard precision mode — Operation at 40,000 ft. AGL to obtain standard vertical accuracy.
- High precision mode — Operation at 20,000 ft. AGL to achieve higher vertical accuracy.

STAR-3i has been verified in independent tests to meet the following performance accuracy's:

Table 1. STAR-3i Performance

Mode	Aircraft AGL	X&Y (CEP)	Z noise
Standard Precision	40,000	5 m RMS	1.5 - 3 m RMS
High Precision	20,000	5 m RMS	0.3 - 2 m RMS

These performance accuracy's assume the GPS base station is within 200 km of the collection site. The performance improvement realized in high precision mode is primarily due to the fact the aircraft is operated at a lower altitude. This provides a better signal-to-noise ratio (SNR) and reduces the effect of any navigational errors present. The Z noise is "localized" variation of the vertical. The localization of the error is dependent on many factors including target type and navigation performance. Ground control could be utilized within "small scenes" of STAR-3i data to remove offsets and provide DEM accuracy's at the noise levels. To apply this process to an entire project area would require a statistically significant number of ground control points.

2.2.4 STAR-3i Aircraft platform

Practical IFSAR operations dictate the need for a high performance aircraft to carry the radar sensor package. The Learjet 36A is considered to be an excellent all-round aircraft to fulfill this role because of its high performance, excellent cabin environment for radar equipment, very robust design and proven field reliability, and two pilot operation.
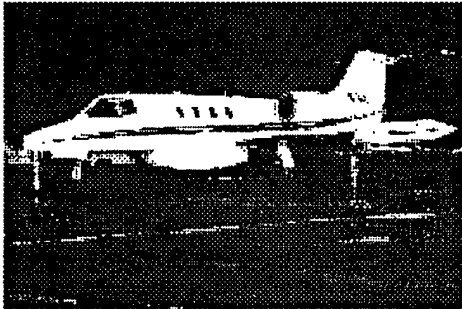
The climb and cruise performance of the Learjet allow the aircraft to reach a project area quickly and to collect data at a very high rate (up to 100 sq. kms/minute). Its nominal true airspeed of 740 km/hr enables rapid deployment to worldwide destinations in order to meet specific deadlines or to monitor natural disasters. The maximum operational ceiling of the Learjet is 45,000 feet. This allows a wide range of field project planning options and the ability to get above most weather.

2.2.5 STAR-3i Ground Processing System

Unlike the IFSARE systems aboard the aircraft, the ground processing system required significant improvements for it to be commercially viable. When operated by ERIM, the IFSARE was used primarily for research studies and periodic mapping projects to support TEC and the DoD. Under this scenario, accuracy of the DEM and SAR image products was the main priority.

During the process to commercialize the IFSARE, it became quite apparent that the ability to process large volumes of data would become equally important to the requirement for product accuracy. A commercially viable system requires that the product generation keep up with the rate of data acquisition. Therefore, in 1996 Intermap initiated an aggressive program to improve the ground processing throughput.

The ground processing system has the function of generating IFSARE products from the collected data. As described in (Sos et al., 1994), the processing system consists of the tape playback unit, the position/attitude processor, two image formation processor channels and the DTE processor. When initially developed by ERIM and JPL, the ground processing system was implemented on a Cray processor.

To improve the data throughput capability as well as the overall system reliability, ERIM recently completed the porting of the Cray software to a Unix environment. Now running on a network of six Sun Ultra^2 workstations, the overall throughput of the ground processor has been increased by approximately a factor of 3. Further optimization of the processing sequence is underway.

In addition, the next major phase of ground processor improvements has already begun. ERIM and Intermap recognized that the Unix port of the original JPL processing software was just an interim solution. The long term solution involves the development of an entirely new ground processing segment that utilizes the latest advances in DTE formation algorithms. An important goal of this next phase is to automate the entire processing chain as far as is reasonably achievable. To realize these goals, Intermap has initiated a contract with ERIM to build this next generation IFSARE processor. Known as the High Throughput IFSARE Processing System, or HiTIPS, this system will offer significant improvements in the areas of motion compensation processing, ambiguity determination, and phase unwrapping. HiTIPS should be fully operational in late 1997.

3.0 COMMERCIAL APPLICATIONS

The worlds of remote sensing and geographic information systems (GIS) are undergoing a revolution that is being propelled by the rapid advance of technology and the continuing discovery of new applications. High resolution commercial satellites are planned for 1997 and onward, thus

providing new capabilities in mapping, earth observation, and resource monitoring.

However, this remote sensing and GIS revolution will require timely and accurate digital terrain data if it is to continue its rapid rate of advance. Accurate digital elevation models (DEMs) are required for most applications that require high geolocation accuracy. In fact, DEMs are a very suitable base map for many GIS applications such as mapping, land use classification, and transportation planning.

Figure 3 shows the trends in topographic mapping. Airborne IFSAR has created a new class of DEM product having high accuracy at costs that can be significantly less than that using traditional photographic means. This is particularly true for tropical regions where cloud cover can make photogrammetry (by aircraft or satellite) impractical in terms of cost and time.

Value of Topographic Mapping
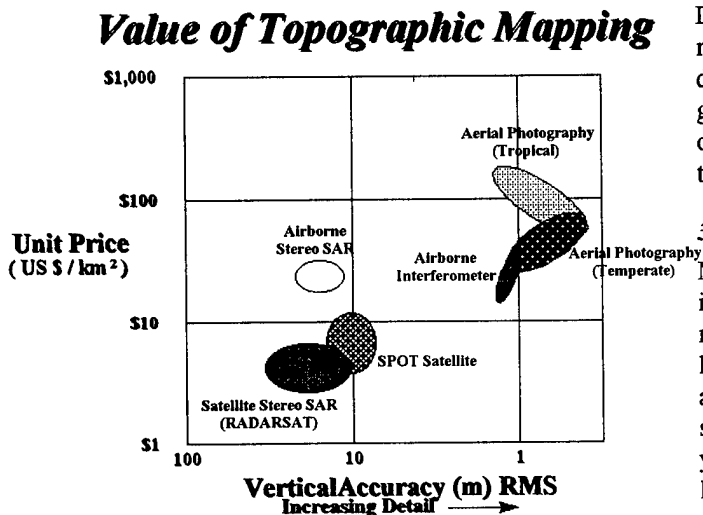
Figure 3. Relation of STAR-3i to Topographic Mapping Trends.

Intermap's STAR-3i produces three main product types:

Digital Elevation Models In a timely manner, the STAR-3i system provides large area coverage DEMs at finer terrain elevation accuracy's than commonly available from other remote sensing systems. Due to the density of the DEM information available from

IFSAR, DEM noise is minimal. In a low altitude area, localized DEM noise can be as little as 30 cm.

Orthorectified Image Maps STAR-3i high resolution radar images are orthorectified using the simultaneously-generated DEM. Consequently the radar imagery is presented with all vertical height distortions removed. These images are registered to a desired projection and are mosaicked into image maps. STAR-3i digital images can be used as base maps for GIS applications or output as hard copy image maps at scales as large as 1:10,000.

Thematic Maps Most DEMs and orthorectified images are used to produce value-added products, including thematic maps by application, contour and topographic maps, and perspective views. Digital STAR-3i data is extremely versatile, allowing presentation forms to suit a wide range of requirements. DEMs can be presented as wire-mesh diagrams or radar image data can be draped over the DEM to produce a realistic perspective view. High resolution STAR-3i images can be interpreted to derive thematic maps such as land cover, land use, geology, forestry, and mining. If satellite or airborne optical imagery is available, it can be draped over the DEM for realistic 3-D fly-through applications.

3.1 FORESTRY

Mapping the world's forests has become an important application. Ecosystem management, resource monitoring, and the preservation of certain habitats and species has created the need for timely and accurate remotely sensed data. Foresters have successfully employed aerial photography for many years and some now look to the possibility of using high resolution satellite imagery (Green, 1996).

However, for many parts of the world the frequent presence of cloud cover make the use of optical remote sensing extremely difficult. For these parts of the world, such as the tropics, the use of radar becomes an attractive solution from the standpoint of product accuracy and cost (Mercer, 1993). STAR-3i now offers the capability to generate high accuracy image maps and DEMs that can serve as the base map for forestry applications. Since the STAR-3i system uses X-band radar, the scattering is generally off the top layer of foliage or other scattering surface that the incident radar beam might encounter. The

derived DEM is therefore with respect to this layer and might more accurately be termed a "surface model." In instances of dense forest canopy, the underlying "bald earth" elevation model can be obtained by removing the tree height through algorithmic post-processing.

Furthermore, orthorectified radar image maps can be collected at planned intervals to monitor the forested regions. It is precisely this ability acquire mapping and land use data on a regular schedule in cloud covered regions that make radar such a useful technology for forestry. To date, Intermap has found forestry to be a key application for the STAR-3i system. Intermap is currently producing DEMs of widespread tropical forests, making these regions among the most accurately mapped in the world.

3.2 EXPLORATION

Many exploration applications require precise knowledge of the terrain to be effective. Development of coal deposits, oil and gas exploration, logistical planning, geological hazard mapping and environmental monitoring are examples of such applications. Petroleum and coal exploration activities in tropical regions and other heavily-vegetated areas are hampered by lack of bedrock exposure and difficult logistics due to surface conditions. This may result in poor quality seismic data. Geological structural mapping in such areas depends on the use of remotely sensed imagery and other reconnaissance exploration tools (*e.g.,* airborne gravity and magnetics). Although geophysical tools provide quantitative subsurface information, surface structural and lithological information is also required in order to accurately determine potential areas of interest. The STAR-3i imaging system is a preferred remote sensing tool because it can penetrate persistent cloud cover, haze and smoke. The radar shadow allows for the interpretation of geological structures, lithology and geomorphologic features covered by dense vegetation. In addition, STAR-3i DEM data and imagery aid in seismic line planning by providing surface topographical information. This is particularly true in areas with limited field control. Orthorectification of the radar imagery eliminates geometric distortions due to layover and foreshortening inherent in radar imagery. Due to the side-looking nature of radar imagery, choice of radar

look direction is critical in obtaining the optimum structural and lithological information. This allows the geologist to map directly from the imagery into a GIS.

3.3 TELECOMMUNICATIONS AND TRANSPORTATION

Telecommunications is an exploding field where accurate DEMs are essential for client services. Cellular telecommunication is dependent upon customer's access to towers. Selection of cellular tower locations is becoming more complex due to the trends in urban growth and stricter zoning regulations. As a result, planning and engineering are becoming even more important to the successful construction of the telecommunications infrastructure.

STAR-3i can quickly provide large area coverage DEMs at finer terrain elevation accuracy's to service providers. For example, the telecommunications industry may require response times of only a few weeks for delivery of DEM and other spatial data products. Thus the ability to respond on these time periods is an important pre-requisite for successful commercial operation of the STAR-3i system. STAR-3i data are used for "line of sight" tower planning, accurate DEM and DTM mapping for microcell planning, land use and clutter mapping for microwave propagation planning.

STAR-3i can also be an attractive solution when mapping long, linear projects. Examples of these applications include: powerline right of way planning and monitoring, pipeline planning and highway planning. Data acquisition for these applications can be much more efficient when using an airborne platform as compared to using a satellite platform, which are generally inefficient for sensing extended linear features that are not aligned with its orbital path. The STAR-3i system allows for the rapid generation of DEMs for these extended linear features without the requirement for ground control.

4.0 CONCLUSIONS

Intermap's STAR-3i is the first commercial implementation of a high performance single pass across track interferometer. The STAR-3i system allows Intermap to provide high quality mapping products to meet the needs of the worldwide imaging and mapping community. DEMs and orthorectified image maps produced by the STAR-3i system are already making important contributions towards a variety of commercial applications such as forestry, exploration, telecommunications, and transportation. As GIS and global navigation and positioning (*i.e.*, GPS) applications continue to proliferate and exploit advances in technology to increase their accuracy, the need for high accuracy DEMs will continue to increase. For example, with the upcoming launch of high resolution commercial imaging satellites by companies such as EarthWatch and Space Imaging-EOSAT, we believe that many new applications of STAR-3i DEMs are on the horizon. Consequently, as the pace of remote sensing and GIS accelerates, IFSAR technology will be an increasingly important element to help advance these industries.

5.0 REFERENCES

G. F. Adams, J. L. Auterman, G. T. Sos, and J. O. Abshier, "Terrain Height Measurement By Fine Resolution Interferometric SAR," *Proc. Ninth Thematic Conference on Geologic Remote Sensing*, Feb. 1993.

L. C. Graham, "Interferometric Radar for Topographic Mapping," *Proc IEEE*, Vol. 62, No. 6, pp. 763 - 768, June 1974.

K. Green, *Panacea or Pandora's Box? How New Satellites Will Affect Our View of the World*, Geo Info Systems, p. 12 - 20, July 1996.

S. N. Madsen and H. A. Zebker, "Automated Absolute Phase Retrieval in Across-track Interferometry," *Proc. Int. Geoscience and Remote Sensing Symp.*, Vol. II, 1992.

B. Mercer, S. Griffiths, and S. Thornton, "Operational Topographic Mapping from Airborne SAR Data," *Proc. of the International Symp. Of Operationalization of Remote Sensing*, ITC Enshede, The Netherlands, p. 19 - 23, April 1993.

G. T. Sos, H. W. Klimach, and G. F. Adams, "High Performance Interferometric SAR Description and Capabilities," *Proc. Tenth Thematic Conference on Geologic Remote Sensing*, San Antonio, Texas, May 1994.

A. Zebker and R. M. Goldstein, "Topographic Mapping from Interferometric Synthetic Aperture Radar Observations," J. Geophysical Research, vol. 91, no. B5, pp. 4993 - 4999, April 1986.

THE AIRSAR/TOPSAR INTEGRATED MULTI-FREQUENCY POLARIMETRIC AND INTERFEROMETRIC SAR PROCESSOR

Jakob J. Van Zyl, Anhua Chu, Scott Hensley, Yunling Lou, Yunjin Kim, Soren N. Madsen

Jet Propulsion Laboratory, California Institute of Technology
4800 Oak Grove Drive, MS 300-227
Pasadena, California 91109
email: jacobv@blacks.jpl.nasa.gov

I. INTRODUCTION

Research on the utility of Synthetic Aperture Radar (SAR) data in many diverse applications has seen great activity in the past decade. In particular, two powerful SAR techniques emerged during this time. Polarimetric SARs were first demonstrated during the 1980's and is described by van Zyl *et al.* [1] and Zebker *et al.* [2]. Since then polarimetric SAR data have been applied to most disciplines of Earth Science. A recent summary of these investigations can be found in [3]. The second powerful SAR technique that has received much attention lately is SAR interferometry. While first published by Graham [4] in the 1970's, interest in this technique has steadily increased since the demonstration of SAR interferometry using digital processing [5]. For a summary of the different applications of SAR interferometry, please see [6].

To really derive the maximum information content from SAR data, it is desirable to combine polarimetric and interferometric techniques, preferably at multiple frequencies. The NASA/JPL AIRSAR/TOPSAR system [14] is capable of simultaneously acquiring interferometric (C- and/or L-band) and polarimetric data (C-, L- and P-band). In this paper we describe a processing approach that is used to process data acquired in these modes. This approach is different from that described by Madsen *et al.* [7] in both the motion compensation approach, as well as in the sense that data are deskewed before interferograms are formed. Using this approach, the same basic SAR processor is used to process data acquired in any of the modes supported by the AIRSAR/TOPSAR system.

II. THE AIRSAR/TOPSAR SYSTEM

The NASA/JPL AIRSAR system is a three-frequency airborne SAR system that was developed to be a general test-bed for advanced SAR techniques. The SAR system is flown on a NASA DC-8 passenger jet operated by NASA's Ames Research Center in Mountainview, California. The AIRSAR antennas are not gimballed; instead the dual-polarized microstrip antennas are mounted fixed to the body of the DC-8 aft of the left wing. The earliest mode implemented in the AIRSAR system (operational since 1988) was the three-frequency polarimetric mode, where fully polarimetric data are acquired simultaneously at C-band, L-band and P-band. This mode was used to provide prototype data for the SIR-C/X-SAR science team and many of the algorithms applied to SIR-C data were developed using AIRSAR data.

In 1990 NASA, in collaboration with an Italian consortium (CORISTA), approved the addition of another set of C-band antennas to implement a single-pass, fixed baseline cross-track interferometer (XTI) for topographic mapping. The C-band antennas were provided by CORISTA, while NASA sponsored the system modifications and processor development described by Madsen *et al.* [7]. This mode of the AIRSAR system became known as TOPSAR [8] and data have been acquired since 1991. The original TOPSAR processing software has been updated several times since the original publication in [7]. One version of this updated software was delivered to the Environmental Research Institute of Michigan (ERIM) under a contract with the Defence Advance Research Projects Agency (DARPA), and is currently being used to process the data from the ERIM IFSARE system. In 1995 TOPSAR was extended to acquire XTI data simultaneously at C-band and L-band [9]. All TOPSAR interferometers can be operated in single or dual baseline modes. For single baseline operation signals are transmitted out of one antenna only, and the received signals are measured simultaneously through two antennas. In the dual baseline mode, signals are alternately transmitted out of the antennas at either end of the baseline, while the received signals are measured simultaneously through both antennas.

III. PROCESSING APPROACH

The aim of the Integrated AIRSAR Processor is to implement a processing strategy capable of processing all the modes described above with the same basic processor. Therefore, the processor must automatically produce co-registered multi-frequency images, whether or not at least one frequency was acquired in the interferometric mode. Madsen *et al.* [7]

describe a way to process single frequency cross-track interferometry data. In this approach, the individual images are never explicitly deskewed. Rather, the deskew forms an integral part of the location algorithm; the along-track offset given by Madsen *et al.* [7] is identical to the deskew used in the traditional range-Doppler processor [10].

This follows from the fact that in traditional (non-interferometric) SAR processing, it is assumed that the imaged pixel is located at the intersection of the Doppler cone (centered on the velocity vector), the range sphere (centered at the antenna) and an assumed reference plane. Since the Doppler cone has its apex at the center of the range sphere, and its axis of symmetry is aligned with the velocity vector, it follows that all points on the intersection of the Doppler cone and the range sphere lie in a plane orthogonal to the velocity vector. The additional information provided by the interferometry is that the imaged point also has to lie on the cone described by a constant phase, which means that one no longer has to assume an arbitrary reference plane. This cone of equal phase has its axis of symmetry aligned with the interferometer baseline and also has its apex at the center of the range sphere. It then follows that the imaged point lies at the intersection of the Doppler cone, the range sphere and the equal phase cone. Using the same argument as before, it is clear that the point still lies in a plane orthogonal to the velocity vector. This along-track offset can still be calculated using the traditional expression for the deskew, as shown in Madsen *et al.* [7].

When processing multi-frequency data, one has two options to ensure that the output images automatically co-register. In the first approach, the sub-patch size is chosen such that the same number of output lines are kept for all frequencies. (This assumes that the radars operate at the same pulse repetition frequency, which is the case for the AIRSAR system.) All frequencies can then be processed with properly scaled Doppler parameters, meaning that the along-track shift for all frequencies will be the same. Therefore, the location parameters derived at any frequency can directly be applied to all the other frequencies. In this case, the size of the sub-patch used, as well as the amount of overlap between adjacent sub-patches are determined by the length of the azimuth reference functions at the lowest frequency.

There are two main disadvantages to this approach. First, the fixed number of output lines for all frequencies means that the processor becomes quite inefficient in the case of the high frequencies for which the azimuth reference functions are much shorter than at the low frequencies, since large parts of the overlap areas between successive sub-patches are unnecessarily recalculated. Secondly, since the size of the patch at the high frequencies is large compared to the

synthetic aperture size, the motion compensation may be less than optimum.

These disadvantages can be overcome by processing each frequency separately into the zero squint geometry before utilizing any interferometric information. After the deskew is applied, the multi-frequency images automatically co-register. This now means that each frequency can be processed with a sub-patch size optimally chosen for that particular frequency. In a sense this follows the same processing paradigm usually employed in repeat-pass interferometry. The disadvantage, at least in our implementation, is that the bookkeeping of the phases during motion compensation is slightly more complicated.

The post processing steps applied after the SAR processing depends on the mode in which the data were acquired. For the three-frequency polarimetric mode the various cross-products are combined into the standard AIRSAR compressed Stokes Matrix format and then radiometrically calibrated.

In the case where interferometric data were acquired, the interferogram phase is first unwrapped and the slant range digital elevation model is formed. The location parameters for each slant range pixel is now calculated using the elevation model just derived. Since all the images acquired at the different frequencies now are co-registered, the same set of locations parameters an be used to geometrically resample all images. These location parameters are then used to resample the calibrated polarimetric SAR images. In addition to the calibrated and geometrically corrected SAR images and the digital elevation model, images of the local incidence angle and the interferometric correlation coefficient are also provided. These images are also geometrically corrected using the location parameters calculated from the interferometric phase information.

IV. RESULTS

The performance of the TOPSAR instrument and processor was previously reported by Madsen, *et al.* [7], who compared the radar derived digital elevation models with ones derived using conventional optical stereo techniques. Their analysis showed the difference between the DEMs to be 2.2 m r.m.s in relatively flat terrain, and up to 5.0 m in mountainous areas. Instead of repeating these analyses here, we compare the results of the Integrated Processor described here to that of the TOPSAR processor described by Madsen *et al.* [7].

To compare the results of the processors, we processed two strips of data through both processors, and then compared the results. First we tested the relative geometrical accuracy of the two resulting data sets. This is done by cross-correlating

small subsections of the images, and measuring the along-track and cross-track offsets between the images. This analysis is repeated for a grid of 100 points spaced uniformly through the images. To test the effect of relief on the results, this comparison was done for a flat area covering the Bolivar peninsula near Galveston, Texas, and a mountainous area covering part of Mount Rainier in Washington State. The total relief in the Bolivar scene is less than 50 m while the total relief in the Mount Rainier scene is about 1500 m. The results of the relative geometry test shows the rms difference between the Bolivar images to be 1.3 m in the cross-track direction, and 2.1 m in the along-track direction for a nominal post spacing of 10 m. For the Mount Rainier scenes, the rms difference are 2.3 m and 4.9 m in the cross- and long-track directions respectively. This confirms previous reports that results for relatively flat areas are typically better than those for high relief areas.

REFERENCES

[1] J. J. van Zyl., H.A. Zebker and C. Elachi, "Imaging radar polarization signatures: Theory and observations," *Radio Science,* 22, pp. 529--543, 1987.

[2] H. A. Zebker, J. J. van Zyl and D. N. Held, "Imaging radar polarimetry from wave synthesis," *Journal of Geophysical Research,* 92, no. B1, pp. 683--701, 1987.

[3] J. J. van Zyl, "SAR polarimetry and interferometry," in *Review of Radio Science 1993-1996,* R.W. Stone (Ed), Oxford University Press, New York, 1996.

[4] L. C. Graham, "Synthetic Interferometer Radar for Topographic Mapping," *Proc. IEEE,* 62, pp.763-768, 1974.

[5] H. Zebker and R. Goldstein, "Topographic Mapping from Interferometric SAR Observations," *J. Goephys. Res.,* 91, pp. 4993-4999, 1986.

[6] C. T Allen, "Interferometric Synthetic Aperture Radar," *IEEE Geoscience and Remote Sensing Society Newsletter,* pp. 6-13, September 1995.

[7] S. N. Madsen, H. A. Zebker, and J. Martin, "Topographic Mapping Using Radar Intereferometry: Processing Techniques," *IEEE Trans. Geosci. Remote Sens.,* GRS-31, pp. 246-256, 1993.

[8] H. A. Zebker, S. N. Madsen, J. Martin, K. B. Wheeler, T. Miller, Y. Lou, G. Alberti, S. Vetrella, and A. Cucci, "The TOPSAR interferometric Radar Topographic Mapping Instrument," *IEEE Trans. Geosci. Remote Sens.,* GRS-30, pp. 933-940, 1992.

[9] J.J van Zyl., H.A. Zebker, S. Hensley and D.R. Haub, "The new dual frequency (C- and L-band) TOPSAR airborne interferometric SAR," *Proceedings of IGARSS'95* , Florence, Italy, July 10-14, 1995.

[10] J. C. Curlander and R. N. McDonough, *Synthetic Aperture Radar Sytems and Signal Processing,* John Wiley and Sons, New York, 1991.

Implementation of the Integral Equation Model for Rough Surfaces with Generic Isotropic Autocorrelation Functions

G. Nesti[1], R. Estevan de Quesada[2], J. M. López[2], and A. J. Sieber[1]

[1] Advanced Techniques, SAI JRC 21020 Ispra (Va), Italy
Tel/Fax: +39 332 785922/5772, E-mail: Giuseppe.Nesti@jrc.it
[2] Departamento de Comunicaciones, ETSIT, UPV
Camino de Vera s/n, 46071 Valencia, Spain

Abstract - An implementation of the Integral Equation Model applicable to rough isotropic surfaces is presented which makes use of Fourier Transform numerical methods to compute the surface spectrum. Different approaches for performing the calculations are compared in terms of computational accuracy and efficiency. Optimum values for window size and sampling step are reviewed and illustrated in practical cases depending on the surface autocorrelation function and the operating frequency.

INTRODUCTION

The computation of the scattering coefficient of rough surfaces through the Integral Equation Model (IEM) requires the estimation of the Fourier Transform of the surface autocorrelation function (ACF) elevated to the nth power, where n takes integer values from 1 to ∞. In practice, a value n_{max} is selected on the basis of a reasonable convergence criterion for the series. In some canonical cases, such as the Gaussian and Exponential ACFs, the spectrum can be computed analytically but in general only a direct numerical calculation is possible. In this numerical approach, two aspects require careful consideration: (1) the computational efficiency to avoid unnecessarily long computation time, and (2) the proper sampling and windowing of the ACF to avoid aliasing and leakage effects.

In this paper, an implementation of the IEM applicable to rough surfaces with azimuth-isotropic ACFs is presented which is based on the computation of the surface spectrum via numerical methods. The criteria for selecting the window size and the sampling step are reviewed and demonstrated in practical cases on dependence of the type of ACF and the operating frequency. Different approaches for performing the calculations are compared in terms of computational accuracy and efficiency.

As an application of the method, simulated results are compared with experimental backscattering data acquired at the European Microwave Signature Laboratory (EMSL) on an artificial rough dielectric surface, in the frequency range 2 - 18 GHz and for incidence angles from 10 to 50 degrees.

THE IEM MODEL

The Integral Equation Method (IEM) Model is based on an approximate solution of a pair of surface integral equations for the tangential fields E and H. This method yields an estimation of the tangential fields by introducing in the formal exact solution the Kirchhoff field as first approximation [1].

The far-zone electric scattered field is computed from the tangential electric and magnetic fields by using the Stratton-Chu integral and finally the scattering coefficient is derived from an ensemble average which takes into account the distribution of the surface heights.

The explicit final formula actually requires the computation of the spectrum ACF elevated to the nth power, where n takes all integer values from 1 to a convenient large value (n_{max}).

For example, the copolar backscattering coefficient from a random surface with height RMS $= \sigma$ and ACF $= \rho(u,v)$ reduces to (for single scattering):

$$\sigma_{pp}^0 = \frac{k^2}{2} e^{-2\sigma^2 k_z^2} \sum_{n=1}^{+\infty} \sigma^{2n} |I_{pp}^n|^2 \frac{W^{(n)}(-2k_x,0)}{n!} \quad (1)$$

$$I_{pp}^n = (2k_z)^n f_{pp} e^{-\sigma^2 k_z^2} + \frac{k_z^n [F_{pp}(-k_x,0) + F_{pp}(k_x,0)]}{2} \quad (2)$$

$$W^{(n)}(K_x,K_y) = \frac{1}{2\pi} \int_{-\infty}^{+\infty} \int_{-\infty}^{+\infty} \rho^n(u,v) e^{-j(K_x u + K_y v)} du dv \quad (3)$$

where θ is the local incident angle, $k = 2\pi/\lambda$, $k_z = k\cos\theta$, $k_x = k\sin\theta$. The explicit expressions for the coefficients f_{pp} and F_{pp} are given in [1], Appendix 4B. They are function of θ, ε_r (frequency dependent dielectric constant) and μ_r (relative permeability) either explicitly or through the surface Fresnel reflection coefficients ($R_{\parallel}$ and $R_{\perp}$).

Approximations to local incidence angle

Two simple approximations to the local angle θ used for the calculation of R in f_{pp} can be considered: (1) replace it with the incidence angle (flat surface approximation) and

(2) set $\theta = 0$ (normal incidence approximation). In the coefficients F_{pp}, the local angle is always approximated by the incidence angle. Comparison between the Moments Method and the IEM Model [1, section 6.4] have shown that the first approximation is good in the low frequency region, while the other is good in the high frequency region. However, a transition region is always present where the two approximations give the upper and lower bound of the correct value. In the simulation results presented here a simple transition function has been used (for all the incidence angles) to weight the two limit cases in the intermediate region and get a good fit with the experimental data:

$$\theta = \frac{\theta_{incident}}{2} \cdot \mathrm{erfc}\left(\frac{f - f_0}{\Delta_f/4}\right) \qquad (4)$$

where f_0 is the center frequency and Δ_f is the measured band.

Up to now, no method is available to select the weighting function on the bases of the surface characteristics (ε_r, σ, ρ).

COMPUTATION OF SURFACE SPECTRUM

In general, the surface spectrum has dependence along orthogonal directions u and v, accounting for geometric anisotropic surfaces. In the following, only azimuth-isotropic surfaces are considered where the ACF$=\rho(r)$ with $r = \sqrt{u^2 + v^2}$. In these cases the power spectrum $W^{(n)}(K_x, K_y)$ will have also circular symmetry and can be computed by taking the Hankel transform of ρ^n:

$$W^{(n)}(K) = \int_{r=0}^{+\infty} \rho^n(r) \cdot r \cdot J_0(Kr) dr \qquad (5)$$

In a few canonical cases, such as the Gaussian and Exponential ACFs, the spectrum can be computed analytically using (5) but in general real surfaces do not follow such simple functions and the spectrum must be computed numerically. We have rejected the possibility of performing the numerical integration due to the oscillating characteristics of $J_0(Kr)$. This function behaves like a sine with period $2\pi/K$, and it is necessary to use a large number of nodes N_{nodes} in the numerical integration in order to obtain accurate results for high values of K [2]. An approximate expression of N_{nodes} based on the Gaussian method to compute the integration is $N_{nodes} = 16 \cdot r_{max}/P$, where $P = 2\pi/K$ is the period and r_{max} is the value of r from which the function becomes negligible. Therefore, we have resorted to use Fourier Transform (FT) methods to compute directly the spectrum.

Discrete Two-Dimensional Fourier Transform

If $s[n, m]$ is the finite sequence obtained by sampling the ACF along x and y with a spatial frequency $f_s = 1/T_s$,

its two-dimensional Discrete Fourier Transform (DFT):

$$S[k, l] = \sum_{n=0}^{N-1} \sum_{m=0}^{N-1} s[n, m] \cdot e^{-j \cdot \left(\frac{2\pi}{N} \cdot k \cdot n + \frac{2\pi}{N} \cdot l \cdot m\right)} \qquad (6)$$

is related to the 2D-FT of the original ACF ($S_c(\omega_1; \omega_2)$) by the following relation:

$$S[k, l] = (1/T_s)^2 \cdot \qquad (7)$$
$$\sum_{k_1=-\infty}^{+\infty} \sum_{l_1=-\infty}^{+\infty} S_c\left(\frac{2\pi}{N} k f_s - 2\pi k_1 f_s; \frac{2\pi}{N} l f_s - 2\pi l_1 f_s\right)$$

Sampling rate

Equation (7) shows that the original surface spectrum is corrupted by the sampling procedure (aliasing effect) if f_s does not satisfy the Nyquist criterion $f_s > BW = 2 \cdot f_{max}$.

As an application example, we will apply the method to a specific ACF:

$$\rho(r) = \exp\left[-r^2/\sqrt{l^4 + (L \cdot r)^2}\right] \qquad (8)$$

where the *gaussian* term l and the *exponential* term L dominate the function shape in the limit of short or long displacement, respectively.

In this case, at high frequency the spectrum is dominated essentially by the *gaussian* term ($\Rightarrow BW = BW_{gaus}$) except if $l \ll L$ ($\Rightarrow BW = BW_{exp}$) where BW_{gaus} and BW_{exp} are estimated from the analytical expressions of the Gaussian and Exponential ACF spectra, respectively. Since those spectra are unlimited, we have to define empirically the bandwitdh by setting a limit value (i.e. 10^{-E_0}) in the normalised spectrum.

In the general case where no *a priori* knowledge is available, a possible approach is to oversample the ACF and apply an anti-aliasing low-pass filter according to the required maximum value of K, i.e., K_{max}.

Data window

Obviously, it is necessary to use a large data window for the ACF to get a good accuracy in the computed spectrum. However, a tradeoff has to be established between window size and sampling rate in order to keep the number of samples within reasonable limits. A criterion for selecting the window size can be established by imposing the level of the ACF to be lower than an arbitrary value i.e. $\rho^n(r) \leq 10^{-E}$.

The application of this condition to (8) yields,

$$r \geq \frac{EL \log(10)}{n\sqrt{2}} \sqrt{1 + \sqrt{1 + \frac{4l^4 n^2}{L^4 E^2 \log^2(10)}}} \qquad (9)$$
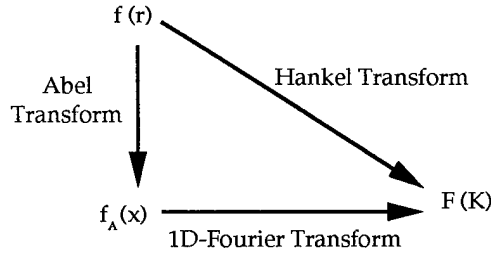
Figure 1: Relationship between Abel, Fourier and Hankel Transforms

Figure 2: Comparison of the computation complexity between 2D-FFT and Abel Transform plus 1D-FFT

COMPARISON OF TRANSFORM METHODS

Simulated data can be required for a few K-values of interest or for a set of K-values covering a large K-range. In the first case the formula (6) can be conveniently used while in the other it is more efficient to apply the FFT algorithm even if not all the computed points are needed. The efficiency of the method can be improved, taking advantage of the surface circular isotropy, by replacing the 2D-FT with an Abel Transform followed by one 1D-FT as discussed below.

The Abel Transform

Given the circular isotropy of the surface ACF we can write:

$$W^{(n)}(K,0) = \int_{-\infty}^{+\infty} \rho_A^{(n)}(x)e^{-jKx}dx \qquad (10)$$

where

$$\rho_A^{(n)}(x) = \int_{-\infty}^{+\infty} \rho^n\left(\sqrt{x^2+y^2}\right) dy \qquad (11)$$

is the Abel transform of $\rho^n(r)$ [3, Chapter 9].

The Abel transform is, for a given x, the line integral of $\rho^n(r)$ in the y-direction. The numerical integration is performed by using integration formulae of Gaussian type. The spectrum is finally obtained by using a 1D-FT along x, as shown schematically in Fig. 1.

Computation efficiency

If N is the number of points where the spectrum is computed, the number of operations in all methods is dependent on N. Computing the spectrum by means of a 2D-FFT, the total number of floating point operations (FLOPS) is known to be proportional to $N^2 \log_2(N)$. However, using the Abel Transform, only N integrations and a single 1D-FFT are needed. The integration method consists on the evaluation of the integrand at a fixed number of points (usually less than 40) and a weigthed summation. Then, the total number is approximately proportional to $N(\log_2(N)+N_{int})$. On the other hand, the above mentioned methods yield the value of the spectrum at N points in the frequency (or K) domain. By using the 2D-DFT one can obtain the spectrum at N_K arbitrary points.

Then, the number of FLOPS of the 2D-DFT will be expressed as $N_K \cdot N^2$, and therefore this method will be more efficient than the 2D-FFT only if $N_K < \log_2(N)$.

In order to show real results we have obtained the number of FLOPS required by Matlab for each method in the range from $N=2$ to 1024. This result is depicted in Fig. 2. As expected, for high values of N the Abel Transform is more efficient, and the 2D-FFT becomes useless due to its great computation complexity and consequent high computation time.

Accuracy

In the application of the IEM Model the spectra will be evaluated at $K = -2k_x$. The upper limit of this value (in modulus) is given by $K_{max} = 2k = 4\pi f/c \approx 42f(\text{GHz})$.

The accuracy of both methods (2D-FT and Abel Transform) and its dependence on parameters has been analyzed in the range $0 \leq K \leq 1000$ corresponding to a maximum frequency of about 24 GHz. Of course, the 2D-DFT and the 2D-FFT have the same accuracy, the difference being only in the number of evaluated frequency points.

The accuracy has been estimated against reference results, obtained in this case from the analytical solution of the Exponential ACF. As described in previous sections, the window size and the spectrum bandwidth depend on n (the exponent). The accuracy of both methods as a function of n, for fixed N, E and E_0, is outlined in Table I.

When n grows the maximum error becomes negligible. Moreover, even with this relatively large error for low n the final backscattering coefficient is quite accurate (error less than 0.2 dB in the worst case).

The parameter E_0 has been fixed to 5 because with

Table I: Maximum error (dB) of the nth power spectra computed by the 2D-FT and the Abel Transform in the range $0 \leq K \leq 1000$. Parameters: Exponential ACF, $E = 7$, $E_0 = 5$, $N = 1024$, $L = 3$ cm

n	1	2	3	4	8	15
2D-FT	1.1	0.13	0.04	0.017	0.0025	0.001
AbelT	0.5	0.09	0.0225	0.009	0.0015	0.0005

lower values accuracy decreases and with higher values the number of points N used in the 2D-FT becomes too large. On the other hand, E produces good results from 4 to 7, being inaccurate for lower values and inefficient for higher values.

COMPARISON WITH EXPERIMENTAL DATA

As an application example, data computed with the method presented here have been compared with experimental data acquired at the EMSL [4] on an artificial rough dielectric surface with $\sigma = 0.9$ cm and ACF defined in (8) ($l = 1.8$ cm, $L = 3.0$ cm), in the frequency range 2 - 18 GHz and for incidence angles from 10 to 50 degrees. The dielectric constant of the material ranged from $5 - i1.4$ at 2 GHz to $3.7 - i0.9$ at 18 GHz. The parameters used in the simulation are: $E = 7, E_0 = 5, N = 1024$.

Fig. 3 shows the comparison versus frequency for an incidence angle of $40°$. No frequency averaging has been applied to the experimental data. The noise is due to the residual speckle after averaging 72 independent samples per frequency point. The line labelled R(erfc) refers to the local angle θ interpolated using (4).

For this incidence angle the agreement is excellent in the whole frequency range, however the same is not true at lower incidence angles where a significant deviation can be noted at high frequency (e.g in Fig. 4b). This discrepancy may be partly due to the contribution of multiple scattering. Further investigation in this direction is in progress.

CONCLUDING REMARKS

The results presented here show that numerical Fourier Transform techniques can be efficiently and accurately applied in the implementation of the IEM model to estimate the surface spectrum of rough surfaces with generic ACF. For azimuth isotropic surfaces, and when the number of data points required to properly sample the ACF is higher than 64, the 2D-FFT can be conveniently replaced by the Abel Transform, followed by a 1D-FFT. The typical parameters values (sampling step, window size) which are required to obtain a good accuracy have been discussed in practical cases.

REFERENCES

[1] A. K. Fung, *Microwave Scattering and Emission Models and Their Applications*. Nordwood: Artech House Inc., 1994.

[2] L. Rakotoarivony, "Validation de modèles de diffusion électromagnétique: comparaison entre simulations et mesures par radar héliporté sur surfaces agricoles de sol nu". *Thèse de doctorat de l' Université de Caen*.

[3] R. N. Bracewell, *Two-Dimensional Imaging*. Prentice Hall International Editions, 1995.

[4] G. Nesti *et al.*, "Experimental Research at the EMSL on Scattering Properties of Non Vegetated Terrains." Proc. IGARSS 1995, Vol. III, pp. 2020-2022.
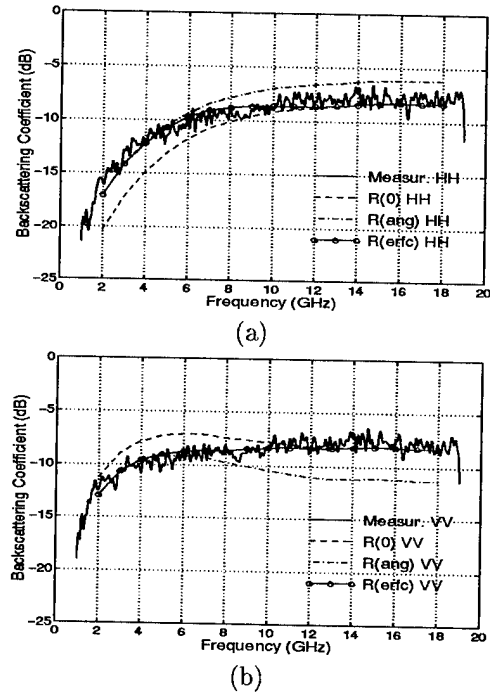
Figure 3: Backscattering Coefficient vs. frequency for a dielectric rough surface. Comparison of measured and IEM simulated data: $\theta = 40°$, (a) HH and (b) VV polarisation
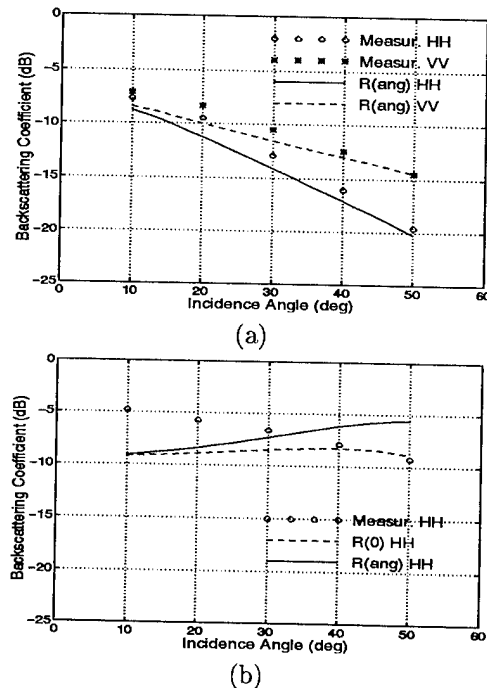
Figure 4: Backscattering Coefficient vs. incidence angle for a dielectric rough surface. Comparison of measured and IEM simulated data: (a) 2 GHz with HH and VV polarisations and (b) 18 GHz with HH polarisation

A Reappraisal of the Validity of IEM Model

T. D. Wu[1], K. S. Chen[1], A. K. Fung[2], Z. Su[3], P. Trouch[3], Rudi Hoeben[3], and Marco Mancini[4]

[1]*National Central University, Chung-Li Taiwan*

Tel: 886 3 4227151 ext. 7961, Fax: 886 3 4255830, Email: s3524015@sparc20.ncu.edu.tw

[2]*WSRC, Dept. EE, University of Texas at Arlington*

[3]*Laboratory of Hydrology and Water Management*

University of Ghent, Ghent, Beligum

[4]*DIIAR Politecnico di Milano, P.za Leonardo da Vinci 32 20133 Milano, ITALY*

ABSTRACT

A surface scattering model based on the integral equation method is examined in terms of its applicability to laboratory measurements. The Fresnel reflection coefficients used in the model have been approximated as a function of the incident angle at low frequency and a function of the specular angle at high frequency. Based on a limited set of experimental measurements, a transition function are suggested for estimating the Fresnel reflection coefficients in the intermediate regions. Results of comparison indicate that the IEM is accurate and practical to use. Issue raised from dielectric information is also addressed.

INTRODUCTION

A surface scattering model based on an integral equation method (IEM) was proposed by Fung et al [1]. It has been demonstrated that the standard Kirchhoff and small perturbation models (SPM) are the special cases of the IEM in the high and low frequency regions respectively. Recently, IEM surface model has been widely used to interpret measurement data from laboratory-controlled experiment and field measurement. Satisfactory results between model and data were reported. Nevertheless, there remains rooms for improvements of model itself and its applications.

In the derivation of applicable approximation for IEM, the Fresnel reflection coefficients are treated as independent of the spatial variable and set the local angle in them as equal to either the incidence angle or the specular angle. An obvious question raised is what do we use in the intermediate region where both approximations fail. In this paper, the transition frequency was investigated and a transition function is suggested to naturally connect these two approximation in the intermediate region. This modification is examined by making comparisons with the laboratory measurement[2] of backscattering coefficients from the Gaussian correlated surface which was irrigated or dried out for each experiment step. The moisture contents measured at different depth and different frequency were converted to dielectric constant. The first data set was measured from a smooth surface with rms height of 0.4 cm and correlation length of 6 cm. The frequency range was from 1 GHz to 10 GHz and the incident angles were 11, 23 and 35 degrees. The second data set was measured from rough surface with rms height of 2.5 cm and correlation length of 6 cm, and its frequency range was from 0.55 GHz to 5.05 GHz. The third data set has the same condition with the second data except for frequency range from 1 GHz to 10 GHz. In the model calculations, we used the measured dielectric constant at smallest depth.

THE IEM SURFACE SCATTERING MODEL

From [1], the form of the single-scatter backscattering coefficient of a randomly rough surface at an incidence angle θ is

$$\sigma_{qp}^s = \frac{k^2}{2} exp(-2\sigma^2 k_z^2) \sum_{n=1}^{\infty} \sigma^{2n} |I_{qp}^n|^2 \frac{W^{(n)}(-2k_x,0)}{n!} \quad (1)$$

where $k_z = k\cos\theta$, $k_x = k\sin\theta$ and

$$I_{qp}^n = (2k_z)^n f_{qp} exp(-\sigma^2 k_z^2)$$

$$+ \frac{k_z^n [F_{qp}(-k_x,0) + F_{qp}(k_x,0)]}{2} \quad (2)$$

The Kirchhoff coefficient f_{qp} and complementary field coefficients F_{qp} are functions of Fresnel reflection coefficient $R_\parallel$ or $R_\perp$ for parallel or perpendicular polarizations; k is the wave number; σ^2 is the variance of the surface heights and $W^{(n)}(-2k_x,0)$ is the Fourier transform of the nth power of the surface correlation function normalized to the surface variance.

For a dielectric surfaces there are two approximations to the local angle in the Fresnel reflection coefficients $R_{\parallel,\perp}$ used in the Kirchhoff coefficient f_{qp}: one approximation replaces the local angle by the incident angle in low frequency region, that is $R(\theta)$, and the other by the normal angle in high frequency region, that is $R(0)$. The local angle in the Fresnel reflection coefficients in the complementary field coefficients F_{qp} is always approximated by the incident angle. It is worth

to note that the single scattering coefficient given by Fqp is always approximated by the incident angle[1]. It is worth to note that the single scattering coefficient given by IEM using the second approximation $R(0)$ will be in agreement with the standard geometric optics model (GOM) which is the Kirchhoff model in high frequency limite and is independent on frequency. It can also be observed that in rough surface case the scattering coefficient computed from IEM with $R(\theta)$ will cross that from GOM near high frequency region, and the cross point depends on the incident angle, dielectic constant, rms height and rms slope of the surface. Therefore, as the frequency increases from low to high, we suggest a transition frequency f_T which is the maximum frequency corresponding the cross point between IEM and GOM. In some cases of vertical polarized scattering which have no cross point, then we set the transition frequency being the frequency corresponding to the peak value of scattering coefficient of IEM with $R(\theta)$, which is the nearest point to GOM. In the special case of surface with small rms slope, the f_T for horizontal polarization is set equal to that for vertical polarization. We also suggest a transition function T to estimate the Fresnell reflection coefficients $R_T = R(\theta) + [R(0) - R(\theta)] \cdot T^2$ as follows:

$$T = 1 + \pi^{-1} \left\{ \tan^{-1} \left[2.5\gamma\sigma^2 \cos^2\theta \cdot \left(k^2 - 1.3k_T^2 \right) \right] - 0.5\pi \right\}, \quad (3)$$

where k_T is the wave number at f_T and γ is the rms slope of the surface. It can be observed that T lies approximately between 0 and 1 which corresponding to $R_T = R(\theta)$ in low frequency and $R_T = R(0)$ in high frequency, respectively; therefore, it satisfies respective approximations at low and high frequency limits discussed above. Fig.1 shows the backscattering coefficient versus $k\sigma$ for GOM and IEM using $R(\theta)$, $R(0)$ and R_T for VV and HH polarizations. It can be seen that the IEM using R_T provides a smooth transition between the one with $R(\theta)$ and with $R(0)$ from small $k\sigma$ (low frequency) to large $k\sigma$ (high frequency).

COMPARISONS WITH MEASUREMENTS

Selected comparisons between model and measurements are given below. Figure 2 shows a comparison of backscattering coefficient between IEM, Kirchoff, SPM and measurement from smooth surface with pretest irrigation at incident angle 11 degrees. In this case the Fresnel reflection coefficient is approximated by $R(\theta)$. It is obvious that IEM is in agreement with measurement all the way from low to high frequency. The second case is the backscattering coefficient of the rough surface measured form 0.55 to 5.05 GHz. The IEM with $R(\theta)$, $R(0)$ and R_T are compared with measurement data for HH and VV polarizations. It is seen that with the use of R_T the IEM matches the data better.

In our comparisons, we find that the IEM can in in excellent agreement with measurement, both trend and level, for all initial and irrigated soil surface. However, in the dried-out
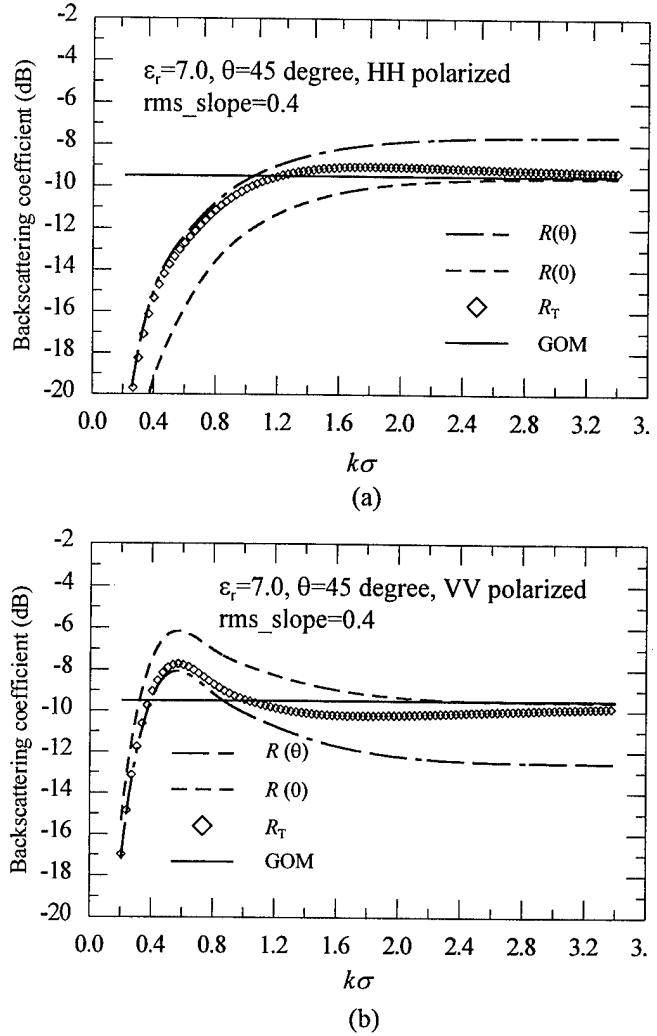
Fig. 1 Comparisons between GOM and IEM with $R(\theta)$, $R(0)$ and R_T for (a) HH polarization, (b) VV polarization.

case, the level of model prediction is slightly higher than measured data. This may be due to the effect of inhomogeneous layer. It was noted from the measured data that the changing rate of dielectric constant with depth in dried-out soil surface is indeed larger than that in irrigated soil surface. To obtain a consistent dielectric constant values, hence, we first calculate the slope of the line fitting the dielectric coefficients of the dried-out soil surface at the depth of 4, 6.5 and 11.5 cm and then shift the dielectric constant by:

$$\varepsilon_{r,shifted} = \varepsilon_r - slope / slope_{ref} - 0.65, \quad (4)$$

where ε_r is the dielectric constant at 4cm depth, $slope_{ref}$ is the slope of dielectric constant in the reference condition from the surface without irrigation or dry-out. Using the shifted dielectric constant in the third case of the measured backscattering coefficient of the rough surface from 1 to 10 GHz, we can see from Fig. 4 that the prediction of IEM with Fresnel reflection coefficient approximated by R_T in in excellent agreement with measurement even in the second dried-out

soil surface.
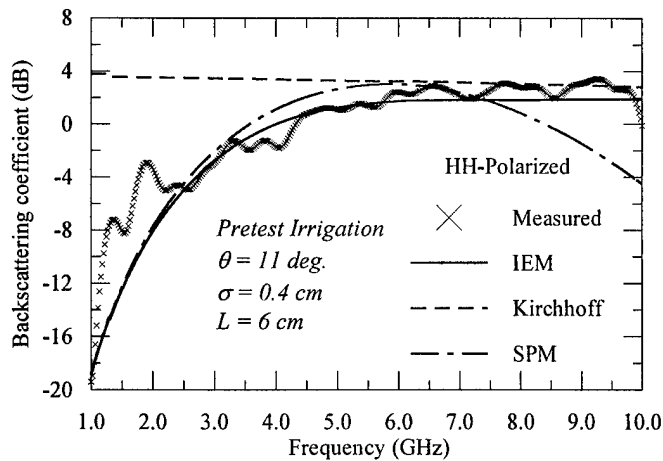
Fig. 2 Comparisons between IEM, GOM, SPM and measurements from a smooth soil surface.
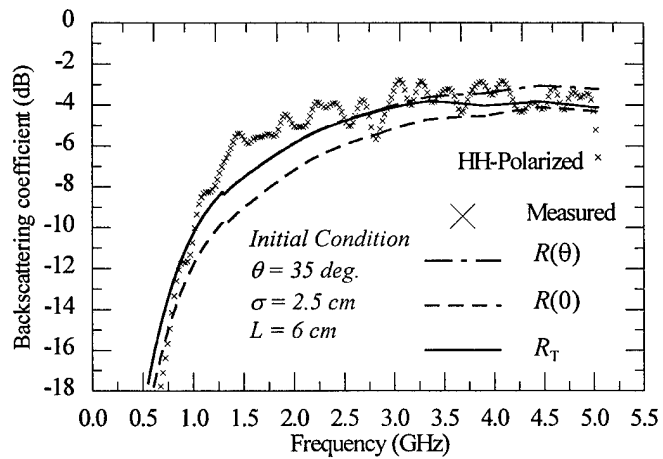
(a)
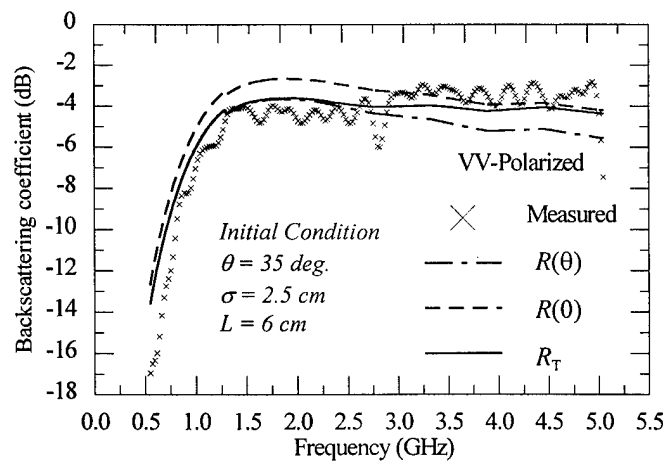
(b)

Fig. 3 Comparisons between model and measurements from a rough soil surface.

CONCLUSION

A modified Fresnel reflection coefficient was proposed based on a limited set of experimental data. The model predictions of IEM are in excellent agreement with data in agular, frequency and polarization dependence. The effect of the inhomogeneity in surface layer remains further study

REFERENCES

[1] A. K. Fung, Z. Li, and K. S. Chen, "Backscattering from a randomly rough dielectric surface," *IEEE Trans. Geosci. Remote Sensing, vol.30, pp. 356–369, 1992.*

[2] Nesti, G.,Pamploni, P., Coppo, P., Hallikainen, M., Mancini, M., Trouch, P., and von Shonermark, M., "Experimental reserach at the EMSL on scattering properties of non vegetated terrains," *Proc. IGARSS95*, pp.2020-2022, 1995.
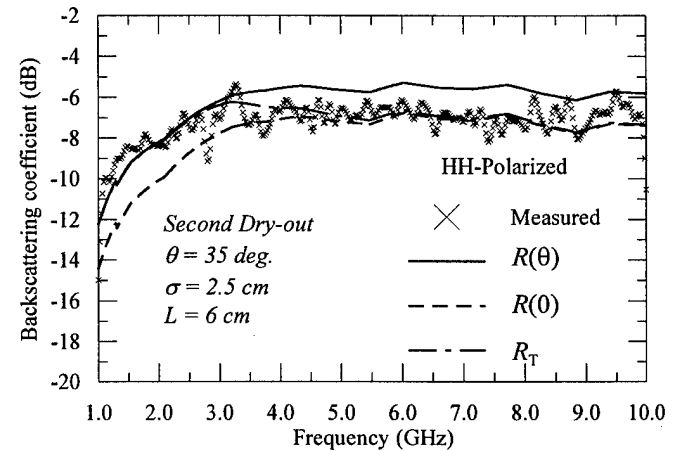
(a)
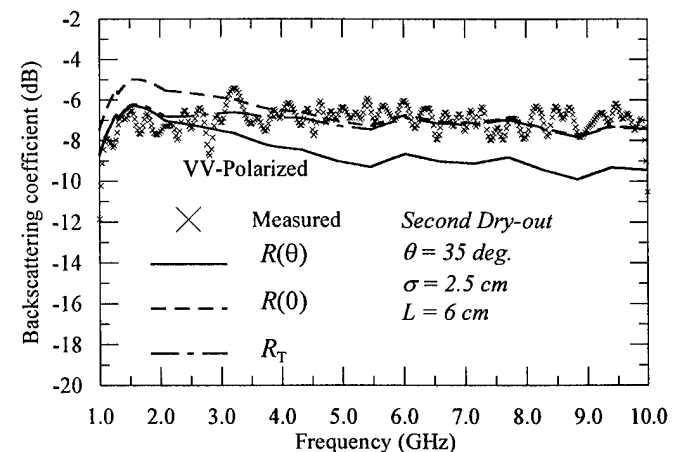
(b)

Fig. 4 Comparisons between model with ε_r shifted and measurements from a dried-out rough soil surface.

Sensitivity of Radar Backscattering to Soil Surface Parameters:
A Comparison Between Theoretical Analysis and Experimental Evidence

Rudi Hoeben,* Peter A. Troch and Zhongbo Su
Laboratory of Hydrology and Water Management, University of Gent
Coupure Links 653, B-9000 Gent, Belgium
tel: +32 9 264 61 38, fax: +32 9 264 62 36; patroch@allserv.rug.ac.be

Marco Mancini,
DIIAR Politecnico di Milano,
Piazza Leonardo da Vinci 32, I-20133 Milano, Italy

Kun-Shan Chen,
Center for Space and Remote Sensing Research, National Central University
Chung-Li, Taiwan, R.O.C.

ABSTRACT

The understanding of the sensitivity of radar backscattering to surface parameters is essential in applying microwave remote sensing to the retrieval of geo- and biophysical parameters. A theoretical model, the Integral Equation Model, is used to investigate the sensitivity of radar backscattering to soil surface parameters. This model is first tested against a dataset retrieved under well controlled conditions at the European Microwave Signature Laboratory, Joint Research Centre, Ispra, Italy. Then the surface roughness parameters are normalised with respect to wavelength and incidence angle to improve our insight into the sensitivity of radar observations to surface roughness. In this way the roughness space can be subdivided in two regions where surface slope controls the dependency of the signal to roughness.

INTRODUCTION

A thorough understanding of the sensitivity of radar backscattering to surface parameters is crucial in developing inversion algorithms for microwave remote sensing of geo- and bio-physical parameters. In this contribution, we aim at evaluating this sensitivity based on both theoretical analysis and experimental evidence. Since it is impossible, in an experimental setup, to mimic all the possible combinations of surface geometrical characteristics, surface dielectric properties and radar configurations, one has to resort to theoretical analysis to generalize what one can experimentally observe under limited conditions. This requires that the theoretical tool used is valid for a wide range and that the experimental data are reliable.

Using a set of well controlled laboratory polarimetric data and soil dielectric data obtained from an experimental research program on the scattering properties of non vegetated terrains conducted at the European Microwave Signature Laboratory (*EMSL*), Joint Research Centre (*JRC*), Ispra, Italy, we shall first validate a theoretical model, the Integral Equation Model (*IEM*) [1]. The IEM is then used to help to interpret the EMSL data in order to generalize the experimental findings as regard to sensitivities of radar backscattering to surface parameters.

THE EMSL EXPERIMENT

The data used are obtained from an experimental research on the scattering properties of non vegetated terrains conducted at the EMSL, JRC, Ispra, Italy. The objectives of the program include validation of surface scattering models and retrieval of soil moisture profiles. The experiment on retrieval of soil moisture profiles was established with the objective to create, under controlled conditions, different datasets which enable the retrieval of soil moisture profiles from microwave observations [2].

The datasets consist of monostatic, multifrequency (0.55 to 10 GHz, step size 11.25 MHz), polarimetric radar measurements at 3 incidence angles θ (11°, 23° and 35°), and measurements of soil moisture and temperature profiles using Time Domain Reflectometry probes (*TDR*) and thermocouples (*TC*). Measurements have been obtained for two soil surfaces. The surface of the soil target is shaped using a mould with specific roughness characteristics. One surface is relatively smooth with a Gaussian autocorrelation function, an root mean squared (*rms*) height σ of 0.4 cm and a surface correlation length L of 6 cm. The other is very rough with a Gaussian autocorrelation function, a σ of 2.5 cm and L equal to 6 cm. The soil sample
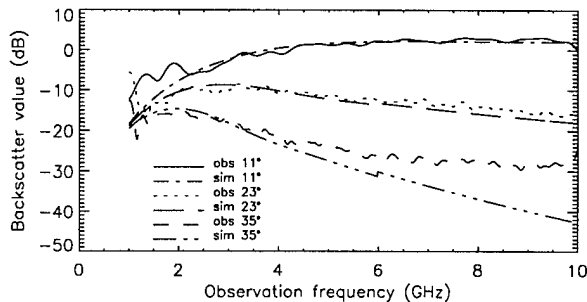
Figure 1: Comparison between measurements and simulations for the smooth surface at 3 incidence angles (VV polarisation, moisture content $m_v = 0.17$)

Figure 2: Sensitivity of σ^o to dielectric constant at different frequencies (exponential correlation function, $\sigma = 1.4$ cm, $L = 10$ cm, $\theta = 35^o$, VV polarisation)

is contained in a cilinder of 2 m in diameter and 0.4 m in depth, placed in the center of the anechoic measurement chamber (radius 10 m). During the radar measurements, stable moisture profiles are realised with a series of irrigation and drying out steps.

Dielectric constant (dc) values at five depths (2.5, 5, 10, 15 and 25 cm) are available. Only the real part of the relative dielectric constant is measured. The measured value is first converted into volumetric soil moisture using a calibration equation, which takes into account soil texture and temperature [3]. A dielectric mixing model [4] is then used to convert the soil moisture into frequency dependent dielectric constants. The measurements at 2.5 cm are used as model input.

VALIDATION OF THE IEM MODEL

The IEM used in this work is an approximate version for surfaces with small to moderate roughness [5]. The validity conditions can be expressed as $k\sigma < 3$, where $k = \frac{2\pi}{\lambda}$ is the free space wave number, λ is the wave length and σ is the surface rms height, and, as only the single scattering term is used, $s < 0.4$, where s is the rms surface slope, $s = \sqrt{2}\frac{\sigma}{L}$ for Gaussian surfaces and $s = \frac{\sigma}{L}$ for exponential surfaces. Due to the large slope, the rough surface falls not within these validity conditions.

In fig.1, comparison between IEM simulation and the measurements is shown. It can be seen that, except for the higher frequencies at 35° incidence angle, the agreement between model simulated and measured backscattering coefficients is very good. The fluctuation in the measured data are due to interference and its treatment is beyond the scope of this contribution. The deviations between measurements and simulations at 35° are possibly due to the neglection of the volume scattering term, which is expected to have an important influence at such low backscatter values.
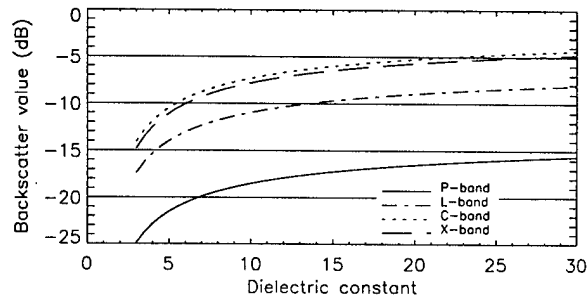
SENSITIVITY ANALYSIS

Generally, moisture content and roughness characteristics (rms height and correlation length for a given type of correlation function) are considered to be the soil surface parameters. As will be shown, frequency and incidence angle will be taken into account, through a redefinition of the roughness parameters.

Fig.2 shows backscatter increasing with dielectric constant. A variation of dielectric constant between 3 and 30 (a shift in moisture content between 2.5% and about 50%, depending on frequency and neglecting soil texture) causes an 8 to 9 dB rise in backscatter coefficient. This shift is almost independent on other parameters, such as incidence angle, frequency or surface roughness. The increment is not linear, but decreases as dielectric constant rises. This implies that the wetter the soil, the lesser the sensitivity of σ^o to dielectric constant will be.

The sensitivity of the backscatter value σ^o to the roughness parameters σ and L has already been discussed [6]. Reference [6] divide the (σ, L) space at C-band in 4 regions, defining different sensitivities to one or both of the parameters. Though we can find some regions also in the (σ, L) spaces at other frequencies, not all can always be found in the range of realistic σ and L values, so conclusions depend on the frequency used. Here we want to generalise their statements concerning the sensitivity to the roughness parameters.

Rescaling this space to the $(k\sigma, kL)$ space makes the sensitivity independent on observation frequency. In fig.3, the $(k\sigma, kL)$ space is divided in 2 regions by drawing a line A. The shaded area is excluded through the validity condition on the slope. In region I the sensitivity of σ^o to kL is small. The sensitivity to $k\sigma$ is very strong at low $k\sigma$ values, but decreases as $k\sigma$ increases. For region II, the situation is just opposite: sensitivity to $k\sigma$ is small, while kL has a strong influence at low kL values, this dependency decreasing with rising kL. The division is
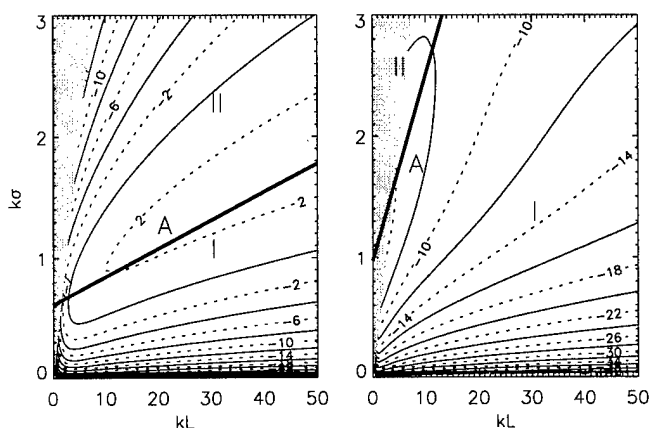
Figure 3: Division of the $(k\sigma, kL)$ space in 2 regions of sensitivity at 11° (*left*) and 52° (*right*) ($dc = 15$, VV polarisation, exponential correlated surface)
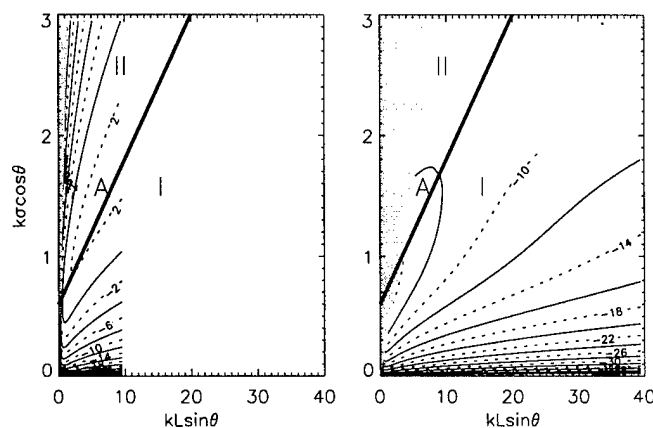
Figure 4: Division of the $(k\sigma \cos\theta, kL \sin\theta)$ space in 2 regions of sensitivity at 11° (*left*) and 52° (*right*) ($dc = 15$, VV polarisation, exponential correlated surface)

independent on frequency, dielectric constant and polarisation, but is still influenced by the incidence angle (rising slope of line A with incidence angle). The incidence angle affects both the shape as the level of the $(k\sigma, kL)$ surface.

A further redefinition of the roughness parameters to $k\sigma \cos\theta$ and $kL \sin\theta$ results in a constant shape of the $(k\sigma \cos\theta, kL \sin\theta)$ surface, though the level of the surface still changes with incidence angle. As can be seen from fig.4, line A can be redrawn in this space through the points (0.6,0) and (20.,3.). The sensitivity in the 2 regions is as mentioned before, but the division is now also independent on the incidence angle. Though the redefinition is only shown for exponential correlated surfaces, it can also be applied to Gaussian ones.

From fig.4, it can be concluded that, for each region (I or II), the only required information to define the backscatter level is the surface slope relative to the incidence angle ($\frac{\sigma}{L} \cot\theta$ for exponential correlated surfaces), as contourlines are near straigth lines through the origin. An important consequence is that once the region in the roughness space for a given application is known, the number of roughness parameters in the retrieval of soil moisture can be reduced from two (rms height σ and correlation length L) to one (surface slope s).

CONCLUSIONS

We conclude that the roughness as seen by the radar can be expressed in terms of $k\sigma \cos\theta$ and $kL \sin\theta$. Apart from the measured roughness parameters, also the observation frequency and the incidence angle are of importance. As the roughness parameters have a large influence at small numerical values, the knowledge about the correlation length L is important at lower incidence angles, while the rms height σ has to be accurately known at higher

incidence angles. It is stated that both dielectric constant and incidence angle affect the level of the $(k\sigma \cos\theta, kL \sin\theta)$ surface, but the introduction of the generalised roughness characteristics simplifies the understanding of the behaviour of the approximated IEM to the roughness characteristics.

The sensitivity of backscattering to the surfaces's dielectric constant decreases as the soil becomes wetter, but is independent on other parameters such as radar configuration or roughness characteristics.

REFERENCES

[1] A. K. Fung, Z. Li, and K. S. Chen, "Backscattering from a randomly rough dielectric surface," *IEEE Trans. Geosci. Remote Sensing*, vol. 30, no. 2, pp. 356–369, 1992.

[2] M. Mancini, F. Vandersteene, P. A. Troch, O. Bolognani, G. Terzaghi, G. D'Urso, and M. Wüthrich, "Experimental setup at the EMSL for the retrieval of soil moisture profiles," in *Proc. International Geoscience and Remote Sensing Symposium (IGARSS)*, T. I. Stein, Ed., Firenze, Italy, 1995, pp. 2023–2025.

[3] M. Wüthrich, *In situ measurement and remote sensing of soil moisture using Time Domain Reflectometry, thermal infrared and active microwaves*, PhD dissertation, Department of Geography, University of Basel, Switzerland, 1996.

[4] M. C. Dobson, F. T. Ulaby, M. T. Hallikainen, and M. A. El-Rayes, "Microwave dielectric behavior of wet soil, Part II: Dielectric mixing models," *IEEE Trans. Geosci. Remote Sensing*, vol. 23, no. 1, pp. 35–46, 1985.

[5] E. Altese, O. Bolognani, M. Mancini, and P. A. Troch, "Retrieving soil moisture over bare soil from ERS-1 synthetic aperture radar data: Sensitivity analysis based on a theoretical surface scattering model and field data," *Water Resour. Res.*, vol. 32, no. 3, pp. 653–661, 1996.

[6] Z. Su and P. A. Troch, "Soil surface parameters and radar backscattering," *Annales Geophysicae*, p. C 361, 1996.

Topography Sensing by Polarimetric SAR: Theoretical Basis and Application using Orthogonal-pass AIRSAR Data

G.F. De Grandi (1), D.L. Schuler (2), T.L. Ainsworth (2) and J.S. Lee (2)

(1) European Commission Joint Research Centre - Space Applications Institute
Monitoring Tropical Vegetation 21020 Ispra (VA) Italy
Tel.: +39 332 789823 Fax: +39 332 789073 Email: gianfranco.degrandi@jrc.it

(2) Remote Sensing Division, Code 7263, Naval Research Laboratory, Washington DC 20375-5351, USA
Tel.: (202) 767-2004, Fax: (202) 767-5599, Email: schuler@imsy1.nrl.navy.mil, lee@imsy1.nrl.navy.mil

ABSTRACT

The authors have recently proposed an algorithm to derive topographical information from polarimetric SAR data. The algorithm is based on empirical comparisons between the terrain local slope angle and the corresponding changes in the relative position of the co-pol polarimetric signature maximum, and was supported by some preliminary theoretical analysis. Also the algorithm has been validated experimentally using data sets acquired over different geographical areas, over different types of natural targets (forest, bare soil) and using different digital elevation models as reference system. This paper presents some theoretical considerations on the scattering mechanisms which underpin the phenomenological aspects of the topography sensing method. A simplified closed form approximation to the relationship between the co-pol maximum shift and the measured covariance matrix elements is introduced. This step highlights the major contributions to the co-pol maximum shift and suggests an interpretation in terms of the azimuthal symmetry properties of the target. Covariance matrices generated from experimental or modelling data can then be used as input variables to establish the relationship between the true and estimated terrain tilt angle. An example of the theoretical analysis relative to the influence of the incidence angle on the estimator error for a slightly rough surface is reported. From the algorithm's application point of view a new technique is finally demonstrated, whereby using two pass orthogonal acquisition data the elevation surface can be generated as a solution of a Poisson type differential equation with only one tie-point.

INTRODUCTION

The authors have recently proposed an algorithm to derive topographical information from polarimetric SAR data [1]. The algorithm is based on the dependency of the co-polarized polarimetric signature maximum position on the terrain tilt angle in the azimuthal direction. The relative displacement of the co-pol maximum can therefore be linked to the resolved terrain slope in a direction perpendicular to the illuminating radar beam, and provides a differential measurement of the terrain elevation profile. The algorithm has been validated experimentally using air-borne polarimetric SAR data acquired over different geographical areas, over different types of natural targets (forest, bare soil) and using different digital elevation models as reference system. The performance assessment reported in [1] indicates that the error budget on the slope measurement is moderately sensitive to the type of scatterer, and therefore the algorithm is self adaptive within the scene heterogeneity (e.g. forest, bare soil). Experimental results also show empirically that there exist a useful quasi-linear relationship between the relative co-pol signature maximum shift and the azimuth tilt angle within ranges of terrain slopes and SAR incidence angles. Since this relationship is at the core of the algorithm, theoretical understanding of the underlying mechanisms is important. Investigations in this direction to predict the technique's performance and the signal to noise ratio using a slightly rough surface model [2] have been reported in [1]. In this communication we want to tackle the problem from a slightly different perspective. The idea is to try to establish, subject to a number of approximations and boundary conditions, a closed form approximation to the relationship between the co-pol maximum shift and the measured covariance matrix elements. This step will highlight the dominating elements in the maximum shift and suggest an interpretation in terms of the azimuthal symmetry properties of the target. Covariance matrices generated from experimental or modelling data can then be used as input variables to derive the link with the terrain tilt angle. The approach is described in detail in the next section.

Finally from the application point of view results of a new technique are reported which allows for the generation of an elevation map using orthogonal two-pass polarimetric SAR data and only one tie point.

METHODOLOGY

As a first approximation we assume that the transmitted and received waves are linearly polarized, and study only the dependency on the polarization orientation angle ψ (ellipticity angle $\chi = 0°$). This is justified because the co-pol maxima alignment is skewed with respect to the ellipticity angle as a

function of $Im[hh \cdot vv^*]$ and is significant only if the mean $hh \cdot vv^*$ phase is largely different from 0. In this case a rotation of the (ψ,χ) coordinate system can be done, to reduce the problem to the mono-dimensional case.

We then establish a relationship between the co-pol maximum relative shift and the measured polarimetric covariance matrix elements $\psi_{COMAX}= f(C_{ij})$.

This is achieved through a decomposition method into basis trigonometric functions [3], which allows us to identify graphically the contribution of each covariance matrix element to the overall co-pol signature. In our case the basis functions can be built from combinations of the following functions:

$$(1)$$

$$C_1(\psi) = 0.5\,(\cos 2\psi + 1)$$
$$C_2(\psi) = \sin 2\psi$$
$$C_3(\psi) = 0.5\,(-\cos 2\psi + 1)$$

The co-pol power in terms of the covariance matrix is given by:

$$(2)$$

$$P = |C_1|^2 \langle hh \cdot hh^* \rangle + |C_2|^2 \langle hv \cdot hv^* \rangle + |C_3|^2 \langle vv \cdot vv^* \rangle$$
$$+ 2\,(C_1 C_2)\,Re\,[\langle hh \cdot hv^* \rangle] + 2\,(C_2 C_3)\,Re\,[\langle hv \cdot vv^* \rangle] +$$
$$2\,(C_1 C_3)\,Re\,[\langle hh \cdot vv^* \rangle]$$

The basis functions are represented graphically in Fig. 1.
The co-pol maxima are then given by the nulls of the first derivative provided that the second derivative is positive. The first derivative of Eq. 2 is:

$$(3)$$

$$\frac{dP}{d\psi} = (\,(-0.5\langle hh \cdot hh^* \rangle + 2\langle hv \cdot hv^* \rangle - 0.5\langle vv \cdot vv^* \rangle +$$

$$Re\,[\langle hh \cdot vv^* \rangle]\,)\,)\,\sin 4\psi + (\,(\langle vv \cdot vv^* \rangle) - \langle hh \cdot hh^* \rangle)\,)\,\sin 2\psi$$

$$+ (2Re\,[\langle hh \cdot hv^* \rangle] - 2Re\,[\langle hv \cdot vv^* \rangle]\,)\,\cos 4\psi$$

$$+ (2Re\,[\langle hh \cdot hv^* \rangle] + 2Re\,[\langle hv \cdot vv^* \rangle]\,)\,\cos 2\psi$$

The derivative of the co-pol power is therefore in the form of a trigonometric polynomial, which within certain boundary conditions can be approximated by an nth degree polynomial in ψ using a Taylor series expansion of the trigonometric functions. As it can be inferred from the basis functions, the co-pol signature has absolute maxima either near $\psi= 0°$ or $\psi= 90°$ according to whether the $hh \cdot hh^*$ or the $vv \cdot vv^*$ term is larger. At first order Eq. 3 can be linearized around these two values,

and the co-pol maxima relative displacements are then given by:

$$(4)$$

$$\psi_{MAX}(0°) = \frac{Re\,[\langle hh \cdot hv^* \rangle]}{\langle hh \cdot hh^* \rangle - 2\langle hv \cdot hv^* \rangle - Re\,[\langle hh \cdot vv^* \rangle]}$$

$$(5)$$

$$\psi_{MAX}(90°) = \frac{Re\,[\langle hv \cdot vv^* \rangle]}{-\langle vv \cdot vv^* \rangle + 2\langle hv \cdot hv^* \rangle + Re\,[\langle hh \cdot vv^* \rangle]}$$

ANALYSIS

Reflection Symmetry Interpretation

The first consideration that we can make from the visual inspection of the co-pol signature basis functions in Fig. 1 is that the co-pol maximum can only be shifted from the "equilibrium" position at $\psi = 0°$ or $\psi = 90°$ if there is a non-zero cross correlation term ($\langle hh \cdot hv^* \rangle$ or $\langle hv \cdot vv^* \rangle$). This suggests an intuitive physical interpretation of the phenomenon in terms of the azimuthal reflection symmetry properties of the target. The polarimetric response from reflection symmetric targets has been studied for instance in [4][5], where it is demonstrated theoretically that for azimuthally symmetric targets the correlations between co- and cross- polarized backscattering components is zero. In simple intuitive terms we can summarize this effect and relate it to our problem in the following way. Consider a deterministic target which is symmetric with respect to a plane (the reflection plane RP) containing the incident radar beam. A complementary problem is defined in wave scattering when the sources (charges and currents) and the fields are the images of the original problem with respect to some operator. In our case the operator is the reflection with respect to RP. If the charge and current distribution is the same for the complementary problem, i.e.the target is symmetric, the H polarized scattered fields will be an odd function of the azi-
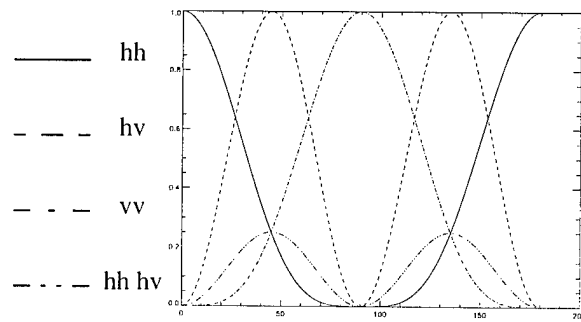

Fig. 1. Basis functions
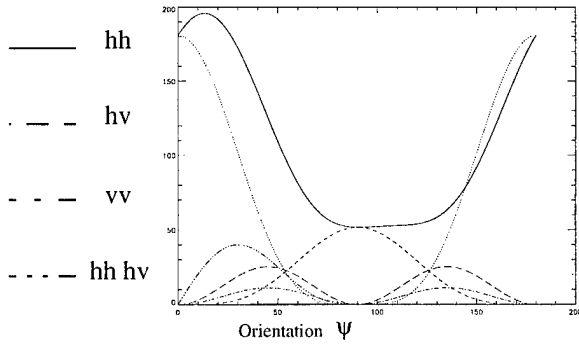
hh
hv
vv
hh hv

Orientation ψ

Fig. 2 Signature decomposition highlighting the influence of the cross correlation term on the co-pol maximum shift.

muthal angle, and the V polarized field will be an even function. This stems form the invariance of the Maxwell equations with respect to reflection operators. Since the excitation sources are the same for the original and complementary problem, this also implies that the co-pol scattering matrix elements will be even functions, and the cross-pol scattering elements will be odd functions. Now consider a random target and compute the ensemble average $hh \cdot hv^*$ over all azimuthal angles; then there will always be a contribution coming from a resolution element in the complementary problem that will cancel out the respective contribution from the' original problem. In other words the cross correlations terms in the covariance matrix will be zero.

On the other hand if the target is tilted with respect to RP, and loses reflection symmetry, the sources in the complementary problem will be different from the original problem, terms in the ensemble average will not be balanced out, and the cross correlation will tend to increase. The signature decomposition illustrates nicely the influence of the cross correlation terms on the polarization maximum shift. An example is shown is Fig. 2 taken from an analysis performed using JPL AIRSAR P-band data, acquired over the Freiburg forest in Germany.

As a side remark, we observe that, following this interpretation, a target which is intrinsically azimuthally non symmetric would exhibit a co-pol maximum shift even for flat terrain. The error introduced should be evaluated and eventually the algorithm should be calibrated for certain natural targets with respect to the absolute co-pol maximum at $\delta = 0°$.

An alternative way of estimating the terrain slope is suggested by the azimuthal symmetry analysis. In fact the tilted terrain will exhibit again reflection symmetry with respect to a plane which is rotated with respect to the original beam incidence plane; if the wave polarization orientation is rotated by the same amount, the cross correlation terms will be minimized. This can be computed by the following polarization basis transformation: $C_S(\rho) = T(\rho) C_S T^\dagger(\rho)$ where $\rho = E_V/E_H$ is the complex polarization ration and:

$$T(\rho) = \frac{1}{1 + \rho\rho^*} \begin{bmatrix} 1 & 2\rho & \rho^2 \\ -\rho^* & 1 - \rho\rho^* & \rho \\ \rho^{*2} & -2\rho^* & 1 \end{bmatrix}$$ (6)

From (4)(5) we can make the following considerations on the dependency of the co-pol maximum relative shift from the cross correlation terms (for first order deviations). We remind that the two equations are respectively valid for a relative shift around 0° and 90° ($hh \cdot hh^* > vv \cdot vv^*$ or $hh \cdot hh^* < vv \cdot vv^*$). Let us consider for simplicity the first case only.

1) The shift is proportional to the cross correlation term and inversely proportional to $\langle hh \cdot hh^* \rangle - Re[\langle hh \cdot vv^* \rangle]$, since the cross-pol power term is usually one order of magnitude less then the co-pol power. For random targets which exhibit low correlation between the co-pol channels (such as forest) the shift is inversely proportional to $\langle hh \cdot hh^* \rangle$ only. Also for small angles the $\langle hh \cdot hh^* \rangle$ term can be considered constant, and the shift will be proportional to the cross correlation term, which is highly linear with tilt angle. On the contrary for targets with high co-pol channels correlation, such as bare soil, the difference $\langle hh \cdot hh^* \rangle - Re[\langle hh \cdot vv^* \rangle]$ becomes important.

2) The effective scattering area on the ground corresponding to a resolution element is a function of the local incidence angle; therefore on sloping terrain the power return will be affected both by the resolution element inclination in range and azimuth direction; variations in the local incidence angle will affect non-proportionally the $\langle hh \cdot hh^* \rangle$ and $\langle hh \cdot hv^* \rangle$ terms, therefore introducing and additional source of error in the azimuth tilt angle estimation.

3) Equations (4)(5) suggest the interesting possibility of constructing a tilt angle estimator (within the limits of the linear assumption) from the power terms $\langle hh \cdot hh^* \rangle$ and $\langle hv \cdot hv^* \rangle$ only. In fact the phase and amplitude statistics of the cross correlation term $\langle hv \cdot hv^* \rangle$ has been fully characterized [6], which would allow us to derive an estimator of the $Re[\langle hv \cdot hv^* \rangle]$ term. If the estimator bias and variance permit, this approach would open up the possibility of using non-fully polarimetric space-borne SAR instruments for topography sensing, such as the foreseen NASDA VSAR aboard the ALOS spacecraft and some acquisition modes of the NASA Shuttle radar.

4) Negative and positive terrain tilt angles can be resolved because the cross correlation term changes sign.

Even this simplified view points out the fact that the underlying mechanisms in the polarimetric topography sensing algorithms depend heavily on the type of target, and that the error budget of the tilt angle estimation is affected by several factors. The full theoretical characterization of the end to end process is therefore a challenging task; we present in the next section some results towards this goal.

As a first step in the algorithm theoretical analysis, an electromagnetic scattering model for a slightly rough surface based on Rice's method was used to compute the polarimetric covariance matrix elements as a function of the incidence and tilt angles. The model is a suitably modified version of the one described in [2] for ocean applications. Results of a numerical simulation for wave scattering from tilted terrain (P-band, $\varepsilon = (9.0 + 1.0i)$, Gaussian power spectrum of the surface) are reported in Fig. 3. Only the covariance terms playing a role in the linearized maximum shift expression are shown. Also the estimated co-pol maximum shift was computed for different incidence angles, using a numerical solution for the roots of the trigonometric polynomial (Eq. 3), and is also reported in Fig. 3. It can be observed that for small incidence angles there is a high non-linearity in the relationship, and the slope angle is over estimated.

APPLICATION

The processing of both single-pass, and orthogonal two-pass polarimetric SAR data sets has been investigated [8]. When single-pass data is used elevation ground truth must be available for at least one point of each profile formed in the azimuthal direction. When orthogonal two-pass slope data is employed, the elevation surface may be generated, in a new algorithm, as an iterative solution of the Poisson equation and only a single elevation tie-point is required. The study reported here uses orthogonal two-pass P-band data as a test of the Poisson equation approach for an area in Death Valley National Park, California. The orthogonal two-pass results have been compared with a co-registered, conventional, U.S. Geological Survey (USGS) Digital Elevation Model (DEM). The SAR look directions for the two data collection passes need not be strictly orthogonal for the method to work.

The data used is NASA/JPL/AIRSAR P-band backscatter, sampled on a 10m x 10m grid, from a desert region of open-terrain centred on Stovepipe Wells in Death Valley National Park. This data set has been chosen for analysis because two nearly orthogonal AIRSAR passes (140° and 220°) were made over a common area of intersection. Orthogonal slopes are generated for each pixel using data from both passes. Slope gradients are then used in the new algorithm to solve for the terrain elevation surface. This algorithm, which is similar to that required in interferometric SAR phase unwrapping problems, requires only one ground truth point to relate the surface to some standard reference ellipsoid. The analytic method attempts though an initial trial solution and iterations to find a solution $\Phi(x, y)$ to the Poisson equation for a rectangular gridded area of terrain elevations. For this problem the Poisson equation may be written in Cartesian coordinates as
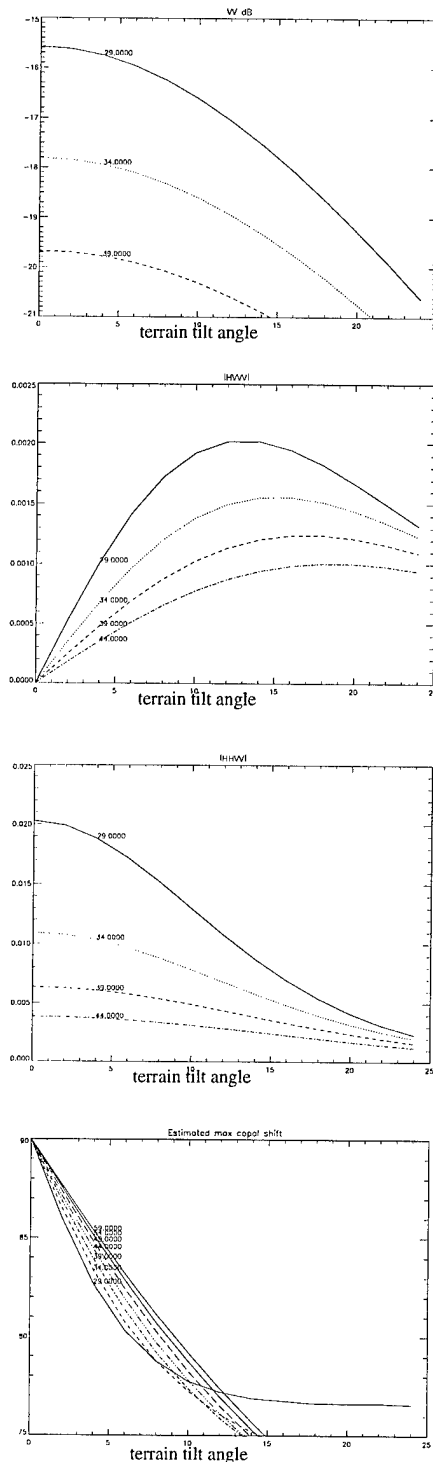

Fig. 3 - Results from the slightly rough surface wave scattering model. Covariance matrix elements and estimated co-pol maximum shift as a function of the azimuth terrain tilt angle and the incidence angle.

$$\nabla^2 \Phi(x, y) = \rho(x, y) \qquad (7)$$

where, ∇^2 is the Laplacian operator. The source function $\rho(x, y)$ consists of values of the surface curvature estimated from input slopes, $S(x, y)$. This Poisson equation algorithm is made more accurate by weighting the individual input slope values by carefully chosen arrays of weights which correspond to confidence levels in the slopes for each image pixel. The weight map that was used heavily weighted areas where the linear-pol polarimetric signature peak was strong.

The resulting elevation surface is given in Fig. 4 and may be compared with an available USGS DEM. Registration of the surfaces was carefully done but was made difficult by terrain layover effects. In Fig. 4 the terrain on the right-side is dominated by the Amargosa Mountain Range. The well-defined V-shaped canyon feature at the lower-right is Mud Canyon and its orifice is known as "Hell's Gate". The central desert basin is partly below sea-level and contains alluvial fans and sand dunes. The sloping area (right side) has localized areas of rough rocks.

The agreement between the two elevation surfaces is good in those regions of the two-pass intersection area where the linear-pol peak of the polarimetric signature is well-defined. In particular, for data regions dominated by Bragg scatter good results were obtained while areas dominated by specular returns introduced errors because the signature peak was weakly defined. Bragg scatter dominated areas in the (central) desert basin and near Mud Canyon. The rms surface differences for these regions were 6m and 18m, respectively. Rms differences over the complete surface were 29m.
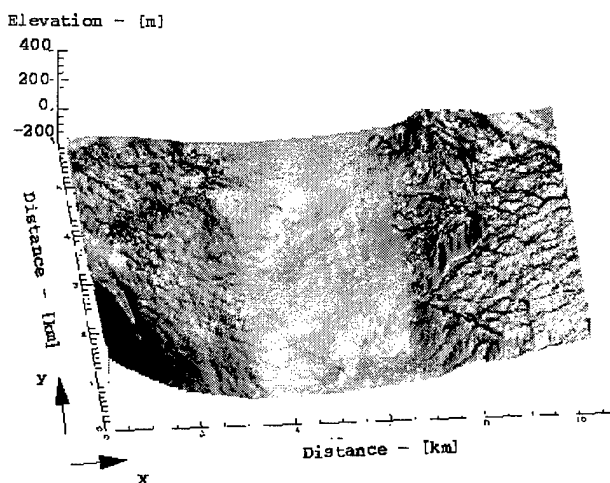
Fig. 4 - Terrain elevation surface produced using polarimetric SAR orthogonal two-pass data.

CONCLUSIONS

We have traced the main lines of a theoretical analysis and physical interpretation of the co-pol signature maximum dependency on the terrain azimuth slope. The suggested approach has some interesting connotations. On a qualitative basis, it allows us to gain an intuitive interpretation of the phenomenon, related to the target reflection symmetry, and to make considerations on the validity range of the algorithm. On a quantitative basis, it will permit, within the boundaries of the assumptions made, and if suitable scattering models are available, to derive sensitivity figures with respect to radiation frequency, incidence angle and type of scatterer. Future work should be directed towards an analysis based on a volume scattering model which could account for the more complicated situation encountered with natural targets such as forest and agricultural areas. Qualitative conclusions have been reached using a modified version of the UTA model [7]. However in order to properly take into consideration the terrain tilt influence on the polarimetric covariance matrix a model based on the solution of the field equations should be used.

Applications for which the new polarimetric SAR technique can contribute are 1) for improving polarimetric image feature classification and 2) for terrain elevation surface measurement/visualization.

REFERENCES

[1] D.L. Schuler, J.S. Lee and G.F. De Grandi, 'The Measurement of Topography Using Polarimetric SAR Images', *IEEE Trans. GARS Vol. 34, No. 5, 1266-1277, 1996.*

[2] G.R. Valenzuela, "Scattering of Electromagnetic Waves for a Tilted, Slightly Rough Surface", *Radio Sci., Vol. 11, No. 3, 1057-1066, 1968.*

[3] G.G. Lemoine, "On Polarimetric Signatures", *Proc. IGARSS'92, Houston, TX, Vol. II, 913-915, 1992.*

[4] S.V. Nghiem, S.H. Yueh, R. Kwok, F.K. Li, "Symmetry Properties in Polarimetric Remote Sensing", *Radio Sci., Vol. 27, No. 5, 693-711, 1992.*

[5] S.H. Yueh, R. Kwok, S.V. Nghiem, Polarimetric Scattering and Emission Properties of Targets with Reflection Symmetry", *Radio Sci., Vol. 29, No. 6, 1409-1420, 1994.*

[6] J.S. Lee, K.W. Hoppel, S.A. Mango, "Intensity and Phase Statistics of Multilook Polarimetric and Interferometric SAT Imagery", *IEEE Trans. GARS Vol. 32, No. 5, 1017-1028, 1994.*

[7] A.K. Fung, 'Microwave Scattering and Emission Models and their Applications', *Artech House, 1994.*

[8] D.L. Schuler, T.L. Ainsworth, J.S. Lee, G.F. De Grandi, "Topographic Mapping using Polarimetric SAR Data", *submitted to the Int. Journ. of Remote Sensing, 1997.*

INTERPRETATION OF RADAR MEASUREMENTS FROM ROUGH SOIL SURFACE WITH A PERMITTIVITY PROFILE

A.K. Fung[1], J. Boisvert[2] and B. Brisco[3]

[1]Department of Electrical Engineering
University of Texas at Arlington
Arlington, Texas 76019 USA
Phone: 817 273-3422
Fax: 817 273-3443
eefung@uta.edu

[2]Centre de recherche sur les sols et les
grandes cultures
2560, boul Hochelaga
Sainte-Foy, Qc, Canada G1V 2J3
Tel: 418-657-7985 ext 272, Fax: 418-648-2402
Boisvertj@em.agr.c

[3]Canada Centre for Remote sensing
588 Booth Street,
Ottawa, Canada K1AOY7

Abstract-- The IEM surface scattering model was applied to interpret sets of multifrequency, multipolarization radar measurements acquired from rough soil surfaces with measured permittivity profiles. The wetness was induced by irrigation and the profile was generated by evaporation. It is known that surface roughness parameters are difficult to estimate and are dependent on the measurement system resolution and record length. Hence, roughness parameters for a soil surface were estimated using the IEM surface scattering model applied to a data set at C- or L-band when the soil condition is wet. Then, the same surface parameters were used at other frequencies and moisture conditions. The measured permittivity profile is used to compute the effective reflection coefficient for the entire soil medium at normal incidence on the air-soil boundary from which an effective permittivity is derived for the soil medium and used for scattering calculation. For soil with a dry upper surface and an increasing permittivity value with depth an additional air-soil transition in permittivity is needed in estimating backscattering.

INTRODUCTION

A quantitative estimation of soil moisture from radar measurements has been a subject of interest for many years. Usually an empirical relationship that maps the measured normalized backscatter coefficient σ° into volumetric soil moisture content m_v is developed using linear regression for this study [1-4]. More advanced empirical non-linear regression models such as those of Oh et al. [5,6], and Dubois et al. [7,8] have also been demonstrated for specific data sets. To make the analysis independent of specific radiometric data sets we want to test the IEM scattering model [9] along with an effective permittivity calculated from the permittivity profile acquired from measurements at discrete intervals as shown in Fig. 1. The input to the reflection coefficient in the scattering model is the standard Fresnel coefficient. In estimating the effective permittivity at the air-soil boundary an incoherent model for reflectivity based on the multi-layer approach is selected. This model is given in the next Section.

It is known that soil surfaces dry up from the top down after rain. Thus it is desirable to incorporate a physical dielectric gradient into our theoretical modeling for this special situation. The modeling of this transition gradient is given in the third section.

In this work, we combine the IEM model with an effective permittivity model based on a discretized vertical soil moisture profile and a dielectric transition model. The purpose of this paper is to illustrate the application of this combined model to two sets of multi-frequency, multi-polarization and multi-angle data taken from soil surfaces with permittivity measured over depth.

PERMITTIVITY FOR MULTI-LAYER

An effective permittivity for a multi-layered medium can be derived by inverting the standard reflection coefficient for a multi-layered medium at normal incidence. However, this quantity is an oscillatory function of frequency not suitable for application. In practice, there is no real boundary between inner layers and hence an incoherent reflection coefficient is determined empirically for a multi-layered medium and is inverted for the desired effective permittivity. The reflection coefficient for reflectivity of a layer of depth d_1 over a half-space is known to be [10]
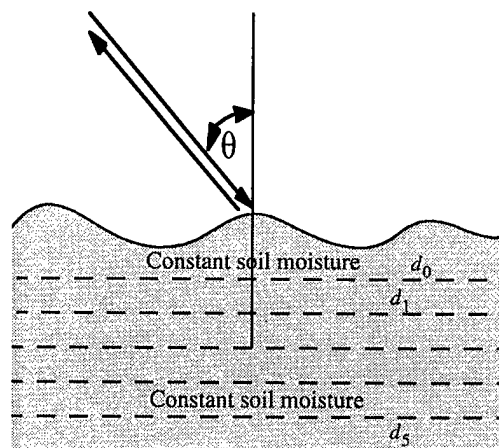
A layered soil medium based on dielectric measurements at 2 cm intervals over a distance of 10 cm.

$$R_l = \frac{R_1 + R_2 \exp[-2(\alpha + j\beta)d]}{1 + R_1 R_2 \exp[-2(\alpha + j\beta)d]} \qquad (1)$$

where R_1, R_2 are the Fresnel reflection coefficients at the boundaries of the layer. This expression can be extended without changing the format to having another layer of depth d_0 above it with R_0 denoting the reflection coefficient at the additional boundary as

$$R_{2l} = \frac{R_0 + R_l \exp[-2(\alpha + j\beta)d]}{1 + R_0 R_l \exp[-2(\alpha + j\beta)d]} \qquad (2)$$

Similar consideration allows us to extend the formula to as many layers as we wish. Based on this formula we choose its incoherent representation by dropping the phase yielding

$$R_{2i} = \frac{R_0 + R_l \exp[-4\alpha d]}{1 + R_0 R_l \exp[-2\alpha d]} \qquad (3)$$

The corresponding effective permittivity becomes

$$\varepsilon_{eff} = \left(\frac{1 + R_{2i}}{1 - R_{2i}}\right)^2 \qquad (4)$$

DIELECTRIC TRANSITION MODEL

We consider the transitional dielectric layer given by [11] in which the permittivity as a function of depth, z, is

$$\varepsilon_r(z) = 1 + \varepsilon_{r_1} \frac{\exp(mz)}{1 + \exp(mz)}. \qquad (5)$$

In the formulation of Brekhovskikh, note that $\varepsilon_{r_1} = \varepsilon_{eff} - 1$, and $-N = \varepsilon_{r_1}$. The inputs to the model are the transition rate factor m and the dielectric constant at $z = \infty$ which is ε_{eff}. The real part of the dielectric will always start at $\varepsilon_{r_\infty} = 1$ which is air and changes to ε_{eff} at a rate of m. The value for m accounts for dielectric transition over the depth of penetration seen at a given wavelength. Hence, it varies with frequency and the condition of the soil being smaller for dryer soil and very large for wet soil where no transition exists.

The standard Fresnel reflectivities are replaced by a modified set of relations which are given by

$$R_\perp = \frac{\Gamma(jS\cos\theta_0)}{\Gamma(-jS\cos\theta_0)} \frac{\Gamma\left[\left(\frac{-jS}{2}\right)(\cos\theta_0 + \sqrt{\cos^2\theta_0 + (\varepsilon_{r_\infty} - 1)})\right]}{\Gamma\left[\left(\frac{jS}{2}\right)(\cos\theta_0 - \sqrt{\cos^2\theta_0 + (\varepsilon_{r_\infty} - 1)})\right]}$$

$$\times \frac{\Gamma\left[1 - \left(\frac{jS}{2}\right)(\cos\theta_0 + \sqrt{\cos^2\theta_0 + (\varepsilon_{r_\infty} - 1)})\right]}{\Gamma\left[1 + \left(\frac{jS}{2}\right)(\cos\theta_0 - \sqrt{\cos^2\theta_0 + (\varepsilon_{r_\infty} - 1)})\right]} \qquad (6)$$

and[1]

$$R_{//} = \frac{\Gamma(jS\cos\theta_0)}{\Gamma(-jS\cos\theta_0)} \frac{\Gamma\left[\left(\frac{-jS}{2}\right)\left(\cos\theta_0 + \frac{1}{\varepsilon_{r_\infty}}\sqrt{\cos^2\theta_0 + (\varepsilon_{r_\infty} - 1)}\right)\right]}{\Gamma\left[\left(\frac{jS}{2}\right)\left(\cos\theta_0 - \frac{1}{\varepsilon_{r_\infty}}\sqrt{\cos^2\theta_0 + (\varepsilon_{r_\infty} - 1)}\right)\right]}$$

$$\times \frac{\Gamma\left[1 - \left(\frac{jS}{2}\right)((\varepsilon_{r_\infty})^{1/3}\cos\theta_0 + \sqrt{\cos^2\theta_0 + (\varepsilon_{r_\infty} - 1)})\right]}{\Gamma\left[1 + \left(\frac{jS}{2}\right)(\cos\theta_0 - \sqrt{\cos^2\theta_0 + (\varepsilon_{r_\infty} - 1)})\right]} \qquad (7)$$

where $S = 2k/m$. An example showing the differences in the reflectivities is shown in Figure 2.

APPLICATION OF SCATTERING MODEL

Backscattering measurements were taken from two soil surfaces at 1.5, 5.17 and 12.8 GHz and the relative permittivities were measured at depth intervals of 0-2, 2-4, 4-6, 6-8, 8-10, and 10-12 cm. For wet and medium-wet soil conditions, the measured dielectric values are fed into the formula corresponding to (3) and (4) but for more layers to estimate the effective permittivities. These permittivities are then used in the backscattering model to predict backscattering. If the soil is dry ($\varepsilon < 3$, in the first layer), an additional transition defined by (5) is included in which the parameter m is selected to fit data.

Figure 3 (a) shows a comparison between data and model at 1.5 GHz when soil is wet. Then the same surface parameters are used to fit data at 5.17 GHz in Fig.3 (b) for both vertical and horizontal polarizations. In Fig. 4 similar comparisons are shown for the same surface when it is dry at the top.

REMARKS

This paper provides an incoherent permittivity for a soil surface with a vertical profile. It also adapted a transition profile for dry soil based on the work of Brekhovskikh. It is shown that for wet soil the incoherent permittivity model
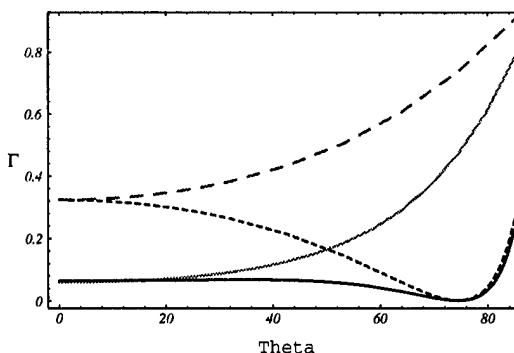

Fig. 2 Comparison of standard Fresnel power reflection coefficients (dashed lines) with reflectivitites including transitional effects.

---

1. This is an approximate relation not derived explicitly in Brekhovskikh [11].

1377

works well and for dry soil both models are needed as inputs to a surface scattering model.

REFERENCES

[1] Ulaby, F.T., P. Batlivala, and M. Dobson, "Microwave Back-scatter Dependence on Surface Roughness, Soil Moisture, and Soil Texture: Part I – Bare Soil," *IEEE Trans. on Geoscience and Remote Sensing*, Vol. GE-16, No. 4, Oct. 1978.

[2] Jackson, T.J., A. Chang, and T.J. Schmugge, "Aircraft Active Microwave Measurements for Estimating Soil Moisture," *Photogrammetric Engineering and Remote Sensing*, Vol. 47, pp. 810-805, June, 1981.

[3] Dobson, M.C., and F.T. Ulaby, "Active Microwave Soil Moisture Research," *IEEE Trans. on Geoscience and Remote Sensing*, GE-24, pp. 23-36, Jan. 1986.

[4] Pultz, T.J., R. Leconte, R.J. Brown, and B. Brisco, "Quantitative soil moisture extraction from airborne SAR data," *Canadian J. of Remote Sensing*, Vol. 16, pp. 56-62, 1990.

[5] Oh, Y., Sarabandi, K. and F. T. Ulaby, "An Empirical Model and an Inversion Technique for Radar Scattering from Bare Soil Surfaces", *IEEE Trans. Geoscience and Remote Sensing*, 1992, pp. 370-381.

[6] Oh, Y., K. Sarabandi, and F.T. Ulaby, "An Inversion Algorithm for Retrieving Soil Moisture and Surface Roughness From Polarimetric Radar Observations," *in Proc. of IGARSS 1994*, Vol. III, pp. 1582-1585.

[7] Dubois, P.C., J. van Zyl, and T. Engman, Measuring Soil Moisture with Imaging Radars, IEEE Trans. on Geoscience and Remote Sensing, Vol. 33, No. 4, July, 1995.

[8] Dubois, P.C., J. van Zyl, and T. Engman, Corrections to Measuring Soil Moisture with Imaging Radars, IEEE Trans. on Geoscience and Remote Sensing, Vol. 33, No. 6, Nov. 1995.

[9] Fung, A.K., *Microwave Scattering and Emission Models and Their Applications*, Chapter 2, Artech House, Norwood, MA, 1994.

[10] F.T. Ulaby, R.K.Moore and A.K.Fung, "Microwave Remote Sensing," *Vol. 1*, pp. 236,Artech House, 1982.

[11] Brekhovskikh, L.M., *Waves in Layered Media*, Second Edition, Translated from the Russian by R.T. Beyer, Academic Press, New York, 1980.

Fig. 3(b) Comparisons at 5.17 GHz, ε_{eff} = 22.67-j3.39.

(a)

(b)
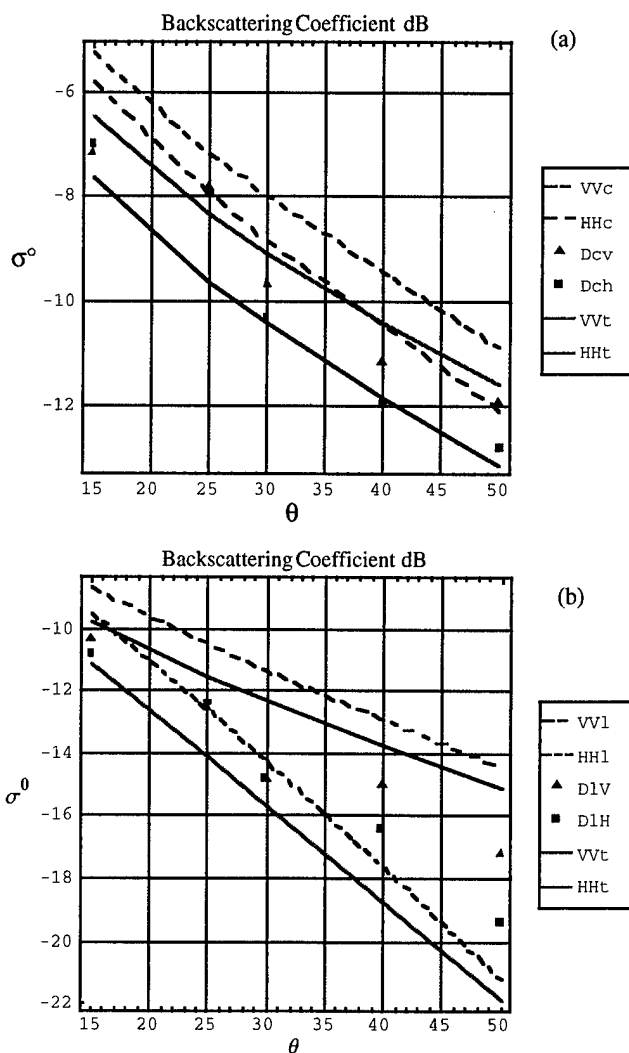
Fig. 4 Similar comparisons as in Fig.3 when the surface is dry on top with (a) ε_{eff} = 5.78-j0.54 at 5.17 GHz and (b) ε_{eff} = 7.8-j1.1 at 1.5 GHz.
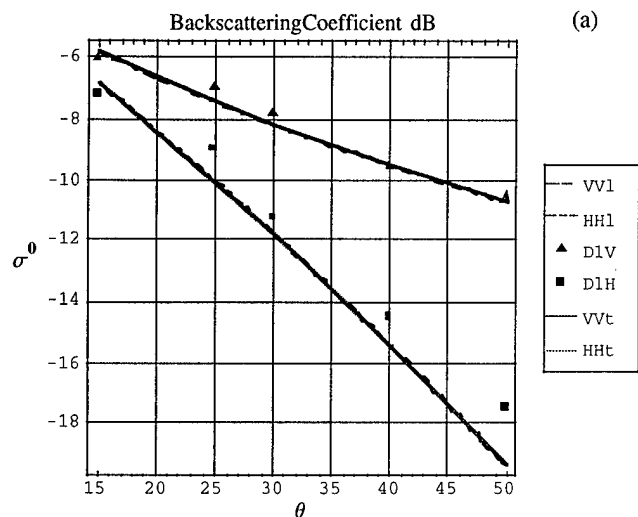

(a)

Fig.3 (a) Comparisons of VV and HH with data at 1.5 GHz for a wet soil with rms height of 1 cm and correlation length of 4 cm. ε_{eff} = 23-j3.65. Exponenetial correlation. VVt and HHt means the same calculations with dielectric transition.
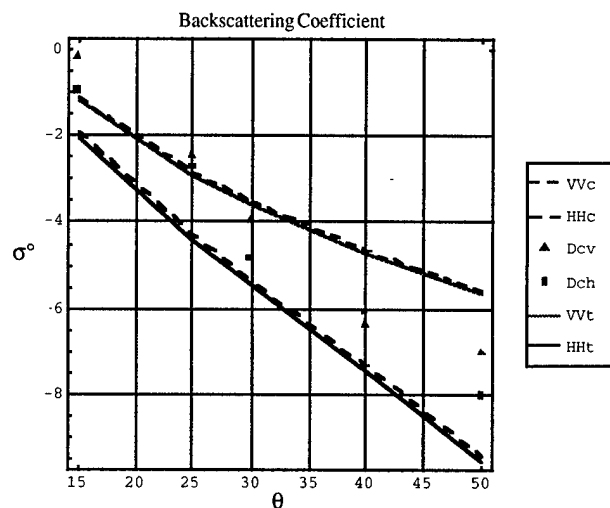
A Successive Approximation Series for TE and TM Scattering from One-Dimensional Conducting Rough Surfaces

M. A. Moyssidis, C. N. Vazouras, P. G. Cottis, and J. D. Kanellopoulos
Department of Electrical and Computer Engineering
National Technical University of Athens
9, Iroon Polytechniou , Athens 15773, Greece.
Tel. (+301) 7723521, Fax (+031) 7723549
e-mail: chvazour@cc.ece.ntua.gr

Abstract -- A successive approximation (SA) scheme is applied to the problem of scattering from a perfectly conducting surface, rough in one dimension. The SA scheme is based on appropriate reformulation of the extinction theorem integral equation, in combination with a convenient representation of the source function. An explicit expression is given for the general term, which allows derivation of the general term of a related perturbation series and of corrections to the Kirchhoff approximation to all orders.

INTRODUCTION

Iterative techniques to treat scattering from conducting rough surfaces are of current interest [1-3]. Such methods appear quite well suited to the complicated nature of the problem at hand; however, treatment of higher order terms often presents difficulties. A very efficient iterative technique was introduced recently [3]; being, however, of a numerical character, it does not lend itself directly to development of explicit expressions for the statistical quantities of interest.

On the other hand, perturbation methods have been in use for quite a long time [4-6]. Notwithstanding their limitations, they have the advantage of simplicity and of being amenable to fairly straightforward statistical treatment, since they provide analytical results. Following a momentum transfer expansion [7], a unified perturbation method (UPM) was introduced recently by Rodriguez and Kim [8] and shown to possess various merits, combining features of both the Kirchhoff approximation and small perturbation models.

The present work is largely based on the UPM approach, combining its basic features with an iterative approach recently proposed by the present authors [9]. The iterative method is based on the extended boundary condition (EBC) formulation, and makes possible the treatment of the general term in an explicit form. This, in turn, may be appropriately manipulated to yield the general term of the UPM. Further on, the Fourier transforms involved may be explicitly inverted in the high frequency region, yielding closed form expressions for corrections of the Kirchoff approximation to all orders. Thus, the momentum tranfer expansion scheme [7] is recovered as a special case. For simplicity, the case of horizontal (TE) polarization is treated in more detail; the analogous procedure for the vertical (TM) polarization case is also outlined.

FORMULATION AND BACKGROUND

We consider a typical geometry of two infinite half-spaces seperated by an interface, rough in one dimension, characterized by a dererministic profile function $z=\zeta(x)$ giving the height of the surface from the $z=0$ plane. The upper half-space is assumed to be the free space, with dielectric permittivity ε_0 and magnetic permeability μ_0, while the lower half-space is taken to be perfectly conducting. An $\exp(-j\omega t)$ time dependence is assumed.

An incident plane wave of linear polarization is considered with the direction of incidence in the xz-plane, so that the only field component is among the y-direction. Thus, the y-component of the incident electric (TE case) or magnetic (TM case) field is given by the following expression

$$\vec{E}_i(\vec{r}) \text{ or } \vec{H}_i(\vec{r}) = \psi_i(\vec{r})\hat{y} = \exp\left(jk_x x - jk_z z\right)\hat{y} \qquad (1)$$

where

$$k_x = k_0 \sin\left(\theta_i\right), k_z = k_0 \cos\left(\theta_i\right), k_0 = \omega\sqrt{\varepsilon_0\mu_0} \qquad (2)$$

and the incidence angle θ_i is measured from the vertical z-direction. More general incident wave forms could easily be considered by superposition.

We apply the well-known EBC equations, taking into account the boundary conditions and the Fourier plane wave expansion for the two dimensional free space Green function. By the usual procedure based on the linear independence of the plane wave functions [4-8], the following operatorial equation is derived for the TE case

$$\int_{-\infty}^{+\infty} \exp\left[j\lambda x + j\upsilon(\lambda)\zeta(x)\right] f(x)dx = 4\pi\upsilon\left(\lambda_0\right)\delta\left(\lambda + \lambda_0\right) \qquad (3)$$

where $\delta(\lambda)$ is the Dirac functional and

$$\upsilon_0(\lambda) = \left(k_0^2 - \lambda^2\right)^{1/2} \qquad (4)$$

with the square root defined so as to satisfy the radiation conditions $\left(\text{Re}(\upsilon_0), \text{Im}(\upsilon_0) \geq 0\right)$. The unknown function is related to the normal derivative of the field through

$$f(x) = j\hat{n} \cdot \nabla\psi(\vec{r})\left[1 + \left(\frac{d\zeta}{dx}\right)^2\right]^{1/2} \qquad (5)$$

A similar equation arises for the TM case

$$\int_{-\infty}^{+\infty} \exp\left[j\lambda x + jv(\lambda)\zeta(x)\right]\left(v(\lambda) - \lambda\zeta^{(1)}(x)\right)f(x)dx =$$

$$= 4\pi v(\lambda_0)\delta(\lambda + \lambda_0) \tag{6}$$

where the unknown function corresponds to the magnetic field values on the surface.

The scattered field in the upper half space is then given by

$$\psi_{sc}(\vec{r}) = -\int_{-\infty}^{+\infty} \frac{A(\lambda)}{v(\lambda)} \exp\left[j\lambda x + jv(\lambda)z\right]d\lambda \tag{7}$$

where

$$A(\lambda) = \frac{1}{4\pi} \int_{-\infty}^{+\infty} \exp\left[-j\lambda x - jv(\lambda)\zeta(x)\right]f(x)dx \tag{8}$$

in the TE case; a likewise expression is found in the TM case.

Following the approach of [8], we write

$$f(x) = 2\exp\left[j\lambda_0 x - jv(\lambda_0)\zeta(x)\right]g(x) \tag{9}$$

The advantages of the representation (9) (the origin of which may be traced back to [10]) have been discussed in [8].

Combining (3) and (9), one gets the final equation to be solved

$$\int \exp\left[j(\lambda + \lambda_0)x + j\left(v(\lambda) - v(\lambda_0)\right)\zeta(x)\right]g(x)dx =$$

$$= 2\pi v(\lambda_0)\delta(\lambda + \lambda_0) \tag{10}$$

From this point on, the infinite limits of the integration will be dropped for brevity of notation, as it has been done in (10).

Expanding g(x) in a perturbation series, with the perturbation parameter being in effect the corrugation height of the surface, one has the UPM series. Inserting the exponential expansion in (10), multiplying the series in the Cauchy sense and equating terms of the same order in $\zeta(x)$, we get the iterative relations

$$g_0(x) = v(\lambda_0) \tag{11}$$

$$\tilde{g}_n(\lambda + \lambda_0) = -\sum_{m=0}^{n-1} \frac{j^{n-m}}{(n-m)!}\left[v(\lambda) - v(\lambda_0)\right] \cdot$$

$$\cdot \int_x \exp\left[j(\lambda + \lambda_0)x\right]\zeta^{n-m}(x)g_m(x)dx \quad , \; n\geq 1 \tag{12}$$

where the tilde(~) denotes Fourier transform.

For flat surfaces the solution is given from the term for n=0 only, whereas the computation of f(x) would require an infinite number of terms. For smooth surfaces, one may extract the well-known Kirchhoff approximation

$$f(x) = 2\exp\left[j\lambda_0 x - jv(\lambda_0)\zeta(x)\right]\left[v(\lambda_0) + \lambda_0\zeta^{(1)}(x)\right] \tag{13}$$

which comes from the contribution of $g_0(x)$, as well as part of $g_1(x)$.

THE SUCCESSIVE APPROXIMATION SERIES

The successive approximation approach is based on reformulation of (10) in a form suitable for iteration

$$\tilde{g}(\lambda + \lambda_0) + Kg(x) = 2\pi v(\lambda_0)\delta(\lambda + \lambda_0) \tag{14}$$

This is done by adding and substracting unity to the term containing the exponential of the surface profile, and taking into account the well known property of the Fourier transform

$$F\{a(x)\} = A(\lambda) \iff F\{\exp(jbx)a(x)\} = A(\lambda+b)$$

In (14), the K operator is defined as

$$Kg(x) = \int_x \exp\left[j(\lambda + \lambda_0)x\right]B(\lambda,x)g(x)dx \tag{15}$$

with

$$B(\lambda,x) = \exp\left[j\left(v(\lambda) - v(\lambda_0)\right)\zeta(x)\right] - 1 \tag{16}$$

Based on (14) and applying the successive approximation technique (Neumann iteration) with the right-hand side as initial guess, one comes up with the following successive approximation (SA) series

$$g(x) = \sum_{n=0}^{+\infty} g_n(x) \tag{17}$$

where the SA terms are given by

$$\tilde{g}_n(\lambda + \lambda_0) = -Kg_{n-1}(x), \; g_0(x) = v(\lambda_0) \tag{18}$$

Thus, the general term of the SA series may be written explicitly as follows

$$g_n(x) = \frac{(-1)^n}{(2\pi)^n}v(\lambda_0)\int_{\lambda_n}\cdots\int_{\lambda_1}\exp\left[-j(\lambda + \lambda_0)x\right]\cdot$$

$$\cdot Q(\lambda_n,\lambda_{n-1})\cdots Q(\lambda_1,\lambda_0)d\lambda_1\cdots d\lambda_n \tag{19}$$

where we have defined

$$Q(\lambda,\mu) = \int_x \exp\left[j(\mu - \lambda)x\right]B(\lambda,x)dx \tag{20}$$

Expanding the exponential in (16) and making use of (20), one gets an alternative expression

$$g_n(x) = \frac{(-1)^n}{(2\pi)^n}v(\lambda_0)\int_{\lambda_n}\cdots\int_{\lambda_1}\exp\left(-j(\lambda_n + \lambda_0)x\right)$$

$$\left[\sum_{m_n=1}^{+\infty}\frac{j^{m_n}}{m_n!}\left(w^{m_n}(\lambda_n)\right)Z_{m_n}(\lambda_{n-1} - \lambda_n)\right]\cdots$$

$$\cdots\left[\sum_{m_1=1}^{+\infty}\frac{j^{m_1}}{m_1!}\left(w^{m_1}(\lambda_1)\right)Z_{m_1}(\lambda_0 - \lambda_1)\right]d\lambda_1\cdots d\lambda_n \tag{21}$$

where we denote by $Z_k(\lambda)$ the Fourier transform of the k-th power of the profile function, and

$$w(\lambda) = v(\lambda) - v(\lambda_0)$$

Expression (21) is well suited for the derivation of the general term of the UPM series. This may be carried out based on the observation that (21) represents a multiple series made up from various conrtibutions, the order of which in $\zeta(x)$ corresponds to the sum $m_1+...+m_n$, which is greater or equal to n. This means that all contributions of order up to m are contained in the first $m+1$ terms of the series (21), i.e. $0 \leq n \leq m$. Thus, collecting all contributions of order m in $\zeta(x)$, one gets the following closed form expression for the general term of the UPM series

$$g_m^{\text{UPM}}(x) = \upsilon(\lambda_0) \sum_{n=1}^{m} (-1)^n \sum_{m_1+...+m_n=m} \frac{j^m}{m_1!...m_n!}$$

$$\int_{\lambda_n} \cdots \int_{\lambda_1} \exp\left(-j(\lambda_n+\lambda_0)x\right) w^{m_n}(\lambda_n) \cdots w^{m_1}(\lambda_1) \cdot$$

$$\cdot Z_{m_n}(\lambda_{n-1}-\lambda_n) \cdots Z_{m_1}(\lambda_0-\lambda_1) \, d\lambda_1 \cdots d\lambda_n \qquad (22)$$

which bears close resemblance to the general term of the field perturbation series given in [11], and may be shown by the method of [11] to satisfy the iterative relation (12).

In the high frequency region, or, otherwise stated, for a surface of sufficiently narrow bandwidth, one may adopt a Taylor expansion for the function $w(\lambda)$ around the point λ_0 and explicitly invert the Fourier transform to get

$$g_m^{\text{UPM}}(x) = \upsilon(\lambda_0) \sum_{n=1}^{m} (-1)^n \sum_{m_1+...+m_n=m} \frac{j^m}{m_1!...m_n!} \cdot$$

$$\cdot \sum_{p_1=m_1}^{+\infty} \cdots \sum_{p_n=m_n}^{+\infty} j^{-(p_1+...+p_n)} a_{m_1}^{p_1} \cdots a_{m_n}^{p_n} \cdot$$

$$\left[\cdots \left[\left[\zeta^{m_1} \right]^{(p_1)} \zeta^{m_2} \right]^{(p_2)} \cdots \zeta^{m_n} \right]^{(p_n)} \qquad (23)$$

where

$$a_m^n = \frac{1}{n!} \frac{d^n w^m(\lambda)}{d\lambda^n} \bigg|_{\lambda=\lambda_0} \qquad (24)$$

Eq. (23) yields the higher order corrections to the Kirchhoff approximation related to higher derivatives of the profile function to all orders. Obviously, an analogous expression may be derived directly from the SA series (21), rather than the rearranged form (22).
For example, the up-to-third-order approximation of g(x) is

$$g(x) = \upsilon(\lambda_0) + \lambda_0 \zeta^{(1)}(x) - j \frac{k_0^2}{2\upsilon^2(\lambda_0)} \zeta^{(2)}(x) +$$

$$+ \frac{k_0^2 \lambda_0}{2\upsilon^4(\lambda_0)} \zeta^{(3)}(x) + \frac{k_0^2 \lambda_0}{\upsilon^3(\lambda_0)} \zeta^{(1)}(x) \zeta^{(2)}(x) \qquad (25)$$

which agrees with the result of [7].
An analogous procedure may be carried out for the case of

TM polarization, with a more complicated kernel of the form

$$B(\lambda,x) = \exp\left[j\left(\upsilon(\lambda) - \upsilon(\lambda_0)\right) \zeta(x) \right] \left[\upsilon(\lambda) - \lambda \zeta^{(1)}(x) \right] / \upsilon(\lambda_0) - 1$$

The corresponding up-to-third-order expression is found to be

$$g(x) = 1 + j\left(\frac{1}{\upsilon(\lambda_0)} + \frac{\lambda_0^2}{\upsilon^3(\lambda_0)} - \frac{k_0^2}{2\upsilon^3(\lambda_0)} \right) \zeta^{(2)}(x) -$$

$$- \frac{2k_0^2 \lambda_0}{\upsilon^5(\lambda_0)} \zeta^{(3)}(x) + j3\left(\frac{k_0^2}{2\upsilon^4(\lambda_0)} - \frac{\lambda_0}{\upsilon^2(\lambda_0)} - \frac{\lambda_0^3}{\upsilon^4(\lambda_0)} \right) \zeta^{(1)} \zeta^{(2)}$$

REFERENCES
[1] P. Tran, V. Celli and A. A. Maradudin, 'Electromagnetic scattering from two-dimensional randomly rough perfectly conducting surfaces: iterative methods', J. Opt. Soc. Am. A, vol. 11, pp. 1686-1689, 1994.
[2] C. Macaskill and B.J. Kachoyan, 'Iterative approach for the numerical simulation of scattering from one-dimensional rough surfaces', Appl. Opt., vol. 32, no. 15, pp. 2839-2847, May 1993.
[3] D. A. Kapp and G. S. Brown, 'A new numerical method for rough surface scattering calculations', IEEE Trans. Antennas Propagat., vol. AP-44, no. 5, pp. 711-721, May 1996.
[4] N. Garcia, V. Celli and M. Nieto-Vesperinas, 'Exact multiple scattering of waves from random rough surfaces', Opt. Commun., vol. 30, no. 3, pp. 279-281, 1979.
[5] J. Shen and A. A. Maradudin 'Multiple scattering of waves from random rough surfaces', Phys. Rev. B, vol. 22, no. 9, pp. 4234-4240, 1980.
[6] D. Winebrenner and A. Ishimaru, 'Investigation of a surface field phase perturbation technique for scattering from rough surfaces', Radio Sci., vol. 20, no. 2, pp. 161-170, 1985.
[7] Rodriguez, E., and Y. Kim (1992), A unified perturbation expansion for surface scattering, Radio Sci., vol. 27, no. 1, pp. 79-93.
[8] E. Rodriguez, 'Beyond the Kirchhoff approximation', Radio Sci., vol. 24, no. 5, pp. 681-693, 1989.
[9] C. N. Vazouras, P.G. Cottis and J.D. Kanellopoulos, 'Application of a successive approximations scheme to scattering from a perfectly conducting surface, rough in one dimension', Proc. 5th International Conference on Mathematical Methods in Electromagnetic Theory, Ukraine, pp. 455-458, Sept. 1994.
[10] G. S. Brown, 'A stochastic Fourier transform approach to scattering from perfectly conducting randomly rough surfaces', IEEE Trans. Antennas Propagat., vol. AP-30, no. 6, pp. 1135-1144, June 1982.
[11] C. N. Vazouras, P. G. Cottis and J. D. Kanellopoulos, 'Scattering from Conducting Rough Surfaces: A General Perturbative Solution', IEEE Trans. Antennas Propagat., vol. AP-41, no. 9, pp. 1232-1241, Sep. 1993.

RADARSAT Elevation Antenna Pattern Determination

T.I. Lukowski, R.K. Hawkins, C. Cloutier, J. Wolfe[1] and L.D. Teany
Canada Centre for Remote Sensing, Natural Resources Canada
588 Booth St., Ottawa, Ontario K1A 0Y7
Phone: (613) 995-0386 Fax: (613) 947-1383
email: tom.lukowski@ccrs.nrcan.gc.ca

S.K. Srivastava, B. Banik, R. Jha[2], and M. Adamovic[3]
RADARSAT Operations, Canadian Space Agency
6767 Route de l'aéroport, Saint-Hubert, Québec J3Y 8Y9
Phone: (514) 926-5133 Fax: (514) 926-5167
email: satish.srivastava@space.gc.ca

[1] Intermap Technologies Ltd. Under Contract to the Canada Centre for Remote Sensing
[2] Array Systems Computing Inc. Under Contract to the Canadian Space Agency
[3] Lockheed Martin Canada Under Contract to the Canadian Space Agency

Abstract -- The operations plan for RADARSAT is based on implicit calibration of the imagery products from this sensor system. The determination of the antenna gain patterns in elevation for RADARSAT is a critical step in the radiometric calibration of this imagery. The shapes of the antenna patterns in elevation were derived from imagery collected over the South American rain forests of Brazil and Colombia with a consistency on the order of ±0.2 dB. The absolute levels of the patterns have been determined by superposing the shapes on results from a set of precision radar ground targets known as the RADARSAT Precision Transponders. As pattern revisions are determined, they are included operationally in the determination of the corrections that are required in the Canadian Data Processing Facility to create radiometrically calibrated image products.

INTRODUCTION

The Canadian Earth observation satellite, RADARSAT, was launched in late 1995. One mission objective of this spaceborne SAR program was to provide operationally calibrated products. To do so, there are a number of systematic corrections that must be performed in the processing. Perhaps the most critical of these is the correction for antenna gain variations across the swath.

Determination of the antenna gain patterns for RADARSAT began during the testing prior to launch when measurements were performed by SPAR Aerospace using a partial set of the final Antenna Assembly on a Near Field Measurement Facility [1]. In flight verification of these pre-flight measurements was required to find the overall system gains which would depend on the particular processing and hardware configuration. Continuing monitoring also had to be established for calibration throughout the mission to cover the possibility of aging and other system changes. As a result, the capability to determine these antenna patterns was made a part of the operational scenario for RADARSAT [2].

ELEVATION GAIN PATTERN SHAPE DETERMINATION

Elevation gain pattern determination is based on rough distributed target measurements as previously shown successful for airborne and spaceborne systems [3][4][5][6][7]. In the RADARSAT analysis, the extraction of clutter is based on the algorithm of Shimada and Freeman [6]. The implementation in the software of the RADARSAT Image Data Calibration Workstations (IDCW) was developed by *Array Systems Computing Inc.* for the Canadian Space Agency [2].

The calculations performed for RADARSAT are based on use of the South American rain forests. These stable targets have a simple backscatter variation across track. Indeed, results from the ERS-1 and -2 scatterometers show that the Amazon is stable over a long period with a mean γ_o of -6.5 ± 0.1 dB over an incidence angle of 18 to 57 degrees [7][8]. As a result, removal of the range dependence of the rain forest backscatter from the resulting imagery is particularly straight forward. The areas of South America used to derive the antenna gain patterns for RADARSAT during the Radiometric Calibration Phase were selected based on examination of rain forest imagery including those used by other groups in the determination of antenna gain patterns [5][6]. Relief considerations can be ignored because the elevation variations are negligible.

The remaining unknown factor, the antenna gain pattern in elevation can be determined from the imagery (processed with antenna pattern correction off) by solving the following:

$$P_r - P_N \propto \frac{\gamma_o G_{ANT}^2(\theta_{el})}{\tan\theta} \qquad (1)$$

where:

P_r power from the rain forest image or apparent Radar Brightness (β_o) when processor and antenna gain are neglected

P_N thermal noise power or apparent Noise Equivalent β_o (β_{oNE}) when processor and antenna gain are neglected

γ_o $\sigma_o \cos\theta$

σ_o normalized backscattering coefficient

θ local incidence angle

G_{ANT} antenna pattern gain

θ_{el} elevation angle from nadir

Following the display of the image on the IDCW, the processing methodology for derivation of an antenna gain pattern from a candidate rain forest image is described below:

1. The geometry of the image acquisition is calculated which makes it possible to optimize determination of geometry dependent parameters of (1).

2. This image is subdivided into strips of a selected width (e.g. 0.015 degrees) each with a number of cells (16 is the typical number used).

3. Areas which are clearly not uniform are excised by the operator.

4. The χ^2 method [6] is used to reject non-uniform cells in each strip in the remaining data. If a majority of the cells in a strip are rejected, the complete strip is rejected.

5. All non-rejected values in a strip are averaged.

6. The data are corrected as shown in (1) by subtracting the contributions of thermal noise and, by multiplication by tan θ which accounts for variations in backscatter (the effect of a constant γ_o).

For each beam, the effective relative roll of the satellite between acquisitions was determined. A minimum of three patterns (except in a single case where only two were available) obtained as described above were superimposed and averaged to obtain a representative pattern. (See Fig. 1). Due to the angular limitations of the measured data, it was necessary to extrapolate the patterns using data from the pre-flight measurements supplied by SPAR. A "touch up" procedure was required to correct for minor discontinuities at the extrapolation seams and to smooth the curves.

At the time of this writing, beams S1 to S7 and W1 to W3 have been completed. In November 1996, the Canadian Space Agency initiated a set of intermediate Fine Beam imaging configurations to fill in the gaps in the high resolution imaging geometries. These configurations push the normal imaging range window on either side of the centre of the elevation pattern giving, for example an F1 Near, F1, and F1 Far capability. This gives effectively 32 single beam configurations. Work on the Fine Beams is nevertheless nearly complete.

ABSOLUTE GAIN DETERMINATION

The antenna gain pattern shape determination as described above does not complete the calibration of the processor in the approach used for RADARSAT. The final step to achieving absolute calibration requires knowledge of the RCS (radar cross section) of a ground target or the normalized backscatter (γ_o, β_o, or σ_o) for a distributed target. For RADARSAT, the derived patterns are scaled by the apparent γ_o and any applied gains in the processing and compared against a similar derivation from the precision transponders. In this case, the integrated response from the transponder was scaled by its RCS as indicated in [9]. For convenience, all pattern gain values were referenced to that at the middle of beam S3. In the final step, the patterns and associated gains were converted into the required formats for input to the CDPF.

The patterns from each of three products used to obtain the final patterns for beam S1 are given in the top of Fig. 1. The final pattern obtained from combining the measurements in the upper graph is given in the lower graph along with point target measurements for the RADARSAT Precision Transponders.

Results show a small variation in the derived patterns, good agreement between point target and distributed target levels, and good agreement on antenna pattern shape as discussed in [10].

CONCLUSION

The methodology described here has made it possible to determine the antenna gain patterns in elevation for the RADARSAT System. These patterns are critical to the production of radiometrically calibrated products for this imaging system which meet and exceed the radiometric design goals[10].
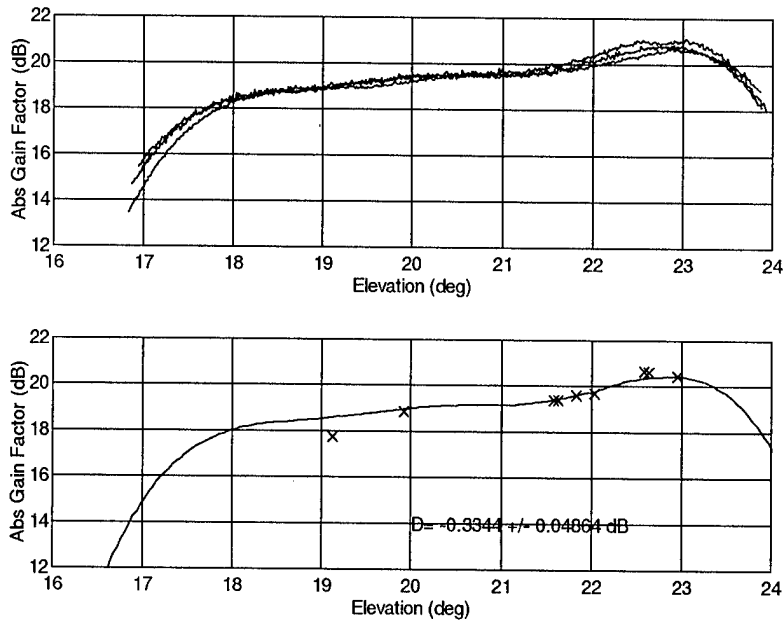
D= -0.3344 +/- 0.04864 dB

Figure 1. Antenna Pattern Determination for Standard Beam S1. The upper graph shows the three constituent beam patterns from the rain forest as they are processed by the CDPF with all gain corrections removed and with an expected $\gamma_o = -6.5$ dB. The lower graph shows the resultant beam pattern when the three curves in the upper graph are optimally combined and averaged. The X's are point target measurements which are assumed to be absolutely correct. The level of the smoothed pattern has been adjusted, from the nominal level expected from the rain forest, in this case by 0.3 dB. The resultant pattern determined from the two methods agrees on average to better than ±0.05 dB.

ACKNOWLEDGMENTS

We acknowledge contributions from and discussions with colleagues M. Shimada (NASDA), P. Vachon and F.Ahern (CCRS), P. Lim (MDA), R. Gray and N. Shepherd (ALTRIX Systems), and A. Luscombe (SPAR Aerospace).

Data were processed by RADARSAT International at the Canadian Data Processing Facility: We thank B. Jefferies, D. Wilson, R. Periard, C. Fabi, G. Fitzgerald, G. Robert, L. Simek, and R. Whetter for their assistance.

REFERENCES

[1] C. Grenier and P. Arsenault, "RADARSAT SAR Antenna RF Performance Report SPAR RML-009-95-031 (RADARSAT Document RSSPR-RT0104)," May 11, 1995.

[2] S.K. Srivastava, N. Shepherd, T.I. Lukowski, and R.K. Hawkins, "Plans for RADARSAT Image Data Calibration," *Adv. Space Res.*, vol. 17, pp. 89-96, 1996.

[3] R.K. Moore, V.S. Frost, H. Westmoreland, D. Frank, and M. Hemmat, "Determining the Vertical Antenna Pattern of a Spaceborne SAR by Observation of Uniform Targets," in *Proc. IGARSS'86*, Zurich, Switzerland, vol. 1, pp. 469-472, September 1986.

[4] R.K. Hawkins, "Determination of Antenna Elevation Pattern for Airborne SAR Using the Rough·Target Approach," *IEEE Trans. Geosci. Remote Sensing*, vol. 28, pp. 896-905, September 1990.

[5] J.E. Laycock and H. Laur, "ERS-1 SAR Antenna Pattern Estimation," ESA Technical Report ES-TN-DPE-OM-JL01, September 1994.

[6] M. Shimada and A. Freeman, "A Technique for Measurement of Spaceborne SAR Antenna Patterns Using Distributed Targets," *IEEE Trans. Geosci. Remote Sensing*, vol. 33, pp. 100-114, January 1995.

[7] E. Attema *et al.*, "ERS-1 and ERS-2 Antenna Pattern Estimates Using the Amazon Rain Forest," in *Proceedings of a Workshop on RADARSAT Data Quality*, St. Hubert, Québec, February 1997, 11p.

[8] P. Lecomte and E. Attema, "Calibration and Validation of the ERS-1 Wind Scatterometer," in *Proceedings of the First ERS-1 Symposium - Space at the Service of our Environment*, Cannes, France, 1992, pp. 19-28.

[9] R.K. Hawkins, L.D. Teany, L. Takken, and T.I. Lukowski, "Absolute Calibration and Other Experiments with the RADARSAT Precision Transponders," in *Proceedings of a Workshop on RADARSAT Data Quality*, St. Hubert, Québec, February 1997, 12p.

[10] S.K. Srivastava, R.K. Hawkins, and T.I. Lukowski, "Operational Calibration for RADARSAT Data," in *Proceedings of GER'97*, Ottawa, Canada, May 1997.

The Effect of Atmospheric Correction on AVIRIS Data to Obtain Consistent Multiyear Foliage Chemistry Results

Alexander F.H. Goetz[1,2], Kathleen B. Heidebrecht[1], Bruce Kindel[1]
[1]Center for the Study of Earth from Space (CSES)/CIRES, Campus Box 216
[2] Department of Geological Sciences, Campus Box 250
University of Colorado, Boulder CO 80309
303-492-5086, fax 303-492-5070
goetz@cses.colorado.edu, kathy@cses.colorado.edu, kindel@cses.colorado.edu

Abstract - During the Accelerated Canopy Chemistry Program (ACCP) study, AVIRIS data were acquired over Blackhawk Island, WI and Harvard Forest, MA to be used to assess the value of imaging spectrometer data in determining canopy chemistry constituents, in particular nitrogen and lignin. An extensive ground sample collection effort was undertaken to provide calibration for the chemical analysis. Correlations between the laboratory chemical analysis of leaves and AVIRIS 224 channel images were derived from a portion of the sample set and the ensuing calibration was used to derive nitrogen and lignin values from AVIRIS. Calibrations were derived from 1992 overflight data by multiple linear regression. However, the same calibrations applied to 1993 overflight data yielded values that were internally consistent but approximately 50% too high for both lignin and nitrogen. Incorrect atmospheric correction is considered the main cause for the discrepancy. Sensitivity tests were applied to the original data by changing multiplicative and additive atmospheric parameters. The main source of error is in the atmospheric water vapor value applied. Empirical-line correction is the most accurate method for spectral image correction.

INTRODUCTION

The NASA Accelerated Canopy Chemistry Program (ACCP) brought together a large number of interdisciplinary researchers to test whether it was possible to determine foliar chemistry, specifically lignin and nitrogen concentrations, by remote sensing with imaging spectrometry. Several methods of data analysis were attempted, but no single method was adopted because no intercomparisons could be completed. In particular, calibrations used in data analysis of AVIRIS overflights in 1992 were not applicable to 1993 data. One of the major uncertainties was the quality of the atmospheric model used to reduce the data to apparent surface reflectance. Another uncertainty was the spectral calibration of AVIRIS which has been shown to vary as much as 3 nm over the 1992 season [1].

AVIRIS data were acquired over Blackhawk Island, WI and Harvard Forest, MA. An extensive ground sample collection effort was undertaken to provide calibration for the chemical analysis. Correlations between the laboratory chemical analysis of leaves and AVIRIS 224 channel images

were derived from a portion of the sample set and the ensuing calibration was used to derive nitrogen and lignin values from AVIRIS [2, 3]. Calibrations were derived from 1992 overflight data by multiple linear regression (MLR) on first-difference pixel spectra. Values of r^2 between 0.85 and 0.9 were obtained for Blackhawk Island and 0.7 and 0.85 for Harvard Forest [3]. However, the same calibrations applied to 1993 overflight data yielded values that were internally consistent but approximately 50% too high for both lignin and nitrogen. The subject of this paper is the determination of the cause, in particular the role played by atmospheric correction, in affecting multi-year calibration by undertaking a sensitivity analysis.

BACKGROUND

The ACCP was designed to help determine whether from orbit, using an imaging spectrometer, it would be possible to measure lignin and nitrogen concentrations in closed forest canopies. The motivation was to be able to document changes in canopy chemistry globally in response to elevating atmospheric CO_2 content [4] to determine whether plants are becoming more efficient in their storage of carbon. The charge was given to the EOS High Resolution Imaging Spectrometer Team, augmented by researchers from related disciplines, that ultimately resulted in a team of 38 investigators [4].

The analysis of AVIRIS data during the ACCP campaign showed clearly the criticality of rapid and accurate atmospheric correction on a pixel by pixel basis. Ultimately, all analyses of vegetation biochemistry require apparent surface reflectance as the raw data form. The experience with ATREM [5] showed that under dry conditions, and with accurate wavelength calibration, that consistent pixel spectra within a single image could be obtained to a precision of approximately 1%. However, as the precipitable water content rose above approximately 1 cm, regions in the spectrum surrounding the major and minor water vapor absorption features became unusable in the analyses because of inaccuracies in the model of the band shape used to correct for the absorption. In particular, the region around the unsaturated features centered at 0.94 and 1.14 μm are not well modeled by ATREM [5], LOWTRAN 7 [6] or MODTRAN [7].

During the ACCP, chemical analyses of samples of the forest canopy from 20 sites at Blackhawk Island, WI, and 20 at Harvard Forest, MA were analyzed by both wet-chemical and near-infrared spectroscopy methods [2]. Using multiple linear regression, Martin and Aber [3]were able to relate field measurements and AVIRIS data for nitrogen and lignin to within an RMS error of 10% of the mean value of the constituent. Similar results were obtained by Gao and Goetz [8] using a curve-fitting method for lignin in the 1.72 μm region after an MNF transformation of the [9]. However, calibrations based on 1992 data were not applicable to 1993 AVIRIS data sets as shown in Fig. 1. The discrepancy possibly can be attributed to an incorrect atmospheric correction, to an error in the AVIRIS calibration, to the effect of a different sun angle and azimuth during the 1993 AVIRIS overflight, or to a systematic error in the data analysis algorithms.

ANALYSIS

The prediction of lignin content in the canopy at Blackhawk Island using the regression coefficients derived from 1992 data applied to 1993 data is in error by approximately a factor of two. Natural variation of less than 10% is expected, and, therefore, the errors must originate from either the viewing geometry, the instrument calibration, or in the correction of instrument radiance measurement to apparent surface reflectance.

The solar zenith angles were 20° in 1992 and 30° in 1993. This difference, most likely, would not produce a BRDF-related effect of the magnitude seen in Fig. 1. The AVIRIS instrument spectral calibration was checked using atmospheric absorption band locations [1]. The radiometric calibration during the 1992 and 1993 flight seasons was monitored by regular, on-runway, standard lamp radiance calibrations. Sources of error would be multiplicative. The largest uncertainty is associated with atmospheric correction from the point of view of overall optical depth, path radiance and column precipitable water vapor.

In order to determine the relative importance of the possible errors described above, we undertook a sensitivity analysis by modifying the data reduction in four different ways and analyzing the resulting data using multiple linear regression [3] and curve fitting techniques [10]. The data used were four pixels for each of 20 sites at Blackhawk Island for which extensive ground data had been collected and foliar chemistry analysis had been performed [3]. The following were applied: (1) Add/subtract a constant representing approximately 1, 5, and 10% of the signal; (2) Multiply by a constant (0.85, 0.9, 1.05, 1.1, 1.15); (3) Add/subtract a scaled scattering curve derived from ATREM using the same atmospheric model and geometry as during the overflight. The scale factors were: .05, 0.1 and 0.5; (4) Multiply/divide by water vapor transmittance curves of varying total column precipitable water vapor amounts derived from ATREM. The amounts were: 0.11, 0.5, 1.06 and 2.05 cm.
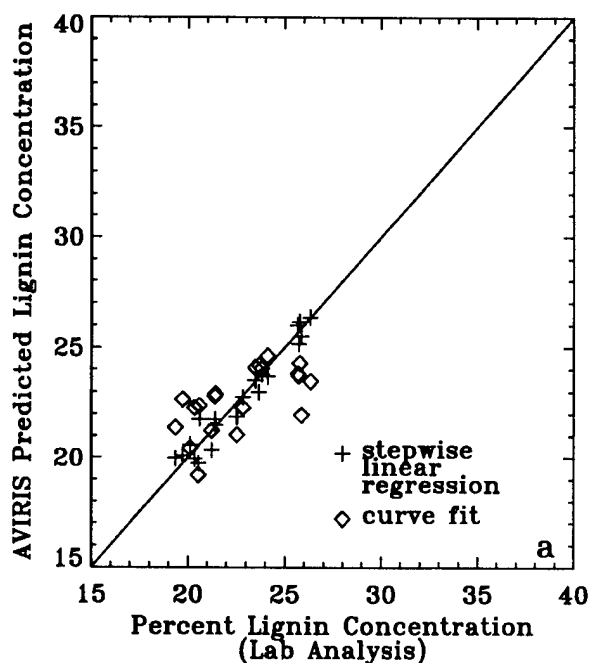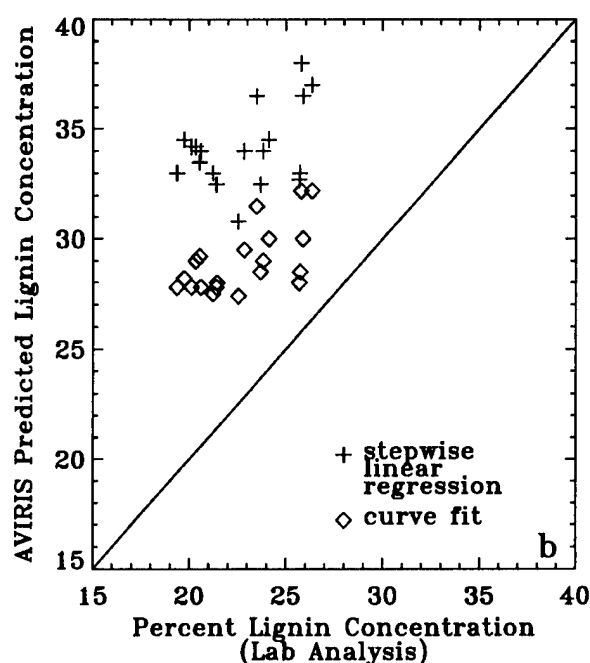

Fig. 1. (a) Lignin content predicted from the 1992 AVIRIS data at Blackhawk Island, WI.

(b) Lignin content predicted from the 1993 AVIRIS data at Blackhawk Island, WI using calibrations based on 1992 data.

The results using the multiple linear regression method are shown in Fig. 2 and those from curve fitting in Fig. 3. The two techniques are very different. The multiple linear regression makes use of first differences among 10 nm spectral bands, in this case at 0.79 and 1.7 µm. The curve fitting technique [10] uses a glass beads and water spectrum to remove the effect of leaf water and a dried leaf spectrum in the 1.5-1.75 µm region to provide the shape of the lignin spectral feature. Therefore, the different methods can be expected to yield different results in the sensitivity analysis.

CONCLUSIONS

The sensitivity analysis shows that both analysis techniques are affected to the greatest degree by inaccurate estimates of water vapor. However, probable errors are not sufficient to create the discrepancy between the 1992 and 1993 data. The multiple linear regression technique is more sensitive than the curve fitting technique to water vapor inaccuracies, most likely because the 1.7 µm band used is on the wings of the.

strong 1.9 µm atmospheric water vapor absorption feature. On the other hand, varying scattering has no effect on the MLR results, and only a small effect on the curve fitting results. The curve fitting method is severely affected by offsets, while the MLR technique is insensitive to them. Other analysis techniques such as Partial Least Squares (PLS) were applied to the data. The results are not shown here because of lack of space. However, the sensitivity to water vapor correction errors for PLS was much greater than for the two techniques described above. A partial solution to the atmospheric correction problem in future missions is to find an invariant target in the area of interest and normalize the spectra to that point.
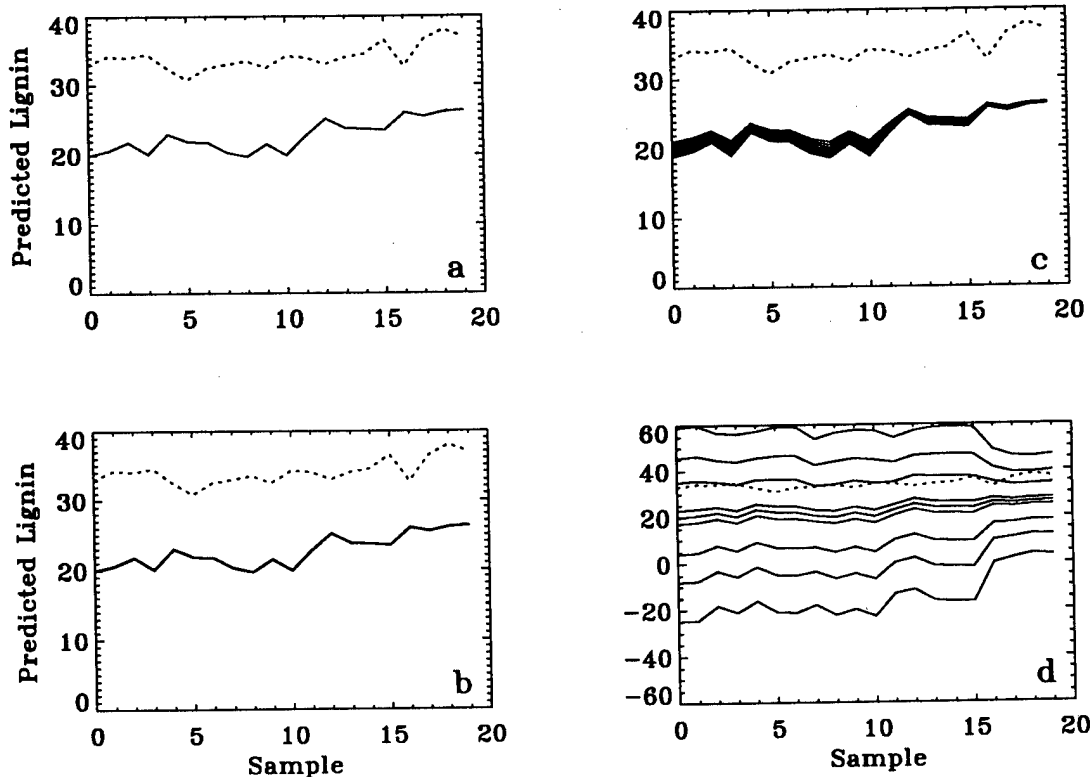
Fig. 2. Plots of predicted canopy lignin using the regression equation derived from multiple linear regression analysis of AVIRIS data from 20 different plots at Blackhawk Island, WI. Solid lines are the 1992 values and the dotted line represents the 1993 data derived using the 1992 regression coefficients.

(a) Offsets applied to the spectra; (b) Scattering added to the spectra; (c) Gains applied to the spectra. The highest value corresponds to 0.85; (d) Corrections made for differing water vapor. The high values correspond to undercorrecting.
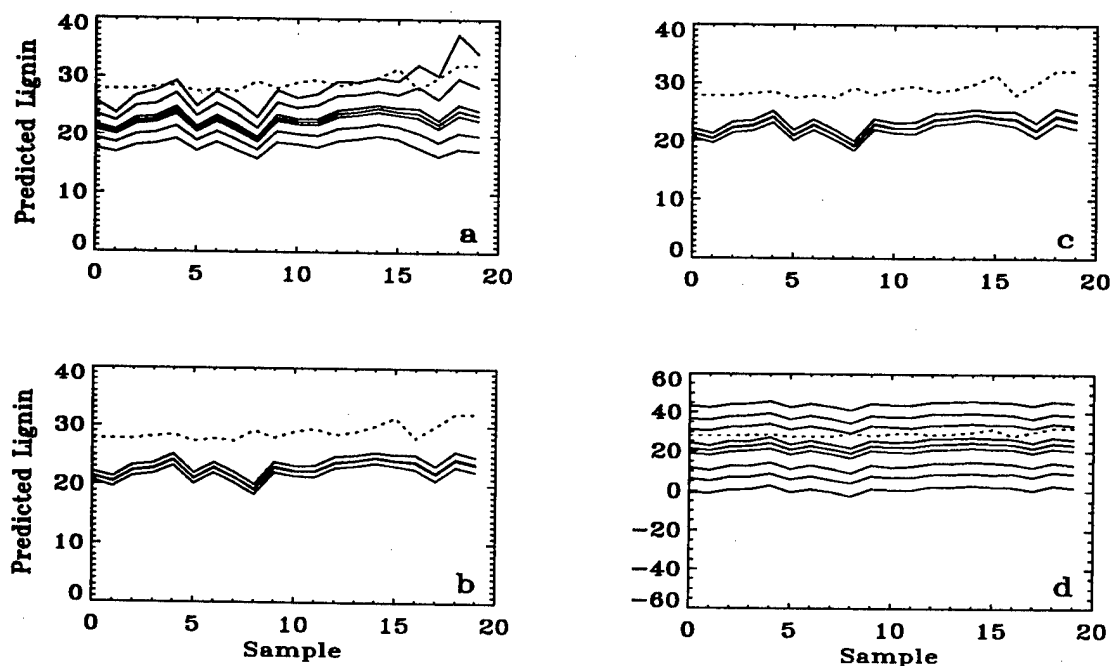
Fig. 3. Plots of predicted canopy lignin using the regression equation derived from the curve fitting technique analysis of AVIRIS data from 20 different plots at Blackhawk Island, WI. Solid lines are the 1992 values and the dotted line represents the 1993 data derived using the 1992 regression coefficients.

(a) Offsets applied to the spectra; (b) Scattering added to the spectra. The upper curve corresponds to a scattering value of -0.5 and the bottom curve to a value of +0.5; (c) Gains applied to the spectra. The highest value corresponds to 0.85; (d) Corrections made for differing water vapor. The high values correspond to overcorrecting.

REFERENCES

[1] A. F. H. Goetz, K. B. Heidebrecht and T. G. Chrien, "High accuracy in-flight wavelength calibration of imaging spectrometry data," *Summaries of the Fifth Annual JPL Airborne Earth Science Workshop*, vol. 1, 67-69, 1995.

[2] M. E. Martin and J. D. Aber, "Analyses of forest foliage III: Determining nitrogen, lignin and cellulose in fresh leaves using near infrared reflectance data," *Journal of Near Infrared Spectroscopy*, vol. 2, 15-24, 1995.

[3] M. E. Martin and J. D. Aber, "High spectral resolution remote sensing of forest canopy lignin, nitrogen, and ecosystem processes," *Ecological Applications*, vol. 7, no. 2, 431-443, 1997.

[4] ACCP, Accelerated Canopy Chemistry Program Final Report presented to EOS-IWG, October 19, 1994.

[5] B.-C. Gao, K. B. Heidebrecht and A. F. H. Goetz, "Derivation of Scaled Surface Reflectances from AVIRIS data," *Remote Sens. Environ.*, vol. 44, 165-178, 1993.

[6] F. X. Kneizys, E. P. Shettle, G. P. Anderson, L. W. Abrew, J. H. Chetwynd, J. E. A. Shelby and W. O. Gallery, "Atmospheric transmittance/radiance: Computer code LOWTRAN 7," AFGL Hanscom AFB, Bedford, MA, 1989.

[7] A. Berk, L. S. Bernstein and D. C. Robertson, "MODTRAN: A moderate resolution model for LOWTRAN 7," Final report, GL-TR-0122, AFGL, Hanscomb AFB, MA, 42, 1989.

[8] B. -C. Gao and A. F. H. Goetz, "Retrieval of equivalent water thickness and information related to biochemical components of vegetation canopies from AVIRIS data," *Remote Sens. of Environ.*, vol. 52, no. 3, 155-162, 1995.

[9] A. A. Green, M. Berman, P. Switer and M. D. Craig, "A transformation for ordering multispectral data in terms of image quality with implications for noise removal," IEEE Transactions on Geoscience and Remote Sensing, vol. 26, no. 1, 65-74, 1988.

[10] B. -C. Gao and A. F. H. Goetz, "Extraction of dry leaf spectral features from reflectance spectra of green vegetation," *Remote Sens. of Environ.*, vol. 47, 369-374, 1994.

The Airborne X/L-band SAR System of CRL/NASDA: System Description and Preliminary Results

Tatsuharu Kobayashi, Makoto Satake, Harunobu Masuko, Masanobu Shimada (+),
Hiromi Oaku (+) and Toshihiko Umehara (++)
Communications Research Laboratory, Ministry of Posts and Telecommunications
(+) Earth Observation Research Center, National Space Development Agency of Japan
(++) Earth Observation Center, National Space Development Agency of Japan
2-1, Nukui-Kitamachi 4-chome, Koganei-shi, Tokyo 184, JAPAN
Phone:(+81)423 27 7547, Fax: (+81)423 27 6110, E-mail: tkoba@crl.go.jp

Abstract – A new airborne multi-frequency Synthetic Aperture Radar (SAR) was developed by Communications Research Laboratory (CRL) and National Space Development Agency of Japan (NASDA). This system observe earth surface by multi-frequency (L and X band), all polarization and high resolution. Furthermore the system has topographic mapping function for X band by a crosstrack interferometric SAR. In this report we describe our SAR system and preliminary results of the test flights.

INTRODUCTION

A new airborne multi-frequency Synthetic Aperture Radar (SAR) system was developed by the joint project of Communication Research Laboratory (CRL) and National Space Development Agency of Japan (NASDA) from 1993 to 1996. It is operated by installing on the airplane, Gulfstream II. The observation is made at the airplane ground speeds between 150 m/s and 250 m/s in the altitude between 6,000 m and 12,000 m. A series of test flight experiments were made in 1996. The resolution of X-band SAR is 1.5 m in both azimuth (after 4 looks processing) and range direction, whereas that of the L-band SAR is 3 m. The both SAR are operated with polarimeter capability, which provide the radar cross sections with phase in all parallel and cross polarizations in order to distinguish surface conditions in detail. Furthermore the X-band SAR has topographic mapping function, which yields the height at each point in the scene by using cross track interferometry with two vertical polarized antennas equipped on the airplane.

SYSTEM

Each of L-band and X-band system is independent and can be operated independently. In the case of multi-frequency observation all frequencies are locked to a crystal oscillator of the X-band system. The L-band system consists of two antennas (installed a radome), a transmitter,a receiver, a data processing system, a recording systems, a control systems, and a calibration system. Whereas the X-band system consists of three antennas (installed two radomes), a transmitter, two receivers,
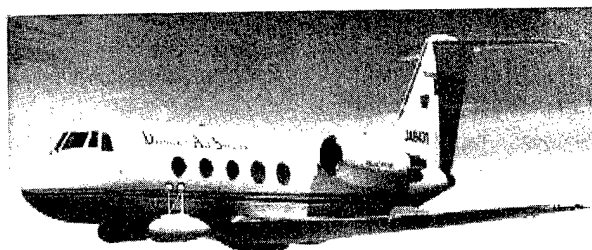
Figure 1: The picture of Gulf Stream II equipped 3 antenna radomes. (Provided by Diamond Air Service)

two data processing systems, two recording systems, a control systems, aircraft data input interface, and a calibration system. This system is controlled throw the touch panel monitor. After landing, SAR image is processed in a work station. The main specifications of our system are shown in Table 1.

The antenna of L-band is microstrip phased-array antennas, covered by a radome under the fuselage. Whereas the antenna of X-band is slotted waveguide phased-array antennas, installed in radomes equipped at the left and right side of airplane. The airplane equipped radomes is shown in Fig. 1. The beam width in the elevation direction at the -10 dB point is nearly 40° (from −30° to +10° around antenna peak). The beam width in the azimuth direction is 2.3° at the -3 dB points. The antenna of L-band is fixed, whereas the antennas of X-bans are variable. The incidence angle of the antenna peak is varied from 40° to 65°. The antenna is moved between ±6.5° in yaw direction using motor drives to roughly compensate the drift angle of the airplane.

The X-band transmitter use a traveling wave tube (TWT) amplifier to generate the high power RF. The peak output power of the TWT is 8.2 kW for the 10 μs long pulse. The output send to the duplexer. It passes through the duplexer to the antenna, and the signal is transmitted. The output power after duplexer become 6.2 kW by the loss of waveguide, duplexer and mismatch.

The return echo signals from the antenna are received by manual gain control or automatically gain control (AGC) and

Frequency	X-band	L-band
weight	707.6 kg (include INS)	422.2 kg
Slant Range resolution	1.5 / 3 m	3 / 5 / 10 / 20 m
Azimuth resolution (4-look Processing)	1.5 / 3 m	3 / 6 m
Noise equivalent NRCS	less than −40 dB for HH	less than −40 dB for HH
S/N	larger than 10 dB for HH	larger than 10 dB for HH
Polarimetry Polarimetric phase accuracy	HH/HV/VV/VH less than 5 degrees	HH/HV/VV/VH less than 5 degrees
Interferometry Base line Phase Accuracy Height accuracy	2.30 m less than 5 degrees less than 2 m (rms)	
Radiometric accuracy	less than 0.5 dB	less than 0.5 dB
Incidence angle	10 – 75 deg. Variable	20 – 60 deg. Fix
Antenna	106.5 cm(length) × 20 cm	155.0 cm × 65.0cm
Antenna gain	26.5 dB	18 dB
Sidelobe (elevation)	-20 dB	-17 dB
Sidelobe (azimuth)	-25 dB	-25 dB
Cross-polarization isolation	-33 dB	-25 dB
Transmitter peak power	6.3 kW	3.0 kW
Pulse length	10 μs	10 μs
Pulse repetition frequency	less than 3000 Hz	less than 1000 Hz
Transmitter bandwidth	100 MHz	50 MHz
Transmitting/receiving	all digital	all digital
Data sampling	123.45 MHz / 61.725 MHz	61.7 MHz / 30.9 MHz
Quantization	8 bits for both I and Q	8 bits for both I and Q
Data rate	512 Mbps	256 Mbps
Recorder	SONY/D1 × 2	SONY/D1

Table 1: System Parameter and Performance

amplified. The I and Q signals are obtained using quadrature demodulators.

The I and Q signals are digitalized in 8 bits by A/D converters with the speed of 123 MHz. These I and Q data, operation parameters, system monitors, and aircraft information are recorded to D1 cassette tape by using SONY DIR-1000. Three tapes is needed for each 50 minutes. The swath width is limited by the record rate. The swath width of X-band is shown in Table.2.

TEST FLIGHT

Our SAR system was installed to Gulf Stream II and tested in the performance. The SAR image is shown in Fig. 2 and 3. This data was taken in the altitude of 12192 m at Noto in Japan. The image is about 3.5 km (Rg) × 1.6 km (Az).

mode	sampling frequency	Swath width in slant range
2 channel (HH/HV, VH,VV)	60 MHz	37.0 km
2 channel (interferometry)	120 MHz	17.7 km
4 channel (polarimetry)	60 MHz	17.5 km
4 channel (polarimetry)	120 MHz	7.9 km
6 channel (polarimetry)	60 MHz	10.8 km
6 channel (polarimetry)	120 MHz	4.7 km

Table 2: Observation mode for X-band system

Range **X-band**

Azimuth

HH

HV

VH

VV

Range **L-band**

Azimuth

HH

HV

VH

VV
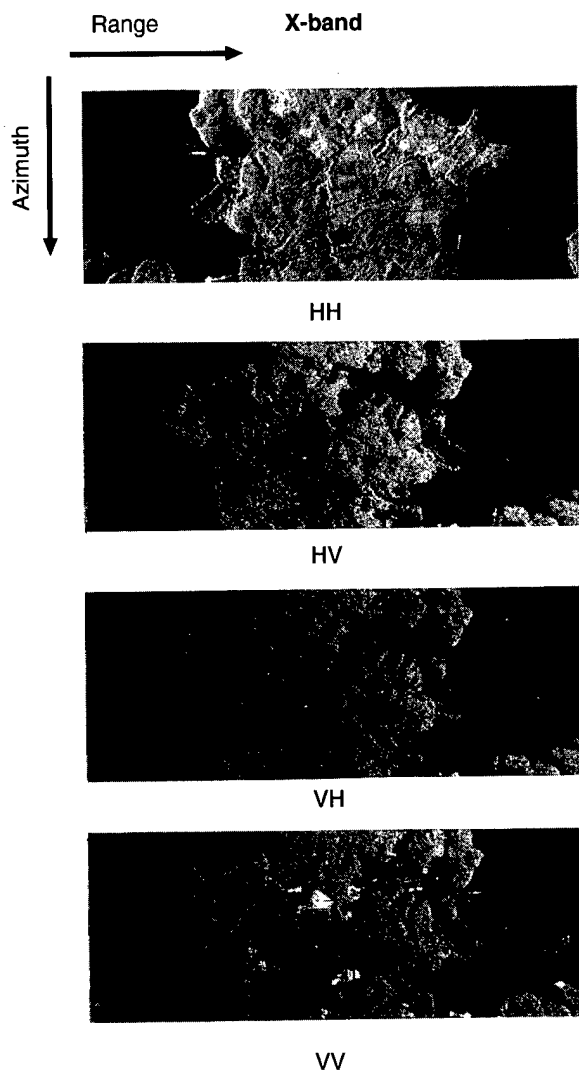
Figure 2: The X-band SAR image of the Noto in Japan. The image is about 3.5 km(Rg) X 1.6 Km(Az). The resolution is 6 m for 2 looks (Rg) x 19 m for 16 looks (Az). (processed by NEC)
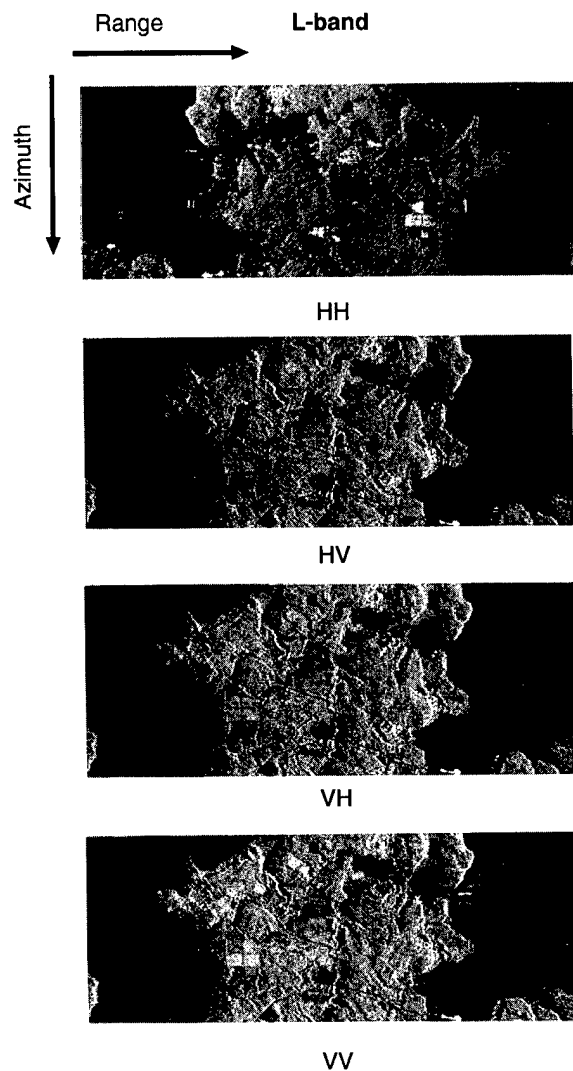
Figure 3: The L-band SAR image of the Noto in Japan. The image is about 3.5 km(Rg) X 1.6 Km(Az). The resolution is 12 m for 4 looks (Rg) x 18 m for 8 looks (Az). (processed by NEC)

A Study on Radiometric Calibration of Next Generation Spaceborne SAR

Yoshihisa Hara, Chikako Ohno, Masafumi Iwamoto, and Natsuki Kondo
Mitsubishi Electric Corporation, Kamakura Works
325 Kamimachiya, Kamakura 247, Japan
Phone: (+81)-467-41-5708, Fax: (+81)-467-41-6920
E-mail: hara@kama.melco.co.jp

Yoshikazu Kamiya and Yoshiaki Nemoto
Japan Resources Observation System Organization
2-20-1 Hatchobori, Chuo-ku, Tokyo 104, JAPAN

Abstract : With the new demands for SAR(Synthetic Aperture Radar), such as variable off-nadir and SCAN SAR, phased array radar technology is required for most of the next generation spaceborne SARs. Radiometric calibration of active phased array type SARs, however, is a very complicated task, because they have hundreds of active devices and phase shifters to be calibrated.

In this paper, we have conducted a study on the internal calibration method for phased array type SAR. First, we derive the error sources of such kind of SARs. These are mainly divided into two categories, the variation in antenna and the variation in transmitter/receiver. Modified REV(Rotating Element Electric Field Vector) method[1] is proposed for the calibration of antenna subsystem. By the compensation, the optimal antenna pattern can be maintained to keep high S/A and S/N of the SAR image, and the accurate antenna gain can be estimated. For the calibration of transmitter/receiver, tone signal method and ERP(Effective Radiated Power) measurement method using REV antenna is proposed. By the compensation, the total gain variation of transmitter/receiver chains can be estimated. It is shown that the radiometric accuracy of 0.8dB can be obtained by the above calibration methods together with the standard external calibration methods.

1. INTRODUCTION

Spaceborne SAR imagery has been supplied by many sensors including EERS-1 SAR and JERS-1 SAR, since Seasat was launched in 1978. SAR was first regarded as a microwave camera and imagery itself was considered important, because the images taken by microwave sensors are completely different from those by optical sensors, and give substantial information which can not be obtained by optical sensors.

Recently, high radiometric accuracy is also necessary to extract more valuable information from the SAR imagery using electromagnetic wave theory. However, SAR imagery suffers from many radiometric errors. Conventional type SARs such as EERS-1 and JERS-1 use the RF replica method to calibrate the imagery , where the high power amplifier output is coupled into the receiver subsystem bypassing the antenna[2]. Calibration process of phased array type SARs such as SIR-C, however, cannot bypass the antenna subsystem, because it has a lot of active devices on it. The RF tone signal method[2] is used to estimate the variations in antenna and transmitter/receiver, and the absolute accuracy is reported to be around 3dB in the case of SIR-C[3].

In this paper, we propose a new internal calibration method for next generation phased array type SAR to get the imagery whose radiometric accuracy is less than 1.0dB.

2. ERROR SOURCES

There are three kinds of error sources for phased array type SARs. The first is the atmospheric propagation such as attenuation, propagation delay, rotation of polarized wave (faraday rotation). The second is variations in antenna such as distortion of antenna panel, phase and amplitude variation of T/R modules due to the temperature change. The last is variations in transmitter and receiver, such as phase and amplitude variation of active devices due to temperature change.

In general, the second and the third error sources are large compared to the first one, and these error must be compensated by the accurate calibrations.

3. CALIBRATION OF ANTENNA PATTERN

Spaceborne phased array type SARs generally have large variations in antenna due to its large physical scale (around 10m)

and a large number of active T/R modules. The antenna pattern is degraded both with the physical distortion and with the variation of the phase and amplitude of T/R modules due to the temperature changes in orbit. The degradation results in the loss of radiometric accuracy as well as that of high S/A and S/N of SAR imagery.

Two calibration methods to compensate the variations in antenna are considered. One is the modified REV(Rotating Element Electric Field Vector) method, and the other is the temperature monitoring method.

REV uses an external calibration antenna which is installed in the main antenna panel, and measures the amplitude and the phase contributed from each T/R module by injecting the calibration signal from the external antenna and rotating the phase shifter value of each module as shown in Fig.1(in the case of Rx pattern)[1]. This method has the capability of compensating the phase and amplitude variation of T/R modules and also the distortion of antenna at the same time. Conventional REV uses only the phase information for the optimal beam forming. Amplitude information is used here to estimate the antenna gain to keep the radiometric accuracy.

On the other hand, temperature monitoring method measures the temperature at each T/R module, and uses the phase and amplitude table which is obtained on the ground and retains the temperature characteristics of each T/R module.

Tradeoff of antenna pattern calibration methods is shown in Table 1. As is clear from the table, the modified REV method is superior in hardware volume because of its simplicity of REV antenna, and test time because it does not need the temperature dependence data of each T/R module. Considering the above superiority and future expandability, we decide to adopt the modified REV method for the antenna pattern calibration.
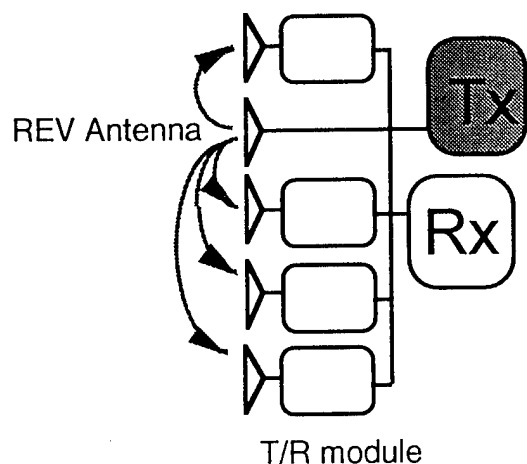
Table.1 Tradeoff of antenna pattern calibration methods

	Modified REV method	Temperature monitoring method
Hardware volume	○	△
On-board software volume	△	○
Calibration accuracy	○	○
Complexity of control software	△	△
Test time	○	△
Future expandability	○	×

3. CALIBRATION OF TRANSMITTER AND RECEIVER

The characteristics variation of analog devices with temperature changes affects radiometric accuracy in the transmitter and receiver subsystem. There are a lot of components, such as HPAs and LNAs, in transmitter/receiver chain of the phased array type SAR. So, measuring the total system characteristics is necessary to obtain high radiometric accuracy.

In this study, the extended RF tone signal method is adopted as a calibration method instead of the conventional RF replica method which bypasses the antenna. This method is an extension of the RF tone signal method applied in SIR-C, and uses the REV antenna to supply or monitor the calibration signal .

To measure the receiver characteristics, the RF tone signal generated and stabilized at the exciter is injected through the REV antenna and coupled with the received signal in T/R modules. The RF tone signal goes through the entire receiver chain, and is extracted by spectral analyses at the ground station after A/D conversion in the signal processor. By constantly monitoring the RF tone signal, the receiver gain of each image can be estimated precisely. The block diagram of the receiver chain characteristics measurement is shown in Fig.2.

To measure the transmitter characteristics, the ERP(Effective Radiated Power) is monitored by the REV antenna by coupling the transmitted signal into the REV antenna and further coupling it into the receiver. The block diagram of the transmitter chain

Fig.1 Block diagram of REV method

characteristics measurement is shown in Fig.3.
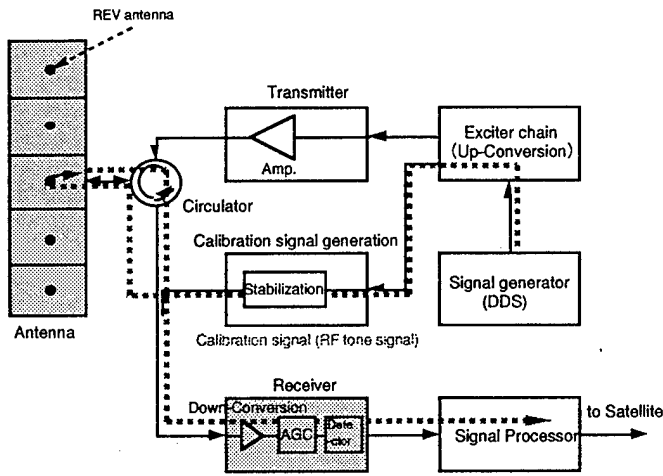
Fig.2. Block diagram of the receiver chain measurement
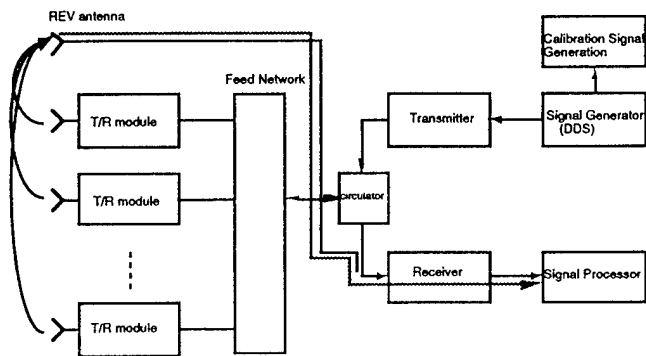
Fig.3. Block diagram of the transmitter chain measurement

4. IMPLEMENTATION

In actual operation, the above calibration methods are implemented in the several modes as shown in Table 2. By the above calibration methods together with the external calibration method using ARC(Active Radar Calibrator), high radiometric accuracy can be obtained. Error budget of the entire SAR system is shown in Table 3. The radiometric accuracy is estimated to be 0.8dB.

5. CONCLUSIONS

A new internal calibration method for the next generation spaceborne SAR is proposed. The modified REV method is used for the antenna calibration, and RF tone signal method using the REV antenna is used for the transmitter/receiver calibration. By using the above methods combined with the standard external calibration methods, radiometric accuracy of 0.8dB can be achieved.

This study was conducted under the contract with MITI (Ministry of International Trade and Industry).

REFERENCES

[1] Seiji Mano and Takashi Katagi, "A Method for Measuring Amplitude and Phase of Each Radiating Element of a Phased Array Antenna," Trans. IECE, vol. J65-B, No.5,1982.

[2]John C. Curlander and Robert N. Mcdonough, "Synthetic Aperture Radar-Systems and Signal Processing", John Wiley & Sons, Inc., 1991.

[3]Anthony Freeman et. al., "SIR-C Data Quality and Calibration Results", IEEE Trans. on GRS, vol. 33, No.4, 1995.

Table 2. The operational mode of internal calibration

Mode	Tx/Rx	Procedure	Objective
Calibration mode	Receiver chain	Inject RF tone signal to the receiver	Receiver characteristics measurement
		Scan the RF tone signal across the passband	Frequency response measurement
		Modified REV in receive mode	Antenna pattern optimization and antenna gain estimation
		Inject RF tone signal to the REV antenna	Receiver chain gain measurement
		Terminate T/R modules LNA inputs	Noise measurement
	Transmitter chain	Modified REV in transmit mode	Antenna pattern optimization and antenna gain estimation
		Monitor ERP by the REV antenna	Transmitted power measurement
Observation mode	Receiver chain	Inject RF tone signal to the REV antenna	Receiver chain gain variation measurement
	Transmitter chain	Monitor ERP by the REV antenna	Transmitted power variation measurement

Table 3 Error budget

	Error Factor		Estimated Error
Relative Error	Antenna	Mechanical boresight pointing error	0.2
		Electrical beam pointing error	0.4
		Antenna pattern variation due to deformation of antenna panels	0.1
	T/R module	Variation of transmitter power	0.3
		Distortion by aging and radioactive ray	0.0
	Tx/Rx	Receiver gain estimation error	0.2
		Polarimetric crosstalk error	0.2
		Variation due to thermal noise	0.1
	Signal Processor	A/D Quantization error	0.2
		Parameter estimation error	0.2
Absolute Error	Measurement error by ARC(Active Radar Calibration)		0.4
	Total estimated error (rms)		0.8dB

ARIES - a simulator for the next generation of spaceborne IR meteorological sounders

S H S Wilson, N C Atkinson, P J Rayer, J Smith and D R Pick
United Kingdom Meteorological Office (UKMO), Remote Sensing Branch
Building Y70, DERA Farnborough, Hampshire GU14 6TD, UK
Tel: +44-1252-395860 Fax: +44-1252-515523 Email: swilson@meto.gov.uk

Abstract – The UKMO has developed an airborne interferometer to act as a simulator for satellite-based infrared sounders. ARIES, the Airborne Research Interferometer Evaluation System consists of a modified commercial interferometer, mounted on the UKMO C-130 aircraft. The instrument is sensitive to the wavelength range 3.3 – 16.6 µm, and has a maximum optical path difference of ± 1.037 cm.

I. INTRODUCTION

The Remote Sensing branch of the UKMO has developed a number of airborne radiometer simulators for forthcoming meteorological satellite instruments. These satellite instruments will provide improved temperature and humidity profiles for operational meteorology, ultimately leading to improvements in forecasting [1]. Airborne simulators are required to test and improve knowledge of the relevant atmospheric spectroscopy, surface characteristics and radiative transfer models. This is a necessary precursor to the routine extraction of the required atmospheric data from the satellite radiance measurements.

Until now, much of this work has focussed on the development of simulators for AMSU – the Advanced Microwave Sounding Unit. This has lead to a pair of microwave radiometers [2] mounted on the UKMO C-130 aircraft, which are capable of making measurements at a number of AMSU frequencies. Recently however, an infrared interferometer called ARIES – the Airborne Research Interferometer Evaluation System has been built as a simulator for a number of new infrared sounding satellite instruments, in particular IASI – the Infrared Atmospheric Sounding Interferometer. These new sounders, which also include IMG and AIRS, offer considerably higher spectral resolution and spectral coverage than previous meteorological sounders, e.g. HIRS [1], with the intention of yielding both higher vertical resolution and accuracy in the retrievals. The feasibility of retrieving the improved data from such higher resolution sounders has been demonstrated experimentally, using HIS – the High-resolution Interferometer Sounder instrument mounted on the high flying NASA ER-2 aircraft [3].

As with the other UKMO simulators, ARIES is mounted on the C-130 aircraft, which is an extremely flexible and well instrumented platform. The aircraft has a range of 5000 km, can fly between 16 m and 10 km altitude, and offers a wide range of instrumentation to measure meteorological, radiative, cloud microphysical and related chemical parameters. Some of these measurements, particularly temperature, humidity and ozone concentration provide co-located 'truth' for comparison with the radiometer simulators. ARIES itself is mounted in a converted fuel tank on the starboard wing (Fig. 1). The instrument consists of a commercial infrared interferometer, modified by the UKMO for aircraft usage. The instrument is sensitive to infrared radiation in the wavelength range 3.3 - 16 µm (600 - 3000 cm^{-1}) and is capable of viewing both the upwelling and downwelling radiation (as well as various angular downward views). Fuller details of the instrument design are provided in the remainder of this paper

ARIES data will be used to provide experimental airborne infrared spectra for comparison with simulations from line-by-line radiative transfer models. The intention in this exercise is to identify areas of uncertainty in the modelling and in the relevant atmospheric spectroscopy, prior to the launch of IASI. It is also hoped to fly ARIES in intercomparison campaigns with other airborne infrared interferometers, for example HIS - which views the upwelling radiation, typically mounted on a stratospheric aircraft [3], and TAFTS, an instrument currently under development (Imperial College, Univ. of London), which will monitor a very broad infrared spectral range (80 - 1000 cm^{-1}) at relatively high resolution (0.1 cm^{-1}).

II. DESIGN

At its heart, ARIES has a rugged commercial interferometer (MB200), developed by BOMEM Inc. of Canada. The interferometer views the external scene by way of a pointing mirror assembly, designed by the UKMO. The pointing mirror can also be directed to view a pair of on-board calibration targets. ARIES data is recorded on a PC located in the main body of the aircraft, connected to the instrument by a fibre-optic cable which runs down the starboard wing. Fig. 2 shows a schematic diagram of the package located in the aircraft wing pod. The design of the interferometer, scan mirror assembly, and acquisition system is now considered.

Figure 1: The UKMO C-130 aircraft; an arrow indicates the wing pod in which ARIES is mounted.

1395
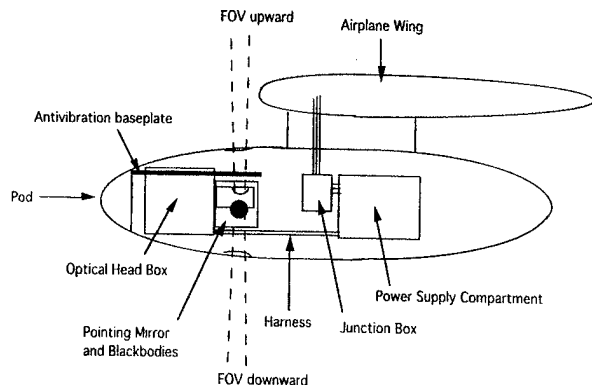
Figure 2: A schematic of the contents of the ARIES wing pod.

II.1 ARIES Interferometer

As with other 'Michelson'-type interferometers, radiation incident on the instrument is partially reflected and partially transmitted by a beamsplitter. A variable optical path difference is introduced between the reflected and transmitted paths, prior to recombination of the beams. The resulting interference pattern is monitored as a function of the path difference; this so-called 'interferogram' contains all the spectral information about the source, which can be recovered using the technique of Fourier transform.

Fig. 3 shows a schematic of the ARIES interferometer optics. Light enters the instrument through a ZnSe window and is partially reflected and partially transmitted by a beamsplitter. The beamsplitter directs the resulting beams to a pair of corner-cube reflectors, which are mounted on a pivoting arm. The motion of this arm rotates the reflectors in opposite directions with respect to the beamsplitter, providing a mechanism for the introduction of a variable path difference. At the corner-cubes, the beams are shifted to a higher vertical plane. Following reflection at the corner-cubes, the beams interfere on return to the beamsplitter and the interference pattern is monitored by a detection system. ARIES has two infrared detectors arranged in a sandwich. A Mercury Cadmium Telluride (MCT) detector is sensitive to the wavelength range 5.5 - 16 μm (600 - 1800 cm^{-1}) and an Indium Antimonide (InSb) detector covers the range 3.3 - 5.9 μm (1700 - 3000 cm^{-1}). The detectors are cooled to ~ 80 K by a Sterling Microcooler.

A 'Second Port' ambient black body is mounted, below mirror A, at the level of the input radiation. The black-body acts as a dump for any reflected light from the detector system which happens to enter the interferometer. The temperature of this black body is monitored using a Platinum Resistance Thermometer (PRT), so that its emission into the interferometer can be calculated [4].

The optical path difference sampling interval is set by the fringe spacing in an interference pattern, generated by a

He-Ne laser. The maximum optical path difference (OPD$_{max}$) defines the instrument resolution. To avoid the description of a particular apodisation function, the resolution can be described in terms of the spectral sampling interval, 1/(2 x OPD$_{max}$). For ARIES, OPD$_{max}$ = 1.037 cm and therefore the spectral sampling interval, is 0.482 cm^{-1}. Typically, at this 'resolution', the sampling rate is 4 scans / sec, but this can be increased by decreasing the 'resolution' i.e. decreasing the OPD$_{max}$. The associated software provides options for a number of such degraded settings.

The interferometer and detector system (see Fig.2, 'Optical Head') is mounted in a machined aluminium box, which is pressurised with dry nitrogen (~ 5 psi overpressure). A series of heaters (Minco 'foil'-type) maintain the unit within its operational temperature range. The entire unit is mounted to the pod via antivibration mounts designed to dampen the severe aircraft vibrations.

II.2 Scan mirror and calibration targets

A pointing mirror assembly (Fig.2) is coupled to the interferometer input window, to allow ARIES to view the external scene.
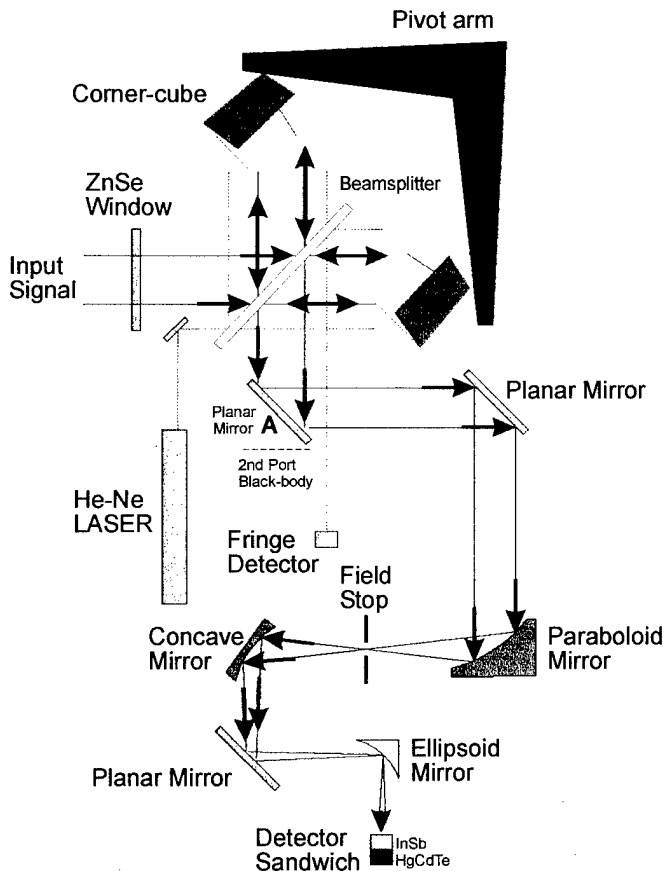
Figure 3: A schematic diagram of the ARIES interferometer optics.

The mirror is gold coated with a SiO protective layer. It can be directed to view upwards through an aperture in the pod (3° off Zenith) and downwards through a slot, with views Nadir and at a series of angles up to 55° towards the main fuselage (across the aircraft track). The ARIES field of view is 44 mrad. The mirror can also be directed to view either of two black-body (Nextel coated) heated calibration targets. The temperature of these calibration targets is monitored via a series of PRTs (Minco type S201PD) and can be set from software (up to 80°C). Typically, the temperatures are set to straddle those of the scene, to facilitate calibration (see § III).

II.3 Software and Data Acquisition

ARIES interferogram data is sent to a PC located within the main fuselage of the aircraft via two fibre-optic cables located in the wing. The data is handled by a dedicated digital signal processing card. Other data, including the PRT temperatures and communication to the scan mirror mechanism, are exchanged via RS-422 twisted pair connections. Using software developed by BOMEM, the operator can specify the acquisition timing, angular view, black-body temperatures and observe temperatures from various other PRTs located around the instrument. As well as recording the interferometer data, the software produces a 'housekeeping file' which records all of these parameters for later use.

III. CALIBRATION

As described above, ARIES can view two temperature stabilised black-body calibration targets, which are mounted on the pointing mirror assembly. Viewing these targets provides the necessary information to calibrate the raw spectral information. The calibration procedure is similar to that described in [5]. In brief, following Fourier transformation of the observed interferogram, the relationship between the raw spectrum S and the calibrated radiance spectrum R is given by:

$$S = G(R - R_{2nd\ Port} - C) \qquad (1)$$

where G is a complex gain and C is a radiance offset, both dependent on frequency. $R_{2nd\ Port}$ is the radiance from the internal black body, which can be calculated from its measured temperature.

By making measurements of the two black-body calibration targets, G and C can be derived. The radiance, R, from the targets can be calculated from their measured temperatures. A pair of simultaneous equations (based on eqn. 1) can then be formed, for the two black-body measurements. These equations can be solved for G and C, which can then be used to calibrate the atmospheric views. To achieve the best calibration, it is important that the target temperatures straddle those of the atmospheric scene; this is

not possible when flying at high level making a Zenith view, as the scene out to space is extremely cold. To alleviate this problem, a ground-use only cold calibration target, cooled to 77 K is under development.

It has been found that the MCT detector has a slightly non-linear output as a function of radiance; an appropriate correction is applied, which is described elsewhere [4].

IV. ARIES DATA

ARIES made its first flight on the UKMO C-130 aircraft in Feb. '96, and since then has participated in a number of campaigns, most notably FASTEX, the Fronts and Atlantic Storm Track Experiment (Jan/Feb '97). However, a hardware fault in the BOMEM electronics, causing a non-linear response in the MCT detector amplifier has caused difficulty in analysis of the data. At the moment, measurements of the amplifier non-linearity are being used to recalibrate the old ARIES datasets, where possible. Following repair of the amplifier circuitry, it is planned to fly ARIES more extensively. In particular, the VIRMEM (Validation of IASI Retrieval Methods: Experiments and Modelling) campaign may provide an opportunity to compare ARIES airborne measurements with those of IMG, ground-based interferometers and radiosondes and Lidar instruments.

V. CONCLUSIONS

A new airborne interferometer, ARIES, has been developed by the UKMO for use on the office's C-130 aircraft. The instrument will be used to improve knowledge of atmospheric spectroscopy and radiative transfer models for the new generation of higher resolution infrared sounding satellite instruments.

REFERENCES

[1] J.R. Eyre, "The information content of data from satellite sounding systems: A simulation study," Q.J.R. Meteorol. Soc., vol 116, pp. 401-434, 1990.
[2] T. J. Hewison, "The design of Deimos: a microwave radiometer with channels at 23.8GHz and 50.3GHz for the UK Met. Research Flight C-130 aircraft." Proceedings of IGARSS'95 conference 10-14 July 1995, pp. 2261-3, Firenze.
[3] H-L. Huang, W.L. Smith and H.M. Woolf, "Vertical Resolution and Accuracy of Atmospheric Infrared Sounding Spectrometers," J. Appl. Meteor., vol. 31, pp. 265-274, March 1992.
[4] N.C. Atkinson, "Signal Processing for ARIES," Met O (RS) Branch Working Paper 103, Meteorological Office, Bracknell, Berks UK, September 1996.
[5] H.E. Revercombe et al, "Radiometric calibration of IR Fourier transform spectrometers," Appl. Opt., vol. 27, pp. 3210-3218, August 1988.

CALIBRATION OF AVHRR DATA GENERATED BY THE INSTRUMENT ON-BOARD TIROS-N USING OCEAN AND CLOUD VIEWS

Arthur P. Cracknell and Ibrahim Busu

Department of Applied Physics and Electronic and Mechanical Engineering,
University of Dundee, DUNDEE DD1 4HN, Scotland, UK.

Fax: ..01382 - 345415
E-mail: a.p.cracknell@dundee.ac.uk

ABSTRACT

Remote sensing images of the Earth have been regarded by many as an important source of data for environmental studies. In order to produce good quality data, all known errors should be removed or eliminated before any of the data are used, especially for time-dependent applications. Over the years a number of post-launch calibration methods and procedures have been suggested and used, particularly for the later spacecraft in the series; each of these has some advantages and disadvantages over the others. This paper reviews a post-launch calibration method which has been established using ocean and cloud views as the main calibration targets; it then applies this method to data from the earlier spacecraft in the series which are no longer in operation.

1.0 INTRODUCTION

In general, the problem addressed in this paper is associated with the data acquisition process with special reference to the archived AVHRR data, that is the data generated by the radiometers onboard the NOAA satellite series. The Dundee AVHRR archive contains data from late 1978 until the present time and it is an important source of data for various applications and has been referred to and used by many geographers and environmentalists. However, the archived AVHRR data set has been generated by about ten different instruments, each of which has been said to be suffering from degradation in responsivity over its lifetime. Therefore, the archived AVHRR data are subject to systematic or instrumental errors. If the archived data are going to be used as input data for time-dependent applications, the systematic errors should be eliminated before the data are blended with data from other sources. An example of such applications is the monitoring of change of the global climate which utilises information generated from long-term AVHRR data.

Satellite sensors in the solar spectrum are very difficult to calibrate due to lack of reliable on-board calibration devices. The pre-launch calibrations are subject to change due to the hostile environment of the sensor during launch, outgasing, deterioration in the sensor system and variation in the spectral characteristics. Some work has been carried out in order to provide alternative calibration methods, which are based on the knowledge of some Earth phenomena as well as on the processing of the digital imagery data generated by the sensor itself. Examples of such work are described in [1] and [2]; however, much of this work is concerned with AVHRRs on spacecraft that were still operating when the work was done.

This paper presents a calibration method for the AVHRR visible and near-infrared channels using oceans and clouds as the main target. An attempt is made to calibrate data from the earlier instruments in the series which are no longer active.

2.0 THE CALIBRATION METHODS

There are two main tasks involved in the proposed calibration method. The first task is to calibrate channel 1 of the AVHRR, which operates in the visible band of the solar spectrum. The second task is to establish the relation between the visible and near-infrared channels. The relation between the two channels is needed due to different radiation and propagation characteristics between them. Once the relation is established, calibration can be transferred between channels 1 and 2.

2.1 Background

Channel 1 of the AVHRR can be calibrated using a technique proposed in [1] using a selected ocean area as the target surface. The method used in the present study is based on radiances measured by the AVHRR over ocean areas, away from the sun-glint area. Theoretically, the upward radiance over a cloud-free ocean surface is greatly influenced by molecular scattering as well as by aerosol scattering. Of the two phenomena, the molecular scattering is more dominant; it contributes about 70 to 80 % of the upward radiance and the remaining 20-30 % is due to aerosol scattering, foam reflectivity and underwater reflectance as in [1]. Based on this background a radiative transfer code using a single order scattering

(SOS) technique has been developed to simulate the satellite-received radiance over a cloud-free ocean area.

The spectral characteristics of channel 2 of the AVHRR are different from those of channel 1; thus its calibration requires a different approach from that developed for channel 1. Sun-glint areas over the ocean have frequently been used to establish the relation between channels 1 and 2; examples can be found from [1] and [2]. The sun-glint area was selected due to the high reflectivity and it is estimated that about 87 % of the glint radiance is due to the specular reflection and it is independent of the radiation wavelength and, therefore, it can be used to determine the relative calibration of band 1 and 2 as mentioned in [1] and [2]. Besides sun-glint areas, cloud bodies were also used by workers for the same purposes of transferring calibration from channel 1 to channel 2 of the AVHRR instrument. Reference [3] indicated that good intercalibration between channel 1 and channel 2 of the AVHRR can be accomplished using high clouds. For the present study, where the area involved is located at high latitude and the chance of having a sun-glint area appearing in the image scene is very remote, the intercalibration between channels 1 and 2 has been established through the use of high altitude clouds.

2.2 The calibration of channel 1

The method described in this section is applied to the image data generated by the AVHRR on-board the TIROS-N satellite which have been received and archived at the receiving station at the University of Dundee. Image data from the Atlantic Ocean have been used for this study. Roughly, the extent of the study area is between latitudes 40^0 N to 55^0 N and longitudes 10^0 W to 25^0 W. However the actual points selected are scattered within this area. In terms of time, the selected image data are from April 1979 to October 1980.

Calibration for channel 1 is performed based on the method described in [1]. The calibration coefficients are defined the following equations:

$$L_i^N = \pi L_i d^2 / E_{oi} \qquad (1)$$

where L_i is the radiance observed in channel i, d is the distance between the Sun and the Earth in astronomical units and E_{oi} is the solar exoatmospheric band average solar irradiance for d = 1.

The normalized radiance L_i^N is equal to the surface reflectance for no atmosphere and for the Sun at zenith. The calibration equation for L_i^N is:

$$L_i^N = \gamma_i (C_i - C_{oi}) \qquad (2)$$

where $\gamma_i = \alpha_i \pi d^2 / E_{oi}$.

The change in the sensor calibration between the true, γ_i (true), and the pre-launch, γ_i (pre-launch), calibration coefficients is given by the calibration ratio (r_i):

$$r_i = \gamma_i (pre - launch) \Big/ \gamma_i (true) \cdot \qquad (3)$$

The pre-launch calibration coefficient is given by NOAA [4]. Therefore, the calibration coefficient α_i can be computed by using the following relation:

$$\alpha_i = \gamma_i (pre - launch) E_{oi} \Big/ (\pi r_i d^2) \cdot \qquad (4)$$

In this case the pre-launch surface reflectance is determined using the information provided on the AVHRR magnetic tape and the pre-launch calibration coefficients; digital counts of channels 1 and 2 can be converted to surface radiance and then further converted to reflectance, see [1] and [4]. The surface radiance at the top of the atmosphere is determined using the radiative transfer codes based on the single order scattering (SOS) with the meteorological parameters provided by the archives of climate data kept at the NOAA Climatic Data Center (NCDC) and other organisations related to meteorological and climatic research.

Using information provided on the magnetic tape and ephemeral data, a normalized radiance for each pixel in the selected areas is computed and divided into the one calibrated using the pre-launch calibration coefficients given by NOAA to produce the calibration ratio (r_1) for channel 1. Therefore the post-launch calibration coefficient for channel 1 of the AVHRR can be determined using (4). On the other hand if calibrated radiances are plotted against the theoretical radiance, the slope of the graph will define the calibration ratio for channel 1 (r_1).

2.3 Intercalibration between channels 1 and 2

In the case where the cloud is high enough (above 12 km) the aerosol and water vapour have a negligible influence on the signal because they are located mainly at a much lower layer of the atmosphere. Thus, the main contributions to the signal received by a sensor are from the cloud reflectance, molecular scattering and absorption by oxygen and ozone. The only contributions to the observed signal are from the cloud reflectance, molecular scattering and absorption by oxygen and ozone. In order to relate the AVHRR measurement directly to the cloud reflectance, the measurements have to be corrected for the atmospheric scattering and absorption. The method described in [3]

has been adopted to establish the relation between channels 1 and 2 in this study.

3.0 RESULTS

A graph in fig. 1 shows the calibration coefficients for channel 1 for both pre-launch and post-launch periods. The best fit line for the post-launch calibration coefficient increases with time. The equation of the best fit line determines the calibration coefficient for channel 1:

$$\alpha_1 = 0.5724456 + 0.0052692 * D \qquad (5)$$

where D is the month after launch date.

The r_{12} values computed using the method described in [3] are then used for transferring the calibration ratio (r_1) from channel 1 to channel 2 and the calibration ratio (r_2) for channel 2 can be determined by the following relation:

$$r_2 = \frac{r_1}{r_{12}} . \qquad (6)$$

Furthermore, the calibration coefficient for channel 2 can be determined using (4), similar to channel 1. Both pre-launch and post-launch coefficients are then plotted against the month of the year in Fig. 2. A significant variation is portrayed by those computed using model predictions. The calibration coefficient for channel 2 can be derived using the equation of its best fit line which is:

$$\alpha_2 = 0.4647135 + 0.0043156 * D . \qquad (7)$$
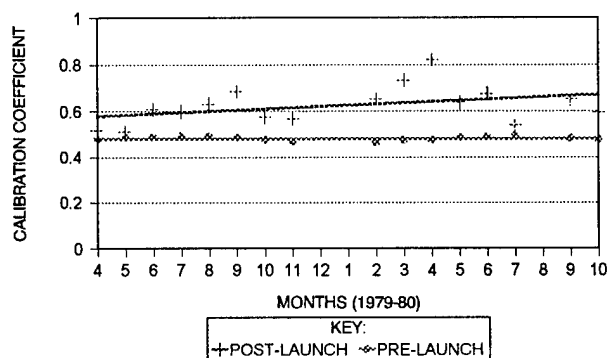
Fig. 1. The calibration coefficients for channel 1 of the AVHRR on-board TIROS-N, based on model prediction (+) and pre-launch information (•)

5.0 CONCLUSION

The applications of AVHRR channel-1 and channel-2 data are gaining in popularity, especially for studies of global vegetation, environmental and other phenomena at regional or continental scale. However, AVHRR users have been hampered by the problems of systematic errors. Now the availability of post-launch calibration methods will enable users to eliminate or minimise these systematic errors. After correcting for the systematic errors, the archived AVHRR data can then be used with confidence for time-dependent applications over long periods. At that stage the validity of the data will be known to the users and then the archived data will be much more valuable than before the calibration.
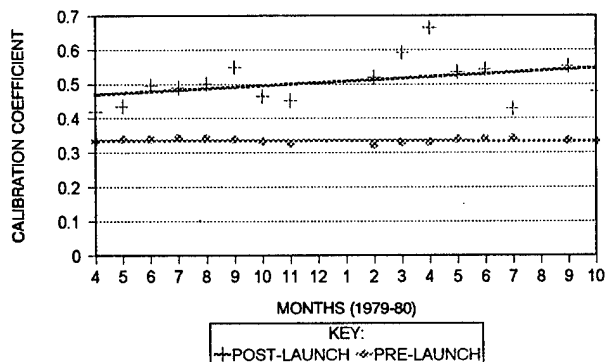
Fig. 2. The calibration coefficients for channel 2 of the AVHRR on-board the TIROS-N, based on model prediction (+) and pre-launch information (•)

REFERENCE

[1] Kaufman, Y. J., and Holben, B. N., "Calibration of the AVHRR Visible and Near - IR bands by atmospheric scattering, ocean glint and desert reflection", International Journal of Remote Sensing, vol. 14, pp. 21 - 52, 1993.

[2] Rao, C. R. N., and Chen, J., "Post-Launch Calibration of the Visible and Near Infrared Channels of the Advanced Very High Resolution Radiometer on NOAA -7, -9, and - 11 Spacecraft", NOAA Technical Report NESDIS 78, p.22, 1994.

[3] Vermote, E. and Kaufman, Y. J., "Absolute calibration of AVHRR visible and near-infrared channels using ocean and cloud views", International Journal of Remote Sensing, vol.16, pp. 2317-2340, 1995.

[4] Kidwell, K. B., "NOAA Polar Orbiter Data Users Guide", U.S. Department Of Commerce, NOAA,1991.

POLARIMETRY IN REMOTE SENSING: Basic and Applied Concepts

Wolfgang-M. Boerner[1], Harold Mott[2] and Ernst Lüneburg[3]

1. University of Illinois at Chicago, UIC-EECS/CSN, M/C 154, 900 W. Taylor St., SELW-4210, Chicago, IL / USA 60607-7018, T&F: +[1](312)996-5480, e-mail: wolfgang.m.boerner@uic.edu
2. University of Alabama, Department of Electrical Engineering, Tuscaloosa, AL / USA 35487-0286. T/F: +[1](205)348-1759/6959, e-mail: hmott@prodigy.net
3. German Aerospace Research Establishment, DLR, Oberpfaffenhofen, Bavaria, D-82230 Wessling, FR Germany, T/F: +[49](8153)28-2343/1135, e-mail: ernst-lueneburg@dlr.de

Abstract: One of the great challenges for modern radar is to classify, sort and identify targets of all kinds for military battlespace surveillance as well as for civilian geo-environmental stress change monitoring purposes. Whereas, in military radar utilization of complete polarization scattering matrix radars is not yet fully accepted, in **Remote Sensing** on the other hand, **Radar Polarimetry** seems to have been accepted as an indispensable tool, and convincing results have ben obtained for geo-environmental applications in agriculture, forestry, hydrology, flood plain and rural infrastructure maintenance, volcanology and seismology, archeology, etc..

However, there still exists a large void in standardization and proper handling of basic and applied polarimetric theory and concepts. In this paper a succinct assessment of the current state-of-the-art is presented summarizing the basic polarimetry concepts spelled out in **Boerner et al. (1997) [1]**. It is the purpose of this paper to draw attention of the **IEEE Geoscience and Remote Sensing community** to this recent compendium on 'Polarimetry in Remote Sensing'.

INTRODUCTION

Polarimetry deals with the vector nature of polarized electromagnetic waves throughout the frequency spectrum from ultra-low frequencies to above the ultraviolet. In regions apart from radiating or reflecting bodies, the electromagnetic field is a **traveling wave** at the velocity of light, with an electric vector field and a magnetic vector field transverse to each other and to the direction of wave travel. Where there are abrupt or gradual changes in the index of refraction (or permittivity, magnetic permeability, and conductivity), the polarization state of a single-frequency wave is transformed, and the wave is **repolarized**. When the wave strikes an object such as a radar target and is reflected, important information about the reflecting body can be obtained from the nature of the reflected wave. The direction of the electric field vector with respect to a transverse reference axis plays a very important role in the interaction between a wave and a target, and much more information about the target can be obtained when the behavior of the transverse electric field is a variable under the control of an operator than can be obtained for fixed electric fields. In nature, polarization effects play a greater role, primarily in the optical regions, than was once believed. Although the human eye has only a rudimentary polarization sense, many crustacians, insects, birds, and especially fish possess a well-developed polarimetric sensory system within the IR to UV spectrum. Some creatures residing in terrestrial surface layers also appear to have a biomagnetic (induction-type) polarimetric snesor that operates in the ULF to VLF (below 3Hz to 30KHz) range.

Radar polarimetry is concerned with control of the polarimetric properties (electric field direction behavior) of radar waves and the extraction of target properties from the behavior of scattered (reflected) waves from a target. It has become an indispensable tool in modern electromagnetic sensor technology, and it is anticipated that within a few years new radars, except those with limited, specific purposes, and scatterometers will have complete polarimetric (scattering matrix) capability. Microwave radars with their ability to penetrate cloud ocover, have already proven to be of enormous value in recent years for environmental monitoring. With the advent of synthetic aperture radar (SAR) the ability now exists to construct high resolution ground maps. The incorporation of coherent polarimetric phase and amplitude into radar signal and image processing promises to bring about further improvements in monitoring capabilities, especially in 'polarimetric doppler radar meteorology' and also in POLarimetric Synthetic Aperture Radar (POL-SAR) image analysis.

WISIP: WIDEBAND (μHz - PHz) INTERFEROMETRIC SENSING AND IMAGING POLARIMETRY

WISIP has become an important, indispensable tool in wide area military battlespace surveillance and global environmental stress change monitoring of the terrestrial and planetary covers. It enables dynamic, real-time optimal feature extraction of significant characteristics of desirable targets and/or target sections with simultaneous suppression of undesirable background clutter and propagation path

speckle at hitherto unknown clarity and never before achieved quality. 'WISIP' may be adopted to the Detection, Recognition and Identification (DRI) of any stationary, moving or vibrating target or distributed scatterer segments versus arbitrary stationary, dynamically changing and/or moving geo-physical/ecological environments, provided the instantaneous 2×2 phasor (Jones/Sinclair) and 4×4 power density (Mueller/Kennaugh) matrices for forward-propagation/backward-scattering, respectively, can be measured with sufficient accuracy. For example, the DRI of stealthy, dynamically moving and/or camouflaged stationary objects occluded deeply into heterogeneous stationary and/or dynamically moving inhomogeneous volumetric scatter environments such as precipitation scatter, the ocean sea/lake surface boundary layers, the littoral coastal surf zones, pack-ice and snow or vegetative canopies, dry sands and soils, etc., can now be successfully realized. A comprehensive overview is presented on how these modern high resolution/precision, complete polarimetric coregistered signature sensing and imaging techniques, complemented by full integration of novel navigational electronic tools, such as DGPS, will advance electromagnetic vector wave sensing and imaging towards the limits of physical realizability. Various examples utilizing most recent image data take sets of the NAWC/ERIM-P3-UWB-TOPIF'E-CATI/LTBL-POLSAR and NASA-JPL-AIRSAR airborne, the NASA/DARA/DASI-SIR-C/X-SAR shuttle, and the ESA ERS-1/2, JERS and RADARSAT satellite imaging systems [2] will be presented for demonstrating the utility of WISIP.

BASIC AND TO ADVANCED THEORY OF OPTICAL - TO - RADAR POLARIMETRY

Great care is taken in separating the **optical forward propagation** (2×2 Jones/4×4 Mueller matrix) **polarimetry** from the **microwave backward scattering** (2×2 Sinclair/4×4 Kennaugh matrix) **radar polarimetry** by developing the following concepts:

Basic Polarimetric Radar Theory: Definition of Polarization State Operators and Polarimetric Matrices
The basic formulation and mathematical representation of polarization vectors and of the set of four distinct scattering matrices, their inter-relations, and their transformations between different polarization bases is considered. Great care is taken in formulating the appropriate transmission (anti-monostatic) versus backscattering (monostatic) coordinate systems for treating the two distinct vector wave medium interaction cases -- in order of complexity -- expressed in terms of a set of four distinct matrices. In each case, these include: (i) the 2×2 complex phasor (coherent) Jones transmission [T] versus Sinclair scattering [S] matrices; (ii)

the associated 2×2 complex coherent power density transmission $[F] = [T]^t[T]$ versus the Graves $[G] = [S]^t[S]$ complex coherent power scattering matrices (with t denoting the Hermitian conjugate); (iii) the 4×4 real power density Mueller [M] propagation versus Kennaugh [K] scattering matrices (of which an optical, but non-identical alternate is the 4×4 Stokes reflection matrix); and (iv) the 3×3 (symmetric: monostatic reciprocal) or 4×4 (asymmetric: general bistatic and/or non-reciprocal) Polarimetric Covariance Transmission [Υ] versus Scattering [Σ] matrices. It is then shown how each set of four unique polarimetric matrices can be strictly related to one another via a matrix tryptic by utilization of the coherence matrix and the SU (2,3,4) Lie and Lorentz transformation groups, where use is made of Cloude's group-theoretic expansion of the covariance matrices for the optical and radar cases, respectively.

Distinct Polarimetric Matrix Optimization Approaches, Huynen Polarization Fork for the Coherent and Partially Coherent Cases, and Target Matrix Decomposition
Although considerable progress was made in advancing the Kennaugh radar target characteristic polarization theory (KRPT) for the determination of the Optimal (characteristic) Polarization States and Huynen's Polarization Fork Concept (HPF) for unique association of these characteristic polarization states on the Poincaré sphere; no fully transparent theory separating the forward scattering (propagation) from the backscattering (monostatic and bistatic) cases and/or its interactive relations was developed until recently. Unfortunately, still today, these distinct wave-scatterer interaction cases are wildly confused in the literature. However, with the recent advances made by Lüneburg in analyzing 'similarity' versus 'consimilarity' eigenvalue/vector problems in radar polarimetry, we are now equipped to resolve the fine points (pitfalls) of the coherent radar transformation phase in the formulation of the proper transformation matrices which differ distinctly for the propagation (similarity) and the backscattering (consimilarity) cases and can be determined uniquely by inclusion of energy conservation principles. Using these two distinct matrix sets and the associated similarity versus consimilarity problems, the resulting five pairs of optimal polarization states (KRPT) are determined together with the complementing set of two Huynen polarization forks (HPFs), where specific reference is made to the recent interactive forward propagation versus backscattering formulation along an idealized lossless, reciprocal polarimetric propagation two-port in terms of generalized transmission/reflection formulation of the 4×4 complex cascading propagation matrices which serves to demonstrate that a clear distinction of the forward propagation (optical: Jones/Mueller) versus back-reflection (radar: Sinclair/Kennaugh) matrix cases must be made in all cases.

APPLICATIONS OF WISIP TECHNOLOGY

The wide ranging applications of WISIP-technology in air/space-borne remote sensing are slowly but steadily being accepted as major, indispensable tools in wide area military battlespace surveillance and local-to-global environmental stress change monitoring. In the complementing papers special attention will be paid to the Detection, Recognition and Identification (DRI) of environmental stress changes of either natural and/or anthropogenic origin such as of: (i) wetland versus flood plain delineation and the stress/pressure build-up along dams, dikes, and levies as well as deformations of the river beds, coastal shorelines and dunes, and surrounding wetlands during major flash flood and storm events; (ii) the DRI of acid rain and acid snow on boreal forests and permafrost tundra environments; (iii) altitudinal height and transverse skewing surface deformations during an entire tectonic stress change episode long before, precisely at, and long after the stress release (earthquake) has occurred; (iv) for sea-quakes, it will include tsunami-mapping and sub-ocean surface ocean-bottom fracture zone delineation; (v) of geo-ecologic stress changes caused by natural and/or anthropogenic secondary/primary source mechanisms; (vi) subtle strategic changes in battlespace scenarios; and/or (vii) the camouflaged construction of hidden bunkers, arms caches and the overnight deployment of minefields, etc.. Various illustrative polarimetric interferometric images, such as applications of most recent **UWB-TOPIF'E-CATI/LTBL-POL-SAR ↔ POL-MTI-TOP-RAR** image data takes will be presented for the purpose of demonstrating the general applicability of the **WISIP** principles introduced in this state-of-the-art-overview.

FUTURE DEVELOPMENTS

In addition to the advances reported here on ultrawideband and multiband polarimetric synthetic aperture radar technology, image processing and analysis in the VHF-to-microwave spectral domain, during the preparation of 'Polarimetry in Remote Sensing' [1], very dramatic changes were made in perfecting space navigational tools such as GPS and precision inertial navigation (INU) systems and merging them into an IGU navigation system. Their merger made possible both spaceborne repeat-orbit and airborne repeat-track, high precision imaging platform operations that give centimeter image overlay accuracies. In addition to single platform cross-and-along-track (CATI) SAR interferometers, such as the JPL AIR/TOP-SAR in the same period satellite (ERS-1/2, JERS-1) and shuttle (SIR-C/X-SAR) LTBL repeat-orbit SAR-image overlay interferometry was conceived and realized. Some of the most impressive applications of high resolution CATI topographic interferometric digital elevation

SAR (JPL-TOPSAR, ERIM-IFSARE, EMI-SAR) imaging have produced high precision digital 3D relief elevation maps approaching cubic-decimeter resolution. These developments will change global cartography to make it freely available on the world-wide web.

Spaceborne repeat-orbit *LTBL (long temporal base line)* image-overlay interferometry has enabled more accurate coregistration of terrestrial surface height deformations caused by tectonic and volcanologic stress changes This has had an impact on earthquake and volcano erruption hazard prediction. With the recent advent of high precision IGU integrated navigation system, airborne repeat-track and satellite and shuttle LTBL image overlay interferometry was realized. In addition, this made possible the delineation of flood plains and changes in riverbeds, as well as ocean-beach and lakeshore deterioration, together with subaquatic sandbank motion as demonstrated for the 1993 Misssouri-Mississippi, the Werra-Fulda and Niederrhein floods. Hurricane and cyclone destruction of estuaries and coastal environments has also been depicted.

As impressive as these CATI and LTBL repeat-track image overlay interferometric imaging results are, they were achieved without complete polarimetric image interferogram optimization. **Interferometric coherence** can be improved substantially by polarimetric speckle reduction. It can also be improved by complete scattering matrix POL-SAR interferometry, crucial for fully realizing all-weather real-time high resolution image overlay interferometric imaging and for advancing this technology to the limits.

In conclusion, the significant achievements of topographic-interferometric and polarimetric SAR to date justify and make desirable the development of more precise systems and the substantial expansion of their use in monitoring natural and cultural features and changes in the planet's surface.

REFERENCES

[1] W-M. Boerner, H. Mott, E. Lüneburg, C. Livingstone, B. Brisco, R. Brown, J.S. Paterson (Authors); S.R. Cloude, E. Krogager, J.S. Lee, D.L. Schuler, J.J. van Zyl, D. Randall and P. Budkewitsch (Contributing Authors), *POLARIMETRY IN REMOTE SENSING - Basic and Applied Concepts*, Chapter 5 (90 p.) in R.A. Reyerson, ed., *The Manual of REMOTE SENSING*, 3rd Edition, ASPRS Publishing, Bethesda, MD, 1997.

[2] H.J. Kramer, *Observation of the Earth and Its Environment: Survey of Missions and Sensors*, 3rd Edition, New York, Springer Verlag, May 1996 (2nd Edition:ISBN:3-540-57858-7/0-387-57858-7,May 1994).

The NASA/JPL Airborne Synthetic Aperture Radar's 1996 PacRim Deployment

Y. Lou, Y. Kim, J. van Zyl, L. Maldonado, T. Miller, E. O'Leary, G. Romero, W. Skotnicki, and V. Taylor

Jet Propulsion Laboratory
California Institute of Technology
4800 Oak Grove Drive, MS 300-243
Pasadena, CA 91109
lou@blacks.jpl.nasa.gov

ABSTRACT

In November and December 1996, the NASA/JPL Airborne Synthetic Aperture Radar system (AIRSAR) embarked on a seven-week campaign to several Pacific Rim countries. This mission was jointly organized by NASA, Australia's Office of Space Science and Application, and University of New South Wales. The major purpose of the mission is to establish a collaborative effort in the area of radar remote sensing application between the United States and the Pacific Rim countries. SAR data were acquired for both U.S. researchers as well as the participating countries. In addition to Hawaii, we imaged areas of interest in New Zealand, Australia, Papua New Guinea, Malaysia, Brunei, the Philippines, Taiwan, Thailand, and Cambodia including coastal regions of some countries. The target areas of this multi-frequency, polarimetric and interferometric SAR system included volcanoes, sites for studies in geology, hydrology, and landuse mapping, and forested mountains to generate height maps of rugged and inaccessible areas.

INTRODUCTION

AIRSAR operates in the fully polarimetric mode at P-, L-, and C-band simultaneously (POLSAR) or in the along-track (ATI) or cross-track interferometric (XTI) mode in L- and C-band simultaneously. The system began collecting data in late 1987 on its first mission aboard a DC-8 aircraft operated by NASA's Ames Research Center in Mountain View, California. Since then, AIRSAR has flown missions every year and acquired images in North, Central, and South America, Europe, Greenland, and Australia. In POLSAR mode, the image products are fully calibrated and are stored in compressed Stokes matrix format that contains all the polarization information. In XTI mode, C-band cross-track interferometer data are used to generate a digital elevation model (DEM) and an incidence angle map. In this case, L-band radar could operate in either cross-track interferometer mode or polarimetric mode whereas P-band radar is always in polarimetric mode. By using the incidence angle map, all output images are geometrically and radiometrically corrected taking the topography into account and resampled to ground range with a 10 m by 10 m pixel spacing. The output images cover 10-12 km in the range direction for the 40 MHz chirp bandwidth mode.

On AIRSAR's 1996 PacRim Deployment, data were collected over the following ten countries: the US, New Zealand, Australia, Papua New Guinea, Malaysia, Brunei, the Philippines, Taiwan, Thailand, and Cambodia as shown Fig. 1. Most of the data were collected in XTI-1 mode, i.e. C-band cross-track interferometer with L- and P-band polarimeter. This mode provides users with a DEM of the imaged site and geometrically corrected L- and P-band polarimetry data. With over 100 sites imaged, investigators will study the following topics: wetlands and peat swamp characterization, mangrove forest mapping, floodplain morphology, archaeology, cultural resource management, crop classification, forest classification, deforestation and regrowth monitoring, biodiversity, soil moisture estimation, carbon dynamics of indigenous rainforests, geologic mapping, DEM generation, volcanic hazards, mining exploration, coastline monitoring, mountain road planning and rehabilitation, and differential penetration of vegetation canopies.

In addition to AIRSAR, three other science instruments were also on-board the DC-8 aircraft. These were TIMS (Thermal Infrared Mapper), AES (Airborne Emission Spectrometer), and Cloud Radar (in Hawaii and New Zealand only). The main objective of TIMS was to image volcanoes and selected geologic sites in Australia. AES provides temperature and humidity profiles for the TIMS imaging of SO_2 concentrations in volcanic gas plumes. AES also monitored gas ratios such as $HCL:SO_2$.

In this paper, we will briefly describe the sites imaged in each country and their respective science objectives. In addition, we will outline our plan for data processing and data analysis.

HAWAII

Sites on three of the Hawaiian Islands were imaged, Oahu, Hawaii, and Maui. The Oahu site located on the summit of the Koolau Mountains was imaged to study differential radar penetration (C-/L-band) through distinct vegetation density

gradients. On the island of Hawaii, the Mauna Kea and Mauna Loa volcanoes were imaged to generate detailed digital elevation models of the summit regions. Two transects, one along the north shore of Hawaii and the other from Kohala Volcano in the northwest to the saddle between Mauna Loa and Mauna Kea, were imaged to study erosion patterns on the windward and leeward sides of the island. In addition, the rainforest on the flanks of Kilauea was imaged to study differential radar penetration along the vegetation gradient. Furthermore, the Kohala Ocean off the northwestern tip of the island of Hawaii was imaged in ATI mode to assist in the development of an ATI processor that will measure the radial component of the ocean current. Finally, we had an opportunity to image Haleakala volcano on the island of Maui on our way back from the PacRim deployment.

NEW ZEALAND

The New Zealand sites were coordinated through Landcare Research of New Zealand. The sites imaged included White Island, several sites on the North Island, Taupo, Ruapehu, Wanganui, Wairarapa, and Baring Head and a portion of the Southern Alps on the South Island.

White Island is a 3 km x 3 km active volcanic island located off the northern shore of the North Island. The objective is to generate a DEM for monitoring the ongoing deformation of the island. Ruapehu is the largest and highest volcano in New Zealand where steam explosions cause hot water to spill over the flanks of the crater lake. Both TIMS and AES data were taken in addition to AIRSAR data. Taupo is an indigenous rainforest and was imaged to study the forest composition and biomass. Wanganui was imaged to evaluate the use of SAR data for landslide detection and vegetation mapping. Wairarapa is an area of active deformation where the growing folds will be examined in three-dimensions. The area contains extensive terraces that act as markers in determining the deformation rates. Finally, the Southern Alps includes a portion of the Alpine fault system, a very active strike-slip fault similar to the San Andreas fault in California. The results from this study will be compared to a study site in the San Gabriel Mountains north of Los Angeles.

AUSTRALIA

AIRSAR spent two weeks in Australia mapping sites in all six provinces in mainland Australia. These sites were selected by Australian scientists and mining companies, and NASA scientists. Sites in Eastern and Southeastern Australia included Condamine, Goulburn, and Tarrawara, which were imaged to generate soil moisture maps. Mt. Fitton is an international radar calibration site rich in minerals and geologic features such as alluvial fans and sand dunes. Lake

Acraman was imaged to study an ancient meteor impact crater whereas Cooper Creek was imaged to study the history of seasonal river channels in this desert region. In addition, a 500 km long transect was imaged over the Cunnamulla region just west of Brisbane to provide a valuable verification data set for the upcoming Shuttle Radar Topography Mapping (SRTM) mission.

In Northeastern Australia, Gilbert Range was imaged for hydrological studies and Lawn Hill was imaged to study a meteor impact crater. Weipa was a site selected for SRTM calibration. Queensland, also imaged in the 1993 AIRSAR Australian campaign, was mapped for a repeat-pass P-band interferometry study.

Central Australia is rich with geologic sites where a number of meteor impact craters were imaged and they included Mt. Toondina, Henbury, Glickson, Connolly, Wolf Creek, Strangways, and Liverpool. In addition, a number of geologic sites were imaged for the mining companies. In the Northern Territory, several mangroves and coastal wetlands were imaged and they included Endyalgout Island, Pt. Farewell, Munmarlary, Mary River, Gunn Point, Humpty Doo, and Daly River. In addition, we also imaged Darwin Harbour for research in coastal ship watch.

PAPUA NEW GUINEA (PNG)

AIRSAR's flight over PNG was flown out of Townsville, Australia. Eight sites were imaged in which three were mining sites. The remaining sites included Manam Island, an active volcanic island which had a violent Strombolian eruption a few days after AIRSAR's overflight. Fly River was imaged for tropical wetland mapping and Lakekamu Basin, a Conservation International site, was imaged to map the topography and ecology of the tropical rainforest. In addition, Huon Peninsula and Ramu-Markham were imaged to study soil erosion, landslide, and landuse mapping.

MALAYSIA

Sites in Malaysia were selected by the Malaysian Center for Remote Sensing (MACRES) and included sites in Sarawak, Sabah, and the Malay Peninsula. The two sites in Sarawak were for landuse mapping of coastal area and mountainous region respectively, whereas Kota Kinabalu in Sabah, the tallest mountain in Southeast Asia, was imaged for land classification and coastal mapping. On the Malay Peninsula, Tioman Island on the east coast was imaged for landuse mapping of mangrove. In addition, Cameron Highland was imaged several times for landuse mapping as well as geologic studies. Muda Merbok was imaged to study landuse and rice crop whereas Terengganu was imaged for coastal zone management studies.

BRUNEI

AIRSAR mapped much of coastal Brunei in six passes and the main objective is to use AIRSAR data to update maps. In addition, the data will provide the Survey Department with their first experience with SAR data for potential applications such as landuse mapping.

PHILIPPINES

The sites in the Philippines were organized by various agencies in the Philippines and coordinated by the National Mapping Agency (NAMRIA) and the Department of Science and Technology (DSTO). They included four volcanoes, ecology sites, and geology sites. The active volcanoes imaged were Taal, Mt. Pinatubo, Mayon, and Kanlaon. In addition, Visayas, a mining site, was imaged for topographic studies of a very rugged mountainous area. Coastal Panay was imaged for landuse mapping as well as soil moisture studies. Los Banos is a rice research site whereas Magat Watershed is a vegetation classification site. Finally, we also imaged Manila and Cebu for urban mapping.

TAIWAN

The Taiwan sites were organized by the Center for Space and Remote Sensing Research Center of National Central University in Chung Li. Two large study sites were selected for land cover and coastal zone mapping using both XTI and POLSAR modes. In addition, two transects were imaged for SRTM verification. One of these transects crossed the tip of the Oluan Peninsula in southern Taiwan whereas the other transect crossed central Taiwan.

THAILAND

Thailand's participation was organized through the Thailand National Research Council (NRCT) and 13 study sites were imaged. They included land cover mapping of Uthaithani, a wildlife sanctuary, and Ranong, a coastal mangrove forest reserve area and rubber plantation. In addition, AIRSAR imaged Lampang, a mining geology site, and Chanthaburi for land use classification. Nakhon Si Thammarat and Songkhla were imaged for wetlands studies whereas Prachuap Khiri Khan was imaged for coastline monitoring. A number of archaeology sites were imaged in northeast Thailand and Cambodia including the famous Angkor Wat in Cambodia. These data will assist the Fine Arts Department of Thailand as well as participants from the World Monuments Fund in cultural resource management and research. Finally, Chiang Mai and Surat Thani were imaged for forestry mapping and classification.

FUTURE PLAN

All the PacRim data have been survey processed and initial evaluation of data quality looks good. We have begun precision processing based on user requests. With just over 100 sites imaged, it could take two to three years to process all the sites. Data collected for agencies and companies in these countries are under a one year proprietary period from the date of precision data processing. In addition, we had the first PacRim Workshop in Pasadena in March, 1997 and began the process of forming research teams by discipline. It is our hope that by teaming up inexperienced SAR users with experienced AIRSAR scientists, this will shorten the learning curve for the former and enable all of us to better utilize the rich data set we collected during the PacRim Deployment. Future PacRim Workshops will be held annually at different participating countries to report exciting research findings and exchange ideas. For more information and updates, please consult AIRSAR's home page at: http//airsar.jpl.nasa.gov.

Location of AIRSAR Flight Lines Collected During Pacific Rim Deployment (Nov.-Dec. 1996)
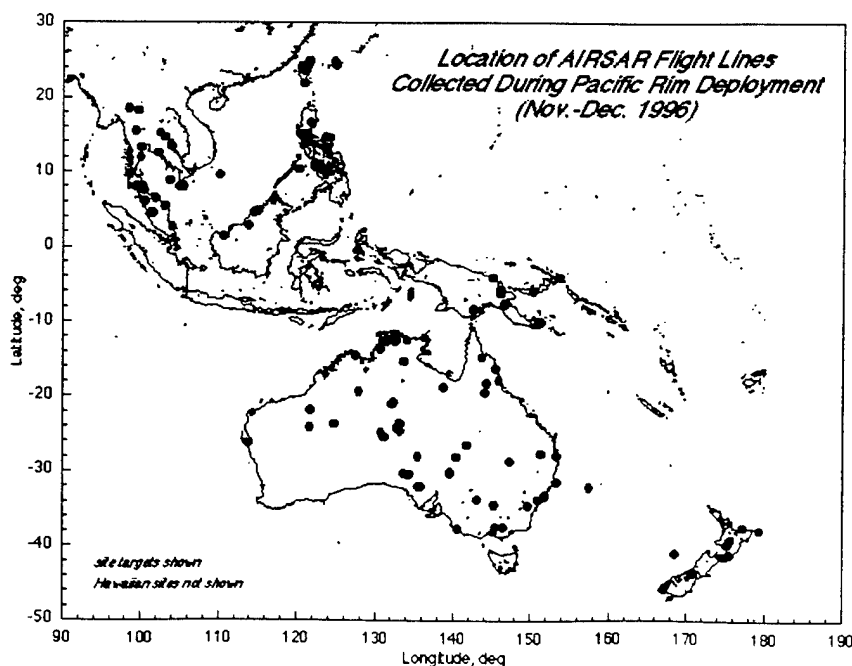
Littoral Remote Sensing Using Polarimetric SAR

J.S. Lee , D.L. Schuler, T.L. Ainsworth and L.J. Du
Remote Sensing Division, Code 7263, Naval Research Laboratory
Washington DC 20375-5351,USA   Tel: (202) 767-2004, Fax: (202) 767-5599
Email: lee@imsy1.nrl.navy.mil

Abstract - Polarimetric SAR has been successfully applied for, terrain and land-use classification, soil moisture and biomass measurements, and many other areas of remote sensing. However, its application to ocean and coastal areas has not been developed. This paper describes several remote-sensing applications for the littoral zone using polarimetric SAR. SIR-C L- and C-band and JPL AIRSAR images are used for illustration.

INTRODUCTION

The polarimetric scattering behavior of a target can be described by a 2x2 complex scattering matrix, S, which relates the incident and scattered electric fields according to

$$\begin{bmatrix} E_h^s \\ E_v^s \end{bmatrix} = \frac{e^{-ik_0 r}}{k_0 r} \begin{bmatrix} S_{hh} & S_{hv} \\ S_{vh} & S_{vv} \end{bmatrix} \begin{bmatrix} E_h^i \\ E_v^i \end{bmatrix} \qquad (1)$$

where the subscripts, h and v, represent horizontal and vertical polarization components, respectively [8]. The superscripts of E, s and i, indicate scattered and incident fields. The E_h^i term denotes the incident complex amplitude of the field component at horizontal polarization, and S_{hv} denotes the horizontal transmitted and vertical received component of the scattering matrix, S. The parameter, k_0, is the wavenumber of the radar, and r is a distance from the target. Polarimetric radar measures the complete scattering matrix, and from the scattering matrix, any combination of transmitted and received polarization can be synthesized by

$$P_{rec} = K \begin{bmatrix} E_h^r & E_v^r \end{bmatrix} \begin{bmatrix} S_{hh} & S_{hv} \\ S_{vh} & S_{vv} \end{bmatrix} \begin{bmatrix} E_h^t \\ E_v^t \end{bmatrix} \qquad (2)$$

In coastal remote sensing, many distinctive scattering mechanisms can be revealed by polarization signatures (van Zyl, 1987) using (2). Polarization synthesis can also be utilized to optimize the target to background ratios. In addition, the target decomposition theorys of Krogager[3], Cloude[4] and Wong[5] are valuable in classification and detection of targets and ocean surface features.   SIR-C, L- and polarimetric SAR images are used for illustration.

CROSS-POLARIZATION RESPONSE

It has been pointed out that cross-polarization HV or VH radar returns are generated by azimuthal asymmetry within the SAR resolution cell. For azimuthal symmetrical media such as, ocean surface, double bounce reflectors, and horizontal or vertical conductors, the scattering matrix can be represented by

$$\begin{bmatrix} a & 0 \\ 0 & b \end{bmatrix} \qquad (3)$$

where a and b are real. Without losing generality, we set the parameter a to be positive. For idealized Bragg scattering, b>a; for dihedral reflector, b= -a; for horizontal conductors, b=0; for vertical conductors, a=0; and for forests on level ground, it can be modeled by a>|b| and b is negative.

Using (2), if we rotate the antenna H-V base vector by an angle δ, the scattering matrix is transformed into

$$S^{(new)} = \begin{bmatrix} \cos(\delta) & -\sin(\delta) \\ \sin(\delta) & \cos(\delta) \end{bmatrix} \begin{bmatrix} a & 0 \\ 0 & b \end{bmatrix} \begin{bmatrix} \cos(\delta) & \sin(\delta) \\ -\sin(\delta) & \cos(\delta) \end{bmatrix} \qquad (4)$$

or

$$S^{(new)} = \begin{bmatrix} a\cos^2(\delta) + b\sin^2(\delta) & (a-b)\cos(\delta)\sin(\delta) \\ (a-b)\cos(\delta)\sin(\delta) & a\sin^2(\delta) + b\cos^2(\delta) \end{bmatrix}$$
$$= \begin{bmatrix} S_{hh}^{(new)} & S_{hv}^{(new)} \\ S_{vh}^{(new)} & S_{vv}^{(new)} \end{bmatrix} \qquad (5)$$

The above equation indicates that HV returns are induced by the rotation. The rotation of the antenna has the same effect as surface or object tilting in the azimuth direction. For desert or grassland characterized by Bragg scattering, higher HV returns are induced by the surface in the azimuthal direction. For dihedral reflectors (b= -a), HV returns are increasing with the tilt, while HH and VV returns are decreasing, and are equal to zero at δ = 45°. For coastal remote sensing, many features display strong cross-polarization signal-to-background ratios.

1) Coastline Detection

Coastlines are difficult to define accurately using single VV or HH polarization SAR, because the wind modulated coastal water frequently creates higher returns than flat beaches and adjacent inland areas[1]. The surface tilt and vegetation on the beaches induces higher HV returns than from ocean waves. Fig. 1 shows an L-band SIR-C image of Malaysia. The coastline can be easily detected by a simple thresholding using HV polarization. It would be much more difficult to detect it using HH or VV images

2) Coastal Feature Detection

Also shown in Fig. 1, the bridge, the pier and ships have higher signal to background ratios in the HV image (Fig. 1(b)) than in the HH or VV images (refer to Fig. 1(a) and
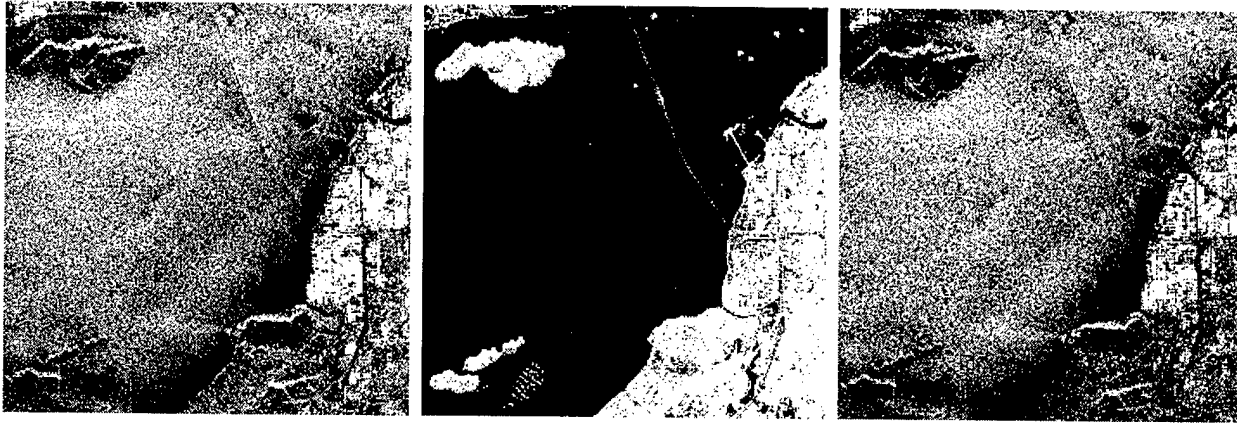
(a) HH amplitude image   (b) HV amplitude image   (c) VV amplitude image

Fig. 1 SIR - C L - band HH, HV and VV images of Malaysia are shown. Coastline and coastal features, such as the bridge and the pier can be easily detected using HV image, however, ocean waves, shipwakes and wind shadows are better defined in HH nad VV images.

1(c)). Also, the fishing activity shown as a cluster of white spots in the lower left of the HV image has a contrast reversal in HH and VV images. Features that are dominated by Bragg scattering, such as oceanwaves, shipwakes and wind shadows, are better discerned with HH and VV.

POLARIZATION SIGNATURES (PolSig)

Coastal features often display distinctive PolSig (van Zyl, 1987). The fishing activity shown as a cluster of white spots in Fig. 1(b) has co-pol signatures given in Fig. 2(a) and (b). Most pixels of this cluster have these kind of signatures with peaks displaced away from HH or VV. This displacement could be caused by surface tilt in a target with Bragg scattering. It can also be formed by objects tilted near 45 degrees. A small amount of helix related scatterings is also present. Helix scattering is measured by the difference between RR (right circular transmit and right circular receive) and LL. The close by ocean area show typical Bragg signatures with the peak located at VV, and helix scattering (see Fig. 2(c)). This SIR-C data has been calibrated, and PolSigs are computed on pixels from a 2x2 average of 4-look processed data.

AZIMUTHAL SLOPE MEASUREMENT

We have shown that surface tilts induce HV polarization. Theoretically, surface tilt can be obtained from the scattering matrix. From (5), we can solve for δ,

$$\delta = \frac{1}{2}\tan^{-1}\left[\frac{2S_{vh}^{(new)}}{S_{hh}^{(new)} - S_{vv}^{(new)}}\right]$$

The above equation reveals that surface tilt, δ, increases with $S_{hv}^{(new)}$, but decreases with $(S_{hh}^{(new)} - S_{vv}^{(new)})$. The sign of the term in the parenthesis of the above equation is determined by the direction of the tilted surface. This equation indicates that polarimetric SAR could also be used to measure surface slope in the azimuthal direction. Schuler, Lee and De Grandi [2] have utilized this to develop a technique of topography measurement. Since the scattering matrix, in reality, is complex, the above equation is difficult to apply. It was found that the displacement of the peak in PolSig corresponds to the surface tilt. A steepest ascent algorithm was derived to efficiently locate the maximum in
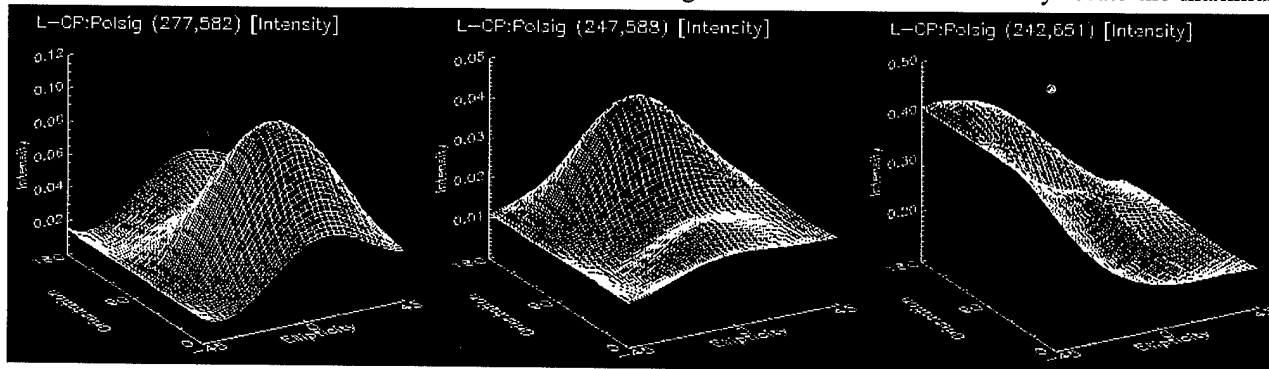
(a) The peak shifts towardr 45°   (b) The peak shifts toward 135°   (c) Helical scattering

Fig. 2 Some peculiar polarization signatures of coastal features. (a) and (b) reveals the Polsig for the fishing activity as shown as a cluster of white spots in Fig. 1(b). Many pixels in the nearby islands shows helicity in signatures.

1408

(a) SAR image of Italy coast (b) Polarimetric SAR derived topography
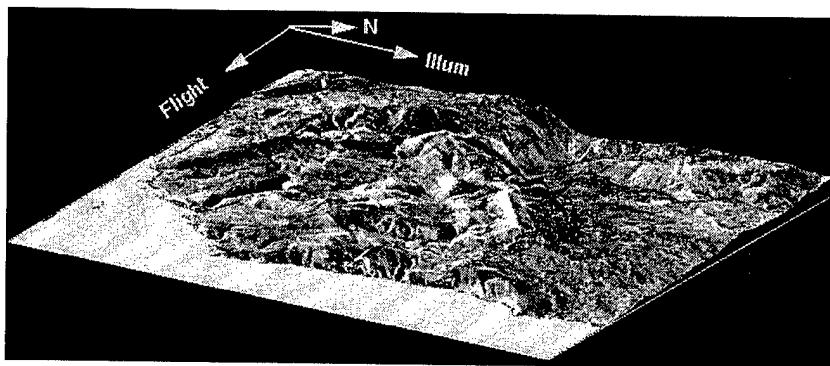
Fig. 3 Using SIR - C L - band polarimetric SAR data of the coast of Italy near Camerota (see (a)), topography are derived by integration azimuthal slopes from the coast upward as shown in (b).

co-pol signatures. For areas with Bragg scattering, the azimuth slope is the displacement from the orientation angle of 90° (VV). For forest areas, the displacement from 0° or 180° corresponds to the slope. To derive topography, tie points along a range line are required for starting integration in the azimuth direction. Alternatively, if orthogonal pass data are available, only a single tie point is needed. For coastal applications, however, topography can be obtained by integration from the coast upward without a priori tie point information on the land.

Fig. 3(a) shows an L-band SIR-C image of Italy coast. The polarimetric SAR derived topography is shown in Fig. 3(b). Currently, this technique is not as accuracy as that from interferometry SAR. Further improvement requires pre-classification of the scattering mechanism of each pixel, and compensation for local incidence angle variations.

This azimuth slope technique was also applied to the ocean surface to detect ocean features with large surface tilts and current fronts (Lee, IGARSS'96).

POLARIMETRIC TARGET DECOMPOSITION

One of the advantages of polarimetric SAR is its ability in

revealing the inherent scattering mechanism of a medium. This unique capability can be utilized for better characterization and classification of targets and terrain types. Coastal features, such as, atolls, tropical rain cells, oil slicks, current fronts, and other atmospherically-induced ocean surface features have many distinctive scattering mechanisms, that include, dipole, Bragg, double bounce, sphere and helix. Recent target decomposition methods by Krogager[3] and Cloude[4] can be utilized to classify terrain and coastal features based on their scattering mechanisms.

Fig. 4 shows an example of Krogager's decomposition. The polarimetric SAR image of Fig. 1 is decomposed into diplane, surface and hecility scatterers. Using circular polarizations, Krogager has shown that Max(RR, LL) represents diplane (i.e., even bounce) scattering, Abs(RR-LL) for helicity, and RL for surface scattering. The city blocks and ships are dominated by corner reflectors, and they are bright as shown in Fig. 4(a). The ocean surface consists mainly of surface scattering and shown with higher returns in Fig. 4(b). Helicity is mainly induced by defused scattering from vegetation as shown in Fig. 4(c).

In Cloude's decomposition, he proposed a quantity named Entropy as a measure of randomness in the scattering

(a) Diplane scattering image (b) Surface scattering image (c) Helix scattering image

Fig. 4 Krogager's decomposition of the Malaysia SIR - C image of Fig. 1. Using circular polarization, the polarimetric image is decomposed into (a) diplane, (b) surface, and (c) helix scatterings

1409

(a) Entropy image   (b) Alpha angle image   (c) HH and VV correlation

Fig. 5 Cloude's target decomposition and its relation to the HH and VV correlation coefficient. Entropy is an indicator of randomness in scattering mechanisms as shown in (a), and the alpha angle as shown in (b) varys from surface scattering in dark, dipole scattering in gray, and dihedral in white. The HH and VV correlation coefficient is also a good measurement of the randomness in scattering mechanisms with ocean areas with high correlation of 0.97 to city areas near 0.4.

characteristics, and an α angle to reveal the dominant scattering mechanism ranging from 0 for surface scattering, $\pi/4$ for dipole scattering and $\pi/2$ for dihedral scattering. Fig. 5(a) shows the entropy image. Ocean surfaces are dominated by the surface scattering with lower entropy. Land, ships and bridges have complex scatterings with higher entropy values. The alpha angle image shown in Fig. 5(b) clearly indicates the surface, dipole and dihedral scatterings.

These decomposition methods can be incorporated into statistical classification algorithms to improve unsupervised terrain and target classification.

STATISTICAL CORRELATION

The statistical correlation between channels, especially, HH and VV reveals additional information for target characterization. The complex correlation coefficient is defined as

$$\rho_c = \frac{E[y_1 y_2^*]}{\sqrt{E[|y_1|^2]E[|y_2|^2]}} = \rho\, e^{i\psi}$$

where ψ is the phase. The magnitude ρ indicates the coherence of HH and VV, and ψ can be used to discern between surface scattering and dihedral scattering. The correlation coefficient is evaluated in a 5x5 moving window. The results applied to the Malaysia SIR-C image are shown in Fig. 5(c). The striking similarity between the correlation image and the Entropy image (Fig. 5(a)) with contrast reversal are clearly shown. In other coastal applications, such as, rain cells and atmospherically induced ocean surface features, low correlation between HH and VV has been observed indicating turbulence on the surface.

CONCLUSION

We have shown that polarimetric SAR is a powerful sensor for sensor for coastal remote sensing. Using synthesis, target decomposition, and statistical correlation, polarimetric SAR provides high target and terrain discrimination and classification and topography capability.

REFERENCES

[1] J.S. Lee and I. Jurkevich, "Coastline Detection and Tracing in SAR Images," IEEE TGARS, Vol. 28, No.4, 662-668, July 1990.

[2] D.L. Schuler, J.S. Lee and G. De Grandi, "Measurement of Topography Using Polarimetric SAR Images," IEEE TGRAS, Vol. 34, No. 5, September 1996.

[3] E. Krogager and W.M. Boerner, "On the Importance of Utilizing Polarimetric Information in Radar Imaging and Classification," AGARD Conference Proceedings, 582, vol.17, 1-13, April 1996.

[4] S.R. Cloude and E. Pottier, "A Review of Target Decomposition Theorems in Radar Polarimetry," IEEE Transactions on Geoscience and Remote Sensing, vol.34, no.2, 498-518, March 1996.

[5] Y. Wang and F.W. Davis, "Decomposition of Polarimetric Synthetic Aperture Radar Backscatter from Upland and flooded forests," Int. J. Remote Sensing, vol. 18, no. 6, 1319-1332, 1997.

Classification using Polarimetric and Interferometric SAR-Data

M. Hellmann S. R. Cloude and K. P. Papathanassiou

DLR, Deutsche Forschungsanstalt für Luft- und Raumfahrt e.V.,
D-82230 Oberpfaffenhofen, Germany. Tel/Fax: (49)8153-28-2367/28-1135
Email: Martin.Hellmann@dlr.de

Abstract – The investigation presented in this paper demonstrate a first order approach to an automatic classification and extraction of cartographic relevant features from SAR data. We propose a fusion of polarimetric and interferometric classification techniques that is able to solve several classification ambiguities which are not resolvable with one method alone and is also able to improve significantly the accuracy of the classification results. The complimentarity of the polarimetric and interferometric coherence based classification approaches and the improvements resulting from their combination are demonstrated using data from the space-shuttle-borne SIR-C/X-SAR radar system.

INTRODUCTION

The extraction of terrain information from SAR data has been a promising area of research for many years. Several algorithms have been developed for the classification of land features from SAR data [1] – [3]. In order to achieve reliable results, multi-parameter meassurements are generally necessary. Multitemporal, multifrequency and multipolarization data have been suggested for remote sensing applications. Recently, radar interferometry gives a new oportunity for the interpretation and classification of different natural surfaces. In this paper we consider the use of a combination of polarimetric and interferometric classification algorithms. Each of these techniques provides a variety of advantages but also some disadvantages. In this paper we demonstrate a fusion of these two techniques in order to improve the classification accuracy and avoid the drawbacks each technique shows if applied alone. In the first two sections we will introduce the polarimetric and intererometric classification algorithms. In the last section we demonstrate the fusion of both methods.

DATA DESCRIPTION

For the presented investigations we use data aquired during the 2nd SIR-C/X-SAR mission of the test site Oberpfaffenhofen, Germany. The interferometric data sets (C– and L–band) were aquired on October 9th and 10th, 1994 (data takes 129.30 and 142.12) and were processed by NASA/JPL in Pasadena, the full polarimetric data sets (C– and L–band) were aquired on November, 2nd 1994 (data take 30.00) and processed by DLR/D-PAF in Oberpfaffenhofen, Germany.

POLARIMETRIC CLASSIFICATION

For the polarimetric classification we use a entropy based classification scheme proposed by Cloude and Pottier in [1]. It is a statistical model which sets out with the assumtion of the existance of one dominant "average" scattering mechanism in each resolurtion cell. Two important parameters arise from this model:

1. The entropy H - as a degree of disorder of the polarimetric backscattered signal - defined in the Neumann sense from the logarithmic sum of eigenvalues λ_j of the coherency matrix [5] as

$$H = \sum_{i=1}^{n} -P_i \cdot \log_n P_i \qquad P_i = \frac{\lambda_i}{\sum_{j=1}^{n} \lambda_j}$$

H ranges from 0 for totaly polarized to 1 for fully depolarized (noise) backscattering.

2. The α-angle which is defined as the propability-weighted sum of the phase-angle α_i of the maximum element of each eigenvector of the coherence matrix [1]:

$$\bar{\alpha} = \alpha_1 P_1 + \alpha_2 P_2 + \alpha_3 P_3$$

α is related to the dominant scattering mechanism, being zero for surface scatter and $\pi/2$ for dihedral-like scattering mechanisms [1].

Figure 1: Polarimetric classification

Figure 2: C–band coherence classification

With these two parameters we can form a 2-dimensional classification space. The number of distinguishable classes is strongly dependent on the entropy H. If H equals zero we have a deterministic measurement of the scattering matrix with zero uncertainty in the elements and therefore we may, in theory, extract an infinite number of classes. On the other side when H equals 1 we can only talk about one class (random noise) which will require higher order statistics for classification. Polarimetric data is very sensitive to the differences between high and low vegetation. For forest as well as for low vegetation the entropy has a medium value because of both classes provide a high randomness of scattering. The discrimination between both classes can be made by the α angle. For low vegetation the dominant scattering mechanism in L–band is surface scattering leeding to an low value for the α angle while in forested area the dihedral component is dominant resulting in a high value for the α angle. The classification is shown in Fig. 1. The difference between forested areas (dark), medium (grey) and low (white) vegetation is clearly visible.

INTERFEROMETIC CLASSIFICATION

The SIR-C/X-SAR Sensor operated on L–, C– and, X–band providing radar data suitable for multifrequency SAR Interferometry (INSAR). With repeat-pass interferometry one is able to measure the amount of temporal decorrelation. The sensitivity of the coherence to changes in the characteris-

tics of the scattering mechanisms in time can be used for the detection of a wide variety of surface processes and therefore for the classification of different surface types. As shown in [2] a single band coherence map is not sufficient for an exact classification due to ambiguities of different surfaces. It turns out that the interferometric coherence maps allow a good classification of water and man-made structures like buildings (high coherence in both bands) and the runway of the Oberpfaffenhofen airfield(low coherence in L-band and medium coherence in C-band) while some ambiguities, especially in the discimination between low vegetation and forested areas, remain. Therefore additional information(.e.g. multifrequency and/or polarimetry innformation) is required. Fig. 2. shows the classification derived from the L–band interferometric classification. The buildings (white), water (dark grey), the runway (pale grey) are clearly distiguisable, while in the vegetated areas a lot of ambiguities remain.

FUSION AND EXPERIMENTAL RESULTS

The important features for map classification are buildings, water, forest, low and medium vegetation. Neither the interferometric nor the polarimetric classification alone allows an exact classification of all classes. Therefore we use the C- and L–band coherence maps in combination with the polarimetric classification to seperate the classes from each other. Considering the demand for automatic and unsupervised classification the polari-

metric method provides the advantage that the results are corelated to the physical behaviour of the scatterer. Therefore it is possible to classify without prior groundtruth knowledge which is a basical condition for unsupervised and automatic classification. On the other hand the interferometric data provide a much higher sensitivity to different terrain types and due to this a better classification accuracy. The combination of both methods leeds to classification with good accuracy which is suiteable for unsupervised and automatic applications.

The fusion of both methods led to the following classification:

- buildings: High coherence in C–band (≥ 0.65) and L–Band (≥ 0.8)

- water: low coherence (below 0.15) in C– and L–band

- forest: Low coherence (below 0.2) in C–band and medium coherence in L–band (0.5 – 0.65) and medium (0.4 – 0.75) entropy and a high α ($\geq 65°$)

- low vegetation: Low coherence (0.15-0.4) in C–band and higher coherence in L–band (0.55-0.7) and medium (0.4 - 0.75) entropy and a small or medium α ($\leq 65°$)

- medium vegetation : High coherence in C–band (≥ 0.6) and L–band (≥ 0.75) and low entropy (≤ 0.2)

- runway: low coherence in L–band (≤ 0.2) and medium coherence in L–band (0.2 – 0.45)

The result of this classification is shown in Fig. ??. (runway: black, water: dark grey, forest: grey, buildings: bright grey, low vegetation: pale grey, medium vegetation: white)

CONCLUSIONS

Our aim was to develop an unsupervised method for classification of SAR-data suitable for automatic applications. The fusion of polarimetric and interferometric classification is a first approach towards this aim. As shown above it is possible to classify the five map relevant features with suficient accuracy. The main advantage of the combination of different algorithms is that due to the strong correlation between the polarimetric results and the physical reality this method is suitable for unsupervised and automatific classification and with the additional interferometric information a good resolution can be acheived an remaining ambiguities can be resolved.
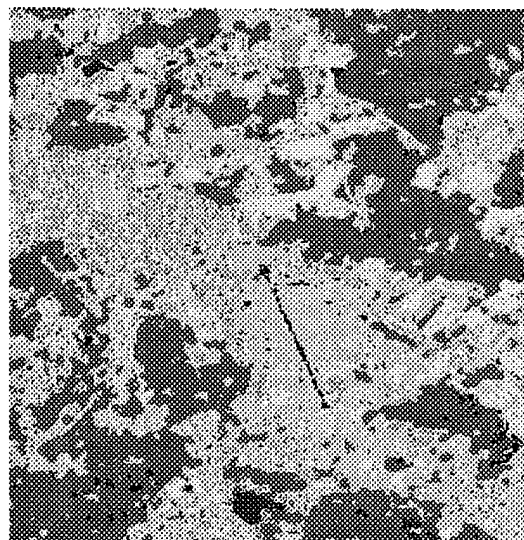
Figure 3: Result of the combined classification

REFERENCES

[1] S.R. Cloude and E. Pottier, " An Entropy Based Classification scheme for Land Applications of Polarimetric SAR", IEEE Trans. Geoscience and Remote Sensing, vol. 35, no. 1, January, 1997

[2] K.P. Papathanassiou, A. Reigber and M. Cotelli, "On the Interferometric Coherence: A Multifrequency and Multitemporal Analysis", ESA Proceedings of Fringe'96, Zurich, Switzerland, October 1996.

[3] J.A. Kong, S.H. Yueh, R.T. Shin and J.J. van Zyl, "Classification of earth terrain using polarimetric synthetic aperture radar images", PIER, J.A. Kong, Ed. New York: Elsevier, vol. 3, ch. 6 1990

[4] A. Freeman and S. Durden, " A three component scattering model to describe polarimetric SAR data", SPIE , Radar Polarimetry , vol. 1748, pp.213-225, 1992

[5] E. Pottier, "On full polarimetric target decomposition theorems with application to classification and identification of real target cross section", in Proc. Int. Rad. Conf., Paris, France, pp.330-335. May 1994,

[6] S.R. Cloude and E. Pottier,"Concept of polarization entropy in optical scattering", Optical Engineering, vol34, no. 6, pp. 1599 - 1610, june 1995

Texture and Speckle Statistics in Polarimetric SAR Synthesized Images

G.F. De Grandi (1), J.S. Lee (2), D.L. Schuler (2),
(1) European Commission Joint Research Centre - Space Applications Institute
Monitoring Tropical Vegetation 21020 Ispra (VA) Italy
Tel.: +39 332 789823 Fax: +39 332 789073 Email: gianfranco.degrandi@jrc.it
(2) Remote Sensing Division, Code 7263, Naval Research Laboratory, Washington DC 20375-5351, USA
Tel.: (202) 767-2004, Fax: (202) 767-5599, Email: schuler@imsy1.nrl.navy.mil, lee@imsy1.nrl.navy.mil

ABSTRACT

A study on the texture and speckle statistics in polarimetric SAR synthesized images was carried out by the authors and presented in preliminary form at the IGARSS'95 Symposium. In this paper some results, which have been recently consolidated, are summarized. We introduce at first a formalism to measure from experimental SAR data and represent graphically and in concise form the dependency of the statistical properties of the image on the polarization state. In particular we focus our attention on the one point statistics and on the second order normalized moment dependency on the polarization state. This is an extension of the classical polarimetric signature, and in the case of the second order moment is called the polarimetric texture signature. Application of this formalism to a data set acquired by the NASA JPL AIRSAR polarimetric radar over the Le Landes forest reveals some distinct and interesting trends in the texture signatures. Theoretical explanation of the phenomenon starts from the consideration of the influence of the synthesis operation, seen as a linear transformation of random variables, on the probability distribution function of the radar signal. A first mechanism that underpins the second moment variation with polarization is defined; this effect arises when multi-look polarimetric data are derived in the space domain from correlated single look data, and is entirely due to the fading statistics. A second mechanism is postulated to account for the observed texture signatures, which is due to the polarimetric diversity of the underlying radar reflectivity. This asymmetry in the response of the scatterer to the polarized wave can be best modelled using a so called polarimetric mixture approach, whereby polarimetrically different scattering mechanisms are combined for each resolution cell. A Monte Carlo simulation approach is used to reconstruct the observed signatures, starting from the assumption of simple physical situations, which can be realizable in scattering processes from natural targets. An example is presented, related to a mixture of deterministic point targets and a vegetation clutter. An interesting consequence from the application point of view is that the polarimetric texture signature is found to be a discriminator of weak targets against a clutter, when only polarimetric diversity and not radiometric diversity plays a role.

INTRODUCTION

A study on the texture and speckle statistics in polarimetric SAR synthesized images was carried out by the authors [1][2]. Topic of this research is the characterization of the statistical properties of polarimetric SAR images, when the power signal is represented in a vector basis, which is different from the one (usually H, V) used for the backscattered electric fields measured by the radar instrument. This transformation is called polarimetric power synthesis. We are in particular interested in investigating statistical properties related to texture. Indeed the central theme is: are the textural properties of a SAR image affected by the vector basis used to represent the observations? Intuitively if the backscattered wave sees different geometrical or dielectric properties of the target according to the wave polarization, and if those properties are spatially modulated then also the image texture should be a function of polarization. Our study tries to give an answer to this intuitive assumption, both from the experimental and the theoretical point of view.

While a full account of the study is given in [2], we want to summarize in this communication some theoretical results, which in our opinion are of general interest in polarimetric remote sensing, and to highlight some examples where the polarimetric texture signature can be linked to the underlying scattering mechanisms in the SAR scene and therefore be of interest for thematic applications.

POLARIMETRIC TEXTURE SIGNATURE

The expected value of the backscattered power in the co-pol and cross-pol configuration can be computed as a function of the transmitted and received wave polarization states:

$$(1)$$

$$E[I] = f\left(\psi_T, \chi_T, \psi_R, \chi_R\right)$$

where $\psi_R = \psi_T$ $\chi_R = \chi_T$ in the co-pol configuration and $\psi_R = \pi/2 + \psi_T$ $\chi_R = -\chi_T$ in the cross-pol configuration. This mapping can be achieved by a linear transformation of the

polarimetric covariance matrix $C_S(\rho) = T(\rho)\,C_S T^\dagger(\rho)$ where $\rho = E_V/E_H$ is the complex polarization ratio and:

$$T(\rho) = \frac{1}{1+\rho\rho^*}\begin{bmatrix} 1 & 2\rho & \rho^2 \\ -\rho^* & 1-\rho\rho^* & \rho \\ \rho^{*2} & -2\rho^* & 1 \end{bmatrix} \tag{2}$$

The intensity expected value is therefore a function of two variables and can be represented graphically as a 3D surface. Such a representation was proposed by Van Zyl [3] and is called the polarimetric signature.

We propose here to extend such a formalism to higher order moments of the single point statistics; in particular since we are dealing with the texture and speckle statistics in polarimetric imagery the normalized second order moment appears to be of interest, because it gives a measure of the speckle strength or of the textural properties of the image.

Accordingly we consider:

$$\text{m2} = \frac{E[I^2]}{E^2[I]} = f\left(\Psi_T,\chi_T,\Psi_R,\chi_R\right) \tag{3}$$

In analogy with the classical Van Zyl signature, we call this representation the polarimetric texture signature. The usefulness of the signature formalism is to allow us to measure from experimental SAR polarimetric data both the first order (strength of the scattering event) and the second order statistical properties (variation of the scattering event), and to represent them synoptically in a graphical object. This in turn lends support to the visual interpretation of properties related to the scene.

PDF TRANSFORMATION

Theoretical characterization of the polarimetric texture signature properties can be achieved from the statistical point of view considering the transformation of the polarimetric vector probability density function when the polarization basis is changed.

The polarization synthesis operation can be considered as a linear operator on the feature vector $\hat{x} = [S_{HH}, S_{HV}, S_{VV}]$ for single look data or on the sample covariance matrix C_S for multilook data. We are interested in investigating how the statistical properties of the polarimetric vector considered as a vector RV (Random Variable), are affected by a change of the orthonormal basis used to represent the vector (e.g. from (H, V) to (A, B):

$$PDF_{(A,B)} = f(PDF_{(H,V)}) \tag{4}$$

In particular an interesting case arises when considering multi-look data with correlated speckle. We demonstrate here that if the multi-look operation is done on an intensity basis starting from single look complex data which are circular Gaussian but correlated, then the probability distribution function of the resulting intensity will be a function of the polarization state. For polarimetric data multi-look processing in the space domain is performed on the Mueller matrices, from which the returned power can be synthesized. The sum and synthesis operators can be commuted:

$$P = \sum G_R^\dagger M_i G_T \quad P = G_R^\dagger \sum M_i G_T \tag{5}$$

Therefore the power corresponding to a certain polarization state ρ in the multi-look operation is equivalent to the sum of single look intensities, which are synthesized in the same polarization state:

$$P(\rho) = \sum_{nlooks} I_i(\rho) \tag{6}$$

The case of addition on an intensity basis of correlated speckle patterns is discussed for instance in [4]. Let us consider for simplicity the case of two correlated speckle patterns. Then the nth moment of the resulting intensity is given by:

$$\langle I^n \rangle = n!\left(\frac{\lambda_1^{n+1}}{\lambda_1-\lambda_2} - \frac{\lambda_2^{n+1}}{\lambda_1-\lambda_2}\right) \tag{7}$$

where λ_i are the non-degenerate eigenvalues of the Hermitian coherency matrix $[\xi] = [A][A^\dagger]$ .where $A = [S_1, S_2]^T$ and S_1, S_2 are two complex Gaussian fields. The normalized second order moment of the multi-look HH channel in the (H, V) basis will then be:

$$\frac{\langle I^2 \rangle_{(H,V)}}{\langle I \rangle^2_{(H,V)}} = \frac{2\left(\lambda_1^2 + \lambda_2^2 + \lambda_1\lambda_2\right)}{(\lambda_1+\lambda_2)^2} \tag{8}$$

If we now transform the single look values into a general polarization state using the linear transformation (2) the new correlation coefficient will be a function of correlations between the other polarimetric channels in the (H, V) basis and of the new polarization state ρ :

$$\langle {}_1S'_p \cdot {}_2S^{*'}_p \rangle = \tag{9}$$

$$\langle {}_1S_{HH} \cdot {}_2S^*_{HH} + {}_1S_{HH} \cdot {}_2S^*_{VV} \cdot \rho^{*2} + {}_1S_{VV} \cdot {}_2S^*_{HH} \cdot \rho^2 +$$

$${}_1S_{HV} \cdot {}_2S^*_{HV} \cdot 4\rho\rho^* + {}_1S_{VV} \cdot {}_2S^*_{VV} \cdot \rho^2\rho^{*2} \rangle \times \frac{1}{(1-\rho\rho^*)^2}$$

Therefore the linear transformation into a new polarization basis changes the statistics of the single look speckle patterns, and in particular the correlation properties of those variables; this in turn modulates the eigenvalues of the coherency matrix and finally the intensity moments.

Numerical solution of (9) has been used to study the dependency of the polarimetric texture signature on the speckle correlation properties. An example is reported in Fig. 1, for $|\langle S1_{HH} \cdot S2^*_{HH} \rangle| = 0.5$, $|\langle S1_{VV} \cdot S2^*_{VV} \rangle| = 0.5$, and $|\langle S1_{HV} \cdot S2^*_{HV} \rangle|$ varying from 0.0 to 0.09

It can be observed that the two characteristic maxima at orientation angle 45° and 135° are present; moreover the depth of the peak modulation is a function of the cross-pol channel correlation: for low HV speckle pattern correlation the moment tends to the nominal value of 1.5 as the basis tends towards the (H, V) basis; for higher values of the HV correlation the normalized moment variation with linear polarization is smoothed out, and the moment assumes higher values than the nominal even in the (H, V) basis.

POLARIMETRIC MIXTURE MODEL

The modulation with polarization state of the second order normalized moment described in the previous section is due entirely to the statistical properties of the radar coherent imaging process (i.e. transformation of RV for correlated single look circular Gaussian data).

A second mechanism which can give rise to polarimetric texture is a polarization dependent modulation of the underlying radar cross section. In other words we can postulate a multiplicative model where the texture variable is dependent on the polarization state, and gives rise to different statistical properties in each component of the polarimetric feature vector, and therefore to polarimetric texture. Such a mechanism can be modelled as an extension of the multiply stochastic approach which gives rise to the class of generalized K distributions. However this line of attack suffers from the difficulty of mapping the statistical properties of the radar reflectivity vector to the underlying physical mechanisms. We propose here an inverse path, where we assume that the polarimetric diversity in the underlying radar cross section is due to a combination or mixture of different physical scattering mechanisms. Each scattering mechanism is assumed to be polarimetrically homogeneous, and is described by simple models (e.g. circular
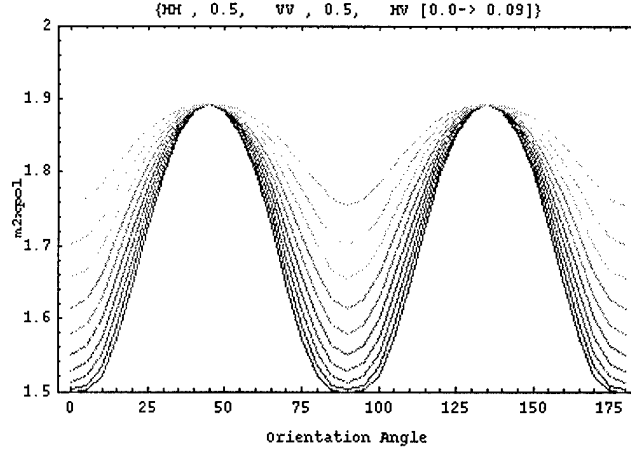
Fig. 1 - Dependency of the polarimetric texture signature from the speckle correlation properties.

Gaussian statistics). Clearly this method lacks of generality, because we do not assume any a priori distribution for the texture variable, but we construct case by case an empirical set of rules according to the scattering scenario; however it can be quite useful to gain physical insight into the polarimetric texture observed in some experimental data, and lends itself nicely to a numerical Monte Carlo type simulation.

To illustrate the approach, we present next a case dealing with a mixture of a grass clutter and deterministic point targets.

TEXTURE SIGNATURES OF WEAK POINT TARGETS AND CLUTTER

In this simulation we want to mimic the situation where a few dihedral reflectors are sprinkled on a vegetation background. Since the dihedral reflectors have a different polarimetric response with respect to the grass clutter, and in particular they have no response in the cross-pol channel and equal return and a phase shift of π in the co-pol channel, they are supposed to introduce an imbalance in the co-pol channel statistics.

We suppose further to be in a fully developed speckle regime with the polarimetric vectors obeying a circular complex Gaussian distribution. The RVs in each class of the mixture are generated using a Monte Carlo approach. The grass clutter is modelled as a reciprocal azimuthally symmetric medium with the following covariance matrix parameters: $\sigma = 1.0$, $e = 0.1$, $\gamma = 1.27$, $\rho = (0.61 + i0.04)$. The dihedral is modelled with the scattering matrix: $S_{HH} = 1$, $S_{HV} = 0$, $S_{VV} = -1$ The two RVs are then combined in a mixture, with the probability of occurrence for the dihedral class of 0.02. Finally the cross-pol texture signature and the power signature are computed. The signatures

of the grass clutter only and the grass clutter with the dihedrals are shown in Fig. 2.

It is interesting to notice that the power signature does not show any difference between the two situations: clutter only Fig. 2.a; clutter and dihedral Fig 2.b; this is due to the fact that the mean power return of the clutter is not affected by the addition of a few different weak scatterers. On the other hand the texture signature shows the two typical peaks at $\psi= (45°,135°)$ only in the case of clutter and dihedral (see Fig. 2.d).

In the perspective of remote sensing applications the polarimetric texture signature seems therefore to be a powerful discriminator to detect polarimetrically diverse but radiometrically weak target embedded in a clutter.

CONCLUSIONS

Selected results from an investigation on speckle and texture statistics in SAR polarimetric images have been reported. The study highlights the fact that polarimetric diversity (the way the underlying scattering mechanism are sensitive to the electromagnetic wave polarization) propagates to the higher order statistical properties of the observed radar signal. An extension of the theoretical speckle and texture models is necessary to account for these effects, and the polarimetric texture signature is introduced as a formalism to analyse experimental data. With these tools at hand we finally arrive at the conclusion that polarimetric texture is useful from the application point of view when different scattering mechanisms can be resolved only due to their polarimetric diversity and not from their radiometric diversity.

REFERENCES

[1] G.F. De Grandi, E. Nezry, J.S. Lee, D. Schuler, "On the Statistics of Polarimetric SAR Synthesized Images", *Proceedings IEEE IGARSS'95, Florence, Italy, July 1995.*

[2] G.F. De Grandi, J.S. Lee, D. Schuler, E. Nezry, "Texture and Speckle Statistics in Polarimetric SAR Synthesized Images", for submission to IEEE Trans. GARS.

[3] Van Zyl, H. A. Zebker, and C. Elachi, "Imaging Radar Polarization Signatures: Theory and Observation", *Radio Science, vol. 22, no. 4, pp. 529-543, Jul. Aug. 1987.*

[4] J.W. Goodman, "Statistical Properties of Laser Speckle Patterns", *in Laser Speckle and Related Phenomena, Edited by J.C. Dainty, ch. 2, 9-75, Springer-Verlag, 1975.*

a)

b)

c)

d)
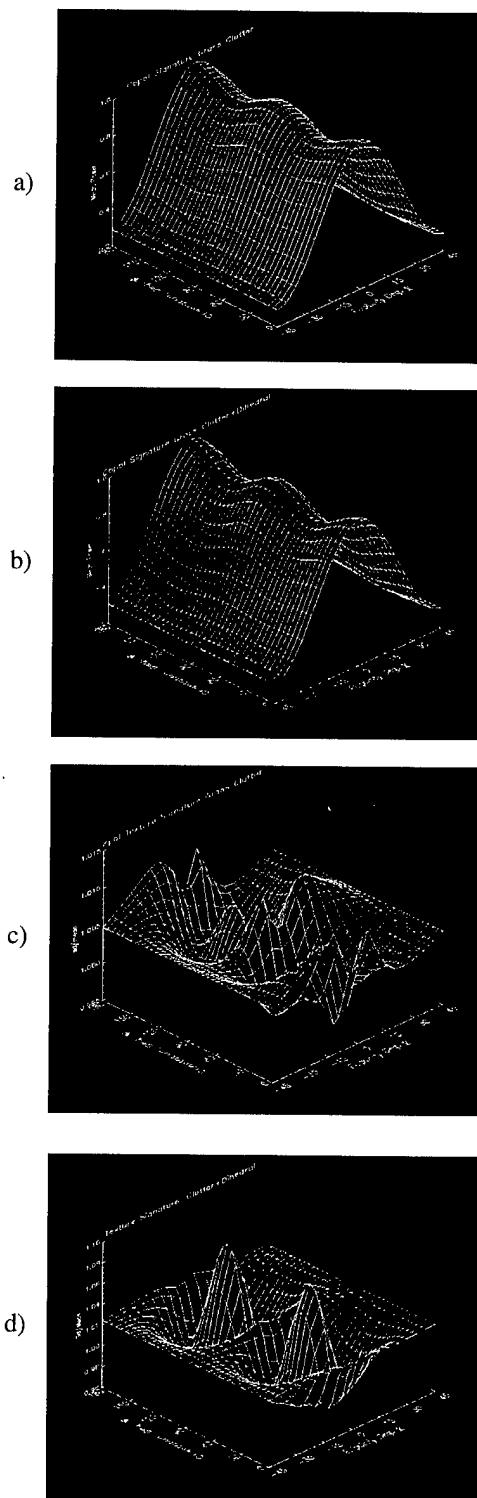
Fig. 2 - Polarimetric power and texture signatures for weak point targets embedded in clutter.

REMOTE SENSING RESEARCH IN MALAYSIA

N. N. Mahmood, K.F. Loh and S.Ahmad
Malaysian Centre for Remote Sensing (MACRES)
City Square Centre, Jalan Tun Razak,
50400 Kuala Lumpur, Malaysia
Tel: 603-2645640 Fax: 603-2645646 E-mail:macres@macres.sains.my

ABSTRACT

The Malaysian Centre for Remote Sensing (MACRES) was established as a research and development organisation with the objectives of developing remote sensing and related technologies and operationalising their applications for resource and environmental management in the country. Apart from implementing a National Remote Sensing Programme which is being fully participated by all the user agencies in the country, MACRES main task is to conduct and support research towards operaional use of relevant technologies for national development. Three main areas of emphasis for remote sensing research and development in the country are microwave remote sensing applications, remote sensing and Geographic Information System (GIS) integration, and multi-sensor/multi-platform data fusion. This paper highlights research and development activities in remote sensing and related technologies in Malaysia and indicates the direction taken towards operationalisation of these technologies in the country.

INTRODUCTION

Malaysian National Remote Sensing Programme (NRSP) which is currently being implemented under the coordination of MACRES since 1998 stipulated that the country involvement in remote sensing is divided into three segments - Ground, User and Space. Successful implementation of this programme has resulted in the widespread utilisation of predominantly optical remote sensing data for the different resource and environmental management objectives. Recent advances in microwave remote sensing, expecially with the availablility in several synthetic aperture radar (SAR) equipped satellite and airborne missions, have offered Malaysia opportunities to exploit the potentaility of SAR data for varied applications in Malaysia.

Under the NRSP MACRES will continue to play a leading role in co-ordinating, operationalising and commercialising remote sensing and its related technologies in the country. Operationisation of the technology for national development is currently the focus and all research actvities in remote senisng and related technologies will be geared towards this direction.

Operationalisation of remote sensing technology normally implies moving from an academic environment to an analysis of what is needed and how the technology can be used to solve practical problems. However, when addressing the same subject in a developing country like Malaysia, it also implies additional facets of capacity building encompassing both human resource and infrastructural development, and institutional arrangement.

To upgrade research and development capacity in Malaysia, three projects are being implemented by MACRES . These are MACRES headquarters to be equipped with the state - of - the - art equipment and facility, Malaysia Earth Observation Ground Receiving Station, and a compehensive Human Resource Development Programme for development of skilled and trained manpower.

In the Seventh Malaysian Plan (1996 - 2000), a special fund has been allocated by the Government under the Intensification of Research in Priority Areas (IRPA) Progamme to conduct research in prioritised fields for indegenious capacity building and commercialisation purposes. Remote sensing and GIS are incorporated in the programme.

RESEARCH AND DEVELOPMENT DIRECTION

Three main priority areas for remote sensing research in the country are microwave remote sensing applications, remote sensing and Geographic Information System (GIS) integration, and multi-sensor/multi-platform data applications.

Microwave Remote Sensing

Research activities in microwave remote sensing in the country are directed towards four major thrust areas :
(i) Basic backscattering behaviour of major cover types in response to different microwave bandwidths, polarisation and look angles;
(ii)Information retrieval and classification of different cover types, effects of canopy, trunk and soil moisture, employing technique like least square, maximum likelihood and neural network;
(iii)Data calibration (system effect removal, speckle filtering, and geometric rectification); and
(iv)Multisensor and multiplatform data fusion of optical and SAR systems.

Microwave research in the country started in early 1980's. Initial efforts focussed on the development of theoretical models to understand electromagnetic wave interactions with random media such as vegetation and forest. The Monte Carlo technique was adopted for backscatter models developed for vegetation canopies and forest stands (2, 3).

While basic research in SAR modelling was on-going, interest was also focussed on applications development, encompassing among others the development of classification and vegetation parameter retrieval algorithms and potentials of SAR technologies for agriculture and geological applications

Most of the SAR applications research projects conducted in the country are undertaken in collaboration with partners from abroad. The first of such projects was implemented in 1991 with the University of New South Wales, Australia (10) to examine the complementarity of airborne SAR (X band , HH polarisation) and SPOT - MLA data for land cover mapping in the state of Kedah. Results obtained indicated that on the RGB composite (SAR, SPOT bands 3,1) slight improvements in visual separability of features - such as mangrove , rubber (different stages of growth), hilly topography, water bodies, urban and linear features were obtained compared to the SPOT RGB composite (bands 3,2,1).

Pilot application studies in Johore state (7) using ERS-1 data acquired under the EC-ASEAN project (1993 - 1996) and in Kedah state in collaboration with NASDA, Japan using JERS-1 data in 1996 (1) , enlightened on the potentials of multi-temporal SAR composite for land cover change detection.

Under the GLOBESAR project implemented in 1993 - 1996 with Canada, the potentials of airborne SAR data for land use classification (5) and geological information extraction (8) was researched in detail. Fractal analysis and neural network technique (4) proved successful in digital land use classification using SAR data in Kedah state. The SAR data enhanced visual analysis and understanding of the geology of Tubau-Bukit Lumut, Bintulu area (8).

In collaboration with NASA of USA, Malaysia is currently implementing AIRSAR PACRIM programme scheduled for completion during 1996 - 1999. The main objective of the programme is to acquire airborne polarimetric AIRSAR and interferometric TOPSAR data over Malaysia for research in terrain analysis, land use/cover change detection, forest density monitoring, coastal zone information extraction and enhancing understanding of local geological formation.

With the establishment facilities like Microwave Anechoic Chamber in 1995 at the University of Malaya

for SAR polametric and biostatic measurements (6) and another similar one with wider frequency range planned at MACRES in 1999, SAR research for backscatter studies as reported above is expected to be tremendously augmented.

Remote Sensing and GIS Integration

Multi-layered resource and environmental data analysis using the integration of remote sensing and GIS technologies is receiving increasing application in Malaysia expecially in the implimentation of development projects. This is an indication that the combined use of these technologies is moving towards operational mode. Successful applicaions of remote sensing/GIS integration can be seen in projects like agro-ecology mapping (9), soil erosion risk assessment and hydrological modelling in Malaysia.

MACRES is presently undertaking a project under the request of Economic Planning Unit of the Prime Minister Department to generate a database using the integration of remote sensing and GIS for National Resources and Environmental Management, NAREM, in short. The database for NAREM will comprise both land and water resources information generated basically from remote sensing data. Derived information like slope stability, water quality, mineral potential and agro-ecology are anticipated deliverables in the GIS environment. Decision on development options of a specific area, resides on a decision support system incorporated also in NAREM, which takes into account socio-economic and other policy considerations.

Future research in futher enhancing the combined use of remote sensing and GIS will focuss on the development of expert systems incorporating both physical and empirical models suitable to Malaysian conditions, for multi - layered GIS analysis.

In most cases the integration of remote sensing and GIS has been unidirectional, that is from remote sensing into GIS to update its database comprising mainly of layers of information collected from remote sensing and other sources. The reverse direction from GIS into remote sensing has not been fully exploited in Malaysia and research in this area is also being given priority as there is vast potential for GIS inputs to improve classification outputs from remote sensing data.

Multi-sensor Data Fusion

Malaysia's experience in the fusion of datasets from different sensors and platforms for thematic mapping is still limited. Research in this direction is essentail to take advantage of the present availibility of several optical and SAR systems.

1419

Complementary use of optical and SAR satellite data for land cover mapping shows that, depending on choice of bandwidths SAR data by themselves are unsuitable for land cover mapping. Combined with optical data there is little advantage in generating more precise land cover map. With the recent launch of high resolution optical satellites such as the IRS-1C and all weather capability Radarsat, there is potential in combining the two datasets for more reliable land cover mapping.

SAR and optical satellite data fusion for hydrocarbon and mineral potential explorations is an area of potential where future research will be focussed.

Production of precision coded satellite image maps requires data fusion to resolve cloud cover problems. Mosaicking of these datasets to ensure geometric accuracy and to remove radiometric anomalies is another focus for research.

CONCLUSION

Under the coordination of MACRES, Malaysia will continue to intensify research efforts in three main focus areas: microwave remote sensing, remote sensing and GIS integration and multi-sensor data fusion. This together with capacity building programmes covering both human resource and infra-structure development will set the country to move forward in operationalising the use of remote sensing and related technologies for national development.

References

1. A. Rosenqvist and H.Oguma , 1994, `Phenological Characteristics of Cultivated Vegetation Covers in JERS-1 and ERS-1 Synthetic Aperture Radar Data - Preliminary Results, International Seminar on Vegetation Monitoring, 29-30 August, 1994, Chiba University, Japan.

2. H.T.Chuah and H.S.Tan (1990), ` A Multi-constituent and Multi-layer Radar Backscatter Model for A Vegetative Medium', Remote Sensing of Environment, vol.31, pp. 137 - 153.

3. H.T.Chuah and H.S.Tan (1992), ` A Radar Backscatter Model for Forest Stands', Waves in Random, vol.2,pp 7-28.

4. H.T.Chuah (1993), An Artificial Neural Network for Inversion of Vegetative Parameters from Radar Backscatter Coefficient ', Journal of Electromagnetic Wave and Applications, vol.7,No. 8,pp 1075-1092.

5. H.T.Ewe, H.T.Chuah and W.Y.Chin (1995), Classification of Landuse in Kedah, Malaysia , Using Fractal Analysis ' GLOBESAR Conference, Beijing, China October 9 -12.

6. B.K.Chung and H.T.Chuah (1996), `Bistatic Microwave Anechoic Chember : Design and Construction'

7. Procceding of the First Malaysian Remote Sensing Society Conference on Remote Sensing and GIS, 25-27 Nov. 1996, Kuala Lumpur, pp. R1-R9.

8. K.F.Loh., L.Nordin and K.M.N. Ku Ramli (1995), ` Complementary Nature of ERS-1 SAR and Optical Data for Land Cover Mapping in Johore, Malaysia ', International Seminar on the Integration of Remote Sensing and GIS Technologies, Jakarta, Indonesia on 6-8 June, 1995.

9. L.N.Ley (1996), `Application of SAR Data in the Geological Mapping of the Tubau - Bukit Lumut Area, Bintulu, Sarawak, Malaysia', Geological Survey Malaysia, Sarawak, Malaysia.

10. N.N.Mahmood, M. Bruneau.M, and H. LeMan (1983), `A Pilot Study on the Use of Satellite Data for Agro-ecological Mapping of Peninsular Malaysia', MARDI, ASAS 02-83.

11. N.N.Mahmood, K.F.Loh and S.Supian (1993),` SAR and SPOT Data for Landcover Mapping : Their Complementary and Integrated Characteristics', Workshop on SAR Data Analysis and Applications , Bangkok , Thailand 2-4 March, 1993.

An Overview of Microwave Remote Sensing Research at the University of Malaya, Malaysia

H.T. Chuah
Department of Electrical Engineering
University of Malaya
50603 Kuala Lumpur
MALAYSIA
Tel: +603-7595229
Fax: +603-7595316
email: htchuah@fk.um.edu.my

Abstract -- The microwave remote sensing research activities at the University of Malaya, Malaysia, is being carried out mainly at the Electrical Engineering Department. Various types of studies are conducted which include (a) development of convenient, practical and physically based scattering and emission models to elucidate multiple scattering processes in different kinds of random media; (b) development of classification and parameter retrieval algorithms for SAR imagery; (c) measurements and modelling of dielectric properties of tropical vegetative samples. Based on measured data over a frequency spectrum 2-14 GHz, a dielectric model using dual-dispersion technique has been formulated to predict dielectric constants of rubber and oil palm leaves at various moisture contents, and (d) monostatic and bistatic radar cross-section measurements in a microwave anechoic chamber. This paper gives an overview of these activities for the past decade.

1. INTRODUCTION

Microwave remote sensing has become one of the targeted areas of intensified research in Malaysia for earth resources monitoring and management. This is primarily due to the capability of microwave to penetrate cloud covers and to transmit through rain since these two reasons limit the use of optical imagery. In the 80's, the Microwave Remote Sensing Research group at the University of Malaya started by concentrating on the development of theoretical models to understand electromagnetic wave-target interaction mechansims in random media such as vegetation and forest. Then the research work has been extended to other areas which include development of classification and parameter retrieval techniques and algorithms, and laboratory and field experiments; as well as in application areas. Based on measured data on rubber and oil palm leaves, a semi-empirical dielectric model using dual-dispersion technique has also been developed. With the setting up of a microwave anechoic chamber in 1995 to support polarimetric and bistatic measurement in the frequency range of 2-18 GHz, many types of measurement activities within the university and collaboration projects with outside research agencies are being conducted.

2. MONTE CARLO MODELS

The complex vector multiple scattering problem for propagation and scattering of em wave in a random medium is treated by a Monte Carlo formulation, in which an incident beam of photons is progressively scattered by scattering centres in the medium. The theory characterizes each scattering event by functions describing the probability of the photons being scattered into different directions, or absorbed by the scatterer. The process is tracked until the photon flux is sufficiently attenuated or is backscattered into the receiver. Several reduction techniques are introduced to reduce the computation time required to achieve acceptable ensemble averages of the statistics. This method of modelling allows the multiple scattering process to be studied in great details with different combinations of different types of scattering centres in multi-layered geometries. This Monte Carlo model has been applied to study microwave radar backscatter from

(a) vegetation canopies and forest stands [1-2]
(b) sea-ice [3]
(c) wet snow [4].

These complex natural media are modelled as multiple layers of ellipsoidal dielectric scatterers of various shapes, representing the components of the medium such as leaves, stems, branches, trunks in the case of vegetation; air bubbles in the case of sea-ice; or water inclusions in the case of snow. These component scatterers are embedded in a suitable background medium and backed by a rough ground surfaces. Figure 1 shows typical comparisons of the theoretical calculations with measured data when the model is applied to a forest stand.

Recently, a phase matrix has been developed to deal with densed random media [5]. In the formulation, both amplitude and phase correction are included to take into account the electrically dense medium effect.

3. LANDUSE CLASSIFICATION OF SAR IMAGES

Natural objects generally present self-similarity and self-affinity in their shapes, structures and groupings. Since the SAR images are basically taken on natural terrains, classification of landuse can be performed based on the fractal analysis. A project is currently underway to study the SAR images on a GlobeSAR site in Kedah, Malaysia using fractal dimension of the images as an additional input to a neural network classifier. This fractal dimension corresponds closely to our general conception of the "roughness" of the intensity surface. Preliminary results [6] show that fractal analysis is useful in classifying the respective sea, urban, forested and paddy areas.

4. DIELECTRIC MODEL FOR TROPICAL LEAVES

Dielectric properties of vegetation samples are important parameters to be investigated for they describe the linkage between electromagnetic properties and physical properties of the samples. The dielectric constants are required in theoretical models that calculate propagation constants and radar backscatter coefficients from a vegetation medium. Investigation into the ecology of tropical plants shows that free-water volume fraction of the moisture content of a tropical leaf should be higher when compared to that of a leaf from the temperate country. Experiments have been conducted in the Department of Electrical Engineering, University of Malaya, to measure dielectric constants of tropical leaves (especially rubber and oil palm, which are two commercial plants in Malaysia) as a function of frequency (4-18 GHz) and moisture content (10-85%). The waveguide thin sheet method is employed. A piece of leaf sample is sandwiched between two waveguide sections. The reflection coefficient is measured using a Network Analyser. The dielectric constant is calculated using the reflection coefficient. Using the dual-dispersion model in Ulaby and El-Rayes [7], the dielectric constant of a tropical leaf is given as a simple additive mixture of a non-dispersive residual component, ε_s; a free water component, $v_{fw}\varepsilon_w$; and a bulk vegetation-bound water component, $v_b\varepsilon_b$:

$$\varepsilon = \varepsilon_s + v_{fw}\varepsilon_w + v_b\varepsilon_b \qquad \ldots\ldots (1)$$

where v_{fw} is the volume fraction of water and ε_w the free water dielectric constant; and v_b the volume fraction of the bulk vegetation-bound water component and ε_b its dielectric constant. Based on the measured data, the following empirical formula is obtained:

$$\varepsilon = \varepsilon_s + v_{fw}[4.9 + \frac{73.5}{1+\frac{jf}{19.7}} - j\frac{18\sigma}{f}] + v_b[2.9 + \frac{55.0}{1+(\frac{jf}{0.18})^{0.5}}] \qquad \ldots\ldots(2)$$

The variations of ε_s, v_{fw}, v_b and the ionic conductivity of aqueous solution σ with gravimetric moisture M_g are obtained by minimization of mean-square errors between measured data for rubber and oil palm leaf samples and calculations from the model, yielding the following values:

$$\varepsilon_s = 1.7 - 0.74M_g + 6.16M_g^2 \qquad \ldots\ldots (3)$$

$$v_{fw} = M_g(0.756M_g - 0.1333) \qquad \ldots\ldots (4)$$

$$v_b = \frac{(1.5306M_g - 2.5909M_g^2 + 1.4355M_g^3)}{(1-0.60M_g)} \qquad \ldots\ldots (5)$$

$$\sigma = 1.27 \qquad \ldots\ldots (6)$$

Figure 2 shows a typical comparison of the model with measurements on rubber leaf samples at 10.0 GHz.

5. CONTROLLED LABORATORY EXPERIMENTS

The Electrical Engineering Department has a polarimetric bistatic microwave anechoic chamber for monostatic and bistatic radar cross-section measurements. It covers a frequency range of 2 to 18 GHz. The structure of the chamber is a quarter goedesic dome with a 12 foot radius, and raised 3 feet above the floor. The chamber consists of 10 dual-polarized quad-ridge antennas. The antenna railing system consists of 6 rails 30 degrees apart in azimuth angle behind the dome-shaped structure. The six antennas can be moved along the rails in the elevation direction, with the microwave beam pointing at the centre of the dome where the target is located. This design thus enables a very large combination of incident and scattering angles in bistatic measurements. 4 transmit antennas are fixed at different elevation angles next to one of the antenna rails. Using an azimuth-over-elevation positioner as the pedestal for the target, and by positioning the movable antenna along that rail beside those fixed transmit antennas, monostatic measurements with incident angles ranging from 0 - 90 degrees can be accomplished (see Figure 3) [8]. A vector network analyser is used to measure the amplitude and phase of the radar returns. IEEE-488.2 interface bus is used to control various hardware components as well as to perform data acquisitions. A computer program was written to automate the measurement system. Data are stored in raw format and processed later with own-designed dedicated software so that different processing methods and parameters can be applied. Using a time-domain gating technique to remove spurious responses due to target-pedestal coupling effect, a measurement precision of 0.5dB can be achieved. Many types of measurement activities are being conducted and planned for the microwave anechoic chamber such as bistatic scattering from discrete sparse/dense random media with known scatterer size and statistically known positions.

6. REFERENCES

[1] H.T. Chuah, and H.S. Tan, "A Multi-constituent and Multi-layer Radar Backscatter Model for A Vegetative Medium," *Remote Sensing of Environment*, vol. 31, pp. 137-153, 1990.

[2] H.T. Chuah, and H.S. Tan, "A Radar Backscatter Model for Forest Stands," *Waves in Random Media*, vol. 2, pp. 7-28, 1992.

[3] H.T. Chuah, and H.S. Tan, "A Numerical Model for Radar Backscatter from a Lossy Inhomogeneous Layer," *International Journal of Remote Sensing*, vol. 11, no. 4, pp. 639-651, 1990.

[4] H.T. Chuah, and H.S. Tan, "A Monte Carlo Backscatter Model for A Layer of A Mixture of Discrete Scatterers," *International Journal of Remote Sensing*, vol. 12, no. 7, pp. 1425-1440, 1992.

[5] H.T. Chuah, S. Tjuatja, A.K. Fung and J.W. Bredow, "A Phase Matrix for a Dense Discrete Random Medium: Evaluation of Volume Scattering Coefficient," *IEEE Trans. Geosci. & Rem. Sensing*, vol. 34, no.5, pp. 1137-1143, 1996.

[6] H.K. Low, H.T. Chuah and H.T. Ewe, "Windowing Technique in An Artifical Neural Network Classifier for Landuse Application," Proceedings of the 1st Malaysian Remote Sensing Conference, 25-27 Nov, 1996, Kuala Lumpur, pp. E1-E9.

[7] Ulaby, F.T., and El-Rayes, M.A., "Microwave Dielectric Spectrum of Vegetation Part II: Dual Dispersion Model," *IEEE Trans. Geosci. & Rem. Sensing*, vol. 25, no.5, pp. 550-557, 1987.

[8] B.K. Chung and H.T. Chuah, "A Bistatic Microwave Anechoic Chamber: Design and Construction," Proceedings of the 1st Malaysian Remote Sensing Conference, 25-27 Nov, 1996, Kuala Lumpur, pp. R1-R9.

Figure 2: Comparison of measurement and model for rubber leaf samples at 10.0GHz
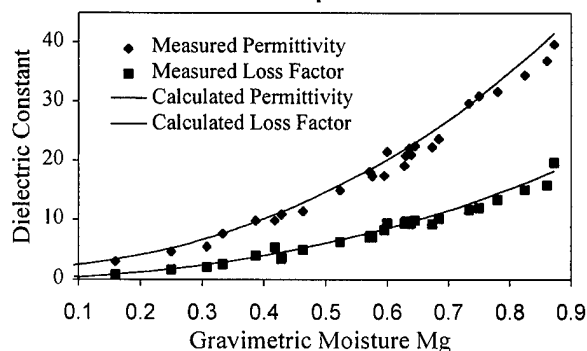
Figure 1: Comparison of Monte Carlo calculations with measurements from Kansas deciduos trees at 8.6 GHz
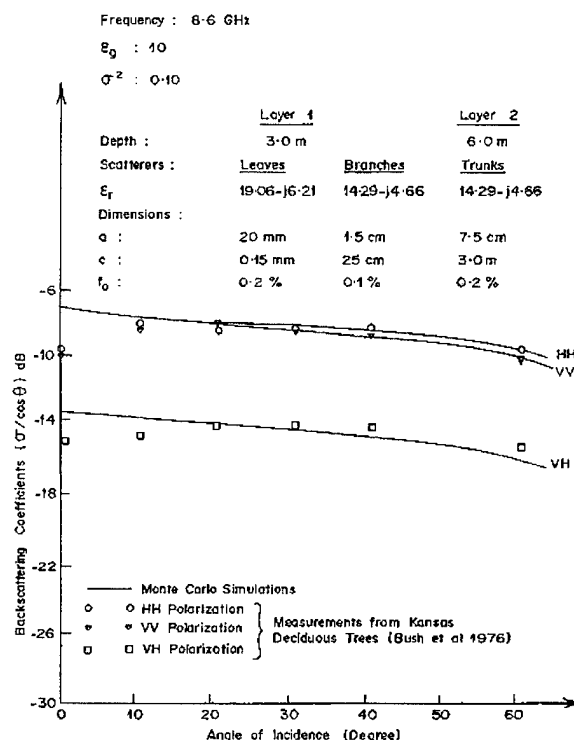
Figure 3: The microwave anechoic chamber at the University of Malaya, Malaysia

1423
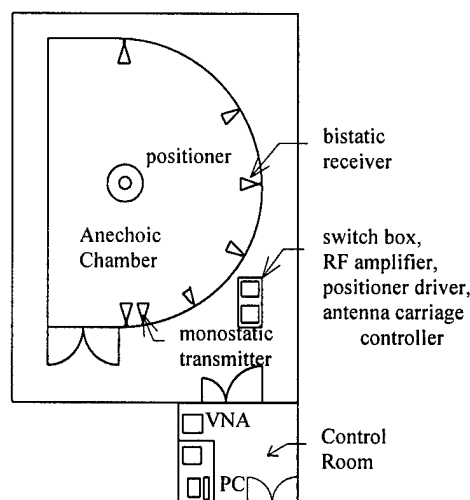
The Use of Satellite Imagery for Monitoring Coastal Environment in Taiwan

C.F. Chen,   K.S. Chen,   L.Y. Chang,   and A.J. Chen
Center for Space and Remote Sensing Research
National Central University
Chung-Li, TAIWAN, R.O.C.
Telephone: 886-3-4227151-7624, Fax: 886-3-4254908, E-mail: cfchen@csrsr.ncu.edu.tw

Abstract--An efficient coastland management is one of the major land development policy in Taiwan, an island with about 1780 miles of shoreline and most of the population resides in the west coast. One main mission of the policy is to closely investigate and watch the coastal environment in order to protect island's limited land resources. In this study we use satellite remote sensing imagery data to monitor the near-shore environment in the coastal area. In particular, the use of ERS1/2 SAR data to detect oil slicks near shore is described here. Because the presence of oil slicks on sea surface increases the surface tension of sea water, the surface wave motion is significantly depressed or disappeared. This effect will relatively lower the sea surface roughness, and accordingly, will decrease the radar backscattered energy. These damping effects are now well understood and it is such effects that enable the oil slicks to be discernible from the radar image. In this study, we shall concern with the digital techniques that effectively delineates the oil slicks pattern from SAR image. Directly using SAR images to detect the oil slicks, however, is not fully straightforward because of complex process of SAR imaging mechanism and the existing of inherent multiplicative speckle noise. The technique we developed here is based on the fact that the oil slicks on the image gray value surface is a concave area. In order to correctly identify these concave areas and suppress the effect of speckle noise, an image pyramid with multiresolution layers is generated sequentially from the original image. Then a top-down approach, which applies both first and second order derivative operators, Difference of Gaussian(DoG) and Laplace of Gaussian(LoG), to the image pyramid, is used to detect oil patches. Two ERS-1 SAR images acquired over Taiwan water area on August 5,1994 and September 5,1994 were used for testing. It was indicated that the proposed method effectively depresses the speckle noise and other sea clutter signal, and clearly enhances the oil slicks pattern.

INTRODUCTION

This study concerns with detection of oil spill on ocean surface using Synthetic Aperture Radar(SAR) image. Because the presence of oil slicks on sea surface increases the surface tension of sea water, the surface wave is significantly depressed or disappeared. This implies that the roughness of sea surface is lower if oil slick exists. It is now well understood that the radar backscattered energy is highly dependent on surface roughness[1,2]. Therefore, the gray value surface of such radar image will become a concave area if that area is corresponding to an oil slick. In this work, we propose a scheme to detect concave area on the SAR images and infer that area is covered by oil slick. Generally, SAR images are not generated by direct interactions with ground target. The information on SAR images comes from some secondary effect, for example, variation of surface roughness. The major problem is that the parameters that affect the roughness of sea water are too many, to name a few, wind field on sea surface, internal wave of sea water, etc. This problem becomes very severe when the area of interest is large. Another drawback is that the SAR system uses coherent polarized wave as a detection source. As a result, the SAR images inherently contain "multiplicative speckle noise" and further complicates the detection of oil slicks. Because of the reasons mentioned above, traditional image classification technique is clearly not suitable for this application, especially

for some algorithms using pixel by pixel approach. In this study we propose a top-down scheme to overcome the aforementioned difficulties. The scheme basically includes two major components: (1) reducing original image resolution serially and generating an image pyramid, (2) applying Laplace of Gaussian[3] and Difference of Gaussian[3] to the multilayers of the image pyramid to locate the position of oil slicks. The detailed methodology will be addressed in next section. The following section will present the experimental results and discussion. Some conclusion remarks will be given in the final section.

METHOD

The proposed method basically consists of two major stages. At first stage, an image pyramid is generated from the original image. The following stage a top-down detection method is applied to the image pyramid. Two major stages are described as follows:

The Image Pyramid Generation

Directly using SAR images to detect the oil slicks, to some extent, is not sufficiently reliable because of complex process of SAR imaging mechanism and existing of inherent multiplicative speckle noise. Therefore, in order to decrease the effect of noise and other sea clutter and to perform the following oil detection, a unit of 2 by 2 pixels is used to reduce the original image sequentially and generate an image pyramid with a multilayer structure. Note that the top level of the pyramid is the coarsest image and the bottom of the pyramid is the original image.

The Top-down Detection Scheme

It was mentioned that gray values of oil slick are lower than that of background. That means that oil slicks on image gray value surface is a concave area and we can use a second order derivative operator, Laplace of Gaussian(LoG)[3], to detect such area. It was firstly repeatedly

applied LoG over a W by W window on the coarsest image of the image pyramid. At this point, we can take the negative portion of the image and delineate the concave areas in image gray value surface. However, not all of such concave areas are oil slicks coverage, some nature phenomena, for instance, the variation of wind field has similar effect. Nevertheless, oil film and sea water are electromagnetically different. In fact, the gradient of image gray value on the boundary of oil-water normally is greater than that made by variation of wind field. Therefore, a first order derivative operator, Difference of Gaussian (DoG)[3], is used to measure the sharpness of the edge on the boundary of the slicks detected by the previous procedure. In order to justify whether the detected area is oil slick or not, a criterion should be empirically chosen.. If the slick boundary pixels whose sharpness is greater than the selected threshold, they are classified as an oil slick boundary. Because the oil slicks may vary in size, the window size of operator also has to be adjusted accordingly. In this paper, we apply lower resolution window (larger window size) to detect the oil slicks initially and then apply higher resolution window (smaller window size) to detect finer oil slicks based on the oil slicks detected by the lower resolution windows. This approach effectively reduces the sea clutter and preserves subtle variations of oil slicks. Up to this point, the oil slicks are found only in the coarsest image. The next step we will use these oil slick pixels as the seeds to perform further refinement from the top to down layers in the image pyramid. . First of all, LoG is used again to further delineate small variation of oil slicks on edge portion. This coarse to fine multilayer approach is to assure that the pixels detected is the oil slicks. Since there may be some small convex surfaces and can not be detected with LoG plus DoG procedure alone. A region growing method[4] is used along to find out the rest of oil slicks.

EXPERIMENT RESULT

We selected two ERS-1 SAR images to test the

proposed scheme. Two Images were acquired on August 5, 1994, and September 5, 1994, respectively. The subscenes were cut from original full scenes for testing. The image sizes of subscenes are 3000 by 3000 pixels and 2048 by 2048 pixels, respectively. In Figures 1 and 2, the dark areas are the detected oil slicks with proposed scheme. Figures 3 and 4 are part of enlarged oil slicks. It is worth to note that the subtle variations of the oil slick edge was detected.

Fig. 1 The detected oil slicks for test SAR image I

CONCLUSION

Three conclusive points can be made from this study:

(1) From the experimental results, the proposed scheme is able to effectively suppress the speckle noise and other sea clutter, and clearly enhances the oil slicks pattern.

(2) In spite of some of empirical parameters introduced in the proposed scheme, acceptable result were obtained when the same set of parameters are applied to different images. Thus, the applicability and robustness of the proposed scheme is demonstrated.

Fig. 2 The detected oil slicks for test SAR image II

(3) Because the field test of oil slicks spilled over on sea is extremely difficult, if not impossible, we have not sufficient ground truth as an evidence. Nevertheless, the effectiveness of the presented method was shown. Further validation may be required, if so necessary.

Fig. 3 Part of enlarged oil slicks of test SAR image I

REFERENCES

[1] Robinson, I. S., "Satellite Oceanography," John Willey&Sons, 1994.

[2] Ulaby, F. T., R. K. Moore and A. K. Fung, "Microwave Remote Sensing, Active and Passive," Volume II, Addison-Wesley, 1982.

[3] Pratt W. K., "Digital Image Processing," 2nd Edition, John Willey&Sons, 1991.

[4] Rosenfeld, A. and A. C. Kak, "Digital Picture Processing," 2nd Edition, Academic Press, 1982.
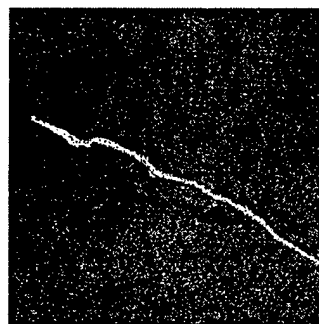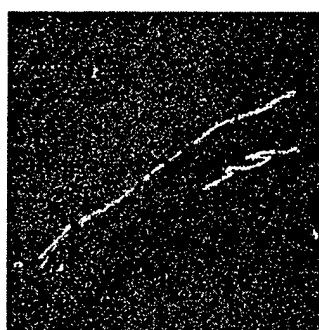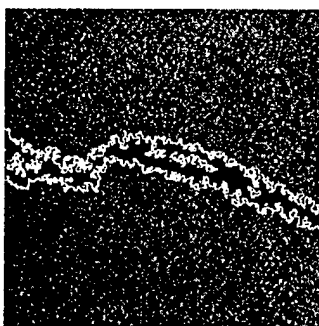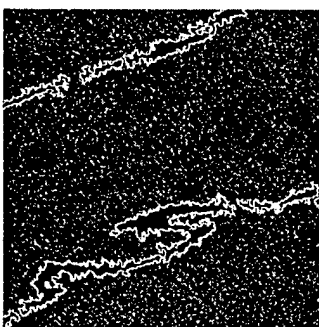
Fig. 4 Part of enlarged oil slicks of test SAR image II

A Study of Dense Medium Effect Using a Simple Backscattering Model

H. T. Ewe and H. T. Chuah
Faculty of Engineering
Universiti Telekom
Bukit Beruang, 75450 Melaka, MALAYSIA
Tel: 60-(6)-252-3420, Fax: 60-(6)-231-8696

Abstract -- In an electrically dense medium, when the spacing between the scatterers is comparable to the wavelength, it is important to incorporate the near field effect, both amplitude and phase, into the backscattering theory. In this paper, a simple backscatter theory based on Radiative Transfer (RT) Theory is presented. The random medium, bounded on top and bottom by a rough surface, contains a layer of randomly distributed spherical scatterers. The phase matrix for these closely packed discrete scatterers is obtained using the Dense Medium Phase and Amplitude Correction Theory (DM-PACT) [1,2] and the rough surface is characterized by the IEM model [3]. The integro-differential equations of Radiative Transfer Theory are solved iteratively up to second order solutions. Scattering terms for direct surface, direct volume, surface-volume and volume-volume interactions are identified. These results are later compared with full model solution using matrix doubling method.

INTRODUCTION

It is vital to study the scattering mechanisms in a dense medium in order to predict the backscattering returns. Over the years, research has shown that for a random medium with high volume fraction of scatterers, the incoherent scattering approach to the problem is no longer valid [1]. When the spacing between the scatterers is comparable to the wavelength, the medium is an electrically dense medium. For these scatterers which are electrically close to each other, the calculated scattered field should include the near field amplitude terms and the phase coherent effect of the volume of scatterers. This incorporation of near field effect has been implemented through the Dense Medium Phase and Amplitude Correction Method [1,2], where both the amplitude correction and the phase correction are applied on the calculation of volume phase matrix of the spherical scatterers. This corrected phase matrix is later used in the radiative transfer equations. The medium is modeled as a layer embedded with the randomly distributed scatterers, bounded on top and bottom by a rough surface, which is characterized by the IEM model. The integro-differential equations of radiative transfer theory are solved iteratively up to second order solutions with respect to the albedo of the medium. The respective solution terms are later regrouped with respect to the scattering mechanisms involved. In this paper, relative contributions of three scattering mechanisms (direct surface, surface-volume and volume interactions) are investigated. The volume interactions include both direct

volume and volume-volume interactions. To examine the range of validity of the simple model, the calculated results are compared with those of full model solution using matrix doubling method [3,4]. For co-polarized returns, predictions from the simple backscatter model solution compare well with those from the matrix doubling solution at low frequency when low order scattering is significant. At high frequency range, when the wavelength is short compared to the spacing between scatterers, it is found that far field phase matrix is applicable because the medium is now electrically sparse even though the medium may be spatially dense. For cross-polarized returns, since they are mainly due to high order scattering, the predictions from the simple backscattering model are not satisfactory as the solution contains only up to second order interactions.

FORMULATION

The dense medium with randomly distributed discrete spherical scatterers is shown in Fig. 1. Both the top (S1) and the bottom (S2) surfaces are characterized by the surface r.m.s. height and the correlation length.

The propagation and scattering of waves inside the random medium can be described by the radiative transfer equation:

$$cos\theta \frac{d\overline{I}}{dz} = -\overline{\overline{\kappa}}_e \overline{I} + \int \overline{\overline{P}} \overline{I} d\Omega \qquad (1)$$

where $\overline{I}$ is the Stokes vector and $\overline{\overline{\kappa}}_e$ is the extinction matrix of the medium. The volume phase matrix, $\overline{\overline{P}}$ is obtained through the Dense Medium Phase and Amplitude Correction Method [1] and is given as

$$\overline{\overline{P}}(\theta,\phi;\theta',\phi') = \left\langle |\Psi|^2 \right\rangle_n \cdot \overline{\overline{S}} = \begin{bmatrix} P_{vv} & P_{vh} \\ P_{hv} & P_{hh} \end{bmatrix} \qquad (2)$$

where $\left\langle |\Psi|^2 \right\rangle_n$ is the dense medium phase correction factor developed using a simple antenna array concept [1]. When the medium is sparse, $\left\langle |\Psi|^2 \right\rangle_n$ will reduce to the number of scatterers per unit volume, n_o. The amplitude correction has been incorporated by modifying the Stokes matrix $\overline{\overline{S}}$ of a
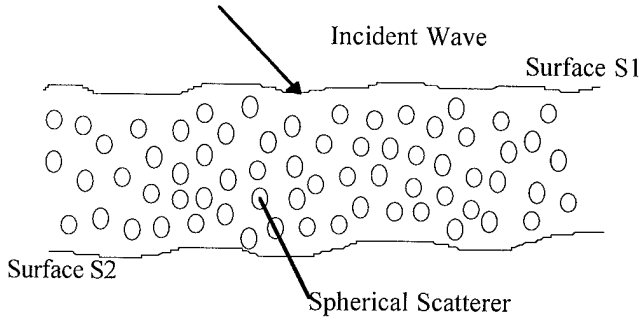
Fig. 1. Physical configuration of the random medium.

single sphere [5].

It is assumed that the transmission across the top boundary can be represented by the Fresnel power transmission T. In this paper, scattering process only up to second order volume scattering process is included. For the top and the bottom rough surfaces, only the single-scatter surface backscattering process for IEM model is considered.

The radiative transfer equation in (1) is then solved iteratively with the albedo of the medium as the iteration parameter [3]. Expressions up to second order solutions are obtained. The zeroth, first and second order solutions of (1) are listed below:

$$\sigma_{pq}(0) = \sigma_{pq}^{s} = \sigma_{pq}^{s1} + \sigma_{pq}^{s2} \qquad (3)$$

$$\sigma_{pq}(1) = \sigma_{pq}^{vs}(m \rightarrow s2) + \sigma_{pq}^{vs}(s2 \rightarrow m) + \sigma_{pq}^{v}(up, down) \qquad (4)$$

$$\sigma_{pq}(2) = \sigma_{pq}^{v}(up, up, down) + \sigma_{pq}^{v}(up, down, down) \qquad (5)$$

where q is the incident field polarisation and p is the scattered field polarisation. The superscripts s, vs and v are used to indicate the surface scattering terms, the surface-volume interaction terms and the volume scattering terms, respectively. σ_{pq}^{s1} and σ_{pq}^{s2} are the surface scattering terms from the top and bottom rough surfaces, respectively. $\sigma_{pq}^{vs}(m \rightarrow s2)$ accounts for the volume to bottom surface scattering terms, whereas $\sigma_{pq}^{vs}(s2 \rightarrow m)$ denotes the bottom surface to volume scattering terms. For volume scattering terms, $\sigma_{pq}^{v}(up, down)$ represents the single volume scattering process where the downward incident waves are scattered back in the upward direction, whereas $\sigma_{pq}^{v}(up, up, down)$ and $\sigma_{pq}^{v}(up, down, down)$ are the double volume scattering

terms for incident waves scattered following the down-up-up and the down-down-up sequences, respectively.

The scattering terms in (3), (4) and (5) are then regrouped into the following three categories, depending on the scattering mechanisms involved.

$$\sigma_{pq}^{s} = \sigma_{pq}^{s1} + \sigma_{pq}^{s2} \qquad (6)$$

$$\sigma_{pq}^{vs} = \sigma_{pq}^{vs}(m \rightarrow s2) + \sigma_{pq}^{vs}(s2 \rightarrow m) \qquad (7)$$

$$\sigma_{pq}^{v} = \sigma_{pq}^{v}(up, down) + \sigma_{pq}^{v}(up, up, down)$$
$$+ \sigma_{pq}^{v}(up, down, down) \qquad (8)$$

$$\sigma_{pq}(\theta_s, \phi_s; \theta_i, \phi_i) = \sigma_{pq}^{s} + \sigma_{pq}^{vs} + \sigma_{pq}^{v} \qquad (9)$$

The surface contribution terms, the surface-volume contribution terms and the volume contribution terms are represented by (6), (7) and (8) respectively. The total backscattering coefficient from the medium is given by (9).

RESULTS AND DISCUSSION

In order to investigate the range of validity of the simple backscattering model, a theoretical study is carried out. For the physical configuration shown in Fig. 1, the thickness of the layer is chosen to be 0.5 m and the volume fraction of the randomly distributed spheres (radius $a = 0.5$ mm) is 30%. The relative permittivity of the background medium is selected to be unity and the scatterers embedded within have a relative permittivity of $3.15 + i0.015$. The lower half-space has a relative permittivity of 5.0. The rms height and correlation length for both the top and bottom surfaces are (0.14 cm, 0.7 cm) and (0.056 cm, 0.28 cm) respectively. Two of the parameters used in DM-PACT [2], σ and l, are chosen to be $0.55 \, d$ and 0.12 mm respectively, where d is the average distance between adjacent scatterers. σ is the standard deviation from mean position of the stationary Gaussian random process representing the random position of the scatterers; and l is the correlation length between two such processes.

An incident angle of $15°$ is selected and the calculated VV polarized backscatter from the simple model is plotted against the frequency (in GHz) and $k_o a$ as shown in Fig. 2. For comparison purposes, the matrix doubling solutions with DM-PACT and without DM-PACT (far field assumption in volume phase matrix of the scatterers) are also included in the same figure. It is found that at frequency lower than 40 GHz ($k_o a < 0.4$), there is a good match between the simple model predictions and the matrix doubling solutions with DM-PACT. However, at the high frequency end, when multiple scattering is dominant, the simple model, which has taken only up to second order volume scattering into account, fails to show agreement with the matrix doubling solutions with DM-PACT. It is also noted that at high frequency (> 40
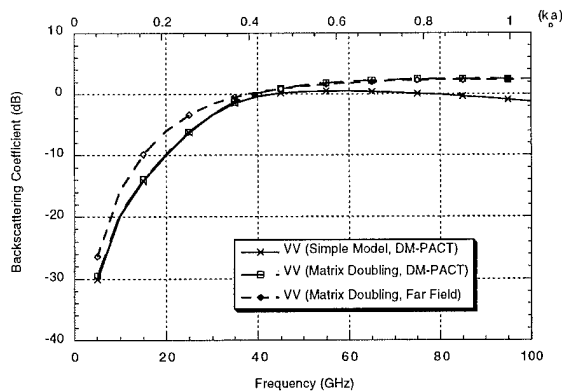
Fig. 2. Comparison of σ_{vv} at 15° incident angle using different models.

Fig. 3. Contributions of different scattering mechanisms at incident angle of 15° for σ_{vv}.

GHz), when the medium becomes electrically sparse, the DM-PACT matrix doubling solutions approach those of the far field matrix doubling solutions.

Fig. 3. shows the relative contributions of different scattering mechanisms at incident angle of 15° for VV backscatter. It is shown that at frequency lower than 18 GHz, surface scattering is dominant, as the long wavelength waves penetrate through the random medium with little scattering loss. When the frequency becomes higher (> 18 GHz), the increasing activity of volume scattering (direct and multiple) in the layer makes the volume scattering contribution more important than the direct surface scattering contribution. It is also noted that although the surface-volume scattering curve shows an increasing trend initially, its backscattering contribution is too small to be significant. When the frequency becomes even higher, increasing scattering loss through the medium allows less energy to reach the bottom surface and thus decreases the surface-volume scattering contribution.

For cross-polarized returns, contributions from high order of volume scattering and multiple scattering between the rough surfaces and the scatterers are important. It is found that the predictions from the simple model are lower than the matrix doubling solutions. Thus, more higher order scattering terms may have to be incorporated into the simple model for better prediction.

CONCLUDING REMARKS

The simple model developed has shown to be a promising model for predicting co-polarized backscattering returns for low frequency when the medium is electrically dense. It is shown that at low frequency, surface scattering is dominant, whereas volume scattering catches up when frequency becomes higher. However, the simple model is not applicable for calculation of cross-polarized returns.
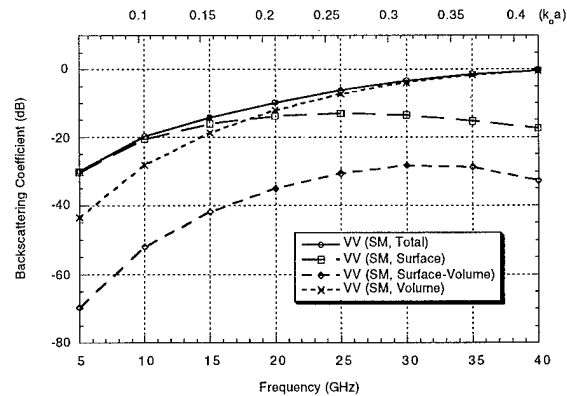
REFERENCES

[1]   Chuah, H.T., S. Tjuatja, A.K. Fung, and J.W. Bredow, "The volume scattering coefficient of a dense discrete random medium," *IEEE Trans. Geoscience & Remote Sensing*, vol. 34, no. 5, pp. 1137-1143, 1996.

[2]   Chuah, H.T., A.K. Fung, S. Tjuatja, and J.W. Bredow, "A scattering model for a densely populated medium: theory and measurement comparisons," *PIERS '95 Proceedings*, pp. 400.

[3]   Fung, A.K., *Microwave Scattering and Emission Models and Their Applications*, Artech House, Norwood, MA, 1994.

[4]   Tjuatja, S., A.K. Fung, and J. Bredow, "A scattering model for snow-covered sea ice," *IEEE Trans. Geoscience & Remote Sensing*, vol. 30, no. 4, pp. 804-810, 1992.

[5]   Fung, A.K., and H.J. Eom, "A study of backscattering and emission from closely packed inhomogeneous media," *IEEE Trans. Geoscience & Remote Sensing*, vol. GE-23, no. 5, pp. 761-767, 1985.

Estimation of Rice Growth Status Using RADARSAT Data

Shao Yun, Wang Cuizhen, Fan Xiangtao, Liu Hao

Institute of Remote Sensing Applications, Chinese Academy of Sciences,
No.3 Datun Rd., Chaoyang District, P. O. Box 9718, Beijing 100101, China,
Tel: 86-10-62925158/Fax: 86-10-64915035/E-mail: yunshao@public.bta.net.cn

Abstract – The Multiple Temporal RADARSAT images were used to monitor the growth status of rice in Zhaoqing test site of south China. The relative brightness of rice fields shows that the radar backscatter increases as the rice grows up, and it is related to the growing period and status of rice and changes over different seasons.

INTRODUCTION

Rice is the staple food in China, especially in south of China. Forty percentage of grain yield in China is rice. It is an important task for remote sensing to monitoring the growing status of rice, however it is limited by the image acquisition. We applied the multiple temporal RADARSAT data to this study in Zhaoqing test site of Guangdong Province. The image acquired at different time show that there are enormous changes of intensity due to the variety of rice growing period and status. The radar backscatter intensity increases as the rice grows up and drops when the rice get matured. This paper discusses the radar backscatter intensity rather than backscatter coefficient of rice in relation to its growth status in term of relative brightness since the calibrated RADARSAT data has not been available for this study at this moment.

RICE GROWTH CALENDAR

Zhaoqing is the only one rice export prefecture in the region of Pearl River Delta. It is very important in the sense of agriculture, and produces a large mount of rice.

It reaps two rice crops a year in Zhaoqing, the early season rice and the late season rice. Fig. 1 shows the rice growth calendar over a year. There are five major growth periods in a life of rice: 1) Transplant period: it transplants the seedling of rice from the seedbed to the paddy field, the transplanting date depends on the weather and temperature; 2) Seedling developing period: the seedling splits up and develops sufficiently in certain mount of quantity; 3) Ear differentiation period: the young ear starts the differentiation; 4) Heading period: it starts to form the heading; 5) Mature period: the rice are maturing and get ready for harvest. The date of those five periods for early season rice are April 4-10, April 20-25, May 10-30, June 10-25, July 15-31; the late season rice are Aug. 1-10, Aug. 10-20, Sept. 1-30, Oct. 1-20, Nov. 1-25.

DATA ACQUISITION

There is a multiple temporal RADARSAT image sets acquired from April to December in the morning for the descending orbit facing west and at the afternoon for the ascending orbit facing east. The imaging date and mode are: 1) June 17, Aug. 4, Sept. 21, Oct. 15, Nov. 8, Dec. 2 in Fine 4 Mode and descending pass, 2) March 6, June 10, Aug. 28 in Standard 5 or 6 mode and descending pass, 3) April 25, Aug. 23, Sept. 16, Nov. 27 in Standard 6 mode and ascending pass.

RELATIVE BRIGHTNESS OF RICE

As we know that water surface acts as a specula reflector and has a little return to SAR antenna. In order to minimize the variations over the scenes of RADARSAT image acquired at 13 dates, we take the difference of a target and the water surface to see the brightness changes of rice over a year.

The brightness of RADARSAT is defined as

$$\beta^{\circ}_{jk} = 10\log10(DN_{jk}{}^2 + A3)/A2_j$$

where DN is a digital number of a pixel's intensity,
A3, $A2_j$ are constants, the range dependent LUT which is supplied with RADARSAT product.

Because RADARSAT data we have are not calibrated, we use the radar backscatter difference of target and water to discuss the relative brightness of the target over the imaging time (Shao, 1996, 1997, Guo, 1997), here rice is the target, we assume that the effect of the range can be ignored, then

$$\beta_r{}^{\circ} = \beta^{\circ}_{jk(T)} - \beta^{\circ}_{jk(W)} = 10\log10(DN_{jk(T)}{}^2)/(DN_{jk(W)}{}^2)$$

Fig. 2 is produced by above approach. It shows the relative brightness of four types of rice. The DN number is taken from the training area defined for classification within RADARSAT image acquired on March 6, April 25, June 17, Aug.4, Aug. 23, Sept. 21, Oct. 15, Nov. 8, Dec. 2. F stands for Fine mode, D for Standard mode/descending pass, A for Standard mode/ascending.

Although there are two breaks of data acquisition, one is in

May, one is in July, we still can see the variations in relative brightness of rice. The R2 in fig.2 represents the moderate mature type of rice which is the most common rice species in that region with 100 days life. It had dense seedling on April 25, got medium radar brightness, and reaches its peak volume with highest radar brightness, was reaped at the end of July; then transplanted again before Aug. 4. The small loose seedling gives weak response to SAR. As it grows up, the radar brightness increases. It reaches the highest point in June for early season rice, and in October for late season rice. R3 in fig. 2 is the late mature type of rice with about 120 days life and transplanted late than R2. It is obvious in fig. 2 that there is a delay of its relative brightness increasing compare to R2. R1 represents a field which was a fish pond in Spring, then become a rice field in Autumn, R4 is the other way round.

RICE GROWTH STATUS MONITORING

The multiple temporal RADARSAT data of 13 scenes were all registered together in three groups of Fine, Standard/descending, Standard/ascending and filtered by Lee filter in PCI image processing system. The combination of images acquired at different dates helps us to understand the variations of rice over seasons and the differences in between of different type of rice. Fig. 3 is a subscene (1100 pixel × 1800 line) of multiple temporal RADARSAT image of Fine mode. The left one was acquired on Oct. 15, Aug. 4, June 17 (R, G, B), the right one was acquired on Oct. 15, Nov. 8, Sept. 21 (R, G, B). There is a big contrast of brightness of rice in left image, R2 in magenta , R3 in yellow in central of image, R1 in red, R4 in light blue, water in black, euryale ferox, a kind of water plant in gray. The variations of the tone is related to the growing status of the agricultural vegetation. Image acquired on Aug. 4 is in green in left image, R2 was just transplanted, has a little response to radar, so shows up as magenta. R3 is in mature status with strong return to SAR antenna. There is much less variations in right image, because three of images are all taken from Autumn of late season rice.

The brightness of rice fields only have small changes, but there are still a little tone variations related to the rice growing status.

CONCLUSIONS

This paper is a primary result of our study. It shows that the RADARSAT image is an effective tool for rice growth status monitoring with its excellent target detecting capability. But it is still not clear enough that what part, which component, what kind of geometry characteristics of rice decide its response to SAR antenna, decide the intensity of the image, and its relationship to incidence angle and the orientation of rice. It is anticipated that the rice backscatter modeling research will give further explanation.

REFERENCE

Y.Shao, H.Guo, H.Liu, X.Lu, GlobeSAR Data for Agriculture Applications-potentials and Limitations, Proc. of the Second Asia-Pacific Regional GlobeSAR Workshop, Science Press, Beijing, 1996.

H.Guo, Y.Shao, Multiple Applications of Airborne Dual-frequency, Fully-polarized SAR Data, Journal of Remote Sensing, vol.1, no.2, Science Press, Beijing,1997.

Y.Shao, C.Wang, X.Fan, H.Liu, Evaluation of SAR Image for Rice Monitoring and Land Cover Mapping, Proc. of Geomatics in the Era of RADARSAT, Ottawa, 1997

ACKNOWLEDGMENT
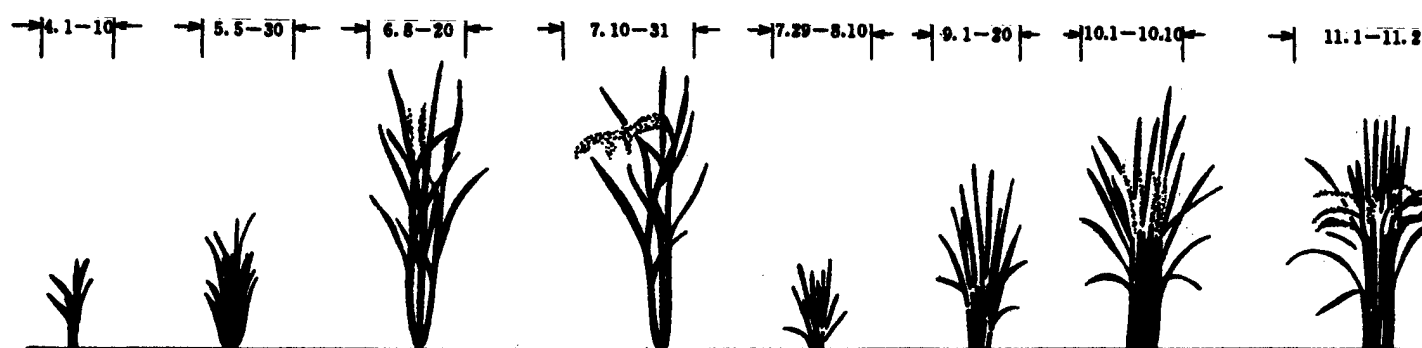
Fig.1 Rice Growth Calendar
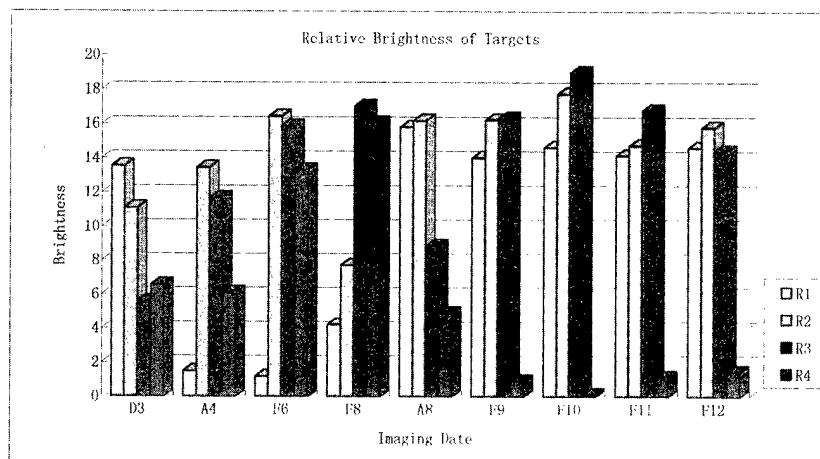
Fig. 2 Relative Brightness of Rice
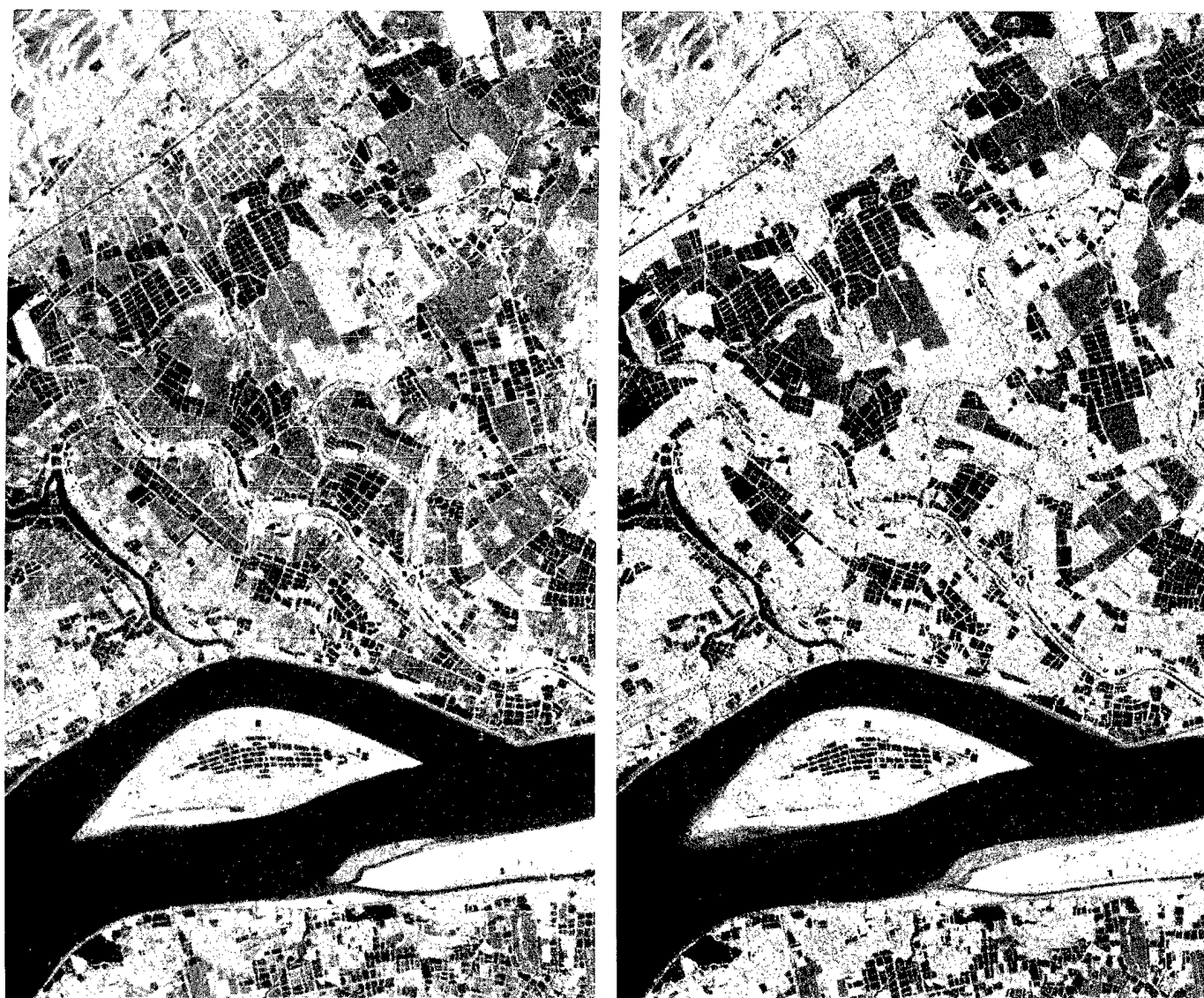
Fig. 3 Multiple Temporal RADARSAT Image of Fine Mode,
left acquired on Oct. 15, Aug. 4, June 17 (R, G, B), right acquired on Oct. 15, Nov. 8, Sept. 21 (R, G, B).

PACRIM, Deployment of AIRSAR in the Australian-ASEAN Region

Anthony K Milne
The University of New South Wales
Sydney, NSW 2050, Australia
Phone: 61 (02) 9385 2731   Facsimile: 61 (02) 9385 3733   E-mail: t.milne@unsw.edu.au

INTRODUCTION

A unique opportunity was afforded Remote Sensing scientists in November 1993 to acquire state-of-the-art radar data over Australian test sites. CSIRO-COSSA and the University of New South Wales Centre for Remote Sensing and GIS collaborated with NASA's Mission to Planet Earth Airborne Sciences Program, and the Jet Propulsion Laboratory (JPL) to bring AIRSAR, the world's most advanced synthetic aperture radar system to Australia.

AIRSAR operates in a full polarimetric mode at L-Band (24.5cm), C-Band (5.6cm) and P-Band (68cm). In addition to this three-frequency polarimetric capability called POLSAR, the incorporation of extra C- and L-band antennas permits interferometric data known as TOPSAR to be acquired.

During November 1993 this system acquired data over 55 sites on the Australian continent for 35 Principal Investigators including both US and Australian scientists and collaborators. This data has been processed and analysed and the research and science findings presented in *Proceedings of the International Workshop on Radar Image Processing and Applications*, Sydney, 6-8 November 1995, (available from the author).

AIRSAR Australia 1993 has made a significant contribution, both in terms of providing the Australian scientific community with advanced polarimetric and interferometric radar data not previously available and in fostering a research community interested in using the unique characteristics of radar to analyse a range of environmental surfaces and conditions. The program has also resulted in a significant increase in technology transfer in bringing together an Australian community not previously experienced in using polarimetric radar and in providing a knowledge base from which radar can be integrated into research aimed at determining geophysical parameters of surface materials. This research community has benefited significantly from collaboration with researchers from the JPL Radar Sciences Group in Pasadena, California.

PACRIM 1996

During a seven week deployment in November and December 1996, NASA's DC-8 aircraft carrying the Jet Propulsion Laboratory's Airborne Synthetic Aperture Radar System (AIRSAR), undertook a major data acquisition program in the Australian-ASEAN region.

Known as the Pacific Rim (PACRIM) Mission, data was acquired over sites in Hawaii, New Zealand, Australia, Papua New Guinea, Brunei, Philippines, Taiwan, Cambodia, Thailand and Malaysia. Distribution of the sites covered in the ASEAN region is shown in Fig 1.

Each country was responsible for identifying sites and determining the scientific objectives of the mission as it related to their own national resource priorities. Workshops and seminars were held in each country before the deployment to instruct potential researchers in the theory and techniques of polarimetric radar and interferometry, to discuss likely applications, and to promote collaborative scientific research.
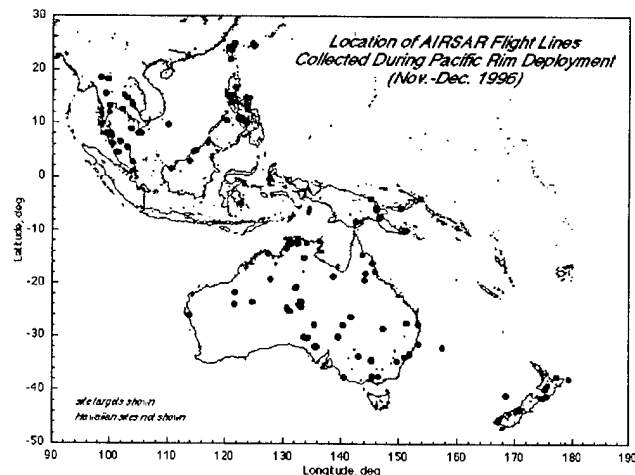
Fig. 1. Location of AIRSAR Flight Lines Collected During Pacific Rim Deployment (Nov-Dec. 1996)

Priorities identified as of interest to all participating countries include:

- geologic studies embracing geomorphic studies, rock weathering and erosional processes, tectonics and geologic boundaries, geobotany, radar stereogrammetry, DEM and interferometry.

- hydrological investigations which cover wetland, humid and arid environment characterisation, and in particular, the assessment of soil moisture conditions

- mapping and identifying vegetation types, assessing the biophysical properties of plant canopies, modelling tree morphologies and examining soil-vegetation boundary layer.

- oceanographic studies to analyse ocean wave spectra, internal wave-current interaction and detection of current-system boundaries, oceanic fronts and mesoscale eddies.

It is anticipated that this data will help provide information for the baseline characterisation of control sites in many different environments for the continued analysis of earth surface, climatic and tectonic processes, with other calibrated radar datasets as they become more readily available from satellite and other airborne radar systems.

A program of collaborative research studies involving scientists from all countries involved is ongoing and programmed for the next three years. This started with a Science and Image Processing Workshop at JPL in Pasadena in March 1997 and will be followed with a Science and Applications Workshop at the Malaysian Centre for Remote Sensing (MACRES) in August 1997.

ACKNOWLEDGMENT

I would like to thank the other members of the PACRIM AIRSAR Management Team in particular, Dr Ian Tapley, Dr Brian Embleton, Ms Jill Huntington, and Ms Jan Smith of CSIRO, as well as Dr Earnest Paylor (Co-Chairman), NASA HQ and Dr Jacob Van Zyl and his staff from the JPL Radar Science Group and the Mission Managers and air crew from NASA Ames, for their contribution in ensuring the success not only of the aircraft deployment but of the ongoing technical and scientific program.

PARTICIPATING AGENCIES AND CONTACTS

Australia

University of New South Wales
Associate Professor Tony Milne (PACRIM Co-Chairman)

CSIRO
Dr Ian Tapley

Brunei Darussalam

Ministry of Development
Haja Salmahwati Joji Mohsin

Malaysia

MACRES
Mr Nik Nasruddin Mahmood

New Zealand

Landcare Research
Dr Stephen McNeil

Philippines

NAMIRA
Mr Virgilio Santos

Taiwan

National Central University
Professor L C Chen

Thailand

NRCT
Dr Suvit Vibulsreth

United States

NASA Headquarters
Dr Earnest Paylor (PACRIM Co-Chairman)

NASA AMES
Mr Christopher Miller

JPL
Ms Ellen O'Leary

SELECTED REFERENCES

A.K. Milne, Ed. "Proceedings of the International Workshop on Radar Image Processing and Applications," 6-8 November 1995, Sydney, pp86.

Conference Author Index